THREE–DIMENSIONAL FINITE ELEMENT ANALYSIS OF SHEET–PILE CELLULAR COFFERDAMS

by

Reed L. Mosher

Dissertation submitted to the Faculty of the
Viginia Polytechnic Institute and State University
in partial fulfillment of the requirements for the degree of

DOCTOR OF PHILOSOPHY

in

Civil Engineering

APPROVED:

G. W. Clough, Chairman
Dean, College of Engineering

T. Kuppusamy
Civil Engineering

J. M. Duncan
Civil Engineering

J. N. Reddy
Engineering Science and Mechanics

N. Radhakrishnan
Waterways Experiment Station

December 1991

Blacksburg, Virginia

Abstract

The conventional design methods for sheet–pile cellular cofferdams were developed in the 1940's and 1950's based on field and limited experimental observations. The analytical techniques of the day were unable to account for the complexities involved. The procedures used only rudimentary concepts of soil–structure interaction which do not exhibit the true response of the cofferdam for most circumstances. During the past decade it has been demonstrated that with proper consideration of the soil–structure interaction effects, the two–dimensional finite element models can be powerful tools in the investigation of cellular cofferdam behavior. However, universal implementation of the findings of these analyses was difficult to justify, since uncertainties remain about the assumptions made in arriving at the two–dimensional models. The only way to address these uncertainties was to perform a three–dimensional analysis.

This investigation has focused on the study of the three–dimensional behavior of Lock and Dam No. 26 (R) sheet–pile cellular cofferdam. The work involved the development of a new three–dimensional soil–structure interaction finite element code for cellular cofferdam modeling, and the application of the new code to the study of the behavior of the first– and second–stage cofferdam at Lock and Dam No. 26 (R).

Abstract

The new code was used to study the cell filling process where the main cell is filled first with the subsequent filling of the arc cell. The finite element results show that interlock forces in the common wall were 29 to 35 percent higher than those in the main cell which are less than those calculated by conventional methods and compare well with the observed values.

After cell filling, the new code was used to model the cofferdam under differential loading due to initial dewatering of the interior of the cofferdam and changes in river levels. The finite element analysis results show that increasing differential water loads cause the confining stresses in the cell fill to increase which results in a decrease in the level of mobilized shear strength in the cell fill. This explains why the cellular cofferdam can withstand extremely high lateral loads and lateral deformations without collapsing.

Acknowledgements

The author wishes to express his deep gratitude to his advisor, Dr. G. Wayne Clough, for his guidance during the course of this research. I am extremely grateful to Dr. Clough for his constant encouragement, tremendous patience, and very sincere personal considerations without which the completion of this work could not have been possible. A special thanks goes to Dr. N. Radhakrishnan for his continual and unceasing support of my quest to complete this research effortt and Dr. T. Kuppusamy for his advice, encouragement, and discussion of the research work from time to time. Much appreciation is extended to my committee members, Dr. J. M. Duncan and Dr. J. N. Reddy, for their interest in my studies and research.

I would like to express my gratitude to the U.S. Army Engineer Waterways Experiment Station for providing me the opportunity to conduct this research and to the U.S. Army Engineer District, St. Louis, and Headquarters, U.S. Army Corps of Engineers, for funding this research effort. Appreciation is extended to Messrs. Donald Dressler, Thomas Mudd, and Paul K. Senter for support and help during the cousre of the work. A special debt of thanks is owed to Mr. H. Wayne Jones for his reviewing the manuscript.

I owe the most to my wife, Loanne, for her continuous encouragement, moral support, patience, and great understanding faced with all the hardship that she has

graciously endured. Without her support, I could hot have accomplished this task. To son Mark, I owe him for the many hours I spent away from the family. Thanks to all my colleagues, friends, and relatives who helped me in this endeavor. And last, but not least, I thank Mr. John Harris and Ms. Gilda Miller for their help in preparing this dissertation.

Contents

Abstract ii

Acknowledgements iv

1 Introduction 1

2 Background 6

2.1 Historical Background 8

2.2 Cellular Cofferdam Geometry 12

2.3 Cellular Cofferdam Failures 16

2.4 Early Cellular Cofferdam Design 18

2.5 Design Considerations 19

2.6 Current Design Procedures for Interlock Stability 22

2.6.1 Main Cell 24

2.6.2 Arc Cell 27

2.6.3 Common Wall 28

2.7 Current Design Procedures for Internal Stability 31

2.8 Instrumented Case Histories of Cellular Cofferdams 43

2.8.1 Cell Filling 44

2.8.2 Differential Water Loading 48
2.9 Early Finite Element Analysis 55
2.10 Lock and Dam No. 26 (Replacement) Cofferdams Studies 58
2.11 Summary and Recommendations 71

3 Basic Finite Element Code **74**

3.1 Introduction 74
3.2 Philosophy 76
3.3 Necessary Capabilities 77
3.4 Development Scheme 82
3.5 Description of Existing Code 83
3.5.1 Element Types 83
3.5.2 Stress and Strain Response 85
3.5.3 Boundary Conditions 87
3.5.4 Equation Solver 87
3.6 Verification of Existing Code 88
3.6.1 Single Element with Concentrated Nodal Loads 89
3.6.2 Single Element with Surface Pressure Loading 89
3.6.3 Thick–Wall Cylinder Problem 89
3.7 Limitation of the Code 97
3.8 Summary 100

4 Additions to the Element Library **102**

4.1 Introduction 102
4.2 Interface Element 103
4.2.1 Zero–Thickness Interface Element 105

4.2.2 Evaluation of Interface Element Formulation 105
4.2.3 Alternative Formulation 106
4.2.4 Interface Element Formulation 111
4.2.5 Implementation of the Interface Element 115
4.2.6 Verification of the Interface Element 117
4.3 Degeneration of Brick–Type Isoparametric Elements 122
4.3.1 Formulation for Degeneration of Quadratic Serendipity Element 125
4.3.2 Implementation for Degeneration of 3-D Element 127
4.3.3 Verification of 15–Node Wedge Element 127
4.4 Shell Element 128
4.4.1 Implementation of Shell Element Formulation 131
4.4.2 Verification of Shell Element 133
4.4.3 Representation of the Sheet Piling with Shell Element 138
4.5 Summary 150

5 Three–Dimensional Soil Constitutive Model 153

5.1 Introduction 153
5.2 Background 154
5.2.1 Incremental Analysis 155
5.2.2 Tangent Shear and Bulk Moduli 156
5.3 New Three–Dimensional Constitutive Model 158
5.3.1 Tangent Shear Modulus Definition 160
5.3.2 Tangent Bulk Modulus Definition 181
5.4 Soil Testing Program for Three–Dimensional Finite Element Study . 188

5.4.1 Background of Soil Testing for Lock and Dam No. 26(R) Cofferdam 189
5.4.2 The New Soil Testing Program 191
5.4.3 Cubical Shear Testing 193
5.5 Comparison of Predicted and Observed Stress-Strain Response 201
5.5.1 Triaxial Test Response 201
5.5.2 Cubical Test Response 205
5.6 Summary 220

6 Cell Filling Analysis **231**

6.1 Project Description 232
6.1.1 Foundation Materials and Properties 237
6.1.2 Cell Fill Materials and Properties 237
6.1.3 Sheet Piles 242
6.1.4 General Construction Sequence 242
6.2 Response of Isolated Main Cell during Filling 244
6.2.1 Verification of the Three–Dimensional Code for Isolated Main Cell Analysis 245
6.2.2 Modeling an Isolated Main Cell During Filling 248
6.2.3 Difficulties in Three–Dimensional Modeling of the Isolated Main Cell Analyses 258
6.2.4 Results of the Isolated Main Cell Analyses 261
6.3 Response of Cellular Cofferdam during Cell Filling 274
6.3.1 Finite Element Representation of Cofferdam 277
6.3.2 Response at Completion of Main Cell Filling 281

6.3.3 Response at Completion of Main and Arc Cell Filling 294
6.4 Summary 319

7 Differential Loading Analysis **326**

7.1 Differential Loads Applied to Cofferdams 327
7.2 Finite Element Models 329
7.3 Construction Simulation 329
7.4 Response to Normal Differential Loading 333
7.4.1 Cell Deflections 333
7.4.2 Interlock Force 343
7.4.3 Lateral Earth Pressure Coefficients 345
7.4.4 Soil Stresses 350
7.5 Response to Extreme Differential Loading 350
7.5.1 Load–Deflection Response 353
7.5.2 Lateral Earth Pressure Coefficient 353
7.5.3 Soil Stresses 358
7.6 Summary 361

8 SUMMARY AND CONCLUSIONS **365**

8.1 Development of New Three–Dimensional Finite Element Code 366
8.2 Additions to The Element Library 369
8.3 Three–Dimensional Soil Model 370
8.4 Analysis of an Isolated Main Cell 372
8.5 Analysis of Main and Arc Cells During Filling 373
8.6 Differential Loading of the Cofferdam 374
8.7 Conclusion 376

Bibliography 378

A Derivation of the Goodman Interface Element 388

B 1–D Example of the Goodman Interface Element 393

C Basic Shell Element Formulation 396

D Determination of Soil Model Parameters 408

VITA 434

List of Tables

2.1 Key Aspects of Cofferdam Case History [38]. 45

2.2 Two–Dimensional Finite Element Models [8] 60

3.1 Comparison of Results for Single Element with Concentrated Nodal Loads. 91

3.2 Comparison Results for Single Element with Surface Pressure Loading. 91

3.3 Comparison of Displacements for Thick–Wall Cylinder Problem. . . 101

4.1 Computed Displacements for Interface Test Problem 1. 152

5.1 Comparison of Stiffness Parameters between WES and Woodward–Clyde Tests. 192

5.2 Comparison of Testing and Sample Preparation Procedures of Previous Efforts 192

5.3 Parameters of Soil Model for a Relative Density of 55 percent 230

5.4 Parameters of Soil Model for Relative Density of 70 percent. 230

6.1 Radial Deflections after Main Cell Filling, Cell with 35–ft Penetration. 285

6.2 Radial Deflections after Main Cell Filling, Cell with 15–ft Penetration. 285

D.1 Three–dimensional hyperbolic model parameters determined from triaxial tests for a relative density of 55 percent. 421

D.2 Three–dimensional hyperbolic model parameters determined from triaxial tests for a relative density of 70 percent. 421

D.3 Parameters of the bulk modulus model. 433

List of Figures

2.1 A sheet–pile cellular cofferdam. 7

2.2 Black Rock Harbor cofferdam [3]. 9

2.3 Battleship *Maine* cofferdam [3]. 11

2.4 Commonly used sheet–pile cellular cofferdam configuration, (a) diaphragm, (b) circular, and (c) cloverleaf. 15

2.5 Possible failure modes. 20

2.6 Interlock force determination by hoop–stress equation. 23

2.7 The four most commonly assumed pressure diagrams for interlock tension [53]. 25

2.8 Free body for the TVA secant formula for determining interlock forces in the common wall. 29

2.9 Free body for the Swatek formula for determining interlock forces in the common wall. 30

2.10 Terzaghi's base pressure [60]. 32

2.11 Vertical shear on the centerline [60]. 35

2.12 Failure plane proposed by Krynine [32]. 38

2.13 Cummings method [10]. 39

2.14 Hansen method [23]. 41

2.15 Measured interlock forces for Trident and Lock and Dam No. 26 (R) cofferdams. 47
2.16 Comparison of interlock forces in the common wall for Lock and Dam No. 26(R). 49
2.17 Trident cell movements [38]. 50
2.18 Lock and Dam No. 26(R) cell movements [38]. 51
2.19 Top of cells movements for Lock and Dam 26(R) [38]. 53
2.20 Comparison of cell movements [38]. 54
2.21 Schematic of vertical slice model [53]. 57
2.22 Schematic of horizontal slice model [53]. 61
2.23 Schematic of axisymmetric model [53]. 62
2.24 Lock and Dam No. 26(R) sheet–pile interlock forces [55]. 65
2.25 Lock and Dam No. 26(R) sheet–pile deflections [55]. 66
2.26 Lock and Dam No. 26(R), effects of E–ratio of sheet–pile deflections [53]. 67
2.27 Lock and Dam No. 26(R), effects of E–ratio on earth pressures applied to sheet piles [53]. 68
2.28 Lock and Dam No. 26(R), effects of E–ratio on sheet–pile interlock forces [53]. 69
2.29 Lock and Dam No. 26(R), interlock forces in sheet piles as predicted from horizontal slice analysis [55]. 70

3.1 Plan view of main and arc cells. 79
3.2 Stress–strain behavior of sand [53]. 81
3.3 Eight to twenty–one variable number of nodes element [29]. 84

3.4 Quarter model of main cell of a cofferdam. 86
3.5 Single element with concentrated nodal loads [29]. 90
3.6 Single element with surface pressure loading [29]. 92
3.7 Thick–wall cylinder problem [29]. 94
3.8 Finite element mesh for the thick–wall cylinder problem [29]. 96
3.9 Variation of radial stress with radius [29]. 98
3.10 Variation of tangential stress with radius [29]. 99

4.1 Typical types of interface elements used in soil–structure interaction analysis. 104
4.2 Penetration of adjacent element [5]. 107
4.3 Example problem to evaluate interface element [63]. 108
4.4 Solid, interface, and shell element configuration for three–dimensional code. 113
4.5 Meshes for interface Test Problem 1. 119
4.6 Desai's interface test problem [14]. 120
4.7 Results for Desai's interface test problem [14]. 121
4.8 Degeneration of a brick–type isoparametric element. 123
4.9 Example problem of degeneration by simple collapsing of one side of brick–type isoparametric elements. 124
4.10 Degeneration for a quadratic serendipity element. 126
4.11 Single–wedge element with a surface pressure. 129
4.12 Results for four–wedge elements with a surface pressure. 130
4.13 Geometry of the shell element [47]. 132

4.14 Composite, thick–wall cylinder problem: a. composite, thick–wall cylinder with an internal surface pressure; and b. finite element mesh for the composite–wall cylinder. 135
4.15 Variation of radial displacements with radius. 137
4.16 Sheet–pile interlock connections for cellular cofferdam. 139
4.17 Measured load–displacement behavior of sheet–pile interlocks [8, 33, 53]. 140
4.18 Comparison of radial deflections for three different E–ratios. 146
4.19 Comparison of interlock forces for three different E–ratios. 147
4.20 Comparison of predicted and measured earth pressures for three different E–ratios. 148
4.21 Change in predicted lateral earth pressure coefficients with maximum radial deflections. 149

5.1 Representation of deviatoric and volumetric stresses in three–dimensional stress space. 157
5.2 Hyperbolic representation of the shear stress and strain curve. 161
5.3 Physical meaning of the parameters a and b. 162
5.4 Variation of stiffness with confining pressure. 164
5.5 Variation of initial tangent modulus with confining pressure. 165
5.6 Stress path plane for triaxial test in principal stress space. 167
5.7 Projection of stress paths on triaxial plane. 168
5.8 Stress paths in q-p stress space. 170
5.9 Shear stress–strain curve for triaxial test. 171
5.10 Shear stress–shear strain data plotted on transformed axis. 172

5.11 Normalized shear stress and shear strain data plotted on transformed axis. 173
5.12 Stress path showing the initial mean normal stress and the normal stress at failure. 174
5.13 Variation of initial shear modulus versus initial mean normal stress. 176
5.14 Simple representation of the Mohr–Coulomb failure envelope. 178
5.15 Three–dimensional representation of Mohr–Coulomb failure criterion. 180
5.16 Volumetric strain versus mean normal stress. 182
5.17 Plot of volumetric strain versus mean normal stress from triaxial consolidation test [15]. 183
5.18 Plot of expression for volumetric strain and mean normal stress on arithmetic scale. 186
5.19 Plot of expression for volumetric strain and mean normal stress on log–log scale. 187
5.20 Gradation curves for cell fill sand [52]. 194
5.21 Stress path from vertical slice model for cell fill at midheight [52]. . . 197
5.22 Stress path from vertical slice model for cell fill at bottom [52]. . . . 198
5.23 Stress path from vertical slice model for foundation soil below dredgeline outside the cell [52]. 199
5.24 Schematic representation of stress paths used in cubical shear tests [52]. 200
5.25 Comparison between soil model and triaxial compression test data for a relative density of 55 percent. 203
5.26 Comparison between soil model and triaxial extension test data for a relative density of 55 percent. 204

5.27 Comparison between soil model and triaxial compression test data for a relative density of 70 percent. 206

5.28 Comparison between soil model and triaxial extension test data for a relative density of 70 percent. 207

5.29 Stress path **B** for cubical shear test. 209

5.30 Stress–strain results from cubical shear test for stress path **B**. . . . 210

5.31 Comparison between two–dimensional model and cubical shear test for stress path **B**. 211

5.32 Comparison between three–dimensional model and cubical shear test for stress path **B**. 212

5.33 Finite element model for cubical shear test. 214

5.34 Comparison of mean normal stress and confining stress. 215

5.35 Comparison of value of Poisson's ratio during cubical shear test for stress path **B**. 217

5.36 Comparison of value of Young's modulus during cubical shear test for stress path **B**. 218

5.37 Stress path **F** for cubical shear test. 221

5.38 Stress–strain results from cubical shear test for stress path **F**. 222

5.39 Comparison between two–dimensional model and cubical shear test for stress path **F** with $\phi = 39\,\text{deg}$. 223

5.40 Comparison between two–dimensional model and cubical shear test for stress path **F** with $\phi = 42\,\text{deg}$. 224

5.41 Comparison between three–dimensional model and cubical shear test for stress path **F**. 225

5.42 Comparison of value of Young's modulus during cubical shear test for stress path **F**. 226

5.43 Comparison of value of Poisson's ratio during cubical shear test for stress path **F**. 227

6.1 Artist illustration of the first–stage Lock and Dam No. 26(R) cofferdam. 234

6.2 Plan view of the first–stage Lock and Dam No. 26(R) cofferdam. . . 235

6.3 Profile section through the first–stage Lock and Dam No. 26(R) cofferdam. 236

6.4 Artist illustration of the second–stage Lock and Dam No. 26(R) cofferdam. 238

6.5 Plan view of the second–stage Lock and Dam No. 26(R) cofferdam. . 239

6.6 Profile section through the second–stage Lock and Dam No. 26(R) cofferdam. 240

6.7 Artist illustration of the third–stage Lock and Dam No. 26(R) cofferdam. 241

6.8 Layout of sheet piles in main and arc cell. 243

6.9 Schematic of isolated main cell and axisymmetric model. 246

6.10 Schematic of isolated main cell and three–dimensional model. . . . 247

6.11 Finite element mesh for an isolated main cell from first–stage of Lock and Dam No. 26(R) using three–dimensional solid elements to represent sheet piles. 249

6.12 Finite element mesh for an isolated main cell from first–stage of Lock and Dam No. 26(R) using shell elements to represent sheet piles. . . 250

6.13 Finite element mesh for two–dimensional axisymmetric analysis of first–stage Lock and Dam No. 26(R) cofferdam using shell elements for the sheet piles. 251

6.14 Radial deflection of sheet piles from linear elastic analyses of an isolated main cell. 252

6.15 Sheet–pile interlock stresses from linear elastic analyses of an isolated main cell. 253

6.16 Finite element mesh for an isolated main cell from second–stage of Lock and Dam No. 26(R) with 10–ft of penetration. 256

6.17 Comparison of radial deflection from the three–dimensional and axisymmetric finite element for isolated main cell with 35–ft penetration. 263

6.18 Comparison of radial deflection from the three–dimensional and axisymmetric finite element for isolated main cell with 10–ft penetration. 264

6.19 Comparison of interlock forces in the cell wall from the three–dimensional and axisymmetric finite element for isolated main cell with 35–ft penetration. 266

6.20 Comparison of interlock forces in the cell wall from the three–dimensional and axisymmetric finite element for isolated main cell with 10–ft penetration. 267

6.21 Predicted lateral earth pressures in an isolated main cell with 35–ft penetration. 268

6.22 Predicted lateral earth pressures in an isolated main cell with 10–ft penetration. 269

6.23 Normalized vertical soil stresses in an isolated main cell with 35–ft penetration. 272
6.24 Normalized vertical soil stresses in an isolated main cell with 10–ft penetration. 273
6.25 Normalized horizontal soil stresses in an isolated main cell with 35–ft penetration. 275
6.26 Normalized horizontal soil stresses in an isolated main cell with 10–ft penetration. 276
6.27 Schematic of cofferdam model. 278
6.28 Mesh for second–stage Lock and Dam No. 26(R) with 35–ft penetration. 279
6.29 Mesh for second–stage Lock and Dam No. 26(R) with 15–ft penetration. 280
6.30 Radial deflections after main cell filling for a penetration of 35 ft. . . 283
6.31 Radial deflections after main cell filling for a penetration of 15 ft. . . 286
6.32 Interlock forces after main cell filling with 35–ft penetration. 287
6.33 Interlock forces after main cell filling with 15–ft penetration. 288
6.34 Predicted lateral earth pressures after main cell filling with 35–ft penetration. 290
6.35 Predicted lateral earth pressures after main cell filling with 15–ft penetration. 291
6.36 Normalized vertical soil stresses after main cell filling with 35–ft penetration. 292
6.37 Normalized vertical soil stresses after main cell filling with 35–ft penetration. 293

6.38 Normalized horizontal soil stresses after main cell filling with 35–ft penetration. 295
6.39 Normalized horizontal soil stresses after main cell filling with 35–ft penetration. 296
6.40 Radial deflections after arc cell filling for a penetration of 35–ft. . . . 298
6.41 Radial deflections after arc cell filling for a penetration of 15–ft. . . . 299
6.42 Interlock forces after arc cell filling with 35–ft penetration. 302
6.43 Interlock forces after arc cell filling with 15–ft penetration. 303
6.44 Comparison of interlock forces from generalized plane strain analysis. 304
6.45 Predicted lateral earth pressures in the main cell after arc cell filling with 35–ft penetration. 307
6.46 Predicted lateral earth pressures in the main cell after arc cell filling with 15–ft penetration. 308
6.47 Predicted lateral earth pressures in the arc cell after arc cell filling with 35–ft penetration. 309
6.48 Predicted lateral earth pressures in the arc cell after arc cell filling with 15–ft penetration. 310
6.49 Comparison of earth pressures from generalized plane strain analysis. 311
6.50 Normalized vertical soil stresses in the main cell after arc cell filling with 35–ft penetration. 313
6.51 Normalized vertical soil stresses in the main cell after arc cell filling with 35–ft penetration. 314
6.52 Normalized vertical soil stresses in the arc cell after arc cell filling with 35–ft penetration. 316

6.53 Normalized horizontal soil stresses in the main cell after arc cell filling with 35–ft penetration. 317
6.54 Normalized horizontal soil stresses in the main cell after arc cell filling with 15–ft penetration. 318
6.55 Normalized horizontal soil stresses in the main cell after arc cell filling with 35–ft penetration. 320
6.56 Normalized horizontal soil stresses in the arc cell after arc cell filling with 35–ft penetration. 321

7.1 Mesh for second–stage Lock and Dam No. 26(R) with 35–ft penetration. 330
7.2 Mesh for second–stage Lock and Dam No. 26(R) with 15–ft penetration. 331
7.3 Schematic of construction simulation. 334
7.4 Movements of inboard and outboard walls after berm placement. . . 336
7.5 Movements of inboard and outboard walls after dewatering. 338
7.6 Movements of inboard and outboard walls for river at flood stage. . 339
7.7 Movement of top of cell due to differential loading for Dam No. 26(R) cofferdam [38]. 341
7.8 Movements of inboard and outboard walls for river at maximum flood stage. 344
7.9 Lateral earth pressure coefficients in x direction at the end of main and arc cell filling. 346
7.10 Lateral earth pressure coefficients in x direction after the initial dewatering. 347

7.11 Lateral earth pressure coefficients in x direction during flood conditions. 348

7.12 Mobilized shear strength after initial dewatering. 351

7.13 Mobilized shear strength during flood conditions. 352

7.14 Lateral load versus deflection of top of sheet piling. 354

7.15 Deformed shape of model for nine times the normal flood load. . . . 355

7.16 Lateral earth pressure coefficients in x direction at nine times the maximum flood load. 357

7.17 Vertical shear factor of safety versus multiples of normal flood load. 359

7.18 Vertical shear factor of safety versus water level. 360

7.19 Mobilized shear strength at two times normal flood load. 362

7.20 Mobilized shear strength at nine times normal flood load. 363

A.1 Goodman, Taylor, and Berkke Interface Element [22]. 392

B.1 Example problem to evaluate interface element [63]. 394

C.1 Geometry of the shell element [47]. 397

D.1 Diverge from hyperbolic expression. 411

D.2 Relationship between normalized initial slope and R_f for a relative density of 55 percent. 413

D.3 Relationship between normalized initial slope and R_f for a relative density of 70 percent. 414

D.4 Relationship between normalized initial slope and shear strength for a relative density of 55 percent. 415

D.5 Relationship between normalized initial slope and shear strength for a relative density of 70 percent. 416
D.6 Relationship between shear strength mobilized and R_f for a relative density of 55 percent. 417
D.7 Relationship between shear strength mobilized and R_f for a relative density of 70 percent. 418
D.8 Relationship between normalized initial slope and normalized mean normal stress for a relative density of 55 percent. 419
D.9 Relationship between normalized initial slope and normalized mean normal stress for a relative density of 70 percent. 420
D.10 Extension triaxial test data plotted transformed axis for relative density of 55 percent. 423
D.11 Extension triaxial test data plotted transformed axis for a relative density of 70 percent. 424
D.12 Comparison of initial slope versus mean normal stress between extension and compression triaxial test data for relative density of 55 percent. 425
D.13 Comparison of initial slope versus mean normal stress between extension and compression triaxial test data for a relative density of 70 percent. 426
D.14 Volumetric strains occurring during a triaxial test. 428
D.15 Mean normal stress versus volumetric strain for relative density of 55 percent. 429
D.16 Mean normal stress versus volumetric strain for relative density of 70 percent. 430

D.17 Volumetric strain versus mean normal stress on a log–log scale for a relative density of 55 percent 431

D.18 Volumetric strain versus mean normal stress on a log–log scale for a relative density of 70 percent 432

Chapter 1

Introduction

The designers of navigation and waterfront structures are faced with the problem of constructing these facilities at a site entirely or partially covered by water. In many cases, the designer must provide a dry construction area. A popular construction technology is to use sheet–pile cellular cofferdams to provide a continuous barrier around a site to exclude the water. Generally, a cofferdam is considered a success if it does not collapse, does not permit water to come in faster than it can be pumped out, and is dry enough to permit the construction to proceed as planned. A cellular cofferdam is formed by driving interlocking steel sheet piles into a series of interconnecting cells and filling the cells with a free draining soil to provide stability. The most common geometry for the cells is a circular configuration, while other shapes, such as cloverleaf or diaphragm cells, are used for special situations. Primarily, sheet–pile cellular structures have been utilized as temporary cofferdams to provide a dry construction area. In recent years, cellular structures are being used as permanent structures, such as locks, drydocks, piers, jetties, mooring dolphins, floodwalls, and bulkheads. They are a viable alternative to more traditional structures.

The conventional design methods for sheet–pile cellular cofferdams were developed in the 1940's and 1950's from field and experimental observations. As a result of the inability of earlier investigators to accurately determine the stresses in the cell fill, no single method of design/analysis was universally accepted by the engineering community. For example, the factor of safety for internal stability is checked by four different methods, each with its own inherent empiricism associated with its development.

Other problems with the conventional design approaches are:

- The various design methods give inconsistent answers which lead to a quandary over which is correct.
- Many of the conventional design methods are overly conservative.
- None of the methods can predict deformations of the cofferdam, the one measurement of performance which is easiest to monitor.
- There are no explicit procedures to consider soil–structure effects.
- There is essentially no consideration of three–dimensional effects.

One of the best examples of problems with the conventional design methods occurred during the design and construction of the Lock and Dam No. 26(R) cofferdam. The plans for the construction of a one billion dollar replacement for the old Lock and Dam No. 26 on the Mississippi River called for the use of a three–stage cellular cofferdam to allow construction of the new lock and dam in the dry. This cofferdam was one of the largest projects of its type in the world. The U.S. Army Corps of Engineers instituted a large–scale instrumentation program for the first–stage cofferdam, because they were concerned by contradictions between existing

conventional design techniques for cofferdams. It also was felt that the conventional procedures could be overly conservative.

The objectives of the instrumentation program were to obtain the field measurements to determine the sheet–pile interlock forces at various levels in the cells, to evaluate the benefits of the interior berm, and to evaluate the overall performance of the cofferdams. Many of the field measurements could not be assessed by conventional cofferdam analysis methods. This led to an effort to develop finite element procedures that could be applied to the modeling of the cellular cofferdams to aid in interpreting the instrumentation results and to assess conventional design methods.

The Lock and Dam No. 26(R) studies was one of the most extensive investigations of a specific project. Three two–dimensional finite element models were developed by modifying the program **SOILSTRUCT** [8, 33, 53]. Many of the complexities ignored or crudely approximated by earlier investigators, such as the circular geometry, the nonlinear material behavior, the interlock behavior, and the interaction between soil and the steel sheet piles were incorporated using the finite element method. The two–dimensional finite element models demonstrated their value for this type of structure. However, the specialized two–dimensional finite element models were not able to represent the full three–dimensional nature of a cellular cofferdam. For example, the two–dimensional models could not consider the nonuniform filling sequence, out–of–plane loadings, and torsional effects on structural connections. Since the response of a cellular cofferdam is three dimensional in nature, full implementation of the findings of the two–dimensional finite element studies was difficult to justify.

The focus of this investigation was to study the three–dimensional behavior of Lock and Dam No. 26 (R) sheet–pile cellular cofferdam. The work involves the

development of a new three–dimensional soil–structure interaction finite element code for cellular cofferdam modeling and the application of the new code to the study of the behavior of the first– and second–stage cofferdam at Lock and Dam No. 26 (R).

Chapter 2 presents an overview of the basic concepts of cellular cofferdams, a review of their history and performance, and an examination of design and analysis procedures. Limitations of these design/analysis procedures are discussed, and recent cofferdam research efforts are reviewed.

Chapter 3 presents the reasons for developing a new three–dimensional, soil–structure interaction finite element code, states the philosophy behind its development, lists the required capabilities for the new code, and describes the basic code that was modified to create a new code.

Chapter 4 describes the development and implementation of a new three–dimensional interface element, the implementation of the higher order wedge, and the shell element in the new code.

In Chapter 5, the development and implementation of a new three–dimensional constitutive model for soil is presented. The new model is a variable moduli type which is based on a hyperbolic relationship between shear stress and shear strain.

In Chapter 6, the behavior of the second–stage Lock and Dam No. 26(R) cellular cofferdam is investigated during the filling process. The behavior of the isolated main cell is used to verify the three–dimensional finite element code by comparing it to the two–dimensional axisymmetric finite element analyses. After verification, the new three–dimensional code is applied to a truly three–dimensional section of the second–stage cofferdam for Lock and Dam No. 26(R) to examine the fundamental behavior of the cofferdam during cell fill placement. The results of the analysis with

the three–dimensional code are compared with those of previous two–dimensional finite element analyses and instrumentation observations.

In Chapter 7, the second–stage Lock and Dam No. 26(R) cofferdam is analyzed under differential loading due to initial dewatering of the interior of the cofferdam and changes in river levels. The deflections of the cofferdam are compared to the survey data collected from the second–stage cofferdam and the instrumentation results from the first–stage cofferdam. Changes in stresses are reported and related to the overall performance of the cofferdam. Also, in this chapter, the finite element model is loaded to near collapse to study the behavior of cofferdams under extreme loading conditions. The deflections and the related stresses are examined to explain the unusual strength of the cellular cofferdams.

The last chapter is a summary of the findings of this research effort along with the conclusions that can be drawn from the results of the study.

Chapter 2

Background

What are sheet–pile cellular cofferdams? A general definition for a cofferdam is a temporary structure built to exclude water from a construction area so that work may proceed in the dry. One type of cofferdam that is well suited to the construction of harbor and navigational facilities is the sheet–pile cellular cofferdam. This structure is formed by installing interlocking sheet piles into a series of interconnecting cells which are filled with a free draining soil to provide stability, Figure 2.1. Very few cofferdams totally exclude all water from the construction area; generally, they perform successfully if they do not collapse and do not permit water to come in faster than it can be pumped out so that a dry construction area can be provided.

This chapter presents an overview of the basic concepts of cellular cofferdams, a review of their history and performance, and an examination of design and analysis procedures. Limitations of these design/analysis procedures are discussed and recent cofferdam research efforts are reviewed.

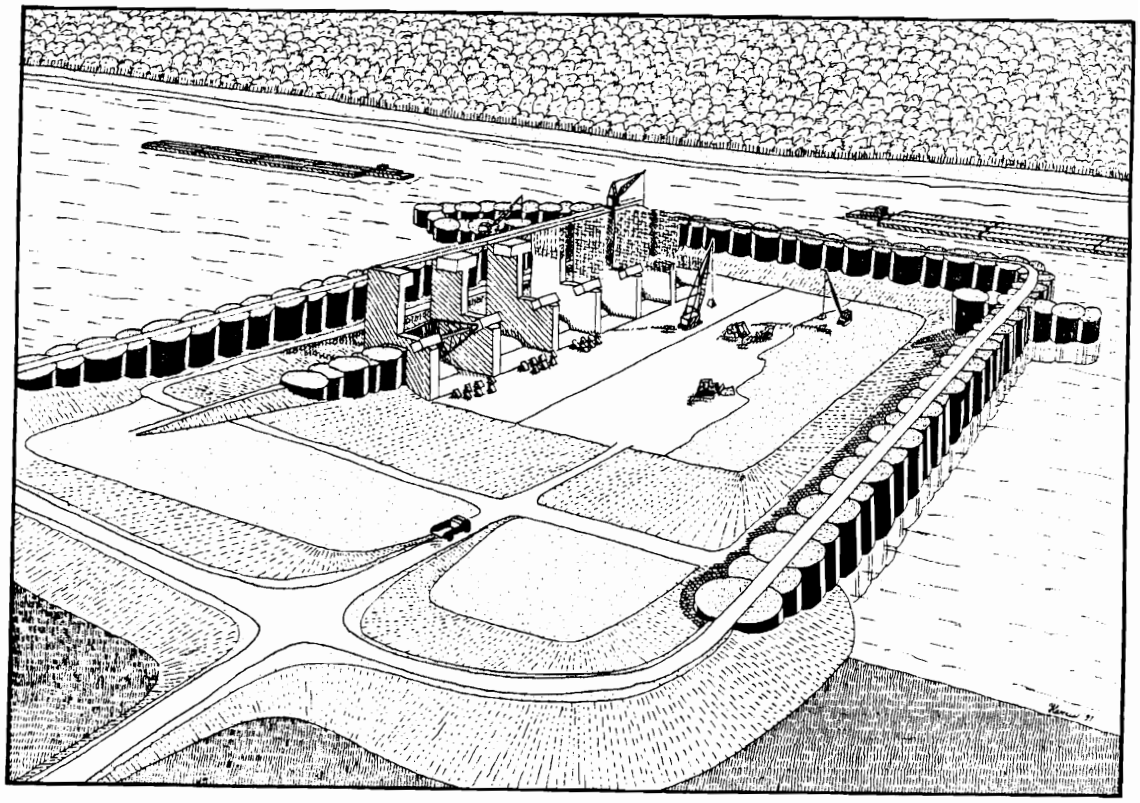

Figure 2.1: A sheet–pile cellular cofferdam.

2.1 Historical Background

Around the turn of the century, designers of river and marine facilities began looking at alternatives to earth dikes and single–wall cofferdams for providing water barriers to permit construction in the dry. Alternatives were needed because many projects had space limitations that precluded the use of earth dikes, and water depth requirements were often beyond the capacity of single–wall cofferdams. In 1908 a new form of cofferdam was used for the construction of a lock at Black Rock Harbor, Buffalo, N.Y. The cofferdam consisted of seventy–seven steel sheet–pile cells (Figure 2.2). Each cell was 30 ft square with straight walls with an average piling length of 50 ft and an average inner free height of 30 ft. Whaling was used around the top of the inner walls of the cofferdam. The whaling was connected to the outer wall of the cells by tie–rods. Initially, the designers felt that the cells by themselves would be stable against external pressure, but during dewatering it was necessary to place a berm of stone against the inner walls of the cofferdam.

The cells for this structure experienced bulging to a maximum of 3.5 ft at the midpoint between cross walls and at a point approximately one–third the cell height above the dredgeline or at the top of the inner berm [3]. During this process, the top of the cells displaced outlined less than 1 ft. Even before the cofferdam was closed the designers realized that by using a cell with curved inner and outer cell walls, much less bulging would occur. As a result, the last four cells were constructed with curved walls.

In 1910, a second steel sheet–pile cellular cofferdam was built to assist in the raising of the sunken battleship *Maine* in Havana Harbor, Cuba [3]. The cofferdam consisted of 20 circular cells, each 50 ft in diameter with connecting arcs between

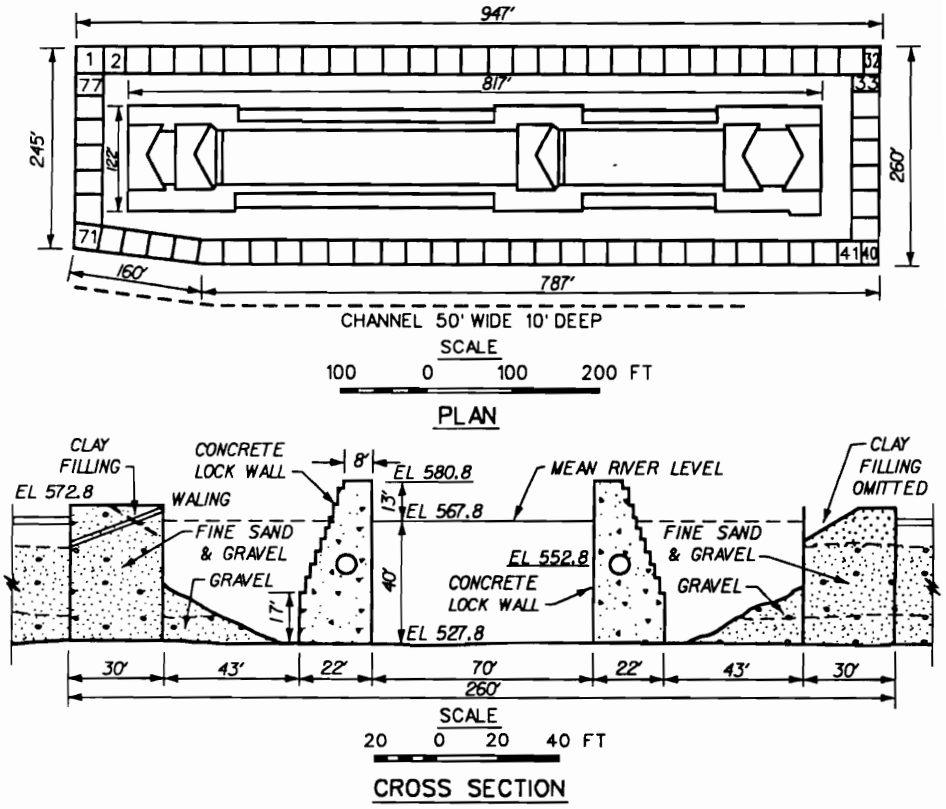

Figure 2.2: Black Rock Harbor cofferdam [3].

the outer wall of the cells, Figure 2.3. The sheet piles for the structure were formed by spicing short sections together to make a 75–ft–long sheet pile.

Initially, it was planned to fill the cells with a heavy clay that was expected to displace a 25–ft layer of very soft harbor silt. It was thought that dropping the heavy clay from a clamshell through water would cause it to sink through the silt to an underlying soft clay, thus displacing the silt. During filling of the cells, time constraints led to the use of hydraulic dredging, and the silt material was trapped in the cells. It was impractical to consolidate or dewater the silt, and it remained in a semiliquid state throughout the use of the cofferdam.

The cells were to be self–supporting. However, during dewatering, the inward movements of the cofferdam became so alarming that it was decided that an inner berm should be added to increase its stability. During the final stages of dewatering and salvage work, the cells had to be braced against the hull of the battleship. The very soft silt was believed to be the major reason for the extensive movements seen during dewatering of the cofferdam.

Despite the difficulties encountered in the construction of these first two sheet–pile cellular cofferdams, some engineers recognized that the basic idea was sound. The cellular cofferdam would provide both an economical and durable structure to act as a water barrier during construction. This opinion was not held by all. Some engineers believed cellular cofferdams were less reliable than other types of cofferdams. This opinion resulted from the failure of several cellular cofferdams for large construction projects. In the book entitled *Cofferdams*, White and Prentis [62], wrote:

> *... Because of the solid appearance and because they are of* **"steel"**, *they are esteemed much more than their performance seems to warrant; there*

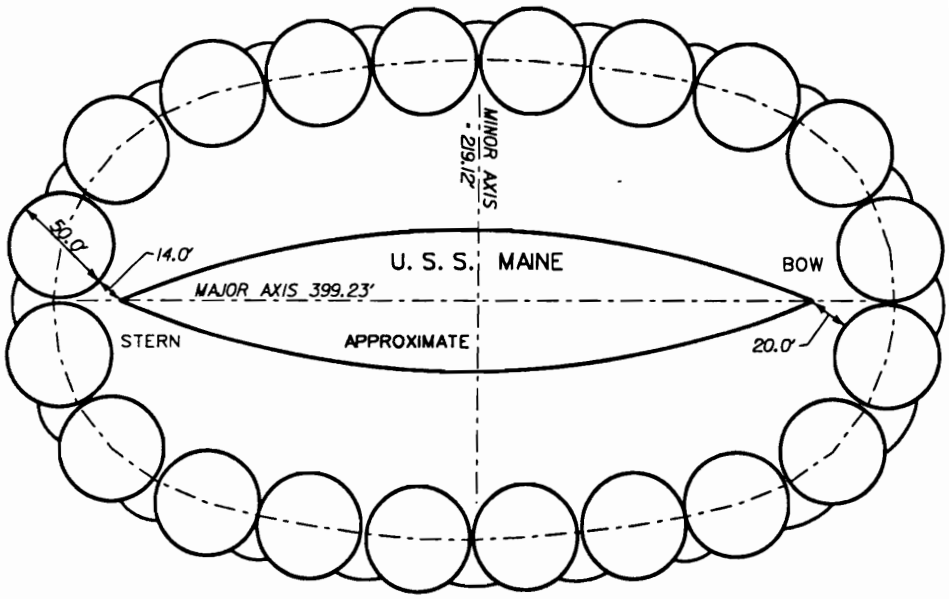

Figure 2.3: Battleship *Maine* cofferdam [3].

have been many failures.

They go on to say that most of the failures were from bursting of the sheet–pile interlocks or from piping of the soil in front of the inboard sheeting.

In 1945, Terzaghi [60] addressed the subject of cellular cofferdam design in what is now referred to as a classic on the topic. He confronted the skeptics who advocated discontinuing use of cellular cofferdams. He felt that the reported failures were due to faulty design and not to an inherent defect in this type of structure. When a cellular cofferdam is to be placed on a foundation other than rock, Terzaghi believed more judgement and experience is needed to design it than other types of cofferdams. Terzaghi notes that the principal weakness of cellular cofferdams lies in the sheet–pile interlock connections. He goes on to say that while cells have burst due to failure of the interlock material or because of sheet piles driven out of interlock, the number of failures are infrequent. In most cases, the costs to repair the cofferdam were so small that the hazard was considered not significant when compared to the overall economic advantages of using this type of structure.

Since Terzaghi's paper [60], the use of steel sheet–pile cellular cofferdams and bulkheads has flourished. Cofferdams have become an integral part of navigation and harbor construction. This does not mean that there has not been some problems with their construction and performance, but they remain a viable technology for water and harbor construction.

2.2 Cellular Cofferdam Geometry

The configuration of cellular cofferdams has been optimized over the years. Initially, they were built with straight sides as was the case at Black Rock Harbor [3]. As

mentioned earlier, curved inner and outer cell walls caused less bulging to occur. As a result, the last four cells at Black Rock Harbor were constructed with curved walls. This is an example of the evolution of the shape of the cellular structure.

Three basic configurations have been used over the years: diaphragm cells, circular cells, and cloverleaf cells, Figure 2.4. The diaphragm configuration was the first type of cellular cofferdam used (Black Rock Harbor) and, initially, was the most common. The diaphragm cellular cofferdam is an adaptation of the double–wall sheet–pile cofferdam. Instead of tie–rods to connect the front wall to the back wall, cross walls are used. Typically, diaphragm cells have curved inner and outer walls with straight cross walls. The connections for the cross walls are usually 120–deg wye piles. This arrangement causes the hoop tension in the cross walls to be the same as that in the inner and outer walls. Diaphragm cells are not self–supporting, and care must be taken in the filling process. During filling, the level of fill in adjacent cells are limited to less than 5 ft to eliminate excessive deformations of the cross wall. For this reason, the construction of diaphragm cells requires that all of the cells in a reach must be formed before filling begins. The cells must be braced to maintain their shape during the construction of the other cells. During filling, if one cell in a reach ruptures, the adjacent cross walls may rupture due to the uneven soil pressure, leading to a chain like rupture of the cells.

The circular cell configuration is the most common shape used today. It consists of a series of circular cells, called main cells, connected by sheet piles arranged in a semicircle, called arc cells (Figure 2.4b). The arc cells are connected to the main cell by means of a **Y** or **T** section. The portion of the main cell shared with the arc cell is referred to as the common wall. The circular cellular cofferdam is constructed by placing the sheet piles for several adjacent main cells. The sheet piles are placed

with the help of a template to obtain the desired shape. Once the sheet piles are placed, the cells are filled with a free draining soil. Next, the sheet piles for the arc cells are positioned with help of a template and then filled. Once a main cell is filled it is self–supporting and can be used as a working platform for the construction of other cells. The circular configuration is preferred for difficult conditions such as water with a strong current since the cells can be stabilized quickly, and one cell of the cofferdam can rupture without adversely affecting the remaining cells. When driving sheet piles in a strong current, an H–pile may be mated with the sheet pile to increase stiffness and maintain alignment.

Cloverleaf cells are used primarily where there are problems with large differential water heights and limited space. Cloverleaf cells can have large base widths without the high hoop tension associated with circular cells. The internal diaphragm walls in the cloverleaf cell reduce the radius of the outer walls resulting in less interlock tension. Cloverleaf cells are difficult to construct because separate templates are required for each quarter of the cell, and the level of the fill in each corner of the cell must stay within 5 ft of each other.

A berm may be placed on the inside of any cofferdam. The berm provides seepage control and additional sliding and overturning stability. A berm may also be used around the outer edge of a cofferdam for scour protection. If a berm can be constructed without encroaching on the working area, it is a cost effective approach to increasing stability of the cofferdam. Berms are usually placed prior to dewatering and shaped after dewatering.

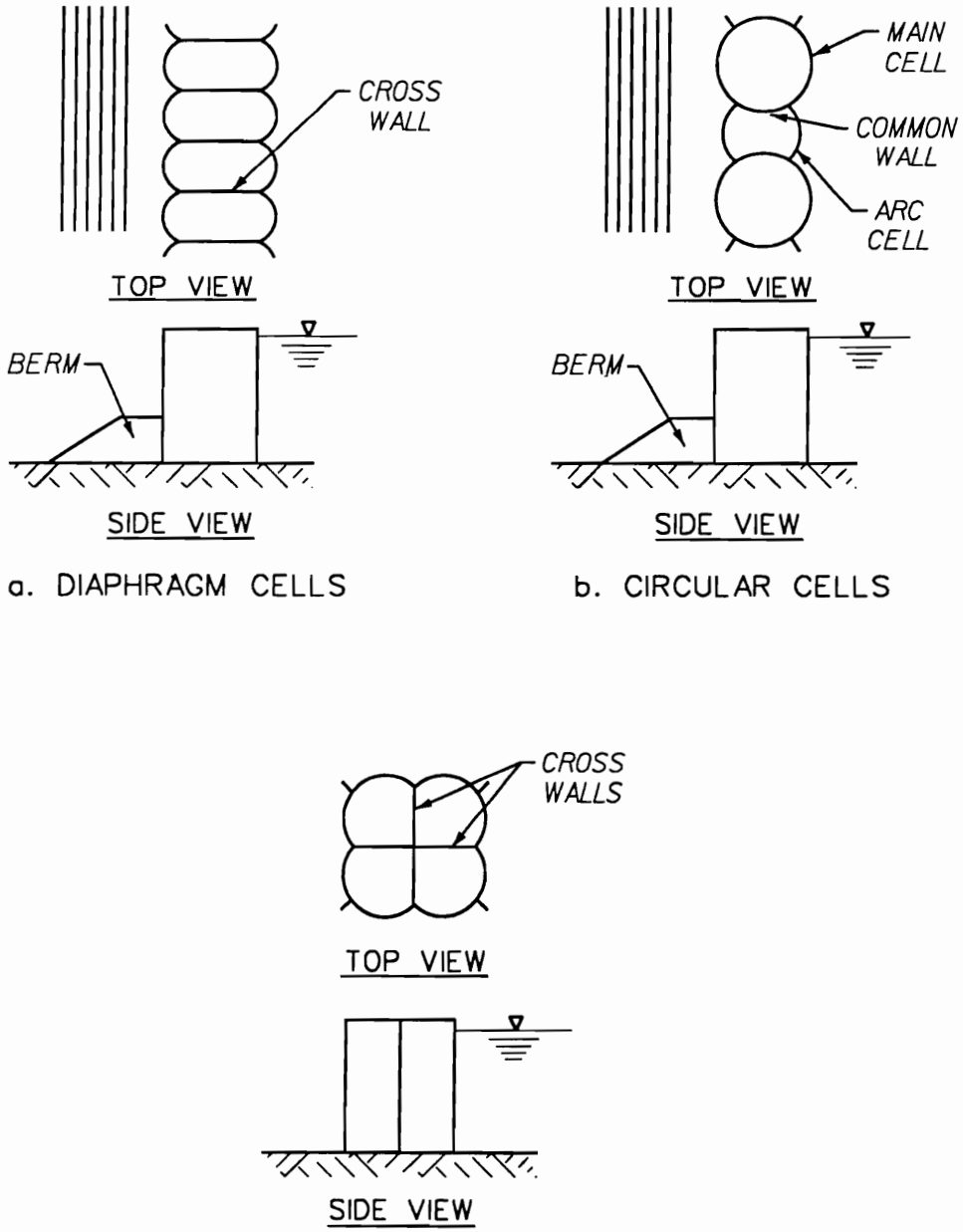

Figure 2.4: Commonly used sheet-pile cellular cofferdam configuration, (a) diaphragm, (b) circular, and (c) cloverleaf.

2.3 Cellular Cofferdam Failures

As reported in the section on historical background, cellular cofferdams initially had a dubious reputation. Some of the early designers of cofferdams believed that cellular cofferdams were less reliable than other types of cofferdams [62]. Terzaghi [60] attributed most of these early failures to faulty design or construction practices, not any inherent flaw in the cellular cofferdam concept.

The most frequent type of failure is due to the separation or rupturing of the sheet–pile interlocks [11, 35, 60, 62]. The Corps [11] reported 35 incidents of failure at 21 construction sites between 1956 to 1971. Of the 35 incidents of failure, the predominant cause of failure was the rupture of the cells. Twenty–four of the 35 incidents were due to either failure of the sheet–pile interlocks or failure of the wyes or tees. Four incidents were due to scour under high–velocity flow. Two failures were due to foundation instability. The remaining five incidents range from a split in a sheet–pile web due to impact of a bulldozer during freezing temperatures to the overtopping by a tsunami.

A large number of failures of welded tees and wyes were reported [11]. The failures generally occurred in the web of the main sheet pile, and often the rupture of the web would occur on both sides of the tee stem. The Corps had recognized the apparent weakness of welded connections in 1965 and directed its offices to utilize only riveted connections in fabricated tees and wyes. In recent years, the Corps has moved away from using tees altogether and now uses 30–deg riveted wyes for circular cells.

In the Corps [11] investigation, the main cause of interlock failure was driving the sheet piles out of their interlocks during construction. Only 2 of the 12 interlock

failures were caused by accidents such as barge impact. Of the twelve, only three incidents involved total interlock failure. The investigation found that cofferdam collapse due to interlock failure was very rare since the interlock failures usually occurred during filling and before dewatering.

Scour from high–velocity flow may elevate a minor construction defect into the primary cause of the collapse of a cell. In the Corps [11] investigation, four failure incidents were attributed to scour of material adjacent to the cells. The scour of the material exposed windows in the sheet piles or interlock separations which allowed piping of the cell fill.

The Corps [11] report states that the design practice for cellular cofferdams at the time of the report generally proved to be adequate as far as the geotechnical aspects of the design are concerned, with the exception of seepage control leading to piping failures. Cofferdam failures due to foundation failure have been infrequent, but when they do occur they have been dramatic. The most spectacular foundation failure was at Uniontown Locks and Dam on February 26, 1971, occurring during a rising river with the cofferdam dewatered. The river level was 60 ft above rock surface and 6 ft below the top of the cofferdam. The cofferdam had been dewatered for only 10 days. The foundation failure occurred when four cells of the first stage cofferdam slid between 37 to 72 ft into the work area. Cells adjacent to these four cells were ruptured, and the work area was flooded within 10 minutes. The slide occurred along a horizontal coal and clay seam about 16 ft below the rock surface. The failure plane surfaced at the center of the work area. Failure was attributed to the low shear strength along this seam and the high pore pressures in the foundation resulting from the high river level.

In summary, the primary cause of cellular cofferdam failures involves the sheet

pile, either by interlock separation or by rupture of the connection of the arc cell to the main cell. As early as Terzaghi's paper [60], problems with sheet–pile interlocks were of concern. He stated that the only inherent weakness of the cellular cofferdams is the vulnerability of the sheet–pile interlock connections. Often the failure can be traced back to problems occurring during construction such as piles driven out of interlock, use of used sheet piles, splicing, or sheet piles from different manufacturers. Other causes are extreme water level, overtopping, and barge impacts. The second most frequent cause of cofferdam failure is piping. This comes from scour problems, or poor seepage control at the connections to existing structures. Although rare, cofferdam collapse due to a foundation failure can occur, but in all cases cited the failures occurred well below the base of the cells and would have occurred regardless of the type of cofferdam. No cases were cited where collapse of the cofferdam occurred by the titling of the cells.

2.4 Early Cellular Cofferdam Design

Prior to Terzaghi's 1945 classical paper [60] on cellular cofferdams, the customary methods for designing cellular cofferdams assumed the cofferdam could be represented as a rigid gravity type structure that must resist sliding, overturning, internal shear of the cell fill, and bursting of the cells [46]. It was stated that to prevent vertical as well as horizontal shear fail of the cell fill, the fill should have a natural slope (angle of repose) greater than 3 to 1. If the cell fill material met this requirement, the cells were designed against overturning as if they were a gravity wall with the resultant of forces on the cells having to passes through the middle one–third of the base.

2.5 Design Considerations

The primary function of a cofferdam is to act as a water barrier and it must be designed to ensure adequate protection of the construction site. The engineer designs the cells of a cofferdam to be stable under loads which result from providing the necessary protection. The designer is concerned with ensuring that the cofferdam is sized appropriately so the applied loads do not cause the foundation material (soil or rock), cell fill, or steel sheet piles to reach a state that would allow radical movements of the structure. Illustrations of these potential failure modes are shown in Figure 2.5.

The considerations for stability of the cells of a cofferdam are essentially the same as for any hydraulic structure with two exceptions, internal and interlock stability. First and foremost, the cells must be able to contain the cell fill without bursting the sheet–pile interlock connections. The interlock strength must be selected to withstand the hoop tension resulting from the combination of soil and water pressures applied to the sheet piles. These pressures are a function of the height and diameter of the cells, the density of the fill material, and the water level in the cells. The condition of interlock hoop tension is normally most critical during the filling of the cells, since at this time the water level in the cells is at its peak. Questions about the maximum values of interlock tension actually experienced in the field generated the studies that led to this research.

The external stability of a cofferdam with regard to sliding, bearing capacity, and settlement are evaluated as for a gravity structure. Contemporary geotechnical design procedures that have been used over the years have demonstrated themselves to be adequate for the design of cellular cofferdams. Depending on the foundation

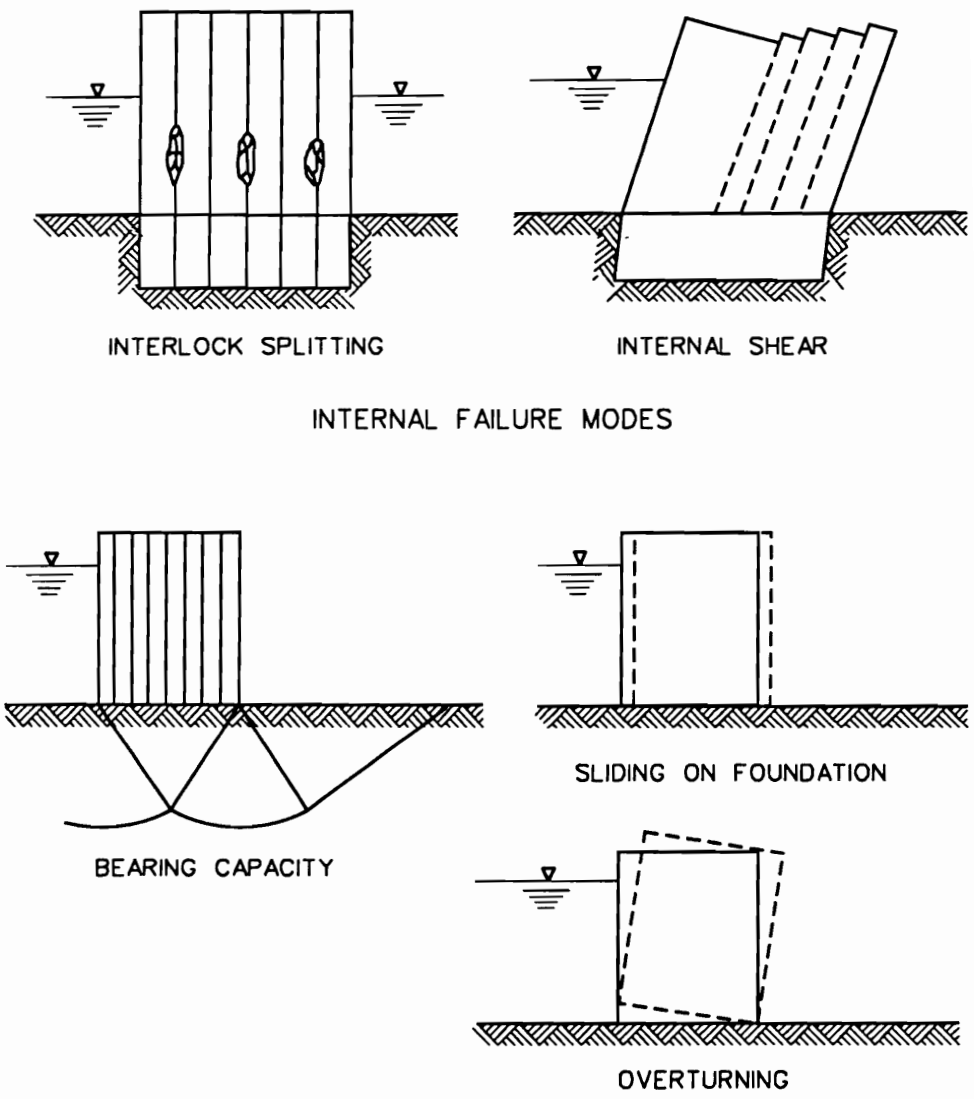

Figure 2.5: Possible failure modes.

material, whether sand, clay, or rock, the different modes of failure (bearing, settlement, or sliding) may play a more important role in determining the external stability. For instance, the external stability of cells founded on rock is controlled by the sliding resistance of the cell–rock interface. The strength and stiffness of the rock are usually so great that bearing and settlement problems do not play a role in sizing the cofferdam.

For soil–founded cofferdams, one or more of the failure modes may control the external stability. In these cases, the shear strength and compressibility of the foundation are important design parameters. For clay foundations, careful consideration must be given to all three modes of failure. Sand–founded cells are normally most sensitive to sliding and, to a lesser degree, bearing failures. While acting as a water barrier, a cofferdam may be subjected to a substantial differential water head. The resulting seepage and uplift pressures may have a significant influence on these modes of failure.

Internal stability pertains to the strength within the cells themselves. The cells have two components which contribute to the internal stability: the sheet piles and the cell fill. Internal stability is a measure of the ability of the cell fill to mobilize its shear resistance to the applied lateral load without excessive shear distortions. The cell fill derives its shear strength through the confinement provided by the sheet–pile membrane. This confinement allows the fill to develop the necessary compressive and shearing stresses to transmit the lateral loads to the foundation.

2.6 Current Design Procedures for Interlock Stability

The interlock strength of cofferdam cells must be sufficient to withstand the forces in the interlocks resulting from the combination of soil and water pressures applied to the sheet piles. Conventional design procedures to predict interlock forces during cell filling are determined as if the cell were a perfect pressure vessel. The maximum interlock force, t_{max}, in the main or arc cell outside the cross wall is calculated from the hoop–stress equation

$$t_{max} = p_{max} r \tag{2.1}$$

where p_{max} is the maximum lateral pressure acting against the wall exerted by the cell fill and water and r is the radius of the cell, Figure 2.6.

The analogy between the pressure vessel and a cell of sheet–pile cellular cofferdam involves several assumptions. First, the cell walls are assumed to be continuous with an uniform thickness. The articulated nature and nonuniform cross–sectional area resulting from the interlock sheet piling are ignored. This assumption is only a problem when attempting to predict cell deformations using membrane theory. Second, the cofferdam cell is an infinitely long cylinder with free ends; the dredgeline imposes an end constraint. To accommodate this issue, most methods for predicting interlock tensions are empirically based. Despite the simplifications associated with using Eq. 2.1, it has served as the principal means for predicting interlock forces for cofferdam design.

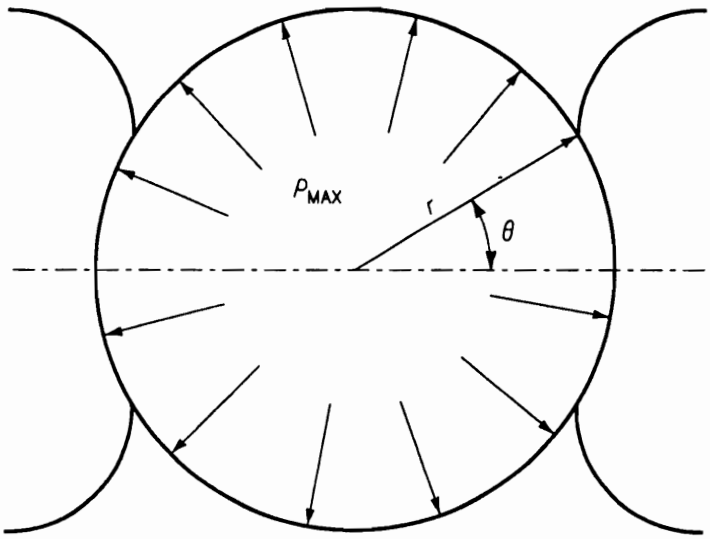

Figure 2.6: Interlock force determination by hoop–stress equation.

2.6.1 Main Cell

The key to assessing the maximum interlock force is the determination of the maximum lateral pressure acting against the cell walls. The maximum pressure, p_{max}, is assumed to occur at the point of maximum bulging of the sheet–pile cell. It is calculated by summing the effective lateral earth pressure and the difference in water pressure between the inside and outside the cell. Figure 2.7 summarizes the four most commonly recommended design pressure diagrams for the determination of the interlock force. These vary from one another by the location of the maximum pressure, the shape of the distribution, and the magnitude of the pressures. The pressure diagrams are empirically based and do not necessarily represent the actual pressures applied to the sheet piling.

The Terzaghi [60], Figure 2.7(a), and the old Corps of Engineers [13], Figure 2.7(c), methods assume that the lateral earth pressure increases linearly with depth to the dredgeline with lateral earth pressure coefficients of 0.4 and 0.5, respectively. Recent studies have shown that these approaches are excessively conservative [38, 49, 51, 55].

Based on their many year of experience in the design and construction of cofferdams in the 1930's and 1940's, the Tennessee Valley Authority (TVA) [1] developed an earth pressure distribution for predicting the maximum interlock force which increases linearly to a point of maximum pressure and then decreases to zero at the bottom of the cell, Figure 2.7(b). The point of maximum pressure was assumed to coincide with the location of the maximum bulge of the cell during filling. Based on field observation, the location of maximum bulge was observed to occur at one–fourth of the free height of cell above the dredgeline. Because most of TVA's

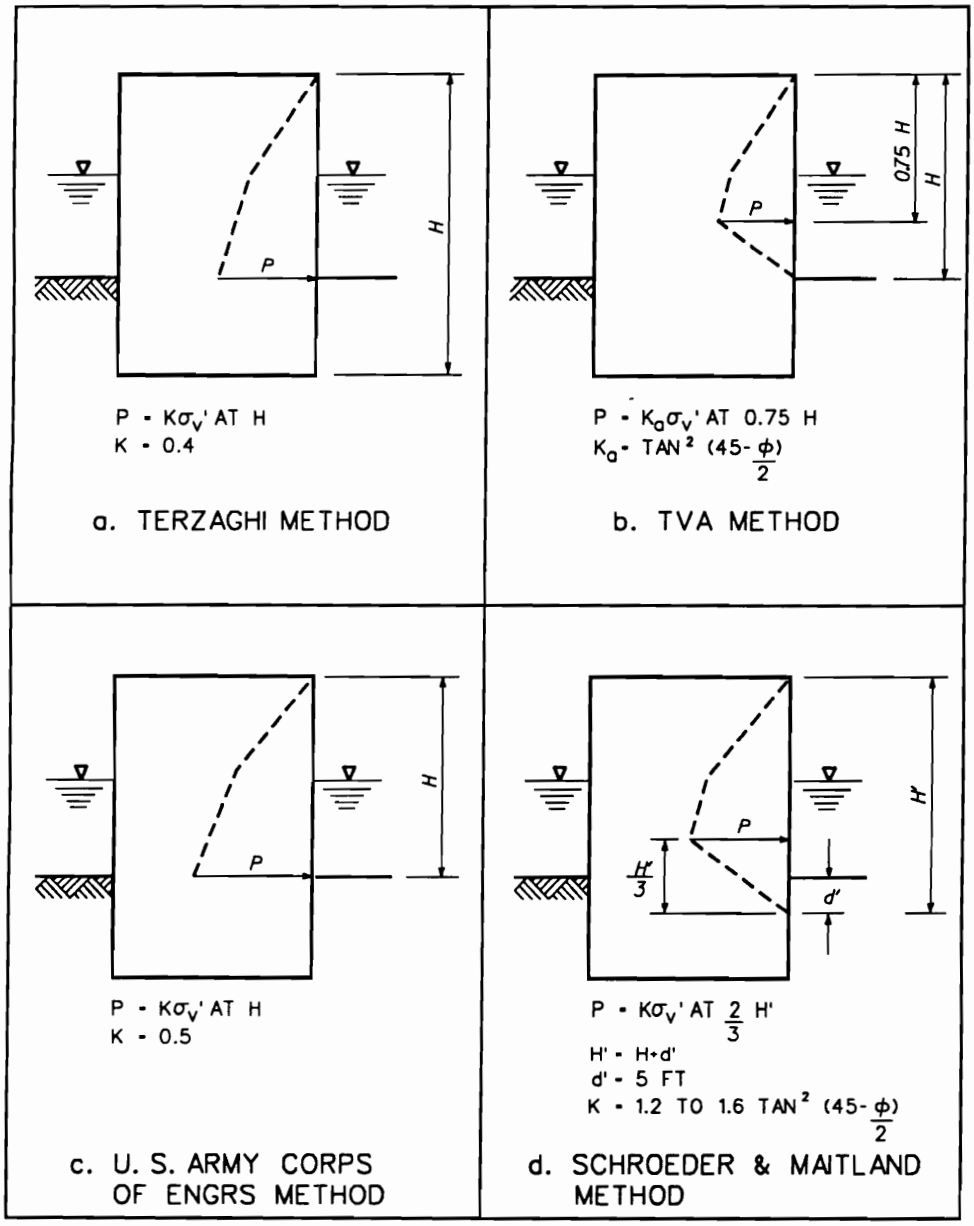

Figure 2.7: The four most commonly assumed pressure diagrams for interlock tension [53].

experience was with rock–founded cofferdam, they set the soil pressure to zero at the tip. The method was subsequently extended to soil–founded cofferdams by assuming the dredgeline played the same role as the rock. Thus, resulting in the same distribution of lateral pressure being used for both rock– and soil–founded cofferdams. TVA assumed that there was sufficient deformation to develop active pressures adjacent to the sheet piling. Thus, allow them to use a Rankine active lateral earth pressure coefficient. The TVA method represented an improvement over Terzaghi's approach, because it recognized that the interlock forces do not increase uniformly for the full depth of the fill and the magnitude of the earth pressure should be closer to active than at–rest.

Schroeder and Maitland [51] proposed a modification to the TVA method based on their observation of large–scale model tests and cellular sheet–pile bulkheads construction at port facilities in the northwest United States. Their approach used a pressure distribution with the same basic shape as that of TVA, but with redefined limits on the extent of the diagram and the lateral earth pressure coefficient. Schroeder and Maitland found that for soil–founded cofferdams with sheet piling penetrating the soil, the lateral earth pressure would be greater that zero at the dredgeline. They proposed that the point of zero pressure would occur where sheet piling developed a plastic hinge in their model tests, and termed this point to be the plane of fixity. For cells founded directly on rock, they assumed the plane of fixity would occur at the top of the rock. For soil–founded cofferdam, Schroeder and Maitland proposed that the plane of fixity is analogous the point of zero rotation of a single laterally loaded pile and the formulas to find the point of zero rotation for a laterally loaded pile could be used to determine the location of the plane of fixity. In their procedure, the maximum interlock force occurs at one–third of the effective

free height of the cell which is the distance from the plane of fixity to the top of the cell, Figure 2.7(d). They also recommended the use a lateral earth pressure coefficient equal to 1.2 to 1.6 times the active pressure coefficient. Schroeder and Maitland's approach compared well with the instrumentation results from Lock and Dam No. 26(R) first–stage cofferdam [55]. The Corps of Engineers [48] has adopted this method in its latest design criteria.

2.6.2 Arc Cell

The interlock forces in the arc cell wall are smaller than those in the main cell or the common wall. One reason for this is the smaller radius of the arc cell, thus, the interlock forces are smaller as shown by Eq. 2.1. A second reason is the lateral pressures in the arc cell are likely to be smaller than those in the main cell at comparable depth is because the smaller diameter arc cell will vertically restrain the fill movements more than the larger diameter main cell. The increased vertical restraint will result in arching in the arc cell fill. This phenomenon is believed to occur, although it has not been shown through numerical modeling or field observation. The three–dimensional finite element analyses developed for this research provides a tool for assessing this phenomenon.

Since, in most cofferdam construction, the same size sheet piling is used for the arc cell and main cell, the margin of safety for the arc cells is greater than for the main cells because of the lower interlock forces in the arc cell walls.

2.6.3 Common Wall

The common wall has greater interlock forces than the main cell because the main and arc cell walls pull on the common wall through the wye. Two conventional methods have been proposed to estimate the common wall interlock forces: the TVA secant formula [1], and the Swatek formula [19]. The TVA secant formula is derived from the free body shown in Figure 2.8. Using this free body, the formula for the maximum interlock force in the common wall is

$$t_{cw} = p_{max} L \sec\theta \tag{2.2}$$

where L is the distance between the centerline of the main cell and centerline of the arc cell, and θ is the angle between the centerline of the wall and a line from the center of the main to the wye. This formula assumes that the lateral pressure on the main and arc cell walls is equal and the wye does not rotate. As discussed in the previous section, the pressure on main and arc cell walls is not equal and therefore, to maintain equilibrium, the wye most rotate. Because of these inconsistencies, the accuracy of the approach is questionable.

The Swatek formula is derived from considering the free body of an equivalent, straight–wall cofferdam geometry used in conventional design procedure for internal stability, Figure 2.9. It is assumed to provide an average common wall interlock. The Swatek formula is

$$t_{cw} = p_{max} L \tag{2.3}$$

This formula results in a smaller common wall interlock force than the TVA secant formula.

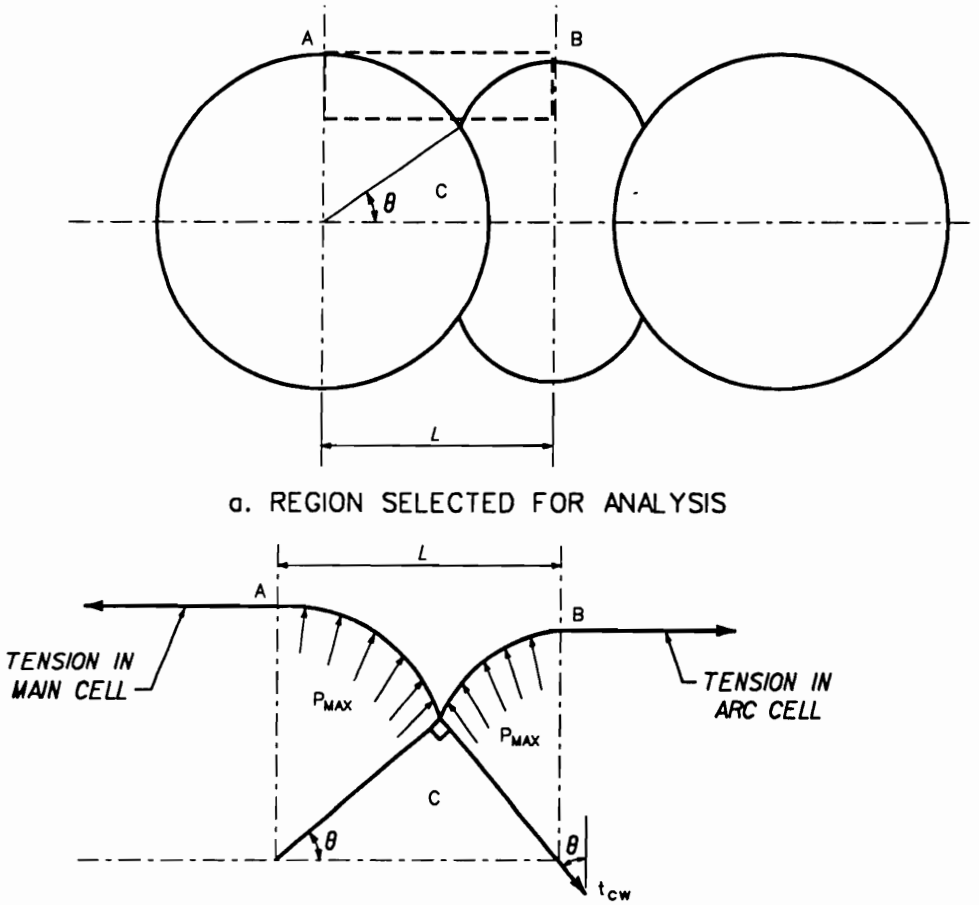

Figure 2.8: Free body for the TVA secant formula for determining interlock forces in the common wall.

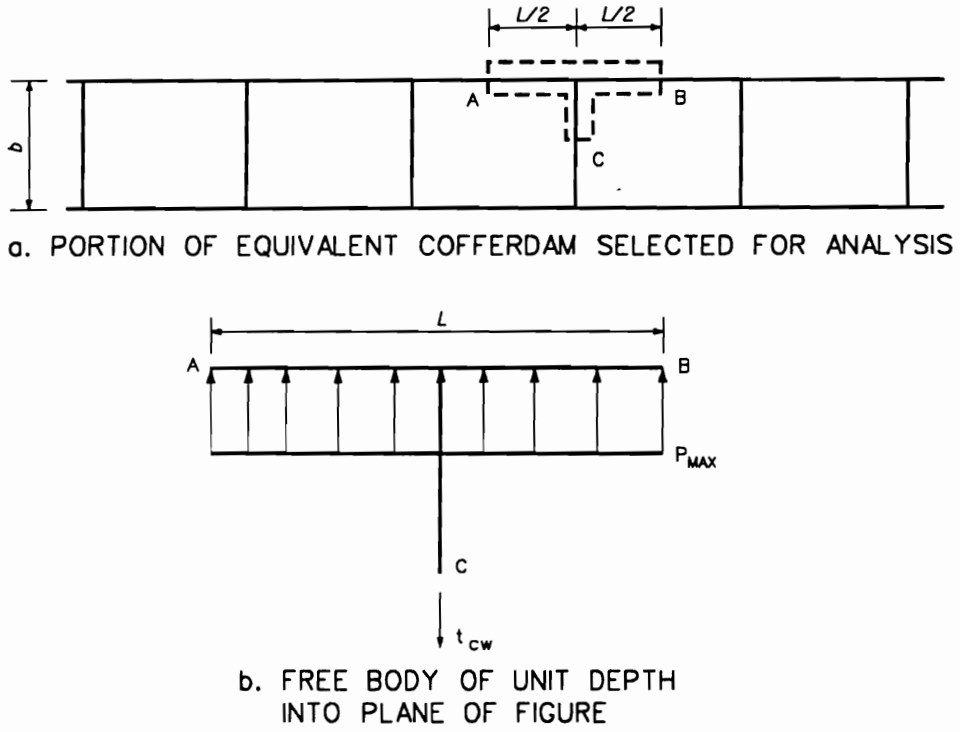

Figure 2.9: Free body for the Swatek formula for determining interlock forces in the common wall.

2.7 Current Design Procedures for Internal Stability

Early concerns about overturning revolved around the assumption that the cell behave as a gravity monolith. In this case, the moments due to the unbalanced lateral load would have to be resisted by a triangular pressure distribution across the base of the cell. Based on this assumption, if the unbalanced lateral load is increased sufficiently, the contact pressure at the outer edge of the cofferdam would have go to zero. Terzaghi [60] noted that this cannot occur in a cell filled with sand. Even if arching developed to its fullest possible extent in the fill above the outer portion of the base, the pressure on the outer edge must have a significant positive value that cannot decrease in spite of increased unbalanced lateral load. Therefore, the most unequal distribution of the pressure on the base that could occur is shown in Figure 2.10. Since the pressure at the outer edge cannot decrease, an increase in unbalanced lateral load will correspond to a shift in the neutral axis of the base pressure distribution and an increase in the pressure at the toe.

Based on these observations, Terzaghi believed it was unlikely that a cofferdam could fail by the monolithic overturning mechanism, but rather increasing the base pressures on the toe side of the neutral axis would cause a shear failure in the cell fill. To demonstrate this hypothesis in simple terms, Terzaghi made the *customary assumption* that the pressure distribution on the base could be represented by a straight line as shown in Figure 2.11. The shaded area in Figure 2.6 indicates the stresses due to the unbalanced lateral load. Terzaghi stated that this unbalanced

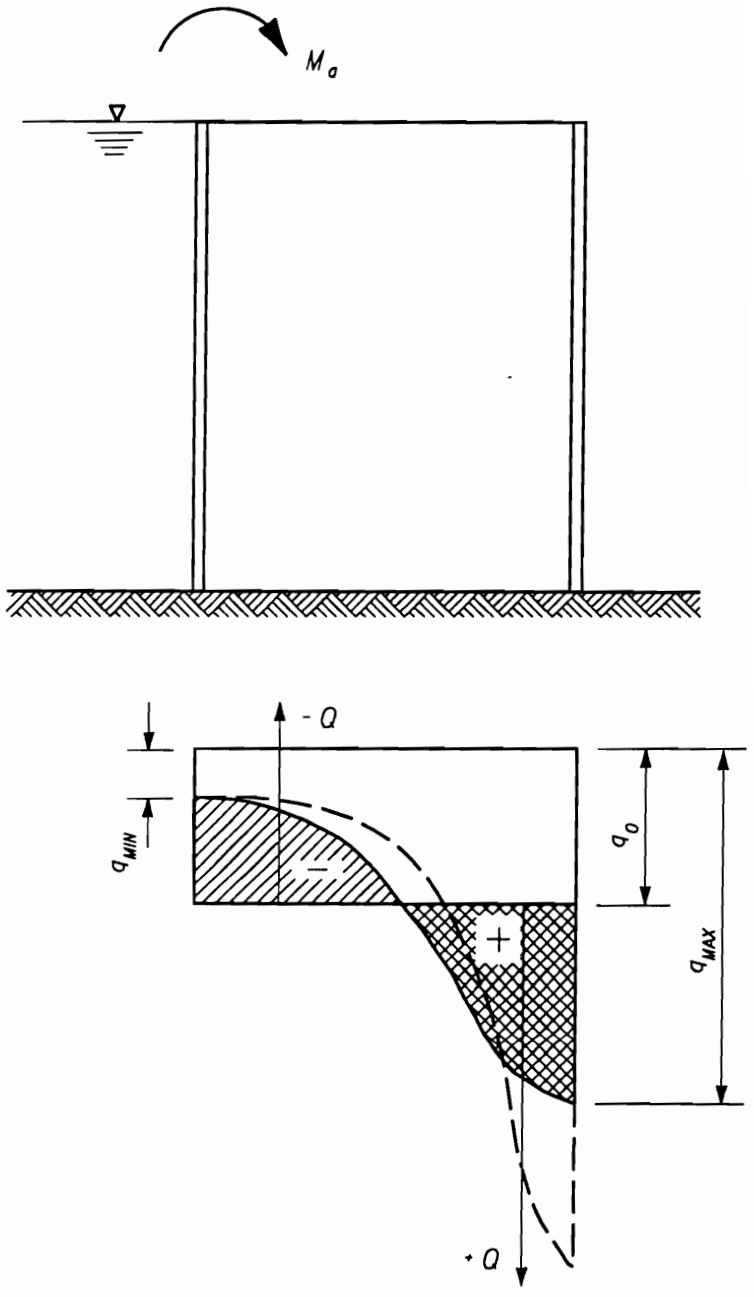

Figure 2.10: Terzaghi's base pressure [60].

lateral load, Q, could be represented as a moment, M, equal to

$$M = \frac{2b}{3}Q \tag{2.4}$$

$$Q = \frac{3M}{2b} \tag{2.5}$$

and the pressure distribution due to this moment could be resolved into two equal and opposite resultant forces with magnitude of Q. Equilibrium required that the total shearing force on the neutral plane per unit length of the cofferdam, Figure 2.11, should be equal to the resultant force on the base, Q.

Terzaghi further stated that the shearing resistance, S_c on this plane was equal to the lateral earth force, P_c, times the coefficient of internal friction, $\tan\phi$, of the fill where lateral earth force, P_c, is determined by

$$P_c = \frac{1}{2}\gamma K_c H^2 \tag{2.6}$$

where K_c is the lateral earth pressure coefficient on the neutral plane, γ is the effective unit weight of the cell fill, and H is the free height of the cell. In addition to this shearing resistance, Terzaghi felt that resistance would also be provided by the friction in the sheet–pile interlocks because no vertical shear failure could occur without simultaneous slippage in the interlock in the same plane. Total tension in an interlock for a height, H, is

$$T = \frac{1}{2}\gamma K_i H^2 r \tag{2.7}$$

where K_i is the lateral earth pressure coefficient at the sheet–pile cell wall. Total resistance against slippage in an interlock is

$$Tf = \frac{1}{2}\gamma K_i H^2 r f \tag{2.8}$$

where f is the coefficient of interlock friction (steel on steel). Circular cells contain two common walls per cell and length of each cell is $2L$; those of the diaphragm type contain one common wall per cell and the length of each cell is L. Hence, the resistance to shearing along the neutral plane contributed by interlock per unit length is

$$S_i = T\frac{f}{L} = \frac{1}{2}\gamma K H^2 r \frac{f}{L} \tag{2.9}$$

For a circular cellular cofferdam, the factor of safety against shear failure on the centerline is the ratio of resisting to driving forces

$$FS = \frac{S_c(2L) + 2S_i}{\frac{3M}{2b}(2L)} \tag{2.10}$$

For the special case of uniform cell fill density, $L = r$, and triangular distribution of interlock forces

$$FS = \frac{\gamma b H^2 \left(K_c \tan\phi + K_i f\right)}{3M} \tag{2.11}$$

Terzaghi proposed that the lateral earth pressure coefficient, K where K is equal to K_c and K_i, within the cell should remain at an at–rest value between 0.4 to 0.5. A constant value for lateral earth pressure coefficient throughout the cell fill was a fundamental assumption in Terzaghi's development of vertical shear analysis. He stated that this was no more than very crude approximation. He believed it very probable that the value for the central part of the fill was much greater than that for the fill adjacent to the inboard sheet piling. He recommended a constant value because of a lack of a way to assess the value throughout the fill.

Although this procedure was developed for cells founded on rock, Terzaghi indicated that the results of such analysis would not differ greatly for cells founded on rock or soil, and it could be applied to cells founded on rock, sand, or hard–to–medium clay foundations. He felt that if the foundation was able to resist the

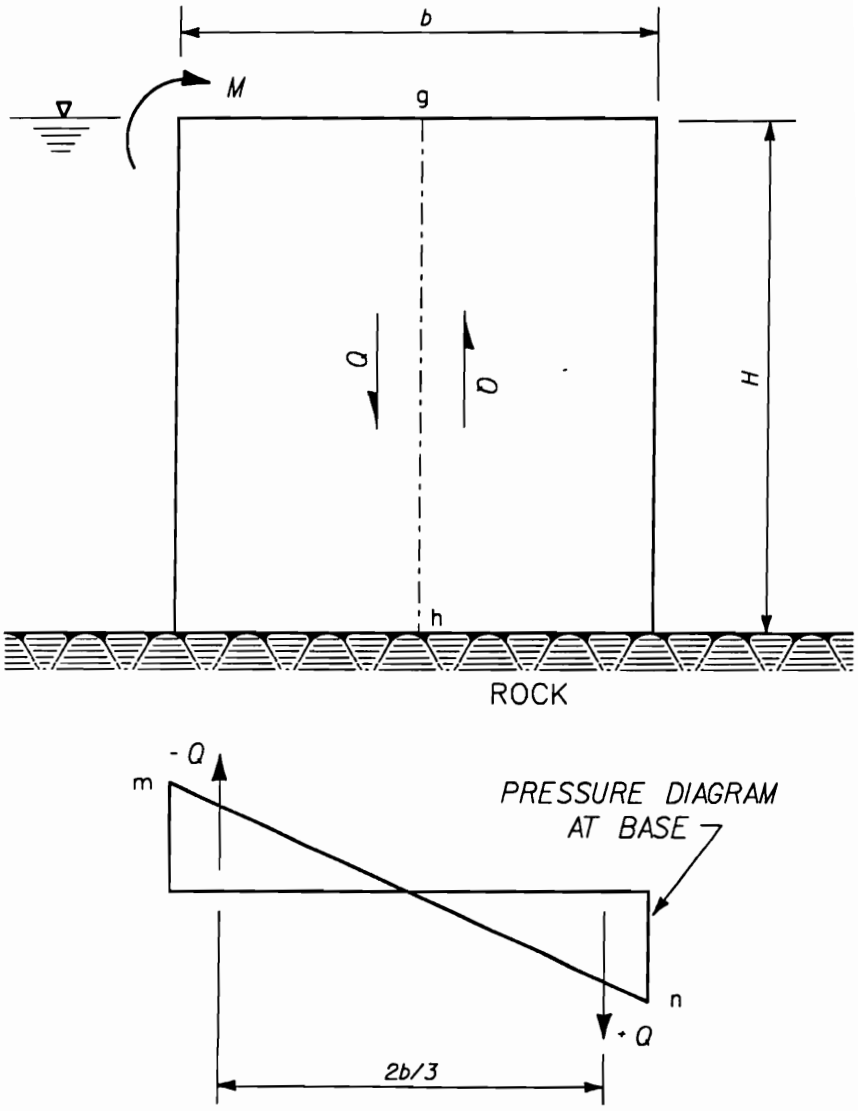

Figure 2.11: Vertical shear on the centerline [60].

unequal base pressure distribution resulting from the combined vertical and horizontal forces acting on the cell, shearing resistance on vertical planes within the fill could be mobilized. Thus, it was recommended that the magnitude of this resistance be considered in evaluating the stability of a cell.

Terzaghi's vertical shear concept received criticism after its publication concerning the assumption of the vertical mechanism of failure and the choice of the at–rest lateral earth pressure coefficient for shear resistance calculations. It was even criticized for being too mathematical. The most outspoken critic was Pennoyer [45] who wrote that a review of completed cofferdams showed that they performed successfully even though the safety factor for vertical shear determined using the Terzaghi's procedure was less than or equal to 0.6. He noted that the resultant force of the base pressure distribution was in the middle–third of the base even if the factor of safety by Terzaghi's procedure was below 1.0. Pennoyer was critical of Terzaghi's recommendation to use the friction in the interlock to provide resistance to vertical shear. Pennoyer maintained that a value of 0.3 for a coefficient of friction for the interlocks was unconservative and would lead to greater resistance from the interlocks than would actually develop.

Krynine [32], in his critic of Terzaghi's paper, pointed out that it was incorrect to use the Rankine active earth pressure coefficient to calculate vertical shear resistance in the cell fill. His reasoning for this was that the assumed failure plane (the vertical plane) cannot be a principal plane because shear stress acts on it. Terzaghi [60] concurred with Krynine's point and agreed that the lateral earth pressure coefficient would be greater than the Rankine active value. Krynine also suggested the possibility of a failure along a curved shear plane beginning at the outboard bottom of the cell and inclined at an angle ϕ as shown in Figure 2.12. This mechanism

allowed for an increased resistance as the width gets larger. However, he presented little to develop or substantiate this hypothesis.

During the 1950's, alternative methods of analysis based on different assumptions for the internal failure surfaces were proposed. Most noteworthy were those of Cummings [10] and Hansen [23, 24]. Cummings [10] proposed a method of analysis shown in Figure 2.13 based on a horizontal shear concept. According to Cummings [10], as the cell begins to tilt under lateral pressure, an inclined rupture surface will form and the cell fill above this plane will begin to slide down the plane. The rupture plane starts at the toe of the cell and is inclined at an angle equal to the internal friction of the fill, although sliding on this plane is inhibited by the confining effects of the sheet piles of the cell. The fill below the rupture plane is transformed into a passive state by the combined effect of the lateral pressure on the exterior of the cell and the weight of the fill above the rupture plane. Cummings felt that failure would occur along a horizontal shear plane below the rupture surface.

The technical literature contains no reports of failure of full–size cells by the forming of horizontal failure planes in the fill. The only positive experimental evidence of such a failure mode comes from Cummings' own paper [10], describing his model studies and theory, and from a TVA experiment using a cigar box with the top and bottom replaced by glass [1]. The walls of both of these models were relatively stiff, and the small size of the models raises serious concern that the surface effects in the fill were far more important than they would be in a full–size cell. Indeed, it is interesting to note Erzen's comments [20] in the discussion of Cummings' paper. Erzen expressed concern that the stress distribution in the fill in Cummings' models was strongly influenced by the proximity of the walls, and as a result, he doubted whether Cummings had really demonstrated that distinct zones of active

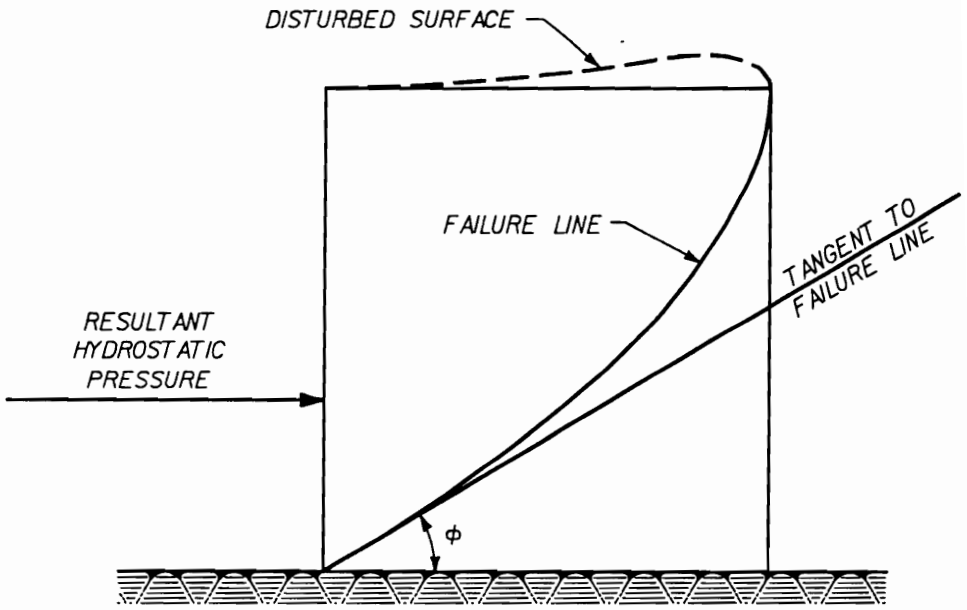

Figure 2.12: Failure plane proposed by Krynine [32].

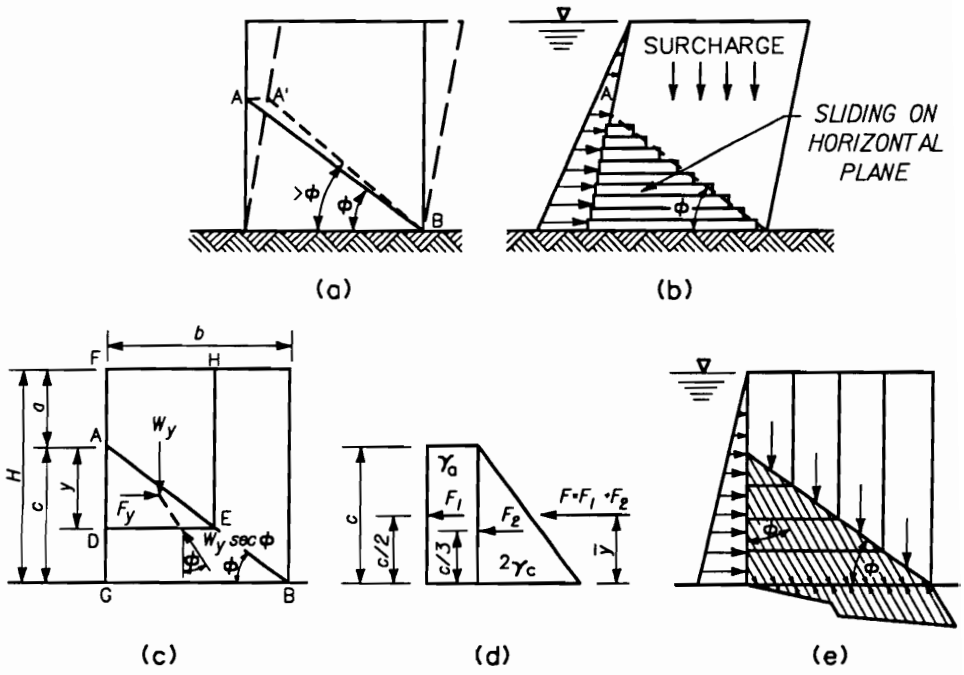

Figure 2.13: Cummings method [10].

and passive pressure exist in the fill.

Hansen [23, 24] took a different approach to internal shear based on a more rigorous analytical treatment. Observations from model studies suggested to him that a cellular cofferdam founded on rock failed near the bottom of the cells by sliding along a circular failure surface formed between the tips of the outboard and inboard walls as shown in Figure 2.14. The portion of the cell above the failure surface rotates as a rigid body about the center of the surface. Some of the assumptions made in Hansen's method of analysis are not consistent with conventional soil mechanics. In particular, Hansen's assumptions do not allow the stress–strain behavior to vary from point to point in the cell fill according to the stresses and deformations. For example, the fill near the inboard wall is assumed to respond the same as the fill near the tip of the outboard wall, even though the confining stresses near the base of the inboard wall are significantly higher than those near the outboard wall. Since the behavior of soil is dependent on confining stress, it is questionable for Hansen to neglect this feature. This, along with the complexity of applying Hansen's method, especially for cells founded on soil, has resulted in the method having limited use by practicing engineers.

Until recently (29 April 1988), the Corps of Engineers' criteria [12] for the design of cellular cofferdams employed five different procedures to check the safety factor for internal stability. At the present time, the design against internal instability is controlled by the Terzaghi's vertical shear and Cummings' horizontal shear methods.

Efforts have been made through the years to sort out the controversy over the rather large number of hypothesized failure modes that have accumulated. Several model studies [1, 10, 37, 44] have been conducted to determine which proposed failure modes best represent the failure of a cell and which ones are inappropriate.

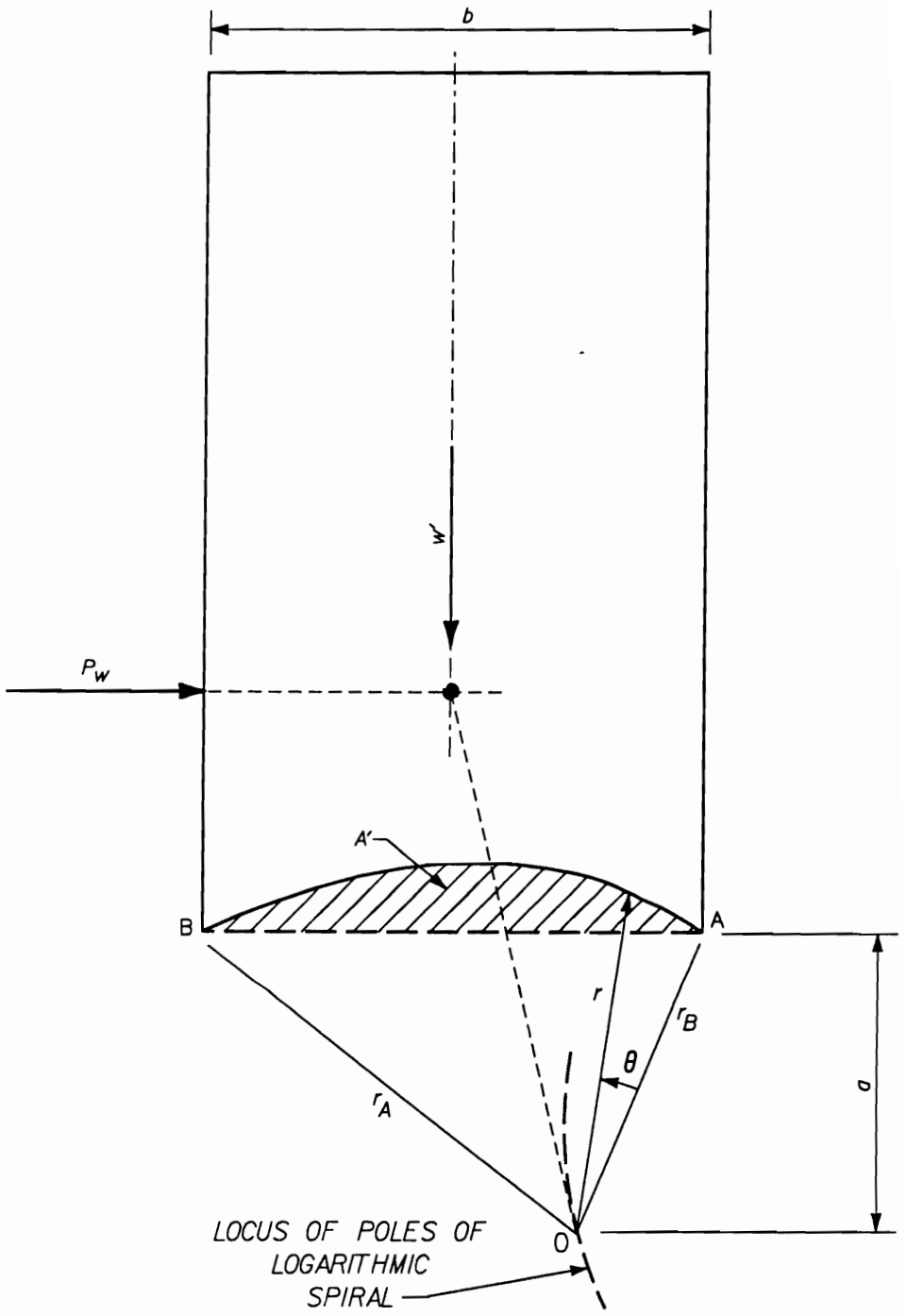

Figure 2.14: Hansen method [23].

With one recent exception, these studies have not been of great help. In some cases, the studies have actually been a hinderance to the understanding of the actual behavior of full–size cellular cofferdams. The use of relatively small models with overly stiff walls led some experimenters to postulate failure mechanisms which are highly unlikely in a full–size cell.

The one exception is Schroeder and Maitland [37, 51]. They performed a series of large–scale model tests that more closely represented a full–size cell than was represented in previous studies. In their tests, the cells were loaded well beyond the point when signs of initial failure were observed. The maximum deformations measured by Schroeder and Maitland reached up to 50 percent of the cell height. With this much deformation, sharply defined terraces formed in the surface of the cells and during excavation of the cell fill, vertical failure planes were found. In addition, slippage was observed along the sheet–pile interlocks starting at the middle of the cell and advanced toward the inboard of the cells. The observed slippage in the cell fill and the sheet–pile interlocks support Terzaghi's hypothesis of a vertical shear failure mechanism.

Although Schroeder and Maitland's model study generally supports Terzaghi's failure mechanism, they disagreed considerably with Terzaghi's recommended value for the lateral earth pressure coefficient for determining the vertical shear resistance. As previously mentioned, Krynine [32] had pointed out that lateral earth pressure coefficient should be greater than 0.5 and could be slightly higher than the at–rest values. By back calculating, Schroeder and Maitland found that the lateral earth pressure coefficient in the test cells were equal to or greater than unity. This results in an internal resistance in cell fill more than twice that calculated using Terzaghi's recommendations.

2.8 Instrumented Case Histories of Cellular Cofferdams

Field measurements of actual cellular cofferdams form a valuable resource in understanding cofferdam behavior [1, 30, 34, 38, 39, 50, 55, 57, 58, 59, 61]. Field measurements provide data that cannot be obtained from laboratory tests of model studies. Therefore, field measurements provide the most valuable source of information on the behavior of cofferdams. Although valuable data on the behavior of cellular cofferdams have been obtained under operating conditions, no instrumented, full–size cell has failed from differential loading, and, thus, no data are available on cell behavior during failure.

Typical instrumentation for a cofferdam consists of slope inclinometers and strain gages. Slope inclinometers are attached to the sheet piling and are used to measure the lateral deformation of the cells. Strain gages are attached to the sheet piling and are used to measure the strain in the web of the sheet piling which is converted to an interlock force.

With increased attention on the development of the analytical aspects of the finite element method for cellular cofferdam analysis, there remains a need for a well–documented data base on field behavior which can be used for validation of these procedures in a wide range of conditions. In an attempt to meet this need, Martin and Clough [38] recently completed a study focusing on measured field response for cofferdams subjected to differential loads. This study examined the case histories of five large cofferdams that were constructed during the past 15 years. In Table 2.1, the key aspects are given for the five cofferdams used in the case history studies. The five cofferdams listed are traditional cofferdams used as temporary barriers to

allow dewatering of a construction site within a body of water.

The cofferdams in the study had various combinations of foundations conditions, cell fills, dimensions, and loadings. Many common trends were found between the different case histories, but when differing conditions existed, differences in the cofferdam response were also found. The findings of the study are summarized in the following paragraphs.

2.8.1 Cell Filling

The filling of the cells of a cofferdam is normally the most critical loading condition for sheet-pile interlocks. Yet, relatively few cofferdams have been instrumented and monitored during cell filling. This can be attributed to the problems with maintaining workable instrumentation on the sheet piles as they are driven and the difficulty of obtaining a reasonable zero reading before filling starts. Fortunately, instrumentation to monitor the cell filling process was successfully installed for two of the cofferdams in the study; Lock and Dam 26(R) Stage 1 cofferdam and Trident Drydock cofferdam. Only in the Lock and Dam 26 (R) Stage 1 cofferdam were inclinometers installed to measure cell movement during filling.

Interlock Forces for Main Cell

In Figure 2.15 the ranges of measured main cell interlock forces for the two cases immediately after filling are shown. The trend in the data is for the interlock forces to increase with depth to a point above the dredge line, and then to decrease with depth. After filling the cells for the Trident cofferdam, the cell fill was compacted by a vibrating probe. With compaction of the fill, the interlock forces increased in

Table 2.1: Key Aspects of Cofferdam Case History [38].

Comparison of Cofferdams: Design

Cofferdam	Ht. (H)	Dia. (B)	B/H	Embed.	Sheet Piles	Cell Fill	Foundation	Berms
Lock and Dam 26 Stage 1	60'	63'	1.05	35'	PS-32, PSX-32, 40 wye	Sand, 55%, Dr, placed by clamshell. Good.	Sand, med. to dense. Good.	Sand, 25' high. In place for dewatering.
Lock and Dam 26 Stage 2	60'-80'	63'	.90*	15'-35'	PS-32, PSX-32, 40 wye	Sand, 55%, Dr, placed by clamshell. Good.	Sand, med. to dense. Good.	Sand, 25'to 35' high. In place for dewatering.
Trident Drydock	80'	76'	.95	2'-4'	PSX-32 40 wye	Sand, densified to 75% Dr. by vibratory probe. Excellent.	Dense Sand and Gravel Till. Excellent.	None used.
Willow Island	55'	65'	1.18	.5-1.5'	MP102	Sand and Gravel. Good.	Sandstone, Hard Clay. Excellent.	Sand, 30'. Placed after dewatering.
Seagirt Terminal	36'	62'	1.72	20'-30'	PS-28 PS-32 30 wye	Silty Sand, placed on top of 10 ft. clay layer. Poor.	Sand and Soft to Stiff Clay. Fair.	Silty Sand. Placed after initial loading. 10' to 25' high.
Williamson CBD Prototype Cells	35'	53'	1.51	30'-35'	---	Sand and Gravel, placed on top of med. clay. Poor.	Sand and Gravel. Good.	None used.

*Average

Comparison of Cofferdams: Performance

Cofferdam	Fmc* (K/in.)	Fcw* (K/in.)	Ht. of Fmc (Ft.)	Maximum Diff. Load	Avg. Defl. Max. Diff. Load	Comments
Lock and Dam 26 Stage 1	4 (1.3 Ka)	5.8	H/4	60 ft. water head.	3.8 in. (.5% H)	Good performance. Negligible creep.
Lock and Dam 26 Stage 2	NA	NA	NA	80 ft. water head.	3.5 in.** (.4% H)	Good performance. Negligible creep.
Trident Drydock	8 (2.1 Ka)	8	H/8	80 ft. water head.	3.0 in. (.3% H)	Very good performance. Some creep during dewatering.
Willow Island	NA	NA	NA	40 ft. water head.	NA	Very good performance. Little creep.
Seagirt Terminal	NA	NA	NA	60 ft. equivalent water head.	Several feet	Clay in cell caused large movements. Much creep. Poor performance.
Williamson CBD Prototype Cells	---	---	---	---	---	Clay in cell caused large fill settlements.

*Fmc, Fcw = Max. Interlock Force after filling: Main Cell, Common Wall, respectively; NA = Not Available ** As of December 1986

magnitude by approximately 35–40 percent, but maintained the same basic characteristic shape. For comparison purposes, only the data recorded immediately after filling are used in this paper. Figure 2.15 also shows a comparison of the predicted interlock forces for the TVA and Schroeder and Maitland methods to the observed values.

Interlock Forces in Common Wall

Figure 2.16 shows a comparison between the observed interlock forces and the predicted interlock forces for the TVA and Schroeder and Maitland methods with interlock forces in the common wall calculated by the TVA secant and Swatek equations for both methods.

Conclusion on Interlock Forces During Filling

The general conclusions that can be drawn from the work to date are:

- The TVA and Schroeder and Maitland methods result in interlock force distributions similar to the trends observed in the instrumentation data.
- The TVA method tends to predict the interlock forces for filling of the main cell closer to the average observed value for Lock and Dam 26 (R) than for the Trident cofferdam which is on the low side of the average. Conversely, the Schroeder and Maitland method is closer for the Trident cofferdam and on the high side for Lock and Dam 26(R).
- The location of the maximum interlock force occurred at a distance above the dredge line of 0.125H and 0.25H for the Trident and Lock and Dam 26 (R),

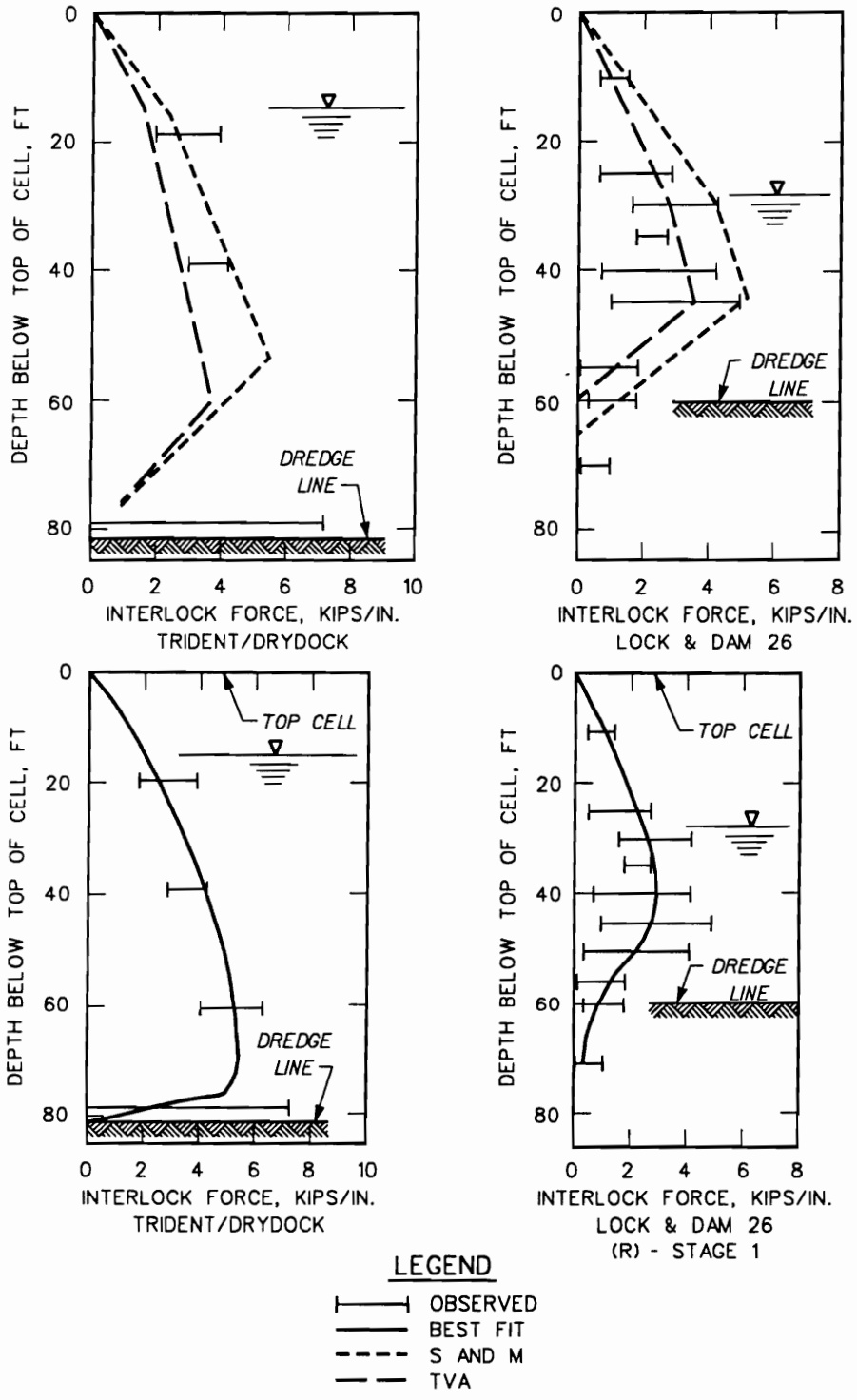

Figure 2.15: Measured interlock forces for Trident and Lock and Dam No. 26 (R) cofferdams.

respectively. The higher location in the Lock and Dam 26 (R) is associated with its greater embedment of the sheet piles.

- As expected, the measured values for the common wall are greater than those in the main cells. However, the measured values are less than those predicted by the TVA secant formula and are more consistent with the Swatek's equation.

2.8.2 Differential Water Loading

The data for the four temporary cofferdams varies in the extent and consistency. The data ranges from only survey measurements of the tops of the cells for the Lock and Dam 26 (R) Stage 2 cofferdam to inclinometer and strain gages measurements as in Lock and Dam 26 (R) Stage 1. The most reliable data obtained from these case histories are the cell movements.

The movements from inclinometer readings for the Trident and Lock and Dam 26 (R) Stage 1 show the displacement patterns of the cell walls, Figures 2.17 and 2.18. The deformed profiles in Figure 8 represent only the displacement that occurred during the dewatering of the cofferdam. The Trident cell rotated in a relatively uniform pattern, while the Lock and Dam 26 (R) Stage 1 cell underwent more of a transnational distortion with the lower portion of the cell being restrained. This difference can be attributed to:

- The greater embedment of the sheet piles for Lock and Dam 26 (R)
- The presence of the berm for Lock and Dam 26 (R)
- The dense condition of the fill for the Trident cofferdam.

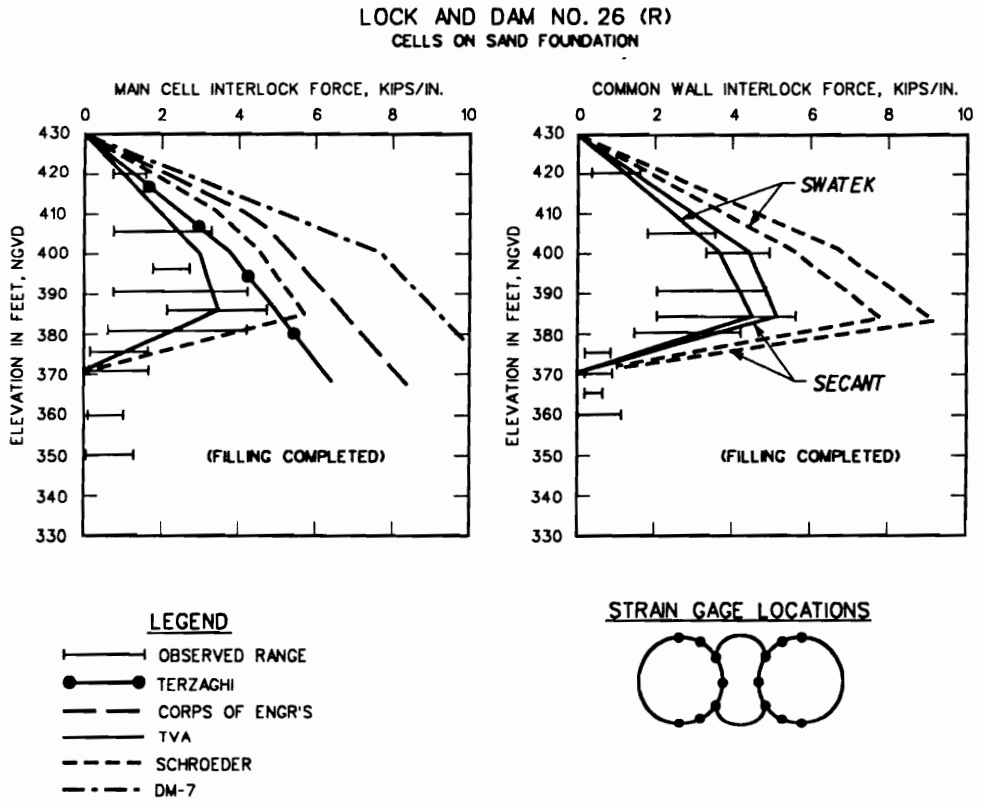

Figure 2.16: Comparison of interlock forces in the common wall for Lock and Dam No. 26(R).

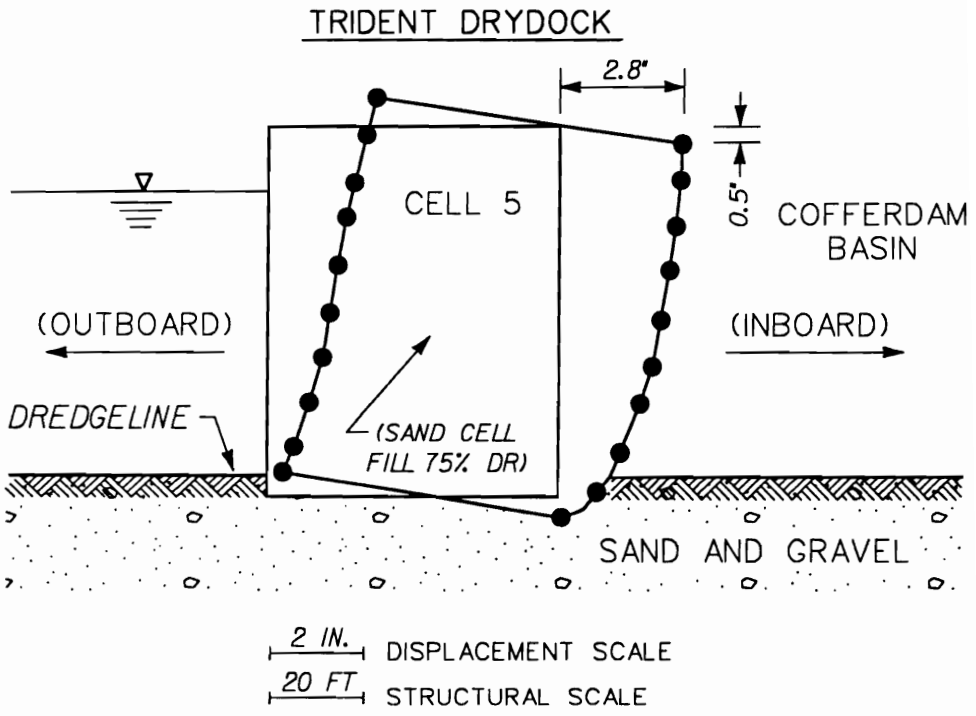

Figure 2.17: Trident cell movements [38].

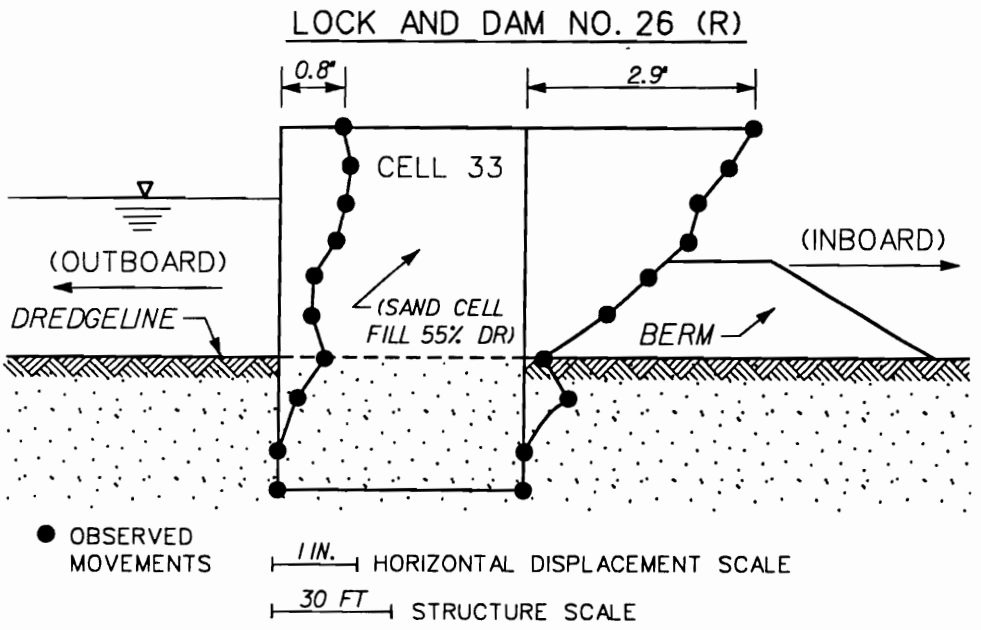

Figure 2.18: Lock and Dam No. 26(R) cell movements [38].

Another interesting segment of cell movement data is the survey measurements of locations on the tops of the cells. This allows an insight into the potential scatter in the data because of the larger sampling number as well as other aspects of the cofferdam response. In Figure 2.19, the movements of tops of cells from the survey measurements for Lock and Dam 26 (R) Stage 1 cofferdam are plotted against differential head during dewatering. The differential head is a simple measure of the load applied to the cofferdam. In spite of the scatter in the data, there is a consistent trend for the deflection of the tops of cells to increase approximately linearly during dewatering.

For comparison of the four temporary cofferdam movements, the measured displacements of the tops of the cells are normalized by dividing by the free height, and then plotted against the differential head, also normalized by dividing by the free height, as shown in Figure 2.20. The figure shows that the nondimensional movements follow the loading in an almost linear fashion until the very high levels of loading which would occur during a flood event. Ranking the cofferdams response by nondimensional movements: Willow Island has the least movement, while the Trident cofferdam has the greatest, Willow Island has the largest diameter–to–height ratio, the strongest foundation, and a stabilizing berm, and it had the smallest displacement. On the other hand, the Trident cofferdam has one of the smallest diameter–to–height ratios, no interior stabilizing berm, the least foundation embedment of the sheet piles, and the greatest free height, and it has the greatest nondimensional movements. The conditions for the two stages of the Lock and Dam 26 (R) cofferdam fall in between the Willow Island and Trident cofferdams as do the nondimensional displacements.

Swatek [18] reports that in his experience the typical temporary cofferdam moves

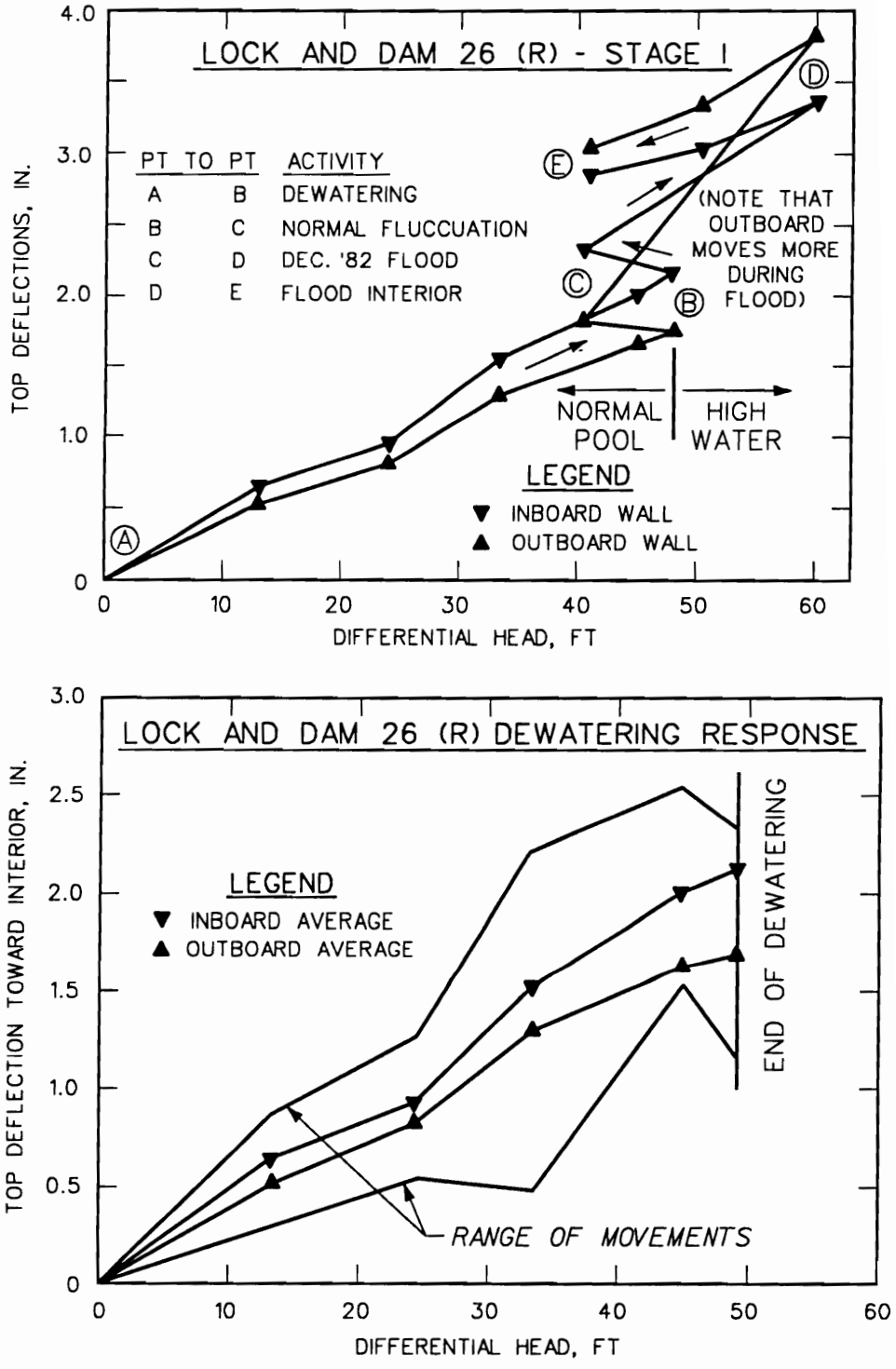

Figure 2.19: Top of cells movements for Lock and Dam 26(R) [38].

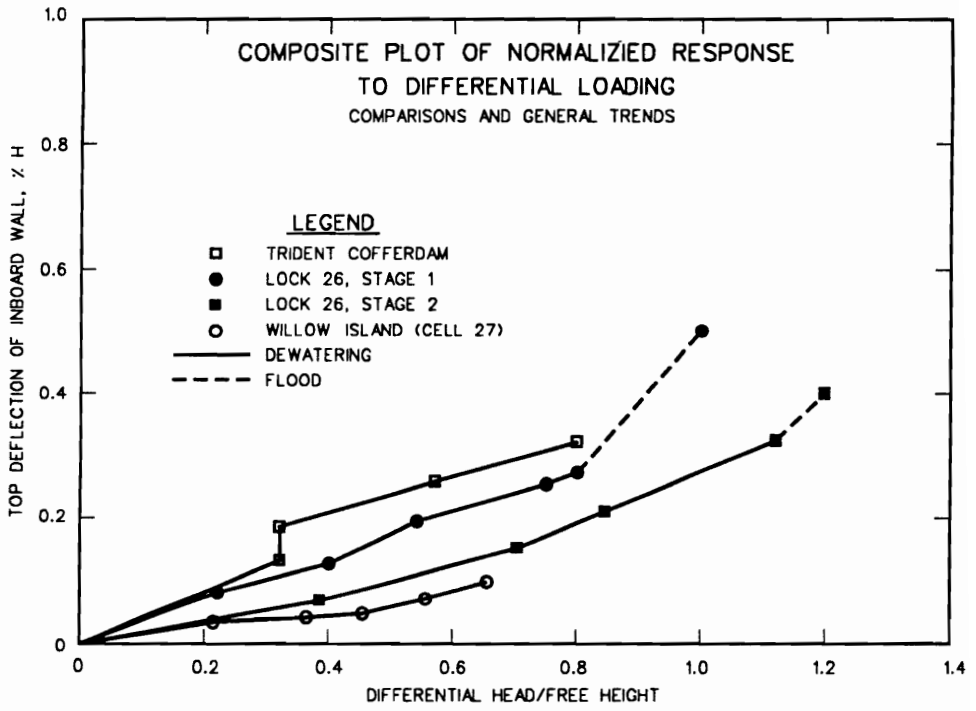

Figure 2.20: Comparison of cell movements [38].

at the top 1 percent of its free height. This would be high for the data shown in Figure 2.20, where all were less than 0.6 percent. Swatek's 1 percent would be in line if the extreme values for a flood event were considered. Two–dimensional, finite element analyses by Singh [56] show that for dewatering, the top movement of a cell should not exceed 0.5 percent of the free height, especially with the presence of a stabilizing berm. It would appear from all of the data and analyses that for a prudent design of a cofferdam on a sound foundation, a value 0.5 to 1.0 percent of the free cell height would be reasonable estimate of the top deflection of a cell.

The condition that had the most significant effect on cell behavior was the presence of a soft layer of compressible soil in the cell above the dredgeline. The movements for cells with such a compressible layer were substantially greater than those with clean sand fill. Other trends found by Martin and Clough [38] were that larger diameter–to–height ratios better the foundation conditions, and the presence of a stability berm all contributed to the lessening of the movement of the cofferdam.

One of the case histories investigated by Martin and Clough [38] was the cofferdam for Lock and Dam No. 26 (Replacement). The results from their investigation will be used in later chapters to compare to the findings of the three–dimensional finite element analyses developed for the investigation presented in this report.

2.9 Early Finite Element Analysis

The first endeavors to apply the finite element method to cofferdam analysis did not recognize the complexities in the sheet pile–soil system and, as a result, the findings were unrealistic. Kittisatra [31] used an axisymmetric model to represent a single main cell assuming that the sheet piles acted as an isotropic shell, the soil

as a linear elastic material, and no slippage could occur between the cell walls and the soil. He investigated the effects of filling the cell by a simple gravity turn–on analysis, and approximated the nonaxisymmetric loading due to a differential water level by a Fourier decomposition technique. Kittisatra's analyses predicted the maximum deflection of the sheet pile during filling to be less than 0.5 in. which was significantly less than what would normally be expected of a cofferdam [58].

Clough and Hansen [7] were the first to apply a more comprehensive soil–structure interaction finite element analysis to cellular cofferdams. They utilized a *vertical slice* model to investigate the potential of sliding failure along shale seams below the base of the Willow Island Cofferdam due to differential water loading from dewatering. The vertical slice model was based on a two–dimensional plane strain representation formed by taking a vertical section through the main cell and assuming the cofferdam to have straight walls as shown in Figure 2.21. The cell walls were modeled by structural elements with the bending properties of steel sheet piles and the inner and outer walls connected by a series of springs. These springs were used to represent the response of the cross walls of the cofferdam, thus tieing the inner and outer walls together. The stiffness of the springs was based on a sheet pile cell acting as a perfect pressure vessel. The cell fill and foundation soil were modeled with nonlinear stress–strain behavior. Slippage between the steel sheet piles and the soil was allowed though the use of interface elements.

The deformation predicted by Clough and Hansen [7] were reasonable under lateral loading, but were unrealistically small for the cell filling condition. Stevens [59] later reanalyzed the Willow Island Cofferdam with Clough and Hansen's vertical slice model using a reduced stiffness for the springs connecting the inner and outer walls. His basis for reducing the spring stiffness was to account for the gaps in the

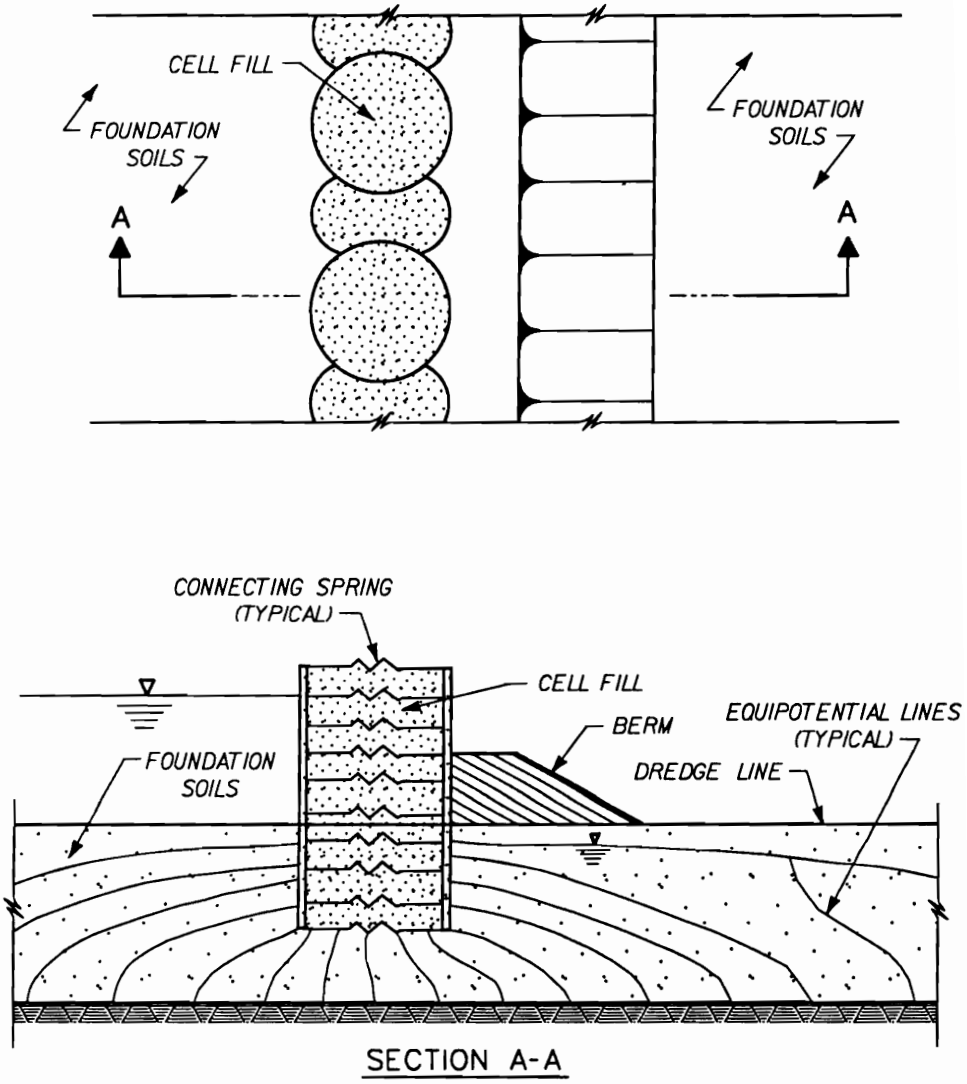

Figure 2.21: Schematic of vertical slice model [53].

interlocks [59]. This approach yielded reasonable predictions for both the lateral loading and cell filling conditions. Stevens reported that the amount of reduction of the spring stiffness was determined by comparing the predicted movements to the observed movements in a trial and error manner. No general procedure for determining the amount of reduction was proposed.

2.10 Lock and Dam No. 26 (Replacement) Cofferdams Studies

In previous applications to cellular cofferdams, the finite element method was employed as an *after–the–fact* or theoretical analysis tool. These applications served to demonstrate the potential of the finite element method for the analysis of cellular cofferdams. They constituted the initial steps in the application of the finite element method to a new problem and laid the ground work for further developments which could lead to significant benefits when applied to actual cofferdams under design or construction. The Lock and Dam No. 26 (R) cofferdam offered an opportunity to use the finite element method as an integral part of the design and performance studies. Details on these studies are provided as needed in this report for comparison and clarification of the findings from this research. An overview of the finite element studies is presented in the remainder of this section.

Initially, the finite element analysis studies for Lock and Dam No. 26(R) cofferdams were used to supplement the instrumentation effort for the first–stage cofferdam. The instrumentation program was designed to monitor key aspects of the cofferdam performance, such as, strains in the inboard and outboard sheet–pile

walls, earth pressures against the cell walls, and the deflections. Many of the parameters which were measured could not be predicted by conventional cofferdam analysis procedures. This led to the incorporation of finite element analyses into the study.

The Corps recognized that the cellular cofferdam is a three dimensional problem, but time and funding constraints required that some form of two–dimensional approach would be taken first. These results would be available before the completion of construction of the first–stage cofferdam. The approach used three different two–dimensional models which incorporated many of the key facets of cofferdam behavior [8, 33, 53]. Each of the two–dimensional models endeavored to investigate different features in the cofferdam construction and operation. Two of the three approaches were developed specifically for this project. The models were referred to as the axisymmetric, the horizontal slice, and the vertical slice models. A brief description of the models is given in Table 2.2, along with their advantages and disadvantages. Schematically, the models are shown in Figure 2.21, Figure 2.22, and Figure 2.23.

The vertical slice model used in this study was essentially the same as the one proposed by Clough and Hansen [7] and allows for the analysis of the entire construction and loading history of the cofferdam. The axisymmetric model allowed a comprehensive analysis of the filling process of a isolated main cell. In contrast to previous works, a more realistic representation of the cell fill, steel sheet piles, and their interaction was employed. The horizontal model was based on a generalized plane strain analysis of a horizontal section cut through the cofferdam. This approach assumes that a constant strain exists in the out of plane direction resulting from the vertical gravity loads above the plane. The model was proposed to allow

Table 2.2: Two–Dimensional Finite Element Models [8]

Model	Purpose	Advantages	Disadvantages
Axisymmetric	Provide data on effects of filling isolated cell	• Simple to perform • Accounts for effects of cell embedment • Provides data on location of maximum deflection and interlock tension upon filling	• Does not consider effects of stage other than filling • No cell interaction
Vertical Slice	Provides data on loading stages other than filling	• Can consider effects of all stages of loading • Provides data on history of behavior from filling to flood stages	• Time consuming to perform if loading is complex • Does not consider 3-D loadings effects
Generalized Plain Strain	Provides data on interaction between cells during filling	• Simple to perform • Accounts for interaction of cells • Provides data on common wall and connection behavior	• Does not consider influence of dredgeline support • Considers only effects of uniform cell filling

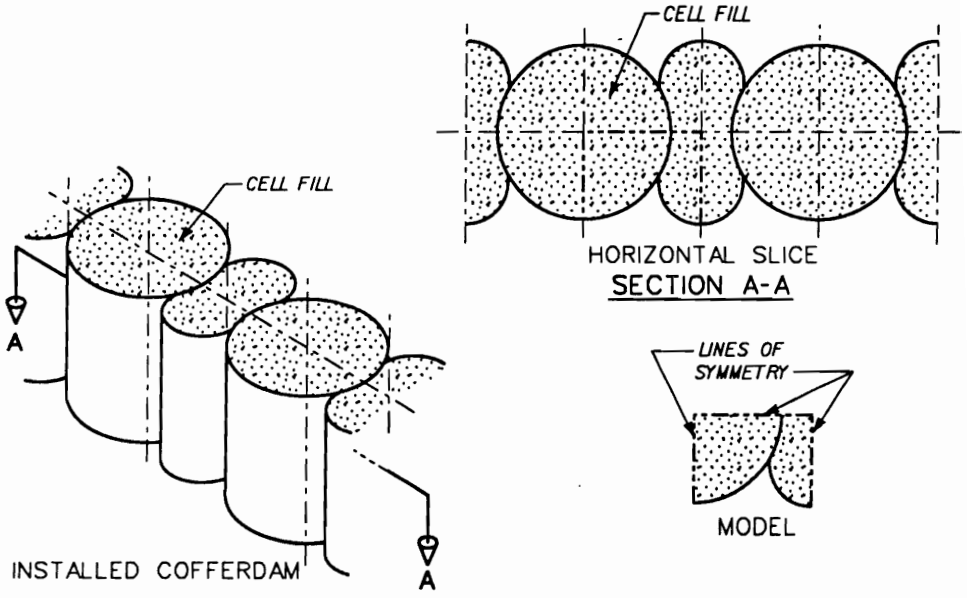

Figure 2.22: Schematic of horizontal slice model [53].

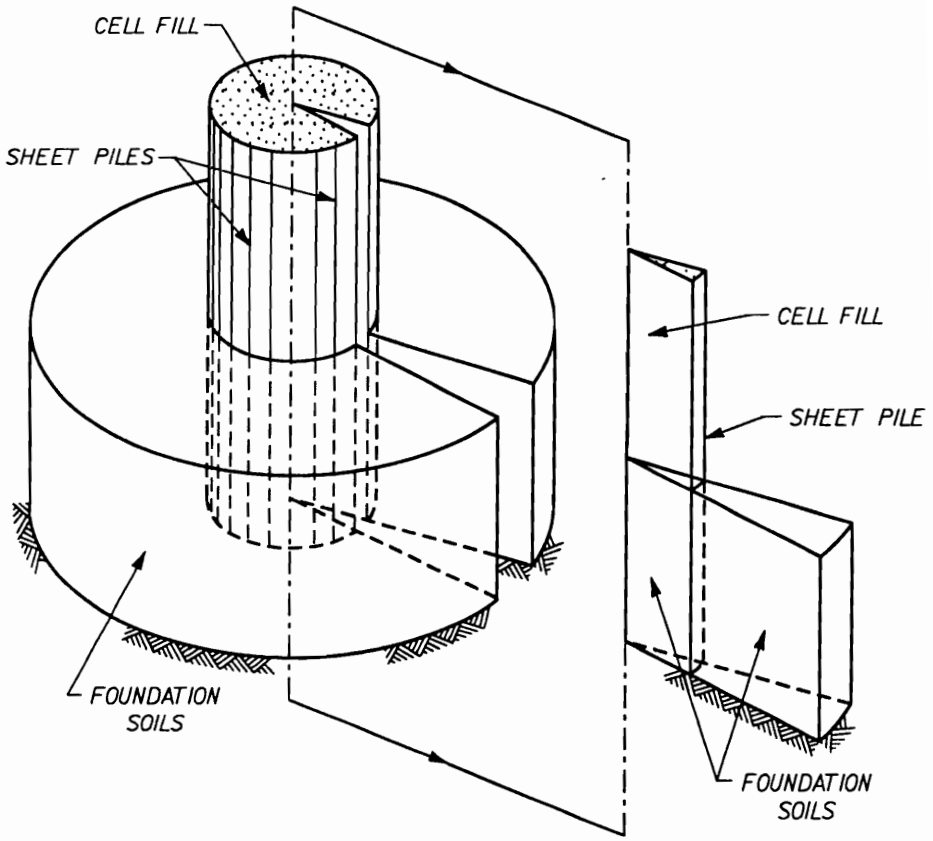

Figure 2.23: Schematic of axisymmetric model [53].

a means of analyzing the interaction between the main and arc cells under uniform filling. Interlock stresses and cell deformations for the main and arc cell walls, the common wall, and the wye connection of the main and arc cells were calculated using this model. This model is unable to account for the lateral support provided by the foundation near the dredgeline. Thus, the model is applicable only to the upper two–thirds or so of the cell where the foundation has a limited effect. The loading conditions for this model are oversimplified in that it assumes the filling of the main and arc cells are done simultaneously which is not the normal construction procedure used in the filling process.

All three of the models were analyzed with three different versions of the computer program *SOILSTRUCT*, developed by Professor G. W. Clough and his–coworkers for the investigation of soil-structure interaction problems. *SOILSTRUCT* allowed the incorporation of the incremental loading and construction, nonlinear soil behavior, slippage between the materials, and yielding of the sheet–pile interlocks.

As previously mentioned, Stevens [59] correctly recognized that the steel sheet piles forming the cells cannot be represented as an isotropic linear elastic pressure vessel. Imperfections and yielding of the interlock connections reduce the horizontal stiffness of the sheet–pile membrane. For the Lock and Dam No. 26(R) study, Clough and his associates introduced the E–ratio concept, where the modulus and/or stiffness of steel sheet piles in the horizontal direction is reduced from that of steel. The E–ratio concept evolved from the axisymmetric model where the sheet piles were represented as an orthotopic membrane with a reduced modulus in the radial direction. The E–ratio concept and supporting experimental data will be presented and discussed in more detail in subsequent chapters. With this reduction in the stiffness of the sheet piles in the horizontal direction, Clough and his associates

were able to accurately simulate the interlock behavior, Figure 2.24. This led to a reasonable model of the cell deformation, Figure 2.25, for the first–stage cofferdam at Lock and Dam No. 26 during filling.

With the use of the finite element results and the instrumentation data, Clough and his associates discovered a number of important points with regard to the behavior of sheet–pile cellular cofferdams. First and most significant, was the influence that the flexibility of the sheet–pile system had on the interlock forces. Since the sheet–pile system is flexible, the cells bulge considerably during filling, Figure 2.26, allowing the cell fill to mobilize its shear strength. This results in a lower lateral earth pressure applied to the sheet–pile walls (Figure 2.27), and thus, yielding lower interlock forces in the sheet piles (Figure 2.28). Second and the primary objective of the investigation, the interlock forces in the common wall were significantly less than that used in the design. The TVA secant formula over predicted the interlock forces in the common wall, Figure 2.29.

Following the initial finite element investigation for the first stage cofferdam at Lock and Dam No. 26(R), additional studies have been conducted to evaluate proposed design changes in subsequent cofferdam stages. One of these additional studies investigated the minimum allowable depth of penetration into the river bottom for the sheet piles. Another compared clam shell filling of the cells with hydraulic dredge filling. Finally, the investigation reported hereto is a continuation of these efforts.

To further capitalize on the Lock and Dam No. 26 (R) efforts, the Corps of Engineers funded a research program on sheet–pile cellular cofferdams. To date, reports by Martin and Clough [38] on the effects of differential loadings on cofferdams, Singh [56] on two–dimensional finite element analysis of cofferdams, and Wu

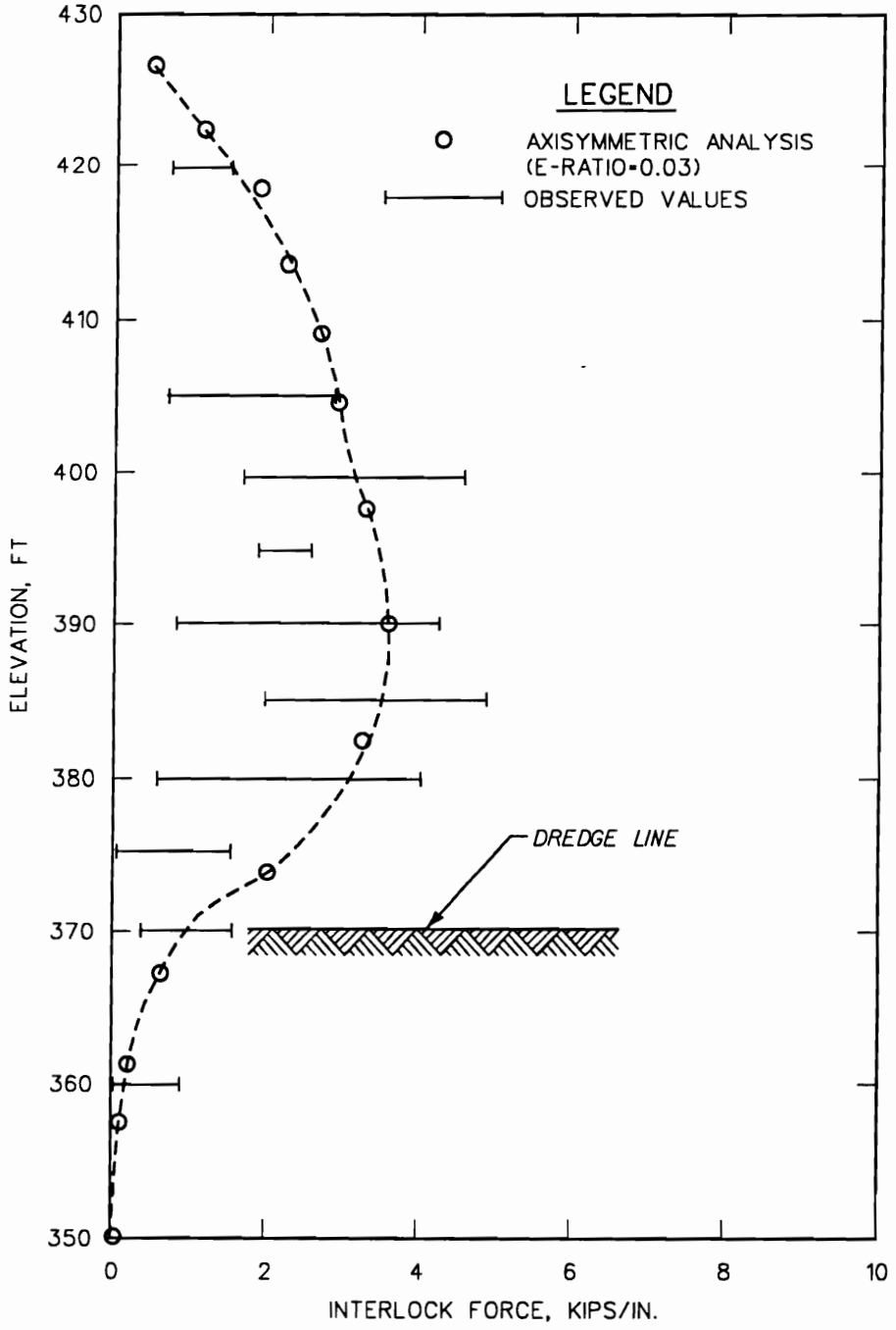

Figure 2.24: Lock and Dam No. 26(R) sheet–pile interlock forces [55].

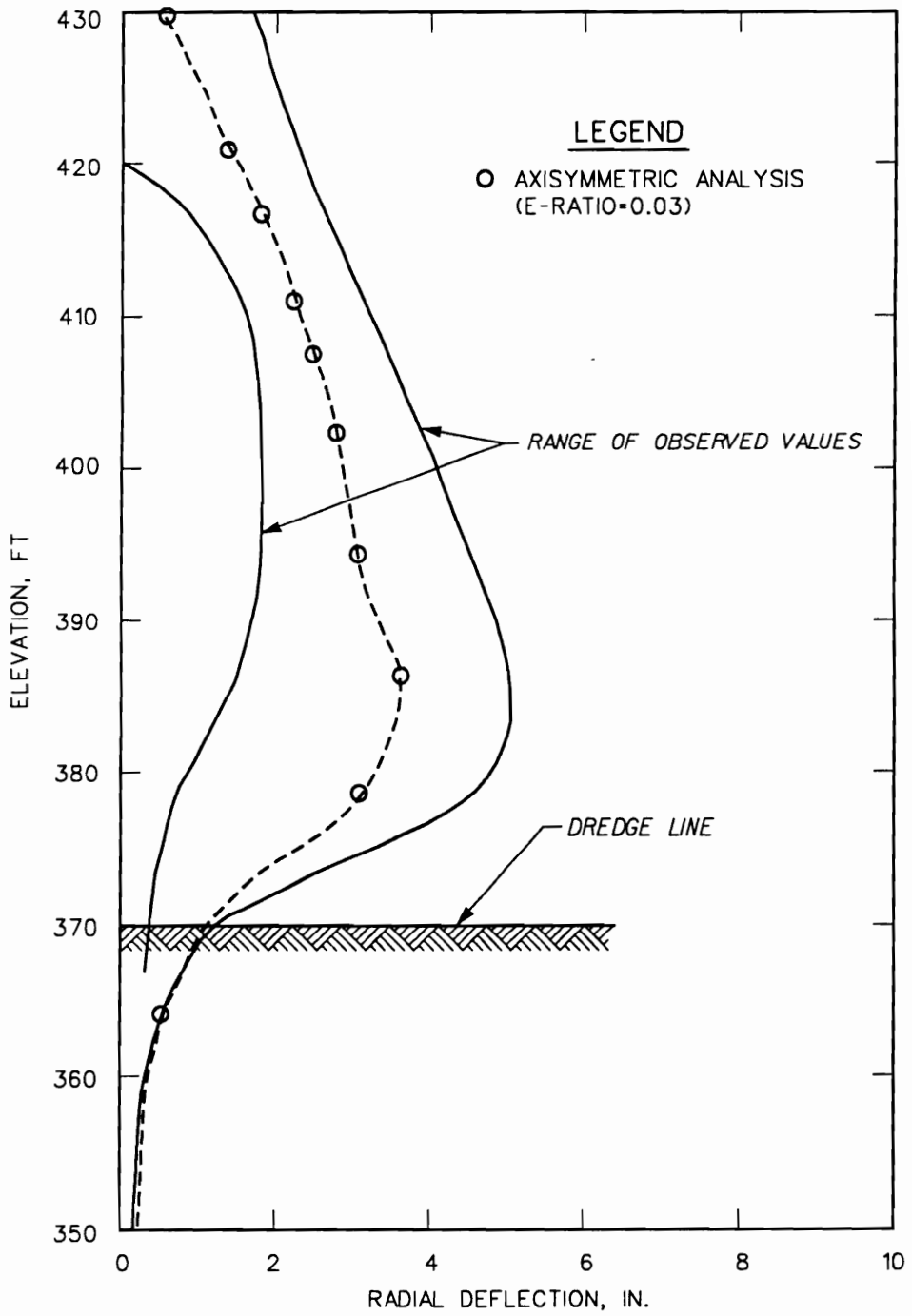

Figure 2.25: Lock and Dam No. 26(R) sheet–pile deflections [55].

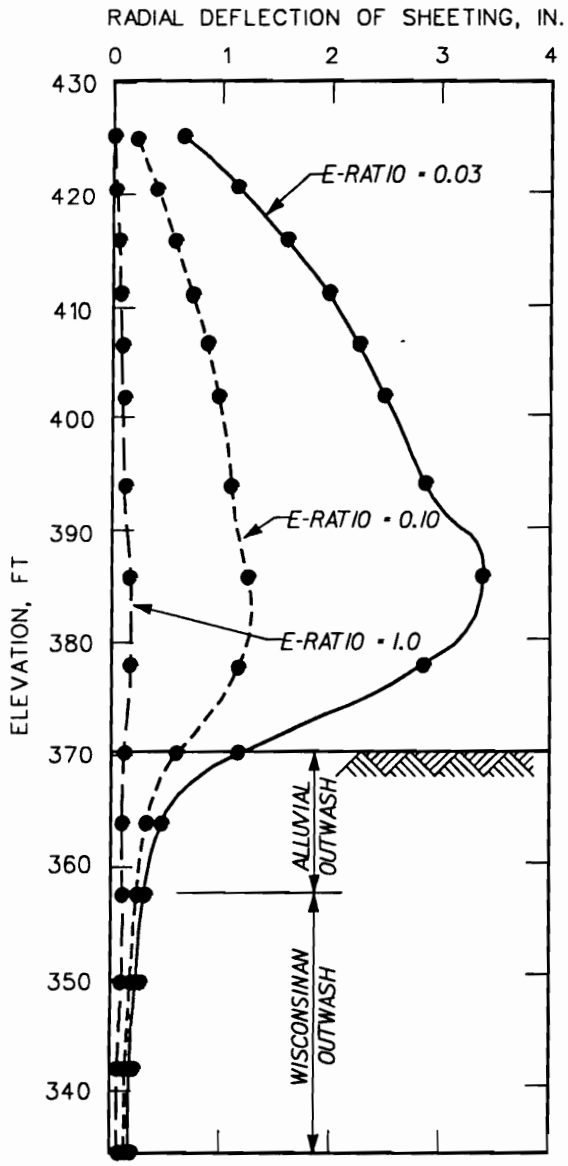

Figure 2.26: Lock and Dam No. 26(R), effects of E–ratio of sheet–pile deflections [53].

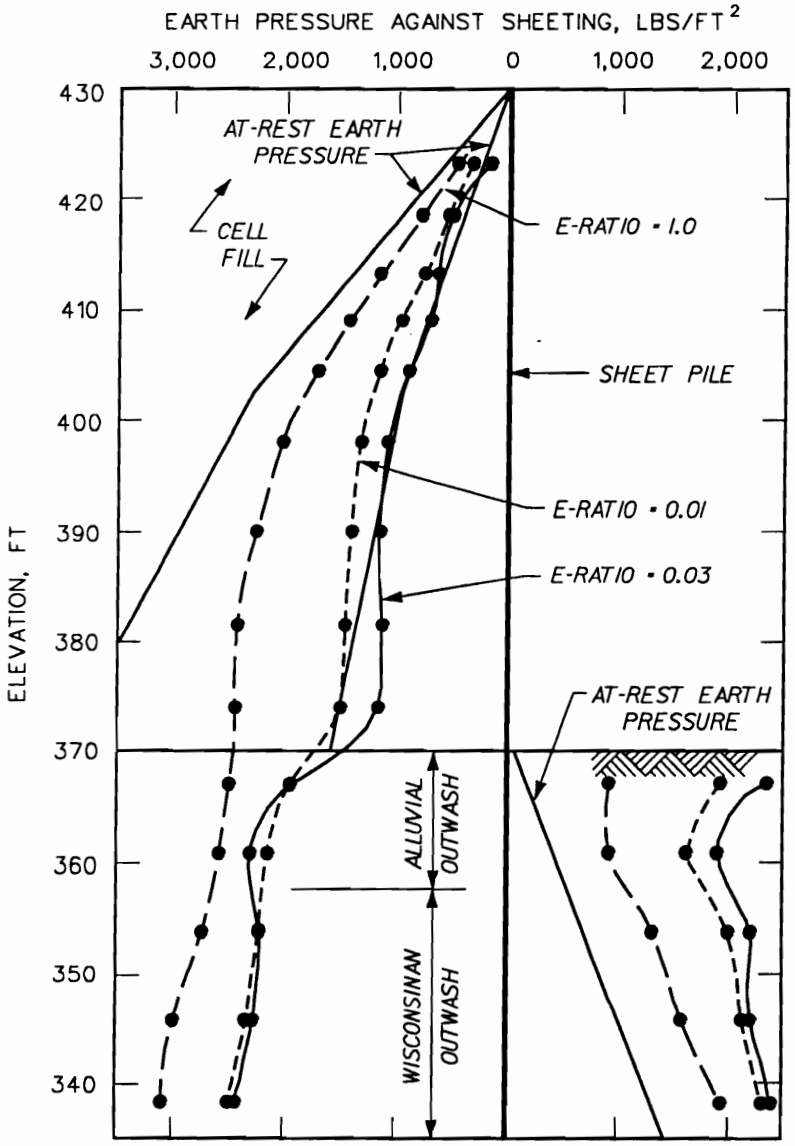

Figure 2.27: Lock and Dam No. 26(R), effects of E–ratio on earth pressures applied to sheet piles [53].

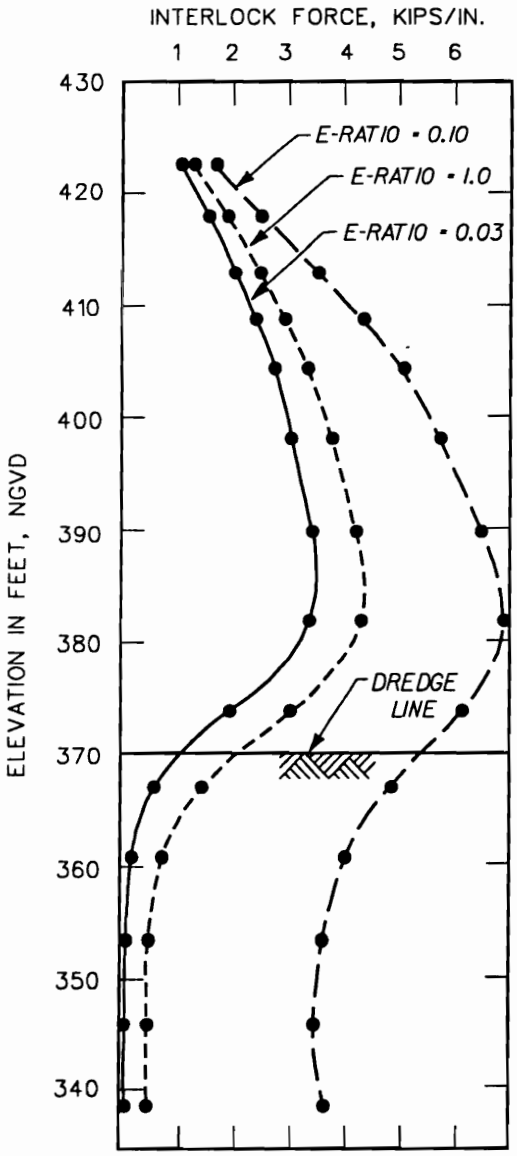

Figure 2.28: Lock and Dam No. 26(R), effects of E–ratio on sheet–pile interlock forces [53].

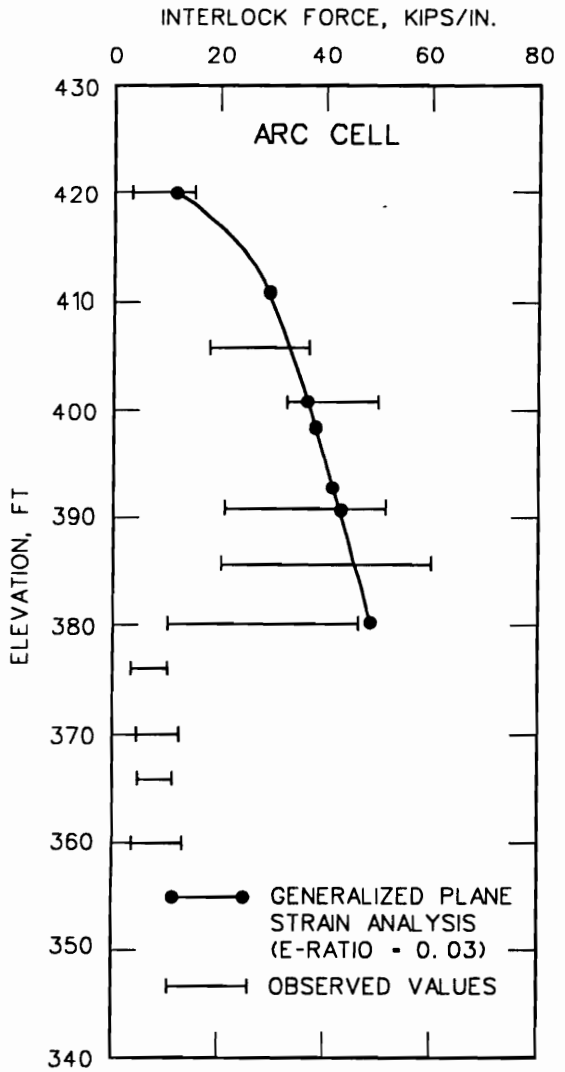

Figure 2.29: Lock and Dam No. 26(R), interlock forces in sheet piles as predicted from horizontal slice analysis [55].

and Barker [64] and Huang and Barker [26] on sheet–pile interlock connections have been produced under this research work.

2.11 Summary and Recommendations

For many years, sheet–pile cellular cofferdam technology had remained relatively unchanged. The conventional design methods for evaluating internal and interlock stability were developed in the 1940's and 1950's from field and limited experimental observations and were semiempirical in nature. As a result of the inability of the earlier investigators to determine the deformations and stresses in the cell fill, no one single method of analysis/design was universally accepted. Instead, the factor of safety for internal stability is checked by all the methods, each with inherent empiricalisms associated with its development. As for interlock stability, the problem in determining stresses in the cell fill is reflected in the almost arbitrary choices of lateral earth pressure coefficient and the shape of the pressure distribution applied to the cell walls. The lateral earth pressure coefficient for these various methods may range from an active value to one greater than the at–rest value depending upon whether it is used in a resistance or driving force.

No actual determination of the stress field in the cell fill is ever made in these conventional methods. The analytical techniques of the day were unable to account for the complexities involved. The procedures used only rudimentary concepts of soil–structure interaction which do not exhibit the true response of the cofferdam for most circumstances. Furthermore, they made no attempt to determine the possible cofferdam deformations that could be expected under the various loading conditions. This last deficiency turns out to be an important missing aspect in predicting

performance when deformations must be limited or when the deformations are used to monitor the field performance of the cofferdam.

Computational capabilities have greatly improved since the early investigators of cofferdams did their work. Many of the complexities they had to ignore or crudely approximate can now be considered more realistically through the use of the finite element method. Early efforts in the finite element analysis of cellular cofferdams were performed without due consideration of the soil–structure interaction involved in the sheet pile–soil system. Clough and his associates [7, 8] have demonstrated that with proper consideration of the soil–structure interaction effects, the finite element method can be a powerful tool for the investigation of cellular cofferdam behavior. The finite element method provides a means to predict cofferdam deformations which were lacking in previous methods.

To date, the finite element analyses have been performed on two–dimensional models which focus on specific facets of cofferdam behavior. A sheet–pile cellular cofferdam has three–dimensional loadings and configuration which may have a significant effect on its response. In the past, the three–dimensional effects have been largely neglected, or only grossly considered, because no practical tools were available to incorporate them in a rational manner. Conventional design procedures are based only on the simplest forms of two–dimensional configurations and loading assumptions. The recent application of two–dimensional finite element models to the Lock and Dam No. 26(R) cofferdam have achieved considerable success in predicting certain aspects of the behavior, in particular, the deformations and interlock forces in the sheet piles during filling. Importantly, it was found in the Lock and Dam No. 26 (R) investigation that most conventional techniques were overly conservative and led to more costly designs. However, universal implementation of

the findings of these analyses is difficult to justify since uncertainties remain about the assumptions made in arriving at the two–dimensional models.

The only way to address these uncertainties is perform a three–dimensional analysis. The basic technology for three–dimensional modeling exists for the finite element method, but the technology had not been developed to the same degree of sophistication as it has been for two–dimensional soil–structure interaction problems. The development of a three–dimensional finite element code to analyses sheet–pile cellular cofferdams requires a significant research effort. Once developed, the model would allow a much more complete assessment of the validity of existing cofferdam analysis and design procedures than hereto were possible. Specific items of interest are:

- Nonuniform filling of the main and arc cells.
- Effects of differential loading.
- Regions of validity of two dimensional models.

It is important to note in regard to the last item mentioned that the three–dimensional finite element code is not an end in itself. Instead, it will be the tool which can be used to define where simpler two–dimensional models can be applied with confidence and where they cannot.

Chapter 3

Basic Finite Element Code

3.1 Introduction

This chapter presents the reasons for developing a new three–dimensional soil–structure interaction finite element code, states the philosophy behind its development, lists the required capabilities for the code, and describes the basic code that was modified to create a new code. In the subsequent chapters, the specific aspects of the development of the code for soil–structure interaction analysis of sheet–pile cellular cofferdams are presented.

It was established in Chapter 2 that one of the major deficiencies with procedures for cofferdam analysis prior to the application of the finite element method was their inability to determine the stress field in the cell fill. The reason for this was the complexity of the geometry, the nonlinear soil behavior, the sheet–pile interlock response, and the interaction between the soil and sheet piles. The finite element method allows us to account for many of these factors. The application of the

method for the Lock and Dam No. 26 (R) cofferdam has demonstrated its value for sheet–pile cellular cofferdams [8, 33, 53].

The sheet–pile cellular cofferdam is a complex structure. The geometry of the main and arc cells and the loadings applied to them are truly three–dimensional in nature and cannot be easily simplified into a two–dimensional representation. In previous finite element studies, the true three–dimensional nature of the sheet–pile cellular cofferdam has been only partially considered or considered only in a simplified form. An axisymmetric model was used by Clough and Kuppusamy [8, 33] to provide a realistic depiction of the three–dimensional response of a single isolated main cell during its filling. Although this model gives a three–dimensional response, it applies only to one aspect of the cellular cofferdam. The horizontal slice model described by Clough and Kuppusamy [8, 33] for the Lock and Dam No. 26 (R) study was aimed at determining the influence on the interlock stresses in the common wall due to the combination of filling the arc cell and main cell. As pointed out in Chapter 2, this model assumes uniform filling of the main and arc cells which contradicts normal construction practice where the main cell is filled first. This representation is further limited by not accounting for the influence of foundation confinement.

The preceding discussions, here and in Chapter 2, support the need for a full three–dimensional analysis of the sheet–pile cellular cofferdam problem. It would be impossible to perform a three–dimensional analysis of the cellular cofferdam problem with closed–form classical continuum mechanics procedures and still maintain the level of complexities and sophistication needed to understand the actual behavior of the cofferdam. The basic technology for three–dimensional modeling exists for the finite element method. The major reason for avoiding a full three–dimensional finite element analysis by previous investigators has been the high cost of the computer

resources and man power. Even with the advances in computer technology and the advent of the *supercomputer*, a nonlinear, three–dimensional, finite element analysis is not for the person with limited funds or a tight schedule.

One of the major decisions faced in undertaking a three–dimensional finite element analysis is whether any of the existing general–purpose finite element codes such as SAPIV, NONSAP, ADINA, NASTRAN, or ABACUS, among others, could be used for the study. Unfortunately, as general as these codes may be, they were developed with a certain class of problems in mind. None of the general–purpose codes could directly be applied for the cofferdam analysis and would require extensive modifications before they could be used. These codes lacked one or more of the following modeling capabilities necessary for the analysis of a cellular cofferdam: nonlinear soil behavior, incremental fill placement, initial gravity stress generation, interface elements, seepage effects, and construction simulation. In addition, these codes contain numerous other sophisticated options not needed for the cofferdam analysis. Furthermore, the commercially available codes require a payment of fees for their use and are difficult, if not impossible, to modify. It was concluded that although the technology for a three–dimensional finite element analysis of the cofferdam problem existed, to utilize it would require the development of a new code designed specifically for the unique aspects of the cofferdam problem.

3.2 Philosophy

The philosophy for developing the new three–dimensional finite element code was to do only the things necessary to have a functioning code which could be verified and documented rapidly so that it could used to test critical phases of the Lock and Dam

No. 26(R) cofferdam. Also, the modeling procedures were to be kept in line with the two–dimensional codes used in earlier cofferdam studies when possible, so that the two–dimensional codes could be validated. Attempts at implementing complex constitutive models for the soil, interfaces, and sheet piles would be avoided so as not to distract from having a functioning code as fast as possible. Yet, the code would be kept flexible so that changes could be made in the future.

3.3 Necessary Capabilities

Once it was decided to develop a code and a philosophy was established, the next step was to formulate the necessary requirements for the code. In keeping with the development philosophy, the capabilities of the two–dimensional code, **SOIL-STRUCT**, were used to form the initial requirements for the three–dimensional code.

To accurately model a sheet–pile cellular cofferdam through its construction and operation, the key aspects that are fundamental to its behavior must be represented as closely as possible. It was felt the code should have the capability to:

- Model the geometry of the cellular cofferdam.
- Model the anisotropic response of the sheet–pile assemblage.
- Model the interaction between the sheet piles and the soil.
- Model the nonlinear response of the soil.
- Determine the initial state of stress in the soil prior to construction.
- Simulate the process of construction of the cellular cofferdam.

- Model the various events experienced during the operational of the cofferdam.

To simulate these aspects, a number of features were required in the code.

The geometry of a sheet–pile cellular cofferdam is complex and does not allow subdivision into simple straight sided brick sections. Looking at a plan view of a cellular cofferdam, Figure 3.1, it is clear that subdividing the main cell and arc cell with elements having only a linear variation between corners (straight lines) would require a large number of elements to approximate the curved geometry. Based on this observation, it was necessary to have higher order isoparametric elements included in the new code's element library to allow the actual curved shape of the cell geometry be considered without requiring an excessive number of elements.

An essential capability for any finite element code used to perform soil–structure interaction analysis is the ability to allow relative movements to occur on the interface between different materials. Typically, this is accomplished through the use of an interface element.

Again looking at a plan view of a main and arc cell, it can be seen that describing the geometry of the connection of the main cell and the arc cell sheet piles would be difficult using any type of three–dimensional solid element, such as a 20–node brick element. Also, the cross–sectional thickness of the sheet piles is only about 0.5 in. Using a solid element to model the sheet piles would require a relatively small thickness when compared with the other dimensions which would lead to the possibility of an ill–conditioned stiffness matrix for the system. For this reason, it was necessary to include a shell and/or membrane element in the element library to model the sheet piles.

As previously mentioned, Stevens [59] correctly recognized that the steel sheet piles forming the cells cannot be represented as an isotropic linear elastic pressure

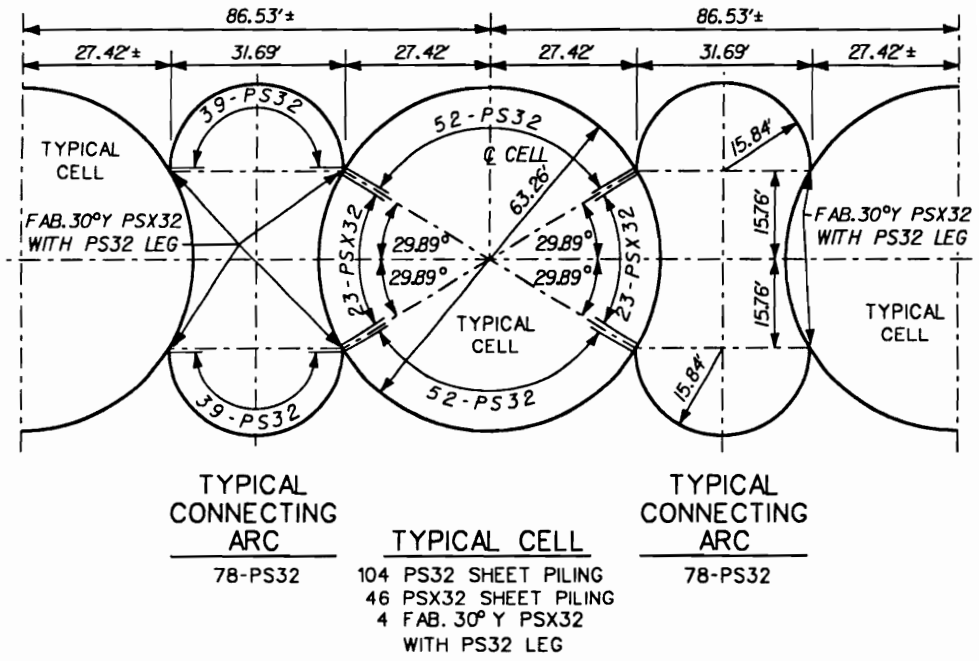

Figure 3.1: Plan view of main and arc cells.

vessel. Imperfections and yielding of the interlock connections reduces the horizontal stiffness of the sheet–pile membrane. Clough and his associates [8, 33, 53] have further demonstrated the necessity to reduce the stiffness of the steel sheet piles in the horizontal direction to account for this phenomena. Thus, the shell and/or membrane element representing the sheet piles in the three–dimensional code should be anisotropic to allow for a different Young's modulus value in the tangential direction.

Soils are known to have complex stress–strain response. For example, consider the stress–strain curves for a sand shown in Figure 3.2. For primary and/or initial loading, the soil response can be represented by a nonlinear curve which is a function of the confining stresses and the strength parameters of the soil. During unloading or reloading, the soil has a hysteretic behavior. If reloading is greater than previous stress levels, response will follow the nonlinear primary curve until failure of the soil is reached. Each of these behaviors is governed by the basic material characteristics as well as the magnitudes of the principal stress difference, the confining stress, and the stress history. To capture the key aspects of the soil behavior, a nonlinear constitutive model for soil had to be incorporated into the code.

The in situ stresses and the changes in stresses play a significant role in the deformation response of the soil. The use of a nonlinear constitutive relationship for the soil requires the implementation of procedures to allow determination of stresses from preconstruction through major flooding events. The initial stress conditions prior to construction have to be computed to determine initial stress–strain response of the soil mass. Procedures had to be provided that would model the application of loads to the finite element model in an incremental manner and allow each soil element to adjust its modulus values in accordance with the stress level at that instant in the load sequence. Also, it was recognized that care had to be taken to

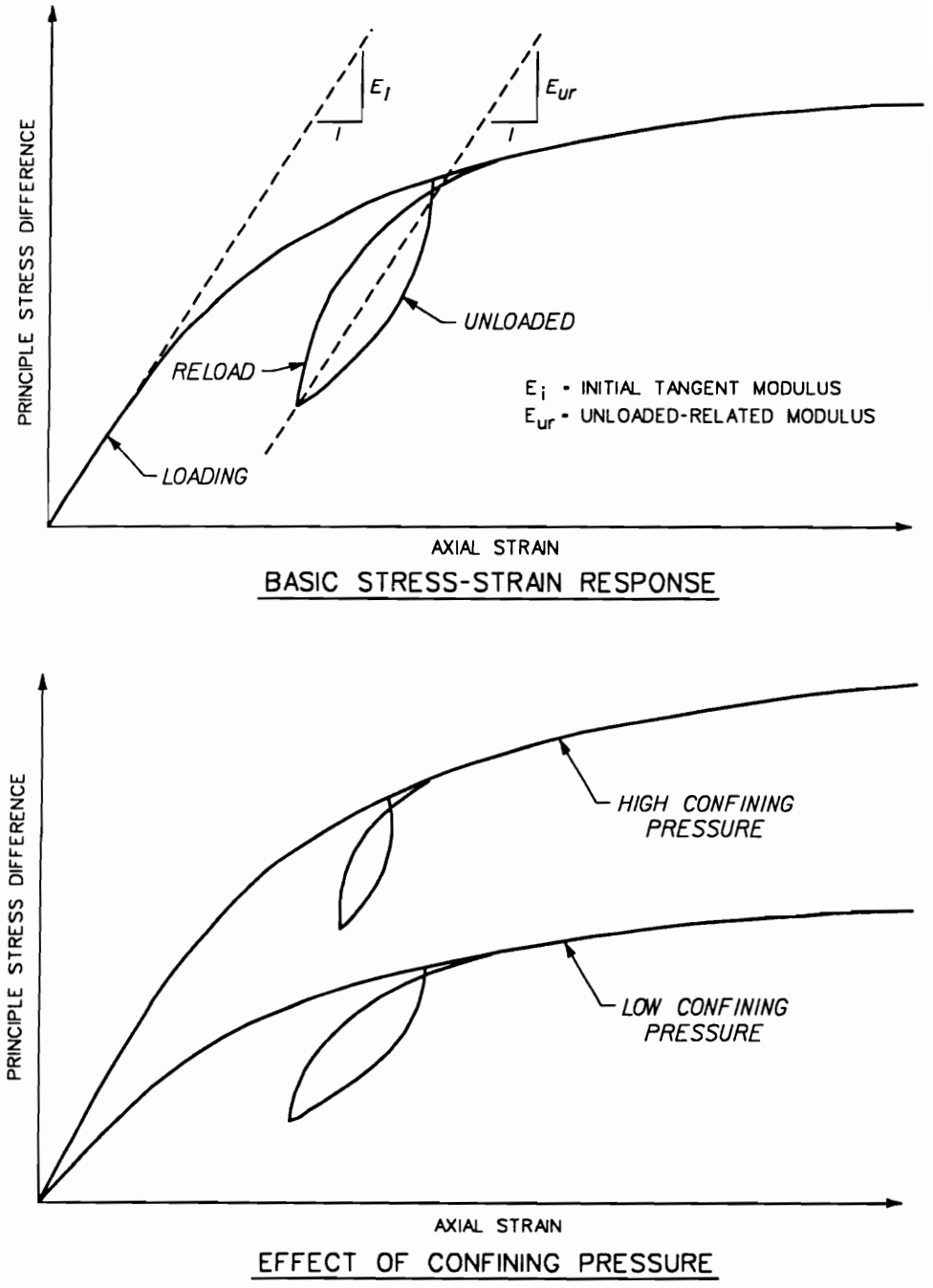

Figure 3.2: Stress–strain behavior of sand [53].

ensure that the stress changes caused by an increment of loading were small enough for the adjustment to moduli at the end of each increment to allow an accurate representation of the stress–strain response of the material.

Procedures had to be created to simulate the construction process of the cofferdam. This includes the placement of the sheet pile and cell fill, dewatering of the interior of the cofferdam, placement of the berms, and raising of the river level on the exterior of the cofferdam. To accomplish this, the code needed the capability to handle concentrated nodal loads and displacements, surface pressure loadings, and the application of body forces. These are common to many finite element codes, but special procedures had to be implemented in the new code to allow them to be use to efficiently in the simulation of the construction and operation of a sheet–pile cellular cofferdam.

3.4 Development Scheme

Knowing that the development of a three–dimensional finite element code would require a significant effort in both time and money, consideration was given to modifying an existing code that had some of the features needed for the cofferdam analysis. The code under consideration was developed by Kasali and Clough [29] for the analysis of advanced and conventional shield tunneling procedures. Many of the same questions and concerns set forth in this investigation were also considered by Kasali and Clough [29]. It was decided that modification of this code would be the most expedite way to develop a new code for this cofferdam study.

3.5 Description of Existing Code

The code developed by Kasali and Clough [29] was written for the analysis of shield tunneling in soft ground. It used some of the existing general–purpose codes as a guide but focused only on those aspects needed for the tunnel model. The code was written in a form suitable for extension. In this section, the major components of Kasali and Clough's code are described along with some of its limitations for a cofferdam analysis.

3.5.1 Element Types

Kasali and Clough's code had a general three–dimensional isoparametric or subparametric solid element which may have from 8 to 21 nodes, Figure 3.3, with three degrees of freedom at each node. The element is commonly referred to as a variable node element. While in its eight–node form, the strains and, hence, stresses are constant across the element. For other forms of the element, the strains and stresses will vary linearly along a side or across a face of the element depending upon the actual number of nodes per side or face. A major advantage of this element is that the 20–node form of the element can be used in areas of high stress gradients or curved geometry for greater accuracy. The variable nodes form of the element can be used to transition to the eight–node form of the element in areas with smaller stress gradients and linear geometry exist. This element was used in Kasali and Clough's work [29] to model the soil as a solid, brick–type element and the tunnel liner as a thick shell element.

One limitation of the element library in the code was that no solid wedge elements were available. After attempting to generate the first finite element mesh for the

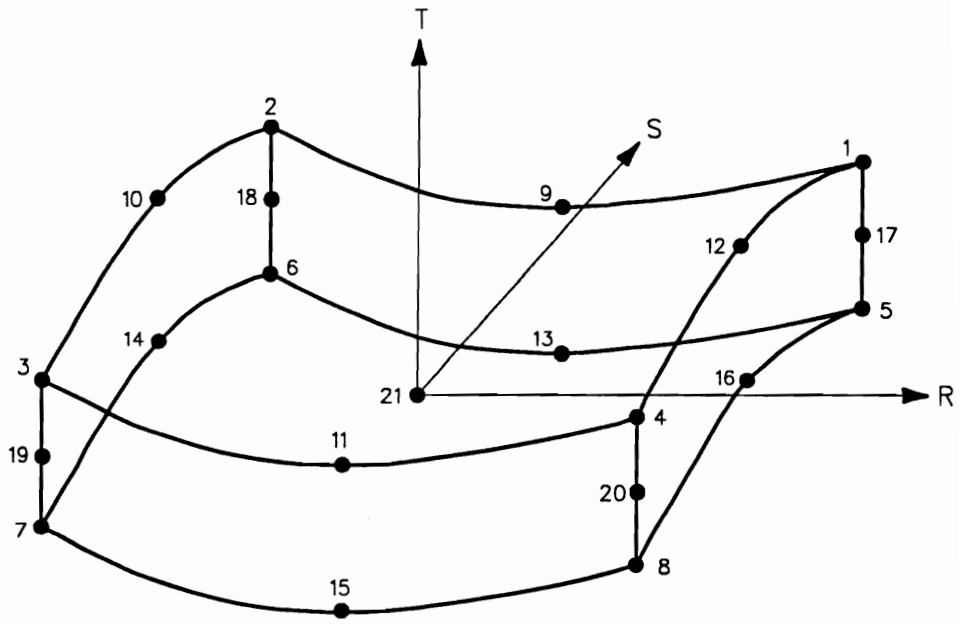

Figure 3.3: Eight to twenty–one variable number of nodes element [29].

cellular cofferdam, it was clear that solid wedge elements were necessary (Figure 3.4). The description of the formulation and implementation of the solid wedge element is presented in Chapter 4.

3.5.2 Stress and Strain Response

The only constitutive relationship incorporated into the Kasali and Clough code was for isotropic linear elastic behavior. The code was written with the intention of incorporation of a nonlinear constitutive model in the future, but that had not been done at the time of this study. The code had an isotropic linear elastic stress-strain relationship given by

$$\{\sigma\} = [D]\{\epsilon\} \tag{3.1}$$

where $\{\sigma\}$ is the stress vector, $[D]$ is the stress-strain matrix and $\{\epsilon\}$ is the strain vector. This can be written in matrix form as:

$$\begin{Bmatrix} \sigma_x \\ \sigma_y \\ \sigma_z \\ \tau_{xy} \\ \tau_{yz} \\ \tau_{xz} \end{Bmatrix} = \frac{E}{(1+\nu)(1-2\nu)} \begin{bmatrix} D_1 & \nu & \nu & 0 & 0 & 0 \\ \nu & D_1 & \nu & 0 & 0 & 0 \\ \nu & \nu & D_1 & 0 & 0 & 0 \\ 0 & 0 & 0 & D_2 & 0 & 0 \\ 0 & 0 & 0 & 0 & D_2 & 0 \\ 0 & 0 & 0 & 0 & 0 & D_2 \end{bmatrix} \begin{Bmatrix} \epsilon_x \\ \epsilon_y \\ \epsilon_z \\ \gamma_{xy} \\ \gamma_{yz} \\ \gamma_{xz} \end{Bmatrix} \tag{3.2}$$

where E is the modulus of elasticity, ν is Poisson's ratio, $D_1 = (1-\nu)$, and $D_2 = 1/2\,(1-2\nu)$. It was necessary to alter this form of the stress–strain matrix for the implementation of the nonlinear analysis needed for the cofferdam model. The description of the implementation is presented in a later chapter.

The strains and stresses are computed at Gaussian integration points as well as at the center of the elements. The code computes the principal stresses from the

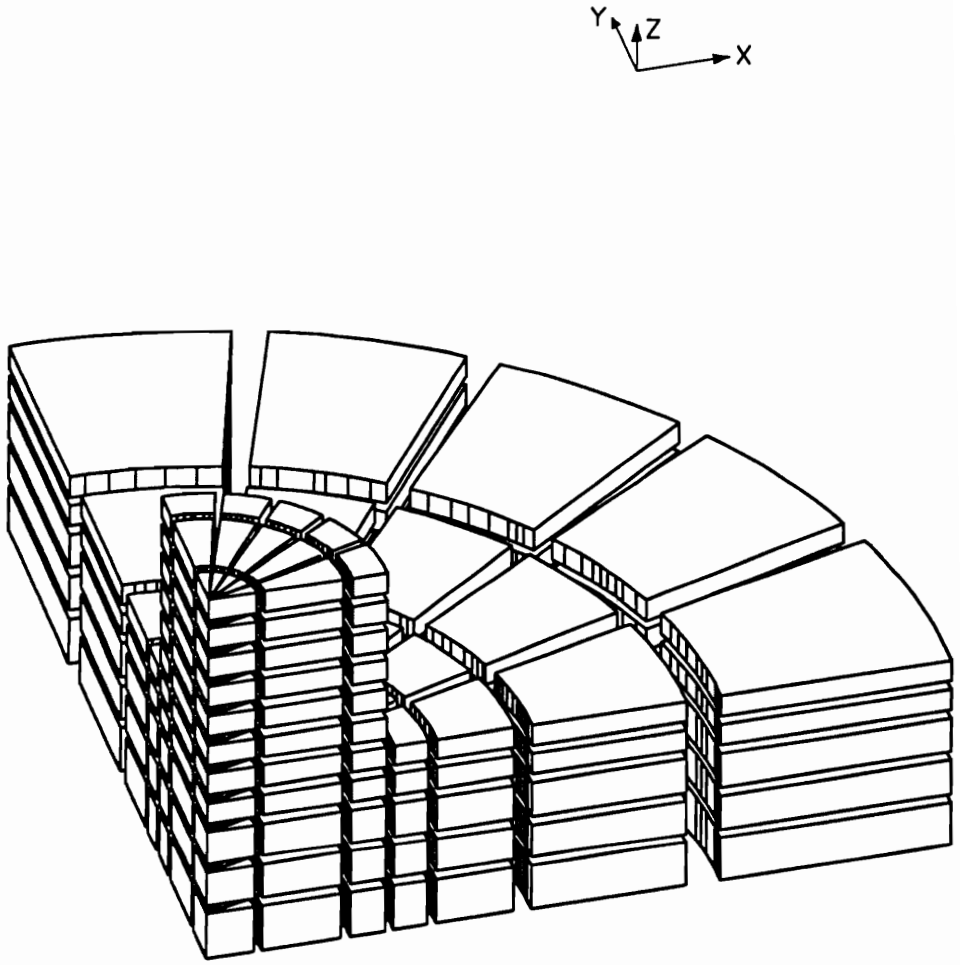

Figure 3.4: Quarter model of main cell of a cofferdam.

general state of stress by the goniometric method [29]. The code also determines the directional cosines for the three principal stresses.

3.5.3 Boundary Conditions

The finite element method for displacement problems has only two permissible ways to apply the boundary conditions, prescription of nodal displacements and concentrated nodal loads. Consequently, forms of loading such as gravity action and pressures assigned to element surfaces must be reduced to equivalent nodal forces before a solution can be found. When the isoparametric element principle is employed in the finite element code, the calculation of equivalent nodal forces is not a process that can be easily performed manually, since area or volume integrations over arbitrarily shaped regions are generally involved. Hence the equivalent nodal forces, due to pressures and body forces cannot be computed for direct input. Inclusion of special procedures for performing these tasks is necessary.

Like any basic finite element code, the Kasali and Clough code has the capability to consider applied concentrated nodal loads or displacement, but in addition it has the ability to handle surface pressure loadings. This is useful in the modeling of the application of water pressures to the cells.

3.5.4 Equation Solver

The storage of the stiffness matrix and the efficiency of the equation solver are important considerations when attempting a three–dimensional finite element analysis. A significant portion of the required computer memory for a finite element code is devoted to the storage of the stiffness matrix. If core memory is limited,

the stiffness matrix may have to be stored on peripheral devices and brought in and out of core during the reduction and back substitution operations. The time required to accomplish these steps is generally far greater than the time required to perform these mathematical operations in–core. Therefore, Kasali and Clough [29] chose an in–core solver for their code. To minimize storage, they used a method called the *skyline* or *profile* storage scheme. Because of the characteristic sparsity of the stiffness matrix formed by the finite element method, the method stores the stiffness matrix by stringing each active portion of the column of the banded matrix compactly into a vector. Where the active portion of a column has only entries associated with that degree of freedom of the system. One advantage of the profile scheme of storage over the typical banded scheme is that it always requires less storage. The only exception to this is when the stiffness matrix is diagonal in which case the storage requirement will be the same. For the type of constitutive relationship use in this investigation, the stiffness matrix is symmetric which allows for storage of only the diagonal entries and nonzero entries above the diagonal. Three–dimensional finite element analyses have a large number of unknowns associated with them. The use of an in–core solver required the use of a supercomputer for this investigation because of the large amount of main core memory required for the stiffness matrix storage.

3.6 Verification of Existing Code

Several simple test problems were analyzed to verify that Kasali and Clough's code [29] was working correctly. The first two problems used a single element. The first used concentrated nodal loads and the second used a surface pressure. The

third test problem was a thick–wall cylinder problem which used twelve 20–node solid elements and surface pressures. These test problems were the same problems used by Kasali and Clough to checkout their code [29].

3.6.1 Single Element with Concentrated Nodal Loads

A single element with eight nodes was loaded with four concentrated loads, 25 lb each at the top nodes as shown in Figure 3.5. The boundary conditions are such that only vertical (z–direction) movements could take place. The displacements may be calculated directly from continuum mechanics and compared to the results predicted by the finite element code. A comparison between the displacements from theoretical computations and finite element analysis are shown in Table 3.1. There is excellent agreement between theoretical computations and finite element results.

3.6.2 Single Element with Surface Pressure Loading

A single element with 20 nodes was loaded with a surface pressure load of 25 psf as shown in Figure 3.6. The boundary conditions are such that only vertical or z movement could take place. A comparison between the displacements from theoretical computations and finite element analysis are shown in Table 3.2. The values of vertical displacement at the nodes indicates that there is excellent agreement between the theoretical and finite elements results.

3.6.3 Thick–Wall Cylinder Problem

The thick–wall cylinder problem was analyzed to verify procedures in the basic finite element code concerning stiffness generation and assembly, equation solution, and

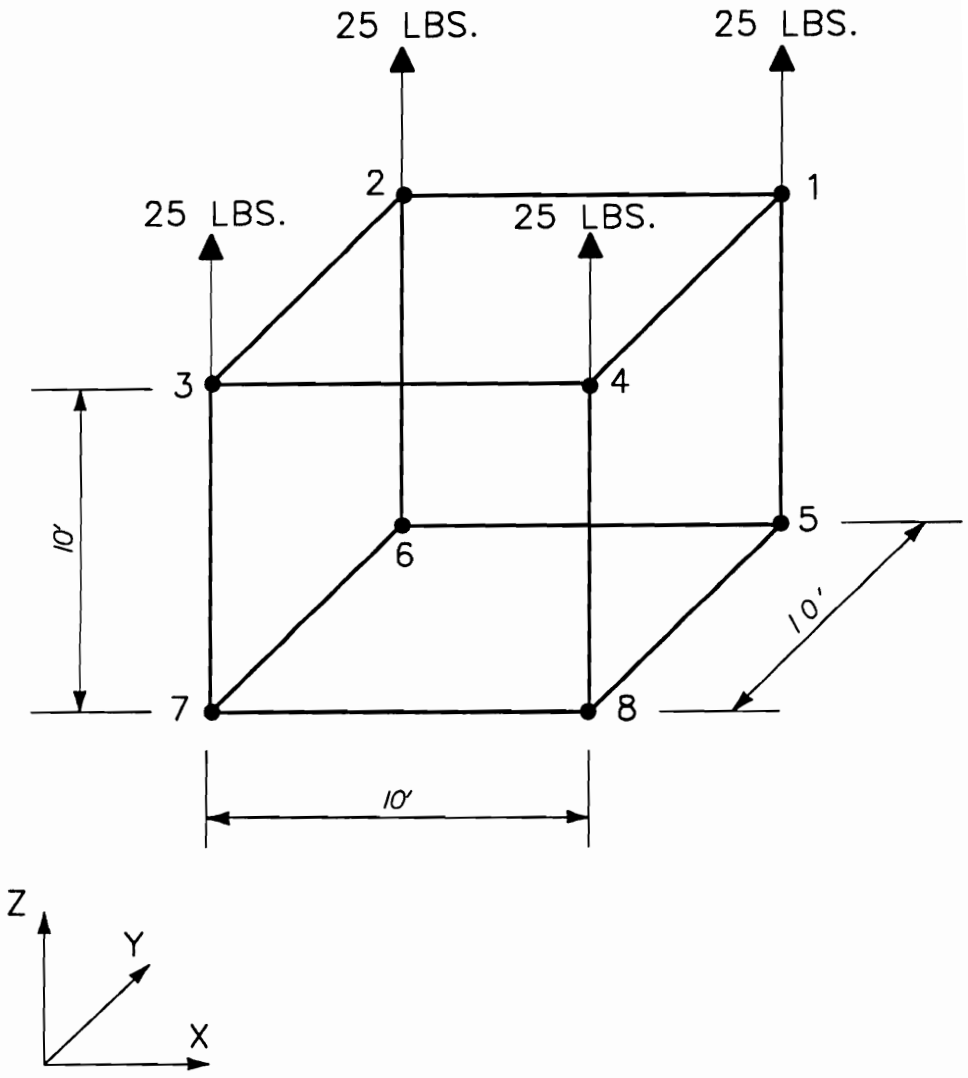

Figure 3.5: Single element with concentrated nodal loads [29].

Table 3.1: Comparison of Results for Single Element with Concentrated Nodal Loads.

Node Number	Vertical or Z Displacement (Feet $\times 10^{-5}$)	
	Finite Element Analysis	Theoretical Calculation
1	7.42857	7.428
2	7.42857	7.428
3	7.42857	7.428
4	7.42857	7.428
5	0	0
6	0	0
7	0	0
8	0	0

Table 3.2: Comparison Results for Single Element with Surface Pressure Loading.

Node Number	Vertical or Z Displacement (Feet $\times 10^{-3}$)	
	Finite Element Analysis	Theoretical Calculation
1, ..., 4	1.85714	1.857
5, ..., 8	0	0
9, ..., 12	1.85714	1.857
13, ..., 16	0	0
17, ..., 20	0.928571	0.9285

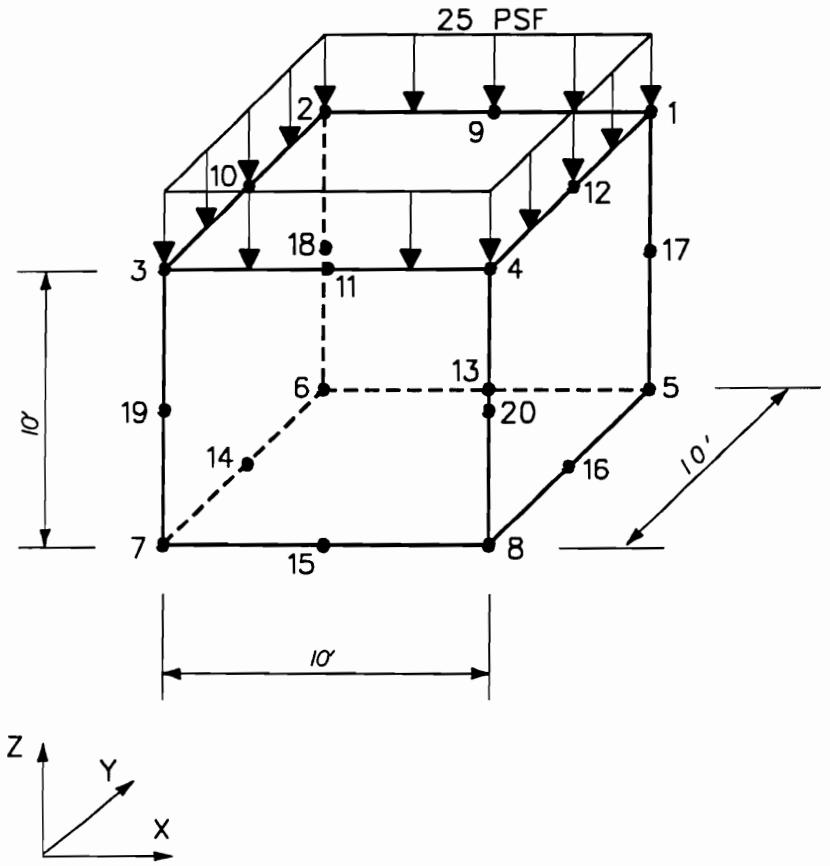

Figure 3.6: Single element with surface pressure loading [29].

displacement and stress computations. The thick-wall cylinder problem is shown in Figure 3.7. The cylinder may be subjected to uniform internal and/or external radial pressures. From the theory of elasticity, the variation of stresses and displacements with the radial distance r is given by:

$$\sigma_r = \frac{a^2 p_i - b^2 p_o}{b^2 - a^2} + \frac{a^2 b^2 (p_o - p_i)}{r^2 (b^2 - a^2)} \tag{3.3}$$

$$\sigma_\theta = \frac{a^2 p_i - b^2 p_o}{b^2 - a^2} - \frac{a^2 b^2 (p_o - p_i)}{r^2 (b^2 - a^2)} \tag{3.4}$$

$$\sigma_{r\theta} = 0 \tag{3.5}$$

$$u = \frac{1-\nu}{E}(r)\left[\frac{p_i a^2 - p_o b^2}{b^2 - a^2}\right] + \frac{1+\nu}{E}\left[\frac{a^2 b^2 (p_i - p_o)}{r(b^2 - a^2)}\right] \tag{3.6}$$

where

r is the radial distance.

σ_r is the stress in the radial direction.

σ_θ is the stress in the tangential direction.

p_o is the uniform external pressure.

p_i is the uniform internal pressure.

a is the inner radius of the cylinder.

b is the outer radius of the cylinder.

$\sigma_{r\theta}$ is the shear stress in the $r\theta$ plane.

ν is the Poisson's ratio of the cylinder material.

E is the Young's modulus of the cylinder material.

u is the displacement in the radial direction.

If $\sigma_{r\theta}$ is identically zero, the polar components of stress, σ_r and σ_θ are the principal stresses.

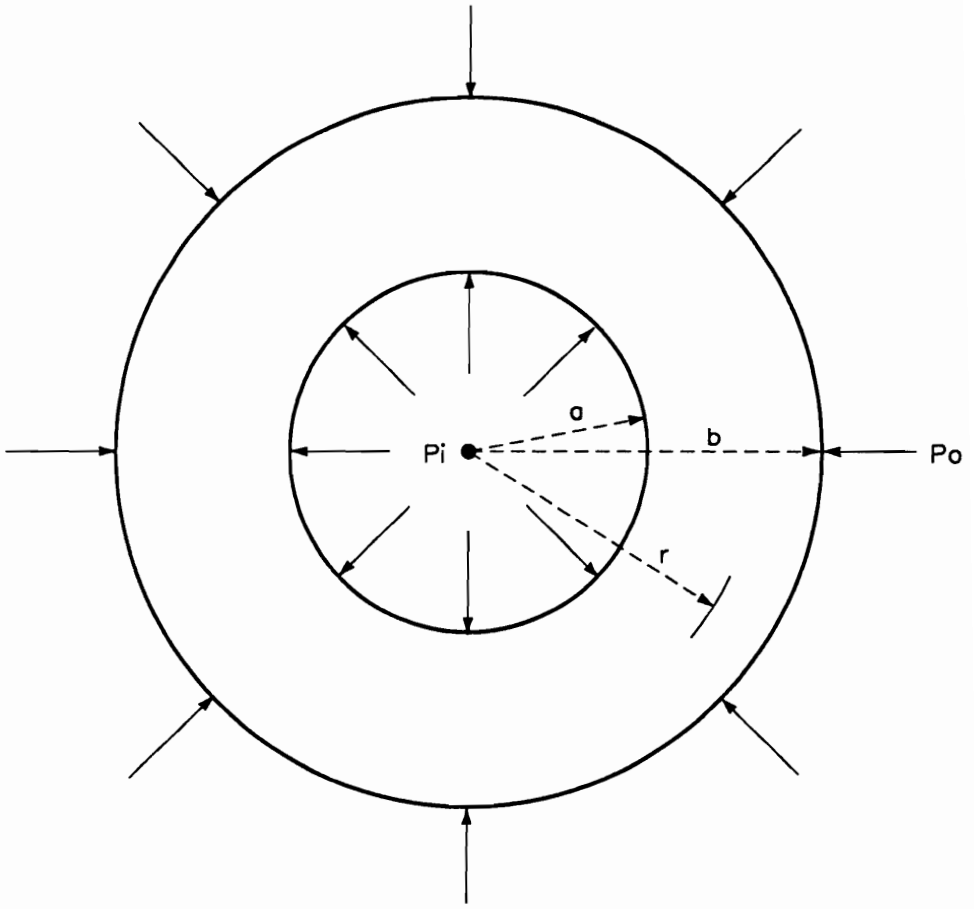

Figure 3.7: Thick–wall cylinder problem [29].

The symmetry of the loading and geometry allowed the representation of the problem by only one quadrant. The finite element mesh used in the analysis is shown in Figure 3.8. The mesh consists of twelve 20–node elements. The nodes at the top and bottom are restrained in the vertical (z) direction.

The problem analyzed is equivalent to that of a thick–wall cylinder subjected to an external pressure and an internal pressure of zero. It is useful to analyze this problem because the circular geometry of the problem corresponds to the circular sheet–pile cofferdam. For the case where p_i in the Equations 3.3, 3.4 , and, 3.6 is zero, the three equations reduce to

$$\sigma_r = \frac{-b^2 p_o}{b^2 - a^2}[1 - \frac{a^2}{r^2}] \tag{3.7}$$

$$\sigma_\theta = \frac{-b^2 p_o}{b^2 - a^2}[1 + \frac{a^2}{r^2}] \tag{3.8}$$

$$u = \frac{1+\nu}{E}[r(1-2\nu)\frac{-p_o b^2}{b^2 - a^2} - \frac{a^2 b^2 p_o}{r(b^2 - a^2)}] \tag{3.9}$$

The problem is modeled by applying a uniform surface pressure, p_o, of 25 psi normal to the outer circumference of the mesh shown in Figure 3.8. The values of the parameters for the problem are:

$$\begin{aligned} \nu &= 0.3 \\ E &= 30,000,000 \quad \text{psi} \\ a &= 5.0 \quad \text{in.} \\ b &= 20.0 \quad \text{in.} \end{aligned}$$

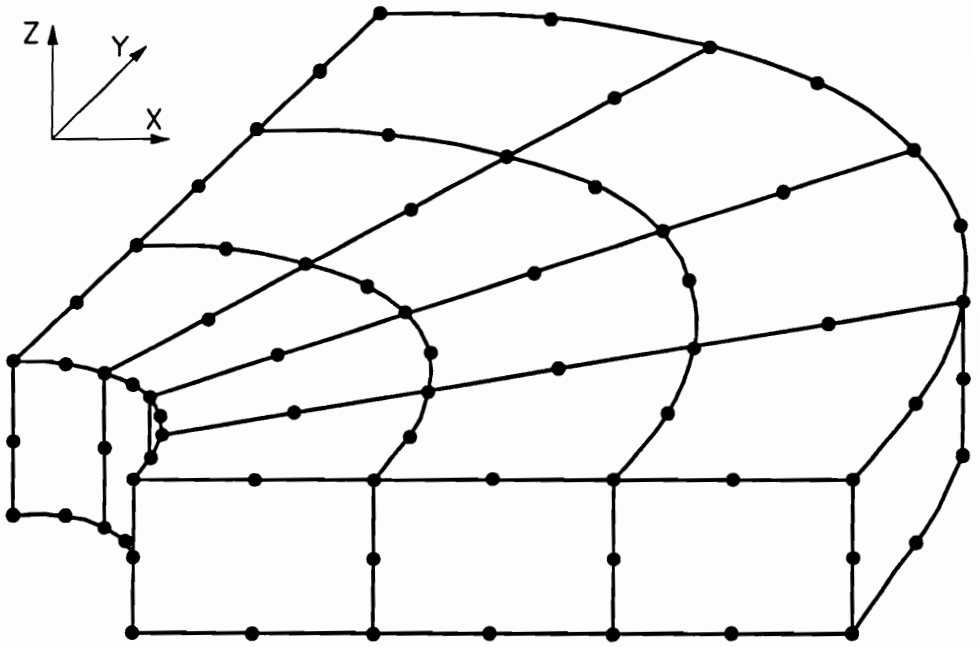

Figure 3.8: Finite element mesh for the thick–wall cylinder problem [29].

The stresses from the finite element analysis and the theoretical solution are compared in Figures 3.9 and 3.10; the displacements are given in Table 3.3. There is excellent agreement between the two sets of results for the radial and tangential stresses and the displacements. This indicates that the basic procedures in the code are accurate.

3.7 Limitation of the Code

Even though the code as written by Kasali and Clough [29] has been accurate, it has a number of limitations with regard to performing a soil–structure interaction study of a sheet–pile cellular cofferdam. The major limitations are the lack of shell/membrane, interface, and quadratic wedge elements, and routines to simulate the placement of fill, seepage effects, and dewatering. Also, important was the lack of nonlinear material response.

Other capabilities had to be modified. The initial stress routine had to be changed to allow the use of total unit weights above the water table and effective unit weights, or pore pressures, and total unit weights below the water table. Also, during the initial stress calculation the modulus values for the three–dimensional soil elements and stiffness values for the interface element had to be determined from their constitutive relationships. Finally, the incremental analysis procedure had to be set into context of a nonlinear analysis.

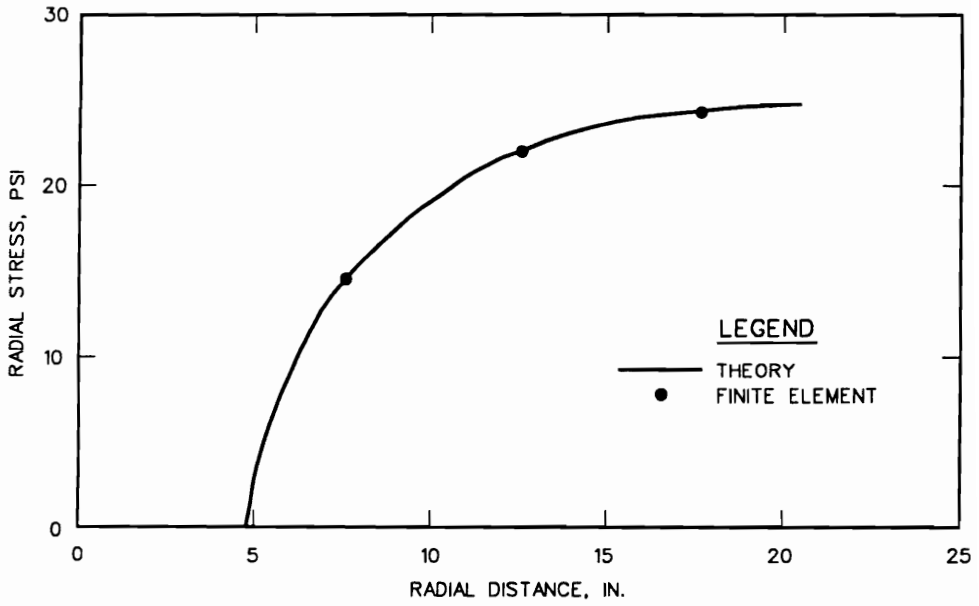

Figure 3.9: Variation of radial stress with radius [29].

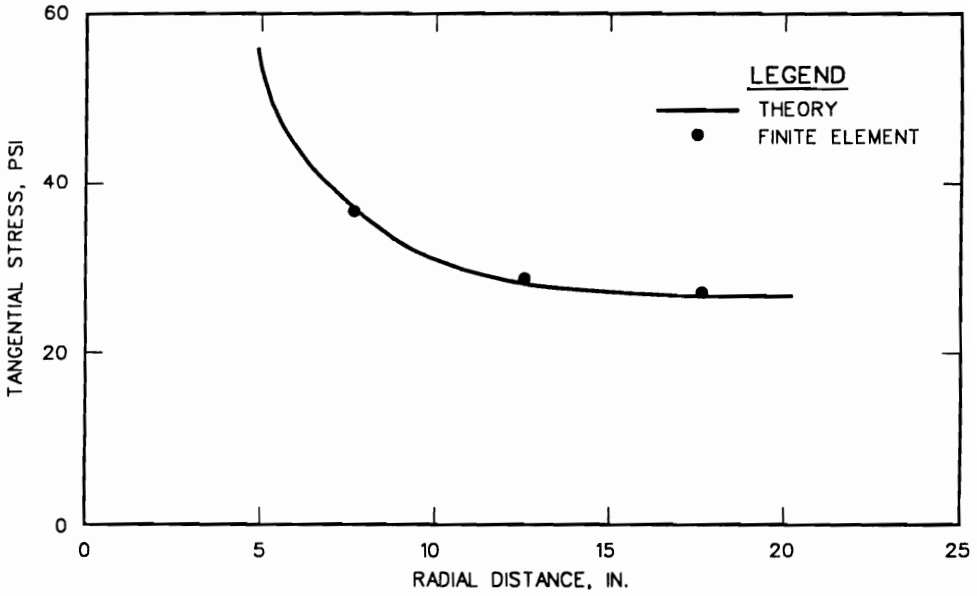

Figure 3.10: Variation of tangential stress with radius [29].

3.8 Summary

In this chapter, the basic philosophy and requirements for developing a new three–dimensional finite element code were established. Instead of using one of the existing general–purpose finite element codes, the decision was made to develop a new code by enhancing a basic linear elastic code written by Kasali and Clough [29] . The code written by Kasali and Clough has many of the features needed for the analysis of a sheet–pile cellular cofferdam, including the use of a higher–order, three–dimensional solid element and an efficient element assemblage and equation solution routine. The basic code was verified with several test problems and was accurate.

While the Kasali and Clough code met the basic requirements for this study, it required considerable modification for three–dimensional analysis of sheet–pile cellular cofferdams. In the next two chapters, details of the additions and modifications to the code are presented.

Table 3.3: Comparison of Displacements for Thick–Wall Cylinder Problem.

Radial Distance Inches	Displacements ($\times 10^{-6}$ inches)	
	Finite Element	Theory
5.0	8.09444	8.08889
7.5	7.31643	7.31852
10.0	7.51381	7.51111
12.5	8.08910	8.08889
15.0	8.85948	8.85926
17.5	9.73956	9.73968
20	10.68930	10.68889

Chapter 4

Additions to the Element Library

4.1 Introduction

In Section 3.3 of the previous chapter, the capabilities necessary to conduct a three–dimensional soil–structure interaction finite element analysis of sheet–pile cellular cofferdams were listed. Included in the list of requirements were a three–dimensional interface element to allow relative movements between different materials and higher–order elements to accurately model the geometry of the cellular cofferdam structure. This chapter describes the three–dimensional interface element, the higher–order wedge element, and the shell element incorporated in the new code.

4.2 Interface Element

One of the most important aspects in soil–structure interaction analysis is the simulation of the behavior of the interface where the soil and the structure meet. Conventional finite element formulation requires compatibility of displacements at the nodal points connecting adjacent elements (no gaps). Furthermore, to ensure numerical accuracy, compatibility of the displacement field along the common sides of adjacent elements should be maintained. These constraints can misrepresent the actual physical phenomenon occurring at the interface between the soil and the structure. This is especially true when the stiffness of the two differ significantly. Relative movements do occur between the soil and the structure, and they play an important role in the overall response of the system. It is important to simulate this behavior in a soil-structure interaction finite element analysis.

Special–purpose elements have been developed to simulate interface response [14, 21, 22, 63, 65].

Two separate philosophies have been followed in this work. The first philosophy follows that credited to Goodman, Taylor, and Brekke [22]. The element is formulated on the basis of the relative nodal displacements of the solid elements adjacent to the interface element, Figure 4.1a, and is referred to as a *zero–thickness* interface element. The second philosophy uses a solid isoparametric formulation for the interface element with the assumption of uniform strain throughout its thickness, Figure 4.1b. This type of formulation was first proposed by Zienkiewicz et al. [65] and is referred to as the *thin–layer* interface element. The thin–layer interface element has been further developed by Desai and his associates [14].

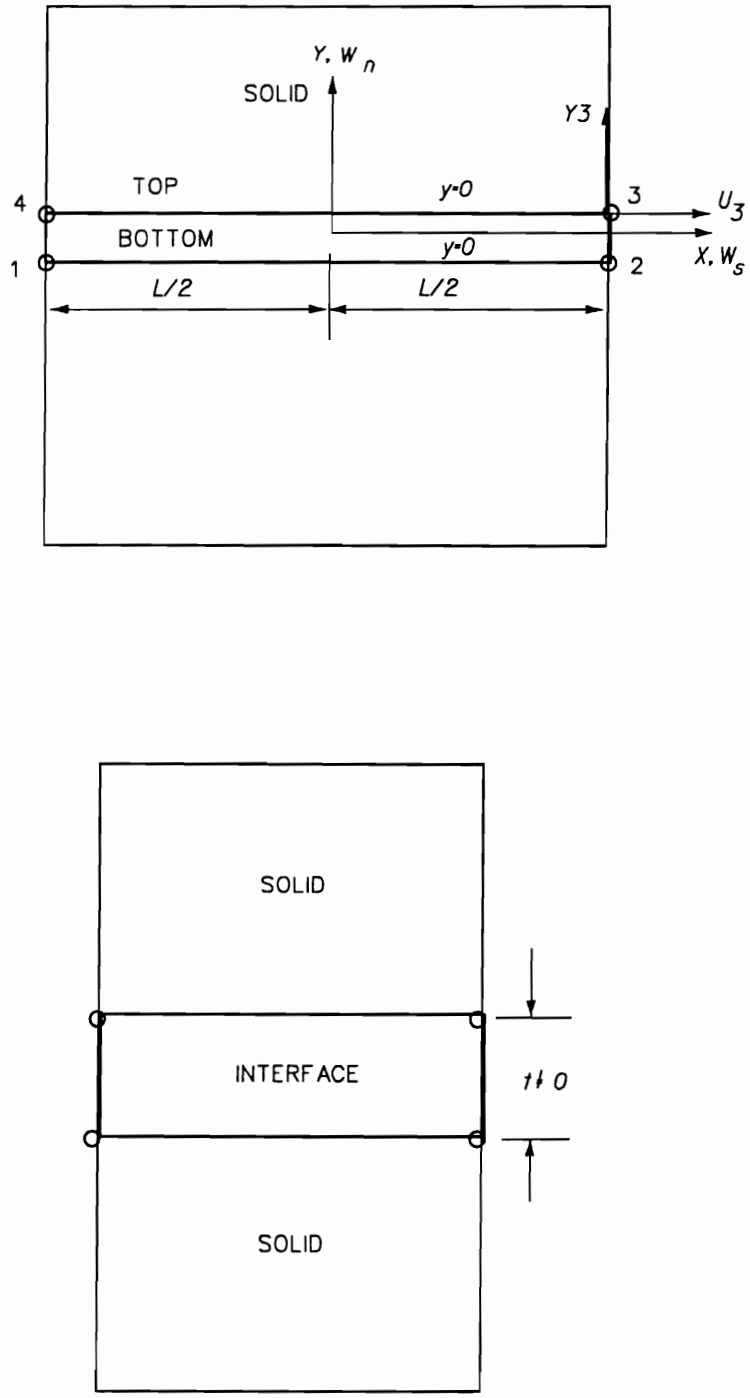

Figure 4.1: Typical types of interface elements used in soil–structure interaction analysis.

While each of these philosophies have their merits and limitations, the zero–thickness element has a number of advantages over the thin–layer element for the cofferdam analysis. The principal advantage is in the development of the mesh for the cellular cofferdam. At the intersection of the main cell and arc cell, the geometry is complex and using the thin–layer elements would significantly add to the difficulty in generating a mesh for the cofferdam.

4.2.1 Zero–Thickness Interface Element

The most commonly used interface element for soil-structure interaction analyses is based on that proposed by Goodman, Taylor, and Brekke [22]. This element type is found in the computer program **SOILSTRUCT**, which was used in the two–dimensional studies for Lock and Dam 26(R) [8, 33, 53]. A schematic of this element is shown in Figure 4.1; has four nodes and zero thickness. Thus, the element has pairs of nodal points with the same coordinates. A brief review of the derivation of the two–dimensional element is presented in Appendix A to provide the background for evaluating the element for use in the three–dimensional code.

4.2.2 Evaluation of Interface Element Formulation

When the formulation for the Goodman, et al. [22] interface element was originally proposed it was based on relative displacements. However, when integrated into a finite element code, it became a function of the absolute displacements of the adjacent solid elements. The stiffness matrix, $[K]$, relates of the absolute displacements of the adjacent solid elements to the internal forces in the system. Reviewing the terms of the stiffness matrix (Appendix A) shows that the off–diagonal terms of the stiffness

matrix may be equal to the diagonal terms, which may lead to an ill–conditioned stiffness matrix. When added into the global stiffness matrix, the interface element stiffness matrix can then cause numerical inaccuracies. An ill–conditioned matrix may occur when the high normal stiffness value in this zero thickness element is needed to keep the two adjacent elements from penetrating one another, Figure 4.2.

Wilson [63] illustrated the possible numerical problems which can develop for this formulation and proposed an improvement. He used a one–dimensional problem consisting of two elements joined by an interface element as shown in Figure 4.3. This example problem for the Goodman, et al. [22] is formulated and solved in Appendix B. The example problem shows the accuracy of computed displacement using the Goodman, et al. [22] interface element formulation dependents on the number of significant figures. The displacement for five significant figures are 0.33283 for u_1 and 0.33333 for u_2. While, the displacement for four significant figures are 0.4995 for u_1 and 0.5000 for u_2. If only three significant figures are used, the set of equations are singular and $u_1 = u_2 = \infty$. This example illustrates that the use of large values for stiffness coefficients in this type of interface element formulation can lead to numerical problems. Even though modern digital computers have 6 to 15 significant figures, the same type of numerical problems can occur.

4.2.3 Alternative Formulation

Wilson [63] showed that numerical problems found in the Goodman, et al. [22] interface formulation could be avoided by stating the equilibrium equations in terms of the absolute and relative displacements rather than the absolute displacements alone. Using the previous example, the displacements for the system can be written as an absolute displacement, u_1, and a relative displacement, Δ, at node 2 with

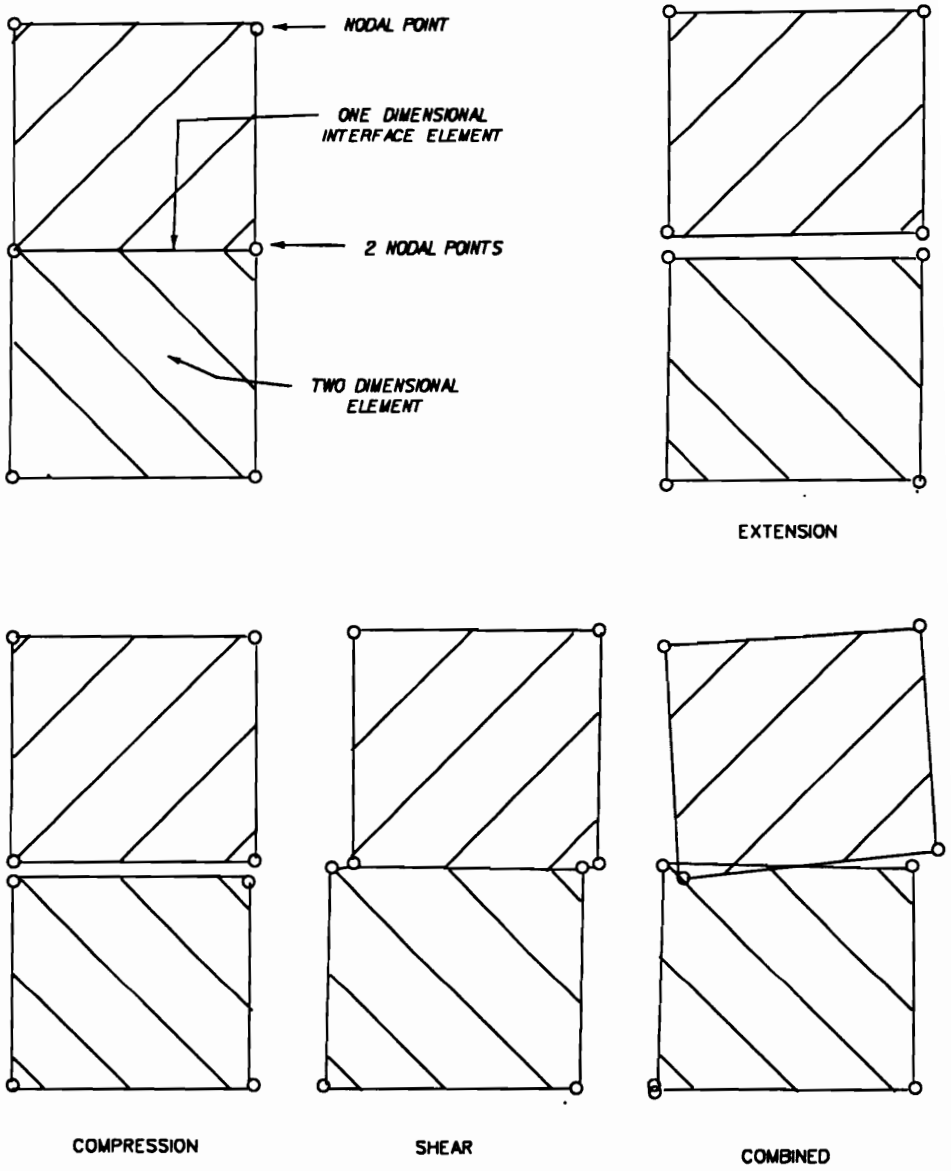

Figure 4.2: Penetration of adjacent element [5].

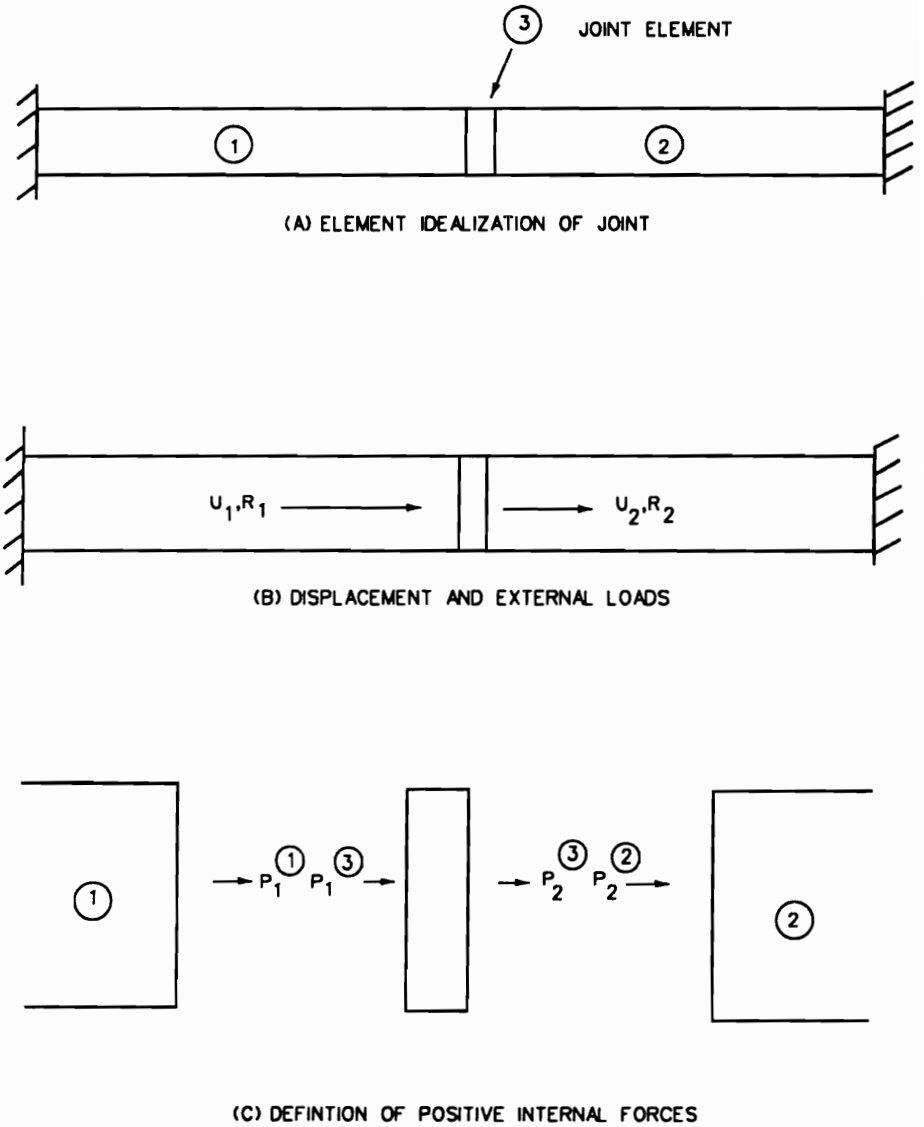

Figure 4.3: Example problem to evaluate interface element [63].

respect to u_1. Therefore, the displacement at node 2, u_2, would be $u_2 = u_1 + \Delta$ and the absolute displacement would be related to the relative displacement by

$$\begin{Bmatrix} u_1 \\ u_2 \end{Bmatrix} = \begin{bmatrix} 1.0 & 0.0 \\ 1.0 & 1.0 \end{bmatrix} \begin{Bmatrix} u_1 \\ \Delta \end{Bmatrix} \text{ or } \{u\} = [T]\{u^r\} \tag{4.1}$$

Substituting this into the basic equilibrium equations,

$$[K]\{u\} = \{F\} \tag{4.2}$$

results in a modified set of equilibrium equations for the system given by

$$[K^r]\{u^r\} = \{F^r\} \tag{4.3}$$

The modified equilibrium equations are formed by premultiplying by $[T]^T$, resulting in

$$\{F^r\} = [T]^T\{F\} \begin{bmatrix} 1.0 & 1.0 \\ 0.0 & 1.0 \end{bmatrix} \begin{Bmatrix} 0.0 \\ 1.0 \end{Bmatrix} = \begin{Bmatrix} 1.0 \\ 1.0 \end{Bmatrix} \tag{4.4}$$

and

$$[K^r] = [K_1^r] + [K_2^r] + [K_3^r] \tag{4.5}$$

where

$$[K_1^r] = [T]^T[K_1][T] = \begin{bmatrix} 1.0 & 1.0 \\ 0.0 & 1.0 \end{bmatrix} \begin{bmatrix} 1.5 & 0 \\ 0 & 0 \end{bmatrix} \begin{bmatrix} 1.0 & 0.0 \\ 1.0 & 1.0 \end{bmatrix} = \begin{bmatrix} 1.5 & 0 \\ 0 & 0 \end{bmatrix} \tag{4.6}$$

$$[K_2^r] = [T]^T[K_2][T] = \begin{bmatrix} 1.0 & 1.0 \\ 0.0 & 1.0 \end{bmatrix} \begin{bmatrix} 0 & 0 \\ 0 & 1.5 \end{bmatrix} \begin{bmatrix} 1.0 & 0.0 \\ 1.0 & 1.0 \end{bmatrix} = \begin{bmatrix} 1.5 & 1.5 \\ 1.5 & 1.5 \end{bmatrix} \tag{4.7}$$

$$[K_3^r] = [T]^T [K_3] [T] = \tag{4.8}$$
$$\begin{bmatrix} 1.0 & 1.0 \\ 0 & 1.0 \end{bmatrix} \begin{bmatrix} 1000.0 & -1000.0 \\ -1000.0 & 1000.0 \end{bmatrix} \begin{bmatrix} 1.0 & 0 \\ 1.0 & 1.0 \end{bmatrix} = \begin{bmatrix} 0 & 0 \\ 0 & 1000.0 \end{bmatrix}$$

Thus, Eq 4.3 can be expressed as

$$\begin{bmatrix} 3.0 & 1.5 \\ 1.5 & 1001.5 \end{bmatrix} \begin{Bmatrix} u_1 \\ \Delta \end{Bmatrix} = \begin{Bmatrix} 1.0 \\ 1.0 \end{Bmatrix} \tag{4.9}$$

With five significant figures, the solution to these equation is

$$\begin{Bmatrix} u_1 \\ \Delta \end{Bmatrix} = \begin{Bmatrix} 0.33308 \\ 0.00050 \end{Bmatrix} \tag{4.10}$$

and

$$u_2 = 0.33358 \tag{4.11}$$

To obtain this accuracy, the Goodman formulation would require eight significant figures. It is important to note that if only two significant figures were retained for the stiffness matrix while performing the solution, the result would be

$$\begin{Bmatrix} u_1 \\ \Delta \end{Bmatrix} = \begin{Bmatrix} 0.33 \\ 0.00050 \end{Bmatrix} \tag{4.12}$$

Furthermore, if the interface stiffness approaches infinity, $u_1 = \frac{1}{3}$ and $\Delta = 0$ without any numerical abnormalities.

Based on these findings and past experience with the program **SOILSTRUCT**, it was decided that the interface element to be implemented into the three–dimensional finite element code would be formulated in terms of both absolute and relative displacements as unknowns.

4.2.4 Interface Element Formulation

In papers by Ghaboussi, Wilson, and Isenberg [21] and Wilson [63], derivations are presented for three–dimensional interface elements in terms of both absolute and relative displacements. However, these derivations require the transformation of the adjacent element stiffness matrix to the local interface coordinate system for each node. For a three–dimensional problem with curved surfaces, as would be the case for the cellular cofferdam, this would require the adjacent element stiffness matrix to be transformed eight times during element assemblage. This would be time consuming and difficult to incorporate in the program. Buragohain and Shah [4] presented an alternative derivation for a curved isoparametric interface surface element which was derived for an arbitrary curved surface as would be the case for the cofferdam analysis. The principal limitation with this formulation was that it used absolute displacements. While neither the elements of Ghaboussi, et al. [21] or Buragohain and Shah [4] had all the desired characteristics, they did come close to that desired. Thus, it was decided to derive a new formulation that would take advantage of the positive aspects of each of the approaches.

A schematic of a 20–node solid element, an 8–node shell element, and an 8–node interface element is shown in Figure 4.4. The unknowns are the three components of absolute displacement, u, v, and w, at each node and the three components of relative displacement Δu, Δv, and Δw, at each node in the global reference system. The geometry as well as the displacements vary quadratically within the element. The variation can be defined in terms of the shape functions, N_i. This variation for the interface is thus compatible with the corresponding variation in geometry and displacement field for the adjacent quadratic isoparametric solid or shell elements.

The shape functions, N_i, are expressed in the natural coordinates (s,t) for the surface and may be written for the corner nodes as

$$N_i = \frac{1}{4}(1+tt_i)(1+ss_i)(tt_i+ss_i-1) \tag{4.13}$$

and for the midside nodes

For $t = 0$

$$N_i = \frac{1}{2}\left(1-t^2\right)(1+ss_i) \tag{4.14}$$

For $s = 0$

$$N_i = \frac{1}{2}\left(1-s^2\right)(1+tt_i) \tag{4.15}$$

Thus, the coordinates of any point on the surface of the interface is described in terms of the nodal coordinates as

$$x = \sum_{i=1}^{8} N_i x_i, \qquad y = \sum_{i=1}^{8} N_i y_i, \qquad z = \sum_{i=1}^{8} N_i z_i \tag{4.16}$$

and the relative displacements at any point are expressed in terms of the nodal relative displacements as

$$\Delta u = \sum_{i=1}^{8} N_i \Delta u_i, \qquad \Delta v = \sum_{i=1}^{8} N_i \Delta v_i, \qquad \Delta w = \sum_{i=1}^{8} N_i \Delta w_i \tag{4.17}$$

The relative displacements in global coordinates at any point are

$$\{\Delta u\} = \begin{Bmatrix} \Delta u \\ \Delta v \\ \Delta w \end{Bmatrix} = [B]\{\Delta q\} = \sum_{i=1}^{8} [B_i]\{\Delta q_i\} \tag{4.18}$$

in which

$$[B_i] = \begin{bmatrix} N_i & 0 & 0 \\ 0 & N_i & 0 \\ 0 & 0 & N_i \end{bmatrix} \quad \text{and} \quad \{\Delta q_i\}^T = \{\Delta u_i, \Delta v_i, \Delta w_i\} \tag{4.19}$$

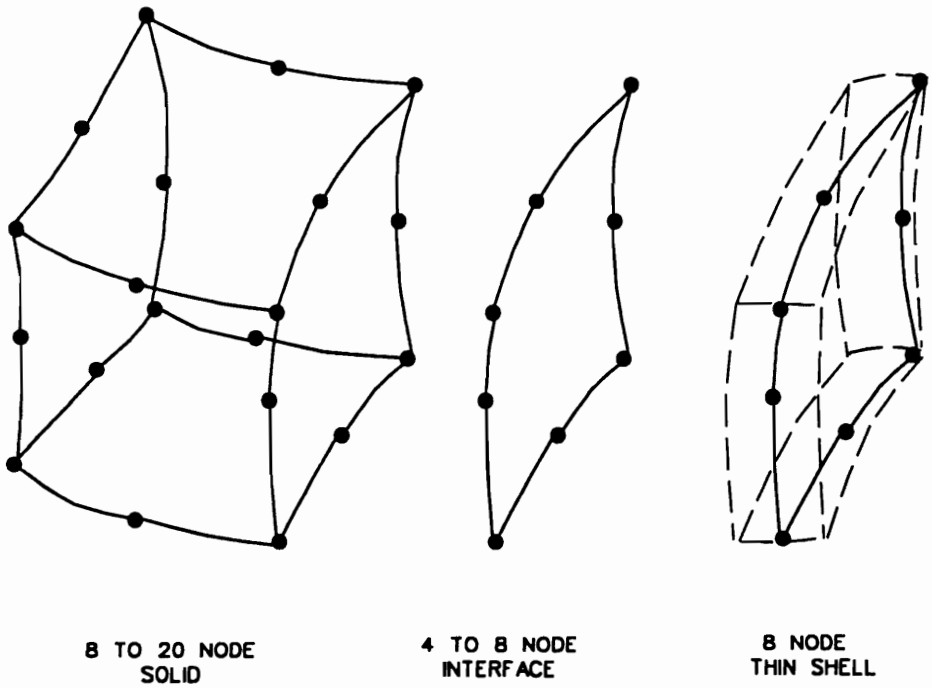

Figure 4.4: Solid, interface, and shell element configuration for three–dimensional code.

The stiffness of the interface is defined in two mutually orthogonal directions along the surface of the interface and a direction normal to the surface. Taking the tangential stiffnesses in the two orthogonal directions as k_{s1} and k_{s2}, and the normal stiffness as k_n with the corresponding unit vectors V_1, V_2, and V_3 defining the two tangential and normal directions, respectively, at any point on the interface surface, the forces on the interface surface are

$$\begin{Bmatrix} f_{s1} \\ f_{s2} \\ f_n \end{Bmatrix} = \begin{bmatrix} k_{s1} & 0 & 0 \\ 0 & k_{s2} & 0 \\ 0 & 0 & k_n \end{bmatrix} \begin{Bmatrix} \Delta u_{s1} \\ \Delta u_{s2} \\ \Delta u_n \end{Bmatrix} \tag{4.20}$$

where f_{s1}, f_{s2}, and f_n are the forces per unit area in the directions V_1, V_2, and V_3, respectively, and Δu_{s1}, Δu_{s2}, and Δu_n are the corresponding relative displacements in directions V_1, V_2, and V_3, respectively. This can be written symbolically as

$$\{f^s\} = [k]\{\Delta u^s\} \tag{4.21}$$

The surface relative displacements, Δu^s, are related to the global relative displacements, $\{\Delta u\}$ by

$$\{\Delta u^s\} = [T]\{\Delta u\} = [T][B]\{\Delta q\} \tag{4.22}$$

where $[T]$ is the transformation which is defined as

$$[T] = \begin{bmatrix} V_{1x} & V_{1y} & V_{1z} \\ V_{2x} & V_{2y} & V_{2z} \\ V_{3x} & V_{3y} & V_{3z} \end{bmatrix} \tag{4.23}$$

where V_{ix}, V_{iy}, and V_{iz} are the x, y, and z components, respectively, of the unit vector V_i.

The unit vectors can be expressed in terms of the local coordinate system of the interface surface at any point. Specifying V_s and V_t as the vectors tangential to the surface, they can be obtained by

$$V_s = \left\{ \frac{\partial x}{\partial s}, \frac{\partial y}{\partial s}, \frac{\partial z}{\partial s} \right\} = \left\{ \frac{\partial N_i}{\partial s} x_i, \frac{\partial N_i}{\partial s} y_i, \frac{\partial N_i}{\partial s} z_i \right\} \tag{4.24}$$

and

$$V_t = \left\{ \frac{\partial x}{\partial t}, \frac{\partial y}{\partial t}, \frac{\partial z}{\partial t} \right\} = \left\{ \frac{\partial N_i}{\partial t} x_i, \frac{\partial N_i}{\partial t} y_i, \frac{\partial N_i}{\partial t} z_i \right\} \tag{4.25}$$

The three unit vectors V_1, V_2, and V_3 are then found by

$$V_1 = \frac{V_s}{|V_s|} \tag{4.26}$$

$$V_3 = \frac{V_s \times V_t}{|V_s| \cdot |V_t|} \tag{4.27}$$

$$V_2 = V_3 \times V_1 \tag{4.28}$$

The stiffness matrix $[K]$ for the interface element in terms of relative displacements is given by

$$[K] = \int_{-1}^{1} \int_{-1}^{1} [B]^T [T]^T [k] [T] [B] |V_s \times V_t| ds dt \tag{4.29}$$

A 3×3 Gauss quadrature was used for the numerical integration for the stiffness matrix.

4.2.5 Implementation of the Interface Element

The first step in implementing the interface element in the finite element code was to write a subroutine to calculate the stiffness matrix for the element as outlined in the previous section. This was accomplished by integrating the normal and tangential stiffnesses of the interface over its surface. The transformation matrix, Eq 4.23,

between the global coordinate system and the local coordinate system tangential and normal to interface surface are found at each integration point by using the direction cosines from the Jacobain. The contribution of stiffness for each integration point is collected to form the stiffness matrix for the interface element.

It was not clear from the literature how the interface element stiffness matrix should be assembled into the global stiffness matrix in the computer code. The method used herein is described in the following text. As mentioned in the previous section, the relative displacements associated with an interface element are actually global degrees of freedom. These relative displacements must be related to the respective absolute displacements at a nodal point. To achieve this in the implementation, the interface element is attached to a three–dimensional solid element which is referred to as the parent element. The interface element is designated in the input by assigning it to the face of a solid element. By assigning the interface element to a face of a parent element, no additional nodal points are required in the mesh. Only additional degrees of freedom are added at the respective nodal points. This is particularly attractive when generating a complex mesh.

The interface element is assigned to the parent element by incorporating its stiffness terms in the stiffness matrix of the parent element. This requires expanding the stiffness matrix of the parent element to include the additional degrees of freedom of the interface element. The procedure for including the interface element in the expanded stiffness matrix requires more than a simple placement of the interface element stiffness terms in the expanded portion of the stiffness matrix. The stiffness matrix for the interface element includes only those terms relating to the relative displacements. As part of the parent element stiffness matrix, the stiffness contribution of the degrees of freedom for the absolute displacements in the parent

element must be included in the expanded portion of the stiffness matrix. This is achieved by copying the terms in the columns and rows of the degrees of freedom for the absolute displacements into the respective columns and rows of the degrees of freedom for the associated relative displacements and then adding the associated stiffness terms of the interface element.

Once the expanded matrix has been formed, the assembly of the global stiffness matrix of the system follows the same procedures as for any other element. The difference being that the relative displacements are now global unknowns to be obtained from the solution.

4.2.6 Verification of the Interface Element

A series of test problems were solved to verify the accuracy of the implementation of the new interface element in the code. The first test problem was a solid block resting on a rigid foundation, Figure 4.5. This problem was used to confirm the correctness of stiffness matrix generation and assembly, displacement and force per area computations for both single– (four and eight node) element and multielement cases. A second problem was chosen from the literature to provide verification with other types of interface elements.

Test Problem 1

The first test problem is a solid block resting on a rigid foundation subjected to a uniform lateral surface pressure, Figure 4.5. An interface is placed between the block and the foundation. Three different meshes were used to analyze the problem, Figure 4.5. The first two meshes consisted of one solid element and an interface element; one with linear interpolation function for displacements (Figure 4.5a) and

the other with a quadratic interpolation function (Figure 4.5b). The third mesh had eight solid elements and four interface elements (Figure 4.5c). A shearing stiffness, k_s, of 100.0 pcf was chosen for the interface to allow easy verification of the results. A high Young's modulus of 30,000,000 psf was used for the block. Thus, the only significant movement should be generated by the interface, and would be equal to:

$$\Delta = \frac{P}{k_s A} \tag{4.30}$$

where P is the shear force and A is the area of the interface. For the problem in Figure 4.5, the block should have a uniform movement relative to the foundation of 0.2500 ft. Table 4.1 presents the displacements of the corner of the block from the finite element analysis. The results are the same from all three meshes. The finite element results are in agreement with the expected result.

Test Problem 2

This problem was reported in the Desai, et al. paper [14] where results are provided for a thin–layer interface element, which lies between two three–dimensional solid elements, (Figure 4.6). Computed displacements from the finite element analyses using (1) no interface; (2) the new interface; and (3) the Desai thin–layer interface are given in Figure 4.7. The two solutions using interface element provide consistent results.

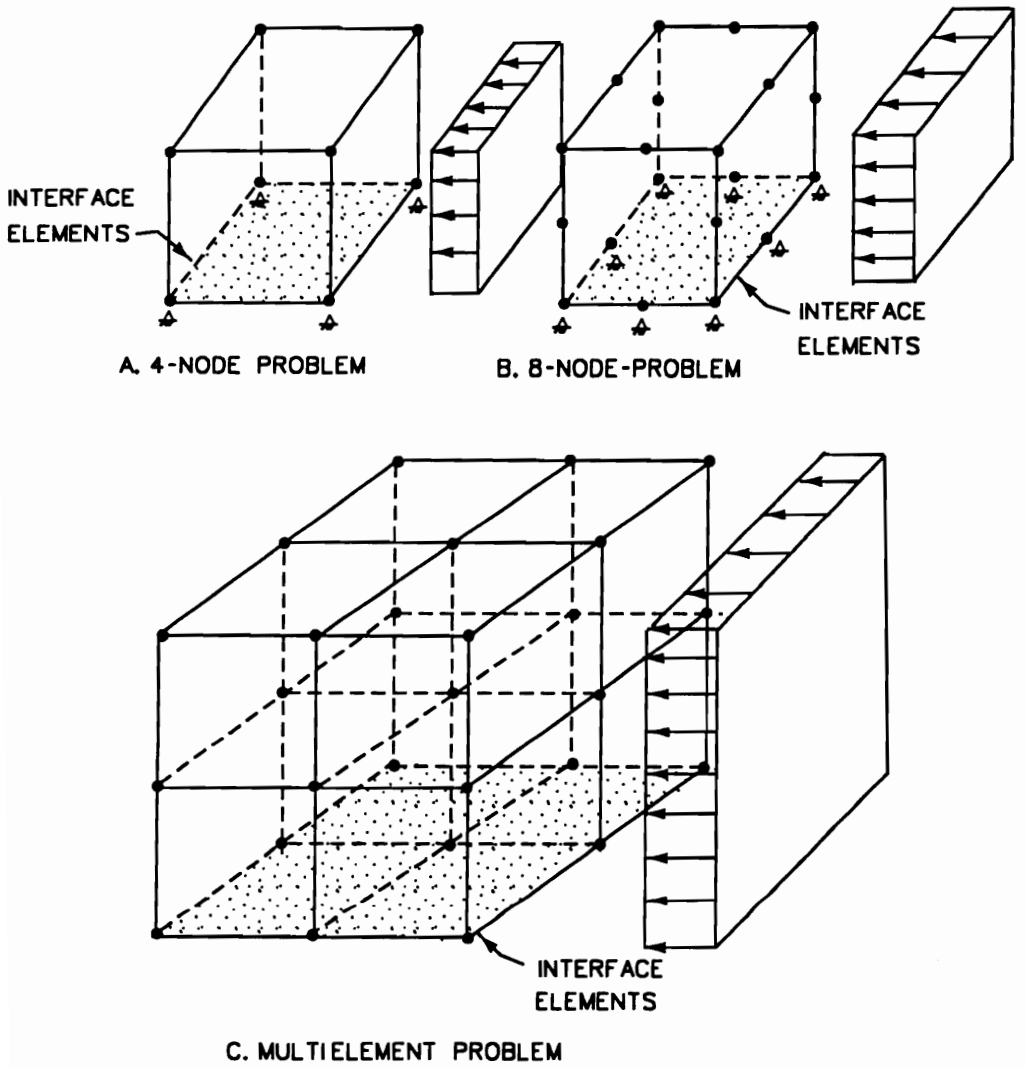

Figure 4.5: Meshes for interface Test Problem 1.

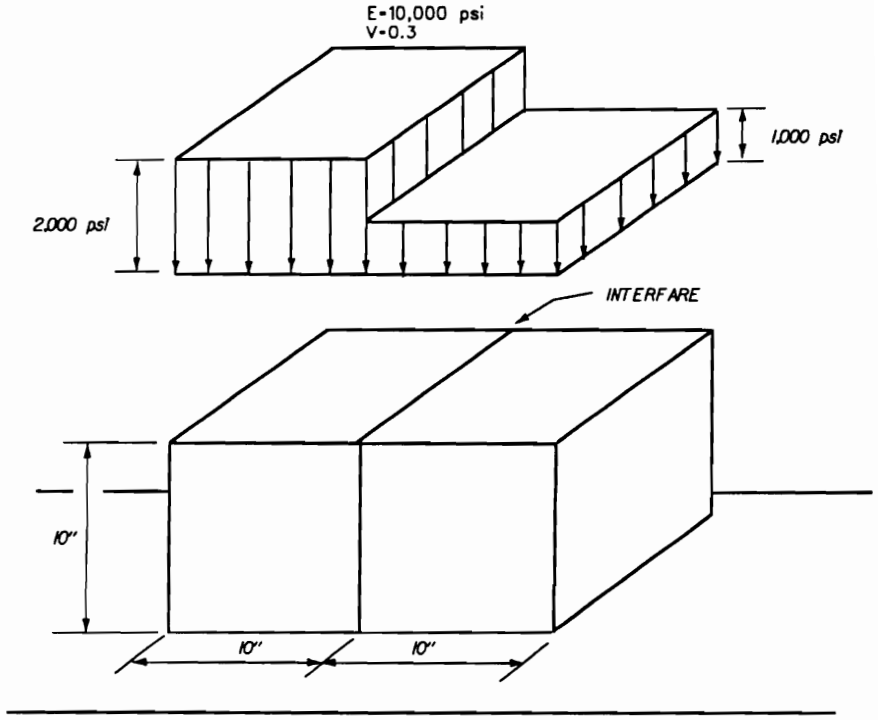

Figure 4.6: Desai's interface test problem [14].

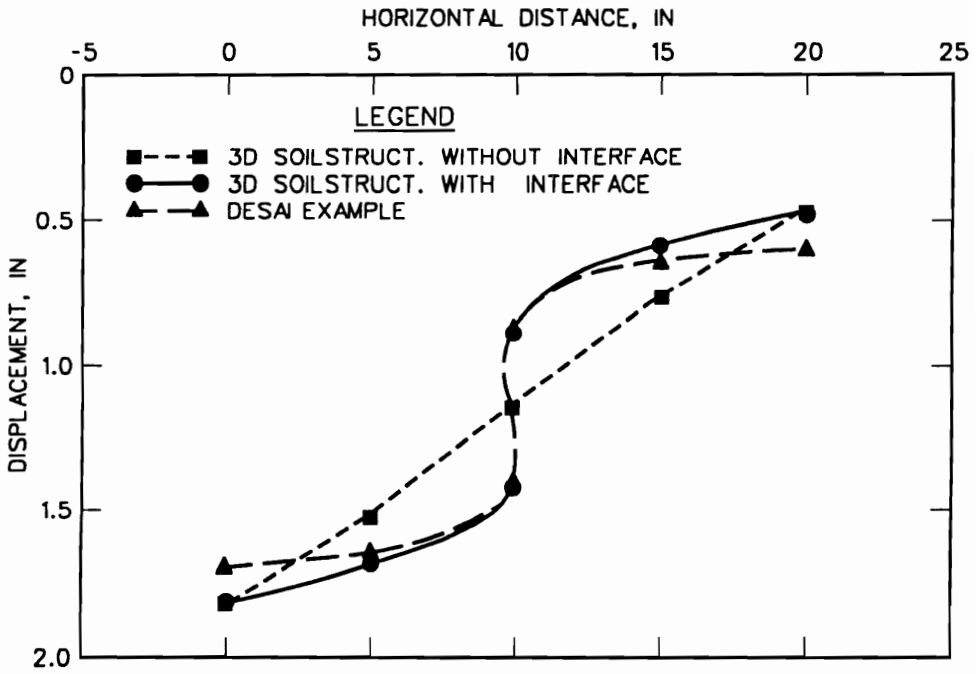

Figure 4.7: Results for Desai's interface test problem [14].

4.3 Degeneration of Brick–Type Isoparametric Elements

The geometry of the cofferdam required the use of wedge shaped elements in locations to generate a smooth consistent mesh. A wedge element for a three–dimensional model would be equivalent to a triangle element in a two–dimensional model. For isoparametric element that uses a linear interpretational function, such as a four–node two–dimensional quadalateral element or eight–node three–dimensional brick element, the elements can be degenerated to a three–node triangle element or six–wedge element by collocating two corners. In the process of verifying the code, it was discovered that the quadratic forms of the brick element in the code would not accurately degenerate to a wedge, as shown in Figure 4.8. Figure 4.9 shows the mesh, loading, and the results of one problem used in the verification of the existing code. The mesh contained four wedge elements which were formed by collocating the three nodes along both top and bottom edges and the two midside nodes on one face of a brick. The shape functions for each location are accumulated. From the Figure 4.9 it is clear that the stiffness coefficients at the collocated points are too large, resulting in nonuniform displacement of the loaded surface.

Irons [27] has exposed some of the problems of degenerating quadratic brick-type isoparametric elements to wedges and trehedrals. Irons proposed procedures for modifying the shape functions of degenerated elements using the hierarchical approach for the shape functions in which the nodal variable at the midside measures the departure from linearity. He was able to first consider the linear effects due to the corner values and then, the additional effects due to the midside values. Using this strategy, the quadratic effects due to the corner values need never be considered.

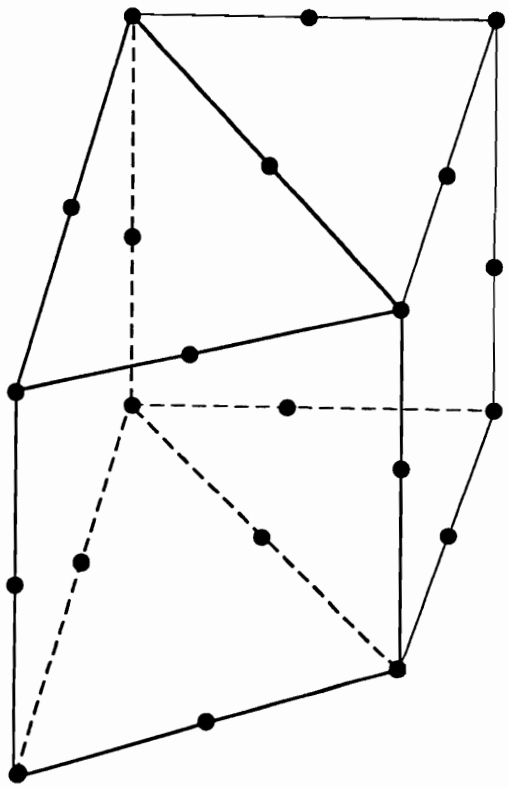

Figure 4.8: Degeneration of a brick–type isoparametric element.

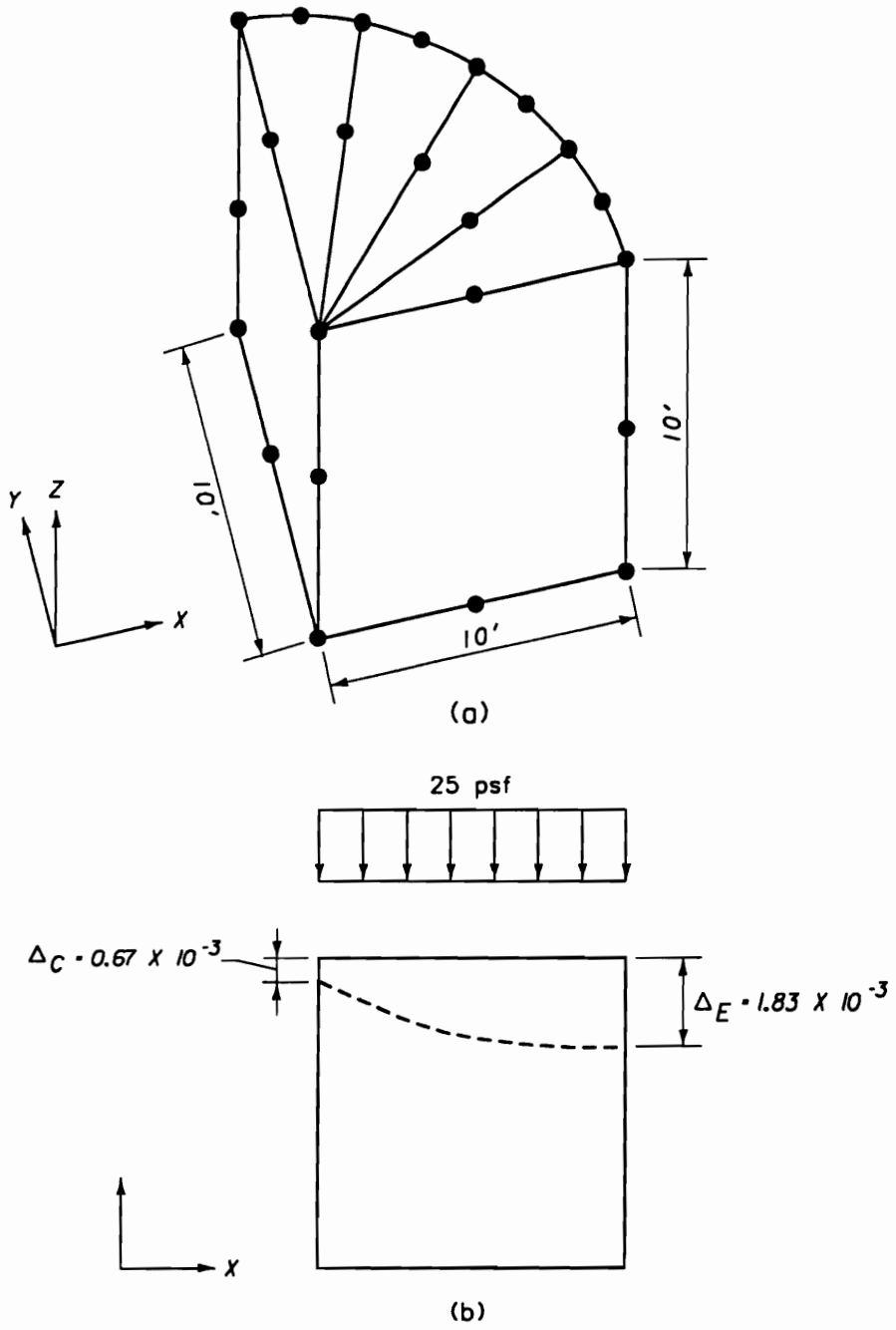

Figure 4.9: Example problem of degeneration by simple collapsing of one side of brick–type isoparametric elements.

Unfortunately this approach does not work for all possible degenerations of the brick element, and it is a special problem since it does not apply to the *Serendipity* family of elements used in the code.

4.3.1 Formulation for Degeneration of Quadratic Serendipity Element

Newton [42] presented a strategy for modifying the serendipity shape functions to accommodate the degeneration of the brick–type element. The shape functions for the 20–node, three–dimensional solid element used in the code (Figure 4.10a) are

$$N_i = \frac{1}{8}(1 + rr_i)(1 + ss_i)(1 + tt_i)(rr_i + ss_i + tt_i - 2) \tag{4.31}$$

for the corner nodes and

$$N_i = \frac{1}{4}(1 + rr_i)(1 + ss_i)(1 + tt_i)\left(1 - r^2 s_i^2 t_i^2 - s^2 r_i^2 t_i^2 - t^2 r_i^2 s_i^2\right) \tag{4.32}$$

for the midside nodes. The degenerate form needed for the cofferdam analysis is shown in Figure 4.10b. The shape functions for the nodes numbered in the figure are the ones that require modification and are denoted by asterisks. The modifications are

$$N_2^* = N_2 + N_3 + N_{10} \tag{4.33}$$

$$N_6^* = N_6 + N_7 + N_{14} \tag{4.34}$$

$$N_{18}^* = N_{18} + N_{19} \tag{4.35}$$

$$N_1^* = N_1 + \Delta N_1 \tag{4.36}$$

$$N_4^* = N_4 + \Delta N_1 \tag{4.37}$$

$$N_{12}^* = N_{12} - 2\Delta N_1 \tag{4.38}$$

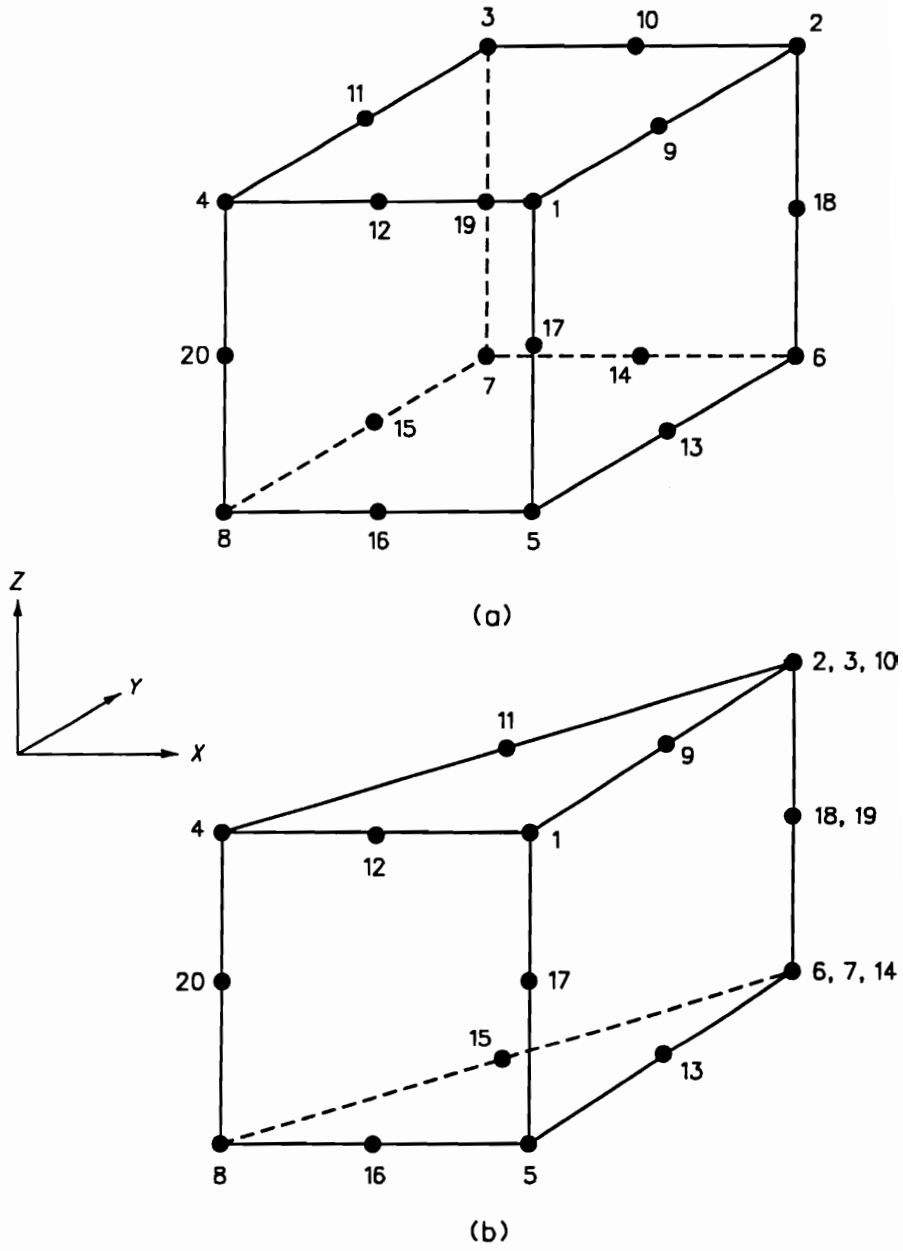

Figure 4.10: Degeneration for a quadratic serendipity element.

$$N_5^* = N_5 + \Delta N_5 \tag{4.39}$$

$$N_8^* = N_8 + \Delta N_5 \tag{4.40}$$

$$N_{16}^* = N_{16} - 2\Delta N_5 \tag{4.41}$$

where

$$\Delta N_1 = \frac{1}{16}\left(1 - r^2\right)\left(1 - s^2\right)(1 + t) \tag{4.42}$$

$$\Delta N_5 = \frac{1}{16}\left(1 - r^2\right)\left(1 - s^2\right)(1 - t) \tag{4.43}$$

For all of the remaining nodes of the element, the original shape functions, Eq. 4.31 and 4.32, hold true.

4.3.2 Implementation for Degeneration of 3-D Element

As previously stated the existing code had an 8 to 21 node, three–dimensional brick–type solid element. The basic code had a scheme for altering the element's shape functions if additional nodes are added above the basic 8–node configuration (linear case).

The modifications for the degeneration of the brick was implemented in a similar fashion. If two corner nodes were collocated and the element face is quadratic, the modification to the shape functions are made. The degenerated elements are input with the same number of nodal entries as the typical brick element but with node numbers repeated at the collocated points.

4.3.3 Verification of 15–Node Wedge Element

Two problems were solved to verify the degeneration of the three–dimensional brick element. The first of these consisted of a single element with a surface pressure as

shown in Figure 4.11a. Figure 4.11b shows the results of the finite element analysis with the implementation. This figure shows uniform settlement across the loading surface as would be expected for successful implementation. The second problem was the example that first revealed the difficulty in collapsing the quadratic brick, Figure 4.9. The results with and without the modifications for degeneration of the brick element given in Figure 4.12 show how the modification led to a solution which is consistent with a uniform surface loading. The test problems demonstrated the new procedures for degeneration of quadratic three–dimensional brick elements into 15–node wedge elements were implemented successfully. It is notable that while the present effort concentrated on the 15–node wedge configuration for the cofferdam analysis, it should also work for the other possible degenerations of the element.

4.4 Shell Element

As pointed out in the Chapter 3, the presence of steel sheet piles in the cofferdam system made it necessary to include a shell element in the element library. The small cross–sectional thickness of the sheet piles, 0.5 in., and the large number of elements needed to model the problem dictated the use of an element other than the solid 20–node element to simplify the mesh generation around the connection of the arc cell to the main cell. The following requirements were in selecting the shell element for this study:

- Nodes only at the midsurface of the element.
- Higher–order shape functions to approximate the curved geometry of the cells.

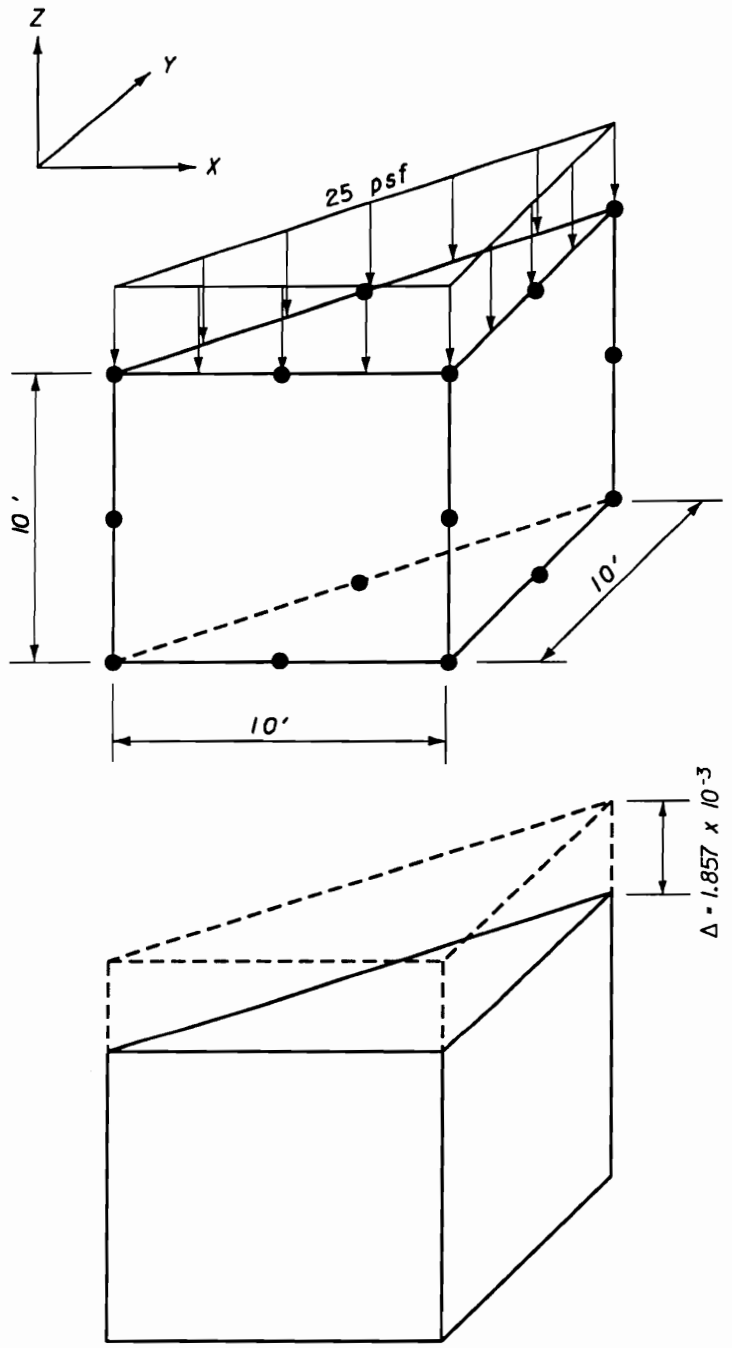

Figure 4.11: Single–wedge element with a surface pressure.

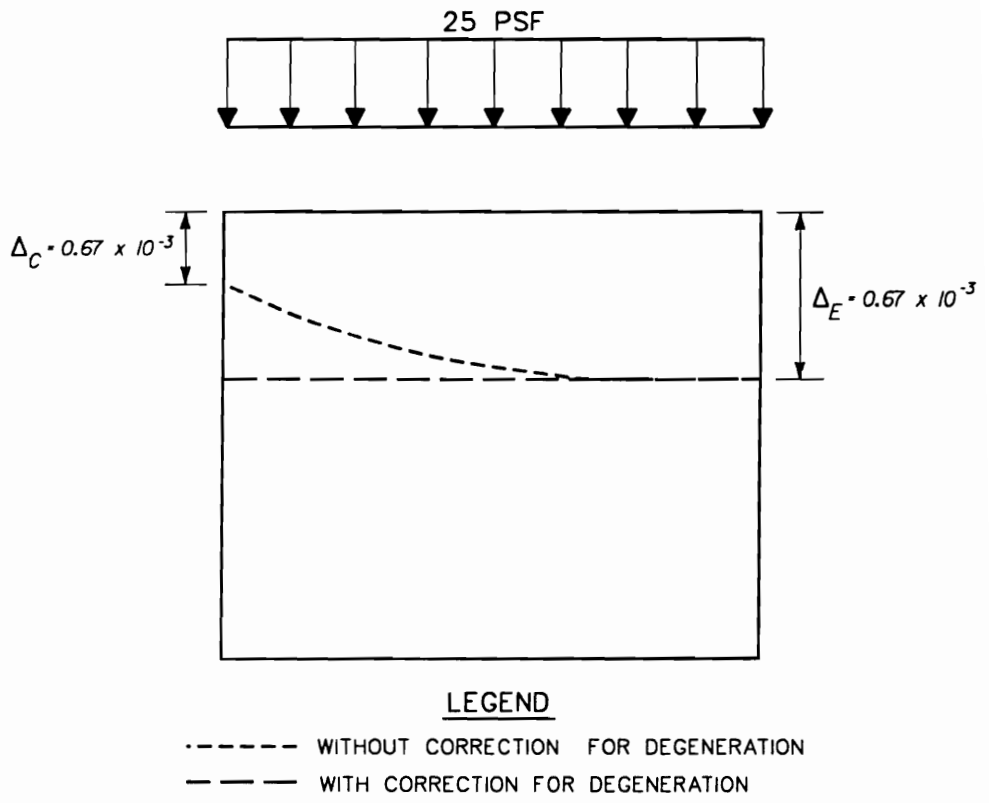

Figure 4.12: Results for four–wedge elements with a surface pressure.

- Anisotropic stress–strain properties to allow for a different Young's modulus value in the tangential direction.

The shell element proposed by Reddy [47] using a doubly curved isoparametric rectangular anisotropic shell element was used in the code. The element derived based on orthogonal curvilinear coordinate (shell coordinates) system with the reference surface of the element midsurface (Figure 4.13). The formulation of the element is presented in Appendix C. The quadratic (8–node) isoparametric form of the element was used in the code. The element stiffness matrix is 40 by 40.

This element is too stiff for thin shells but yields good results for moderately thick shells. To avoid the overstiffening (i.e locking) of the elements for thin shells, reduced integration is required in the evaluation of the stiffness coefficients associated with shear energy terms. For the quadratic isoparametric element, the 2×2 Gauss rule was used for shear energy terms and the standard 3×3 Gauss rule was used for bending terms.

4.4.1 Implementation of Shell Element Formulation

The three–dimensional code was based on cartesian coordinates in contrast to the shell element which was based on orthogonal curvilinear coordinates. This meant that the input coordinates for the geometry defining the shell elements had to be transformed to curvilinear coordinates to develop the local stiffness for the shell element, while the stiffness of the shell elements had to be transformed to the global coordinate system (cartesian) for assembly. This posed some difficulty in maintaining a generalized shell element for the new code. Therefore, only a shell element specifically geared for the sheet–pile cellular cofferdam was implemented.

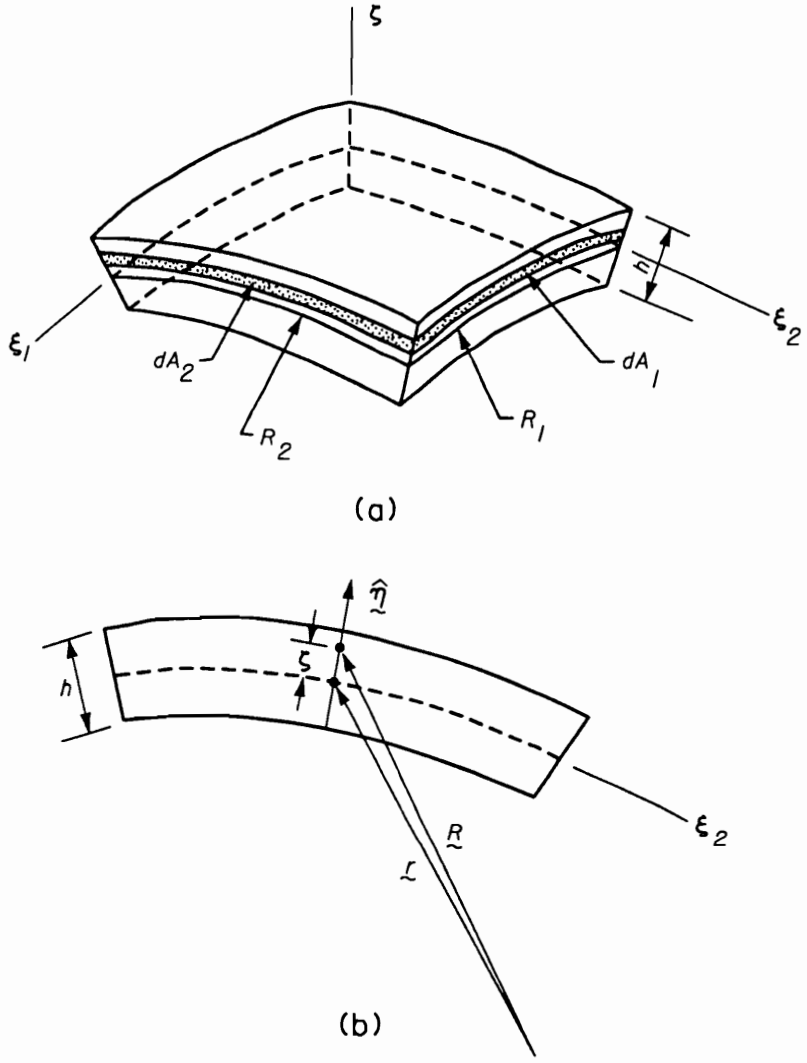

Figure 4.13: Geometry of the shell element [47].

For the formulation for a doubly curved, isoparametric, rectangular, anisotropic shell element, the coordinates of the shell element are defined by two radii, two angles, and a z–coordinate. For the cofferdam analysis, the element needs to be curved in one direction only. This was accomplished by approximating one of the radii as infinity. Thus, the coordinates for the shell element can be defined by a radius, an angle, and a z–coordinate. Local origins for the different radii of the cofferdam geometry had to be designated to compute the shell element coordinates. This was accomplished by specifying a different material type for each curved region of the cell configuration and specifying the origin for each of the regions.

4.4.2 Verification of Shell Element

The validity of the formulation for the shell element was provided Reddy [47]. The primary goal here is verify the implementation of the shell element in the new code.

To verify the implementation, a cylinder subjected to internal surface pressure was used (Figure 4.14a). The cylinder has a composite wall consisting of an inner thick–wall cylinder surrounded by an outer thin–wall cylinder. If the outer thin–wall cylinder is assumed to have the same material properties as the inner thick–wall cylinder, the basic equations for an open–end thick–wall cylinder presented in Section 3.6.3 should give the stresses and displacements of the cylinder walls. The equations from Section 3.6.3 are

$$\sigma_r = \frac{a^2 p_i - b^2 p_o}{b^2 - a^2} + \frac{a^2 b^2 (p_o - p_i)}{r^2 (b^2 - a^2)} \tag{4.44}$$

$$\sigma_\theta = \frac{a^2 p_i - b^2 p_o}{b^2 - a^2} - \frac{a^2 b^2 (p_o - p_i)}{r^2 (b^2 - a^2)} \tag{4.45}$$

$$\sigma_{r\theta} = 0 \tag{4.46}$$

$$u = \frac{1-\nu}{E}(r)[\frac{p_i a^2 - p_o b^2}{b^2 - a^2}] + \frac{1+\nu}{E}[\frac{a^2 b^2 (p_i - p_o)}{r(b^2 - a^2)}] \tag{4.47}$$

where

r is the radial distance.

σ_r is the stress in the radial direction.

σ_θ is the stress in the tangential direction.

p_o is the uniform external pressure.

p_i is the uniform internal pressure.

a is the inner radius of the cylinder.

b is the outer radius of the cylinder.

$\sigma_{r\theta}$ is the shear stress in the $r\theta$ plane.

ν is the Poisson's ratio of the cylinder material.

E is the Young's modulus of the cylinder material.

u is the displacement in the radial direction.

The symmetry of the loading and geometry allowed the representation of the problem by only one quadrant. The finite element mesh used in the analysis is shown in Figure 4.14b. The mesh consists of eight 20–node solid elements for the inner thick–wall cylinder and four shell elements for the outer thin–wall cylinder. The nodes at the top and bottom are restrained in the vertical (z) direction. The problem is modeled by applying a uniform internal surface pressure, p_i, of 20 psi normal to the interior elements of the mesh shown in Figure 4.14b. The values of the parameters for the problem are:

$$\begin{aligned} \nu &= 0.3 \\ E &= 1390 \quad \text{psi} \\ a &= 360 \quad \text{in.} \end{aligned}$$

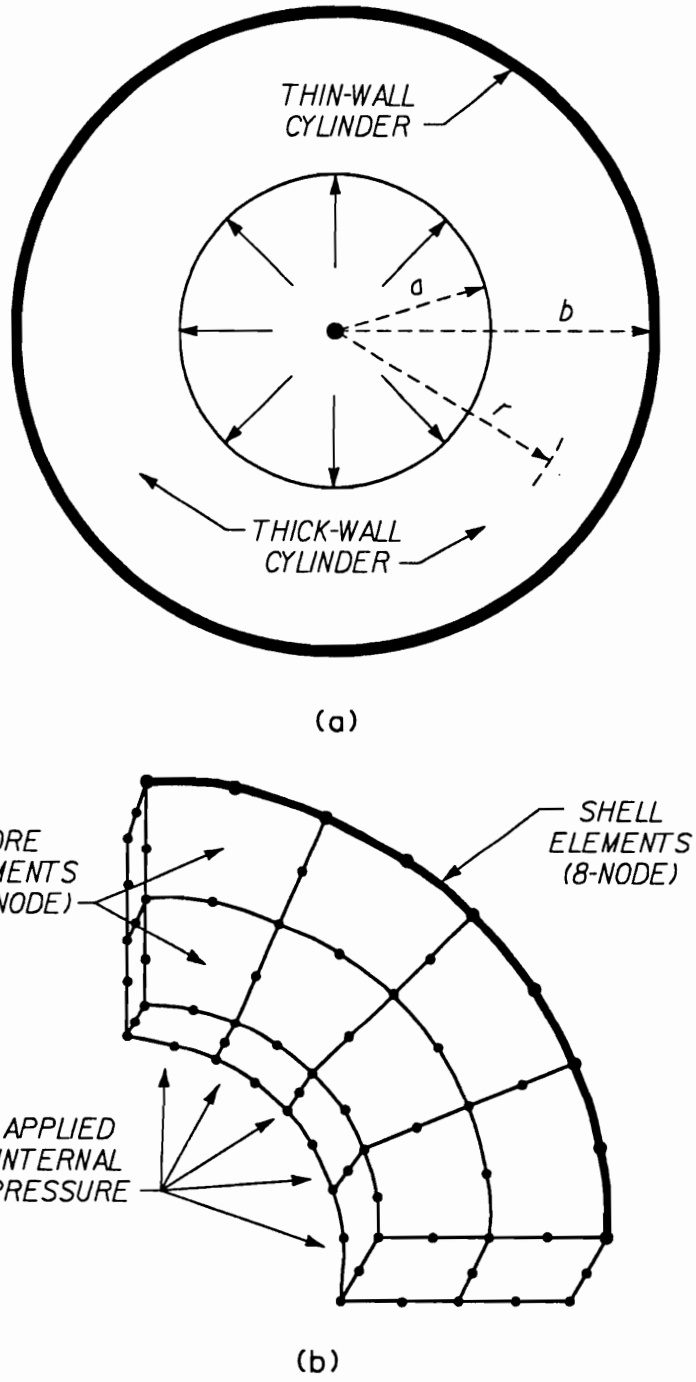

Figure 4.14: Composite, thick–wall cylinder problem: a. composite, thick–wall cylinder with an internal surface pressure; and b. finite element mesh for the composite–wall cylinder.

$$b = 720 \quad \text{in.}$$

The displacements from the finite element analysis and the Eq 4.47 are compared in Figure 4.15 and there is excellent agreement between the two sets of results.

The problem was reanalyzed with an increased Young's modulus, ($E = 30,000,000$ psi), for the outer thin–wall cylinder. No exact theoretical solution was available for this problem. An approximate analytical solution for the problem was obtained by taking the radial displacement of the outer cylinder from the finite element analysis and using it in the equation for the deformation of thin–wall pressure vessel to compute the internal pressure needed to get that displacement in the inner thick–wall cylinder. The deformation of a pressure vessel is given as:

$$u_r = \frac{qR^2}{Et} \tag{4.48}$$

where

u_r is the displacement of pressure vessel in the radial direction.

q is the uniform internal pressure in the vessel.

R is the radius of the pressure vessel.

t is the wall thick of the pressure vessel.

The resulting internal pressure was then substituted in Eq 4.47 as a uniform external pressure, p_o, with a uniform internal pressure, p_i, of 20 psi to compute the radial displacement of the inner thick–wall cylinder. These calculated displacements are compared with the finite element results in Figure 4.15, and this indicates that the shell element is computing the stiffness of the shell element accurately.

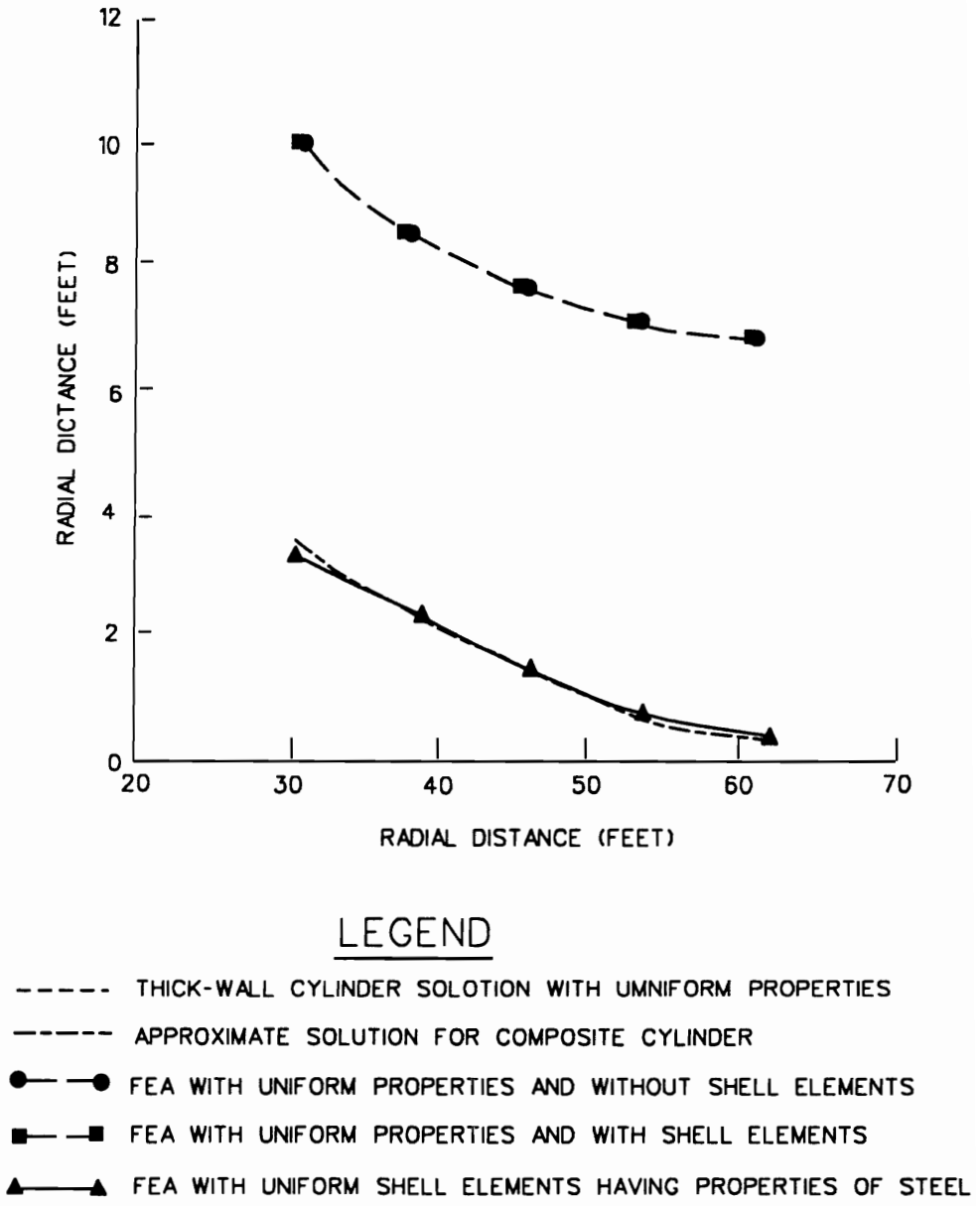

Figure 4.15: Variation of radial displacements with radius.

4.4.3 Representation of the Sheet Piling with Shell Element

The cell membrane is made up of individual sheet piles connected through interlocks (Figure 4.16). For example, a single main cell at Lock and Dam No. 26(R) was made up of 154 sheet piles, while 78 more were needed for the arc cell. To realistically model a cellular cofferdam, it is necessary to account for the primary aspects of the response of the sheet piles comprising the cell membrane. In conventional analysis procedures, the sheet–pile cell is assumed to respond as a perfect pressure vessel. With this assumption, the sheet piles comprising the cells are expected to be in perfect alignment after installation, and the interlocks are to serve as a ideal connections which generate no movement in themselves. This perfect pressure vessel assumption over simplifies the behavior and is far from the actual behavior of the sheet–pile cell system. Load testing of interlocks shows a strongly nonlinear load–displacement pattern caused in the main by imperfect initial contact along the interlock (Figure 4.17). In the initial phase of the test, the interlock undergoes significant movement under a low level of loading. Gradually the interlock stiffens, and for subsequent levels of loading, the displacements are smaller. Each of these phases of loading reflect a different portion of the interlock behavior. In the initial phase of loading there are major gaps and openings along the interlock where the steel in the *thumb and finger* connection is only in partial contact. As the load level increases, the gaps and openings close, and the steel–to–steel contact increases, causing the stiffening of the interlock response.

The membrane theory of thin–wall pressure vessels is a simple, yet representative, tool for predicting the response of a sheet–pile cell filled with soil. Using membrane

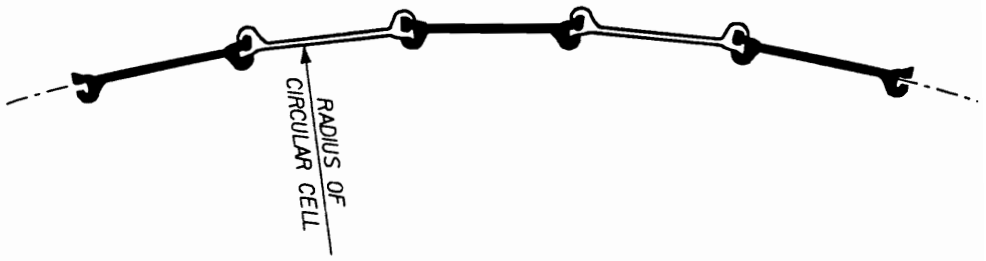

Figure 4.16: Sheet–pile interlock connections for cellular cofferdam.

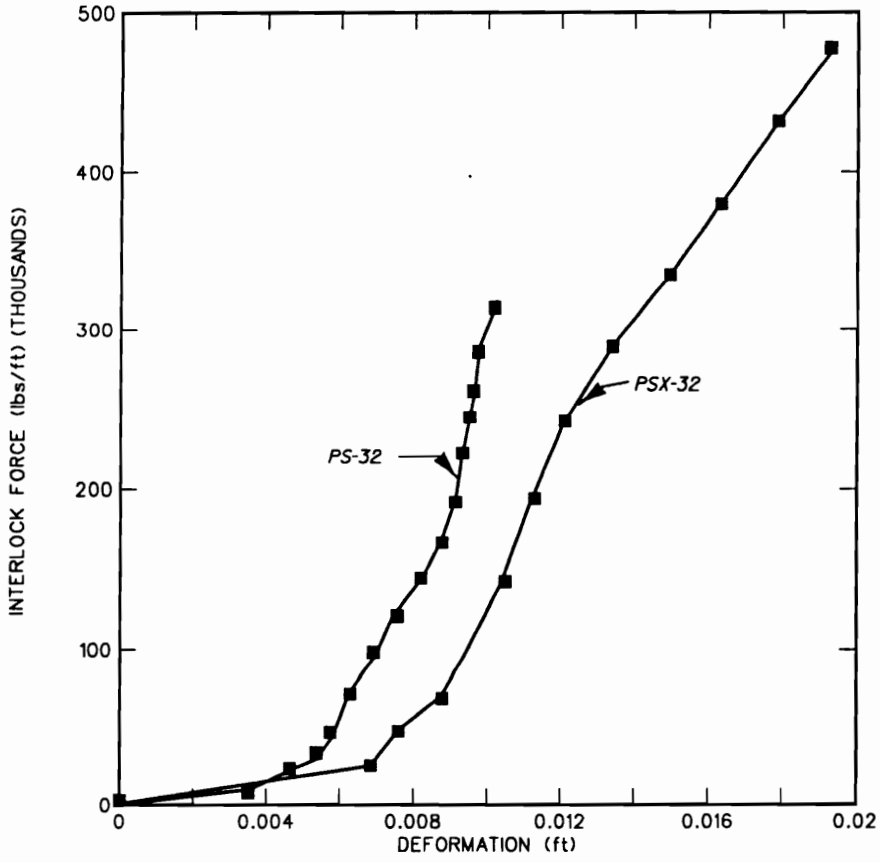

Figure 4.17: Measured load–displacement behavior of sheet–pile interlocks [8, 33, 53].

theory, the interlock tension (hoop stress), t, in the sheet–pile of a cell is computed by

$$t = pr \tag{4.49}$$

where p is the lateral pressure acting against the wall and r is the radius of the cell. The displacement is computed by

$$w_p = \frac{pr^2}{Eh} \tag{4.50}$$

where p and r are as previously defined, E is the Young's modulus, h is the uniform thickness of the idealized cell wall. The principal unknown in this computation is the lateral pressure. The variation in radius for a given cell has a negligible effect on the results. The lateral pressure is the earth pressure against the cell walls resulting from the placement of cell fill. The magnitude of the earth pressure against the cell walls is a function of the movement of the cell walls. If the cell fill is placed in a rigid, unyielding cell, the lateral earth pressure would be at an at–rest condition, but a sheet pile is flexible and will spread lateral. As the cell fill moves laterally, it shears and mobilizes its shear strength. The shear strength of the fill tries to resist this lateral movement. Thus, reducing the lateral earth pressure applied to the cell walls in turn reduces the interlock tension and the interlock tension is a function of the flexibility of the cell walls.

In Clough and Hansen's [7] finite element analysis of the Willow Island cofferdam, they were unable to accurately predict the deflections of the sheet piles during cell filling. Stevens [59] later reanalyzed the Willow Island cofferdam with Clough and Hansen's vertical slice model using a reduced stiffness for the springs connecting the inner and outer walls. With this reduction in spring stiffness, he could more accurately predict deformations in the sheet–pile cell during filling. Stevens [59]

correctly recognized that the steel sheet piles forming the cells cannot be represented as an isotropic linear elastic pressure vessel.

Separately, Clough and his associates [8, 33, 53] recognized that the sheet–pile membrane of the cells for the Lock and Dam No. 26(R) did not deform as a perfect pressure vessel with the properties of steel. Measured deformations ranged from 10 to 30 times those computed by the finite element analyses using the elastic properties of steel. They felt in light of the construction process and nature of the sheet–pile system, it is unlikely that the perfect pressure vessel assumption used in previous finite element analysis was realistic. First, the slack and gaps found in the interlock connections must be taken up during filling of the cell. Second, the hoop tension in the cells is transmitted over a small bearing area in the interlock. This can lead to rotation and/or local yielding of the interlocks which is supported by the fact that the hoop strength is controlled by the interlock connection. Third, it appears probable that a certain amount of realignment of the sheet piles takes place during filling to reach a more stable configuration which would lead to greater movements than would occur if the system was perfectly aligned initially. All of these factors suggest that movements in the radial direction of a cell would exceed those of a perfect pressure vessel during filling. This explained the reason that previous finite element studies using the perfect pressure vessel concept had seriously underestimated the deformation of the cells during filling.

A major aspect in the three–dimensional modeling of the cellular cofferdams with the new three–dimensional finite element code was in accounting for this flexibility of the sheet piling. The shell element described in this section allows the sheet piling to be modeled as an orthotopic shell and to reduce the elastic modulus in the horizontal direction with respect to that in the vertical direction (actual material modulus).

The resulting ratio of the horizontal modulus to material modulus is called the E–ratio. This approach was adopted by Clough and his associates in the axisymmetric model used for Lock and Dam No. 26(R) first–stage cofferdam [8, 33, 53].

Clough and his associates [53] used inclinometer and strain gage data to estimate the modulus along the circumference of the cell membrane and compute the corresponding E–ratio. They used the inclinometer readings to arrive at an average radial movement at the point of maximum bulge. They converted this radial displacement to an average circumferential strain. Next, they used the stain gage data to arrive at an average interlock force. The average interlock force was converted to a hoop stress by using the thickness of the web. An estimate for the average circumference modulus was calculated by dividing the average hoop stress by the average circumferential strain and this value was then divided by the Young's modulus for steel to obtain an E–ratio.

For the first–stage cofferdam for the construction of Lock and Dam No. 26(R), the E–ratios estimated ranged from 0.01 to 0.03 for hoop stresses at one standard deviation from the average measured. This estimate is crude because only four inclinometers could be used to arrive at an average radial deflection, but it is useful for estimating the order of magnitude of the E–ratio to be used in the analyses and should predict stresses and deflections in the cells which correspond to those measured in the field.

As a follow–up to the estimate of E–ratio, Clough and his associates [53] conducted a parametric study with the axisymmetric model with E–ratios of 1.0, 0.1, and 0.03. Cell filling is the primary cause of lateral expansion of the cell membrane. The axisymmetric model which most closely represented the behavior of main cell during filling was the best of the two–dimensional models for examining the effects of

different E–ratios. Varying the E–ratio from 1.0 to 0.03 gives a wide range of possibilities to consider. Figure 4.18 compares the radial deflection of the cell membrane after completion of filling for the three E–ratios along with the range of measured values. It shows that the smaller the E–ratio, the more flexible the cell membrane, the larger the radial deflection. The maximum radial deflection occurs at the same elevation in all instances, but the magnitudes were 3.4, 1.3, and 0.2 in. for E–ratios of 0.03, 0.10, and 1.0, respectively. An E–ratio of 0.03 best represented the field measurements, but is still slightly lower than the approximate average measured observations. Figure 4.19 compares the interlock forces in the cell membrane after completion of filling for the three E–ratios along with the range of measured values. They found that there was a general trend between magnitude of the interlock forces and the logarithm of the E–ratio. The maximum values for the interlock forces are 6.8, 4.5, and 3.4 kips per in. for E–ratios of 1.0, 0.1, and 0.03, respectively. The predicted interlock forces for the three E–ratios show similar trends as the measured data. The predicted interlock forces using an E–ratio of 0.03 agrees more closely with an approximate average of the observed data, while predicted values using an E–ratio of 1.0 are far greater than nearly all of the measured values. Figure 4.20 compares the predicted and measured earth pressure after completion of filling for the three E–ratios. The pressures against the cell walls above the dredgeline vary proportionately with the E–ratio value. An E–ratio of 1.0 yields pressures nearly equal to at–rest pressures, an E–ratio of 0.1 yields pressures between the at–rest and active states, and an E–ratio of 0.03 yields pressures approximately equal to the active state. Although many of the pressure cells in the upper part of the cofferdam did not function properly, the measured earth pressures in the lower portion of the cell follow similar trends to the predicted earth pressures for an E–ratio of

0.03. The magnitudes of the coefficients for E–ratios of 0.03 and 0.1 fall within the range of observed data, while the values for E–ratio of 0.03 lie closer to the mean observed values.

These results illustrate the importance of soil–structure interaction: the more flexible the cell, the higher the radial displacements, and the lower the horizontal earth pressures on the cell walls, consequently, the lower the interlock forces within the sheet piling. It appears that the flexibility offered by an E–ratio equal to 0.03 achieves essentially the optimum situation in reducing the earth pressures and interlock forces, since an active earth pressure state was nearly reached in the cell fill. Figure 4.21 shows the predicted average earth pressure coefficients versus the maximum radial deflections for the three E–ratios. The earth pressure against the cell membrane drops sharply at small levels of movement, and the rate of decrease in earth pressure flattens significantly at the larger movements. A greater degree of flexibility than that offered by the E–ratio of 0.03 would not result in any significant reduction in earth pressure, since the near active state is reached at this level of flexibility.

Experimental results [2, 43, 54] show that the E–ratio for the sheet piling at Lock and Dam No. 26(R) was between 0.01 and 0.14. The experimental results were from simple pull tests [43, 54] and from a assembly of four sheet piles with a internal pressure to simulate the earth pressure from the cell fill [2]. The E–ratio of 0.03 used in previous two–dimensional finite element studies is within the experimental range of values and supports its use in the Lock and Dam No. 26(R) studies.

The general philosophy for this research was to develop a three–dimensional finite element code that would be consistent with the previous two–dimensional finite

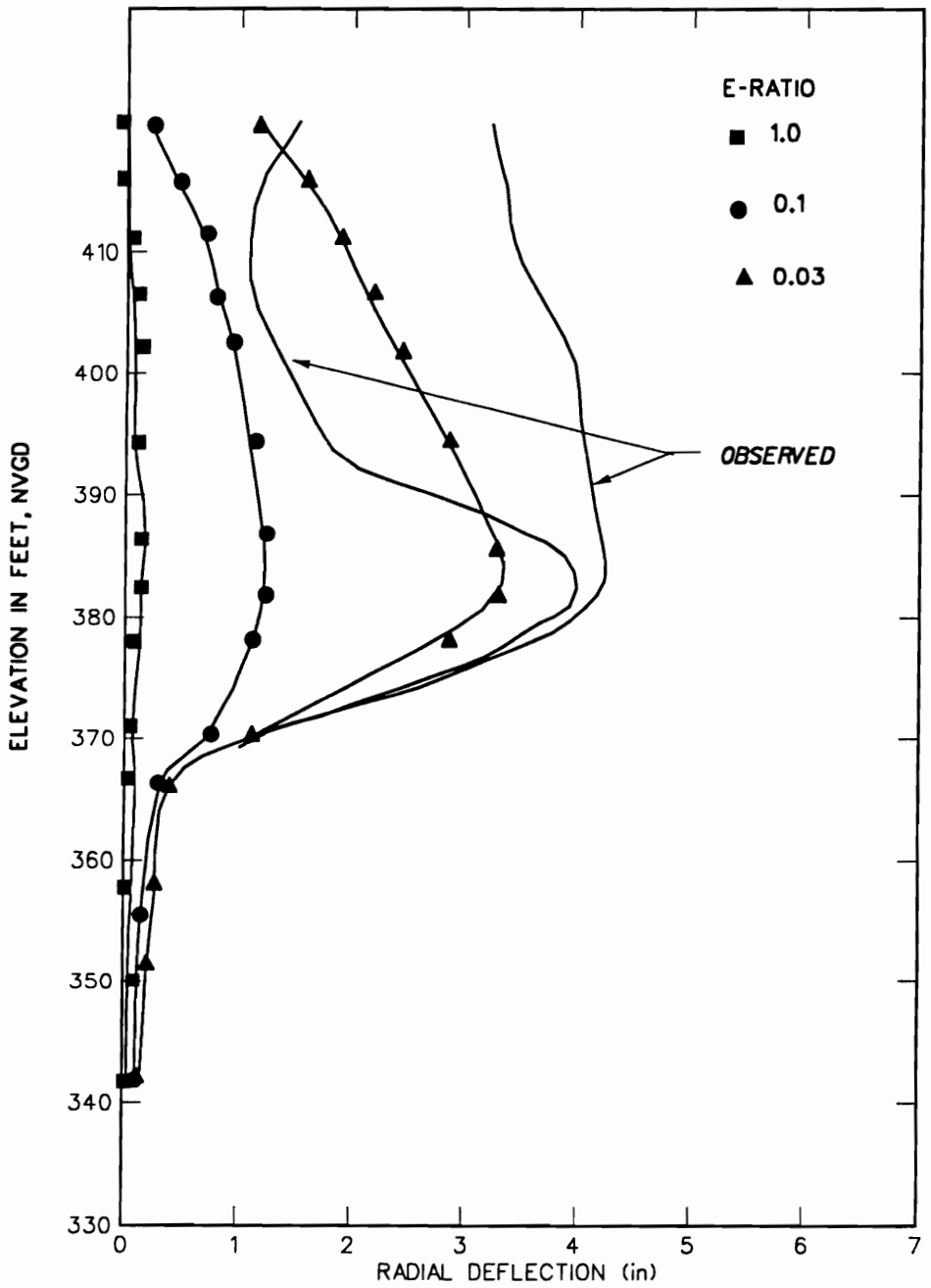

Figure 4.18: Comparison of radial deflections for three different E–ratios.

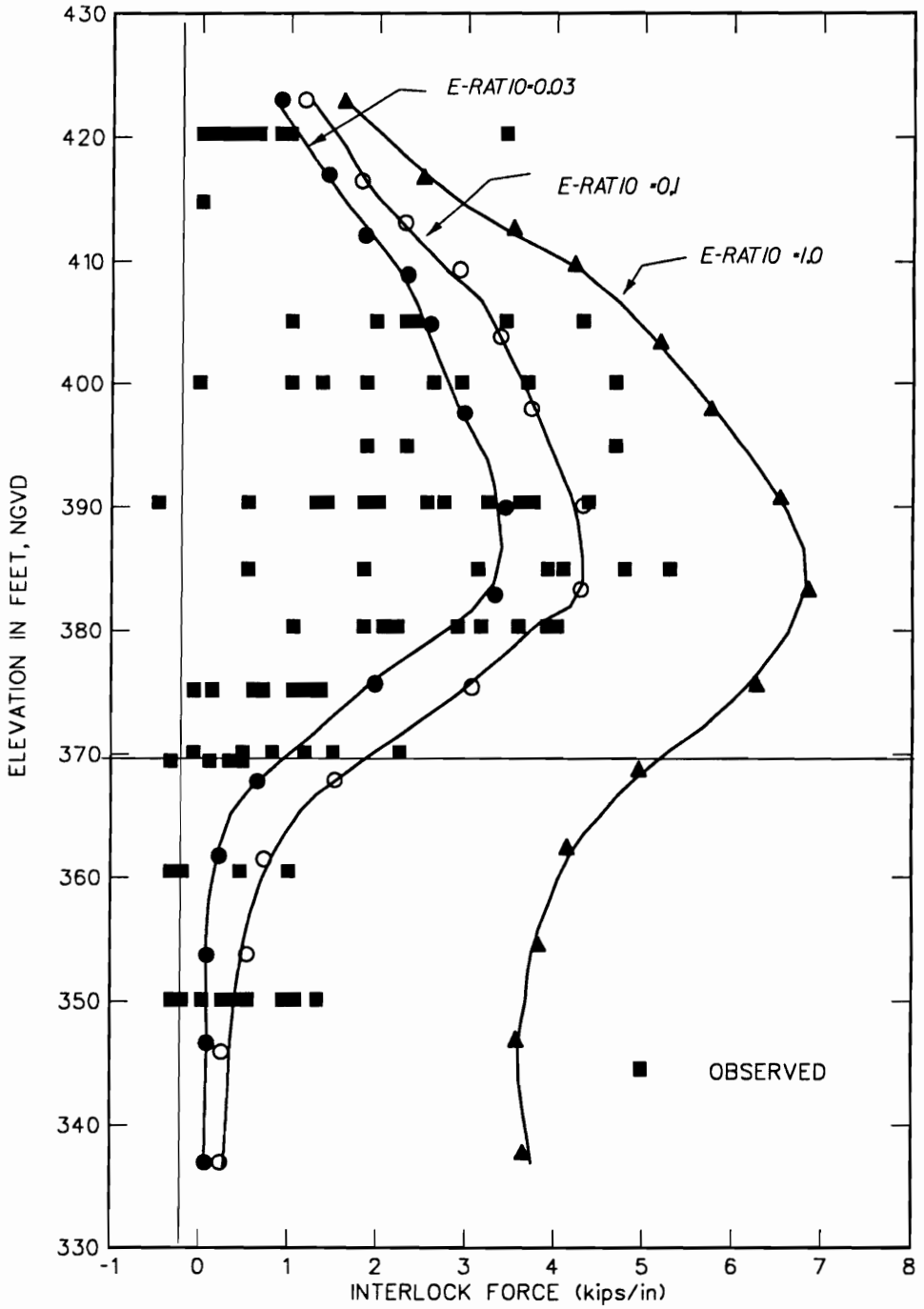

Figure 4.19: Comparison of interlock forces for three different E–ratios.

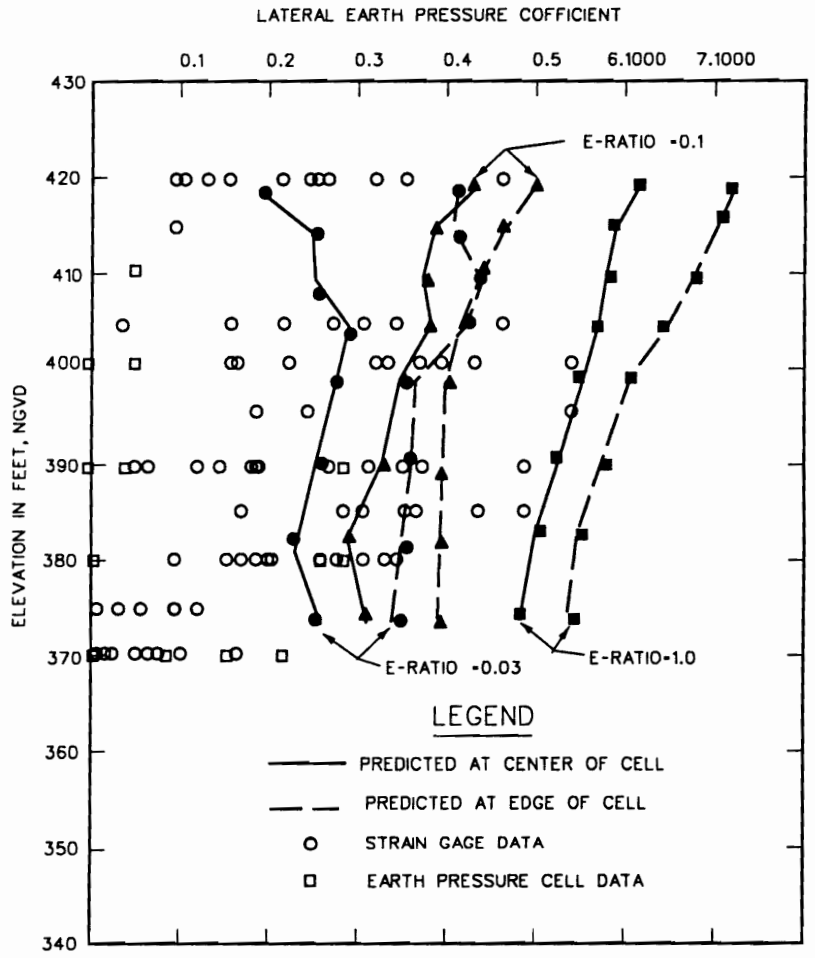

Figure 4.20: Comparison of predicted and measured earth pressures for three different E–ratios.

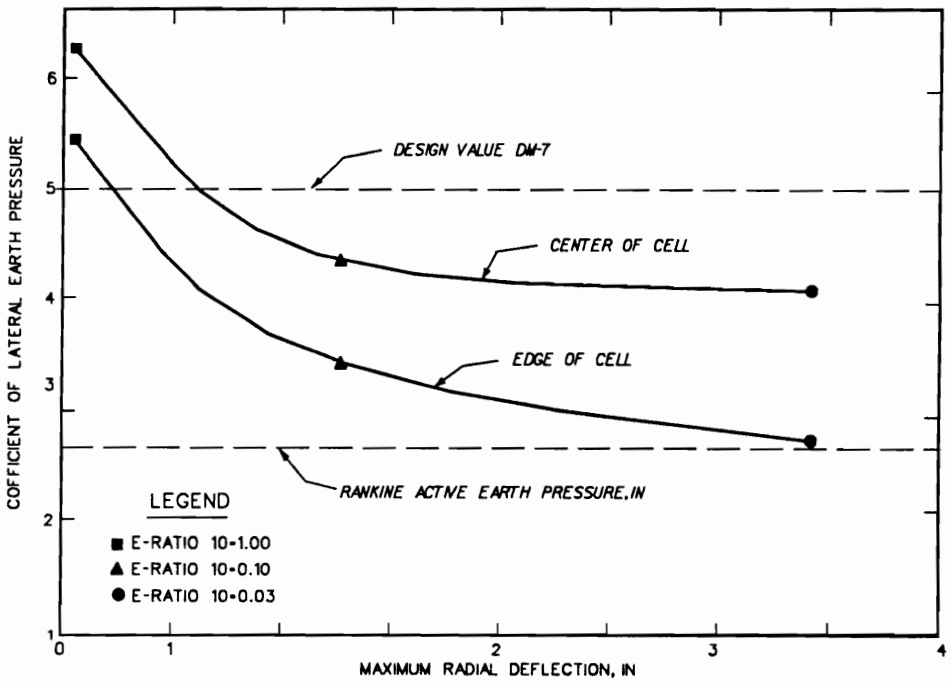

Figure 4.21: Change in predicted lateral earth pressure coefficients with maximum radial deflections.

element codes used in the Lock and Dam No. 26(R) studies [8, 33, 53], and to compare the two–dimensional results for the Lock and Dam No. 26(R) cofferdam to the three–dimensional findings. In keeping with this philosophy, the E–ratio of 0.03 was used in all of the analyses simulating the filling of the cells, while an E–ratio of 1.0 was used during differential loading.

4.5 Summary

In this chapter, the necessary additions to the element library for the new three–dimensional finite element code were presented. The limitations of previous interface elements were discussed and the new three–dimensional interface element was described. Advantages of the new interface element were demonstrated as increased stability and improved modeling of soil-structure interaction over the older elements.

The geometry of the cofferdam required the use of wedge shaped elements in locations to generate a smooth consistent mesh. In the process of verifying the code, it was discovered that the quadratic forms of the brick element in the original code would not yield the correct displacements when degenerate to a wedge element. Procedures were described to solve this problem. The implementation and verification of the procedures in the code were presented.

The small cross-sectional thickness of the sheet piles, 0.5 in., and the large number of elements needed to model the problem made it necessary to have a shell element in the new code. The presence of such an element simplifies mesh generation around the connection of the arc cell to the main cell. A functional shell element was selected which allows for:

- Nodes at the midsurface of the element only.

- Higher–order shape functions to approximate the curved geometry of the cells.
- Anisotropic stress-strain properties to allow for a different Young's modulus value in the tangential direction.

Table 4.1: Computed Displacements for Interface Test Problem 1.

Corner Nodes	Finite Element Solution Relative Displacements (Feet)			Closed Form Solution Relative Displacements (Feet)		
	x	y	z	x	y	z
1	0.2500	$\ll 10^{-10}$	$\ll 10^{-10}$	0.2500	0.0000	0.0000
2	0.2500	$\ll 10^{-10}$	$\ll 10^{-10}$	0.2500	0.0000	0.0000
3	0.2500	$\ll 10^{-10}$	$\ll 10^{-10}$	0.2500	0.0000	0.0000
4	0.2500	$\ll 10^{-10}$	$\ll 10^{-10}$	0.2500	0.0000	0.0000
5	0.2500	$\ll 10^{-10}$	$\ll 10^{-10}$	0.2500	0.0000	0.0000
6	0.2500	$\ll 10^{-10}$	$\ll 10^{-10}$	0.2500	0.0000	0.0000
7	0.2500	$\ll 10^{-10}$	$\ll 10^{-10}$	0.2500	0.0000	0.0000
8	0.2500	$\ll 10^{-10}$	$\ll 10^{-10}$	0.2500	0.0000	0.0000

Chapter 5

Three–Dimensional Soil Constitutive Model

5.1 Introduction

To accurately represent the behavior of the sheet–pile cellular cofferdam system, the complex response of the soil must be included in the three–dimensional finite element model. The stress–strain response is a function of the basic material characteristics, relative density, water content, stress history, stress path, principal stress difference, and confining pressure. For the analysis of the cofferdam, it was important to capture the key aspects of the soil behavior and the parameters that control that behavior within a constitutive relationship. In this chapter, the development of a new three–dimensional constitutive model for soil is presented.

5.2 Background

In keeping with the general philosophy for developing the finite element code, the constitutive model for the soil was to be of the same order of complexity as the one employed in the finite element code, **SOILSTRUCT**, used in the two-dimensional analyses of the Lock and Dam 26(R) cofferdam. **SOILSTRUCT** uses a version of the Duncan-Chang model which is often referred to as the hyperbolic model because a hyperbola is used to approximate the relationship between shear stress and strain during primary loading. A substantial amount of experience has been gained over the years with this model along with a wealth of data related to its parameters used in the model [16, 17]. One of the main reasons for its longevity is its simplicity. The parameters for the model can be obtained from triaxial tests by a straight-forward procedure, and when test data are not available there is a large data base of published values for estimating parameters [16, 17]. However, direct implementation of this model into the code is impossible because it is limited to two-dimensional problems. Therefore, it was necessary to develop a new model or to find an appropriate model in the literature.

The criteria for the model were: to keep it as simple, and conceptually similar to the Duncan-Chang model, and to keep the parameters definable by commonly used laboratory tests. Three important characteristics of the stress-strain response of soils that the model must emulate are nonlinearity, stress-dependency, and inelasticity.

The Duncan-Chang model falls into a special class of constitutive relationships called variable moduli models. Variable moduli models are mathematical representations that describe the relationship between the increments of stress and strain,

yet, have no unique relationship or explicit yield condition. These models are essentially elasticity based. To account for inelastic behavior during unloading, a special load criterion is needed and separate stress–strain relationships are used for loading and unloading.

5.2.1 Incremental Analysis

For incremental analysis, the stress–strain response is formulated simply by replacing the elastic constants in an isotropic linear model by the tangent moduli which are functions of the stress and/or strain. Using the variable moduli model, the three–dimensional incremental stress–strain relationship can be described mathematically as

$$ds_{ij} = 2G_t de_{ij} \tag{5.1}$$

$$dp = 3K_t de \tag{5.2}$$

where ds_{ij} and de_{ij} are the incremental deviatoric stress and strain, respectively, and dp is the incremental mean normal stress and de is the incremental volumetric strain. Writing the equations in this fashion implies that the material is isotropic. Furthermore, separation of the constitutive relationship into deviatoric and volumetric parts prevent any coupling between them as occurs when a soil dilates during shearing. However, for application to the cofferdam problem, this simplification should yield a sufficiently accurate representation of the soil.

For an incremental finite element analysis, the stress–strain relationship is

$$\{d\sigma\} = [C_t]\{d\epsilon\} \tag{5.3}$$

where $\{d\sigma\}$ and $\{d\epsilon\}$ are the incremental stress and strain vectors, respectively, and $[C_t]$ is the tangent constitutive matrix. For the variable moduli model, the tangent

constitutive matrix has the form

$$[C_t] = \begin{bmatrix} K_t + \frac{4}{3}G_t & K_t - \frac{2}{3}G_t & K_t - \frac{2}{3}G_t & 0 & 0 & 0 \\ K_t - \frac{2}{3}G_t & K_t + \frac{4}{3}G_t & K_t - \frac{2}{3}G_t & 0 & 0 & 0 \\ K_t - \frac{2}{3}G_t & K_t - \frac{2}{3}G_t & K_t + \frac{4}{3}G_t & 0 & 0 & 0 \\ 0 & 0 & 0 & G_t & 0 & 0 \\ 0 & 0 & 0 & 0 & G_t & 0 \\ 0 & 0 & 0 & 0 & 0 & G_t \end{bmatrix} \tag{5.4}$$

where K_t and G_t are the tangent bulk and shear moduli, respectively. The tangent bulk and shear moduli are the slopes of the stress–strain curve at a given stress and strain level for the pure hydrostatic stress state and pure shear stress state, respectively. As pointed out earlier, for the three–dimensional variable moduli model, the deviatoric (shearing) and volumetric behavior are independent. Looking at the principal stress space as shown in Figure 5.1, the deviatoric and volumetric stress level can be represented as two components. Changes in the volumetric stress level occur along a line referred to as the hydrostatic stress axis where $\sigma_1 = \sigma_2 = \sigma_3$. Changes in the deviatoric stress occur on a plane perpendicular to the hydrostatic line which is called the octahedral plane.

5.2.2 Tangent Shear and Bulk Moduli

Experimental work [41] has shown that the tangent shear modulus, G_t, and bulk modulus, K_t, are dependent on the stress and/or strain level. Commonly, the tangent bulk modulus is taken as a function of the hydrostatic or mean normal stress, while the tangent shear modulus is assumed to depend on both the hydrostatic stress and a measure of the shear stress such as the variable moduli model proposed by

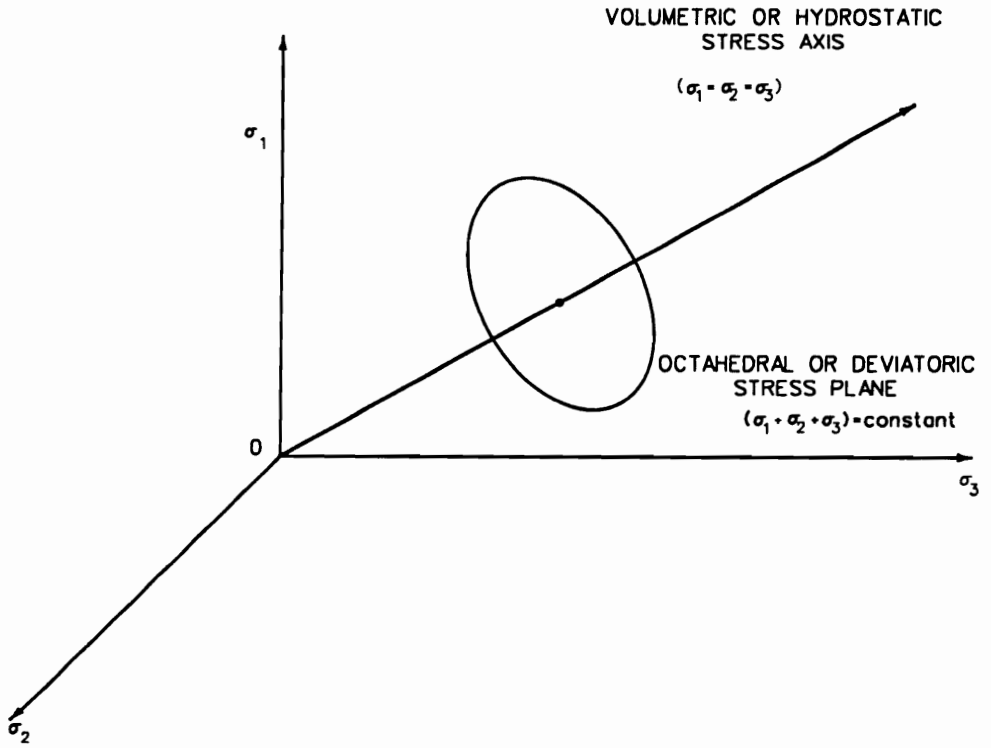

Figure 5.1: Representation of deviatoric and volumetric stresses in three–dimensional stress space.

Nelson and Baron [41].

$$K_t = K_t(\epsilon) = K_0 + K_1\epsilon_v + K_2\epsilon_v^2 \tag{5.5}$$

$$G_t = G_t\left(p, \sqrt{J_2}\right) = G_0 + \alpha_1 p + \alpha_2\sqrt{J_2} \tag{5.6}$$

where K_1, K_2, α_1, and α_2 are constants obtained by curve fitting to laboratory test data and J_2 is the second invariant of the stress deviator. K_0 and G_0 are the initial slope of the curves. This type of representation can be considered as the first terms in a series expansion of more general analytical functions for K_t and G_t.

5.3 New Three–Dimensional Constitutive Model

Although elegant, these above expressions for the tangent shear and bulk moduli lack simplicity and consistency with conventional soil mechanics concepts as found in the Duncan–Chang model. For these reasons, it was decided that a new model would be developed for the cofferdam analysis. The basic idea of a variable moduli models would be maintained, but new expressions for the tangent shear and bulk moduli would be derived.

To establish new expressions for the tangent shear and bulk moduli, the following stress and strain definitions were used:

for shear stress

$$q = \frac{3}{\sqrt{2}}\tau = \frac{1}{\sqrt{2}}\left[(\sigma_1 - \sigma_2)^2 + (\sigma_2 - \sigma_3)^2 + (\sigma_3 - \sigma_1)^2\right]^{\frac{1}{2}} \tag{5.7}$$

for mean normal stress

$$p = \sigma_{oct} = \frac{1}{3}(\sigma_1 + \sigma_2 + \sigma_3) \tag{5.8}$$

for shear strain

$$\epsilon_s = \frac{1}{\sqrt{2}}\tau = \frac{\sqrt{2}}{3}\left[(\epsilon_1 - \epsilon_2)^2 + (\epsilon_2 - \epsilon_3)^2 + (\epsilon_3 - \epsilon_1)^2\right]^{\frac{1}{2}} \tag{5.9}$$

for volumetric strain

$$\epsilon_v = \epsilon_{oct} = \frac{1}{3}(\epsilon_1 + \epsilon_2 + \epsilon_3) \tag{5.10}$$

For the state of stress and strain in a triaxial test ($\sigma_2 = \sigma_3, \epsilon_2 = \epsilon_3$), these expression for stress and strain would reduce to

$$p = \frac{1}{3}(\sigma_1 + 2\sigma_3) \tag{5.11}$$

$$q = (\sigma_1 - \sigma_3) \tag{5.12}$$

$$\epsilon_v = (\epsilon_1 + 2\epsilon_3) \tag{5.13}$$

$$\epsilon_s = \frac{2}{3}(\epsilon_1 - \epsilon_3) \tag{5.14}$$

The tangent bulk and shear moduli are defined as function of the mean normal and shear stress, respectively

$$K_t = K_t(p) \tag{5.15}$$

$$G_t = G_t(q) \tag{5.16}$$

and the incremental stress–strain relationships are

$$dp = 3K_t d\epsilon_v \tag{5.17}$$

$$dq = 3G_t d\epsilon_s \tag{5.18}$$

5.3.1 Tangent Shear Modulus Definition

To define the expression for the tangent shear modulus, it was assumed that the relationship between shear stress and strain during primary loading is represented by a hyperbolic curve, as shown in Figure 5.2, and described mathematically as

$$q = \frac{\epsilon_s}{a + b\epsilon_s} \tag{5.19}$$

This is analogous to the approach used by Duncan and Chang [16, 17], but in their model they used a different definition for strain.

The physical meaning of the parameters a and b is show in Figure 5.3. Defining a and b as

$$a = \frac{1}{3G_i} \tag{5.20}$$

$$b = \frac{1}{q_{ult}} \tag{5.21}$$

where $3G_i$ is the initial slope of the stress–strain curve, and q_{ult} is the asymptote of the stress–strain function, the expression for shear stress versus shear strain can be written as

$$q = \frac{\epsilon_s}{\frac{1}{3G_i} + \frac{1}{q_{ult}}\epsilon_s} \tag{5.22}$$

The tangent shear modulus can be written as

$$G_t = \frac{dq}{3d\epsilon_s} \tag{5.23}$$

Differentiating Eq. 5.22 with respect to ϵ_s yields

$$\frac{dq}{d\epsilon_s} = \frac{1}{3G_i\left[\frac{1}{3G_i} + \frac{\epsilon_s}{q_{ult}}\right]^2} \tag{5.24}$$

Writing Eq. 5.22 in terms of the shear stress gives

$$\epsilon_s = \frac{q}{3G_i\left[1 - \frac{q}{q_{ult}}\right]} \tag{5.25}$$

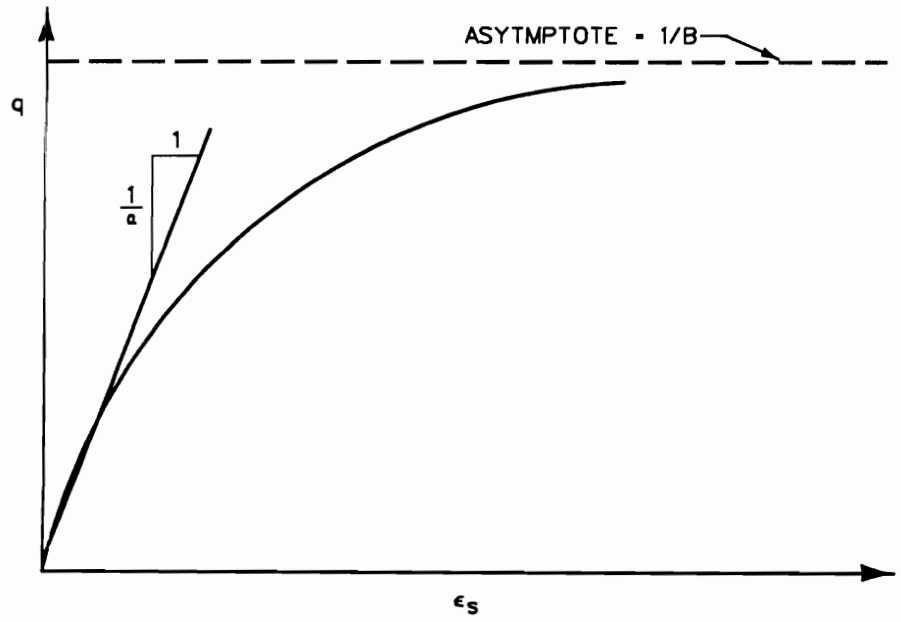

Figure 5.2: Hyperbolic representation of the shear stress and strain curve.

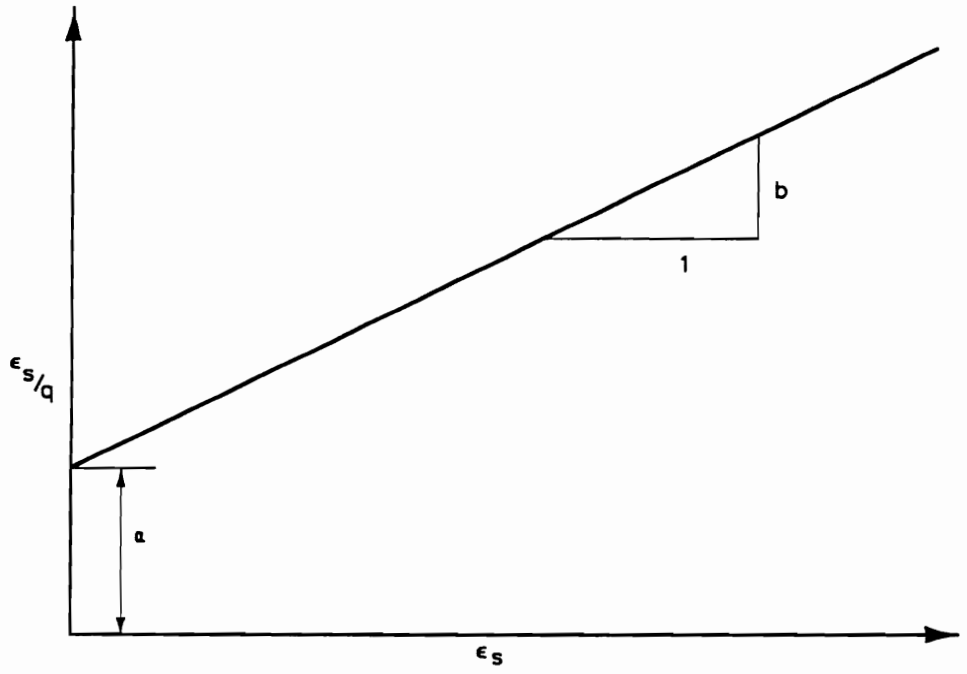

Figure 5.3: Physical meaning of the parameters a and b.

Substituting for the shear strain in Eq. 5.24 and rearranging terms gives the expression for the tangent shear modulus as

$$G_t = G_i \left[1 - \frac{q}{q_{ult}}\right]^2 \tag{5.26}$$

The stress–dependency of soils must also be included in the model. For all soils, the stress–strain curve is stress dependent under most loading conditions. For example, if drained triaxial tests are performed on two samples of the same soil at different confining pressures, the sample with the larger confining pressure will have the greater stiffness and the higher shear strength. Therefore, the initial slope and the asymptote must be related to the stress level. This is taken into account in the new model using empirical relationships to represent the variation of G_i and q_{ult} with the stress level.

Initially, it was believed that the same relationship for the variation of initial slope with the confining pressure for the stress–strain curve of a conventional triaxial compression test used in the Duncan–Chang model could be utilized in the new three–dimensional model. Duncan and Chang based their model on soil behavior observed in the conventional triaxial compression test where the minor and intermediate principal stresses are equal and constant. The stress difference or shearing stress, $\sigma_1 - \sigma_2$, is related to the axial strain (major principal strain) by a variable Young's modulus. The stiffness or slope of the stress–strain curve for a given soil is dependent on the confining pressure, Figure 5.4. The variation of initial slope with confining pressure used in the Duncan–Chang model can be determined directly from the drained triaxial test because confining pressure remains constant during the test, Figure 5.5.

Figure 5.6 shows a schematic representation in the principal stress space of the

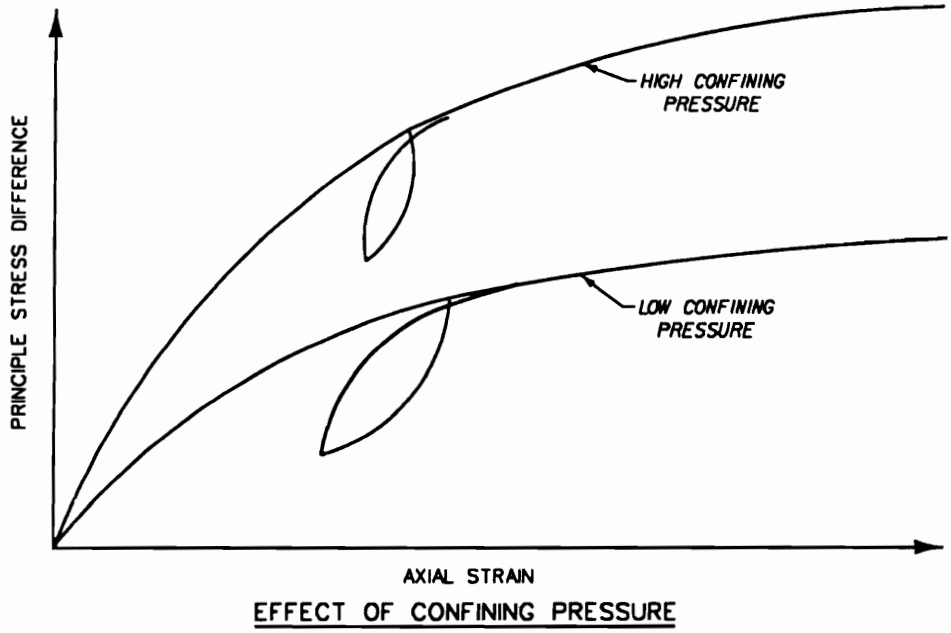

Figure 5.4: Variation of stiffness with confining pressure.

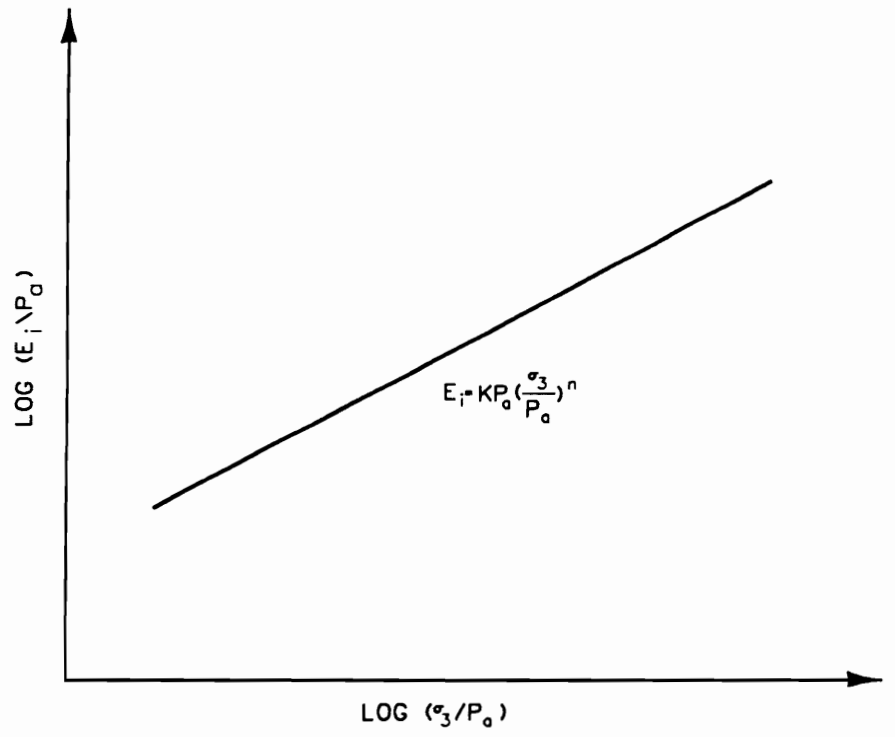

Figure 5.5: Variation of initial tangent modulus with confining pressure.

plane on which the stress paths for conventional triaxial compression test lie. Figure 5.7 shows the stress path for a conventional triaxial compression (CTC) test on the triaxial plane along with the hydrostatic compression (HC) stress path. For a truly three–dimensional state of stress, the minor and intermediate principal stresses are not always equal, and the confining pressure is not relevant in a truly three–dimensional state of stress. Instead of the confining pressure, the mean normal stress, p, is used to relate stress–dependency characteristics in a three–dimensional stress space. As previously mentioned, the variable moduli model separates the deviatoric and volumetric behavior and represents them as two components. The stress path for the volumetric portion moves along the hydrostatic line and the stress path for the deviatoric portion moves within the octahedral plane. The changes in mean normal stress results in volumetric changes and are related to volumetric strains by the tangent bulk modulus. Although the deviatoric stresses and strains are uncoupled from the volumetric portion, the shear strength and the stiffness (slope of the stress–strain curve) of soils are dependent on the mean normal stress. This is analogous to their dependence on the confining pressure in a triaxial or two–dimensional stress state.

The stress path for a conventional triaxial compression test in the q–p stress space shows the mean normal stress varies throughout the test (Figure 5.8). To perform a test that would separate the deviatoric and volumetric behavior, the stress path labeled TC in Figure 5.8 must be followed. On the triaxial plane, this stress path is shown in Figure 5.7. The variation of mean normal stress in the conventional triaxial tests makes it impossible to use the stress–strain curve from triaxial tests to directly determine the parameters for the model. Yet, it is important to be able to utilize triaxial test results for determining parameters because they are the primary

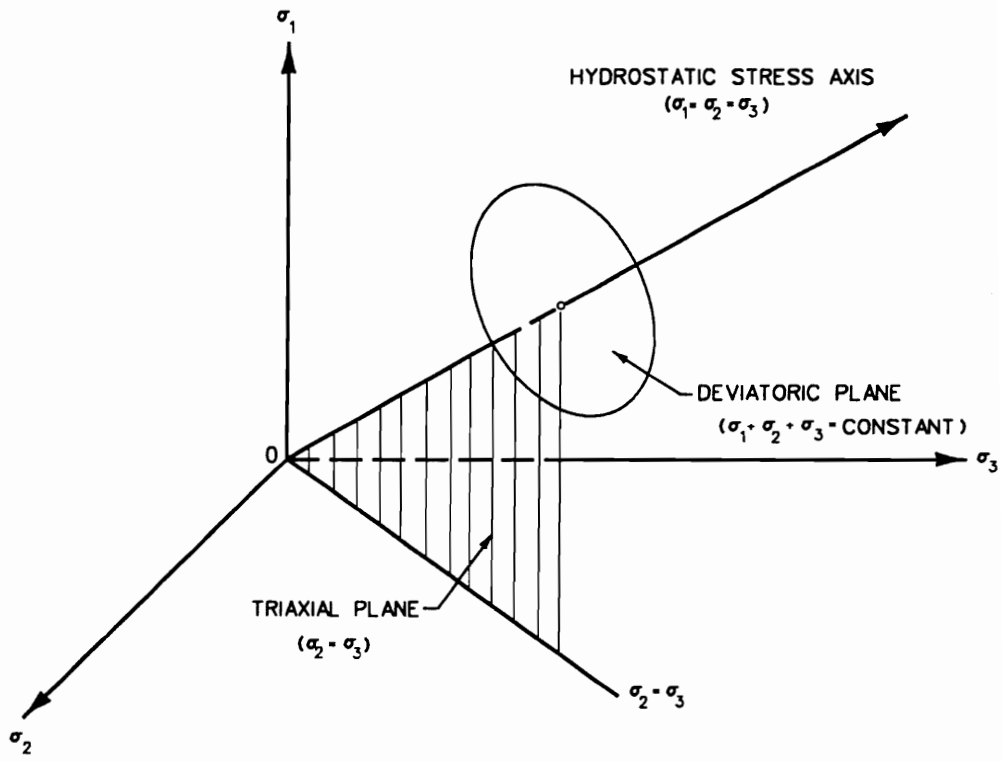

Figure 5.6: Stress path plane for triaxial test in principal stress space.

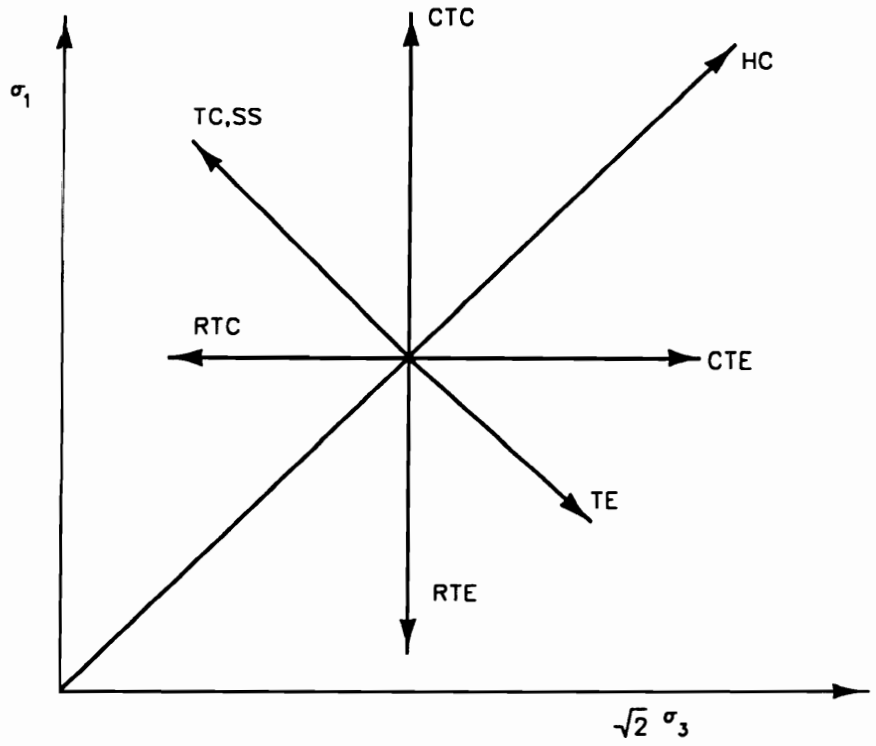

Figure 5.7: Projection of stress paths on triaxial plane.

source of data. Therefore, a procedure had to be developed to extract the necessary information from the triaxial test results.

To utilize conventional triaxial compression test data for parameter determination, a procedure was developed to normalize the test data with respect to the mean normal stress. The procedure evolved from similar steps to those used in determining the parameters from triaxial test results for the Duncan–Chang model. First, the triaxial test results are plotted in terms of the shear stress, q, and the shear strain, ϵ_s, as shown in Figure 5.9. Next, the data are plotted on a transformed axis, Figure 5.10, where the results follows a straight line that can be expressed as

$$\frac{\epsilon_s}{q} = a + b\epsilon_s \tag{5.27}$$

Normalizing this equation with respect to the mean normal stress yields,

$$\left(\frac{\epsilon_s}{q}\right)\left(\frac{1}{p}\right) = a\left(\frac{1}{p}\right) + b\epsilon_s\left(\frac{1}{p}\right) \tag{5.28}$$

This expression is shown in Figure 5.11. At $\epsilon_s = 0$, the normalized intercept, $\frac{a}{p}$ is

$$\frac{a}{p} = \frac{1}{3G_i}\frac{1}{p_i} \tag{5.29}$$

where p_i is the initial mean normal stress, $\sigma_c = \sigma_1 = \sigma_2 = \sigma_3$, shown in Figure 5.12 and $p = p_i$. Thus, the intercept, a, is

$$a = \frac{1}{3G_i} \tag{5.30}$$

Plotting the data as shown in Figure 5.12 allows the determination of the initial slope for the shear stress versus shear strain curve for a given confining pressure from conventional triaxial compression test data.

It is now necessary to establish an empirical expression for the variation of G_i with the mean normal stress. The variation of G_i with p_i can be shown to fit a

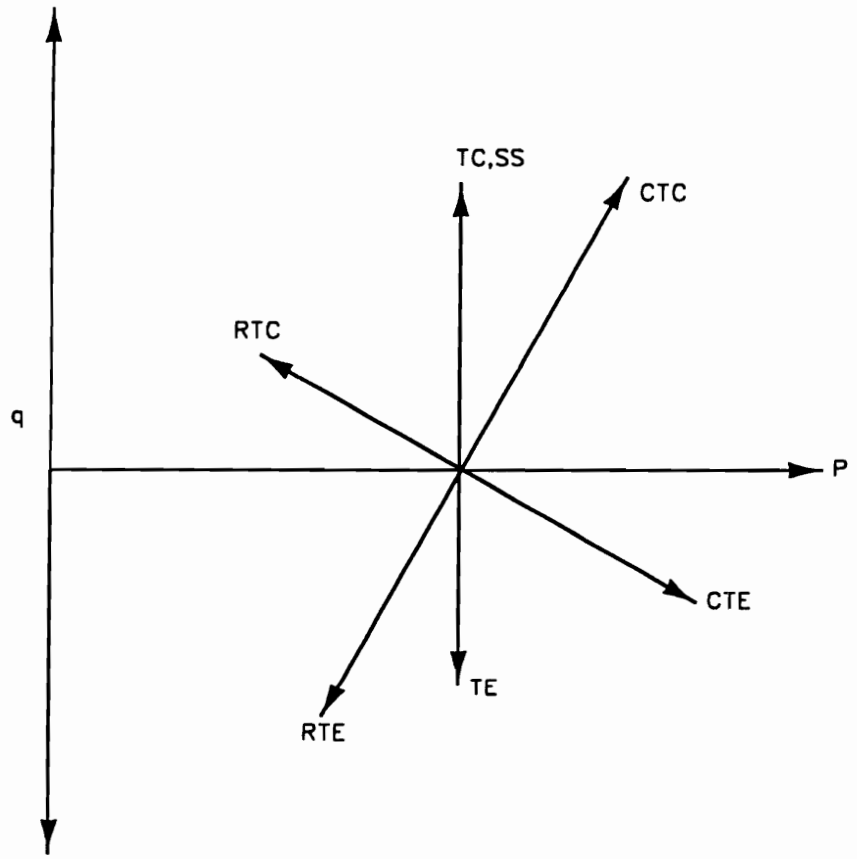

Figure 5.8: Stress paths in q-p stress space.

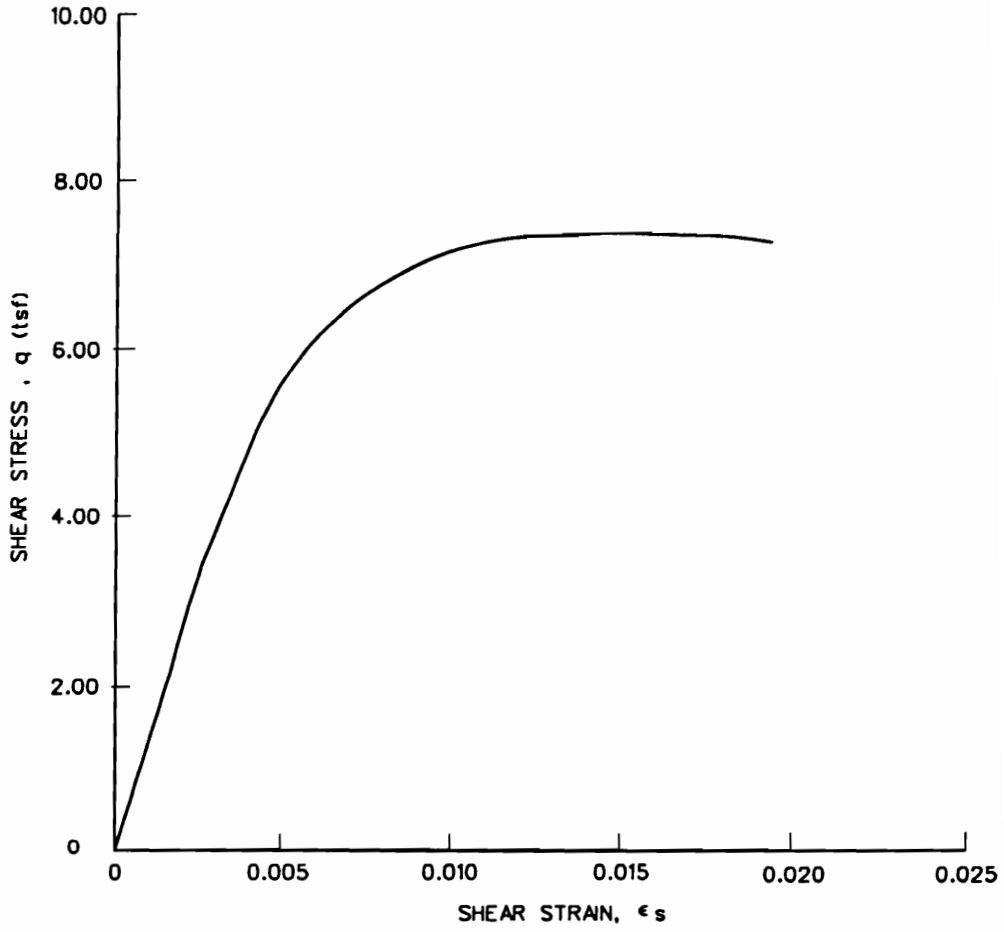

Figure 5.9: Shear stress–strain curve for triaxial test.

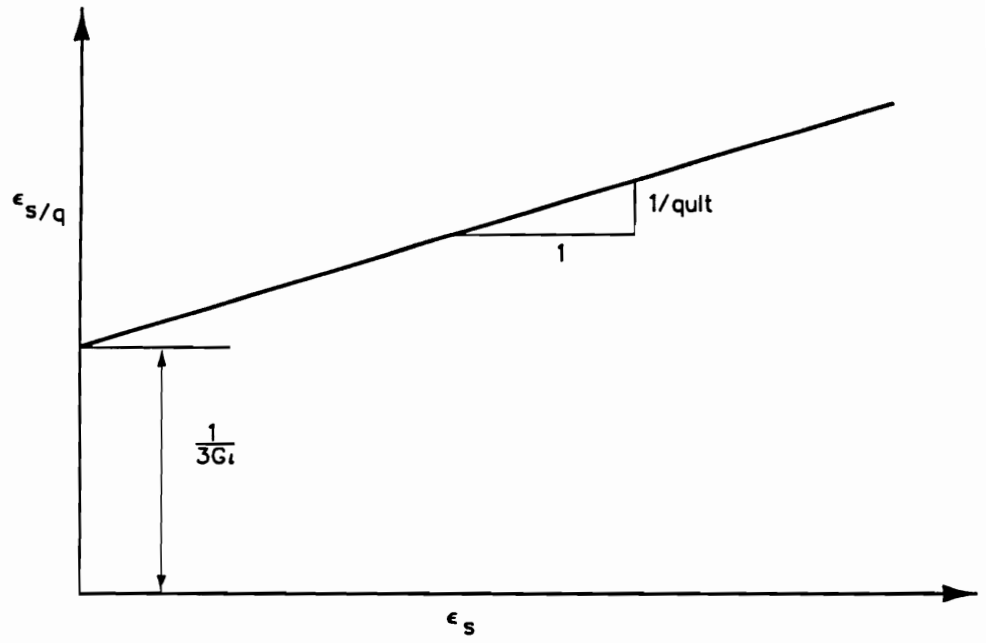

Figure 5.10: Shear stress–shear strain data plotted on transformed axis.

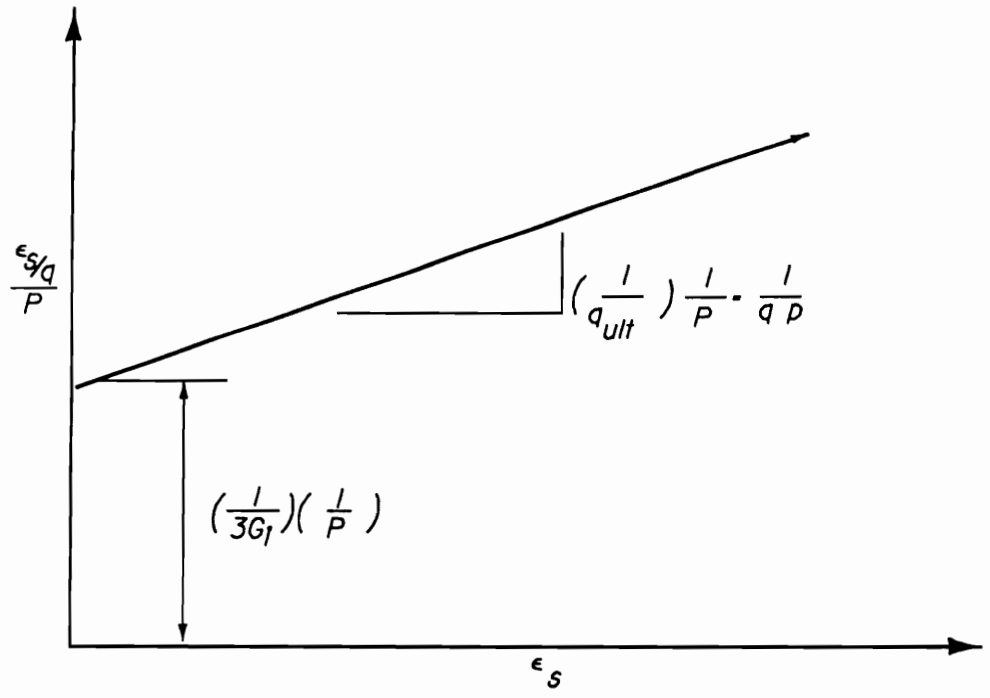

Figure 5.11: Normalized shear stress and shear strain data plotted on transformed axis.

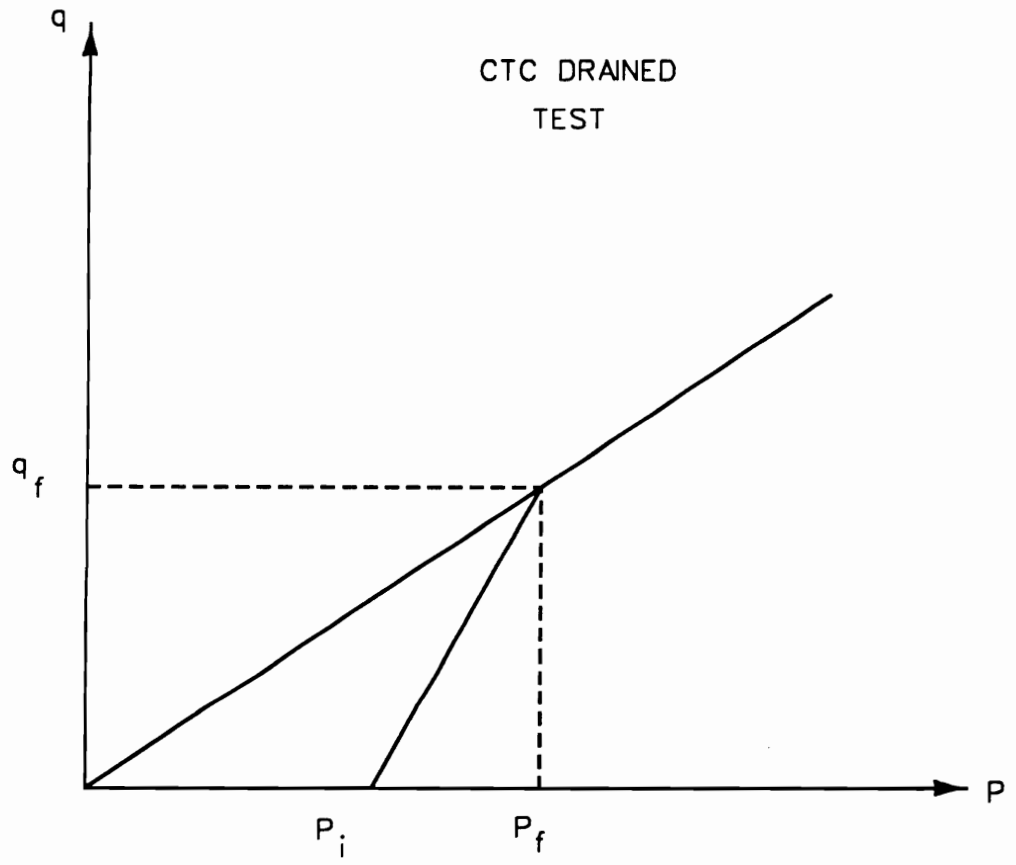

Figure 5.12: Stress path showing the initial mean normal stress and the normal stress at failure.

logarithmic expression which plots as a straight line on a log–log axis, as shown in Figure 5.13, and has the form

$$G_i = K p_a \left(\frac{p_i}{p_a} \right)^n \tag{5.31}$$

This is similar to the expression used in the Duncan–Chang model between ϵ_i and σ_3 that was suggested by Janbu [28]. The parameters K and n in Eq. 5.31 are called the modulus number and modulus exponent, respectively, and are dimensionless. The atmospheric pressure, p_a, was introduced to allow for conversion from one system of units to another. The parameters K and n can be found directly from the plot of the data on the log–log axis and by drawing a straight line through the data points. The value of K is equal to the value of the normalized initial slope at the point where the normalized mean normal stress is equal to unity . The value of n is equal to the slope of a straight line drawn through the data points

The stress–dependency of the asymptote, q_{ult}, of the hyperbolic expression used to describe the shear stress–strain response of the soil is obtained by relating it to the shear strength of the soil. In essence, the asymptote is the limit value of the shear stress and can be expressed in terms of the shear stress at failure of the soil by [16, 17]

$$q_f = R_f q_{ult} \tag{5.32}$$

where R_f is the ratio of shear stress at failure, q_f, to the asymptote. In conventional soil mechanics, the shear stress at failure is described by Mohr–Coulomb failure criterion. The Mohr–Coulomb failure criterion states that the shear stress at failure of the soil is governed by the normal stress as

$$|\tau| = f(\sigma) \tag{5.33}$$

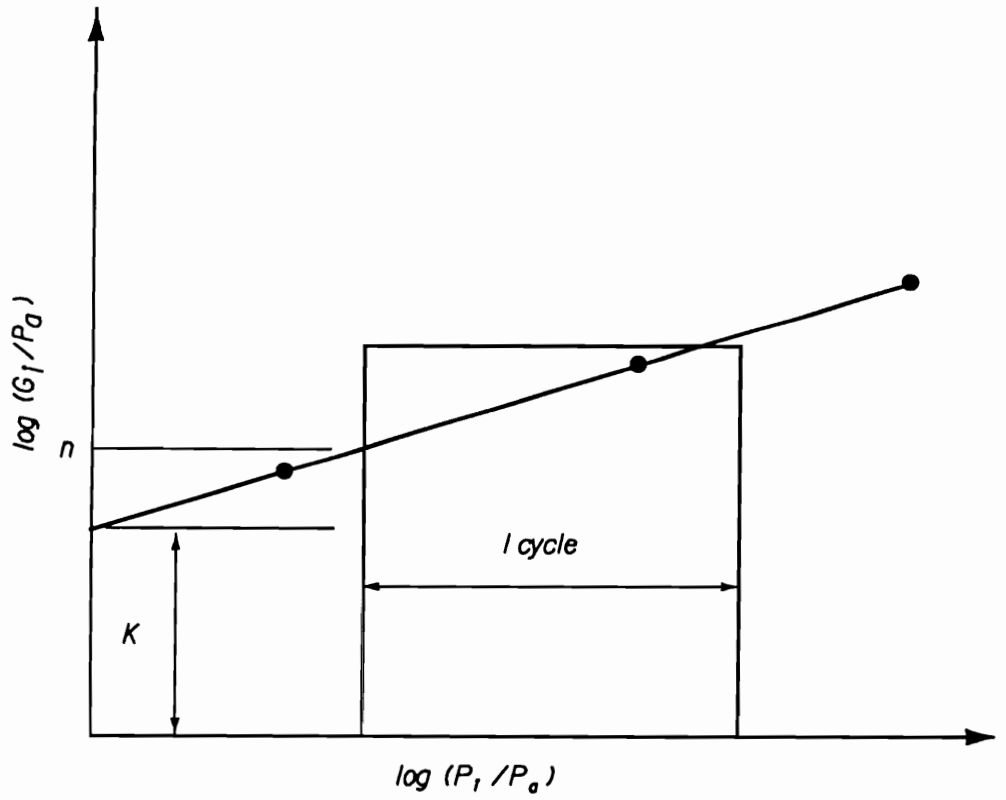

Figure 5.13: Variation of initial shear modulus versus initial mean normal stress.

where the limiting shearing stress, τ, on a plane is dependent only on the normal stress, σ, on the same plane. Eq. 5.33 defines a failure envelope for all states of stress for which the largest Mohr circles are tangent to that envelope. This means that the intermediate principal stress, σ_2, ($\sigma_1 \geq \sigma_2 \geq \sigma_3$), has no influence on the failure condition. The simplest form of the Mohr–Coulomb failure envelope is the straight line as shown in Figure 5.14 and can be written as

$$|\tau| = c + \sigma \tan \phi \tag{5.34}$$

where c and ϕ are commonly referred to as the strength parameters, cohesion and angle of internal friction, respectively. In terms of principal stresses, ($\sigma_1 \geq \sigma_2 \geq \sigma_3$), the failure condition, Eq. 5.34, can be written as

$$1 = \sigma_1 \frac{1 - \sin \phi}{2c \cos \phi} - \sigma_3 \frac{1 + \sin \phi}{2c \cos \phi} \tag{5.35}$$

For a three–dimensional stress state, the Mohr–Coulomb failure criterion is shown in Figure 5.15 and can be written in terms of the stress invariants as

$$f(I_1, J_2, \theta) = -\frac{1}{3} I_1 \sin \phi + \sqrt{J_2} \sin\left(\theta + \frac{\pi}{3}\right) - \frac{1}{\sqrt{J_2}} \cos\left(\theta + \frac{\pi}{3}\right) \sin \phi - c \cos \phi = 0 \tag{5.36}$$

where I_1 is the first stress invariant of the stress tensor and can be written in terms of principal stresses as

$$I_1 = \sigma_1 + \sigma_2 + \sigma_3 \tag{5.37}$$

and is to equal to three times the mean normal stress. J_2 is the second invariant of the deviatoric stress tensor and can be written in terms of principal stresses as

$$J_2 = \frac{1}{6}\left[(\sigma_1 - \sigma_2)^2 + (\sigma_2 - \sigma_3)^2 + (\sigma_3 - \sigma_1)^2\right] \tag{5.38}$$

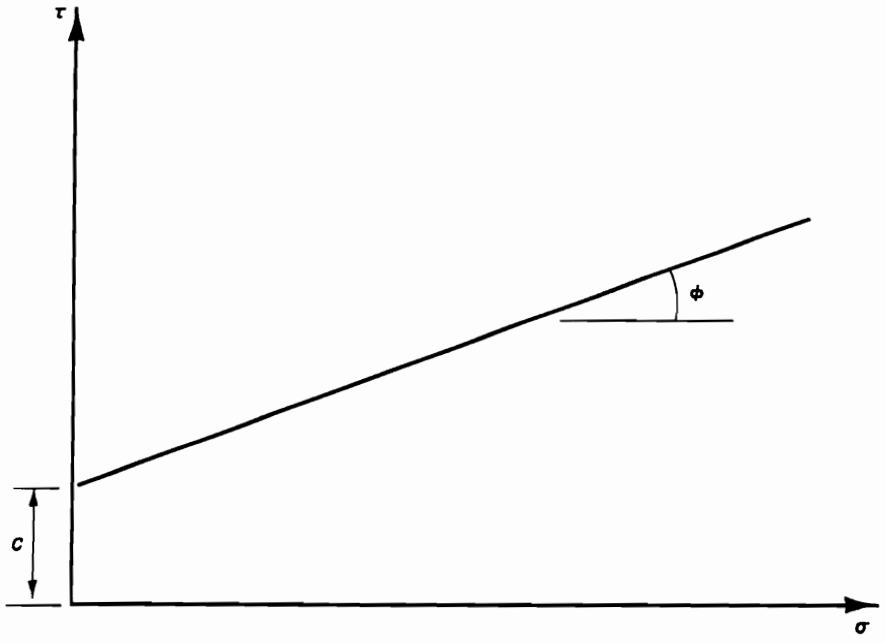

Figure 5.14: Simple representation of the Mohr–Coulomb failure envelope.

and can be related to the octahedral shear stress as

$$\tau_{oct} = \sqrt{\frac{2}{3}J_2} \tag{5.39}$$

θ is defined as

$$\theta = cos^{-1}\left(\frac{2\sigma_1 - \sigma_2 - \sigma_3}{2\sqrt{3J_2}}\right) \quad \text{where} \quad 0 \leq \theta \leq 60\,\text{deg} \tag{5.40}$$

Expanding the terms

$$\sin\left(\theta + \frac{\pi}{3}\right) \tag{5.41}$$

and

$$\cos\left(\theta + \frac{\pi}{3}\right) \tag{5.42}$$

in Eq. 5.36, the failure criterion can be written as

$$f(I_1, J_2, \theta) = -I_1 \sin\phi + \frac{1}{2}\sqrt{J_2}\left[3(1+\sin\phi)\sin\theta + \sqrt{3}(3-\sin\phi)\cos\theta\right] - 3c\cos\phi = 0 \tag{5.43}$$

The above equation can be rewritten in terms of p and q as

$$f(I_1, J_2, \theta) = -p\sin\phi + \frac{q}{6}\left[3(1+\sin\phi)\sin\theta + \sqrt{3}(3-\sin\phi)\cos\theta\right] - 3c\cos\phi = 0 \tag{5.44}$$

Rearranging terms so that the shear stress at failure can be found, yields

$$q_f = \frac{6(p\sin\phi + c\cos\phi)}{\left[\sqrt{3}(1+\sin\phi)\sin\theta + (3-\sin\phi)\cos\theta\right]} \tag{5.45}$$

For the case of triaxial compression, $\theta = 0$, $\sigma_2 = \sigma_3 < \sigma_1$, the failure criterion is

$$q_f = (\sigma_1 - \sigma_3)_f = \frac{2\sigma_1\sin\phi + 4\sigma_3\sin\phi + 6c\cos\phi}{3 - \sin\phi} \tag{5.46}$$

Expressing σ_1 in terms of σ_3, the confining stress as

$$\sigma_1 = \sigma_3\frac{1+\sin\phi}{1-\sin\phi} + \frac{2c\cos\phi}{1-\sin\phi} \tag{5.47}$$

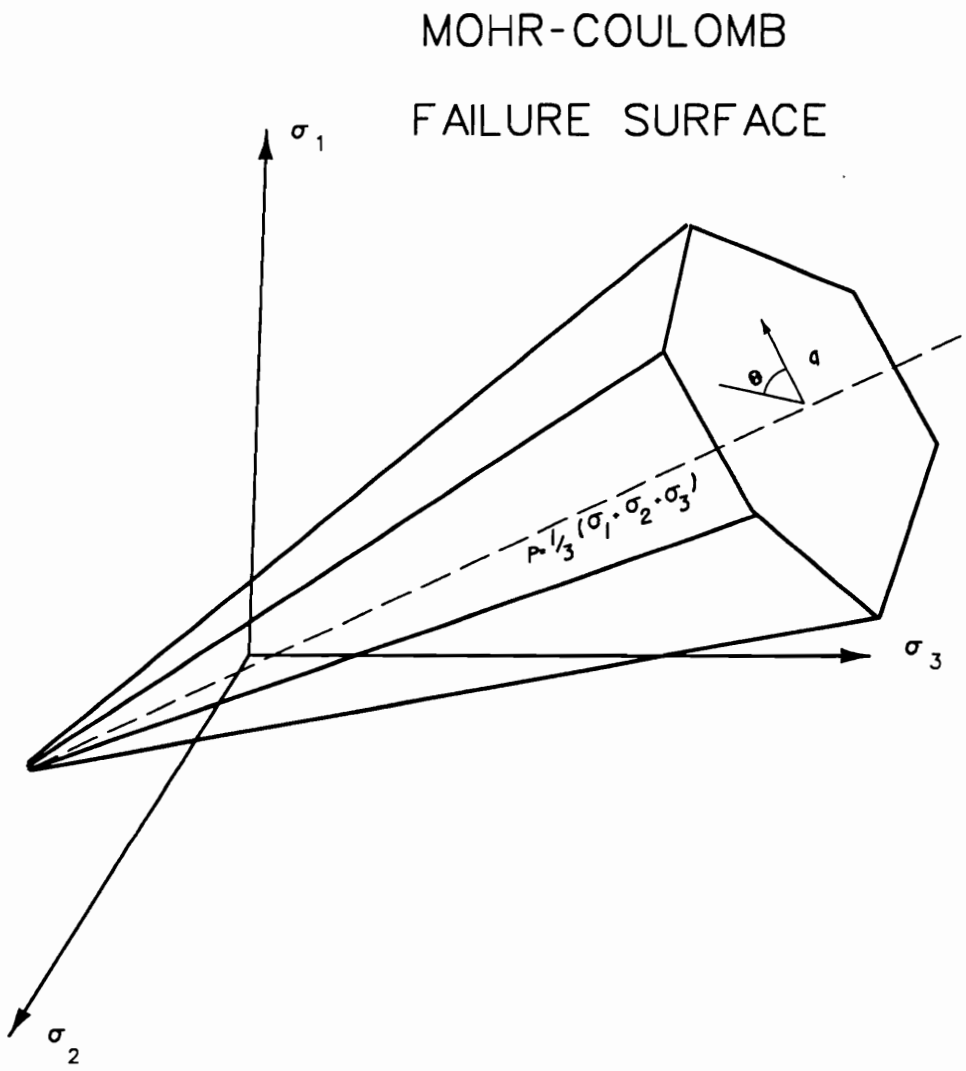

Figure 5.15: Three–dimensional representation of Mohr–Coulomb failure criterion.

and substituting it into Eq. 5.45 gives

$$(\sigma_1 - \sigma_3)_f = \frac{\left[2\sigma_3 \frac{1+\sin\phi}{1-\sin\phi} + 4c\frac{\cos\phi}{1-\sin\phi}\right]\sin\phi + 4\sigma_3 \sin\phi + 6c\cos\phi}{3 - \sin\phi} \tag{5.48}$$

Rearranging Eq. 5.48

$$(\sigma_1 - \sigma_3)_f = \frac{2\sigma_3 \sin\phi}{1 - \sin\phi} + \frac{4\cos\phi\sin\phi + 6c\cos\phi - 6c\cos\phi\sin\phi}{(1 - \sin\phi)(3 - \sin\phi)} \tag{5.49}$$

and combining terms yields

$$q_f = (\sigma_1 - \sigma_3)_f = \frac{2\sigma_3 \sin\phi + 2c\cos\phi}{1 - \sin\phi} \tag{5.50}$$

This is the familiar conventional soil mechanics expression for the shear stress at failure based on the Mohr–Coulomb failure criterion.

5.3.2 Tangent Bulk Modulus Definition

To define an expression for the tangent bulk modulus for the new constitutive model, a relationship between the mean normal stress and the volumetric strains had to be established. Figure 5.16 illustrated the nonlinear stress–dependent nature of the volumetric strain found in a soil under hydrostatic loading. Figure 5.17 shows the results of a series of isotropic consolidation tests performed on sands in a conventional triaxial device by Domaschuk and Wade [15] to determine the volumetric strain response due to increasing mean normal stress. These results indicated that the volumetric strain increases at a decreasing rate as the mean normal stress is increased. It is clear from Figure 5.16 that soils exhibit a nonlinear behavior under hydrostatic loading. During unloading to the initial stress state, only a small portion of the volumetric strain is recovered. The major portion of the strain is unrecoverable and permanent.

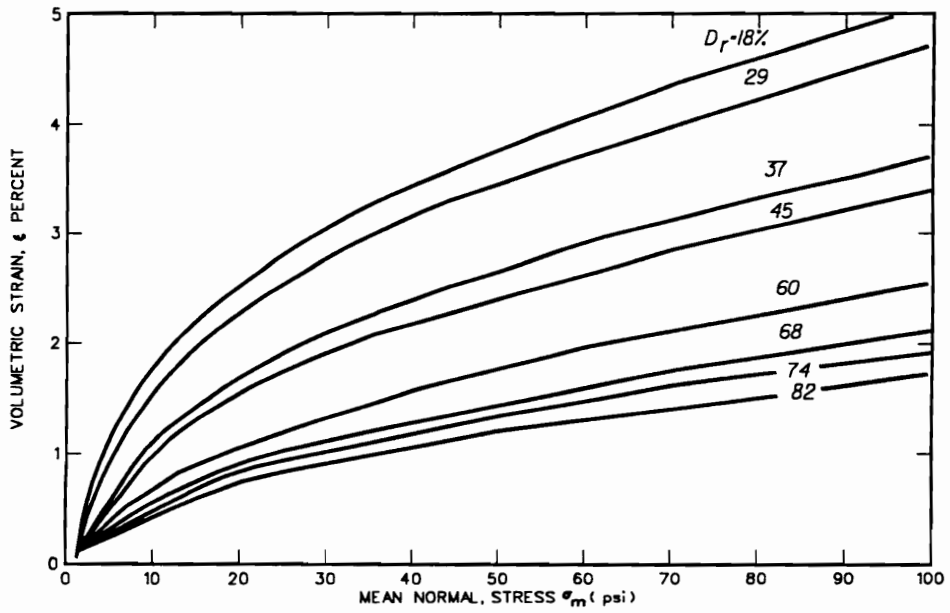

Figure 5.16: Volumetric strain versus mean normal stress.

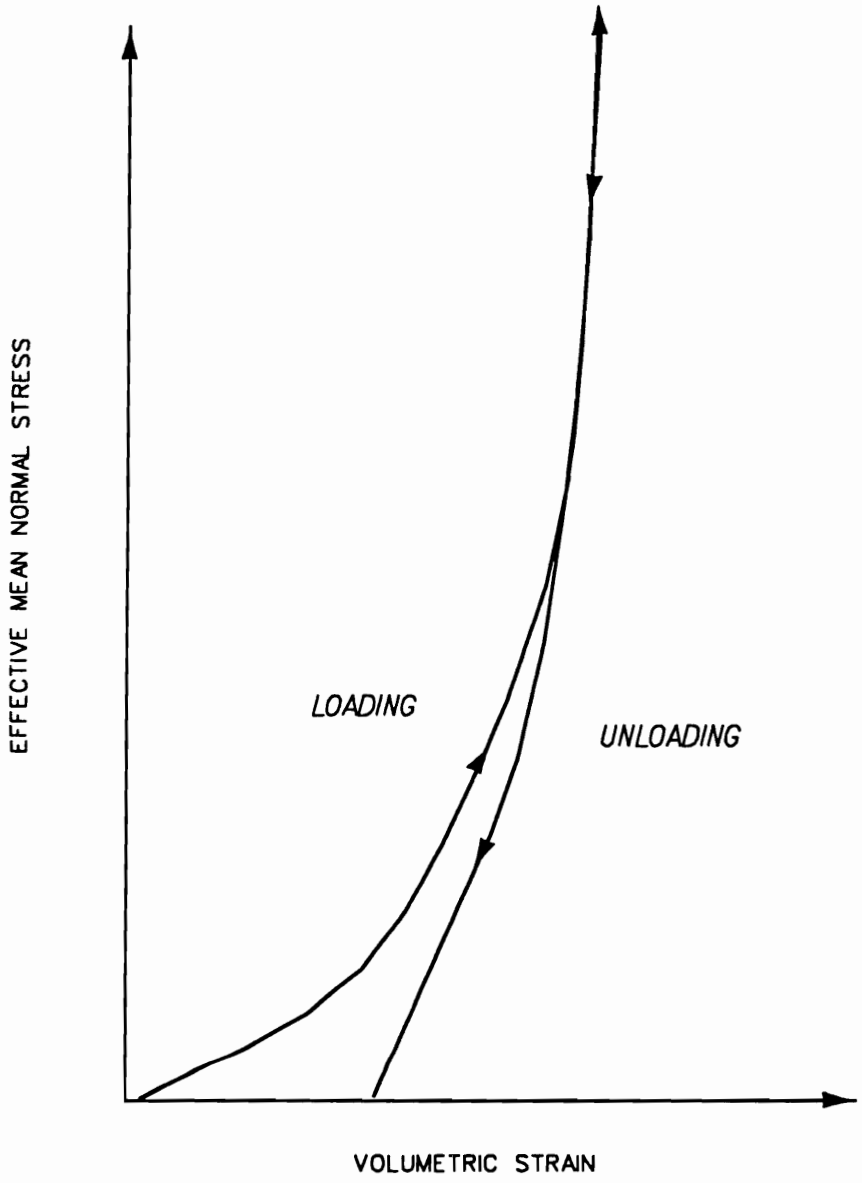

Figure 5.17: Plot of volumetric strain versus mean normal stress from triaxial consolidation test [15].

By definition, the bulk modulus relates the mean normal stress to the volumetric strain in the soil. Duncan et al. [16] proposed the use of a variable bulk modulus in conjunction with the two-dimensional hyperbolic model. The expression for K is given as a function of the confining pressure, σ_3, as

$$K = K_b p_a \left(\frac{\sigma_3}{p_a}\right)^m \tag{5.51}$$

where K_b and m are dimensionless material constants determined in a similar manner as K and n. Domaschuk and Wade [15] proposed that the relationship between the volumetric strain and mean normal stress over a limited stress range could be expressed by an equation of the form

$$\epsilon_v = \frac{1}{m}\left[ln\left(K_i + mp\right) + C_1\right] \tag{5.52}$$

in which K_i is defined as the bulk modulus intercept, and m is the rate change in bulk modulus. Using this expression, the tangent bulk modulus would be

$$K_t = K_i + mp \tag{5.53}$$

Neither of the expressions provide a sufficient model for the new, three-dimensional finite element code. Eq. 5.51 does not account for the three-dimensional state of stress through a variation in mean normal stress, and Eq. 5.52 can only be used over a limited range of mean normal stress. After examination of the volumetric behavior under hydrostatic loading, the following expression was used to define the relationship between volumetric strain and mean normal stress

$$\epsilon_v = K_b \left(\frac{p}{p_a}\right)^m \tag{5.54}$$

Figure 5.18 illustrates a plot of this expression on an arithmetic scale. The K_b and m are nondimensional curve-fitting parameters. The atmospheric pressure, p_a, was

introduced to allow ease in conversion from one system of units to another. Plotting this expression on a log–log scale, as shown in Figure 5.19, produces a straight line of the form

$$\epsilon_v = K_b + m\left(\frac{p}{p_a}\right) \tag{5.55}$$

The parameters K_b and m can be found directly from the plot of the data on the log-log axis. K_b is equal to the value of the normalized initial slope at the point where the normalized mean normal stress is equal to unity . The value of m is equal to the slope of a straight line drawn through the data points.

The tangent bulk modulus, K_t, is the instantaneous slope of the mean normal stress, p, versus volumetric strain, ϵ_v, curve. The instantaneous slope is described as

$$K_t = \frac{dp}{d\epsilon_v} \tag{5.56}$$

Rearranging Eq. 5.55 as

$$p = p_a\left(\frac{\epsilon_v}{K_b}\right)^{\frac{1}{m}-1} \tag{5.57}$$

and differentiating with respect to the volumetric strain, ϵ_v, yields

$$\frac{dp}{d\epsilon_v} = \frac{p_a}{mK_b}\left(\frac{\epsilon_v}{K_b}\right)^{\frac{1}{m}-1} \tag{5.58}$$

Substituting for volumetric strain, ϵ_v, using Eq. 5.55 into Eq. 5.58, yields the final form for the tangent bulk modulus

$$K_t = \frac{dp}{d\epsilon_v} = \frac{p_a}{mK_b}\left(\frac{p}{p_a}\right)^{1-m} \tag{5.59}$$

Some restrictions are necessary on the range of values of the tangent bulk modulus, K_t. As the value of K_t approaches $\frac{2}{3}G_t$, the off–diagonal terms of the constitutive matrix, Eq. 5.4, will approach zero. This is equivalent to allowing the tangent Poisson's ratio to approach zero [16]. Therefore in the finite element computer program,

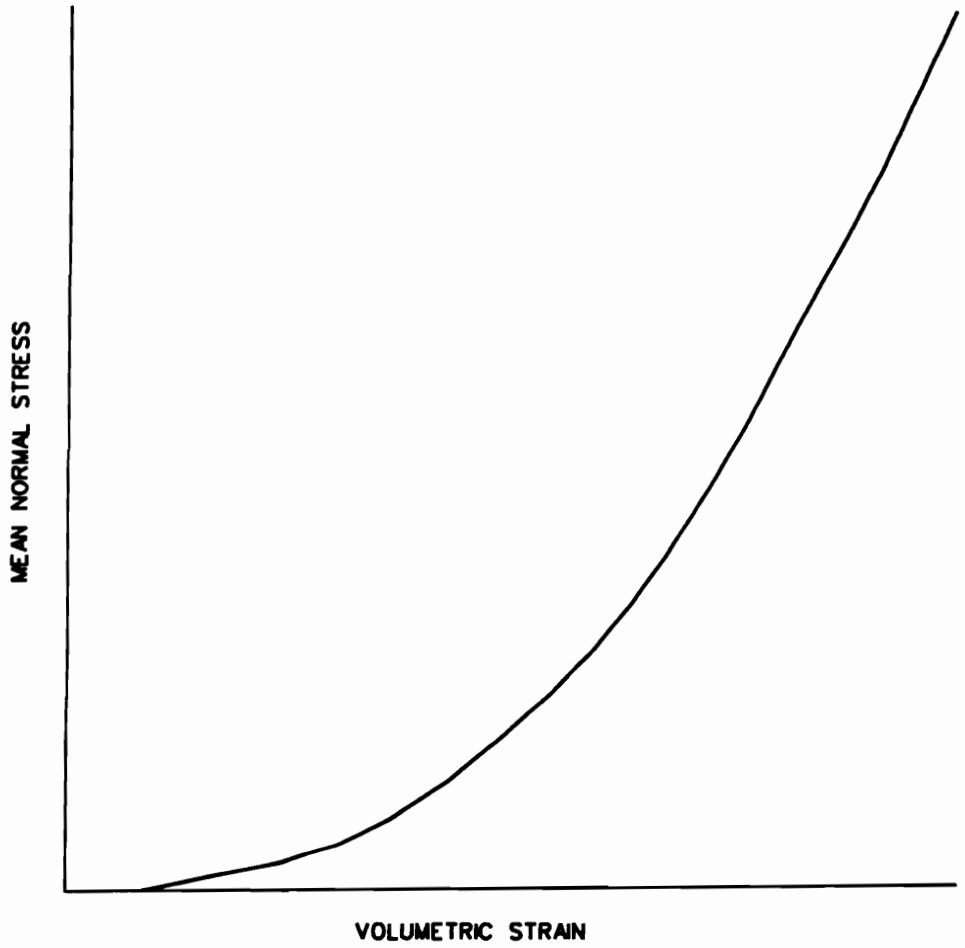

Figure 5.18: Plot of expression for volumetric strain and mean normal stress on arithmetic scale.

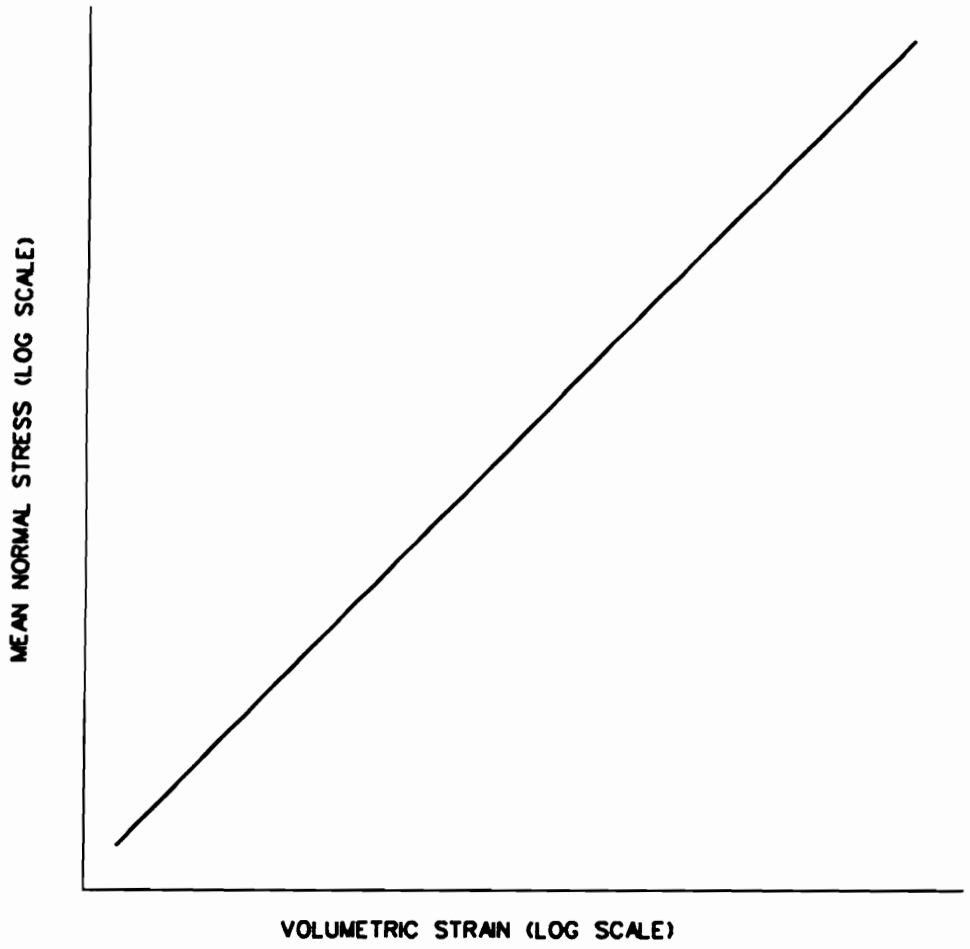

Figure 5.19: Plot of expression for volumetric strain and mean normal stress on log–log scale.

the value K_t is restricted to values greater than $\frac{2}{3}G_t$ to provide a lower bound. Restrictions must also be placed on the upper limits of values of K_t. As a material approaches incompressibility the tangent bulk modulus approaches infinity. This is equivalent to allowing the tangent Poisson's ratio to approach 0.5. The tangent bulk modulus approaching infinity will cause numerical instability in the finite element solution. K_t is restricted to be no greater than $50.0 \times G_t$ in the finite element computer program. This is equivalent to setting Poisson's ratio to 0.49. Studies have shown that the results of the finite element analysis may become inaccurate as Poisson's ratio approaches 0.5 from 0.49.

5.4 Soil Testing Program for Three–Dimensional Finite Element Study

In conjunction with the development of the three–dimensional finite element code described in this report, a soil testing program was conducted by Virginia Polytechnic Institute and State University [52] (VPI). The testing program had three principal objectives:

- Explain and resolve differences which appeared in the results of two previous triaxial test programs which had been performed on the Lock and Dam 26 (R) cell fill sands.
- Provide a data base that could be used to establish parameters for a range of possible constitutive models that might be used in the finite element analyses.
- Provide stress–strain data for the cell fill sands following stress paths that are realistic for the types of loadings expected for the cellular cofferdam problem,

and that can be used to test soil model capabilities.

The soil testing program involved classification, strength, and deformation tests, with the principal emphasis on the latter. The soil testing program was designed around a series of triaxial compression and extension tests and a series of cubical shear tests, along with basic classification tests. In addition, the US Army Engineer Waterways Experiment Station (WES) Geotechnical Laboratory conducted a series of triaxial compression tests for comparison to those conducted at VPI.

5.4.1 Background of Soil Testing for Lock and Dam No. 26(R) Cofferdam

The cell fill for the cofferdam at Lock and Dam No. 26(R) was a sand dredged from the Mississippi River bed. From the grain size analyses of the material performed for the design of the cofferdam, the cell fill was classified as a medium sand with 50 percent of the material by weight passing the No. 30 sieve and less than 10 percent passing the No. 200 sieve.

After dredging the fill from the river bed and placing it on a barge for drainage, it was dropped in the cells by a clamshell bucket. Once the surface of the fill was above the water, it was leveled by a bulldozer. In situ tests performed in the cell fill after completion of construction indicated a relative density of the fill in the range of 55 to 60 percent [55].

The WES Geotechnical Laboratory performed a series of triaxial compression tests for the design of the cofferdam. The primary emphasis of the series of tests was to establish the shear strength of the cell fill. Subsequently, a second series of triaxial tests were conducted by Woodward–Clyde Consultants under the direction

of Mr. Richard Ladd of the Clifton Office [9]. The data from the two testing programs for the cell fill were reported in terms of the stress–strain curves and the failure envelopes.

This stress–strain data were assessed to determine the parameters for the hyperbolic model utilized in the two–dimensional finite element analysis of the first–stage Lock and Dam No. 26(R) cofferdam [8]. The procedure involved examining the data to see that it can be represented by the Mohr–Coulomb criteria, and that the initial tangent modulus values are related to the confining pressure in the tests by a prescribed power function. The Duncan–Chang soil model provided a reasonable representation of the stress–strain response for both sets of tests. There was also good agreement between strength envelopes from both series of tests. However, there was a significant difference in the parameters for the relationship between the initial tangent modulus and the confining pressure for the two sets of tests, Table 5.1. The WES tests yielded modulus values about one–half of those of the Woodward–Clyde tests. For the finite element analyses, the parameters from the two sets of data were averaged and used to specify the soil response.

The reasons for the discrepancies between the two sets of data were not obvious, but not an uncommon occurrence. The modulus is a sensitive parameter which is influenced by factors that do not affect the strength values. Before undertaking a new cell fill testing program for three–dimensional finite element analysis, the test procedures for the previous two series of tests were examined to see if certain differences in the test procedures may have contributed to the discrepancies and to prevent introducing yet another set of procedures in the new testing program that could led to another set of modulus values. Table 5.2 shows the key features of the sample preparation and the testing procedure for the two series of tests.

The principal differences in the test procedures were the sample preparation and the rate of load applied to the sample. The literature shows evidence that sample preparation has a significant influence and that the simple dry tamping method used in preparing the WES samples for the first test series may result in a nonuniform specimen [36]. The undercompaction procedure used in preparing the Woodward–Clyde samples was designed to circumvent this problem of a nonuniform specimen. Thus, on the surface it, appeared that the results of the Woodward–Clyde testing program were more reliable and should be the procedure used in the new cell fill testing program.

5.4.2 The New Soil Testing Program

Sieve analyses were performed on cell fill material obtained from Lock and Dam No. 26(R) site. In Figure 5.20 the average results of the grain size analyses are compared with the overall range for the cell fill and the earlier test programs. The VPI sample results fell near the middle of the overall range and are similar to those for the sand used in the first WES and Woodward–Clyde investigations. The maximum and minimum void ratios for the VPI cell fill material were determined to be 0.588 and 0.400, respectively. These values are slightly different than those found in the Woodward–Clyde investigation which were 0.616 and 0.375, respectively. This difference is likely due to the slightly different gradation.

The VPI test program included 23 triaxial (12 compression and 11 extension) and 9 cubical shear tests. Samples for the triaxial test were prepared to three different densities (26, 55, and 70 percent). These values were intended to bound the density for the cell fill in the field. Specimens were constructed using moist tamping compaction with an undercompaction procedure similar to that used in

Table 5.1: Comparison of Stiffness Parameters between WES and Woodward–Clyde Tests.

Investigation	Relative Density (%)	Friction Angle Degrees	K	n	R_f
Woodward–Clyde	57	36	1,250	0.65	.8
WES I	60	35	400	0.65	0.8

Note: For two–dimensional soil model:

$$E_i = K p_a \left(\frac{\sigma_c}{p_a}\right)^n$$

$$E_t = E_i \left[1 - R_f \frac{(\sigma_1 - \sigma_3)}{(\sigma_1 - \sigma_3)_f}\right]^2$$

where E_i is the initial Young's tangent modulus and E_t is the Young's tangent modulus.

Table 5.2: Comparison of Testing and Sample Preparation Procedures of Previous Efforts

ITEM	WES	WOODWARD–CLYDE
Sample	2.8" dia × 7" high	2.96" dia × 6.6" high
Maximum particle size	> 1/2 sieve	> 1/2 sieve
No. of layers	7	8
Compaction	dry tamp	undercompaction-wet tamp
No. of membrane	2	1
Saturation	back pressure saturation with vacuum assist	back pressure
Consolidation time	2-3 hours	1 day approximation
When D_r reported	after consolidation	after consolidation
Strain rate	0.44 % per min.	0.05 % per min.
Corrections for:		
membrane thickness	yes	yes
membrane strength	no	?
membrane penetration	no	?

the previous Woodward–Clyde study. Confining pressure ranged from 1 to 14 ksf. A density of 55 percent was used for the cubical shear tests. Details on these tests can be found in the report by Sehn et al. [52].

5.4.3 Cubical Shear Testing

The basic philosophy of the cubical shear testing was to develop data on the soil response for stress paths similar to those experienced by the cofferdam fill. Also, the test data are to be used to test the capabilities of both the two–dimensional and three–dimensional soil models used in the finite element analysis of cellular cofferdams. For the new three–dimensional soil model, these cubical shear tests would provide a significant test of its ability to represent the behavior of the cell fill under a truly three–dimensional stress condition.

One of the problems facing the investigation was to first identify the stress paths to be used in the cubical shear testing. Because there were no other three–dimensional analyses or instrumentation data to provide guidelines for this, the two–dimensional finite element analyses of the cofferdam were used. These analyses allow the examination of the stress changes for a large number of points within the cell under the simulation of various stages of loadings experienced by the cofferdam during construction and operation. These results were already available from the work performed by Clough and his associates for the first–stage cofferdam of Lock and Dam No. 26(R) [53].

As discussed in Chapter 2, three two–dimensional finite element models were used; axisymmetric, vertical slice, and horizontal slice. The vertical slice model is the only one of the two–dimensional analyses that was used to analyze the cofferdam through construction and operation. For that reason, its results were used to develop

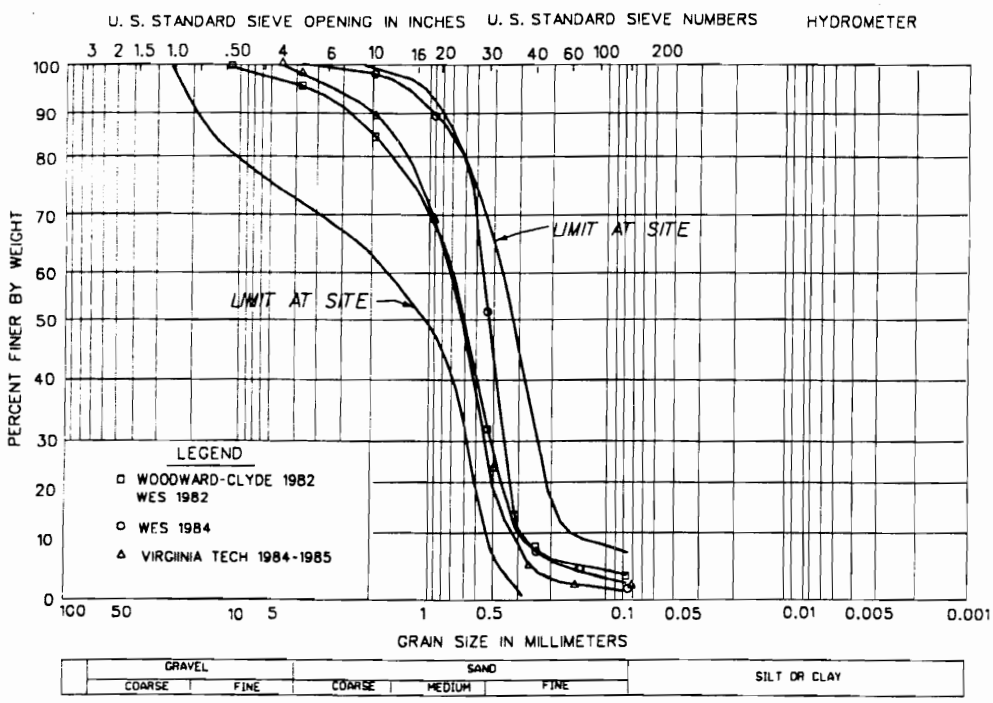

Figure 5.20: Gradation curves for cell fill sand [52].

the stress paths for the cubical shear testing. The vertical slice model assumes plane strain conditions, while the actual conditions are more complex than plane strain. With only two-dimensional stress path information for guidance, it was decided that plane strain conditions would be maintained for one of the three axes in the cubical shear tests. The principal reason for this is that an infinite number of possibilities exist for the stresses in the out-of-plane axis, and those resulting from the plane strain conditions are known and reasonable. In comparing the test data with the three-dimensional soil model, out-of-plane stress values play a significant role in the behavior of soil. This will be discussed later in this section.

Stress paths for selected key elements inside and adjacent to the cofferdam are shown in Figures 5.21, 5.22, and 5.23 . In these figures, the stress path is defined as a plot of the maximum shear stress in the plane versus the average value of the major and minor principal stresses in the plane. Two reference lines are shown. One representing the stress state during conventional one-dimensional consolidation, and is referred to as the K_0 line. The other reference line establishes the limit between failure and nonfailure stress states, and is referred to as the K_f line. The slope of the K_0 line is defined as

$$\beta = \arctan\left[\frac{1 - K_0}{1 + K_0}\right] \tag{5.60}$$

where K_0 is defined in the finite element analysis in terms of the Poisson's ratio, ν, as

$$K_0 = \frac{\nu}{1 - \nu} \tag{5.61}$$

The slope of the K_f line is defined in terms of the maximum shear stress, $(\sigma_1 - \sigma_3)_f$, and an average principal stress, $(\sigma_1 + \sigma_3)_f$, at failure by

$$\alpha = \arctan\left[\frac{(\sigma_1 - \sigma_3)_f}{(\sigma_1 + \sigma_3)_f}\right] \tag{5.62}$$

All stress paths exhibit significant similarity during the cell filling stage, where the soil undergoes a loading corresponding to that defined by the K_0 line. The maximum shear stress and the average principal stress increase at approximately a linear rate. After the cell is filled, the stress paths for the different locations diverge depending upon their response to the differential loading on the cofferdam. In almost all cases, the maximum shear stresses hold constant or decrease under subsequent differential loading of the cofferdam.

The stress paths in Figures 5.21, 5.22, and 5.23 were used as guides to develop a series of the idealized stress paths to be applied in the cubical shear testing. Schematic plots of these idealized stress paths are shown in Figure 5.24. Stress paths A, B, and C were selected to follow average trends seen in the results of the vertical slice analyses. Two sets of cubical shear tests were performed with the stress paths A, B, and C. The first set used stress magnitudes comparable to those at the midheight of the cell. The second set used stress magnitudes equivalent to those found near the base of the cell. Stress path D in Figure 5.24 was intended to duplicate the loading found in the triaxial extension test. The last two stress paths E and F are constructed to serve as a critical test of the soil model to follow a loading that is very close to failure. Either of these types of loading path could occur in the field if the sheet–pile system is extremely flexible, allowing large lateral deformations of the cell and a relaxation of the horizontal stress in the fill. In the subsequent stages of the tests, shear stresses are reduced from the critical state to zero to to simulate a complete unloading. A detailed description of the cubical shear testing can be found in reference by Sehn et al. [52].

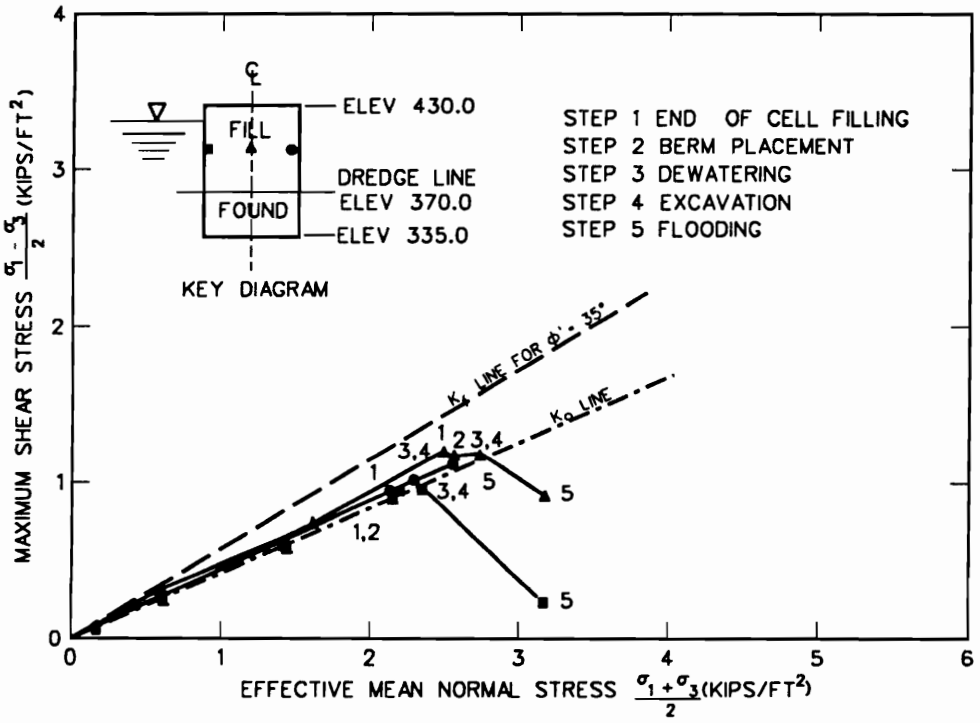

Figure 5.21: Stress path from vertical slice model for cell fill at midheight [52].

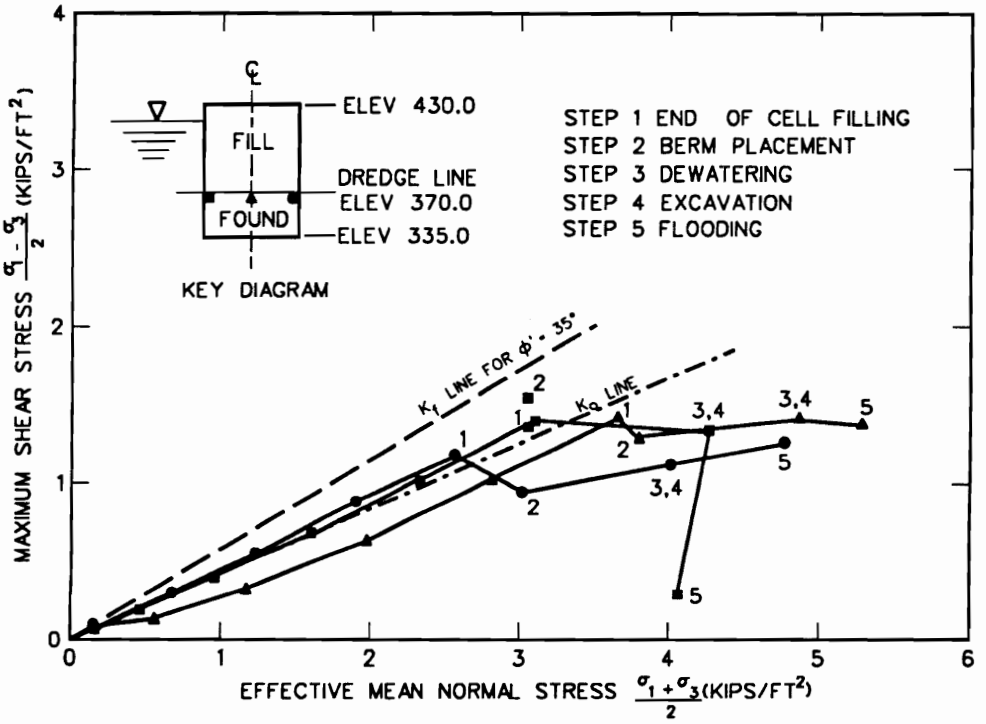

Figure 5.22: Stress path from vertical slice model for cell fill at bottom [52].

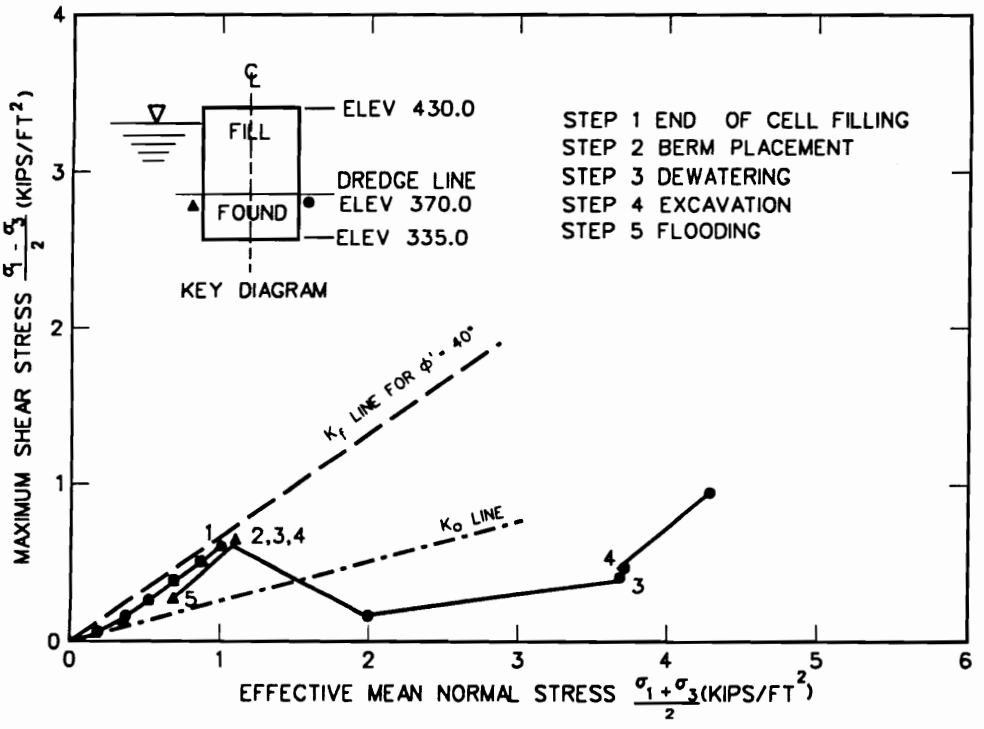

Figure 5.23: Stress path from vertical slice model for foundation soil below dredgeline outside the cell [52].

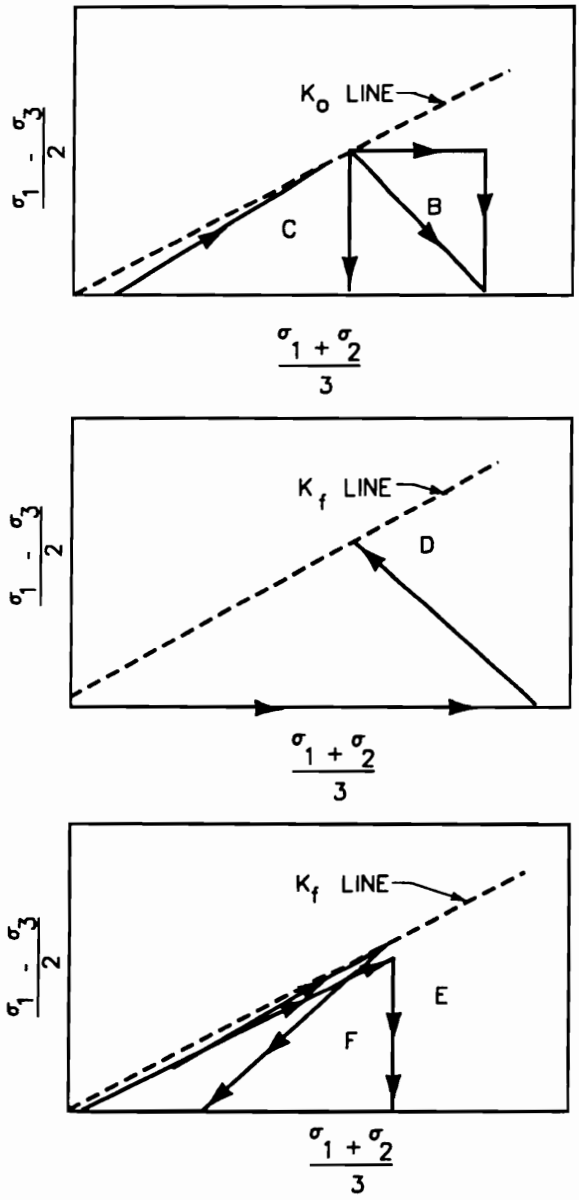

Figure 5.24: Schematic representation of stress paths used in cubical shear tests [52].

5.5 Comparison of Predicted and Observed Stress-Strain Response

To assess the soil model and refine the model's parameters determined in the proceeding section, the new three–dimensional finite element code with the new constitutive model was used to predicted the stress–strain response from the testing program. This evaluation concentrated primarily on the tests for a relative density of 55 percent and secondarily on the tests for a relative density of 70 percent. The three–dimensional soil model is used to predict results from the compression and extension triaxial test and the cubical shear test. The differences in predictions of the cubical shear test results between the two–dimensional and three–dimensional soil models are also discussed.

5.5.1 Triaxial Test Response

The parameters determined from the procedures described in Appendix D are used in the three–dimensional soil model to predict the triaxial test results. In the triaxial tests only the primary loading curves were generated, thus no comparison could be made between the test results and the unload–reload modulus parameters. The comparison of the three–dimensional model to the primary loading curve for the triaxial tests involves the use of six parameters; ϕ, K, n, R_f, K_b, and m.

Various combinations of these parameters can be used to obtain a fit to the observed data. It was shown in the preceding section that the procedures for determining these parameters can yield several possible combinations of the parameters. Since the model was new and there was no experience base to help in the selection

of parameters, the analysis of the triaxial tests and the cubical shear tests were conducted concurrently.

In the first attempts to fit the observed data, it became apparent that the model was sensitive to the value of R_f. When the value of R_f was less than or equal to 0.8, a better fit was obtained for the results at the lower shear stress values. Conversely, when the value of R_f was greater than 0.95, the shear stress and strain produced by the model could accurately match observed value at the higher levels of shear stress. Recognizing this limitation, the model was adjusted so that R_f is equal to 0.8 when the shear stress level is at 85 percent or less of the mobilized shear strength and 0.95 at 100 percent of the mobilized shear strength.

After several iterations of fitting the model to the test data for both the triaxial tests and the cubical shear tests, the parameters presented in Table 5.3 gave the best fit to the observed tests for samples with a relative density of 55 percent. Figures 5.25 and 5.26 show comparisons between the triaxial test data and the model for the compression and extension tests, respectively. No one single set of parameters fit both the compression and extension tests. Further comment is provided in the discussion of the cubical shear tests.

Table 5.4 gives the parameters that produced the best fit to the observed data for the triaxial tests with a relative density of 70 percent. Figures 5.27 and 5.28 show comparisons between the triaxial test data and the model for the compression and extension tests, respectively. As was the case for a relative density of 55 percent, no one single set of parameters can duplicate the observed data for both compression and extension tests. Again, the differences were small. For a relative density of 70 percent there were no cubical shear tests to help in selection of the final parameters,

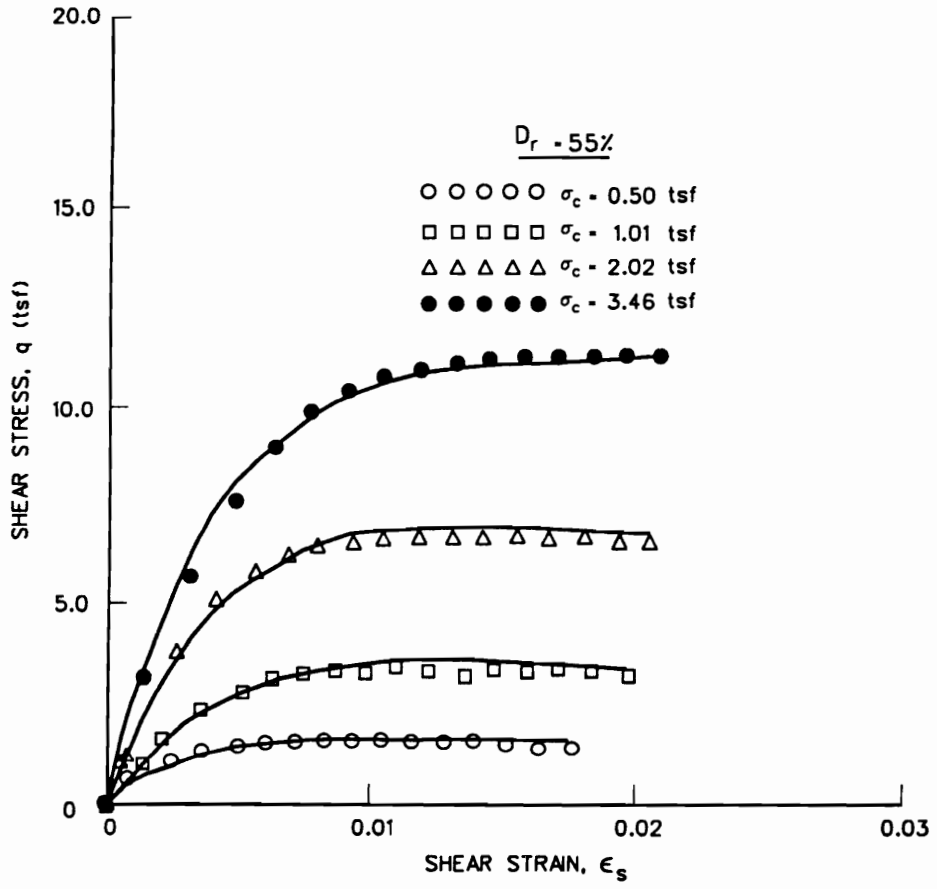

Figure 5.25: Comparison between soil model and triaxial compression test data for a relative density of 55 percent.

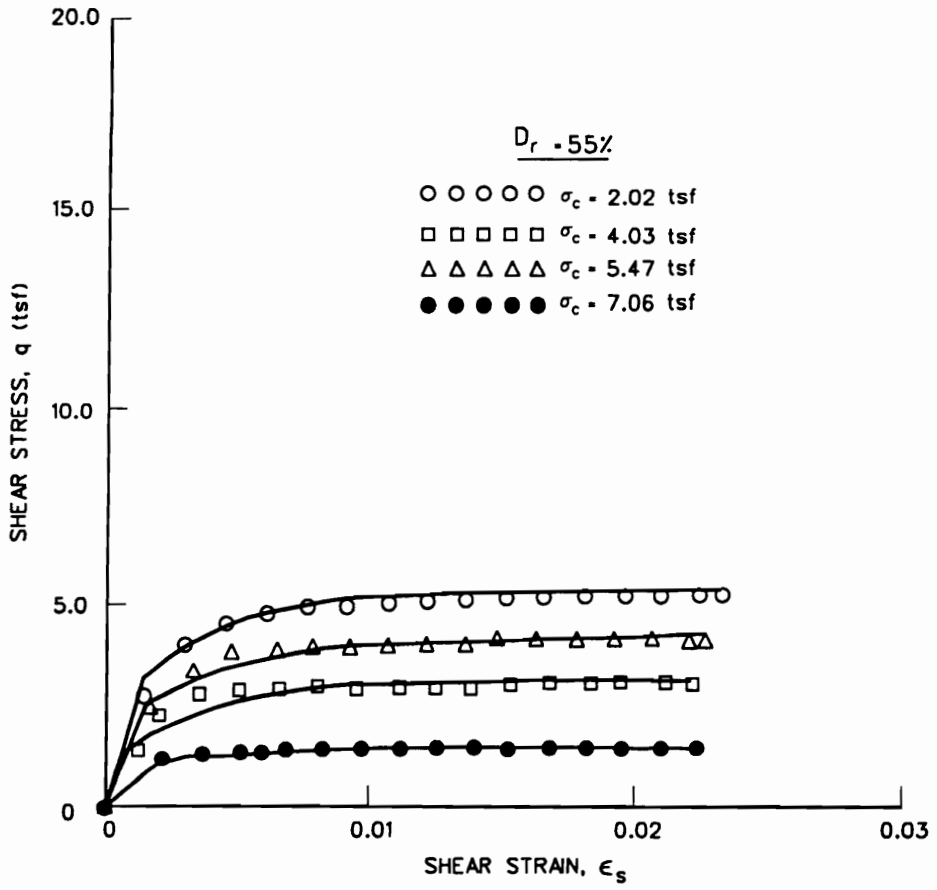

Figure 5.26: Comparison between soil model and triaxial extension test data for a relative density of 55 percent.

and in this case parameters were selected based on the findings of the fitting of the cubical shear tests for relative density of 55 percent.

5.5.2 Cubical Test Response

The matching of the cubical test results with the soil model test predictions proved a more difficult task than was the case with the triaxial tests. The response in the cubical shear tests involve a significant Poisson's effect which, in turn, influences the stress–strain response of the soil. Thus, the predictions for the cubical shear tests were sensitive to the bulk modulus.

In the first six cubical tests, the initial phase of loading was essentially the same as a conventional, one–dimensional consolidation test. Three of the tests used a loading magnitude representative of the midcell height, while the other three used a loading closer in magnitude to that found in the lower portion of the cell. The response in all cases was very similar, following almost identical stress–strain curves. For the unloading phase, three different paths were used for each of the two different initial loading paths. Nevertheless, the soil stress–strain response was almost identical in all cases. The similarity of the response in the first six cubical tests simplifies the fitting of these results. If a set of model parameters are determined which match one of the curves, it will also work for the others. Consequently, for the purposes of discussion, only one of these tests is presented in detail.

The test selected for discussion is stress path **B**, shown in Figure 5.24, with the higher loading magnitude. The stress path and the stress–strain curves are shown in Figures 5.29 and 5.30, respectively. Figure 5.31 shows a comparison with the cubical test results and the results predicted with the two–dimensional soil model. The best fit for the two–dimensional model to the test results is obtained using the

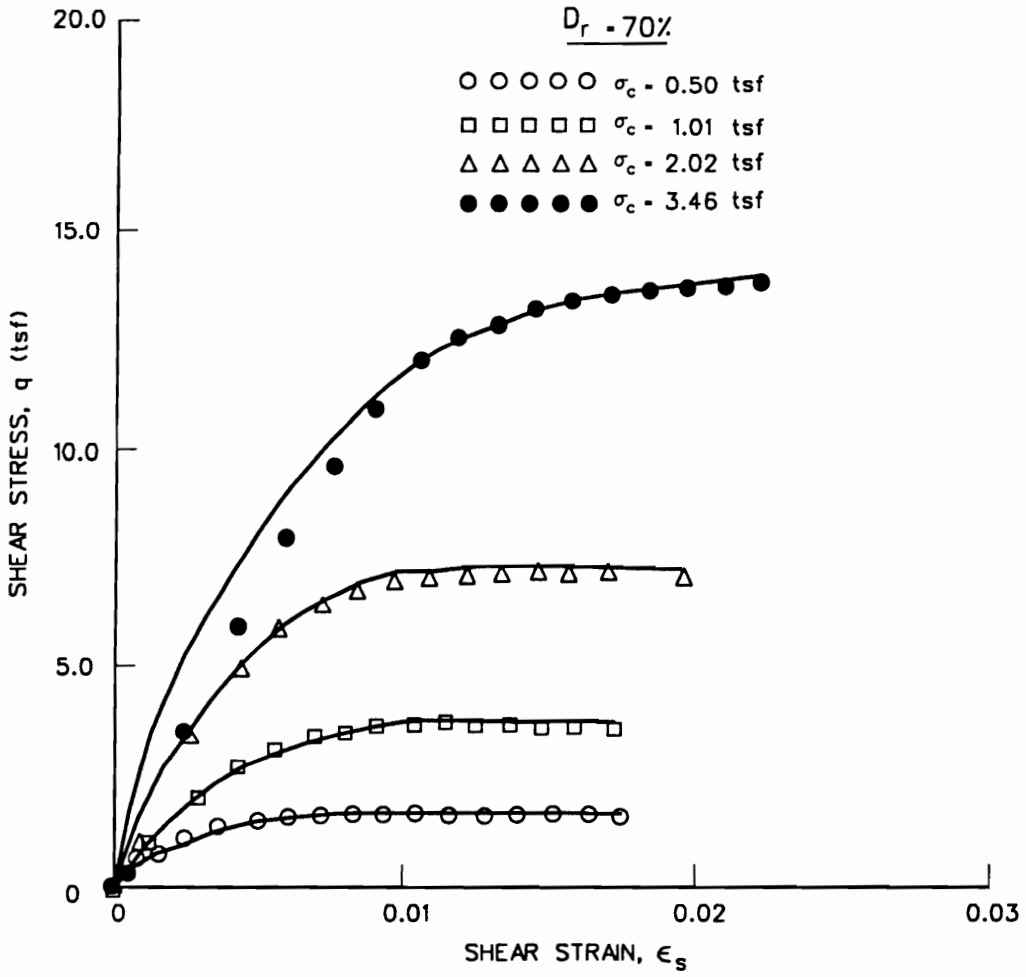

Figure 5.27: Comparison between soil model and triaxial compression test data for a relative density of 70 percent.

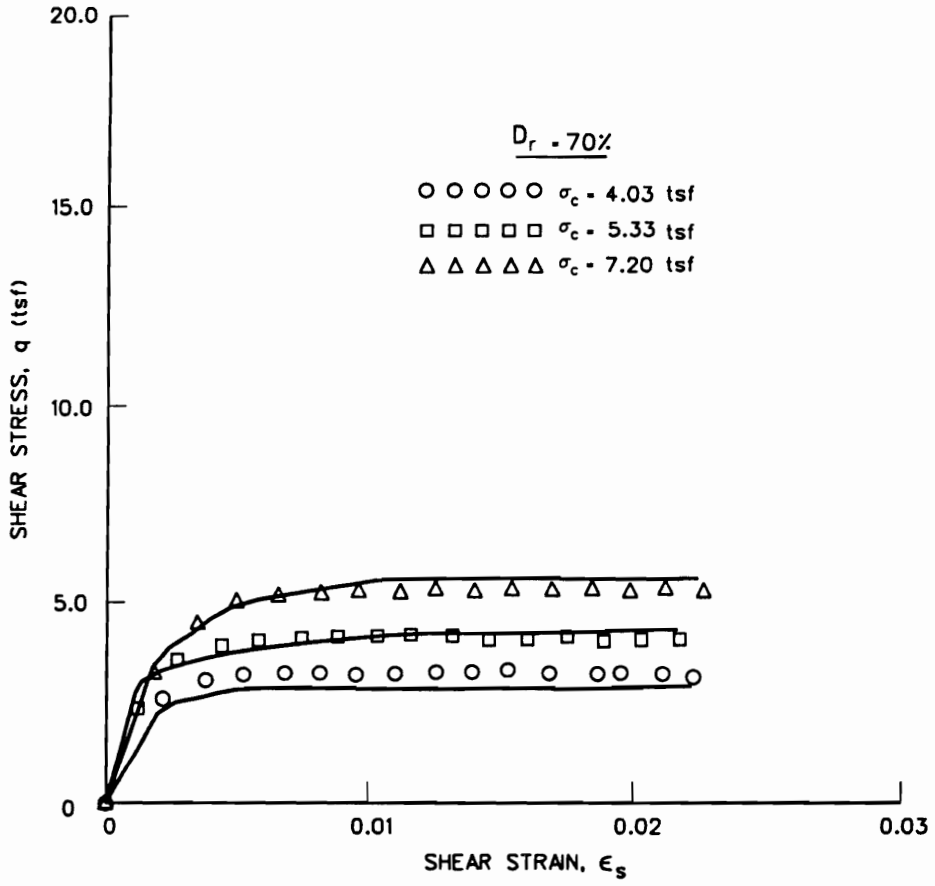

Figure 5.28: Comparison between soil model and triaxial extension test data for a relative density of 70 percent.

parameters derived from the triaxial extension tests with a Poisson's ratio of 0.3. The two–dimensional soil model yields an almost linear relationship between the deviatoric stress and the major principal axial strain during the loading stage of the test. During unloading, the axial strain remains constant. The two–dimensional predictions produce a good fit to the test data at the higher deviatoric stress levels and during the unloading stage of the test. At the initial stage of loading, the two–dimensional predictions show less strain than the test data and do not demonstrate the nonlinear nature of the behavior.

Figure 5.32 shows the comparison between test results and the new three–dimensional soil model. The comparison reveals a good fit with the observed data. The model parameters for the extension test in Table 5.3 were used to fit the cubical shear test results. The three–dimensional predictions capture the nonlinear nature of the principal axial strain with increased deviatoric stress. The relationship between the major principal axial strain and deviatoric stress during the loading stage of the test can be divided into two portions; an initial soft response and a subsequent stiffer, almost linear, response. The three–dimensional model simulated this response, while the two–dimensional model was unable to capture this behavior. The reasons for the difference between the two soil models can be explained by examining the state of stress in the three–dimensional model under the plane strain conditions and the differences in the formulation of the models.

Figure 5.33 shows the simple, one–element finite element model used for the three–dimensional predictions. The principal stresses and strains coincide with the normals of the element faces. To impose plane strain conditions on the model, the nodes on faces 1 and 2 were fixed against movement along the z-axis, as in the cubical shear tests. Remembering that the ultimate shear strength of the soil is defined only

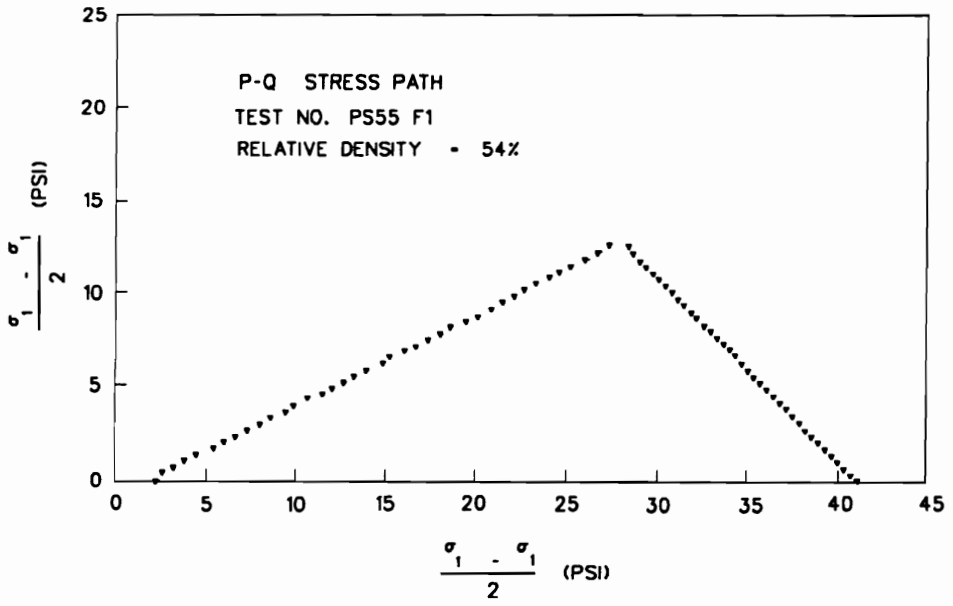

Figure 5.29: Stress path **B** for cubical shear test.

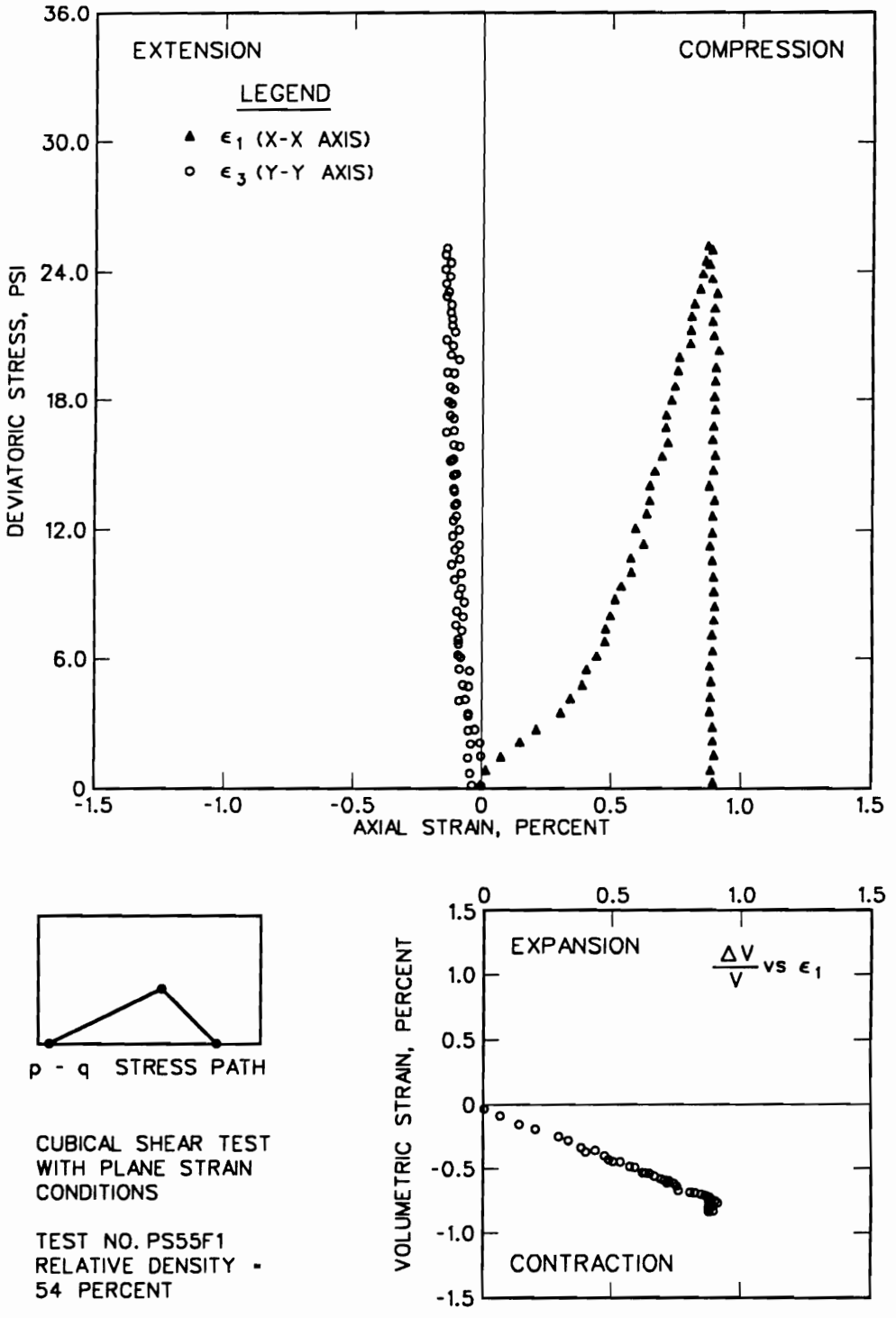

Figure 5.30: Stress–strain results from cubical shear test for stress path **B**.

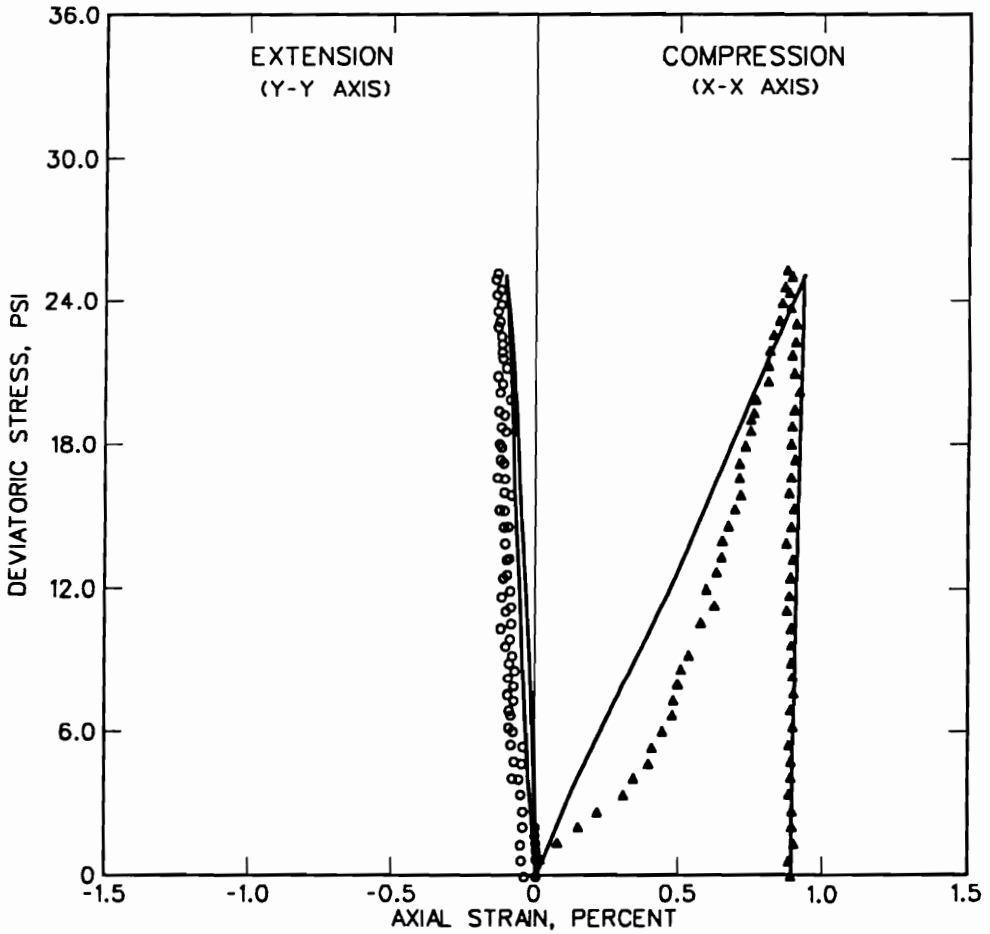

Figure 5.31: Comparison between two-dimensional model and cubical shear test for stress path **B**.

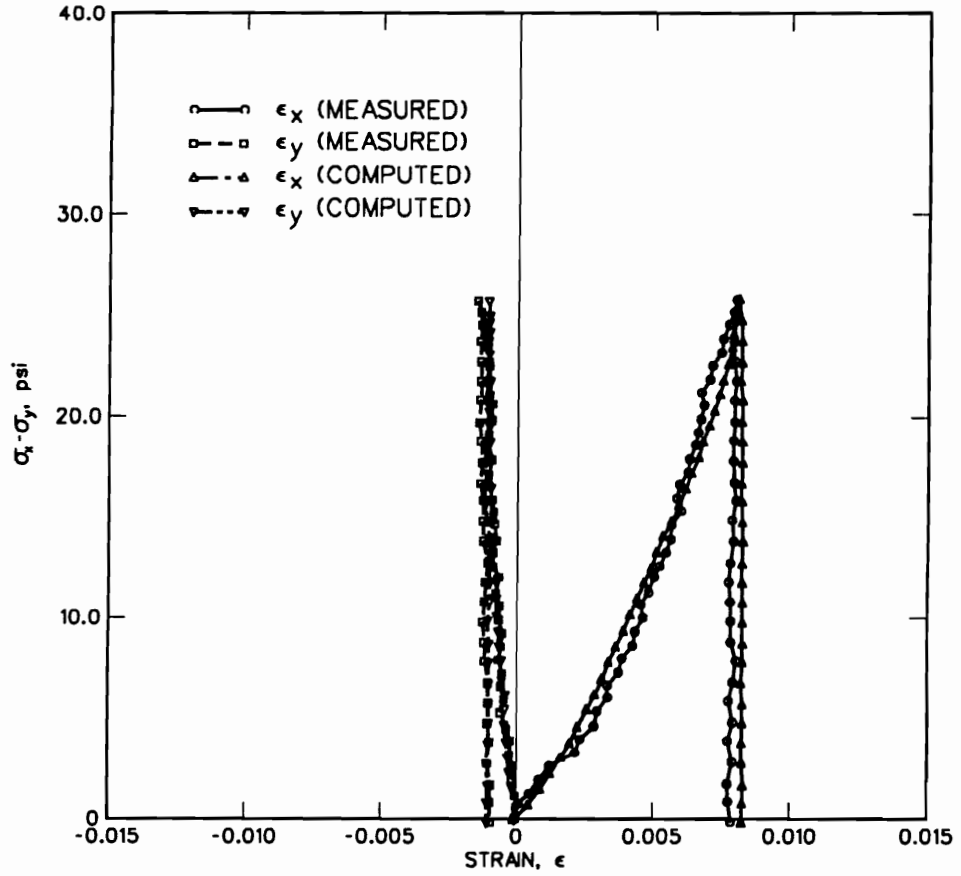

Figure 5.32: Comparison between three–dimensional model and cubical shear test for stress path **B**.

by the major and minor principal stresses and the intermediate principal stress has no influence, an examination of the three–dimensional finite element predictions reveals that during the commencement of the loading the minor principal stress is along the z-axis. As the loading increases, the minor principal stress changes from the out–of–plane axis under plane strain conditions, z–axis, to the in–plane axis, and the x–axis. This was approximately the point where the major principal axial strain changed to the stiffer response. The initial tangent modulus, E_i, for the two–dimensional model is a function of the confining pressure and increases at a rate equal to the log of the confining pressure. Under the plane strain conditions, the confining stress is equal to the minor principal stress in the plane of loading (x–y plane). During the loading stage of the test, the confining stress increases at a constant rate with the major principal stress and deviatoric stress. In the three–dimensional model, the initial tangent shear and bulk moduli are functions of the mean normal stress, p, and increase at a rate equal to the log of the mean normal stress. The three–dimensional model yields a mean normal stress that increases at a faster rate than the confining stress in the two–dimensional model, Figure 5.34. This faster rate of increase in mean normal stress is one of the reasons that the three–dimensional model provides a better fit to the observed data, but the primary reason is the effect of mean normal stress in the formulation of the model.

The formulation for the three–dimensional soil model is in terms of the shear and bulk moduli, while the two–dimensional model is in terms of Young's modulus and Poisson's ratio. In the three–dimensional model, the tangent shear and bulk moduli vary as a function of the mean normal stress and the shear strength ratio. In the two–dimensional model, the Young's tangent modulus varies as a function of the confining stress and the shear strength ratio, while Poisson's ratio remains

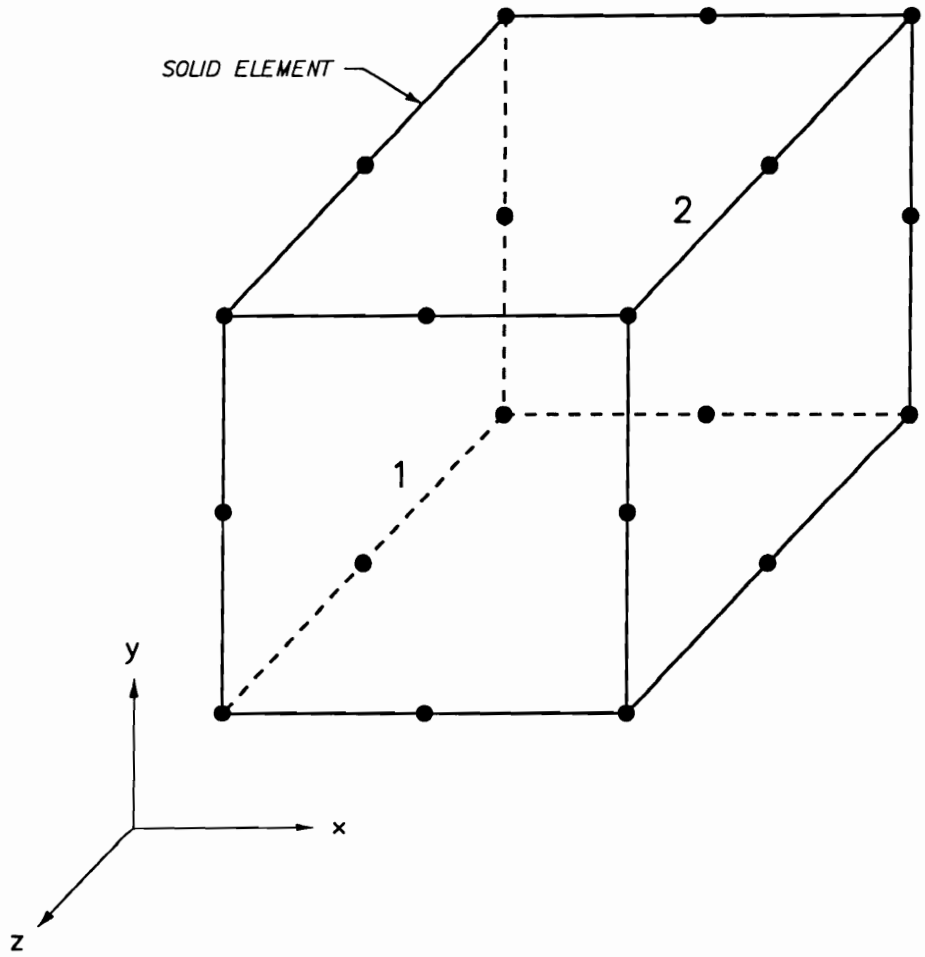

Figure 5.33: Finite element model for cubical shear test.

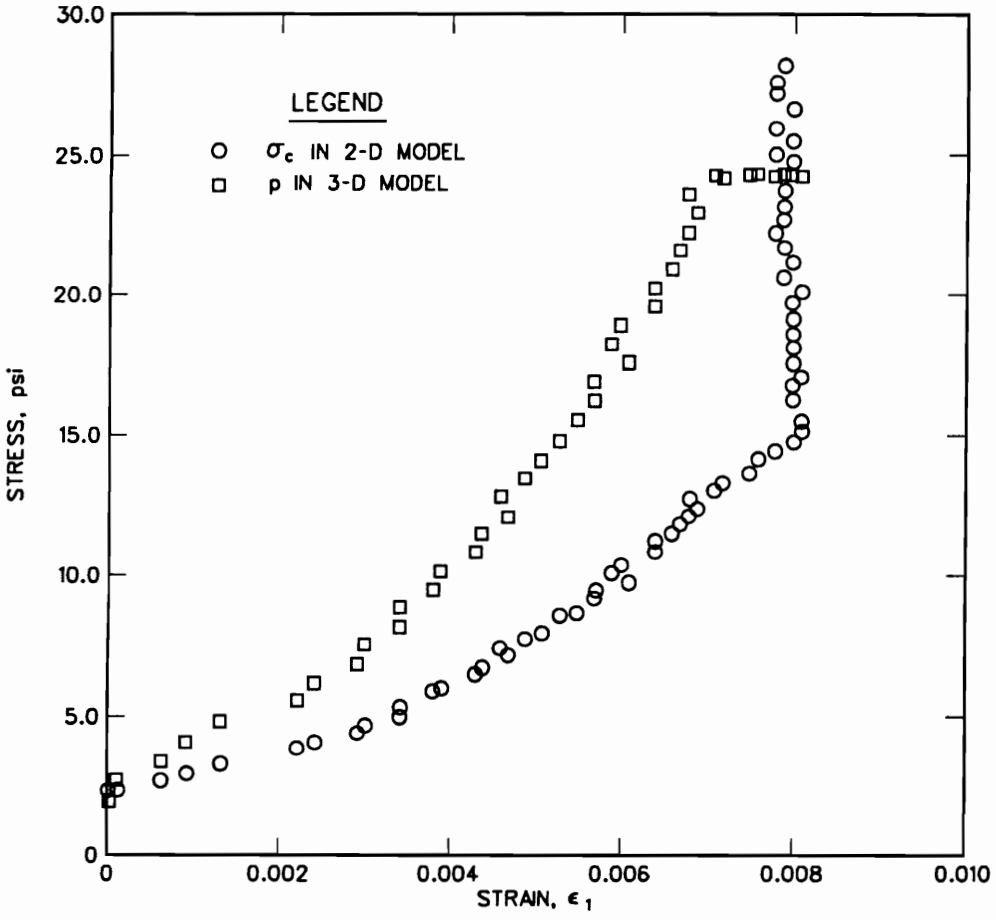

Figure 5.34: Comparison of mean normal stress and confining stress.

constant. To illustrate the differences in the response of these two formulations, the tangent shear and bulk moduli from the three–dimensional formulation are used to compute an equivalent Young's tangent modulus and Poisson's ratio by

$$E_t = \frac{9K_tG_t}{3K_t + G_t} \tag{5.63}$$

$$\nu = \frac{3K_t - 2G_t}{6K_t + 2G_t} \tag{5.64}$$

In Figure 5.35, the values of Poisson's ratio from the two models are compared. The two–dimensional model used a constant Poisson's ratio throughout the test. In the three–dimensional model, Poisson's ratio increases throughout the loading stage of the test. Poisson's ratio from the three–dimensional model starts at a value of approximately 0.15 and increases to 0.37 at the end of the loading stage of the test. This lower value of Poisson's ratio during initial loading in the test is the principal reason for the minor principal stress being in the out–of–plane axis.

The plot in Figure 5.36 compares the Young's tangent modulus from the two–dimensional model to the equivalent Young's tangent modulus from the three–dimensional model. The modulus values are plotted against the major principal strain. The plot reveals that the Young's tangent modulus from the three–dimensional model, thus the stiffness of the soil, increases constantly throughout the loading stage of the test, while the tangent modulus from the two–dimensional model deceases slightly at the start of the test and then increases back to its initial value. The increasing tangent modulus from the three–dimensional model is the primary reason for a better fit to the observed data.

The three–dimensional model did a good job of representing the soil response during the plane strain K_0 loading in the cubical shear device. However, before drawing final conclusions, it is necessary to consider the tests that are closer to the

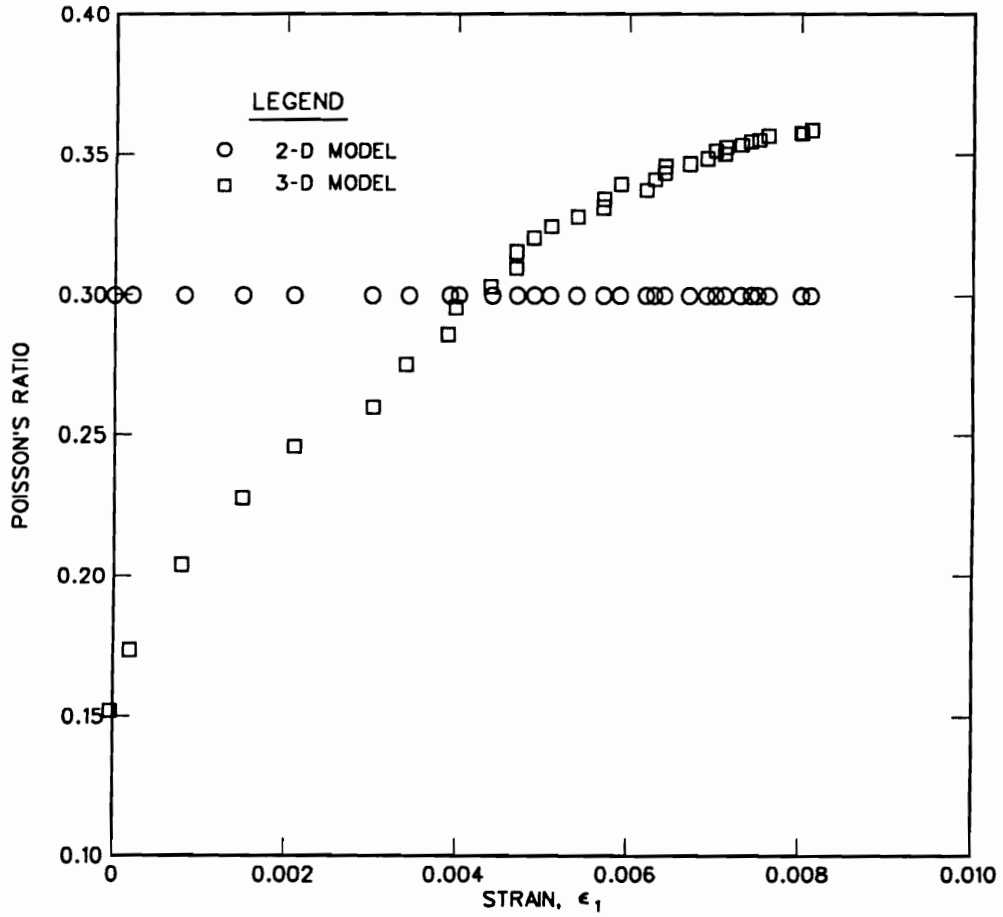

Figure 5.35: Comparison of value of Poisson's ratio during cubical shear test for stress path **B**.

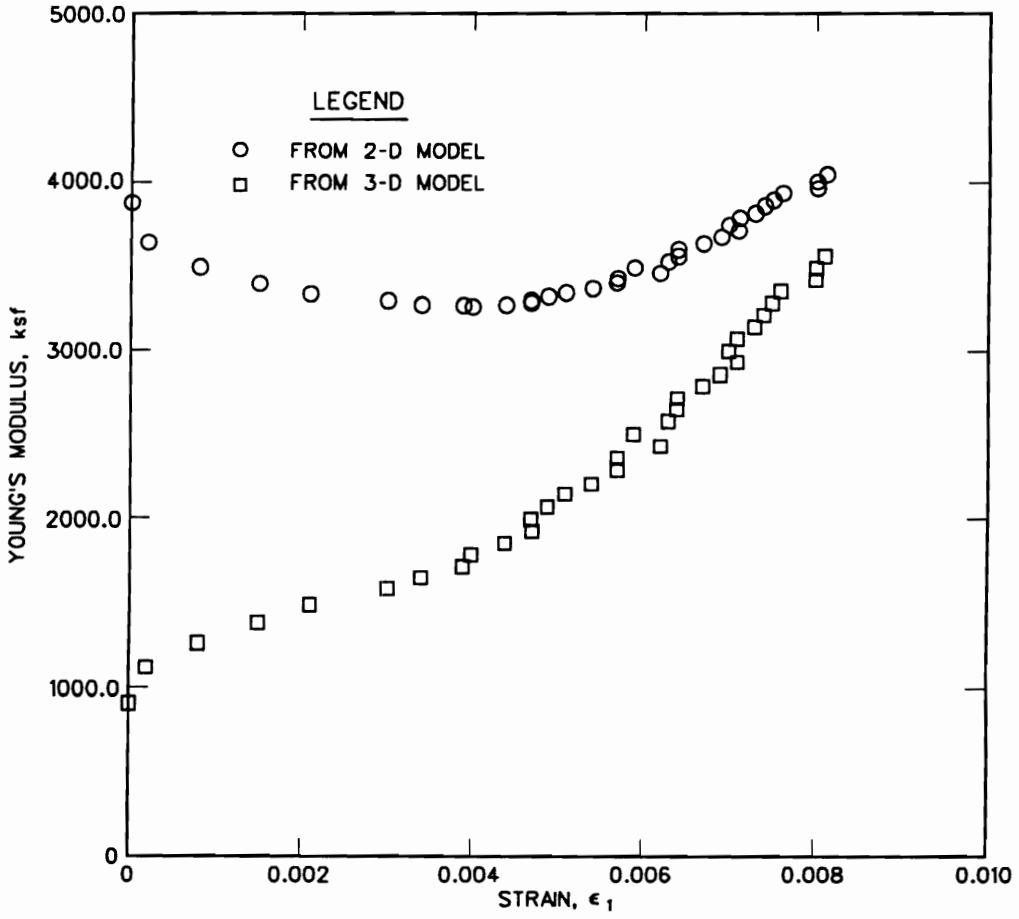

Figure 5.36: Comparison of value of Young's modulus during cubical shear test for stress path **B**.

failure state of the soil.

Figures 5.37 and 5.38 show the load path and test results for hypothetical load path **F**, as referred to in Figure 5.24. This specimen is loaded so that the stress path travels along and slightly below the K_f line. The test shows a significantly greater amount of strain in both minor and major principal strains due to the high shear stress level. Figure 5.39 shows a comparison of the two–dimensional model using the best fit parameters in the K_0 loading tests. These parameters result in a response significantly softer than the observed response. A better fit was obtained by increasing the friction angle in the model from 39 to 42 deg, as can be seen in Figure 5.40. The two–dimensional model has decreasing stiffness with increasing shear stress, while the observed test data has increasing stiffness with increasing shear stress. Figure 5.41 shows the comparison of the three–dimensional model with the parameters used in the previous K_0 tests. The comparison reveals that the three–dimensional model yields a much better representation of the soil response during the test. The primary reason for this is that the stiffness computed in the three–dimensional model increases with shear stress and mean normal stress.

This contradictory response of the two–dimensional model is more pronounced in this test than in the previous K_0 tests. The reason for this is that at high stress levels the value of E_t in the two–dimensional model is markedly reduced as the deviatoric stresses increase, Figure 5.42. With ν constant, this reduction in E_t implies that both values of tangent bulk and shear moduli, K_t and G_t, are reduced at the same ratio as E_t. The reduction in G_t with increasing deviatoric stress is realistic, but the marked decrease in K_t with increasing deviatoric stress is contrary to observed experimental behavior. Test results indicate that the value of the bulk modulus is essentially independent of the magnitude of the deviatoric stress and is primarily

dependent upon the mean normal stress or hydrostatic pressure. At or near failure, both the G_t and K_t are reduced to a negligible amount as a result of reducing E_t to a very small value. As a result of this, with any subsequent loading, the soil is assumed to have essentially no resistance to any type of deformation. This phenomenon has been referred to as a *black hole* [40]. Tests results clearly show that this is not characteristic of real soils, which are capable of sustaining additional hydrostatic stresses even after failure. Figure 5.43 shows the plot of Poisson's ratio for the two–dimensional model and the equivalent Poisson's ratio from the three–dimensional model. In the three–dimensional model, Poisson's ratio increases as the shearing takes place. This equivalent Poisson's ratio increased to a higher value, 0.43, than in the previous K_0 test. By increasing ϕ in the two–dimensional model, the failure deviatoric stress for the soil is increased, resulting in the predicted deviatoric stress for the test being further from the failure envelope.

This, in turn, increases E_t and produces a better fit to the data.

5.6 Summary

In this chapter, a new three–dimensional constitutive model for soil was developed based on the variable moduli concept. The general philosophy for the model was to keep it in the same order of complexity as the one employed in the finite element code, **SOILSTRUCT**, used in the two–dimensional analyses of the Lock and Dam 26(R) cofferdam. The primary criteria for the model were; to keep it as simple and as close as possible, conceptually, to the Duncan–Chang model, and definable by commonly used laboratory tests. There are three important characteristics of the

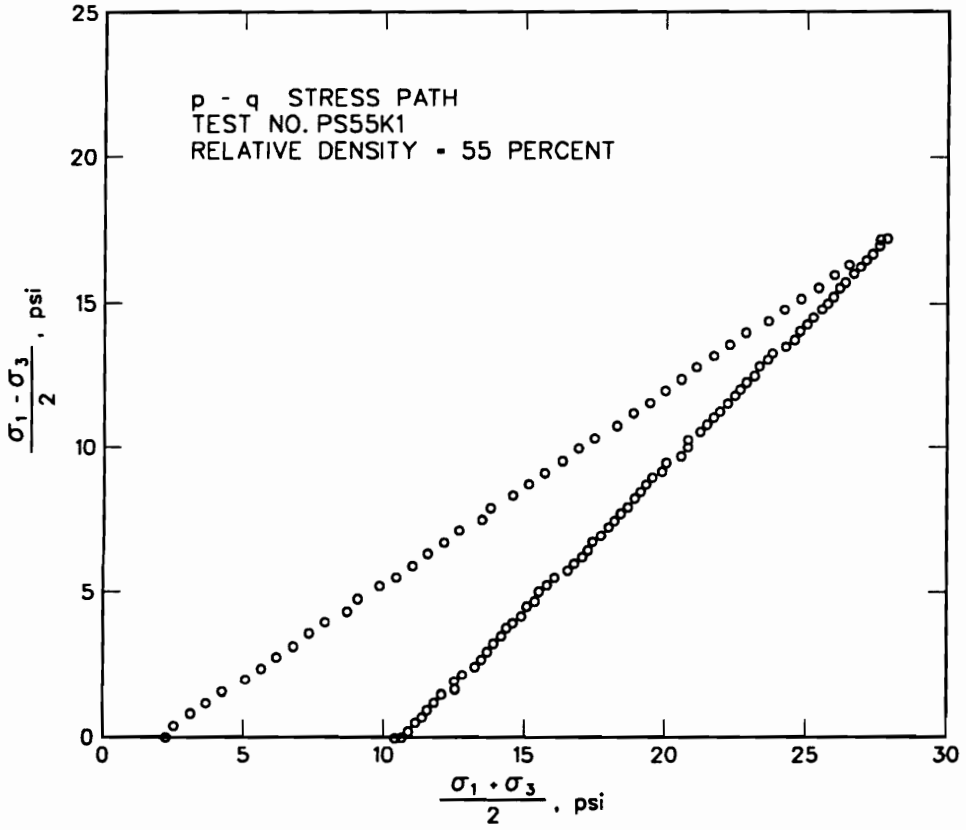

Figure 5.37: Stress path **F** for cubical shear test.

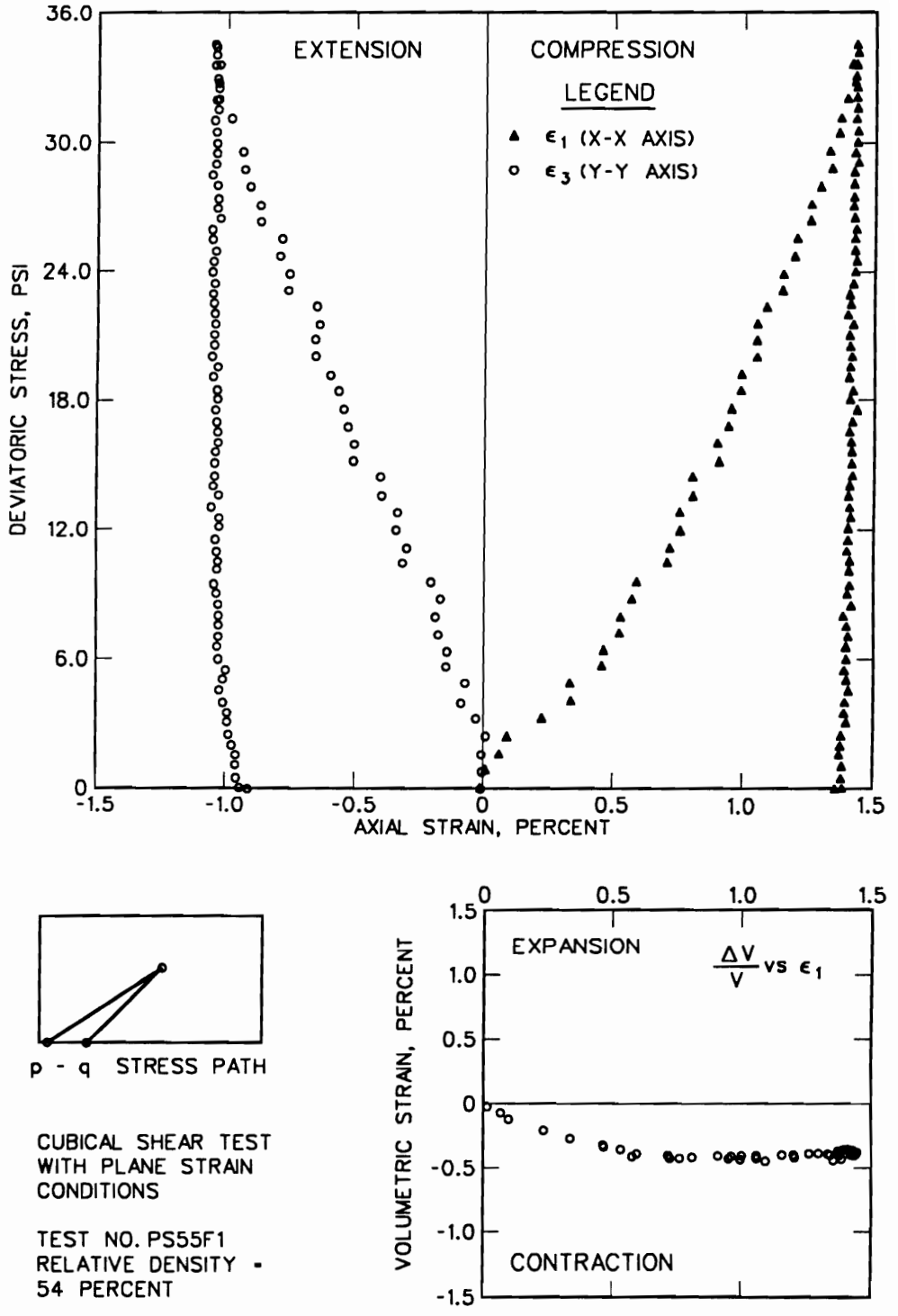

Figure 5.38: Stress–strain results from cubical shear test for stress path **F**.

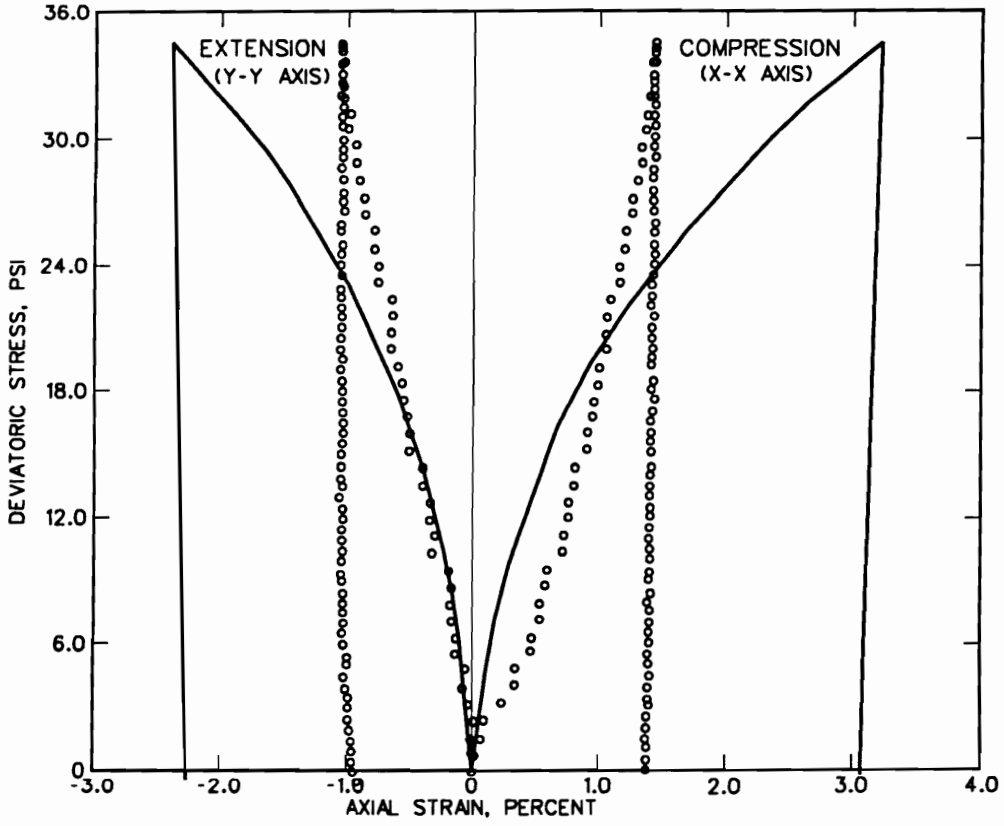

Figure 5.39: Comparison between two–dimensional model and cubical shear test for stress path **F** with $\phi = 39$ deg.

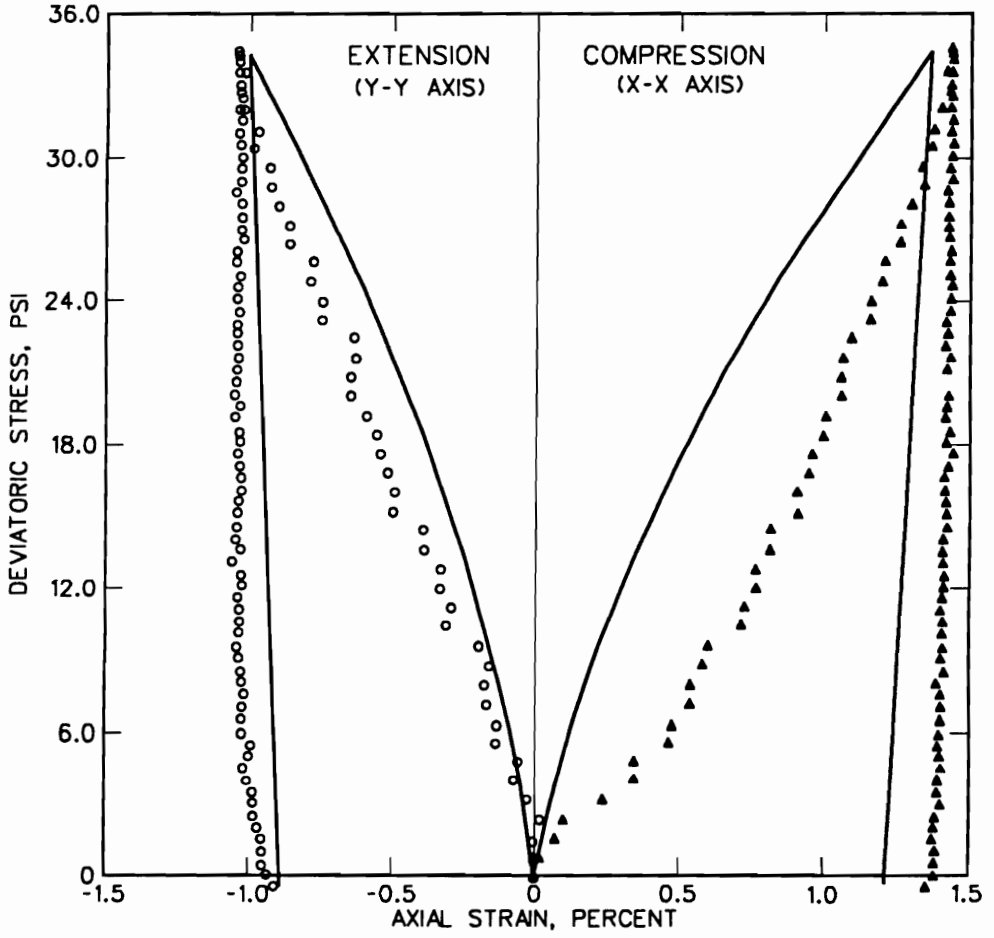

Figure 5.40: Comparison between two–dimensional model and cubical shear test for stress path **F** with $\phi = 42$ deg.

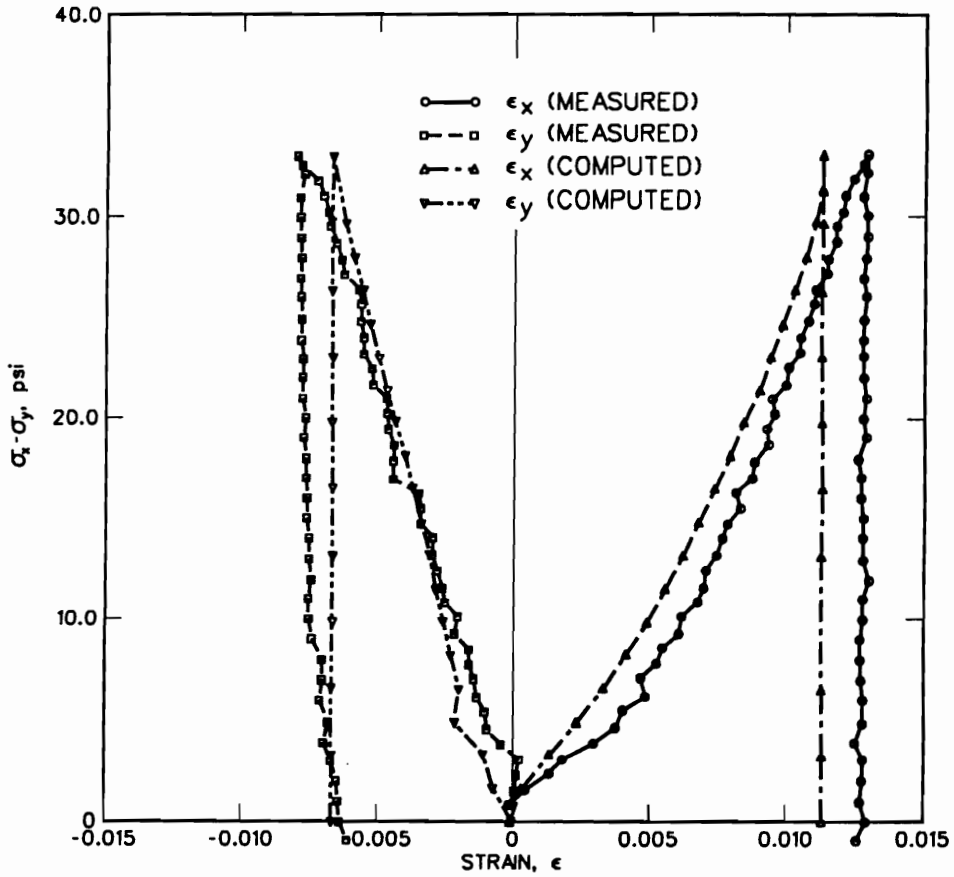

Figure 5.41: Comparison between three–dimensional model and cubical shear test for stress path **F**.

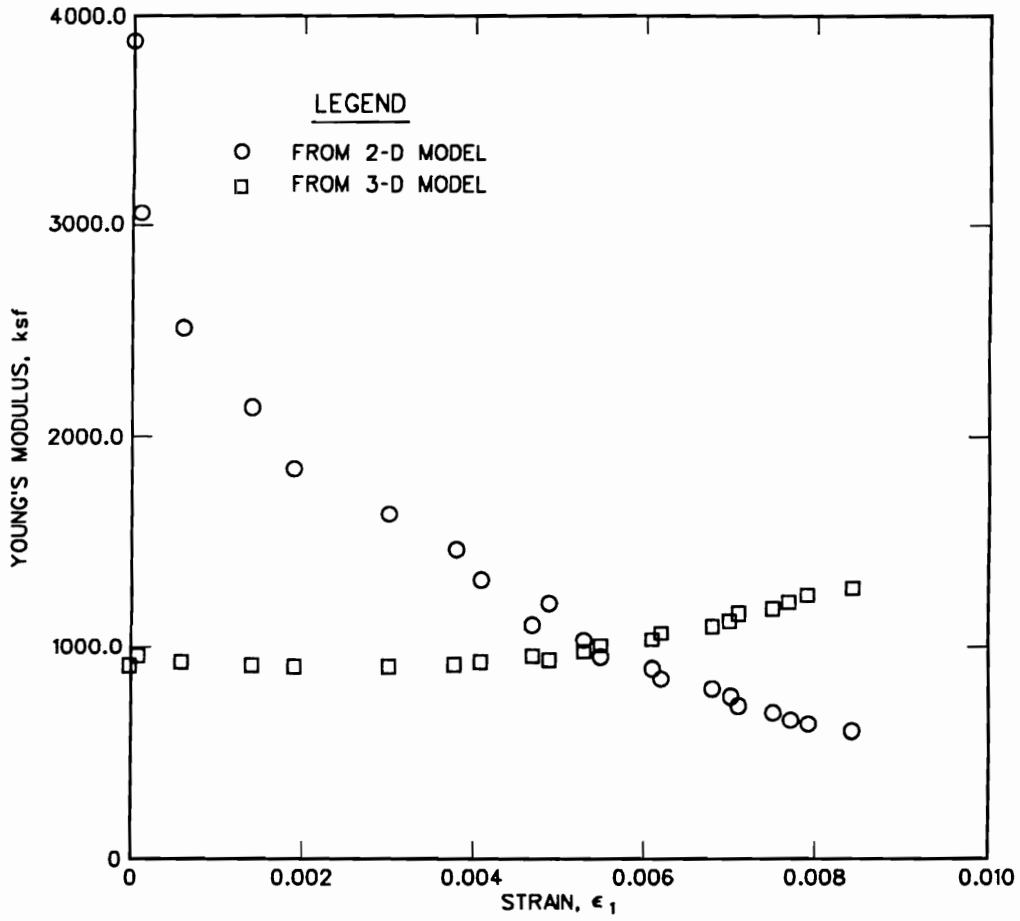

Figure 5.42: Comparison of value of Young's modulus during cubical shear test for stress path **F**.

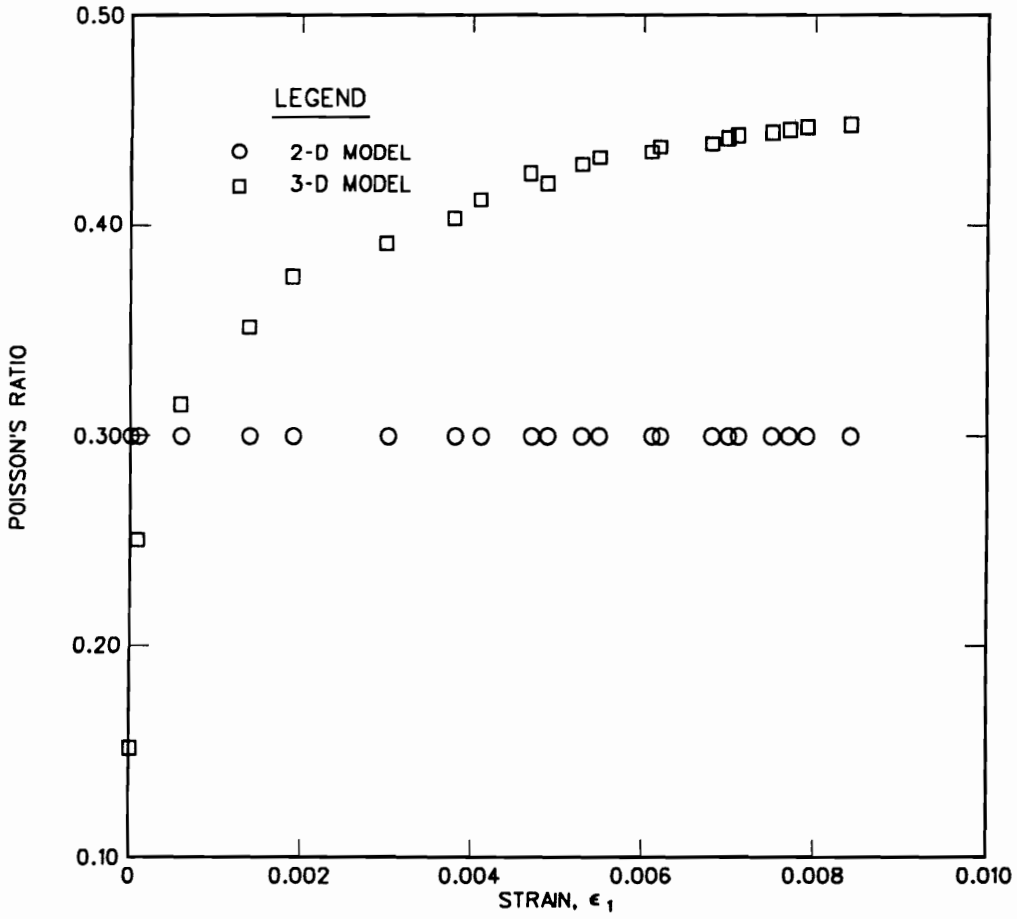

Figure 5.43: Comparison of value of Poisson's ratio during cubical shear test for stress path **F**.

stress–strain response of soils that the model had to emulate. These were nonlinearity, stress–dependency, and inelasticity.

The new model was formulated in terms of the tangent shear modulus, G_t, and bulk modulus, K_t. For the tangent shear modulus, it was assumed that the relationship between shear stress and strain could be represented by a hyperbolic curve and the stiffness was dependent on the mean normal stress and the shear stress ratio. For the tangent bulk modulus, it was assumed that the relationship between mean normal stress and volumetric strain could be represented by power function and the stiffness was a function of the mean normal stress.

A testing program was conducted to explain and resolve differences between two previous testing programs, to provide a data base to be used to establish parameters for new and existing constitutive models, and to provide a stress–strain data base to test the capabilities of the new and existing constitutive models. A total of 23 triaxial (12 compression and 11 extension) and 9 cubical shear tests were performed. The triaxial compression tests were performed to compare with results from the previous testing programs and to add to the data base for determining the constitutive model parameters. As a first step to examining the influence of load path, triaxial extension tests was performed to look at the soil response under a load path that would be the limiting condition during cell filling. To further examine the influence of load path dependence of the stress–strain response of the cell fill, cubical shear tests were performed along a series of stress paths which reasonably duplicated those experienced at critical locations in the cell fill. The data from these tests were used to test the new three–dimensional constitutive model.

To assess the new soil model and refine the model's parameters, the new three–dimensional finite element code with the new constitutive model was used to predict

the stress–strain response from the compression and extension triaxial test and cubical shear tests. The differences in predictions of the cubical shear test results between the two–dimensional and three–dimensional soil models were examined in detail. Several interesting discoveries were made. First, even though the shear strength determined from compression and extension tests were the same, the stiffness of the stress–strain curves were different. The differences were not great, but they were significant. Secondly, the stiffness parameters that matched the extension tests also gave the best match to the cubical shear tests. Finally, the difference in the formulation of the three–dimensional model in terms of shear and bulk moduli from the two–dimensional model in terms of Young's modulus and Poisson's ratio had a significant influence on the ability of the models to predict the cubical shear test results.

Table 5.3: Parameters of Soil Model for a Relative Density of 55 percent

Test	K	n	R_f	K_b	m	ϕ
Compression	350	0.5	0.8	0.0025	0.8	39 deg
Extension	250	0.5	0.8	0.0025	0.8	39 deg

Table 5.4: Parameters of Soil Model for Relative Density of 70 percent.

Test	K	n	R_f	K_b	m	ϕ
Compression	550	0.5	0.8	0.0025	0.8	41 deg
Extension	450	0.5	0.8	0.0025	0.8	41 deg

Chapter 6

Cell Filling Analysis

In Chapter 2, the history of sheet–pile cellular cofferdams and their design was presented. The deficiencies in the conventional design procedures were illustrated by recent experiences in the design and construction of cofferdams for Lock and Dam 26 (R) and the application of two–dimensional soil–structure interaction finite element techniques was described. The two–dimensional finite element analyses have focused on specific facets of cofferdam behavior successfully. However, universal implementation of the findings of these analyses is limited since uncertainties remain about simplifications in the two–dimensional models. This research has led a new three–dimensional nonlinear soil–structure interaction finite element code for sheet–pile cellular cofferdams. In this and the next chapter, the results of the analysis of the second–stage cofferdam for the construction of Lock and Dam No. 26(R) with the new three–dimensional code are presented and compared with the results of previous two–dimensional finite element analyses and instrumentation observations.

In this chapter, the behavior of the second–stage Lock and Dam No. 26(R) cellular cofferdam is investigated during the filling process. The presentation of the

results of the analyses are divided into assessment of: (1) the behavior of an isolated main cell and (2) the three–dimensional section of the cofferdam including a main cell and an arc cell during filling. The behavior of the isolated main cell is used to verify the three–dimensional finite element code by comparing it to the two–dimensional axisymmetric finite element analyses. The three–dimensional analyses of a truly three–dimensional section is used to examine the fundamental behavior of the cofferdam during cell fill placement.

6.1 Project Description

The old Lock and Dam No. 26 near Alton, Illinois, was a bottleneck on the Mississippi River for the last 2 decades. To remove this obstruction to river traffic, the US Army Engineer District, St. Louis, has been constructing a one billion dollar replacement lock and dam 2 miles downstream from the old Lock and Dam No. 26.

The construction scheme calls for the use of a three–stage cofferdam to permit the construction of the replacement lock and dam in the dry. This cofferdam is one of the largest sheet–pile cellular cofferdams ever to be built. Construction began on the first–stage of the cofferdam in the summer of 1981 and was completed the following summer. In 1985, after completion of the construction of six dam monoliths, the first–stage cofferdam was removed and the placement of the second–stage cofferdam began. The second–stage was completed in late 1985 and was used for the construction of the main lock which was completed in 1989. The third–stage of the cofferdam will be used for the construction of a second lock and river closure. The construction of the third–stage cofferdam began in the 1989 with completion and dewatering in 1990.

The first–stage of the cofferdam was built to provide a dry work area for the construction of six of the seven gate sections of the dam. It enclosed the largest area of the three stages, 25 acres, and measured approximately 1,500 ft in length and 800 ft in width. The cofferdam consists of forty–five, 63–ft diam circular main cells, linked together by 43 connector arc cells, Figures 6.1 and 6.2. The cells extended 60 ft above the river bottom to El 430 and had an approximate embedment of 35 ft into the river bed, Figure 6.3.

The second–stage of the cofferdam was built to allow for the construction of the 1,200 ft main lock and the connecting gate section of the dam. This stage of the cofferdam is comprised of 54 main cells and 52 arc cells with the same geometric configuration as the first–stage. It encompassed an area 1,900 ft in length and 600 ft in width, Figures 6.4 and 6.5. The second–stage was designed for a top elevation of 430 ft resulting in a height above the dredgeline ranging from 60 ft on the Missouri leg to 80 ft on the Illinois leg. The embedment depth of the cell ranged from a maximum of 35 ft on the Missouri leg to a minimum of 15 ft on the Illinois leg, Figure 6.6.

The third–stage of the cofferdam is presently under construction and will allow the construction of a second 600–ft–long lock and the closure between the lock and the Illinois river bank, Figure 6.7. This stage of the cofferdam is comprised of 29 main cells and 28 arc cells with the same geometric configuration as the first– and second–stage. For this stage, the elevation of the top of the cofferdam will be raised to 431 ft to avoid the necessity to flood the cofferdam to circumvent damage during extremely high river stages. Both the first– and second–stages were flooded to eliminate possible damage due to overtopping during high river conditions. If the cells for these stages had been 1 ft higher, the need for flooding would not have

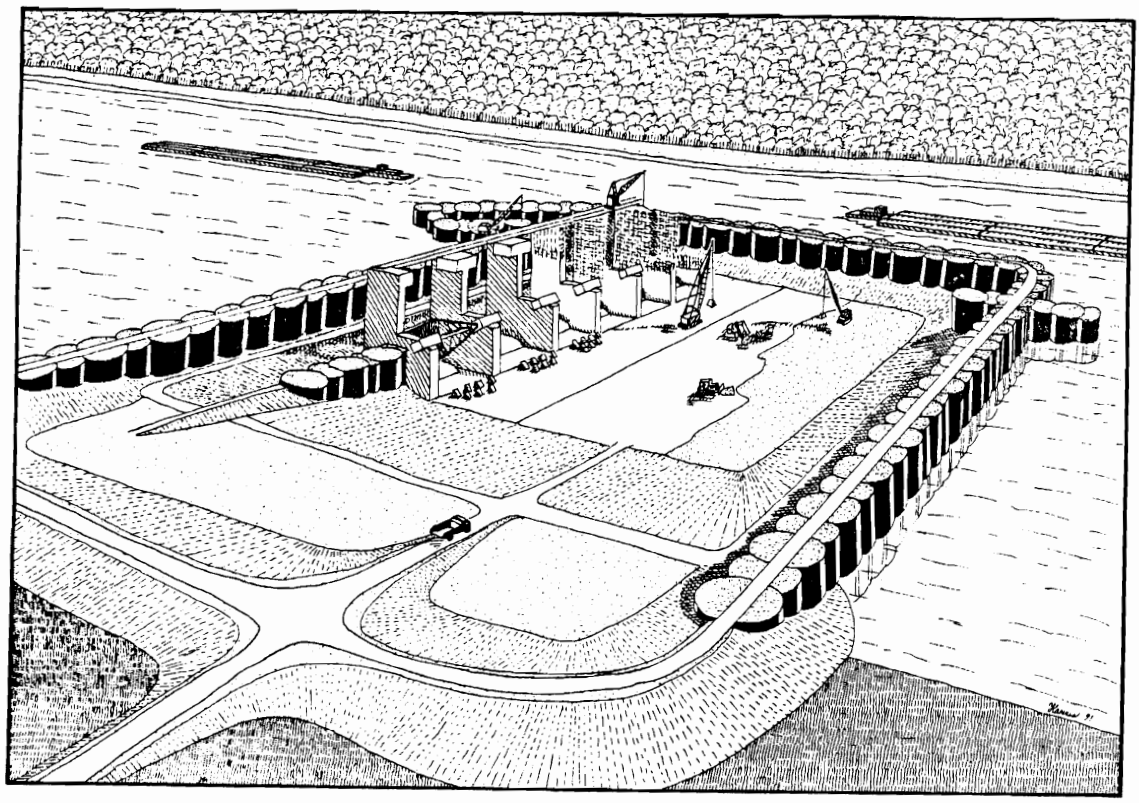

Figure 6.1: Artist illustration of the first–stage Lock and Dam No. 26(R) cofferdam.

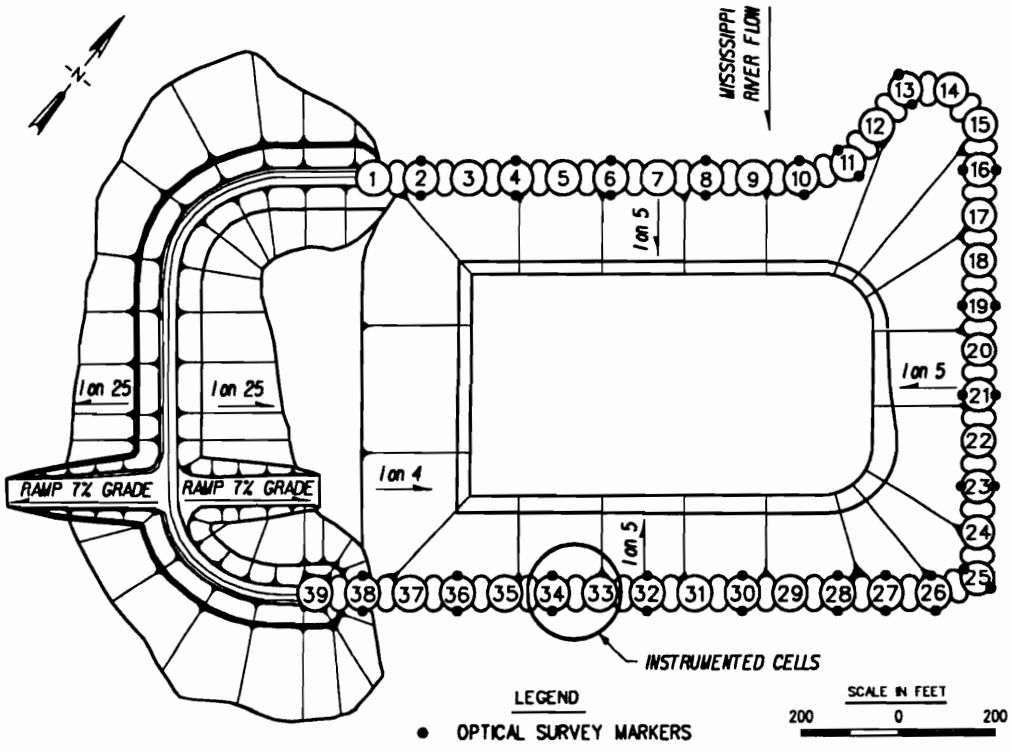

Figure 6.2: Plan view of the first-stage Lock and Dam No. 26(R) cofferdam.

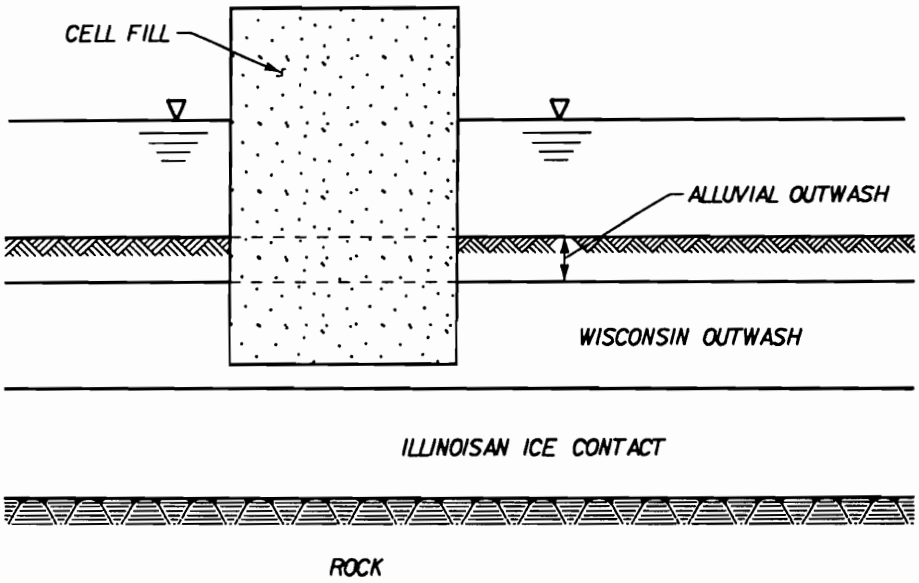

Figure 6.3: Profile section through the first–stage Lock and Dam No. 26(R) cofferdam.

been necessary, and millions of dollars and time lost in construction would have been saved.

6.1.1 Foundation Materials and Properties

The Lock and Dam 26(R) cofferdam is founded on a 70–ft–thick alluvial sand deposit underlain by bedrock. The deposit is composed of a series of dense to medium–dense sand layers, Figure 6.3 and Figure 6.6. Lenses of cobbles and boulders are present in some of the lower layers. For the most part, however, there is little variation among sand layers throughout the deposit. Standard penetration tests show that the deposit was fairly uniform in density with average relative density of approximately 70 percent [53]. The soil properties for a relative density of 70 percent from the laboratory testing program were used in the analyses for the foundation materials.

6.1.2 Cell Fill Materials and Properties

The cell fill is a sand dredged from the Mississippi River bed. After dredging the fill from the river bed and placing it on a barge for drainage, it was dropped in the cells by a clamshell bucket. Once the surface of the fill was above the water level, it was leveled by a bulldozer. From the grain size analyses performed for the design of the cofferdam, the cell fill was classified as a medium sand with 50 percent of the material by weight passing the No. 30 sieve and less than 10 percent passing the No. 200 sieve [53]. In-situ tests performed in the cell fill after completion of construction indicated a relative density of the fill in the range of 55 to 60 percent [6]. The soil properties for a relative density of 55 percent from the laboratory testing program were used in the analyses for the cell fill.

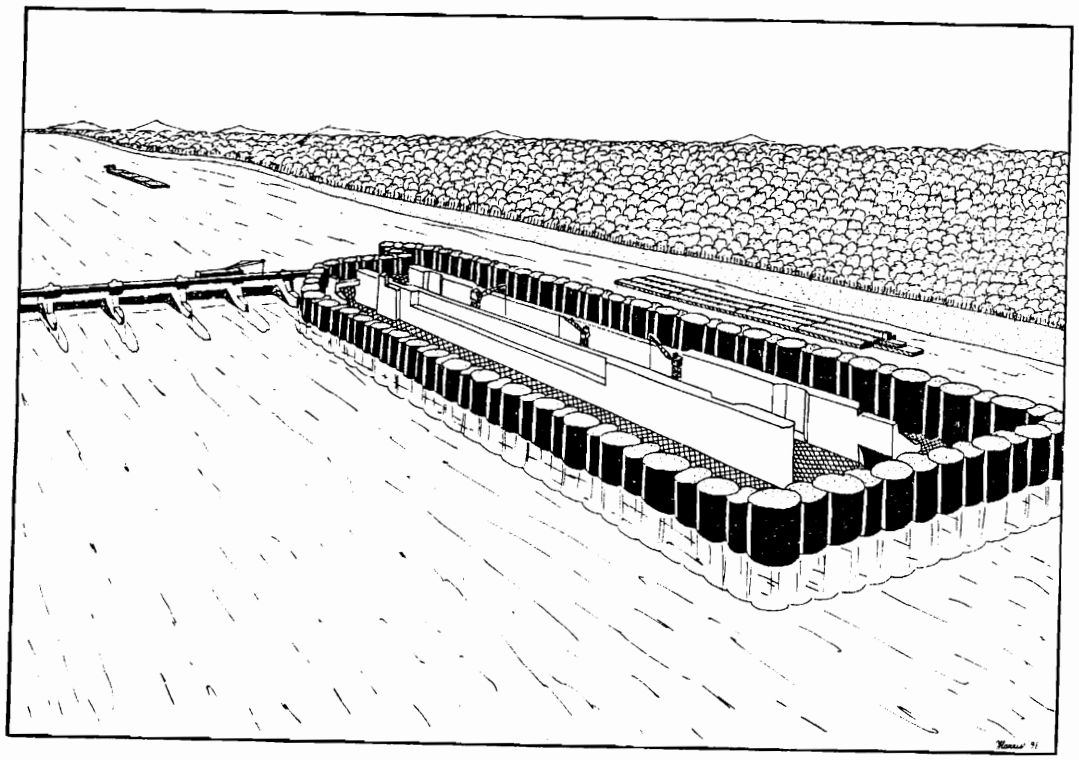

Figure 6.4: Artist illustration of the second–stage Lock and Dam No. 26(R) cofferdam.

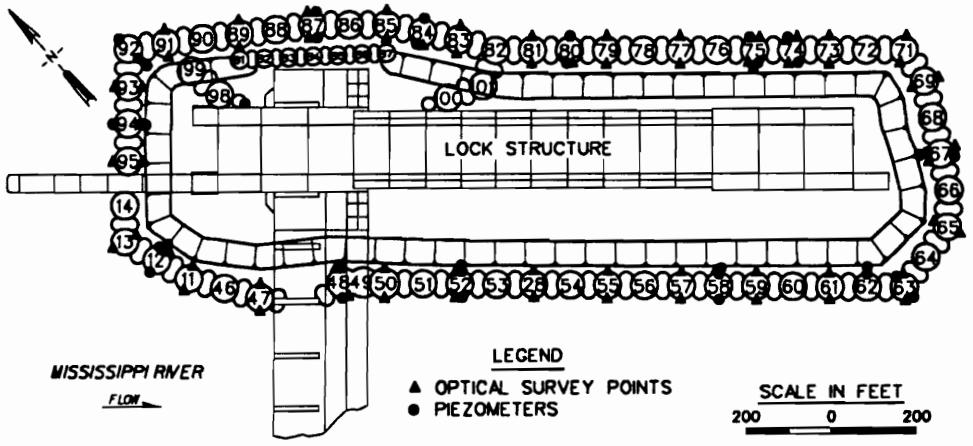

Figure 6.5: Plan view of the second–stage Lock and Dam No. 26(R) cofferdam.

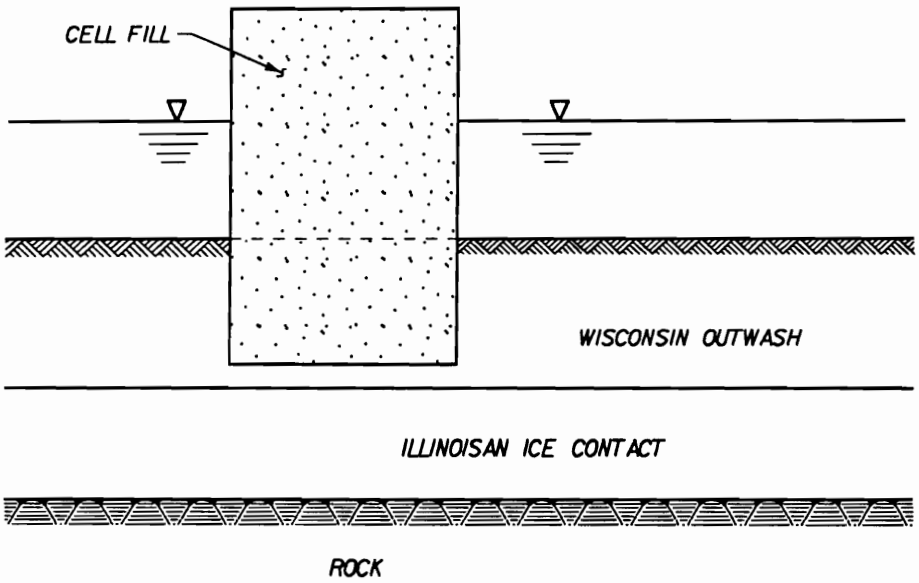

Figure 6.6: Profile section through the second–stage Lock and Dam No. 26(R) cofferdam.

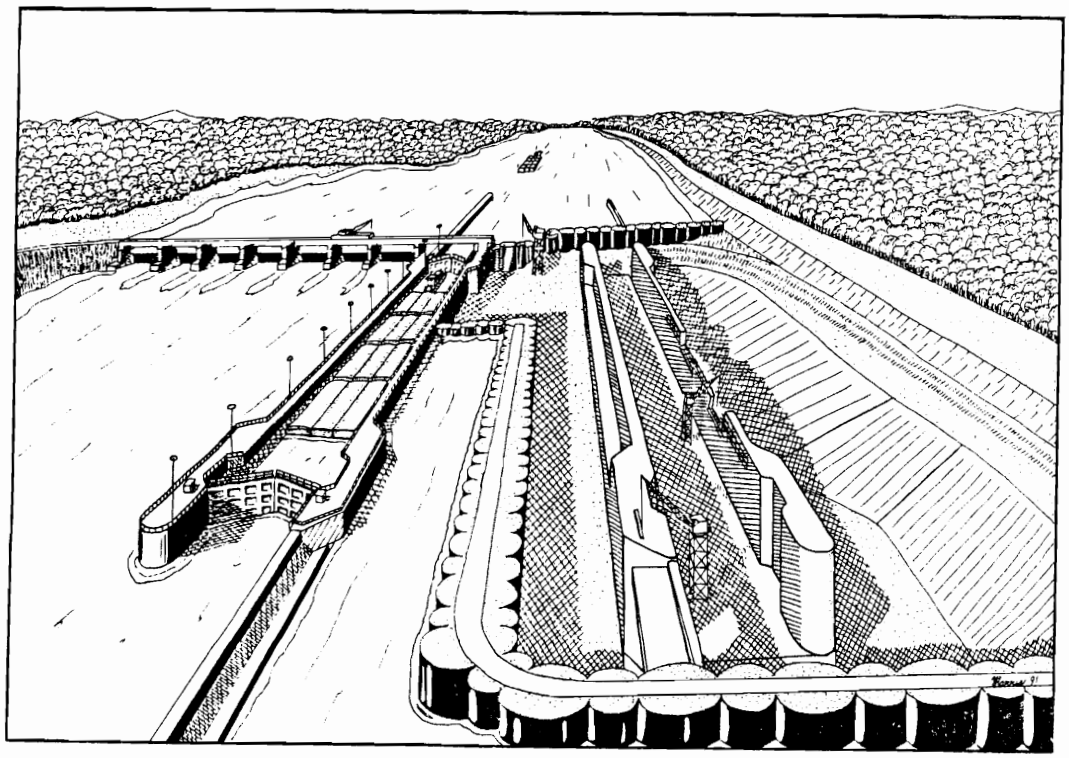

Figure 6.7: Artist illustration of the third–stage Lock and Dam No. 26(R) cofferdam.

6.1.3 Sheet Piles

Each main cell in the cofferdam consists of 154 steel sheet piles while the connecting arc cells are made up of 78 sheet piles, Figure 6.8. The supplier of the steel sheet piling was U.S. Steel Co. For the first–stage cofferdam, high–strength steel sheet piles, PSX–32, were used in the common walls between the main and arc cells where higher loads were expected. PS–32 sheet piles were used in all other sections of the cells. The sheet piles from the first–stage were reused for the second–stage cofferdam. The high–strength sheet piles were used in the common walls for the cells along the Illinois leg of the cofferdam.

6.1.4 General Construction Sequence

The first operation in the construction of the cells for the Lock and Dam No. 26 (R) cofferdam was to place the steel sheet piling. The sheet piles for the main cell were placed with assistance of a template to maintain the cell's shape. The main cell was then filled. Once two adjacent main cells were filled, the sheet piles for the connecting arc cell were driven and the arc cell was filled. The cell fill was dredged from the riverbed, placed on barges, and allowed to drain. The fill was placed in the cells with a clamshell bucket. A bulldozer was used to level the fill once the fill was above the river surface. After all of the cells were placed and filled, sand stability berms were placed against the interior by clamshelling the sand over the sides of the cell. Once the berms were in place, the dewatering of the cofferdam began with aboveground pumps which pumped water directly from the pool. Well points were installed once the water level was low enough to allowed it. The well points were lowered in stages to draw down the pool until the final dewatered state

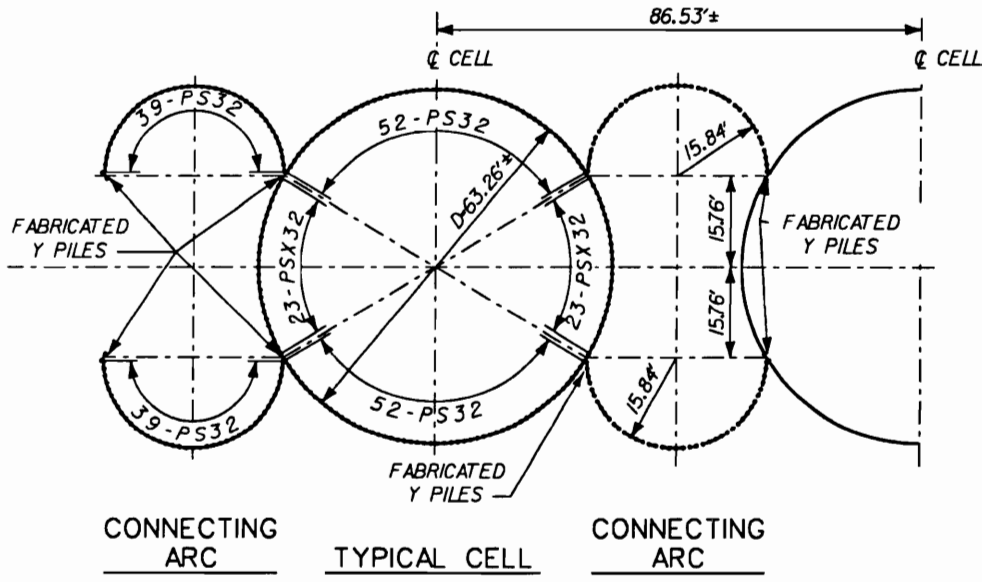

Figure 6.8: Layout of sheet piles in main and arc cell.

was achieved. After final dewatering, the berms were shaped and the river bed silts were excavated to ready the site for construction to begin.

6.2 Response of Isolated Main Cell during Filling

In the investigations of the first–stage Lock and Dam No. 26(R) cofferdam, the behavior of a main cell during filling was studied by analyzing an isolated main cell with a two–dimensional axisymmetric finite element model [8, 33, 56, 53]. In the isolated main cell model, it was assumed that adjacent connecting arc cells and main cells were empty and had no influence on the response of the isolated main cell being filled. It was further assumed that no differential loading was applied to the isolated main cell. Under these boundary conditions, an isolated main cell during fill could be modeled as an axisymmetric problem, Figure 6.9. For the analysis of the first–stage Lock and Dam No. 26(R) cofferdam, an axisymmetric model was developed by Clough and his associates [7, 8] that provided a near complete description of the process of filling an isolated main cell. The axisymmetric finite element model accounted for the staging of load due to filling, the nonlinear behavior, slippage along the interface between the soil and sheet piles, and yielding in the interlocks of the sheet piles.

The new three–dimensional finite element code has similar capabilities as the axisymmetric model and should provide comparable results under the same boundary conditions and loading. The analysis of an isolated main cell provides a verification tool for new three–dimensional code. The symmetry about the center of the cell (z-axis) allows it to be represented in three dimensions by modeling one–quarter of

the cell and the surrounding foundation, Figure 6.10. This three–dimensional case will be referred to as the quarter model.

6.2.1 Verification of the Three–Dimensional Code for Isolated Main Cell Analysis

A series of linear elastic analyses were performed using the axisymmetric and quarter models of the first–stage Lock and Dam No. 26(R) cofferdam. Two different finite element meshes were used in the evaluation. The first mesh used 275 three–dimensional 20–node solid elements for the cell fill and foundation, and forty–five 1–ft–thick three–dimensional 20–node solid elements to represent the sheet piling, Figure 6.11. In the second mesh, the one foot thick solid elements representing the sheet piling were replaced by 8–node shell elements, Figure 6.12. The purpose of the investigation of the two different meshes was to verify the shell element implementation.

The foundation for the models was extended laterally 100 ft from the edge of the cell so that the fixed boundary would influence behavior of cell during filling of the cell. The mesh for the foundation was extended in depth to the bedrock surface, El 300, approximately 70 ft below the Mississippi River bottom, El 370. Bedrock provided an incompressible lower boundary for the model.

Figure 6.13 shows the mesh used for the two–dimensional axisymmetric finite element analyses of the first–stage cofferdam [56]. The foundation is extended approximately 130 ft from the edge of the cell with the same depth of the foundation as the meshes for the three–dimensional analyses. The same values of Young's modulus of elasticity were used for like materials in the two–dimensional and three–dimensional

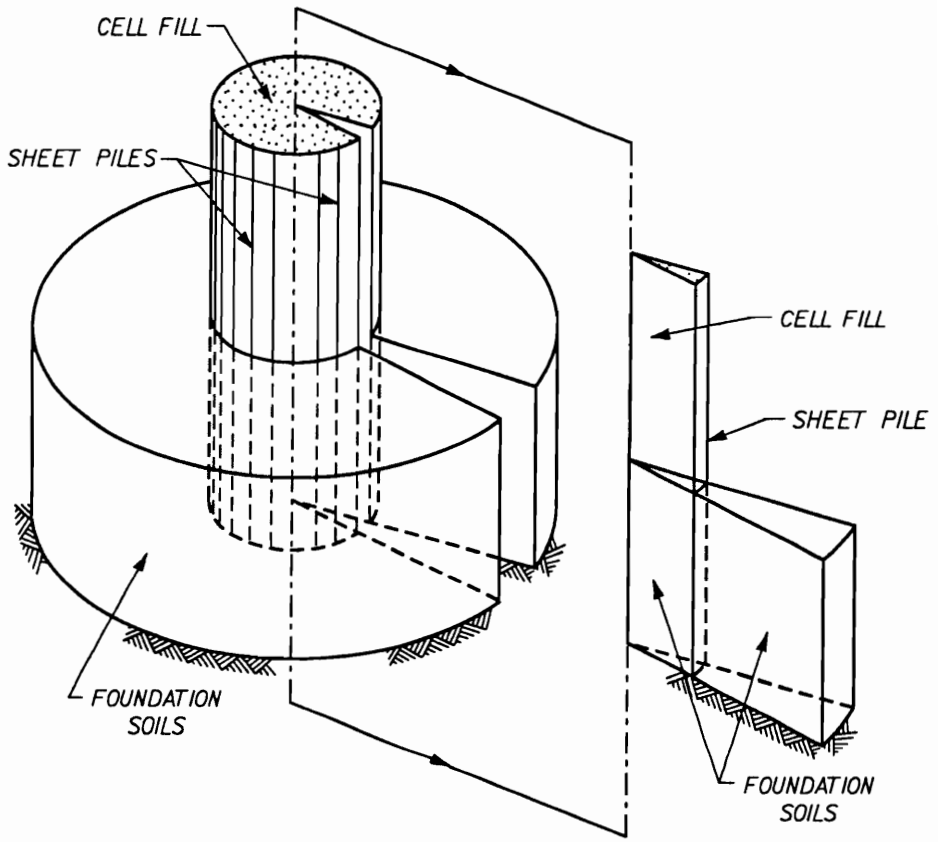

Figure 6.9: Schematic of isolated main cell and axisymmetric model.

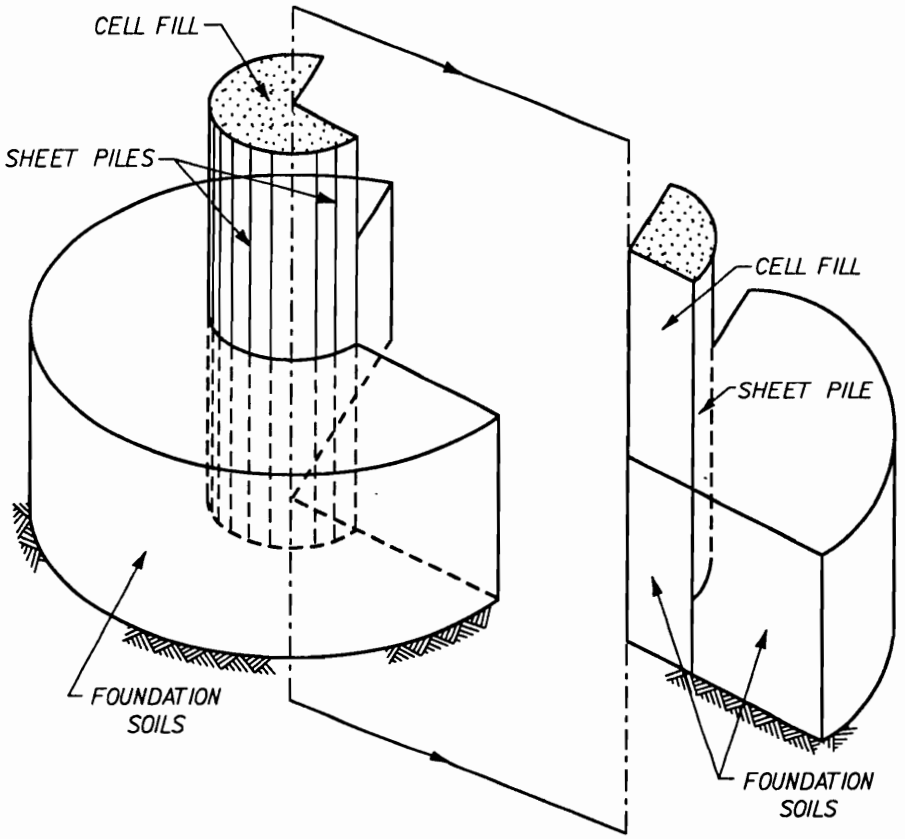

Figure 6.10: Schematic of isolated main cell and three–dimensional model.

models.

Figure 6.14 shows the radial deflection of the sheet piles from the analysis of the isolated main cell under simple gravity, turn–on loading. The deflections for both the axisymmetric and the three–dimensional analyses with 1–ft–thick elements for the sheet piles are essentially identical. The deflections for the analyses with shell elements representing sheet piling were more than twice that obtained from analyses using the 1–ft–thick elements for the sheet piling. Figure 6.15 shows the sheet–pile interlock stresses for the four analyses. Along the free height of the sheet piles, the magnitude of the interlock stresses for the four analyses are essentially the same. Near the dredgeline, the interlock stresses and deflections for the analyses with shell elements are more responsive to the restraint provided by the foundation.

In the course of the research effort, the three–dimensional analyses with the shell element were completed prior to implementation of the shell element in the axisymmetric code. Therefore, the deflections from three–dimensional analysis with the shell element were looked at with suspicion. The interlock stresses from the three–dimensional analysis with shell elements were very reasonable. After careful assessment of the results, it was determined that the results were accurate and the shell element was implemented correctly. This was later confirmed by the development of a shell element for the axisymmetric code [56]. The deflections from the axisymmetric analysis using shell elements were of the same magnitude as those in the three–dimensional analysis, Figure 6.14.

6.2.2 Modeling an Isolated Main Cell During Filling

The linear elastic analyses confirmed the soundness of the element formulation, implementation, and application of the code to large problem (approximately 4,000

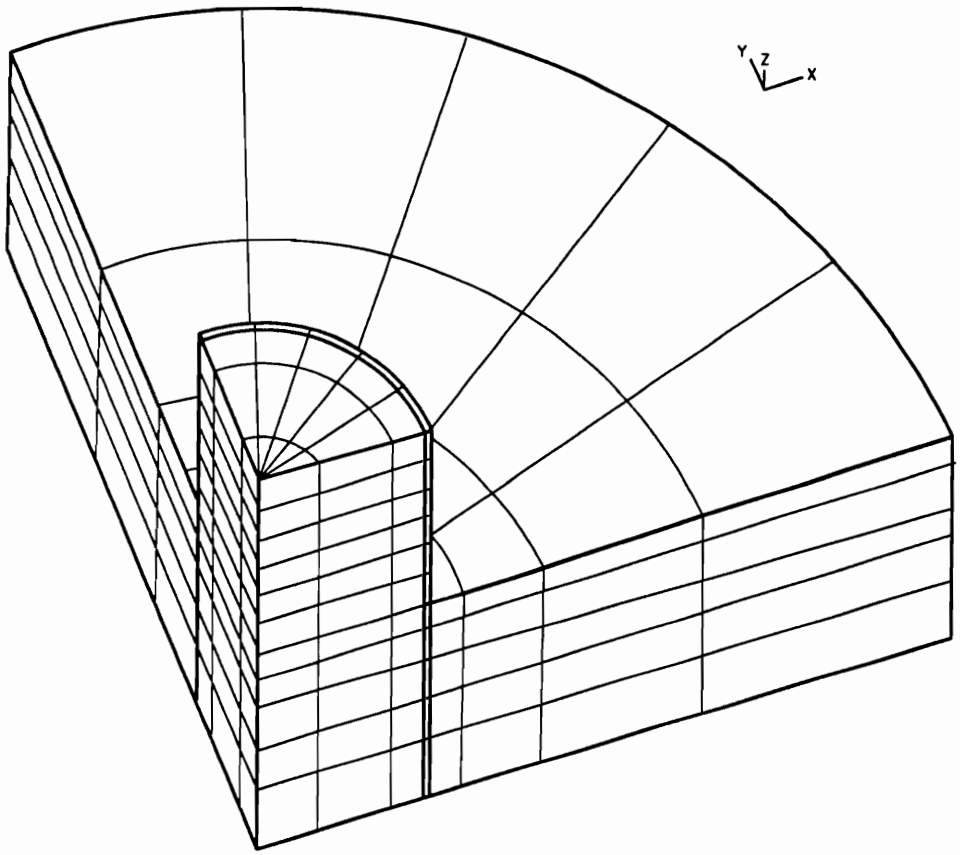

Figure 6.11: Finite element mesh for an isolated main cell from first–stage of Lock and Dam No. 26(R) using three–dimensional solid elements to represent sheet piles.

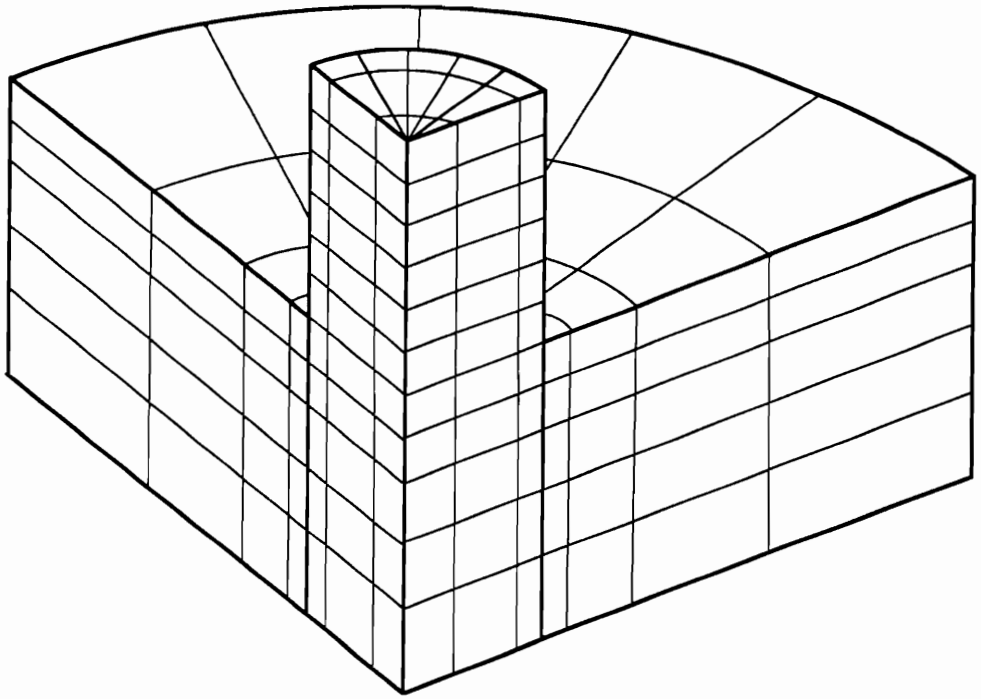

Figure 6.12: Finite element mesh for an isolated main cell from first–stage of Lock and Dam No. 26(R) using shell elements to represent sheet piles.

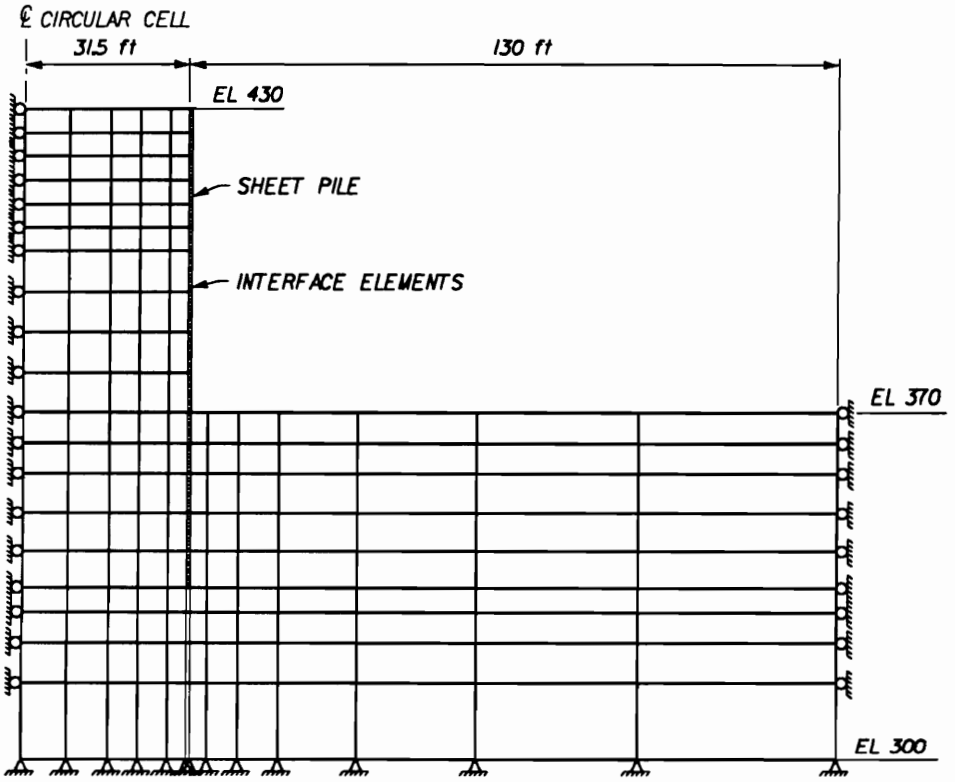

Figure 6.13: Finite element mesh for two–dimensional axisymmetric analysis of first–stage Lock and Dam No. 26(R) cofferdam using shell elements for the sheet piles.

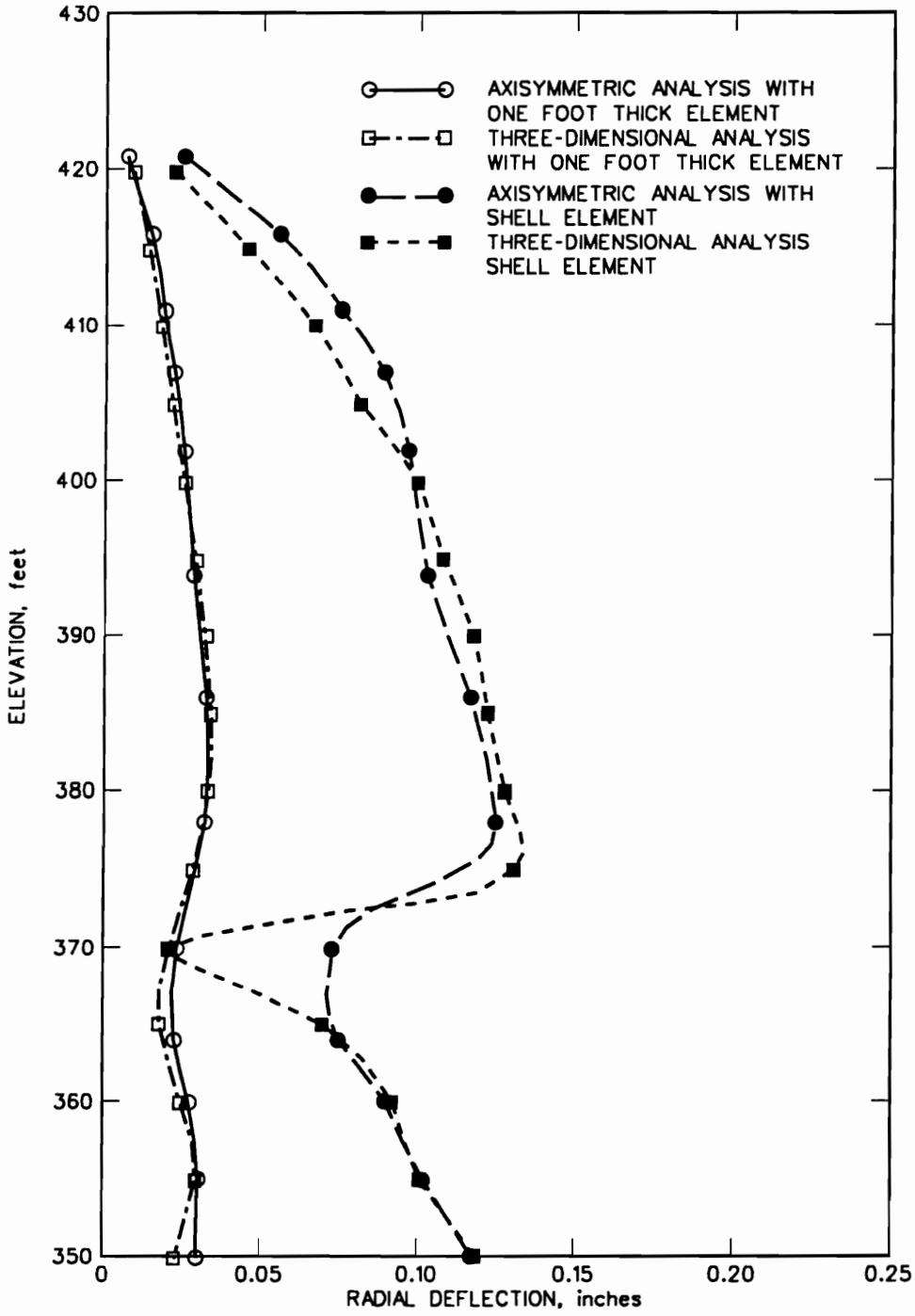

Figure 6.14: Radial deflection of sheet piles from linear elastic analyses of an isolated main cell.

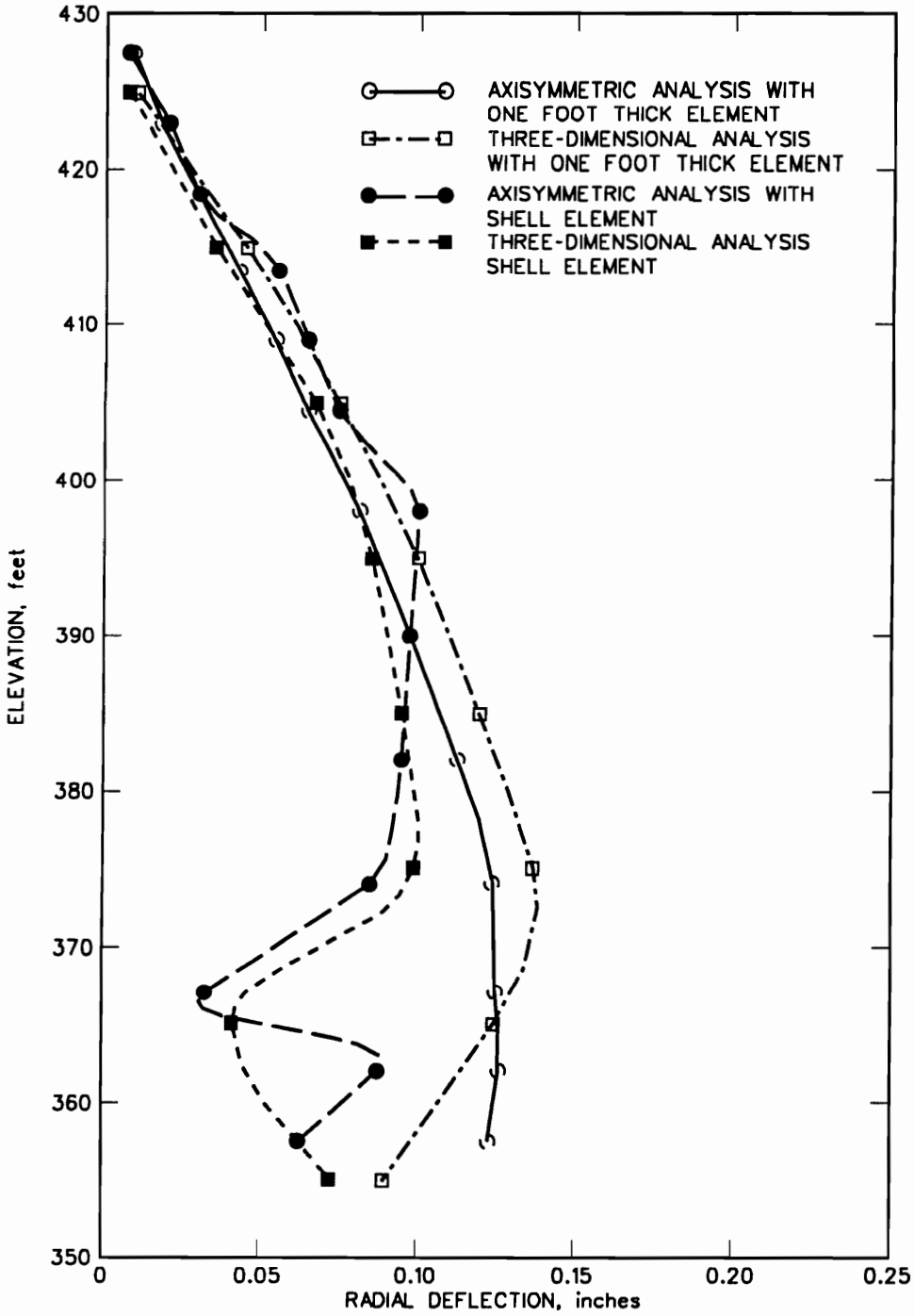

Figure 6.15: Sheet–pile interlock stresses from linear elastic analyses of an isolated main cell.

unknowns). The next step in applying the new code was to perform a nonlinear three–dimensional soil–structure interaction analysis of a sheet–pile cellular cofferdam for a case that had comparable two–dimensional results, such as an isolated main cell during filling.

As previously stated, the purpose of the isolated main cell analysis is to model the response of a main cell during its construction. It is assumed that the adjacent connecting arc cells are empty while the main cell is being filled, a horizontal water level is maintained throughout the filling operation, and that other unfilled connecting arc cells and main cells in the cofferdam have no influence on the behavior of the main cell.

Finite Element Meshes

Three analyses were performed for three different penetrations of the cell into the foundation. These different penetrations represent the possible varying conditions that could be found for the second–stage Lock and Dam No. 26(R) cofferdam. At one end of the spectrum was a penetration of 35 ft which was the same penetration found in the first–stage Lock and Dam No. 26(R) cofferdam. This depth of sheet–pile penetration was found along the Missouri leg of the cofferdam. The mesh from the linear analysis that utilized the shell elements, Figure 6.12, was used to model this penetration. As noted, this mesh consisted of 1,361 nodes, 275 three–dimensional 20–node solid elements for the cell fill and foundation, and 45 eight–node shell elements for the sheet piles. Sixty three–dimensional 8–node surface interface elements were located between the soil and sheet piles. The foundation was extended laterally 100 ft from the edge of the cell and extended in depth to the

top of bedrock, approximately 70 ft below the Mississippi River bottom, providing an incompressible lower boundary for the model.

The two other penetrations analyzed were 15 ft and 10 ft. The 15–ft penetration was the design penetration of the Illinois (channel) leg of the cofferdam. The 10–ft penetration was used to consider possible scour effects. The mesh shown in Figure 6.16 was used for both the 15– and 10–foot penetration analyses. The mesh consisted of 1,635 nodes, 330 three–dimensional, 20–node solid elements for the cell fill and foundation, 55 three–dimensional, 8–node shell elements for the sheet piles, and 70 three–dimensional 8 node surface interface elements between the soil and sheet piles. The lateral boundary was the same as in the previous mesh and the depth of the mesh was 50 ft and 45 ft for the 15–ft and 10–ft penetrations, respectively. The 10–ft penetration was modeled by not activating the surface row of the foundation elements in the model shown in Figure 6.16.

Construction Simulation

The construction of the circular main cell was simulated by applying incremental loads which were designed to represent placing of the cell fill material. The simulation of the filling of a main cell began by establishment of in situ stress conditions in the foundation prior to initiation of construction. The soil in the foundation was assumed to be in an at–rest condition determined in accordance with the specified soil properties and the initial groundwater and soil levels. The code computes the stress level in each element by a gravity turn–on analysis with appropriate unit weights for the soil and values of Poision's ratio, ν, as a function of the at–rest lateral earth pressure coefficients, K_0,

$$\nu = \frac{K_o}{1 + K_o} \tag{6.1}$$

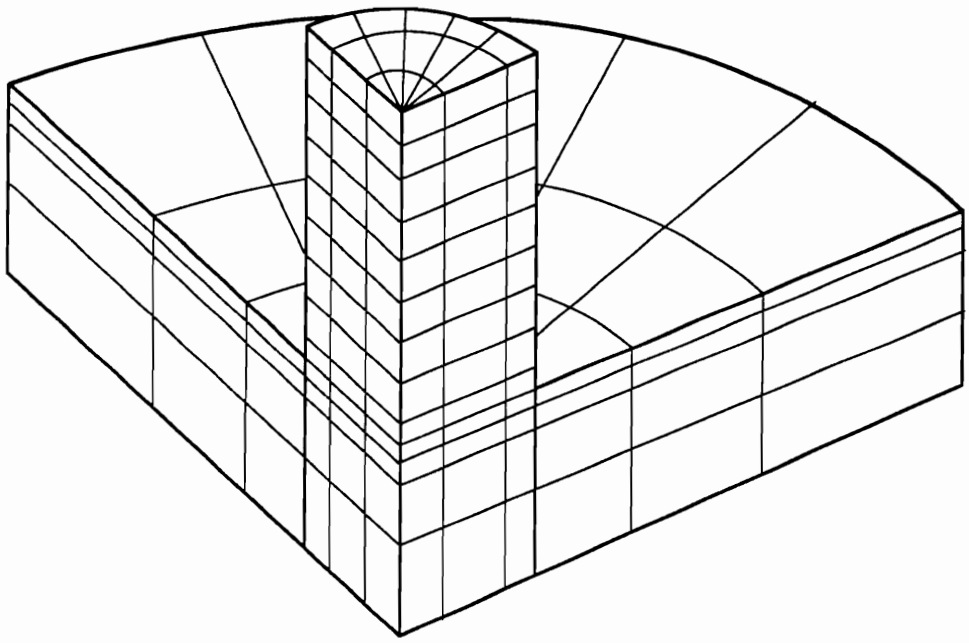

Figure 6.16: Finite element mesh for an isolated main cell from second–stage of Lock and Dam No. 26(R) with 10–ft of penetration.

For the analysis of the 35–ft penetration, the soil surface was at El 370, 70 ft above bedrock, and a river level of El 402 was used. The subsurface consisted of three layers: (1) Alluvial outwash from El 370 to El 358; (2) Wisconsin outwash from El 358 to El 330; and 3) Illinoisan ice contact from El 330 to El 300. Below El 300, the soil was assumed to be underlain by rigid bedrock. For the 15–ft and 10–ft penetrations, the Alluvial outwash was removed and the soil surfaces were at El 350 and El 345, respectively, beginning in the Wisconsin outwash.

The elements in the mesh representing the cell fill, the sheet piles and sheet pile-soil interfaces were not activated during the initial stress determination. Before filling starts, the shell elements representing the sheet piles along with the interface elements between the sheet piles and foundation soils were activated. The stresses in the foundation were assumed to be unchanged from the installation of the sheet piles.

The procedure used to model the fill placement is referred to as the *dense liquid* technique [5]. In the procedure, each layer is placed as a dense liquid, i.e. to have weight but no ability to resist shear. As the next layer is placed, the previous layer is assumed to behave as a solid. Fills are generally constructed in a series of thin layers compared with the total thickness of the fill. It is usually necessary to use much thicker layers in numerical modeling of fill placement than used in the actual construction. The number of layers needed to accurately simulate fill placement depends on the information required from the analysis. If the analysis is focusing on the soil underlying the fill, very few layers are required since both stresses and displacements are not sensitive to the number of layers. However, in the cofferdam analyses the focus is on the behavior of the fill itself, and more layers are necessary. Obtaining accurate values for the cell fill deformation in the cofferdam problem is

especially significant since they influence the shear transfer between the sheet piles and the soil, and thus, the degree of arching in the cell fill.

Clough [5] found that the accuracy of the fill placement simulation was a function of the number of layers, the stresses used to calculate the modulus values, and the rate of change in the modulus due to the confining stress. For the three–dimensional analyses of an isolated main cell during filling, the soil placement in the cell was modeled with six to eight lifts with six substeps per lifts. To check the accuracy of the fill placement, the responses of the elements were monitored from load step to load step. Changes in shear and mean normal stresses were generally much less than 10 percent indicating that the code could update modulus values at intervals that would provide an accurate representation of the stress–strain curve.

6.2.3 Difficulties in Three–Dimensional Modeling of the Isolated Main Cell Analyses

The results of the isolated main cell analyses are presented with the results of the previous axisymmetric analyses for comparison. As will be shown subsequently, the results from the new three–dimensional finite element code compare well with the axisymmetric results, but before examining these findings it is necessary to discuss some of the problems encountered in modeling the isolated main cell with a nonlinear, three–dimensional finite element code. In formulating the axisymmetric model, certain degrees of freedom of the problem are eliminated or constrained by assuming that an axisymmetric condition prevails. This luxury is not afforded in the three–dimensional model. In the three–dimensional model, a vertical plane of symmetry exists at 45 deg from the x and y axes. The coordinates of the nodal

points and the angles formed by a line from the origin to the nodal points should be mirror images of one another from one side of this plane of symmetry to the other. The resulting displacements and stresses from an analysis should also be symmetric about this plane.

The results from the initial nonlinear analysis were not symmetric and at the end of filling the analysis showed that the cell had twisted with it displacing outward from the origin along the x axis and inward along the y axis. This was of great concern and instigated a long search to find out why the results were not symmetrical.

First, the results from the linear verification analyses were reexamined and were symmetric for the five significant digits printed in the output. Next, the coordinates of the nodal points were reexamined to make certain they were a mirror image from one side of the plane of symmetry to the other and they were symmetrical. A number of small problems with rectangular geometry were analyzed, and no problems with the code were discovered. The problem only occurred when the geometry of the main cell was used. It was not practical to search for the problem with the full model because one complete analysis cost about $ 9,000 or about $ 1,500 per load step. To arrive at a model that would be economical to analyze and would reproduce the same problem, two rows of elements from the main cell were used to form a new model. With this smaller model the problem persisted, yet no error in the code was found. After numerous examinations of the code, the individual stiffness matrices were examined. The components of the stiffness matrices of the elements were printed to the full precision of the machine, 15 significant digits. It was discovered that some of the diagonal terms of the stiffness matrices for two elements that should be identical because of symmetry were off from one another in the fifth or sixth significant digit even though the modulus values were identical. This led to the conclusion that there

was an error in the geometry.

As stated earlier, the coordinates of the nodal points were a mirror image of one another about the plane of symmetry, but on further examination only five significant digits were used to define the coordinates. The grid generation software reported only the coordinates to this number of significant digits. At the time, this did not seem likely to make a significant difference. The angles formed with the plane of symmetry and lines passing through the origin and mirror image nodal points were not absolutely identical.

To increase the accuracy of the coordinates of nodal points, a computer program was written to calculate the coordinates of nodal points to 28 significant digits (double precision). Using the newly calculated coordinates, the diagonal terms of mirror image elements matched for 15 significant digits (all that are available in single precision).

Although this was the principal reason for the unsymmetric results in the nonlinear, three–dimensional analysis of an isolated main cell, it was not the only reason. New tangent shear and bulk moduli are calculated during each increment in the construction simulation. These moduli are calculated based on the stress level in the element. If all things are equal in two elements except for a slight difference in stress level from one element to the other, the moduli value computed for the two elements will be different and with additional increments of loading the difference between the stress in the two elements will get greater. Even with 15 significant digits of accuracy, if the stresses in these elements that are mirror images of one another are off in the tenth to twelfth significant digit during the first increment of loading, the moduli for the two elements will not be calculated exactly the same for both for use in the next increment of loading. After 10 or 15 increments, the

differences will grow to an intolerable level. To correct this, the stresses used in the calculation of the moduli were rounded off to five significant digits. With this procedure in place, the displacements, stresses, and moduli values remained symmetrical to five significant digits throughout the analysis.

6.2.4 Results of the Isolated Main Cell Analyses

Results are presented for the sheet–pile penetrations of 35–ft and 10–ft. These are the two extreme conditions that were possible for the second–stage cofferdam, and they are also conditions for which both two–dimensional axisymmetric results and observed measurements were available for comparison. Results from the axisymmetric analyses of main cell filling with an E–ratio of 0.03 are compared with results of the three–dimensional analyses. For the axisymmetrical analyses of the first–stage Lock and Dam No. 26(R) cofferdam, an E–ratio of 0.03 provided the best agreement with the observed behavior. The E–ratio was also used in the three–dimensional analyses.

Sheet–Pile Movements

At the end of filling, radial deflections of the cofferdam from the three–dimensional analysis were 0.3 in. at the top of the cell, 3.1 in. at 15 ft above the dredgeline, and 1.82 in. at the dredgeline. The radial deflections continued to decrease below the dredgeline to 0.3 in. at the tip of the sheet piles. Figure 6.17 shows the predicted radial cell wall displacements for the three–dimensional and axisymmetric analyses along with a range of observed movements for two instrumented cells in the first–stage Lock and Dam No. 26(R) cofferdam. The two analyses give essentially the same predictions, as they should in this case. The observed radial deflections

bound the predicted results from both of the finite element analyses. The predicted deflections reasonably match an average of the observed measured deflections.

Similar results was found in the analysis of the model with a penetration of 10 ft. The three–dimensional analysis yielded a radial deflection of the cell to 0.3 in. at the top, 4.3 in., 15 ft above the dredgeline, and 2.6 in. at the dredge line. The radial deflections continued to decrease below the dredgeline to 0.6 in. at the tip of the sheet piles. Figure 6.18 shows the predicted radial cell wall displacements for the three–dimensional and axisymmetric analyses along with the range of those observed movements from an instrumented prototype test cell used to verify the second–stage Lock and Dam No. 26(R) cofferdam design. Again, the two finite element analyses produce essentially the same prediction of the radial movements. The predicted radial deflections fall within the observed range. The range of observed deflections shows more spread than found in the observed deflections of the first stage, a behavior thought due to the cells not being plumb during filling.

Interlock Forces

The predicted distribution of interlock forces in the sheet piles by the three–dimensional, finite element analysis for the model with 35–ft penetration is shown in Figure 6.19 along with the results from the axisysmmetric analysis and the measured field values. The interlock force distribution is similar to the shape of the radial deflections of the cell wall with the maximum interlock force of 3.1 kips per inch occurring at approximately the same height above the dredgeline as the maximum deflection. The predicted interlock forces compares favorably with the measured values. The predicted values are also significantly less than the design values determined from conventional procedures. The three–dimensional and axisymmetric finite element

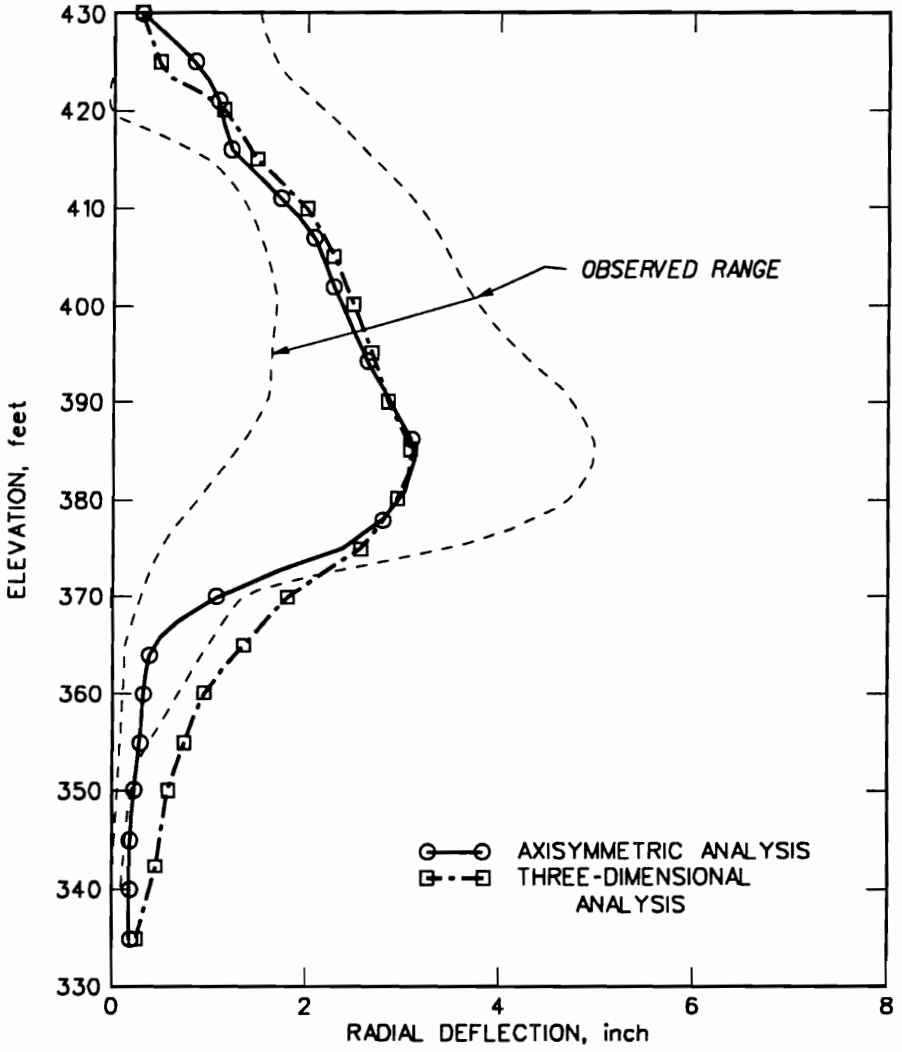

Figure 6.17: Comparison of radial deflection from the three–dimensional and axisymmetric finite element for isolated main cell with 35–ft penetration.

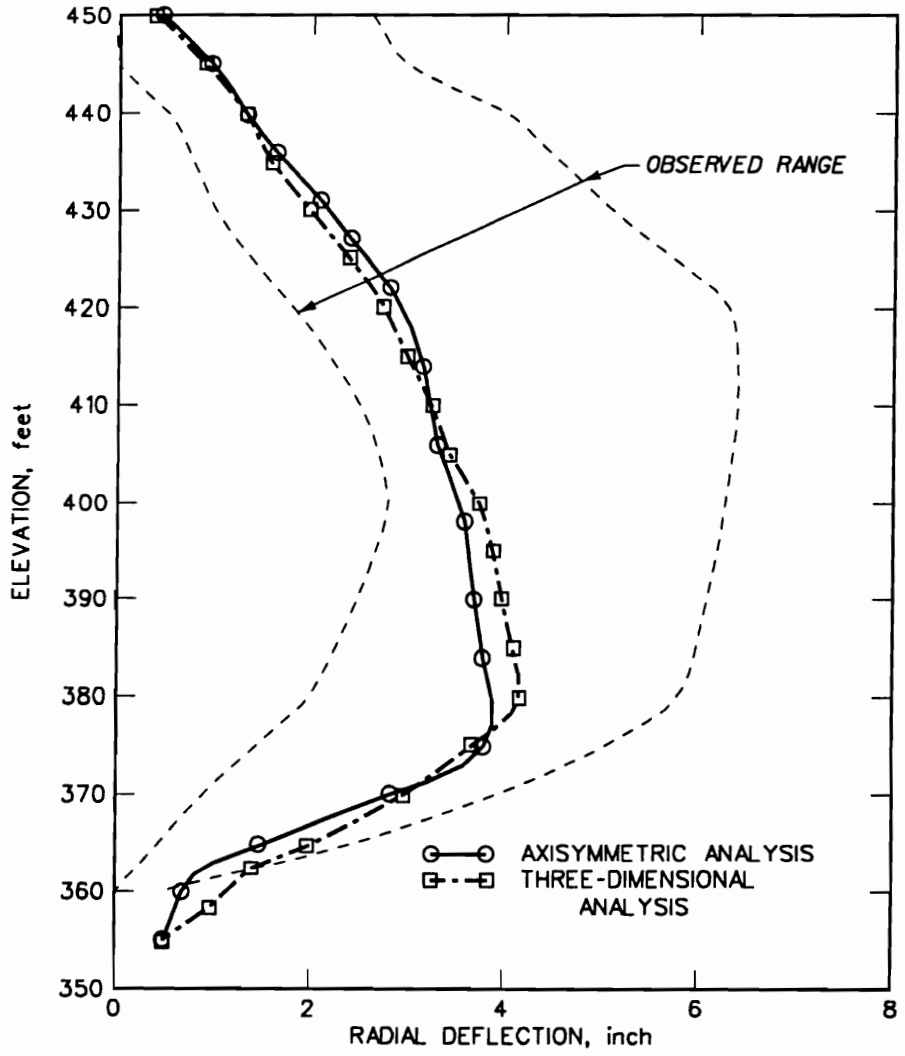

Figure 6.18: Comparison of radial deflection from the three–dimensional and axisymmetric finite element for isolated main cell with 10–ft penetration.

results are in close agreement.

The predicted interlock force distributions for the cell with a sheet–pile penetration of 10 ft are compared in Figure 6.20. A maximum interlock force of 4.2 kips per inch predicted by the three–dimensional analysis is located at approximately the same point as the maximum radial deflection. The two predictions of interlock forces are similar with the three–dimensional analysis producing slightly higher values than the axisymmetric results.

Earth Pressures

The predicted lateral earth pressures against the sheet–pile cell walls are shown in Figures 6.21 and 6.22 for the models with penetrations of 35 ft and 10 ft, respectively. Reference lines denoting the at–rest and the active pressures are also shown in the figures. At the top of the cell, finite element results show at–rest earth pressures are applied against the sheet–pile wall. This represents the earth pressure of recently placed layer of soil elements. Between El 420 and 390, the finite element lateral earth pressures are less than the at–rest and greater than active. From El 390 to the dredgeline, the finite element earth pressures are essentially active. Below the dredgeline, pressure against the inside of the cell wall increase to values between at–rest and active pressures.

Soil Stresses

Figures 6.23 and 6.24 show the vertical soil stresses in the cell fill and portions of the foundation normalized with respect to the vertical overburden pressure. A vertical stress ratio of 1.0 indicates a simple gravity stress condition. The figures show that the normalized vertical stress ratios in the cell fill vary from slightly less than 1.0 in

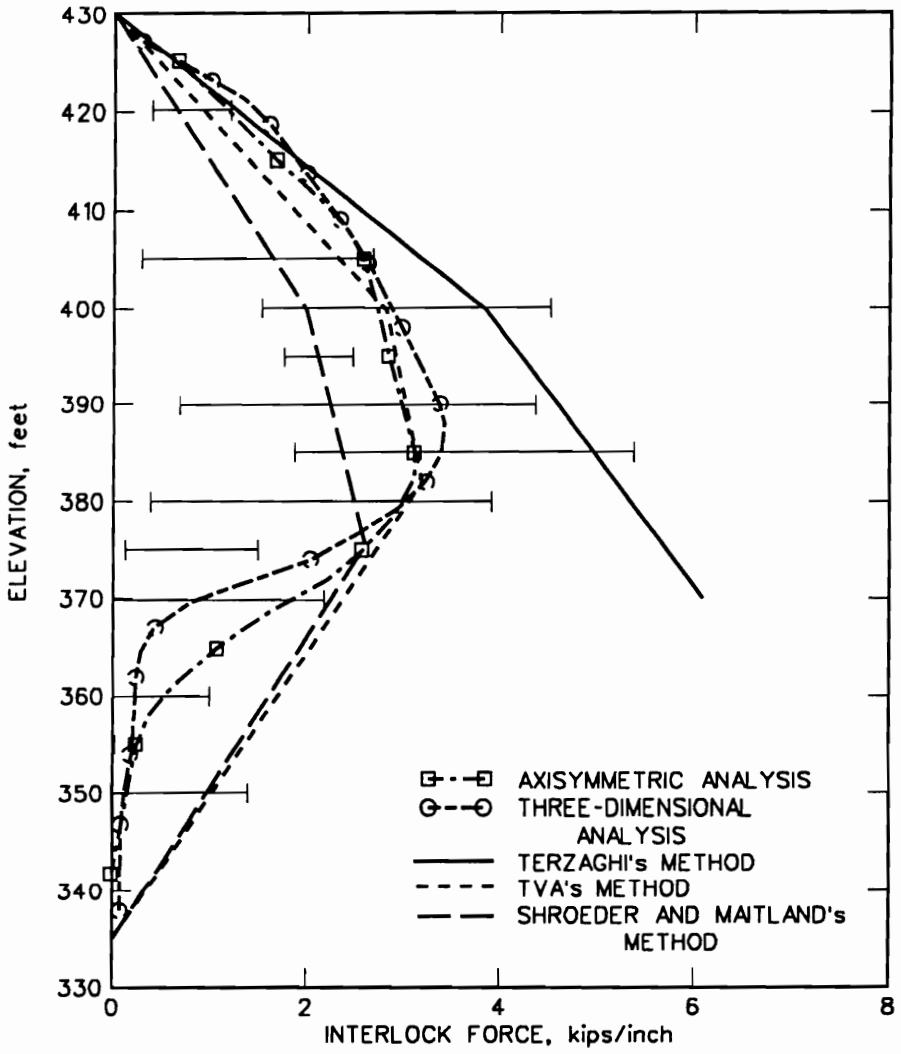

Figure 6.19: Comparison of interlock forces in the cell wall from the three-dimensional and axisymmetric finite element for isolated main cell with 35-ft penetration.

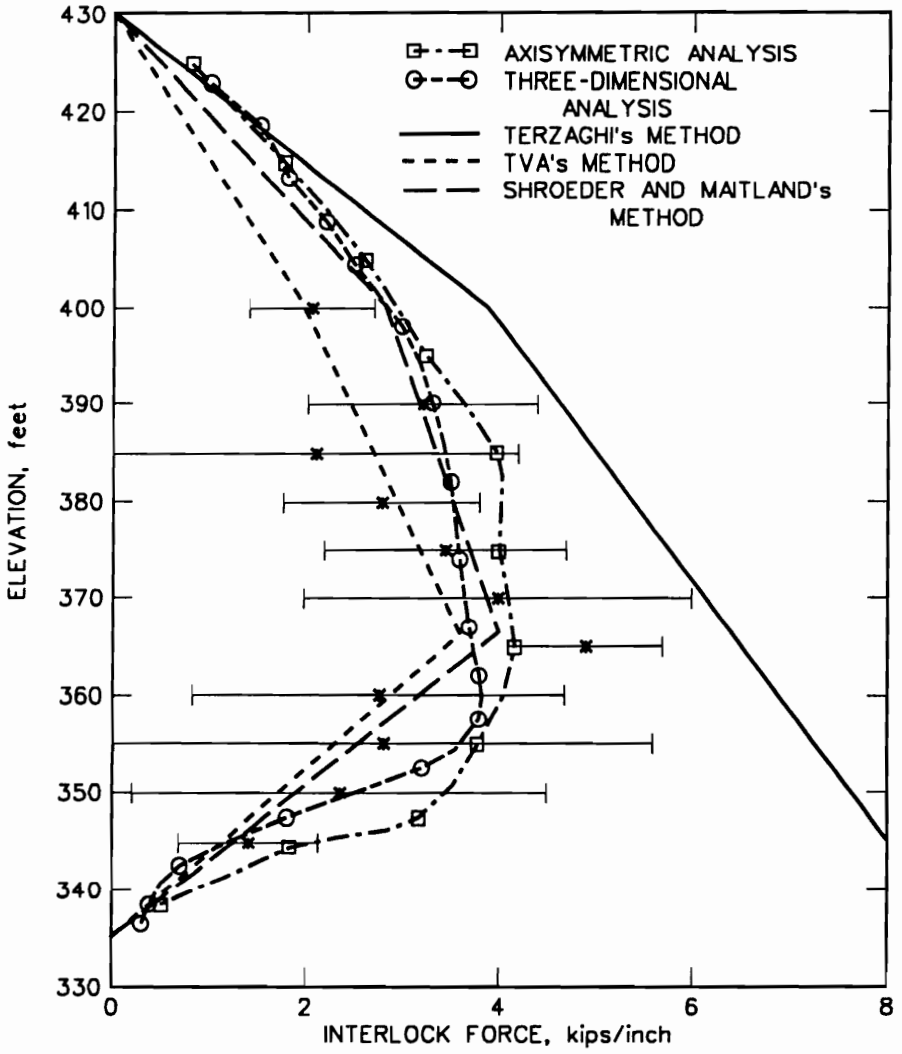

Figure 6.20: Comparison of interlock forces in the cell wall from the three–dimensional and axisymmetric finite element for isolated main cell with 10–ft penetration.

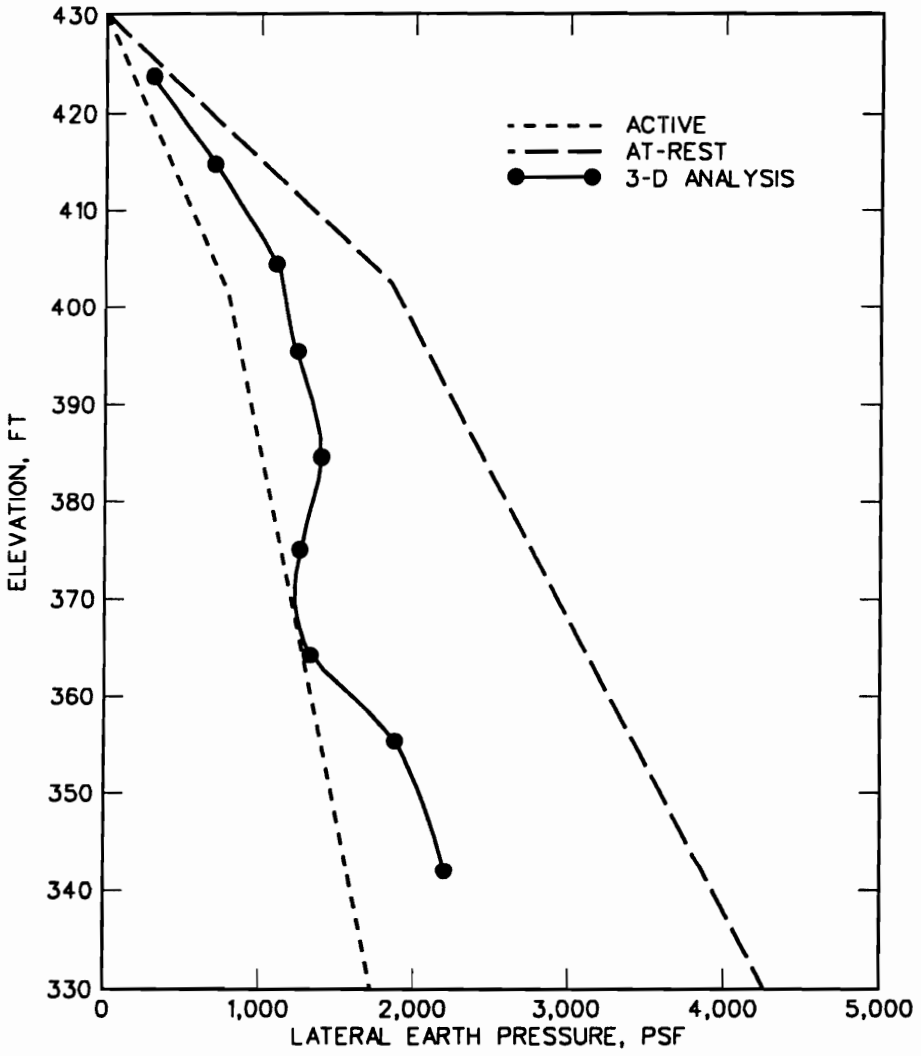

Figure 6.21: Predicted lateral earth pressures in an isolated main cell with 35-ft penetration.

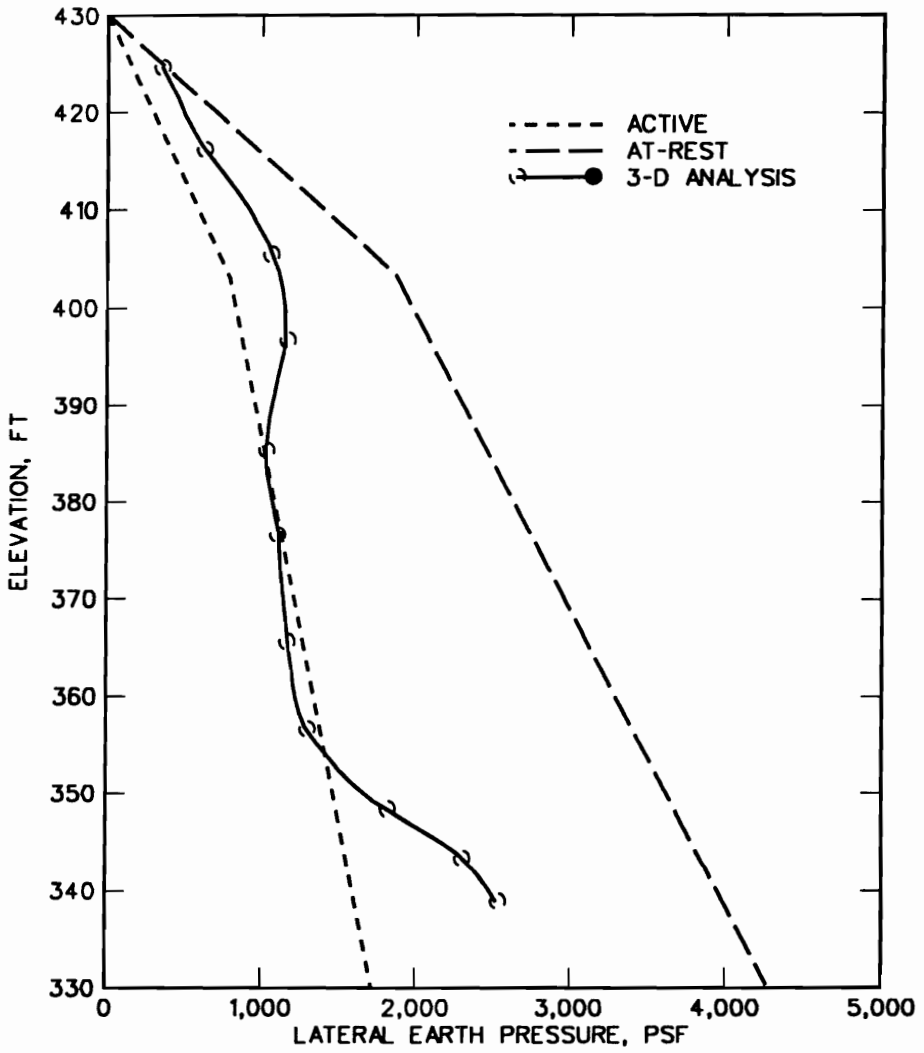

Figure 6.22: Predicted lateral earth pressures in an isolated main cell with 10–ft penetration.

the center of the cell to substantially less than 1.0 near the sheet–pile walls. Since vertical stress ratios in some areas are less than 1.0, it is apparent that a form of stress transfer is taking place in the cell. Near the sheet–pile walls, where the vertical stress ratios are significantly less than 1.0, there is a shear transfer between the walls and soil resulting in a redistribution of the stresses in the cell fill. This occurs because the walls deflect vertically less than the soil and settlement of the soil is resisted by the friction between soil and the wall (also know as arching). Near the center of the cell, away from the influence of the sheet piling, the vertical stresses are substantially closer to the simple gravity stress condition.

The arching phenomena in cellular cofferdams has been investigated by Hardin [25]. He reported that there were two types of arching likely to occur in a main cell. These are arching due to friction between the sheet–pile walls of the cell and the cell fill, as described previously, and arching due to shear strength mobilization. Arching due to shear strength mobilization is caused by a section of soil moving laterally which is sandwiched between regions that have less lateral movement. This occurs in the cofferdam when the sheet piling bulges during filling. At the point of maximum bulge, the soil mobilizes more of its shear strength than directly above or below, thus redistributing the stresses around this area of high movement. Hardin isolated the two separate types of arching in his parametric studies with the axisymmetric finite element model.

In the foundation beneath the cell, vertical stress ratios are fairly constant, but below the tip of the sheet piling the vertical stress is greater than 1.0. In the foundation outside the cell, the vertical stress ratios are greater adjacent to the sheet piling and decreases with distance from the cell. The shear stresses between the sheet piling and cell fill which reduce the vertical stresses in the cell fill also

tend to apply a downdrag load on the piling. This vertical loading on the piling is reflected in higher values of vertical stress ratio in the foundation soils near the wall and below the piling. As the sheet piling settles, the shear strength of the soil is mobilized to resist the increase in stress.

Figures 6.25 and 6.26 show the horizontal stresses normal to the wall and normalized with respect to the vertical overburden pressure. These values represent the lateral earth pressure coefficients that might be used in a traditional cofferdam analysis or design. The horizontal stress ratios decrease from the center to the cell walls and with depth in the cell fill. The values of horizontal stress ratios are fairly constant in the foundation beneath the fill. However, in the foundation outside the fill, the horizontal stress ratios are high adjacent to the cell walls and decrease with distance from the cell. These trends of horizontal stress ratio can be attributed to a combination of arching and radial deflection of the cell walls. Within the cell fill, the lowest values are found near the cell walls where the radial deflections are the greatest. These outward movements reduce the horizontal stress from its initial at–rest state. Near the center and top of the cell, the radial deflections are less and the horizontal stresses are higher.

Adjacent to the cell walls, the horizontal stress ratios vary from a high of 0.50 near the top of the cell to approximately 0.20 near the point of maximum bulge of the cell. The Rankine active earth pressure coefficient in this case is 0.27, and the predicted values range from 0.74 to 1.85 times the Rankine active value. Note that the true earth pressure coefficients are, in fact, somewhat higher than those indicated in Figures 6.25 and 6.26 since the vertical stresses in the cell are generally less than the vertical overburden pressure assumed in calculating the earth pressure coefficients. For example, the vertical stress near the cell walls is as low as 0.45 of the

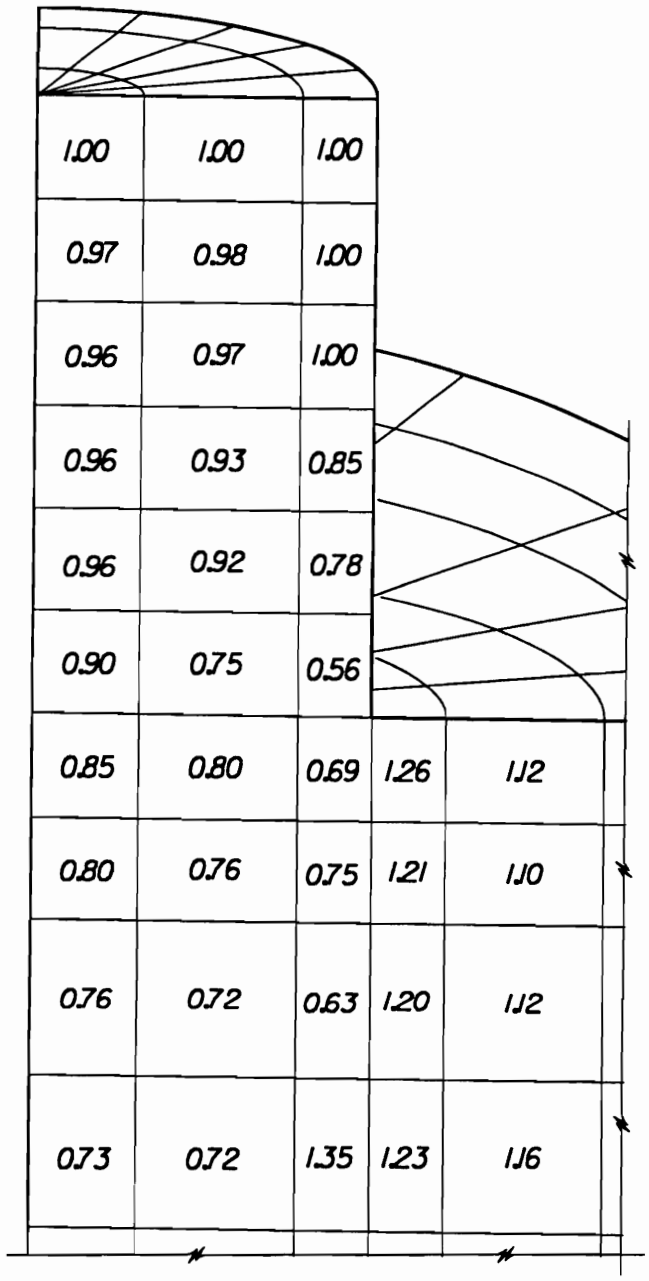

Figure 6.23: Normalized vertical soil stresses in an isolated main cell with 35–ft penetration.

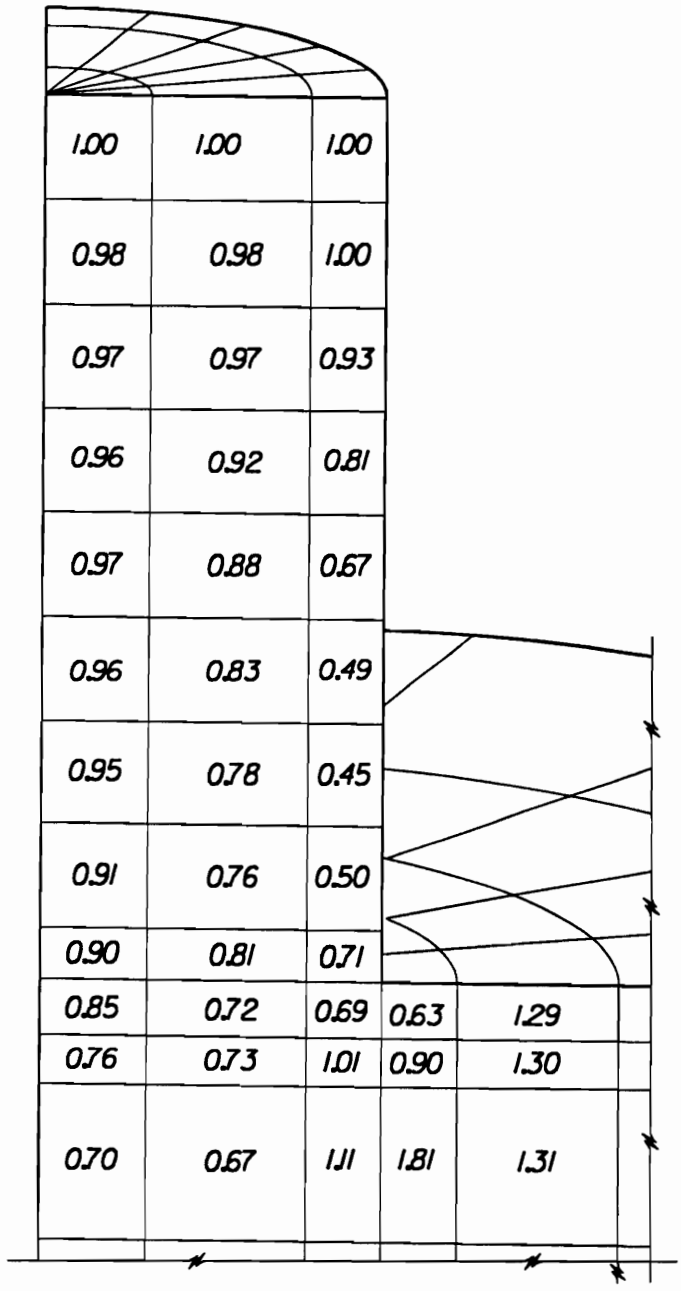

Figure 6.24: Normalized vertical soil stresses in an isolated main cell with 10–ft penetration.

vertical overburden pressure. Also, the Rankine coefficient does not account for the effect of wall friction which would lower the lateral earth pressure coefficient. The higher values in the foundation outside the cell can be attributed to the compression of the soil due to the outward radial deflection of the cell walls. Lateral earth pressure coefficients are approaching those of passive earth pressure coefficients just below the dredgeline and adjacent to the cell.

6.3 Response of Cellular Cofferdam during Cell Filling

The three–dimensional analysis provides an opportunity to more accurately simulate the process of filling the cells of the cofferdam than any previous model. In the two–dimensional axisymmetric model, only the filling of an isolated main cell could be assessed. The generalized plane strain model is used to evaluate the main and arc cell during filling, but it assumes that main cell and arc cell are filled simultaneously while in actuality two adjacent main cells are filled first, followed by the filling of the arc cell between them. filled.

In this section, the results of the three–dimensional finite element analyses of the cofferdam during filling are presented and compared with other approaches and instrumentation observations where possible. These three–dimensional analyses attempted to model as closely as possible the actual filling process of the cells, The main cell was filled first, followed by the filling of the arc cell.

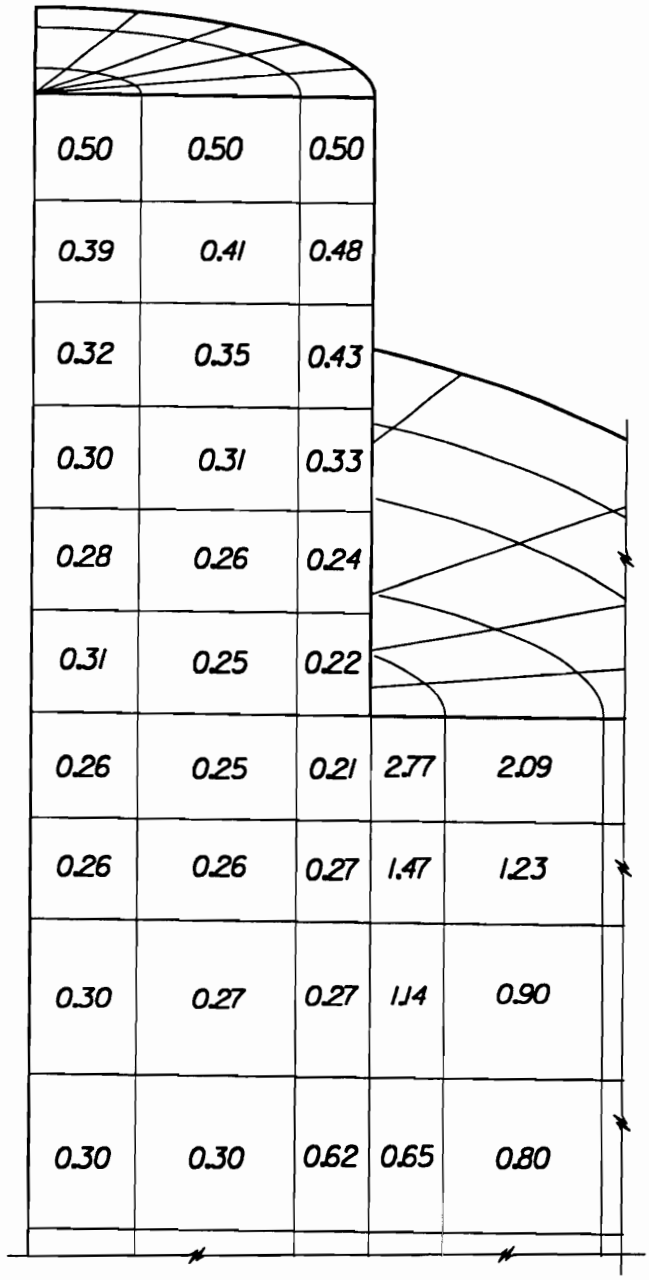

Figure 6.25: Normalized horizontal soil stresses in an isolated main cell with 35-ft penetration.

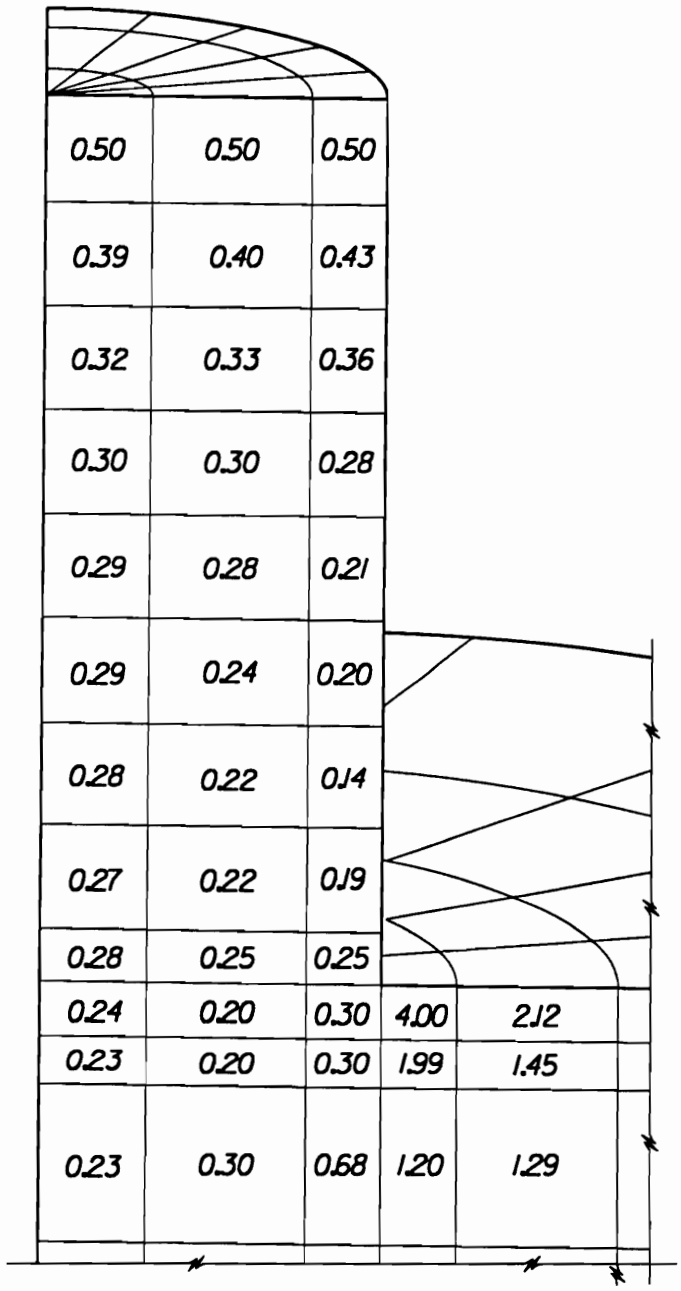

Figure 6.26: Normalized horizontal soil stresses in an isolated main cell with 10–ft penetration.

6.3.1 Finite Element Representation of Cofferdam

To bound the penetrations of the sheet piling found in the second–stage Lock and Dam No. 26(R) cofferdam, analyses were performed for penetrations of 35 ft and 15 ft. Each model consisted of one–half of a main cell and one–half of an arc cell. The models represent a portion of the cofferdam that is not influenced by corners or changes in direction of the cofferdam perimeter, as shown in Figure 6.27. The models are formed by the two parallel planes of symmetry, perpendicular to the cell and passing through the center of the main cell and arc cell.

Finite Element Meshes

The two meshes are shown in Figures 6.28 and 6.29. The mesh for a penetration of 35 ft consists of 2,458 nodes, 417 three–dimensional, twenty–node solid elements for the foundation soil and cell fill, 198 eight–node shell elements for the sheet piling, and 336 three–dimensional, eight–node interface elements. The mesh for a penetration of 15 ft consists of 2646 nodes, 466 three–dimensional, twenty–node solid elements for the foundation soil and cell fill, 198 eight–node shell elements for the sheet piling, and 318 three–dimensional, eight–node interface elements. In Figures 6.28 and 6.29, the inboard of the cofferdam and stability berm are located on the right and the outboard and river are on the left. The slice through the cofferdam is 43.207 ft wide and extends 162 ft on the river side of the cofferdam and 205 ft on the dewatered side.

During the analysis of the cell fill placement, only one–half of the model is required in the analysis. This reduction in the problem size is achieved by taking

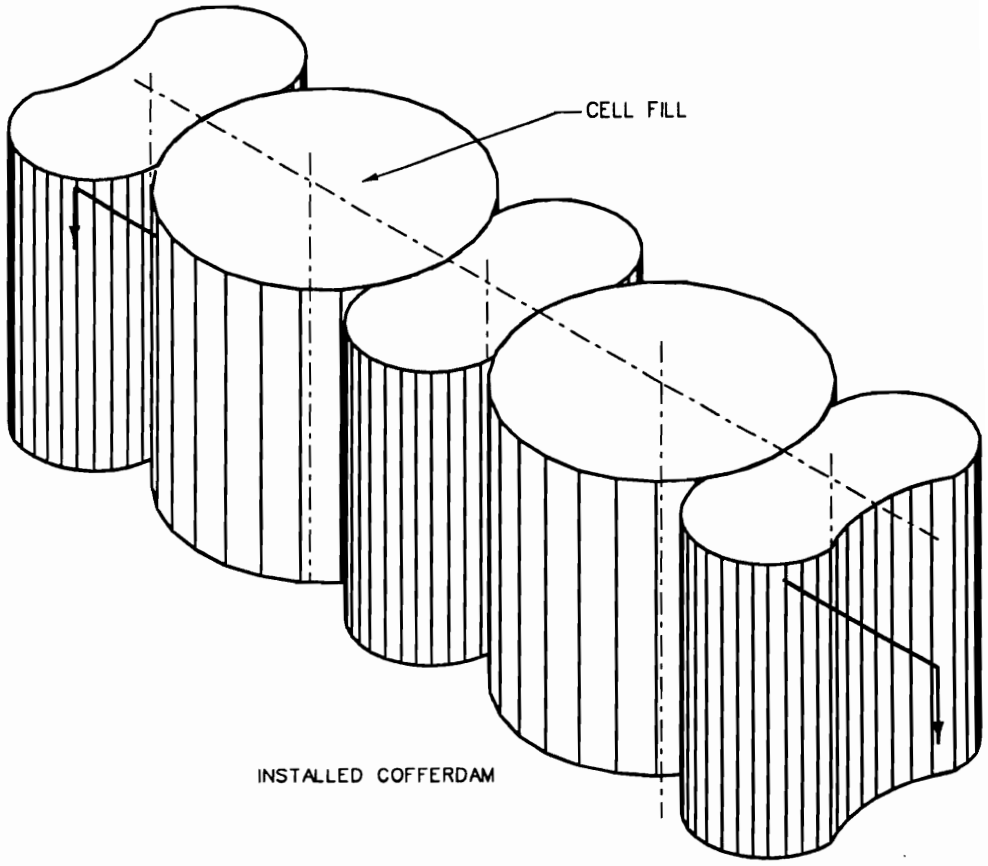

Figure 6.27: Schematic of cofferdam model.

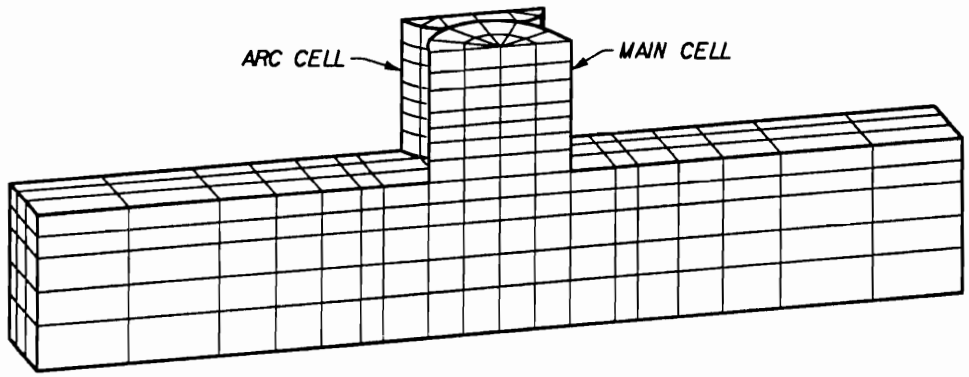

Figure 6.28: Mesh for second-stage Lock and Dam No. 26(R) with 35-ft penetration.

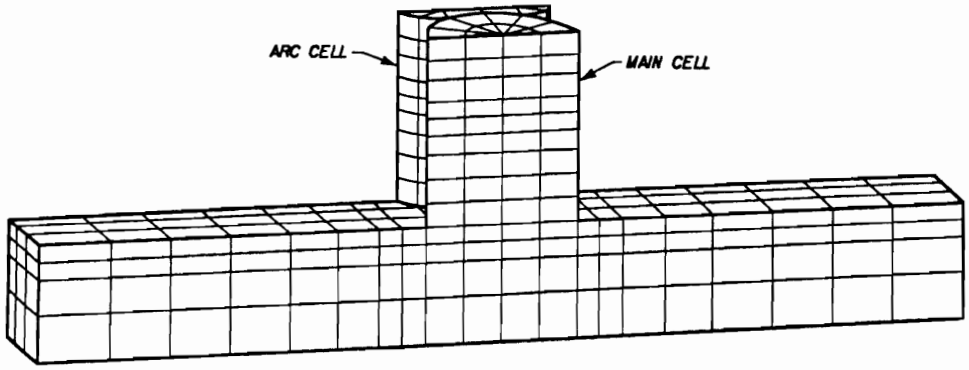

Figure 6.29: Mesh for second–stage Lock and Dam No. 26(R) with 15–ft penetration.

advantage of the symmetry about the centerline of the cell parallel to the leg of the cofferdam. This reduces the size of the problem and, thus, the expense.

Construction Simulation

The first step in simulating the cell filling is to establish the state of stress in the foundation before construction. For the cells with 35–ft penetration, the before–construction state of stress is established as the at–rest stress in accordance with specified soil properties, stratigraphy, a river bottom at El 370 and water pressures based on a river El 402. For the cells with 15–ft penetration, the before construction state of stress is based on a river bottom at El 350. During this stage of the analysis, the elements in the mesh representing the cell fill and sheet–pile elements above the dredgeline are not activated. The elements representing the sheet piling below the dredgeline are also not activated. All independent degrees of freedom associated with these inactive elements are fixed.

The construction of the circular main cell was simulated by applying incremental loads which were designed to represent placing of the cell fill material as described in the previous section on the analyses of isolated main cell. The filling process was simulated by placing the fill in main cell and the subsequent placing of the fill in the arc cell.

6.3.2 Response at Completion of Main Cell Filling

The first major construction step in this analysis was the filling of the main cell. This section describes the results at the completion of the filling of the main cell.

Cell Movements

At the end of filling only the main cell, the three–dimensional model with a penetration of 35 ft had predicted main cell radial deflections of 0.55 in. at the top of the cell increasing to approximately 2.05 in. at 14 ft above the dredgeline. Figure 6.30 shows a comparison of deflections of sheet piling at completion of the filling of the main cell for the new three–dimensional model and those of the previous isolated main cell model. The results from the current model are symmetric about the centerline of the cofferdam, and the deflections of the sheet piling at four locations on the cofferdam are used to describe the response. These results are compared with the range of observed instrumentation measurements and the results of the isolated main cell analysis. The deflections for the three–dimensional model are less than those obtained from the isolated main cell model. This may be due to number element in modeling the cells and the location of the boundaries. Included in the figure are four slices through the cofferdam that show the deformed shape compared to the undeformed configuration. Table 6.1 summarizes the radial deflections of the four pile locations for these slices.

The deflections from finite element analyses of the main and arc cell model are less than those calculated from the isolated main cell model. They are also on the low side of the observed movements.

A similar response was obtained in the analysis of the main cell for the model with a penetration of 15 ft. The main cell radial deflections increase from approximately 0.57 in. at the top to approximately 2.71 in. at 20 ft above the dredgeline and then decrease to approximately 1.75 in. at the dredgeline. Figure 6.31 presents the predicted radial movements of the sheet piling due to filling for four locations

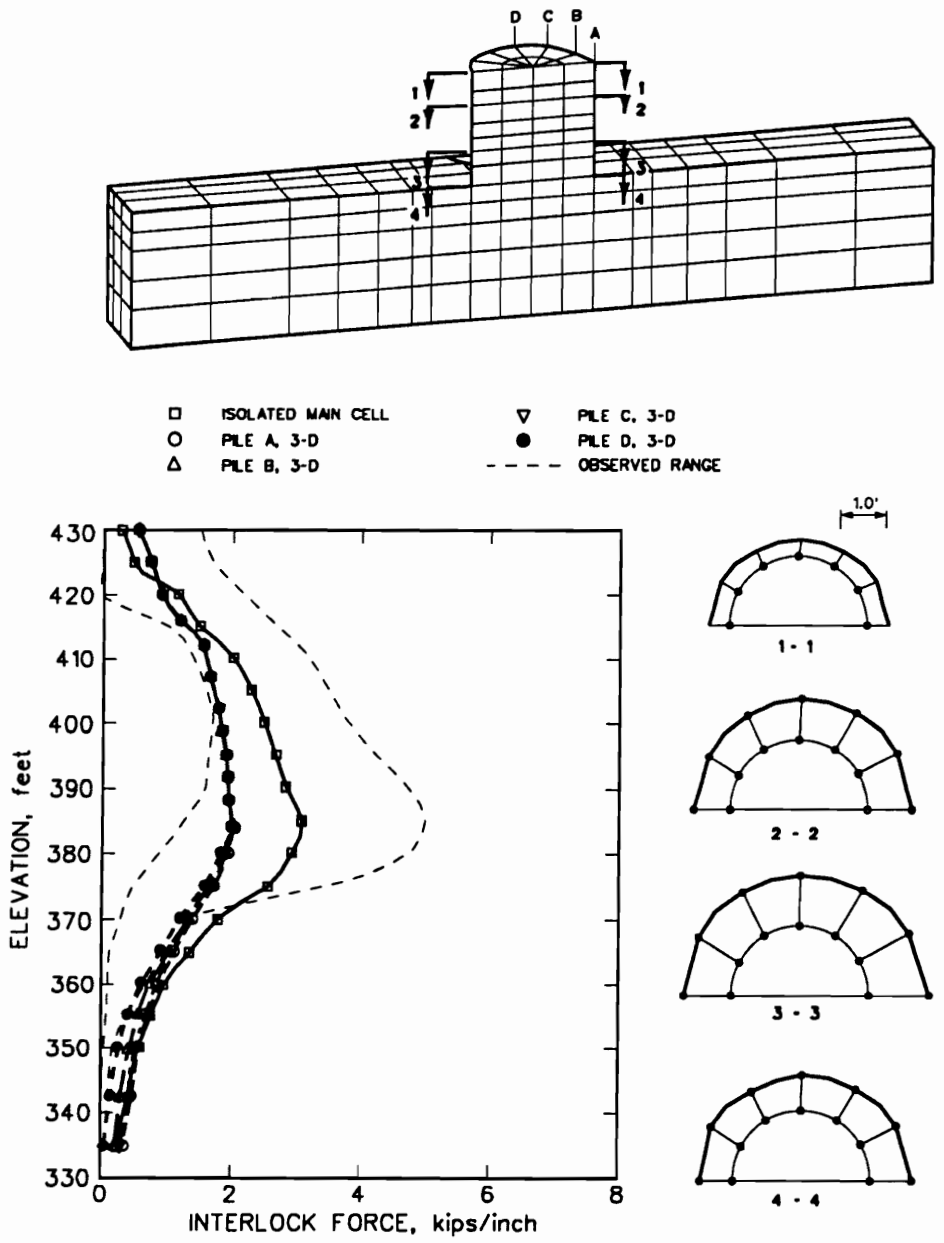

Figure 6.30: Radial deflections after main cell filling for a penetration of 35 ft.

around the main cell. Again, four horizontal slices through the cell are shown in the figure. Table 6.2 summarizes the radial deflections of the four pile locations for these slices.

The deflections of the sheet piling at the four locations (Pile A - Pile B) in Figures 6.30 and 6.31 are virtually the same above the dredgeline. Below the dredgeline, the deflections of the piling differ slightly from one another with the greatest deflections occurring in the direction to the furthest fixed boundary and the least deflection in the direction to the closest fixed boundary. The other two fall within these extremes.

Interlock Forces

The distribution of sheet–pile interlock forces in the main cell predicted by the three–dimensional finite element analysis for models with penetration of 35 ft and 15 ft are shown in Figure 6.32 and 6.33, respectively. The distributions of interlock forces from the three–dimensional main and arc cell models are similar in shape to that ascertained in the isolated main cell analysis but are of smaller magnitude. The maximum predicted interlock forces for penetrations of 35 ft and 15 ft are 2.1 kips per inch and 3.7 kips per inch, respectively, as compared with the maximums of 3.1 kips per inch and 4.2 kips per inch for penetration of 35 ft and 10 ft, respectively, from the isolated main cell analyses.

Earth Pressures

The distributions of lateral earth pressures against the sheet piling of the main cell computed from the three–dimensional finite element analyses are shown in Figures 6.34 and 6.35 for the penetrations of 35 ft and 15 ft, respectively. Reference

Table 6.1: Radial Deflections after Main Cell Filling, Cell with 35–ft Penetration.

Location	Radial Deflection (in.)			
	Top	Maximum	Dredgeline	Bottom
Pile A	0.55	2.09	1.41	0.36
Pile B	0.55	2.07	1.36	0.33
Pile C	0.55	2.05	1.30	0.22
Pile D	0.55	2.02	1.02	0.08
Isolated Cell	0.3	3.10	1.82	0.26

Table 6.2: Radial Deflections after Main Cell Filling, Cell with 15–ft Penetration.

Location	Radial Deflection (in.)			
	Top	Maximum	Dredgeline	Bottom
Pile A	0.57	2.73	1.83	1.25
Pile B	0.57	2.72	1.77	1.15
Pile C	0.56	2.71	1.71	0.99
Pile D	0.56	2.70	1.68	0.90
Isolated Cell	0.4	4.20	2.00	0.5

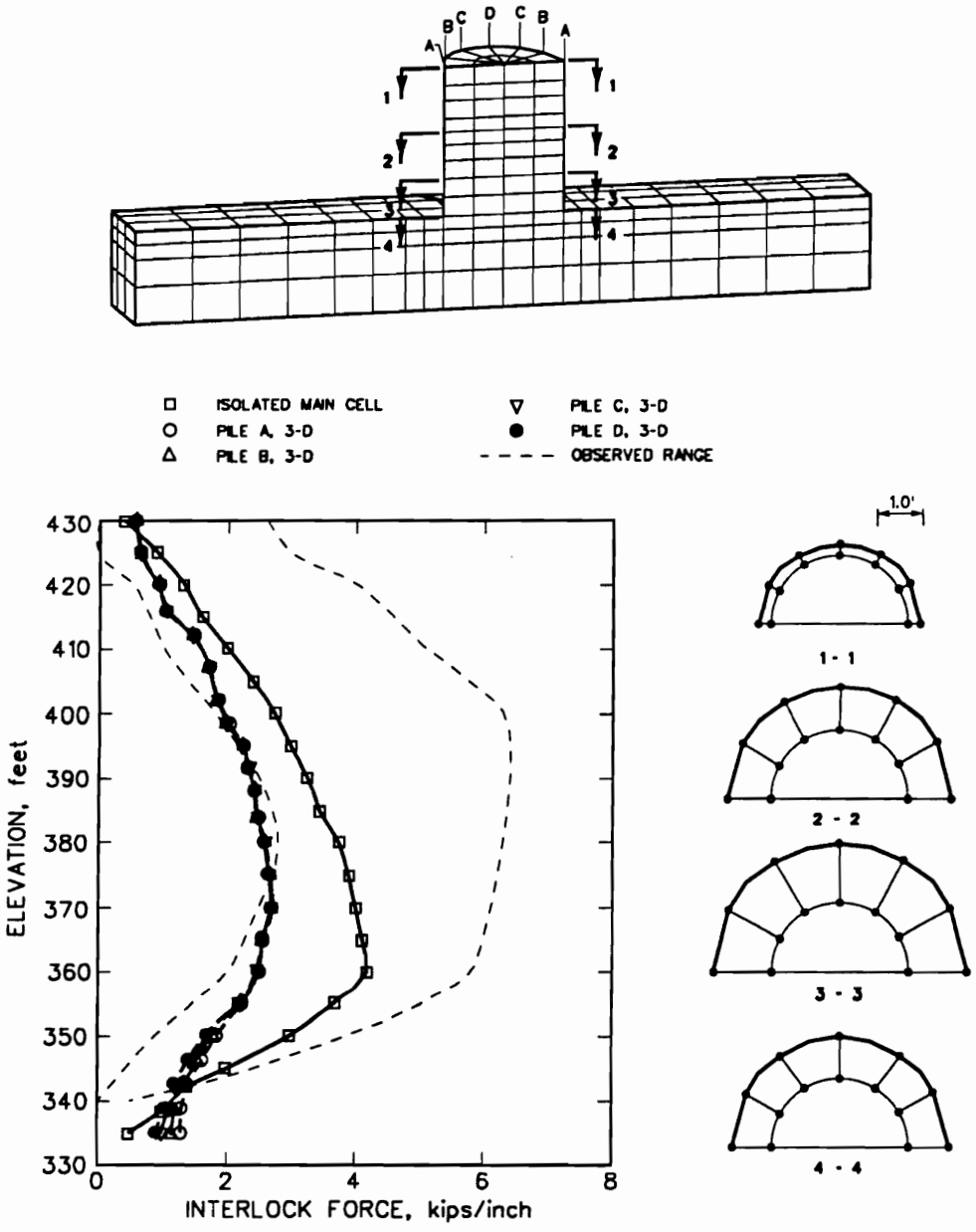

Figure 6.31: Radial deflections after main cell filling for a penetration of 15 ft.

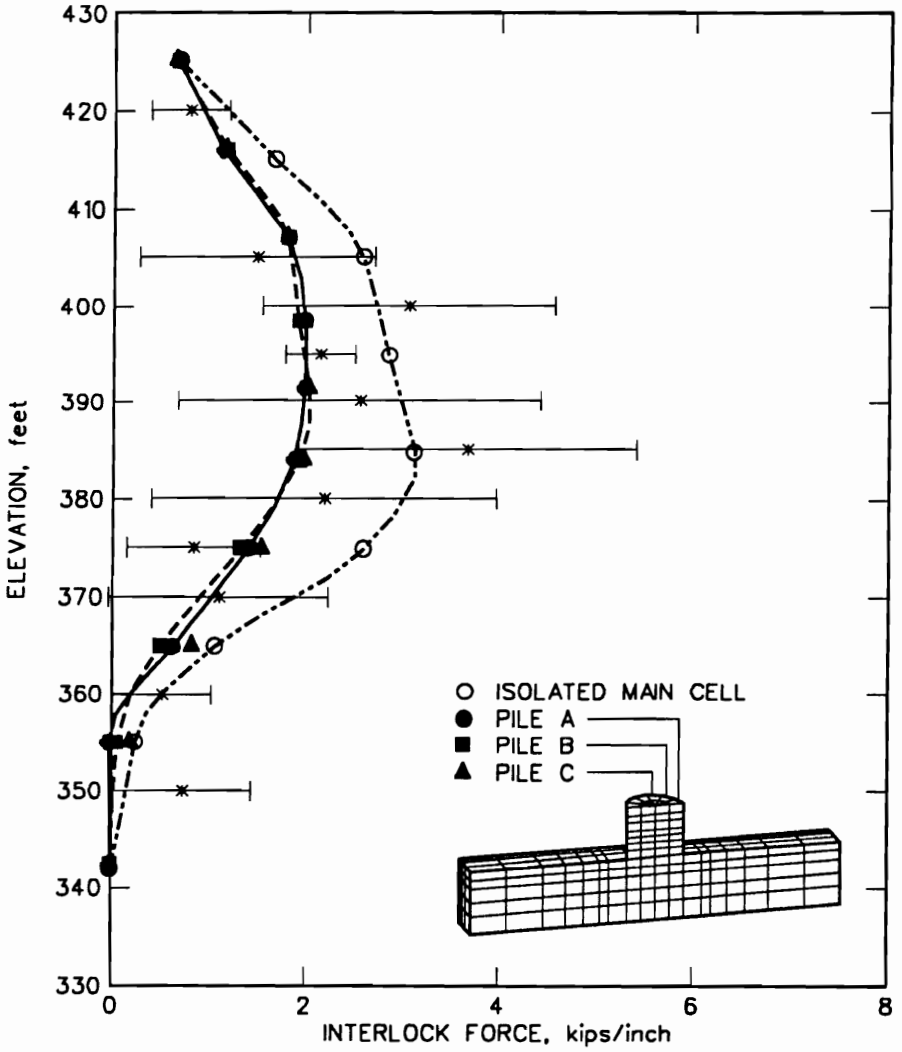

Figure 6.32: Interlock forces after main cell filling with 35–ft penetration.

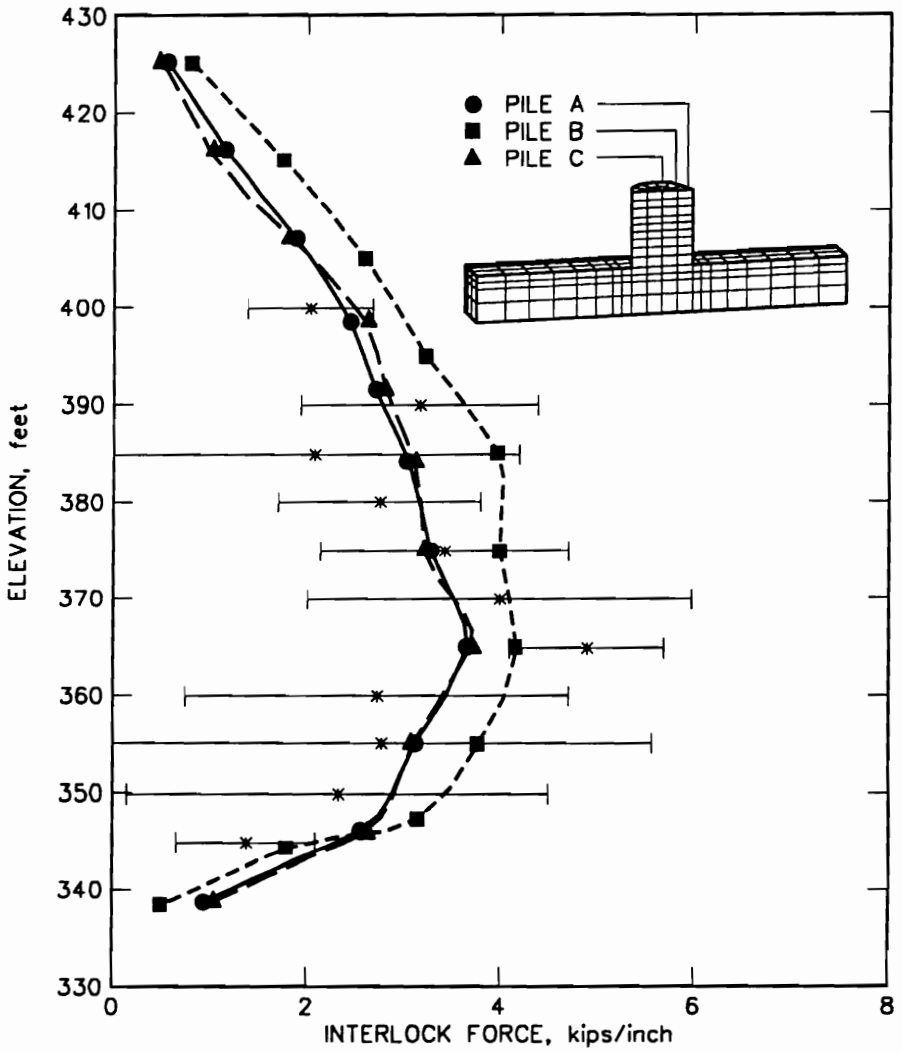

Figure 6.33: Interlock forces after main cell filling with 15–ft penetration.

lines denoting the at–rest and the active pressures are also shown in these figures. Pressures against the wall, above the dredgeline, after filling are at an at–rest value at the top of the cell and approach an active value in the lower portion of the cell. This is similar to the lateral earth pressure distributions found in the isolated main cell analyses.

Soil Stresses

Figures 6.36 and 6.37 present the vertical soil stresses normalized with respect to the vertical overburden pressure for the elements on planes that pass perpendicular and parallel to the centerline of the cofferdam leg and through the center of the cell, respectively, for the model with a penetration of 35 ft. As in the isolated main cell analyses, the normalized vertical stress ratios in the cell fill vary from slightly less than 1.0 near top of the cell to substantially less than 1.0 as the dredgeline is approached. Further down the cell, the vertical stress ratio decreases with depth. The vertical stress ratio varies from the center of the cell to the cell walls. This variation in vertical stress ratio from the center to the wall is similar to that found in the isolated main cell analyses.

Figures 6.38 and 6.39 present the horizontal soil stresses normalized with respect to the vertical overburden pressure for the elements on these same reference planes for the model with a penetration of 35 ft. The normalized horizontal soil stresses reported in the these figures are for the direction normal to the sheet–pile walls. These values represent lateral earth pressure coefficients. As in the case of the vertical stresses in the cell fill, the horizontal stress ratios decrease with depth in the cell. The horizontal stress ratios vary from a high of 0.5 at the top of the cell to 0.27 and 0.24 near the location of maximum bulge of the cell for a penetration of

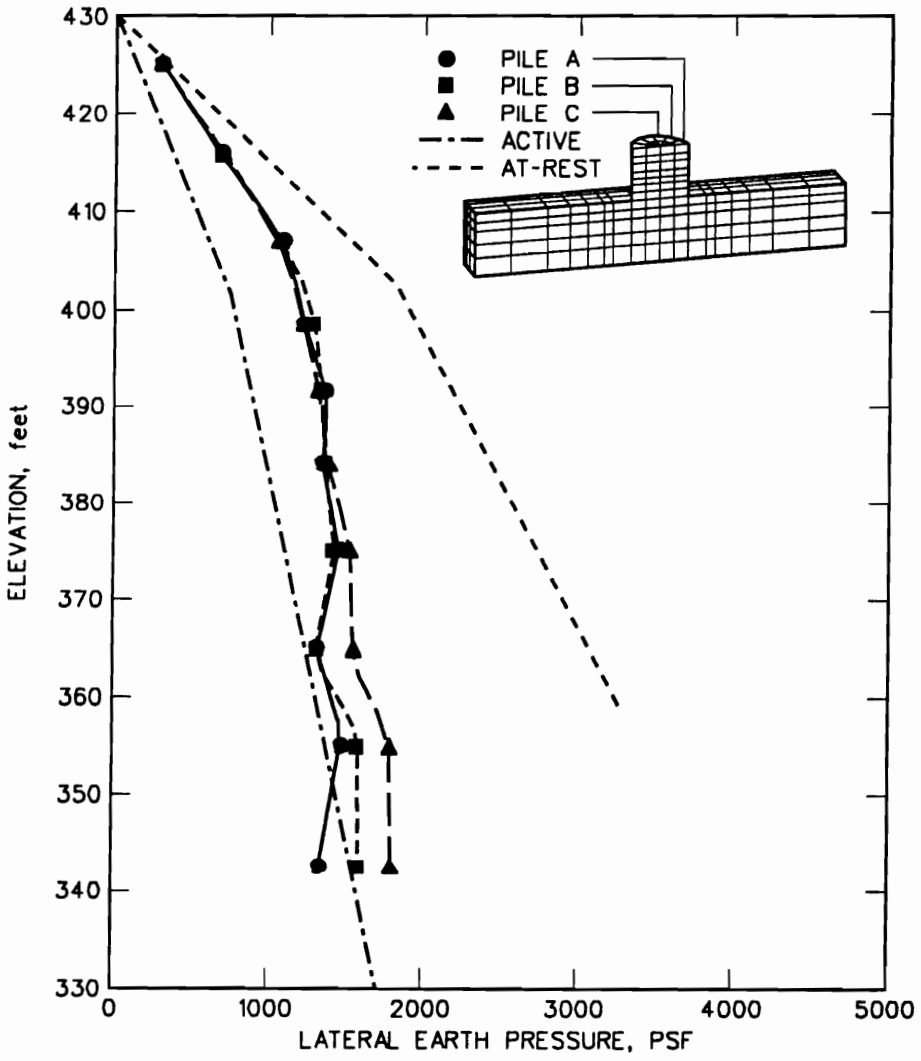

Figure 6.34: Predicted lateral earth pressures after main cell filling with 35–ft penetration.

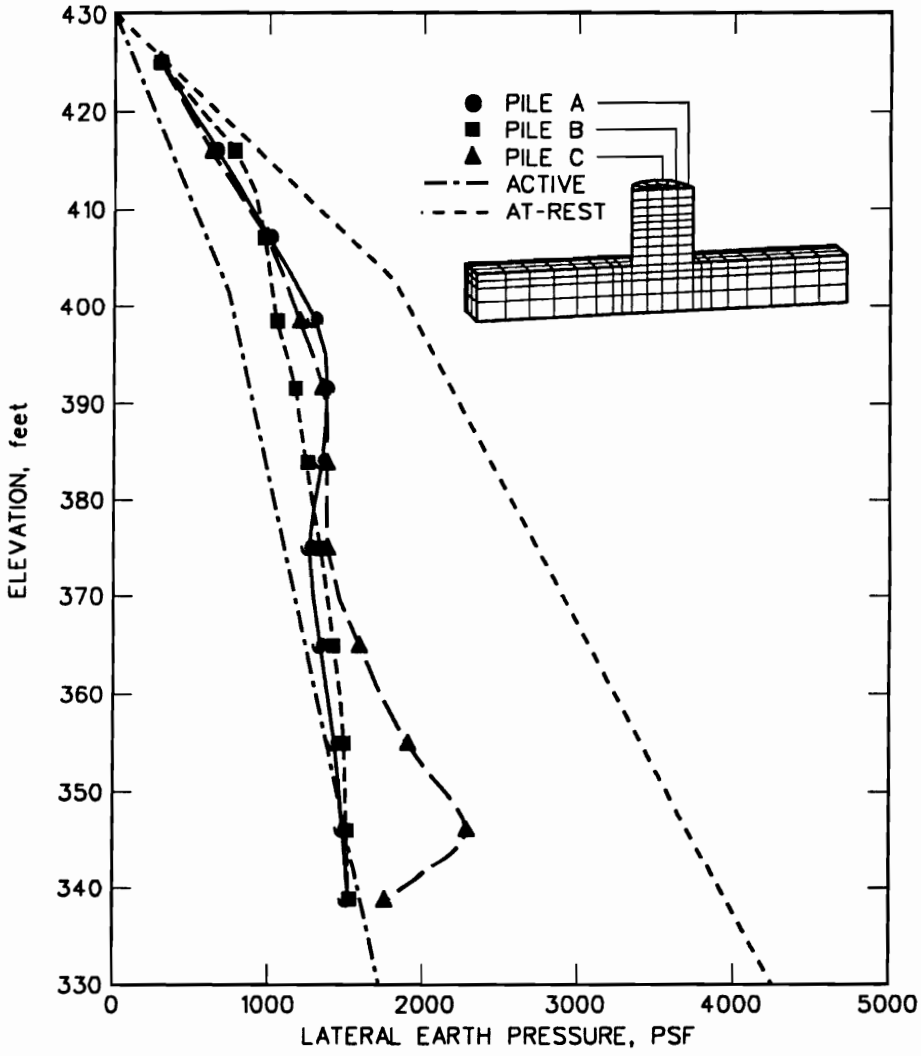

Figure 6.35: Predicted lateral earth pressures after main cell filling with 15–ft penetration.

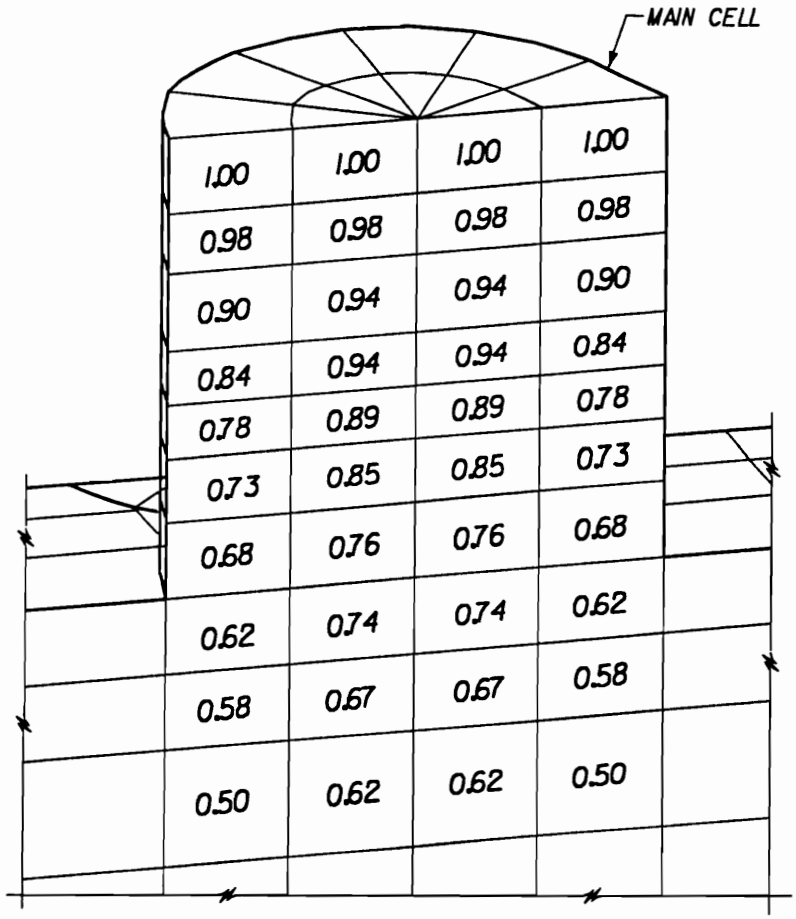

Figure 6.36: Normalized vertical soil stresses after main cell filling with 35–ft penetration.

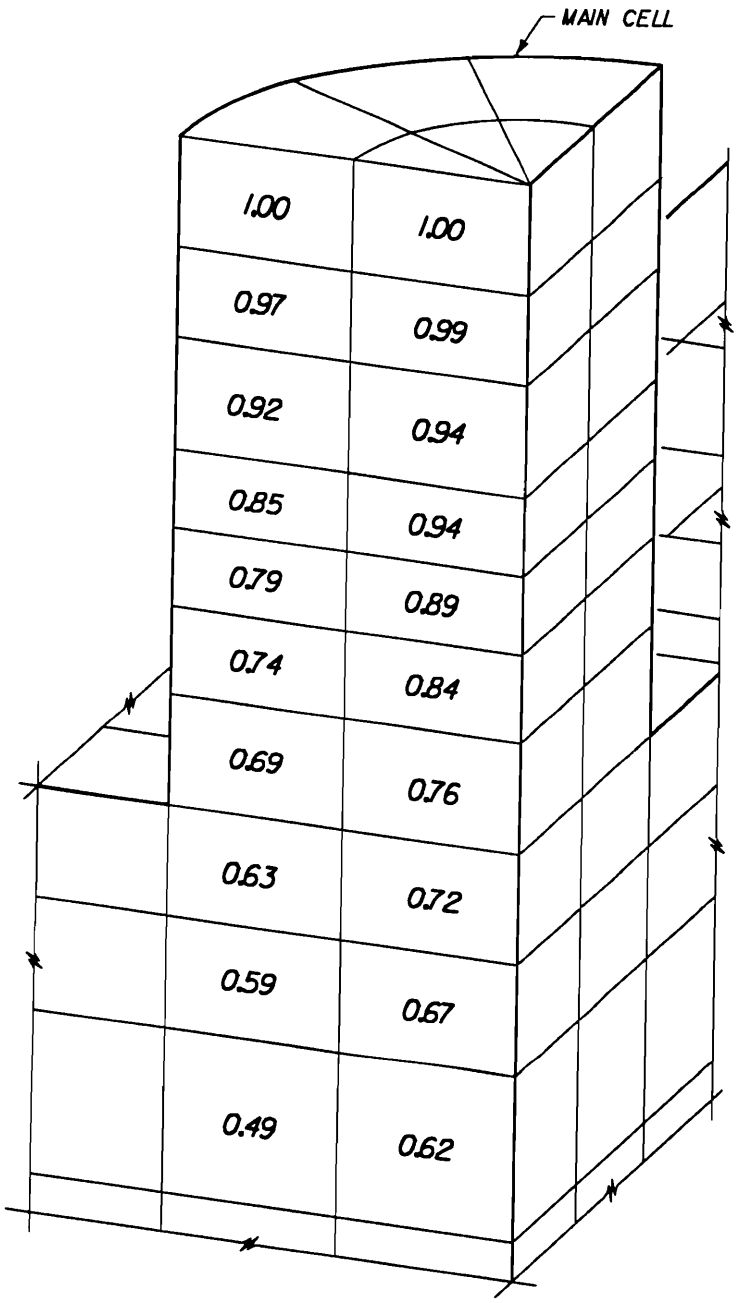

Figure 6.37: Normalized vertical soil stresses after main cell filling with 35–ft penetration.

35 ft and 15 ft, respectively. Below the dredgeline, the horizontal stress ratio drops to as low as 0.20.

6.3.3 Response at Completion of Main and Arc Cell Filling

The second major construction step in this analysis is to fill the arc cells. This section describes the results with the arc cell filling process complete.

Cell Movements

Figures 6.40 and 6.41 show the comparison of deflections of sheet piling at the completion of the filling process for the models with penetrations of 35 ft and 15 ft, respectively. The results from the isolated main cell analyses and the observed instrumentation measurements are presented for comparison. As in the previous analyses, the results are symmetric about the centerline of the cofferdam. The response of the cofferdam can be described by looking at the deflections of the sheet piling at six locations as shown in Figures 6.40 and 6.41.

The deflections of sheet piling vary from one location to another (Figures 6.40 and 6.41). The movement centerlines are captured by Pile A and Pile D. Pile A is along the upstream–downstream centerline of the main cell, while Pile D is found along the centerline perpendicular to upstream–downstream centerline. Not surprisingly, Pile A has the greatest deflection while, Pile D has the least deflection when all filling is complete. At the end of main cell filling only, the deflections of Piles A, B, C, and D were essentially the same, Figures 6.30 and 6.31. Therefore, the differences in the deflections for piles A, B, C, and D, shown in Figures 6.40 and 6.41, are due to the influence of the filling of the arc cell. The differences in the deformations throughout the cell depend on their relative location to the arc cell. Pile A and

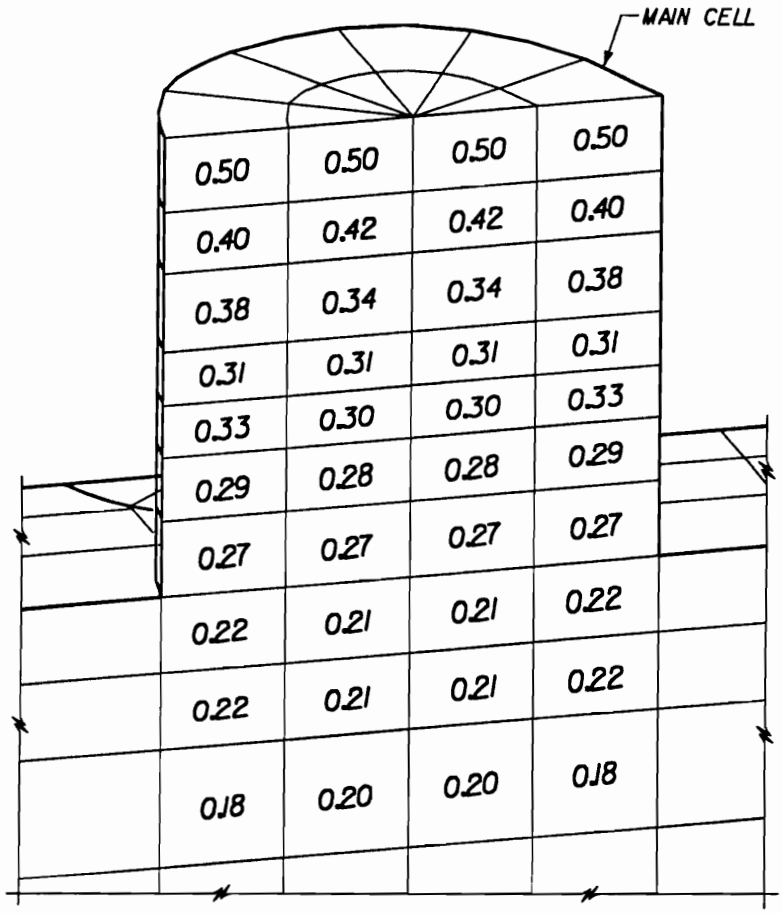

Figure 6.38: Normalized horizontal soil stresses after main cell filling with 35–ft penetration.

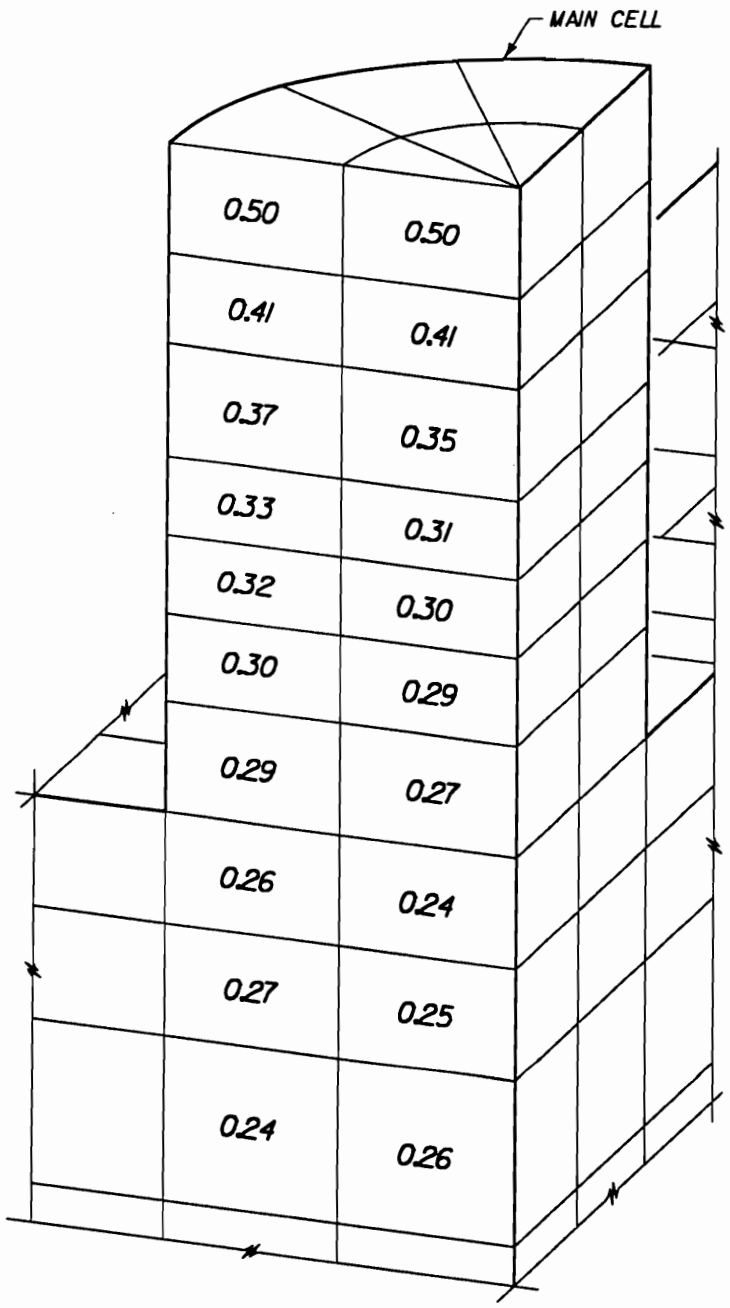

Figure 6.39: Normalized horizontal soil stresses after main cell filling with 35–ft penetration.

B, being furthest away from the arc cell and having no arc cell fill placed against them, had the greatest deflections. Notably, after filling the main and arc cells, the deflections of Pile A are close to those predicted for the analysis of an isolated cell. For Pile C, located at the wye connection of the arc cell to the main cell, the overall radial deflections are actually reduced slightly in magnitude from that reported at the end of main cell filling. Pile D, located in the common wall between the main and arc cells, is pushed back in the direction of the main cell decreasing the magnitude of its radial deflections from that which had occurred during main cell filling.

For Piles E and F, located in the arc cell, the deflections are due solely to the filling of the arc cell. Yet, their deflections are influenced by their proximity to the main cell. Pile F has the greater deflections and is further from the main cell. The radial deflections for both Piles E and F are less than those found in the main cell at the conclusion of its filling.

The three–dimensional analyses reveal that the sheet piling in the main cell undergoes some twisting as a result of filling of the arc cell. This can be seen by examining the plots of the horizontal slices through the cofferdam in Figures 6.40 and 6.41. At the top of the cell, Pile C deformed in a direction normal to the sheet piling. However, at the point of maximum bulge, Pile C deformed in a direction at some angle to the normal demonstrating the twisting induced at this location. A similar twisting is found at Pile B. Piles A and D are not allowed to twist because of the specified boundary conditions.

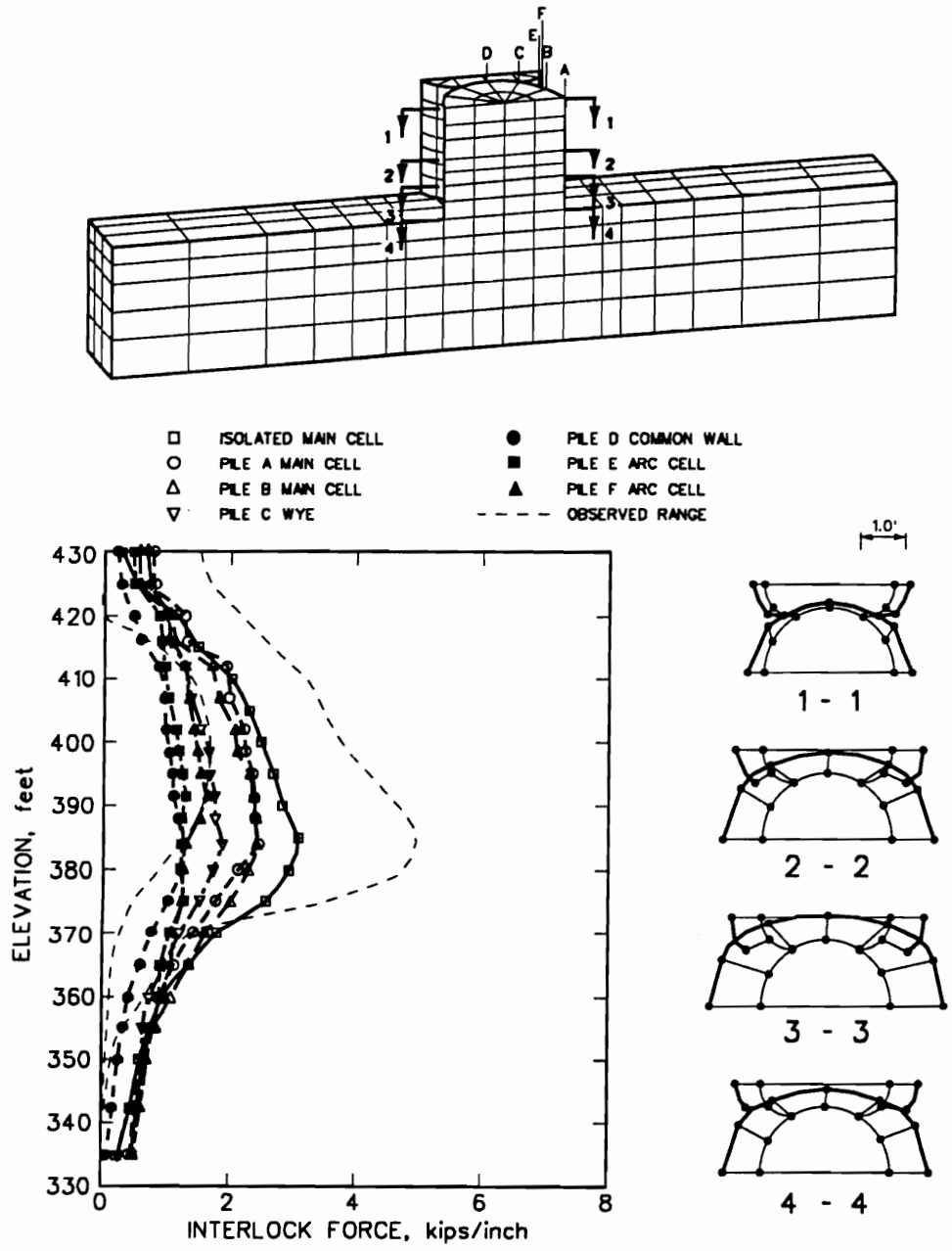

Figure 6.40: Radial deflections after arc cell filling for a penetration of 35–ft.

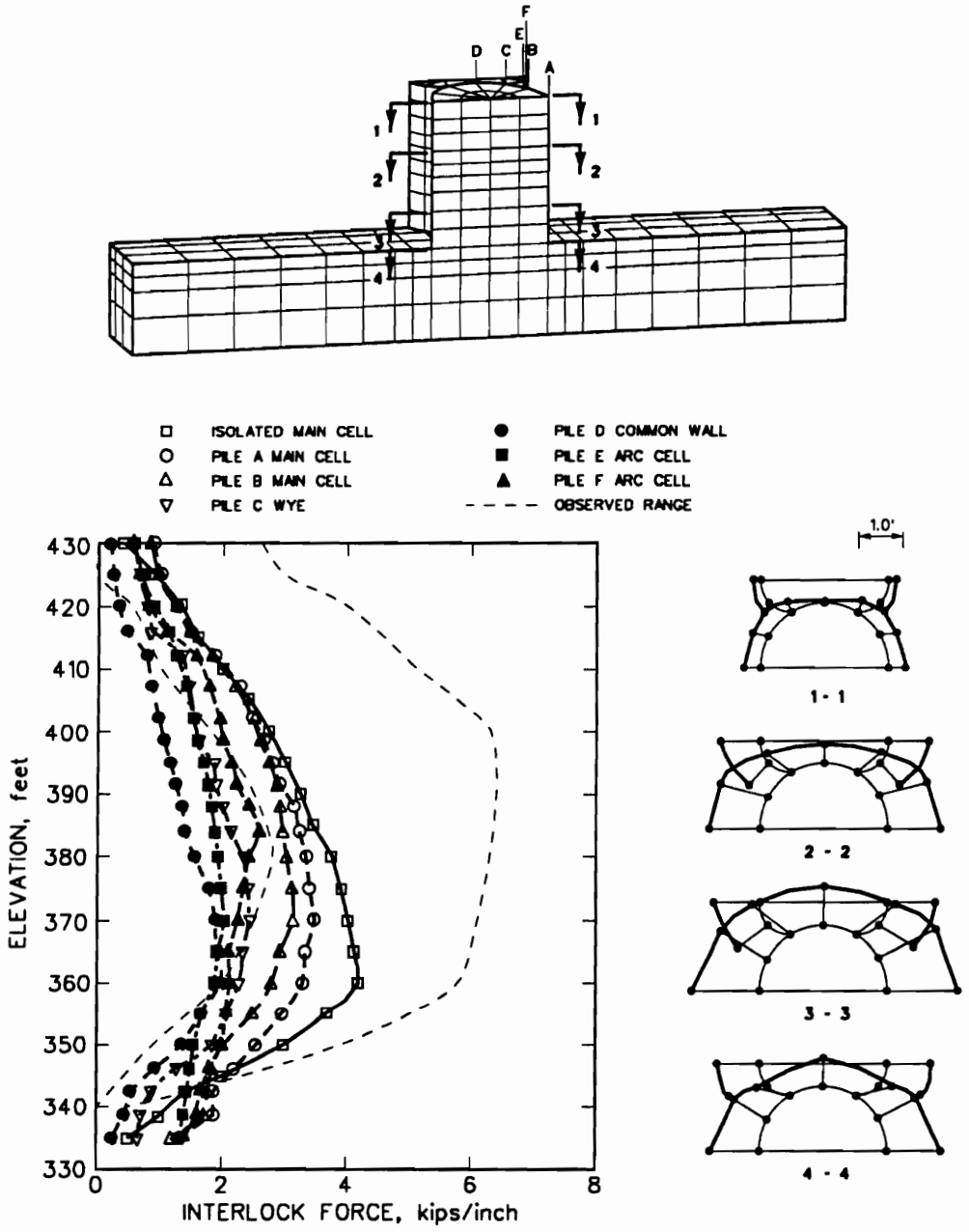

Figure 6.41: Radial deflections after arc cell filling for a penetration of 15–ft.

Interlock Forces

Figures 6.42 and 6.43 show the distribution of sheet–pile interlock forces at five locations in the main and arc cell system for models with penetrations of 35 ft and 15 ft, respectively. Included in the figures are the results of the isolated main cell analyses and the observed instrumentation measurements. The distribution of the interlock forces are similar in shape at all five locations, but different in magnitude. The two locations in the main cell, A and B, are essentially the same in shape and magnitude. For a penetration of 35 ft, maximum interlock forces are 3.43 kips per inch and 3.40 kips per inch for Piles A and B, respectively. For a penetration of 15 ft, maximum interlock forces are 4.44 kips per inch and 4.32 kips per inch for Piles A and B, respectively. These values are an increase over those reported at the end of main cell filling. These interlock forces are similar to those in the isolated main cell analyses. The highest interlock forces are found in the common walls as would be expected. The maximum interlock forces in the common walls for models with penetrations of 35 ft and 15 ft show an increase of 29 and 35 percent, respectively, over the maximum interlock forces in the main cell. The interlock forces in the common wall are 29 to 35 percent higher than those in the main cell. This is less than the maximum interlock forces in the common wall computed by Swatek's equation, given in Chapter 2 (Eq. 2.3), which would yield a 36 percent increase over main cell values for a cell of the same main and arc cell configuration. The TVA's secant equation, given in Chapter 3 (Eq. 2.2), would yield a 58 percent increase for the same geometry. The interlock forces in the arc cell are significantly less than those found in the main cell with maximum interlock values for penetrations of 35 ft being 32 and 36 percent less than the maximum interlock forces found in the

main cell for Piles D and E, respectively. For a penetration of 15 ft, the maximum interlock forces for Piles D and E are 26 and 29 percent, respectively, less than the maximum interlock forces found in the main cell. This can be attributed to the lower lateral earth pressures in the cell due to the high level of arching taking place.

The question arises of how well do interlock forces predicted with generalized plane strain compare with the three–dimensional analysis. Hardin [25] reported on a series of generalized plane strain analyses for a cell of the same main and arc cell configuration as the Lock and Dam No. 26(R) cofferdam cells and at depth of 40 ft. Comparison of the three–dimensional model and the generalized plane strain model (Figure 6.44) shows that the three–dimensional analysis yielded main cell interlock forces that were equal to the piecewise–linear elastic analysis with a Poisson's ratio of 0.45, less than the nonlinear elastic analysis with a Poisson's ratio of 0.45, but greater than the linear elastic analysis with a Poisson's ratio of 0.45. The interlock forces in the common wall from the three–dimensional analysis were less than all of the generalized plane strain analyses (16 percent for the nonlinear and 6 percent for piecewise–linear), and the interlock forces in the arc cell were greater than all the generalized plane strain analyses (17 percent for the nonlinear and 4 percent for piecewise–linear). While the three–dimensional and piecewise–linear elastic generalized plane strain results compare closely to one another, as whole the generalized plane strain analyses had wide range values for the interlock forces at a given location. This leaves considerable uncertainty about the accuracy of the generalized plane strain model.

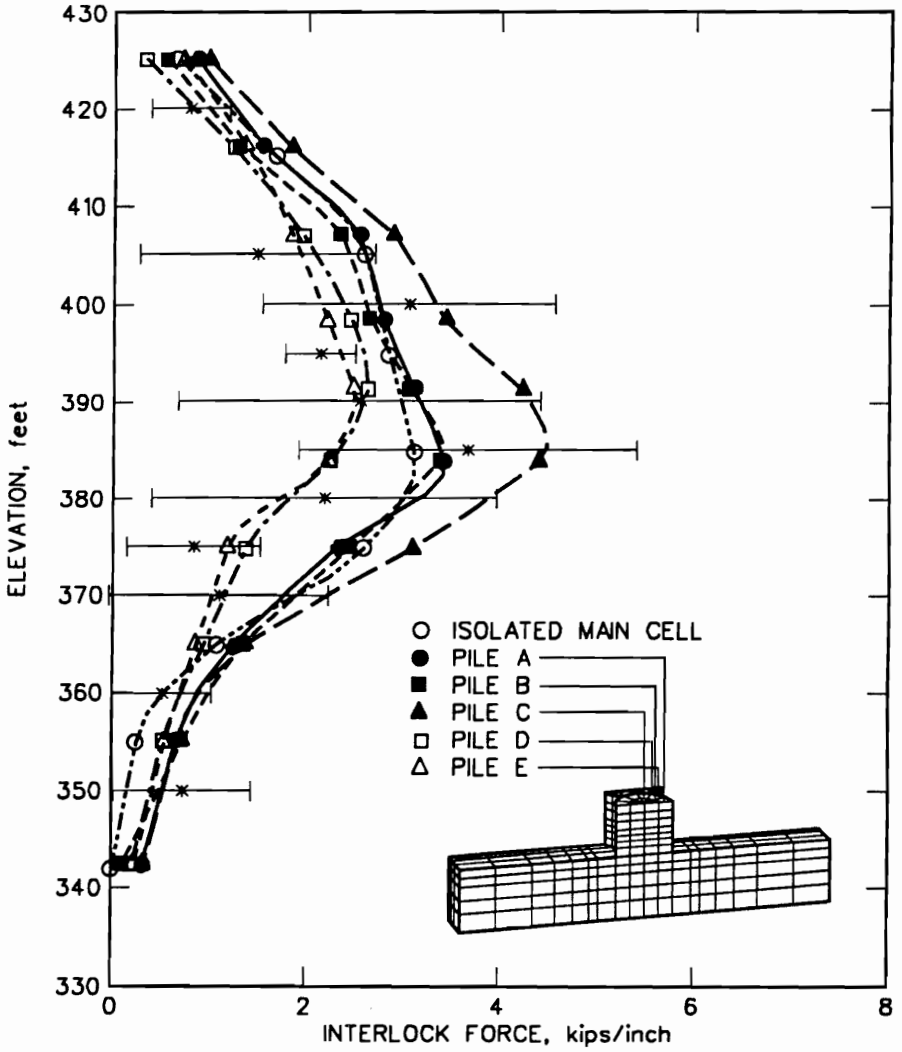

Figure 6.42: Interlock forces after arc cell filling with 35–ft penetration.

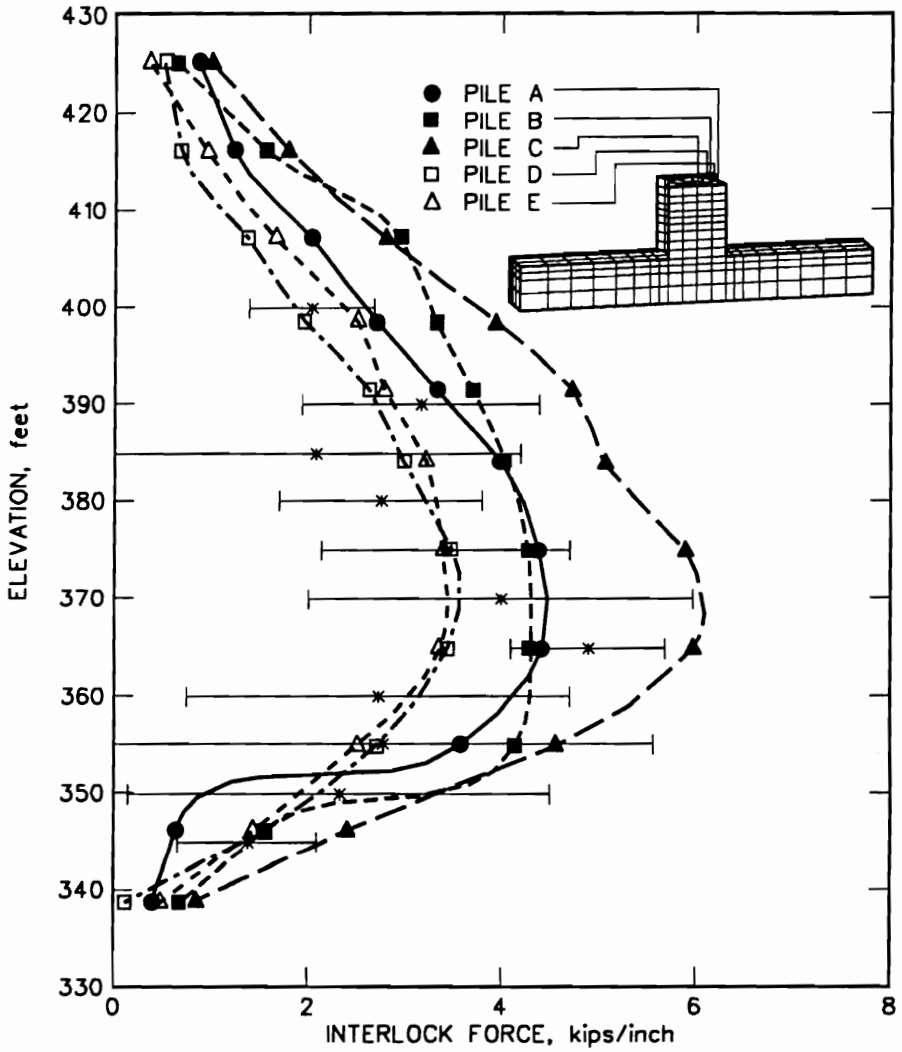

Figure 6.43: Interlock forces after arc cell filling with 15–ft penetration.

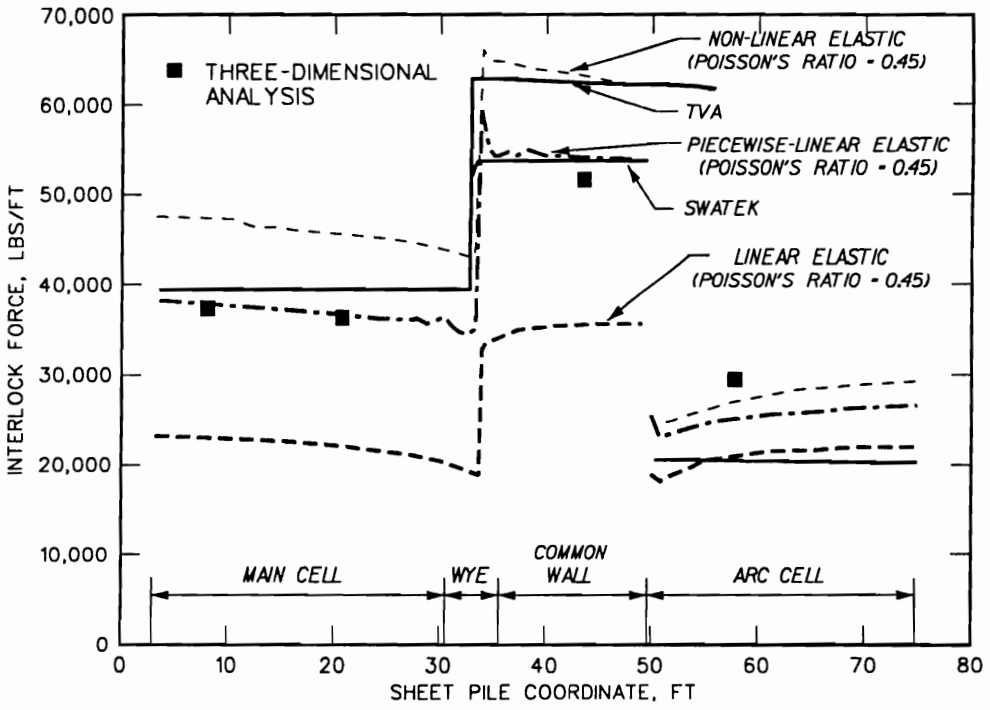

Figure 6.44: Comparison of interlock forces from generalized plane strain analysis.

Earth Pressures

As would be expected from the results presented in the previous two sections, the distribution of lateral earth pressures against the sheet piling varies from location to location throughout the main and arc cells. Figures 6.45 and 6.46 present the distribution of lateral earth pressures after the arc cell filling for three locations in the main cell for models with the penetrations of 35 ft and 15 ft, respectively. The reference lines in the figures are denoting the at–rest and the active pressures for the cell fill.

During arc cell filling, the earth pressures at Piles A and B stay essentially unchanged from those reported at the completion of main cell filling. There is a slight increase in the earth pressures below the dredgeline in the model with a penetration of 15 ft during arc cell filling. For the model with a penetration of 35 ft, at the dredgeline and directly below, the earth pressures remain approximately the same as they were at the end of main cell filling, but near the tip of the sheet piling the earth pressure decreases for Pile A and increases for Pile B.

The earth pressures against the main cell side of the common wall, Pile C, shows the most significant change in magnitude and distribution of any location in the main cell. The earth pressures in the upper portion increase during arc cell filling. This is expected because soil is placed against the common wall during arc fill placement which would tend to push the sheet piling back toward the main cell. This can be seen by examining the sheet–pile movements in Figures 6.40 and 6.41.

The distributions of earth pressures in the arc cell fill for the models with penetrations of 35 ft and 15 ft are shown in Figures 6.47 and 6.48, respectively. Near the top of the cell, the earth pressures are between at–rest and active. In the middle

and lower portion of the cell, the earth pressures drop below active values. The fact that the pressures are lower than active is a sign of significant soil arching is taking place in the arc cell. This arching is seen in the soil stresses.

Below the dredgeline, the earth pressure for locations at Piles E and F location increases to values just greater than active with the Pile F having the greatest value. This increase below the dredgeline for Piles E and F is due to their proximity to the main cell. The results show that the closer to the main cell, the higher the earth pressure.

Comparing the earth pressures normal to the sheet piling from the three–dimensional analysis with those from the generalized plane strain analyses, Figure 6.49 shows that earth pressures in the main cell are between the values from the linear elastic generalized plane strain analysis and the piecewise–linear elastic generalized plane strain analysis and are approximately equal to active values. The earth pressures against the main cell side of the common wall from the three–dimensional analysis are less than those computed by all of the generalized plane strain analyses with the linear elastic analysis being the closest. The three–dimensional analysis shows a 64 percent increase in the earth pressures along the main side of the common wall over the earth pressure in the main cell. The earth pressures in the arc cell are significantly less than those computed in the generalized plane strain analyses. This would be consistent with the high level of arching in the arc cell seen in the three–dimensional analysis and the inability of the generalized plane strain to account for the arching.

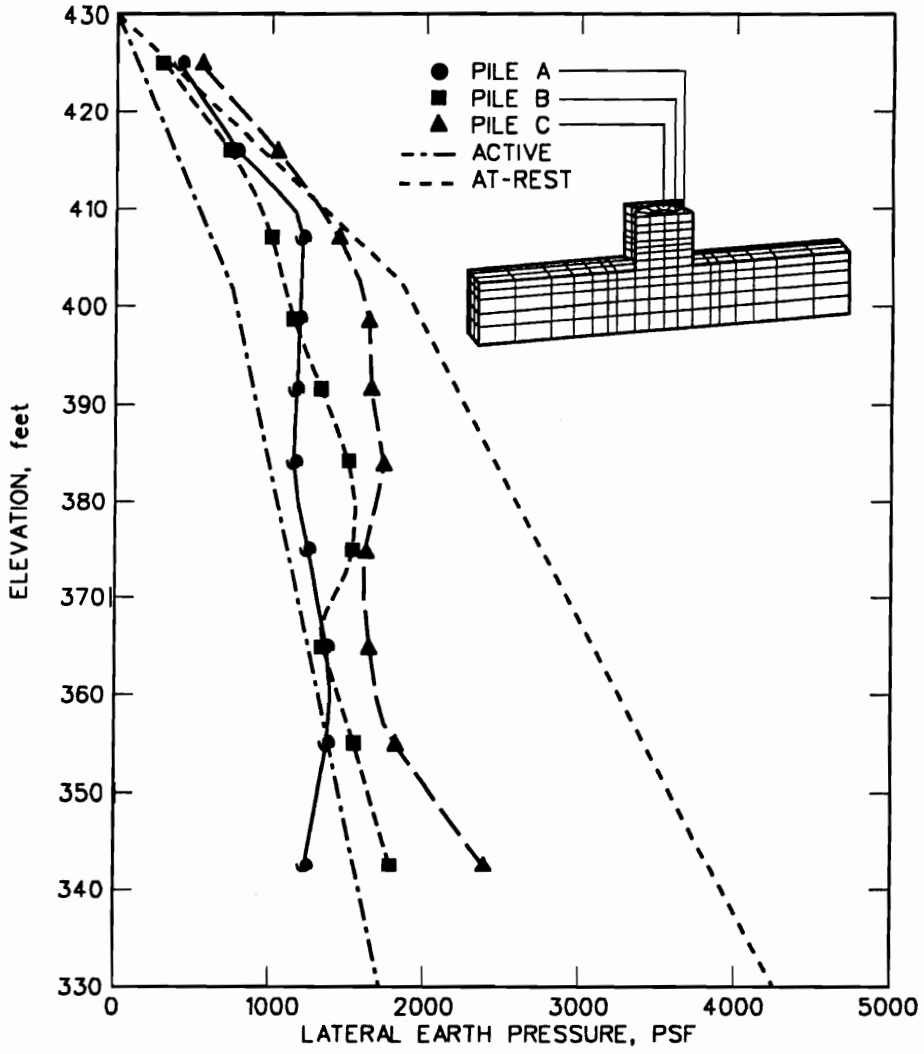

Figure 6.45: Predicted lateral earth pressures in the main cell after arc cell filling with 35–ft penetration.

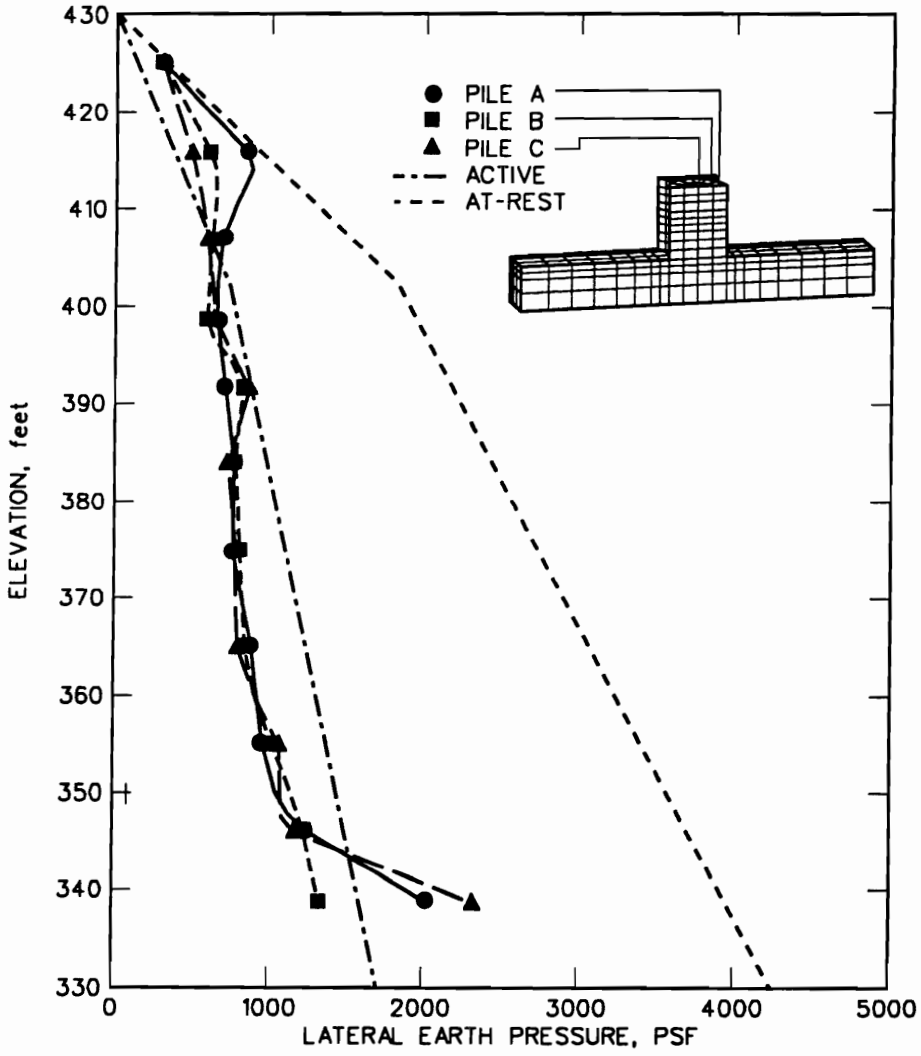

Figure 6.46: Predicted lateral earth pressures in the main cell after arc cell filling with 15–ft penetration.

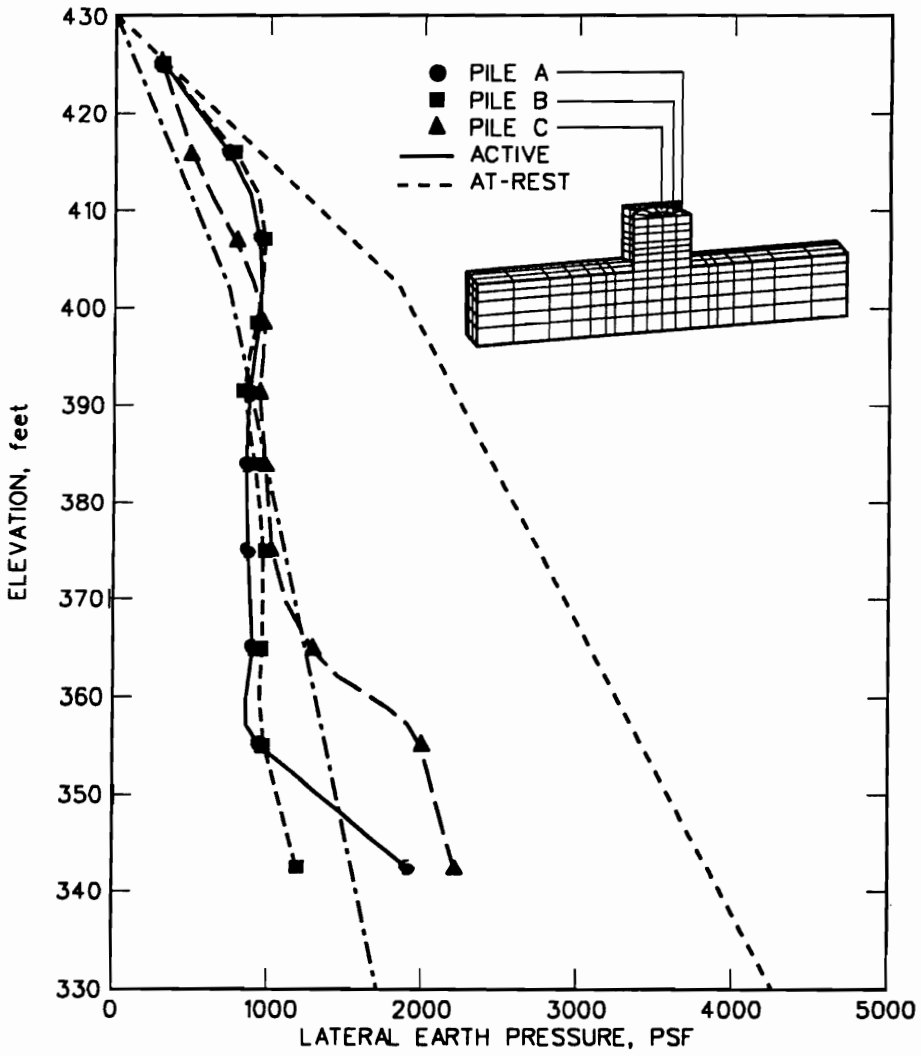

Figure 6.47: Predicted lateral earth pressures in the arc cell after arc cell filling with 35–ft penetration.

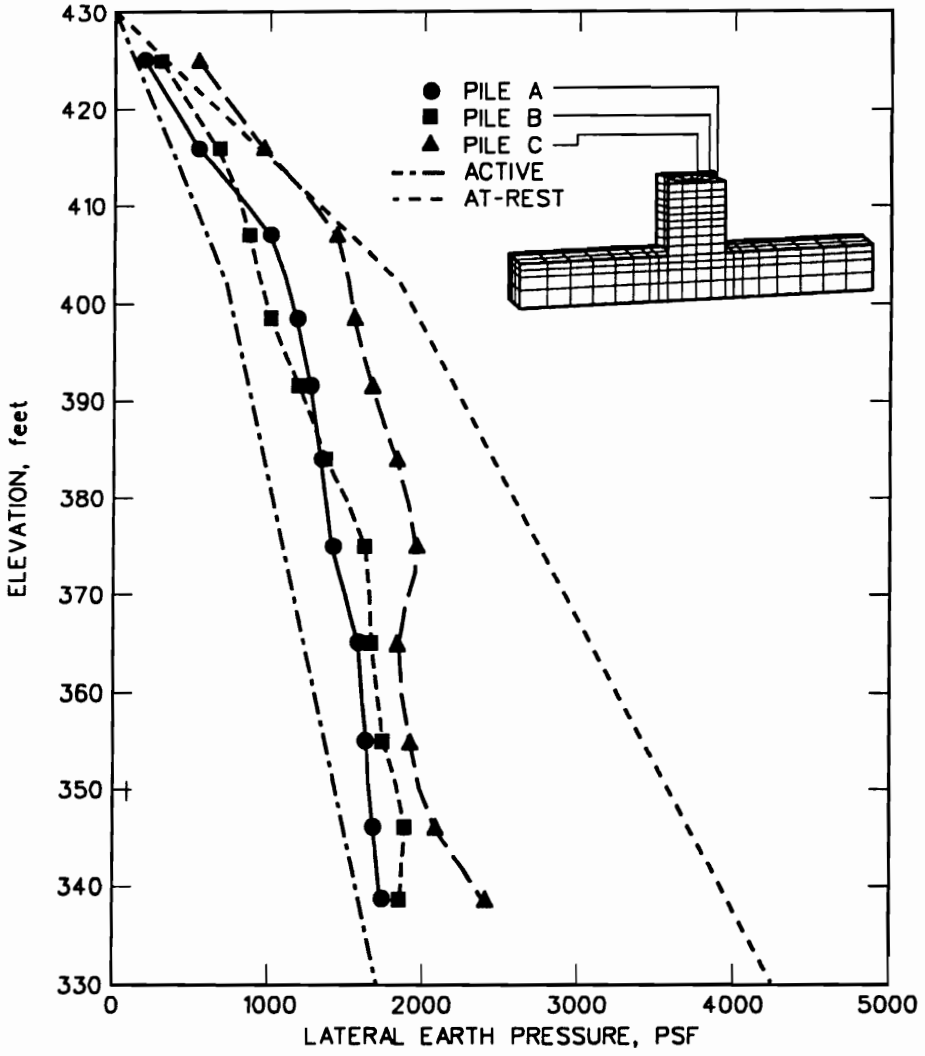

Figure 6.48: Predicted lateral earth pressures in the arc cell after arc cell filling with 15–ft penetration.

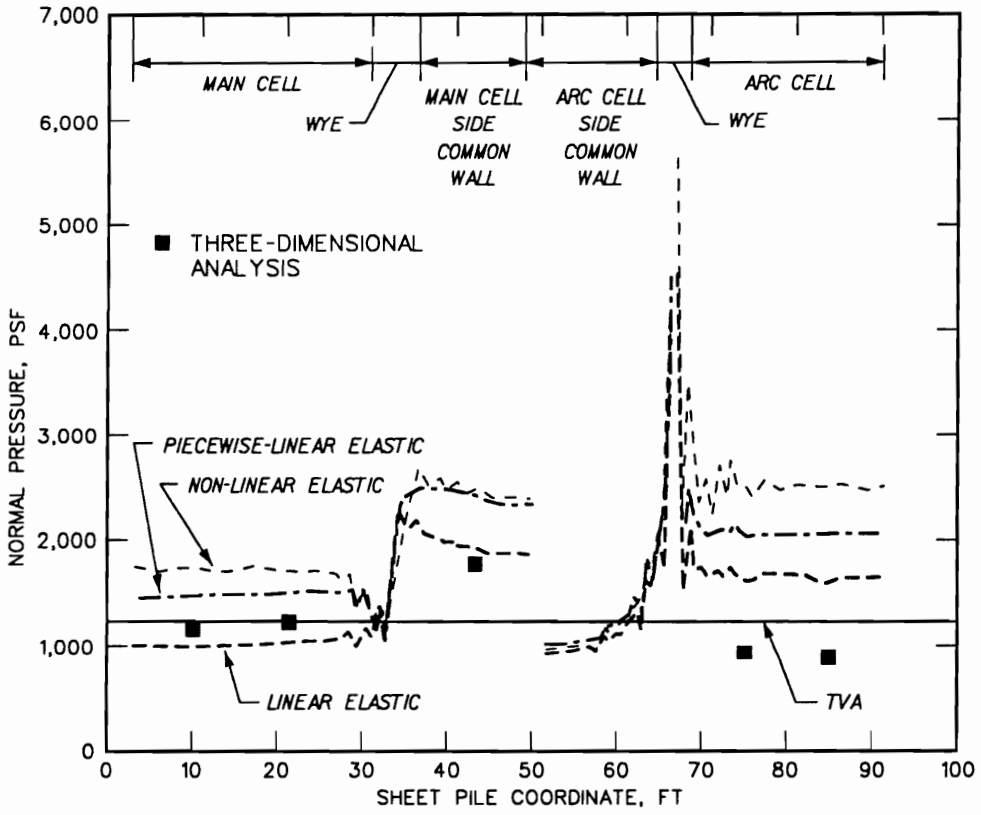

Figure 6.49: Comparison of earth pressures from generalized plane strain analysis.

Soil Stresses

Figure 6.50 shows the normalized vertical soil stresses at the end of arc cell filling for the elements on a plane perpendicular to the centerline of the cofferdam leg and passing through the center of the main cell for the model with a penetration of 35 ft. This figure shows a general increase in the vertical stress ratios over that found at the end of main cell filling, Figure 6.36. The increases are greatest at the center of the cell for this section. The increase in vertical stress for this section varies from a low of 0 percent to a high of 30 percent with an average increase of approximately 10 percent. Similar results were found for the model with 15 ft of sheet–pile penetration. In the rest of this section, the results for a penetration of 15 ft will be presented only when they are different from those for a penetration of 35 ft.

Figure 6.51 shows the normalized vertical soil stresses at the end of arc cell filling for the elements on a plane passing through the centerline of the cofferdam leg for the model with a penetration of 35 ft. This figure shows the same general trend for an increase in the vertical stress ratios over that found at the end of main cell filling, Figure 6.37, but the distribution with respect to depth in cell fill is somewhat different. The increase in vertical stress ratio is higher in upper portion of the cell near the cell walls. The placement of the arc cell fill adjacent to the sheet piling in the common wall is the primary reason for the increase being more pronounced near the cell wall for this section.

The vertical stress ratio in the arc cell fill indicates that a significant amount of arching is taking place. Figure 6.52 shows the vertical stress ratios for the fill in the arc cell for the model with a penetration of 35 ft. This figure shows that the vertical

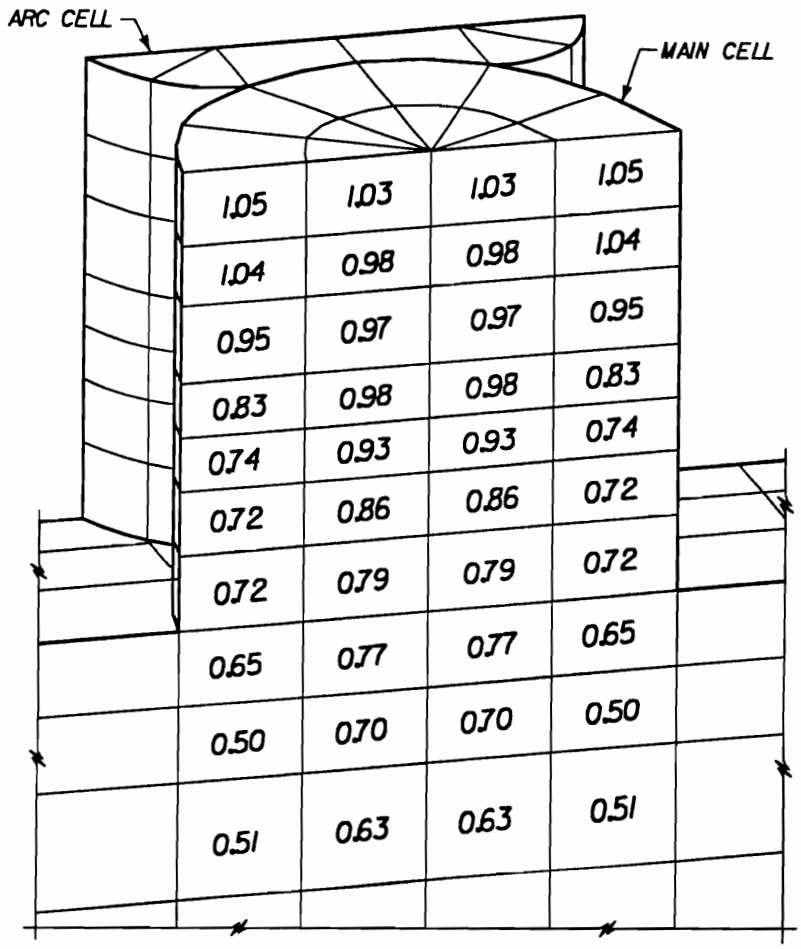

Figure 6.50: Normalized vertical soil stresses in the main cell after arc cell filling with 35–ft penetration.

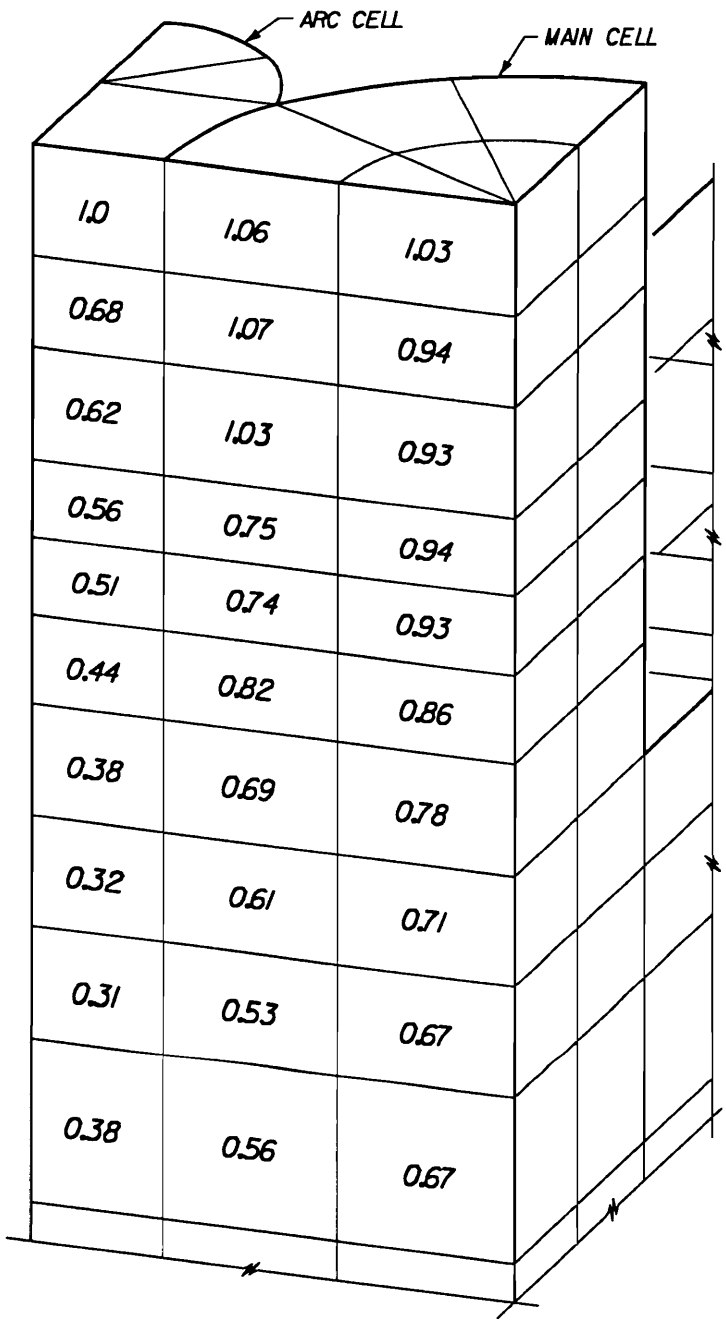

Figure 6.51: Normalized vertical soil stresses in the main cell after arc cell filling with 35–ft penetration.

stress ratio decreases from a value of 1.0 at the top of the cell to values of less than 0.35 near the dredgeline. This means at the dredgeline less than 35 percent of the gravity stress is being transferred through the soil, and this is the principal reason that the lateral earth pressures in the arc cell, reported in the previous section, are below the active values. The type of arching is predominately frictional and is so highly developed due to the slenderness of the arc cell.

An examination of the horizontal stress ratio in the main cell reveals no general trend of increase or decrease for the cells as a whole, but rather a trend for increase and decrease within certain regions in the cells. Figures 6.53 and 6.54 show the normalized horizontal soil stresses at the end of arc cell filling for the elements on a plane perpendicular to the centerline of the cofferdam leg and passing through the center of the main cell for models with penetrations of 35 ft and 15 ft, respectively. These figures show that the horizontal stress ratio has decreased over those at the completion of main cell filling for the elements near the center of the main cell and for the elements adjacent to the cell walls in the region of maximum bulge. This reflects the increase in radial deflections occurring in this section during the arc cell filling. The model with 35 ft of penetration shows a slight increase in horizontal stress ratio in the upper portion of the cell near the cell walls, while the model with the 15–ft penetration shows a decrease. This decrease is probably due to the greater settlement and lateral deformation experienced by the model with the 15–ft penetration.

Figure 6.55 shows the normalized horizontal soil stresses at the end of arc cell filling for the elements on a plane along the centerline of the cofferdam leg for the model with a penetration of 35 ft. This figure shows a major increase in the horizontal stress ratios for the elements in the main cell over those reported at the

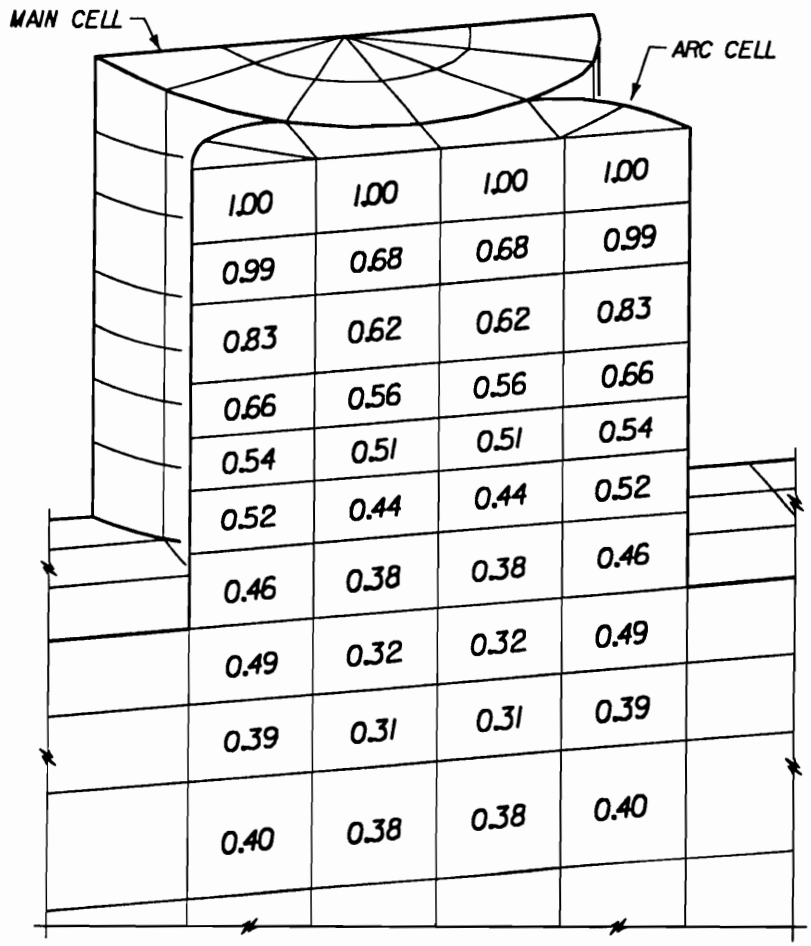

Figure 6.52: Normalized vertical soil stresses in the arc cell after arc cell filling with 35–ft penetration.

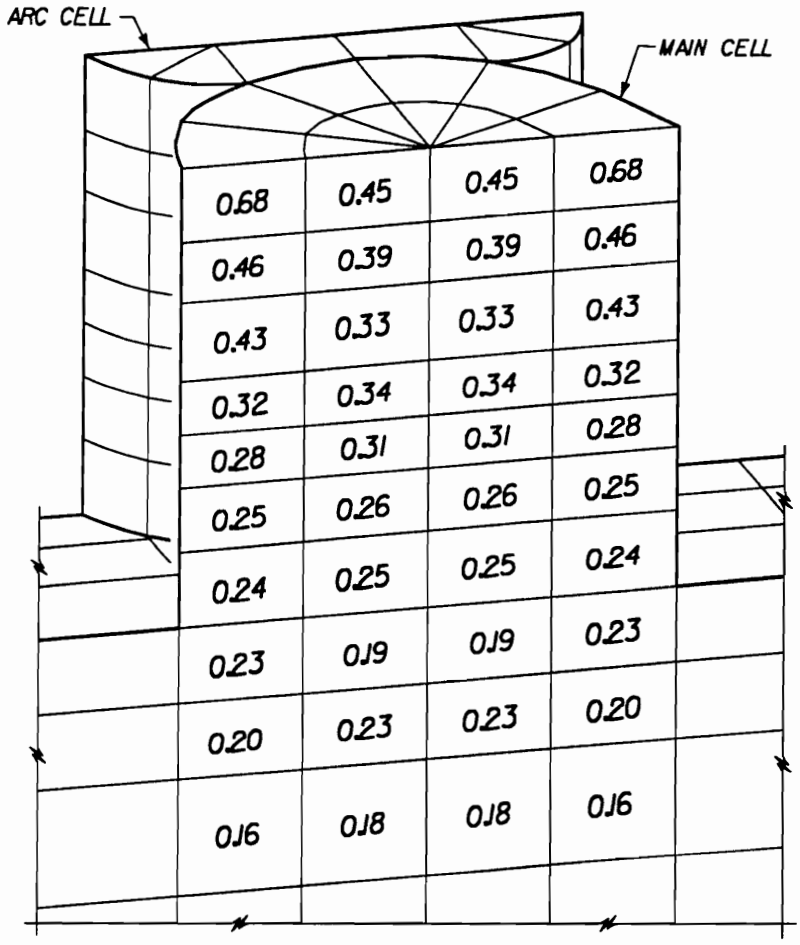

Figure 6.53: Normalized horizontal soil stresses in the main cell after arc cell filling with 35–ft penetration.

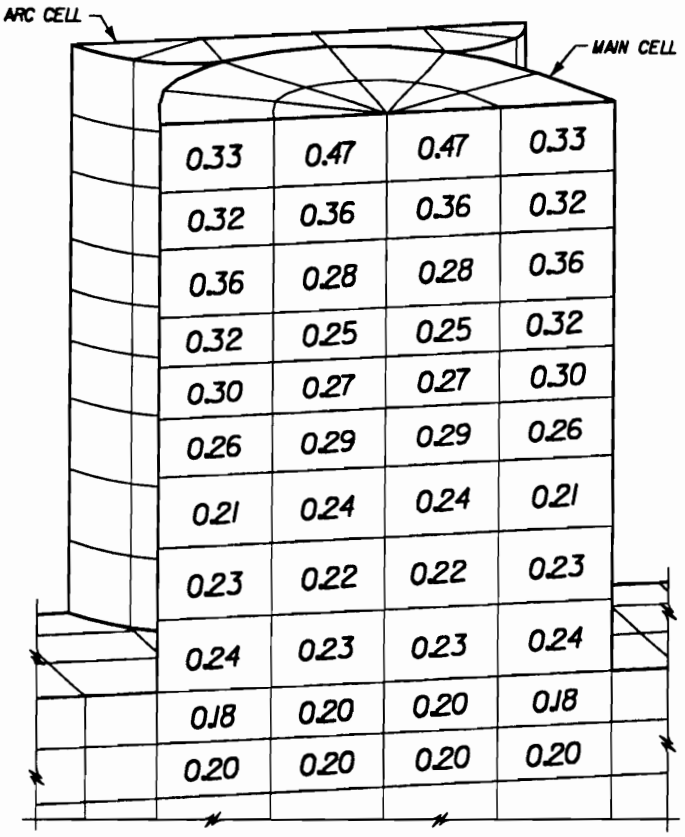

Figure 6.54: Normalized horizontal soil stresses in the main cell after arc cell filling with 15–ft penetration.

completion of main cell filling, Figure 6.39. The increase is greatest in the upper portion of the cell near the cell walls and at the dredgeline where there is little change. The increase in horizontal stress ratio is a result of the arc cell fill being placed against the sheet piling of the common wall.

As would be expected after seeing the lateral earth pressures and vertical stress ratios in the arc cell, the horizontal stress ratios in the arc cell, shown in Figure 6.56 for the model with a penetration of 35 ft are below active lateral earth pressure coefficient values for all except the last two layers of elements placed in the arc cell. The top layer reflects only the stress at the end of placement and next layer below the top has not had sufficient vertical movement to fully develop the friction between the cell fill and the sheet–pile walls. The lower values in the remaining elements are due to the high amount of arching in the arc cell fill.

6.4 Summary

The analyses of the isolated main cell presented in this chapter serve several purposes. First, they confirm the basic formulation and implementation of the various elements used in the new three–dimensional finite element code. Secondly, they verify the new three–dimensional nonlinear constitutive soil model and the incremental analysis procedure used in the new code. In the initial isolated main cell gravity turn–on analyses, the deflections from the models, both three–dimensional and two–dimensional and using shell elements to represent the sheet piling, were over twice that obtained from the analyses of models using a 1–ft–thick solid elements for the sheet piling. The sheet–pile interlock forces from analyses with both types of elements were practically the same. This demonstrated that the shell elements are

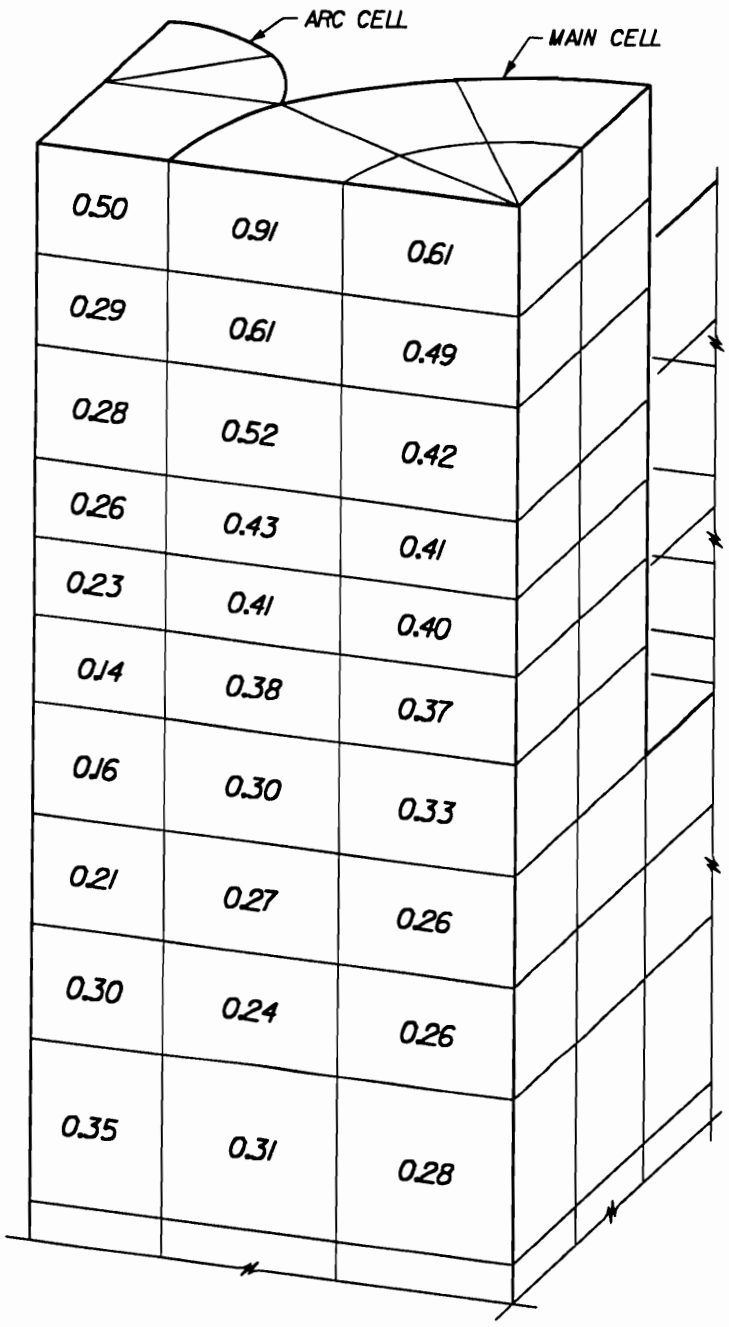

Figure 6.55: Normalized horizontal soil stresses in the main cell after arc cell filling with 35–ft penetration.

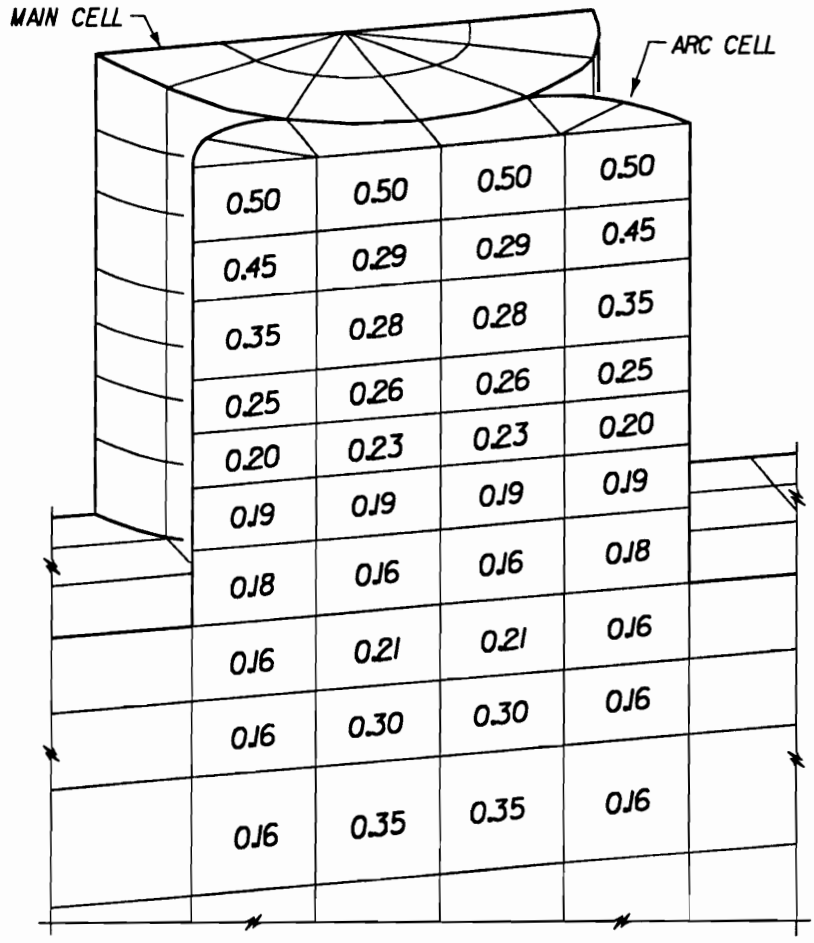

Figure 6.56: Normalized horizontal soil stresses in the arc cell after arc cell filling with 35–ft penetration.

more flexible than the 1–ft–thick solid elements and should provide a more accurate representation of the sheet–pile behavior. In the nonlinear soil–structure interaction analyses, the displacements are over one order of magnitude greater than those in the gravity turn–on analyses. The displacements in the nonlinear analyses are predominately due to the movements of the cell fill. The differences in deflections between the two types of elements for the sheet piling are so small when compared with the overall movements of the cell in the nonlinear analyses that they are not discernible, and, therefore, they are not as significant as once thought.

In general, the predicted sheet–pile movements from the nonlinear analyses of the isolated main cell are characterized by outward radial deflections increasing from the top of the cell until approximately 15 ft above the dredgeline and then decreasing thereafter due to the constraints provided by the embedment of the sheet piling in the foundation. The radial deflections computed by the new three–dimensional code compared well with the two–dimensional finite element results.

The predicted distribution of interlock forces by the nonlinear analyses were comparable to those from previous two–dimensional finite element results and compare well with the mean of the instrumentation measurements. The location of the maximum interlock force approximately coincides with the location of the maximum bulge in the sheet–pile

cell wall.

The arching in the cell fill had a substantial effect on the lateral earth pressures applied to the sheet–pile cell walls. Earth pressures in the cell were above active values in the upper to midportion of cell fill, but less than active in the lower portion of the cell, due to arching effects [25]. The arching reduces the effective vertical and horizontal stresses throughout the cell fill. The arching is more pronounced in the

lower portion of the cell due to the higher vertical deformations and is greatest adjacent to the sheet piling because of the arching mechanism. The arching is principally due to the friction between sheet piling and cell fill.

A general conclusion from the study of the isolated main cell problem, is that the three–dimensional and two–dimensional analyses predicted essentially the same response of the isolated main cell, and the results are supported by the instrumentation measurements. These analyses provided confidence in the new code for its application to more complex aspects of the cofferdam.

After confirmation of the new three–dimensional finite element code by the study of the isolated main cell problem, the code was used to study the filling of a main and an arc cell. This problem is truly a three–dimensional problem that no two–dimensional analysis is fully capable of modeling. The point of primary interest is the effect of the arc cell filling on the interlock forces in the common wall. This has been studied with the two–dimensional generalized plane strain finite element analyses [8, 33, 53] which assumes that both the main and arc cell are filled simultaneously, and this is not the actual case in the field. The three–dimensional analyses uses a scenario that has the main cell being filled first, followed by the filling of the arc cell.

At completion of the filling of the main cell, the analyses reveals that the deformations of the sheet piling are generally radial in direction (normal to the sheet piling), as in the isolated main cell analyses, but are slightly smaller in magnitude which may be due to the model itself. The deformations of the sheet piling of the main cell are uniform within a horizontal plane for the cell above the dredgeline. Below the dredgeline, the deformations of sheet piling decrease in accordance with their distance to the nearest fixed boundary. The interlock forces are also less than those reported in the isolated main cell analyses. The reason for this is that

a higher degree of arching is taking place in the cell fill, thus reducing the lateral earth pressure on the cell walls, even though the soil may not have moved sufficiently to develop the same level of shear strength mobilization, the reduction in vertical stresses resulting from the arching causes lower lateral earth pressures.

After the filling of the arc cell, the cell movements were no longer simply radial. The deflections of the sheet piling had a variation from one location to another due to the influence of the arc cell filling, the deflections of the sheet piling depended on their relative location with respect to the arc cell. For the sheet piling further away from the arc cell and having no arc cell fill placed against them, the deflections were the greatest and are comparable to those found in the isolated main cell analyses. The outward deflections of the sheet piling lessened with proximity to the arc cell.

The three–dimensional finite element interlock forces in the main cell after arc cell filling were approximately the same as those reported in the isolated main cell analyses, although they were increased over those reported at the end of main cell filling. The interlock forces in the common wall were 29 to 35 percent higher than those in the main cell. These three–dimensional interlock forces in the common wall were less than those calculated by conventional methods. The three–dimensional interlock forces compare well with the measured values at Lock and Dam No. 26(R). The interlock forces in the arc cell were significantly less than those found in the main cell. This can be attributed to the lower lateral earth pressures in the cell due to the high level of arching taking place.

In conclusion, the results of the three–dimensional analyses of the cofferdam filling process presented in the chapter have shown the important aspects of cofferdam behavior that can be studied only by a three–dimensional model. The most important is the interlock forces in the common wall due to arc cell filling. The analyses

demonstrate the importance of consideration of the arching in the cell fill. This is believed to be one of the three major reasons that the generalized plane strain model is unable to accurately predict the interlock forces in the common wall. The second major reason is the simultaneous placement of the main and arc cell fill required in the generalized plane strain model. The filling of the main cell has the effect of stiffening the main cell prior to the arc cell fill placement and altering the overall response of the model as compared with the general plane strain analysis. The third reason is the inability of the generalized plane strain model to consider the three–dimensional response of the soil. Chapter 4, it was shown how important it is to use a three–dimensional constitutive soil model when a true three–dimensional state of stress is present as is the case in the generalized plane strain model.

In the next chapter, the new three–dimensional code is used to investigate the behavior of the first and second–stage Lock and Dam No. 26(R) cofferdam under differential water loading. This is a continuation of the analyses performed in this chapter.

Chapter 7

Differential Loading Analysis

In the preceding chapter, the construction process for the second–stage Lock and Dam No. 26(R) cofferdam was analyzed with the new three–dimensional finite element code. The construction of the cells is a significant loading event in the life of the cofferdam. During the cell filling process, interlock forces are at their highest value. Other critical design events pertaining to the internal and external stability occur once the cofferdam has been dewatered and placed in operation.

In this chapter, the second–stage Lock and Dam No. 26(R) cofferdam is analyzed under differential loading due to initial dewatering of the interior of the cofferdam and changes in river levels. As the water in the interior of the cofferdam is lowered, a net hydrostatic head develops between the exterior and interior walls of the cofferdam. This loading causes the cofferdam to deflect toward the interior. The second–stage Lock and Dam No. 26(R) cofferdam is modeled from the time of berm placement and initial dewatering through a major flood event. The deflections of the cofferdam are compared to the survey data collected from the second–stage cof-

ferdam and the instrumentation results from the first–stage cofferdam. Changes in stresses are reported and related to the overall performance of the cofferdam.

Also, in this chapter, the finite element model is loaded to near collapse in order to study the behavior of cofferdams under extreme loading conditions. The deflections and the related stresses are examined to explain the unusual strength of the cellular cofferdams.

7.1 Differential Loads Applied to Cofferdams

After completion of the cell filling, the first differential loading felt by the cofferdam cells is due to the placement of interior and exterior berms. The interior berm provides additional sliding stability for the cofferdam, and the exterior berm provides scour protection for the outboard sheet piling. The berms are generally placed before dewatering of the interior of the cofferdam. For the Lock and Dam No. 26(R) cofferdam, the sand stability berm and the stone scour protection berm placement occurred shortly after completion of the cell filling operation. The material for the stability berm was the same dredged river sand that was used in the filling of the cells, and it had an estimated relative density of 55 percent. The exterior berm was made of rip-rap stone.

The placement of the berms apply a net lateral force to the cell in the direction of the exterior of the cofferdam. This is in an opposite direction to future differential water loads. The cells at Lock and Dam No. 26(R) were observed to move less than 1 in. toward the outboard of the cofferdam at the top of the cells, a movement that is relatively insignificant compared to the movements occurring during dewatering and high water. Although the movements may be insignificant, the importance of

the berm is not insignificant. The berms play a major role in providing strength to the cofferdam and reducing lateral deflections in later loading [38].

Dewatering of the second–stage Lock and Dam No. 26(R) cofferdam was achieved in several phases. First, the interior pool of the cofferdam was lowered by pumping water directly from the pool and discharging it into the river. Once, the interior pool was low enough, well points were placed along the inboard side of the cells. As the interior pool receded, additional well points were placed at lower elevations. Several stages of well points were used to lower the interior pool to a level below the surface of the river bottom.

Upon lowering the water level in the interior of the cofferdam, a net hydrostatic head develops between the exterior and interior walls of the cofferdam resulting in the deflection of the cofferdam towards the interior. This deflection is made up of both a lateral movement and a rotation of the cells. The amount of horizontal deflection at the top of the cells during the initial dewatering is usually less than one percent of the free height of the cofferdam [18]. Dewatering also lowers the phreatic surface in the cell fill. This can lead to significant settlement of the cell fill. The Lock and Dam No. 26(R) cofferdam had settlement as high as 2 ft during dewatering.

During high water or flood stages, the water head on the exterior of a cofferdam increases, and the cofferdam is subjected to a new, higher load than previously applied. The cofferdam cells respond by moving toward the interior of the cofferdam until they reach equilibrium under this new loading. As the high water from the flood recedes, the cofferdam moves toward the outboard but without fully recovering the deformation occurring during the flood event.

7.2 Finite Element Models

The starting points for the analyses presented in this chapter are the end of the cell filling process. The two finite element models, for the cell penetrations of 35 ft and 15 ft, consisting of one–half of a main cell and one–half of an arc cell as used in the cell filling analyses.

To develop the finite element meshes for the analyses of differential loading, the finite element meshes used in the cell filling analyses had elements added to them to represent the stability and scour protection berms. The new meshes are shown in Figures 7.1 and 7.2. The mesh for a penetration of 35 ft consists of 2,458 nodes, 483 three–dimensional, twenty–node solid elements to represent the foundation, cell fill, and berms, 198 eight–node shell elements to represent the sheet piling, and 360 three–dimensional, eight–node interface elements. The mesh for a penetration of 15 ft consists of 2,646 nodes, 512 three–dimensional, twenty–node solid elements to represent the foundation, cell fill, and berms, 198 eight–node shell elements to represent the sheet piling, and 372 three–dimensional, eight–node interface elements. In Figures 7.1 and 7.2, the inboard of the cofferdam and stability berm are located on the right and the outboard and river are on the left. The slice through the cofferdam is 43.207 ft wide and extends 162 ft on the riverside of the cofferdam and 205 ft on the dewatered side.

7.3 Construction Simulation

Figure 7.3 schematically depicts the key construction phases modeled in the three–dimensional finite element analyses. The preceding chapter presented the results for

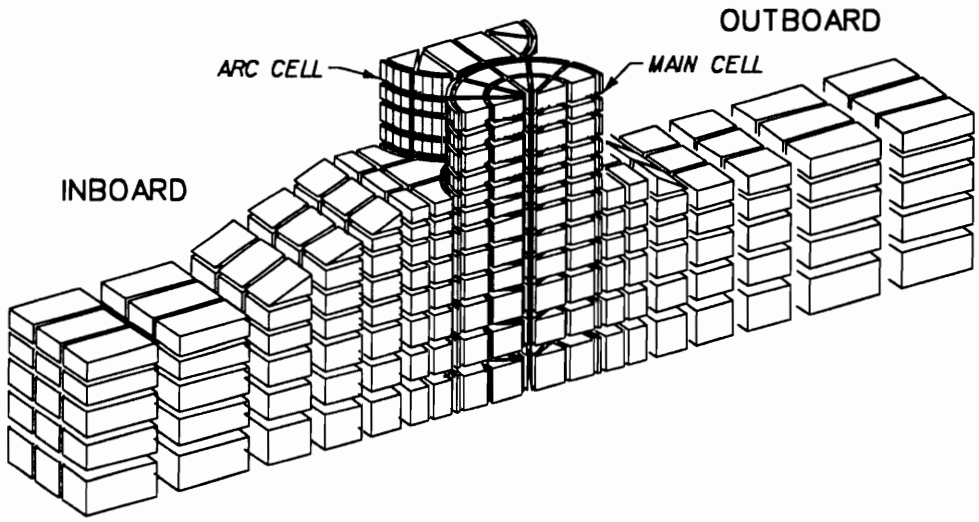

Figure 7.1: Mesh for second–stage Lock and Dam No. 26(R) with 35–ft penetration.

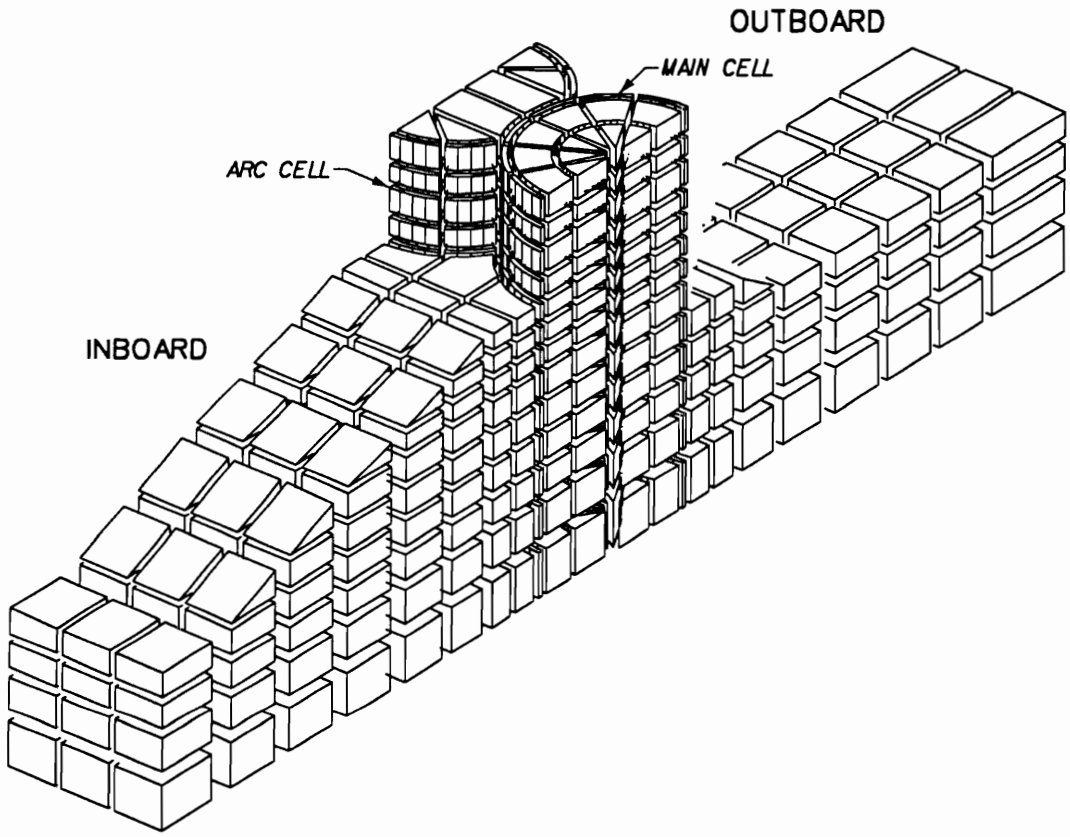

Figure 7.2: Mesh for second–stage Lock and Dam No. 26(R) with 15–ft penetration.

the initial conditions, placement of the sheet piling, and main and arc cell filling, as shown in Figure 7.3a, b and c. The remaining phases of construction simulation are presented in this chapter.

Following the filling of the main and arc cells, the stability berm and scout protection berm are placed, Figure 7.3d. The stability berm has a slope of one vertical on five horizontal with top elevations of 395 ft and 385 ft for the models with 35 ft and 15 ft of penetration, Figures 7.1 and 7.2, respectively. The inboard and outboard river level is maintained at El 402 throughout berm and scour protection placement.

After berm placement, the interior of the cofferdam is dewatered, Figure 7.3e. The river level is maintained at El 402 on the outboard side of the cell while the water level inside the cofferdam is incrementally lowered to a minimum El 345. The flow nets from Shannon and Wilson study [55], assuming the horizontal permeability in the foundation soils is four times greater than in the vertical direction, were used for the pore water pressures in the model. It is further assumed that the sides and the bottom of cells form an impervious barrier to seepage. The water levels corresponding to the fully dewatered state within the cofferdam vary from El 361 adjacent to the inboard cell wall to El 345 at the center of the dewatered area.

The last step considered in these analyses of the cofferdam is the raising of the river level on the exterior of the cofferdam to simulate high water and flood conditions for the river, Figure 7.3f. The river level on the outboard side of the cofferdam is raised to El 420 in 2 steps with 10 substeps and then to the top of cells at El 430 in 1 step with 10 substeps. The rise in the river level is assumed to occur rapidly enough so that the water levels within the foundation and the cell fill do not have sufficient time to respond to the increased head in the river outside the cofferdam.

The increased water loading on the outboard side of the cofferdam is modeled as a boundary pressure load against this side of the cofferdam.

7.4 Response to Normal Differential Loading

This section presents the results of the three–dimensional finite element analyses of the second–stage Lock and Dam No. 26(R) cofferdam from berm placement through dewatering to an exterior river level equal to the top of the cells. The results presented here concentrate on deflections of the cell walls and soil stresses in the cell fill. Only the results from the model with 35–ft penetration are presented, since they are representative of the overall behavior of the second–stage cofferdam and are directly comparable to the instrumentation results from the first–stage cofferdam. The inclinometer readings presented in this section represent only the net lateral movement during the differential loading and do not necessary represent the true shape of the sheeting.

7.4.1 Cell Deflections

Berm Placement

Figure 7.4 shows the movements of the inboard and outboard cell walls, respectively, of the cofferdam after placement of the interior stability berm and exterior scour protection. These results are compared with the inclinometer readings from cells 33 and 34 in the first–stage cofferdam. The placement of the stability berm against the inboard of the cells causes the entire cell to move toward the outboard. The movement at the top of the cell is on the order of 0.3 in. for the inboard and 0.4 in. for the outboard. The predicted inboard movements show a localized response at

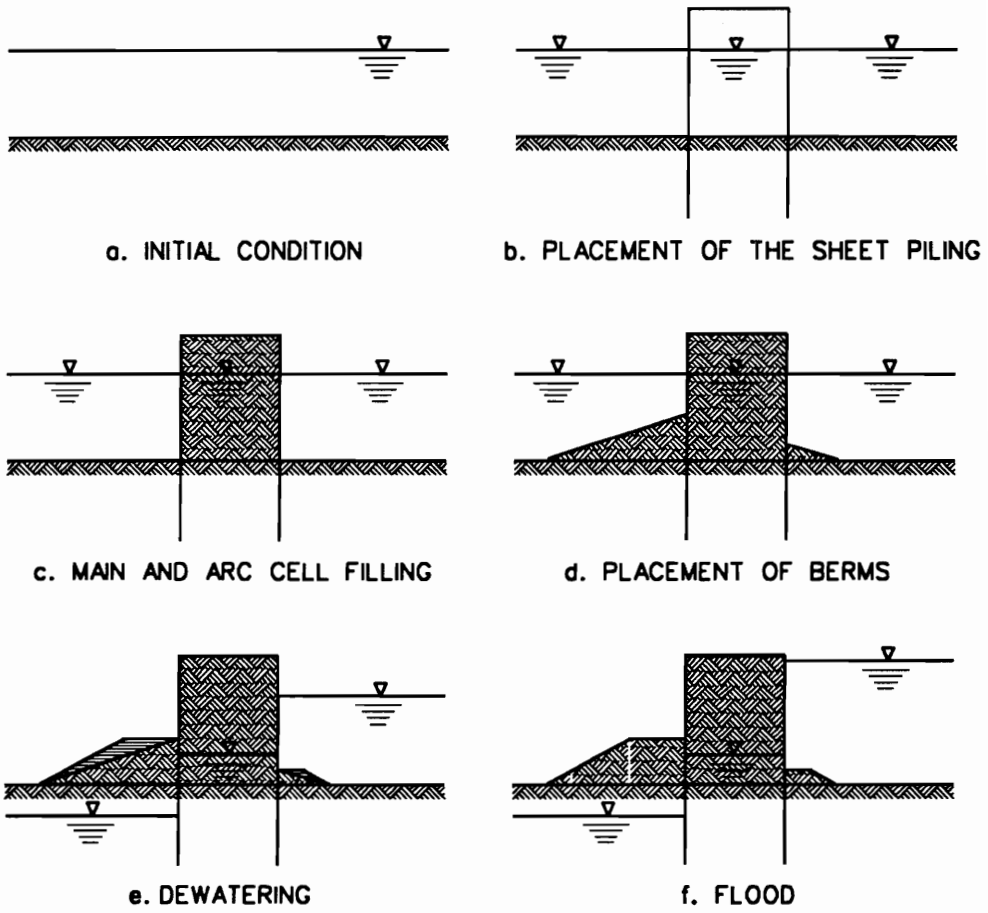

Figure 7.3: Schematic of construction simulation.

the dredgeline to the placement of the berm that is not found in the inclinometer readings. Below the surface of the berm, El 395, the inboard wall movements are greater than at the top of the cells. The predicted inboard movements below the surface of the berm are greater than the inclinometer readings. This difference in the predicted deflection from the field measurements is believed to be due to the initial shape of the cell in the field. The cells after fill placement are not perfectly shaped as assumed in the finite element model. The instrumented cells had an initial shape after filling that had a bias towards the outboard wall which was in the direction of the river flow. Above the top of the berm the predicted movements provide a favorable comparison with the inclinometer readings. The predicted outboard movements compare extremely well with the inclinometer readings.

Initial Dewatering

Figure 7.5 shows the deflections of the inboard and outboard cell walls, respectively, of the cofferdam after dewatering. Dewatering causes both cell walls to move toward the interior of the cofferdam in response to the net hydrostatic pressure on the cofferdam and the seepage forces in the foundation. The predicted incremental movements at the top of the cell as a result of dewatering are approximately 1.8 in. for the inboard and 0.6 in. for the outboard. The outboard wall exhibits smaller movements and has a different profile relative to the inboard wall.

This behavior is explained by Martin and Clough [38] by examining the manner in which the differential loading is applied to the cofferdam as a result of dewatering. During dewatering, the water level on the exterior of the cofferdam remains essentially constant. The differential head on the cofferdam is created by reducing the head on the inboard. The removal of a balancing force on the interior walls of the

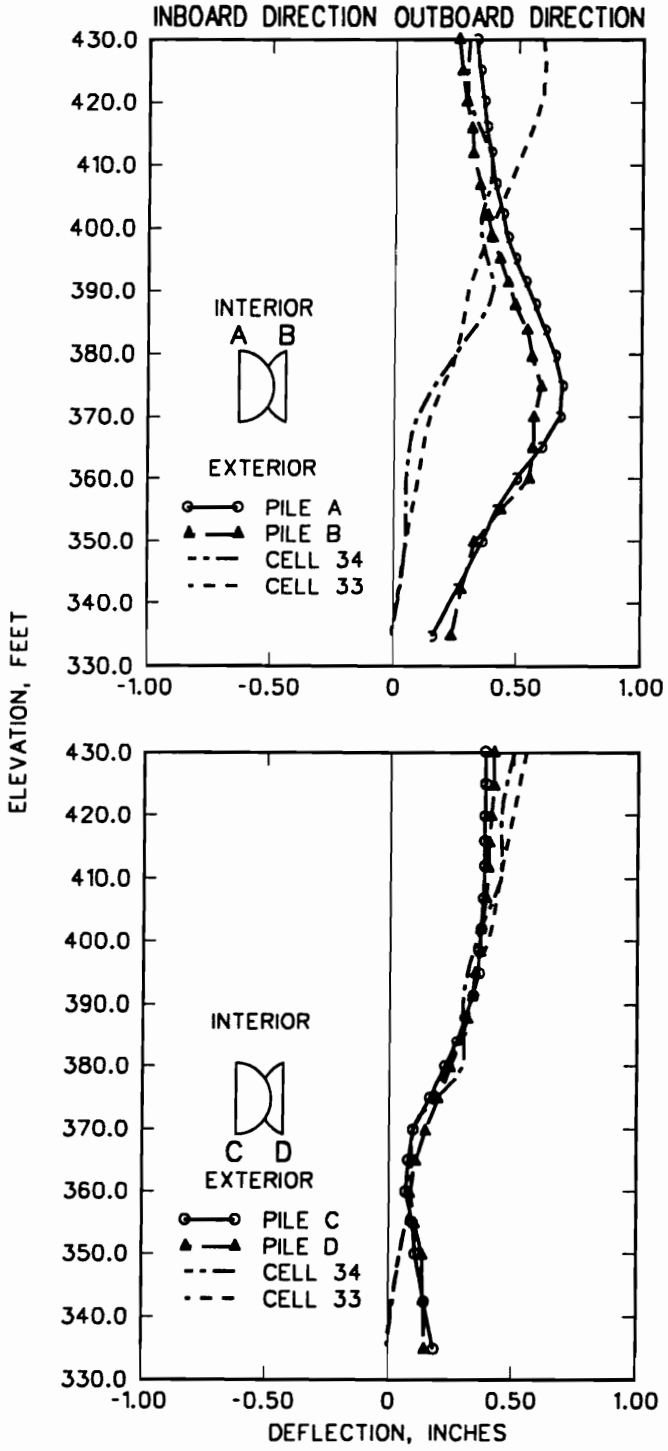

Figure 7.4: Movements of inboard and outboard walls after berm placement.

cells creates the driving forces which induces cell movements. In the finite element model, this is simulated by incrementally applying pressures to the outboard sheeting equal to pressures due to the differential head between the inboard and outboard of the cofferdam at various stages of the dewatering process. The inboard sheeting is free of any loading and moves laterally toward the interior of the cofferdam. The movement is caused by the cell fill pushing against the inboard sheeting toward the interior of the cofferdam.

The outboard sheeting is more nearly vertical in profile which is consistent with the outboard sheeting pushing against the cell fill. At the dredgeline a small reverse curvature in both the inboard and outboard wall is found. Below the dredgeline, the inboard sheeting profile is near vertical. Figure 7.5 shows that the berm limits movements and bulging of the inboard sheeting near the dredgeline and reduces the deflections between the dredgeline and the top of the berm.

River at Flood Stage

A flood was simulated by increasing the pressure on the exterior of the cofferdam by an amount equal to the difference between the differential water load at the flood level and that which it had experienced during the initial dewatering. Figure 7.6 shows the deflections of the inboard and outboard cell walls, respectively, of the cofferdam for the river at a flood stage resulting from a differential head of 62 ft.

A differential head of about 48 ft was exerted on the cofferdam at the completion of dewatering. The additional 14 ft of differential head from the rising flood waters cause both the inboard and outboard walls to translate toward the interior of the cofferdam; approximately 1.3 in. at the top of the cell and 0.5 in. at the top of the berm for the inboard cell wall and approximately 1.9 in. at the top of the cell and

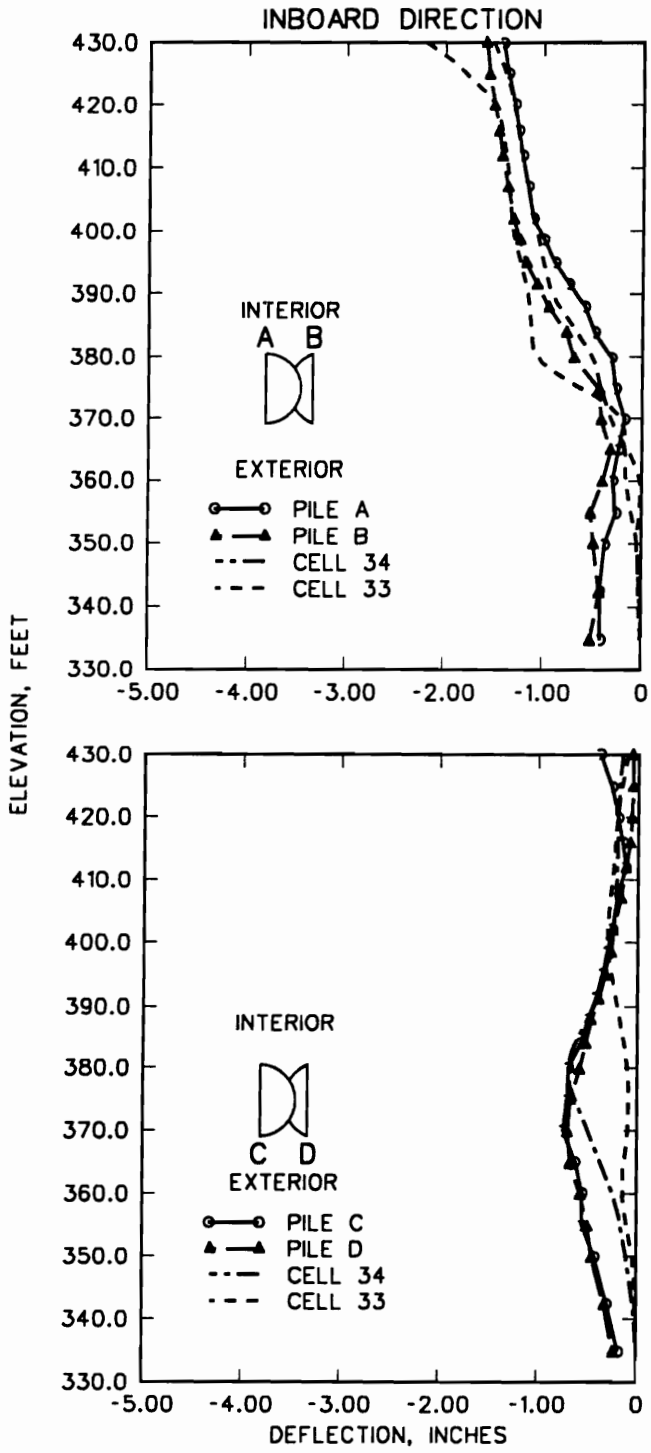

Figure 7.5: Movements of inboard and outboard walls after dewatering.

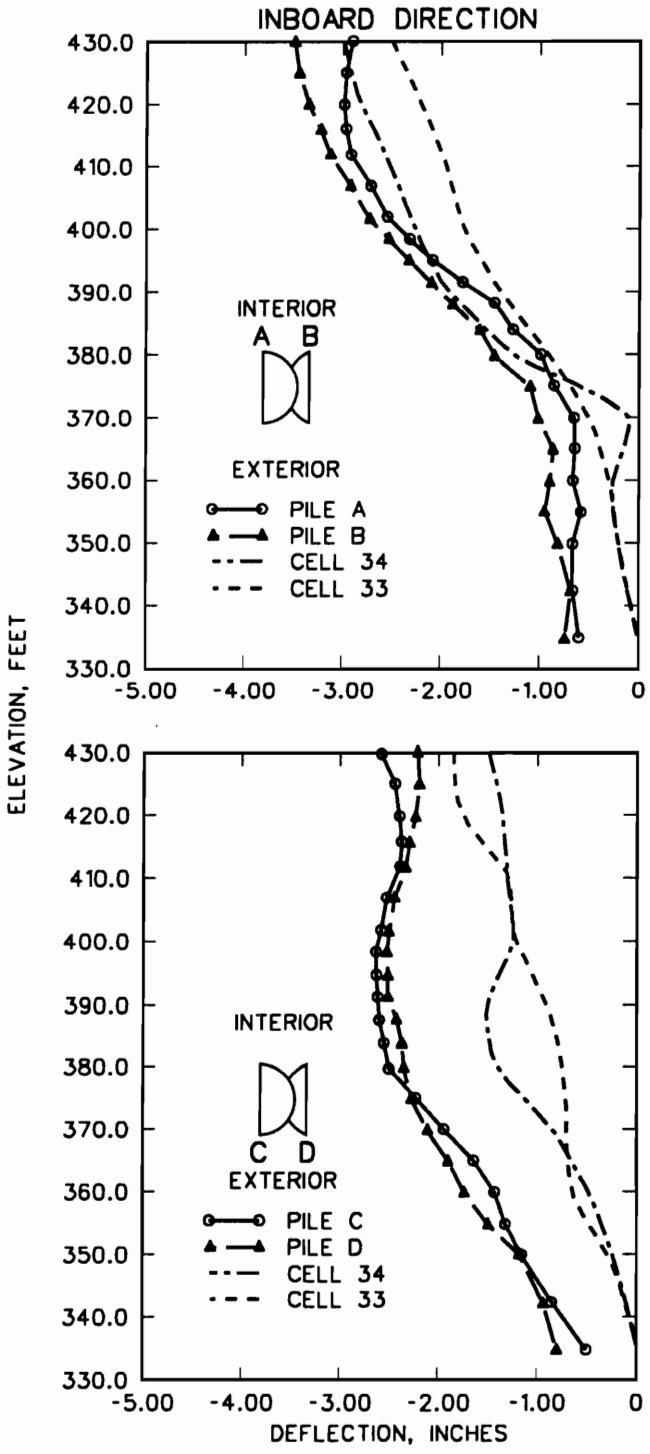

Figure 7.6: Movements of inboard and outboard walls for river at flood stage.

1.4 in. at the dredgeline for the outboard cell wall. The distinctive difference in the deformed shape between the inboard and outboard walls seen during the dewatering are also observed at this flood stage. The cell movements computed for the flood stage are greater than the movements resulting from dewatering even though the change in differential head is less during this stage of loading.

Figure 7.7 shows a comparison of the predicted and observed response of the top of the cells to the change in differential water head. Figure 7.7 also shows the average deflection of the top of the inboard and outboard cell walls as a percentage of the free height of the cell along with the ranges of values [38]. As the differential head grows larger, the deflections at the top of the cell increase for both the observed values and the three–dimensional finite element results.

Both the predicted and observed responses show that during flooding the outboard walls of the cells move more than the inboard walls. This trend is not consistent with the cell response during dewatering, where the inboard wall movements were larger. Martin and Clough [38] proposed an explanation for this reversal by relating it to the way in which the differential head is applied. They felt that the additional differential head during a flood is created by an increase in the load on the outboard wall of the cofferdam as opposed to dewatering where the differential head is created by lowering the water on the inboard walls of the cofferdam. They felt that the load on the outboard wall tended to accentuate its movements. This explanation does not seem to fully explain the differences. In the finite element analysis, both the dewatering and the flooding are simulated by applying boundary pressures to the outboard wall. Yet, the same reversal is found in the finite element results.

Another possible explanation for this phenomenon is that the greater lateral

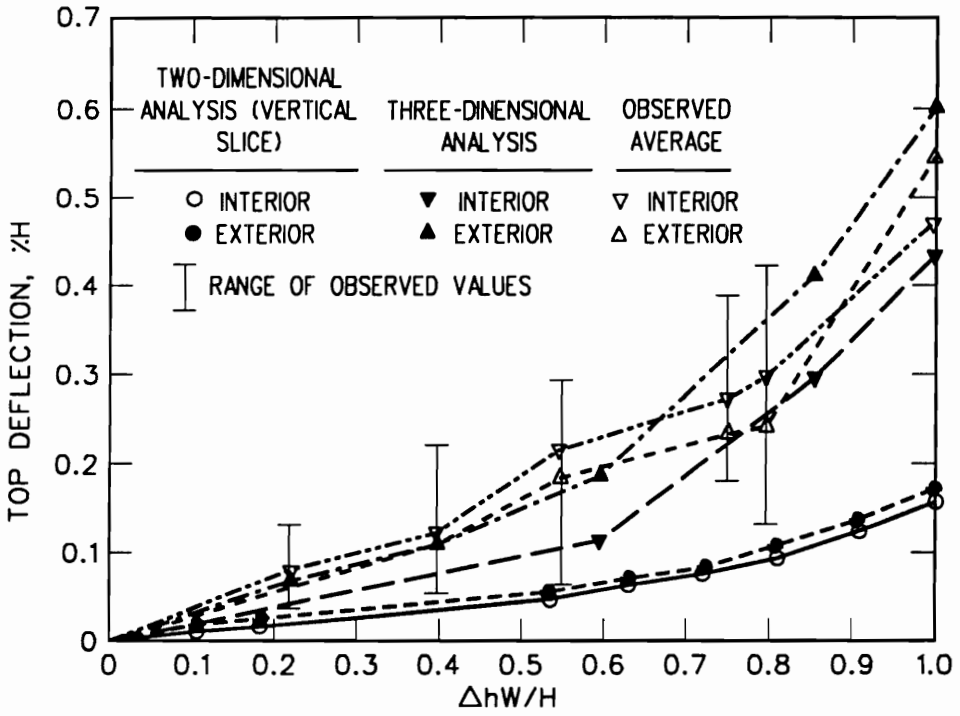

Figure 7.7: Movement of top of cell due to differential loading for Dam No. 26(R) cofferdam [38].

movement of the inboard wall of the cofferdam is a result of the lowering of the phreatic surface in the cell fill. During dewatering, the phreatic surface is lowered from a river level of El 402 to El 360 resulting in an increase of effective stresses in the cell fill. The increase in effective stresses leads to vertical settlement and lateral deformation of the cell fill. With the exception of the inboard wall above the berm, the lateral deformation is resisted not only by the sheet piling but also by the external pressures applied to the cells resulting from the berm, foundation, and water. The inboard wall above the berm is free of any external pressures, allowing the inboard wall to have a greater lateral movement toward the interior of the cofferdam than the outboard wall during dewatering. During flooding, the phreatic surface in the cell fill and the water level in the interior of cofferdam remains constant and the water level on the outboard walls is increased, resulting in a greater lateral movement of outboard walls.

Also shown in Figure 7.7 are the results from a two–dimensional finite element analysis presented in Shannon and Wilson's report [53]. They show a stiffer response than the three–dimensional finite element results to differential water loading by underpredicting the movement of the top the cell. This may be due to the two–dimensional assumptions that do not consider the geometry or the soil stresses in the third dimension.

The predicted results for the flood are for a loading condition that coincides with the greatest differential head on the cofferdam that was reported by the instrumentation readings. No instrumentation readings were available for the most severe possible loading condition of a water level to the top of the cells on the exterior of the cofferdam and a fully dewatered interior. However, it is useful to consider this case in the finite element analysis. Figure 7.8 shows the predicted deflections of the

inboard and outboard cell walls, respectively, of the cofferdam for a river flood stage resulting in a differential head of 80 ft. The additional differential head causes both the inboard and outboard walls to translate toward the interior of the cofferdam; approximately 2.0 in. at the top of the cell and 0.8 in. at the top of the berm for the inboard cell wall and approximately 2.1 in. at the top of the cell and 1.1 in. at the dredgeline for the outboard cell wall. The movements at the top of the cell for both inboard and outboard walls are essentially the same and the cumulative movements are within 10 percent of each other at the end of this stage of loading. The berm has a significant influence on the deformed shape of the inboard wall. The constraint provided by the berm restricts lateral movement of the inboard wall below and just above the top of the berm. The berm has the effect of moving the effective dredgeline to the top of the berm.

7.4.2 Interlock Force

The loading from berm placement, initial dewatering, and a river flood stage influenced the interlock forces. The maximum interlock forces changed in response to each of these changes in the loading, but the maximum interlock forces were less than those experienced during the main and arc cell filling. The magnitude of the change depended upon the specific elevation and plan location in the cell. During the river flood stage, the maximum interlock forces tended to increase slightly, but they remained less that those occurring during main and arc cell filling. The finite element analysis results show the same trends found in the instrumentation results described in the Shannon and Wilson report [55].

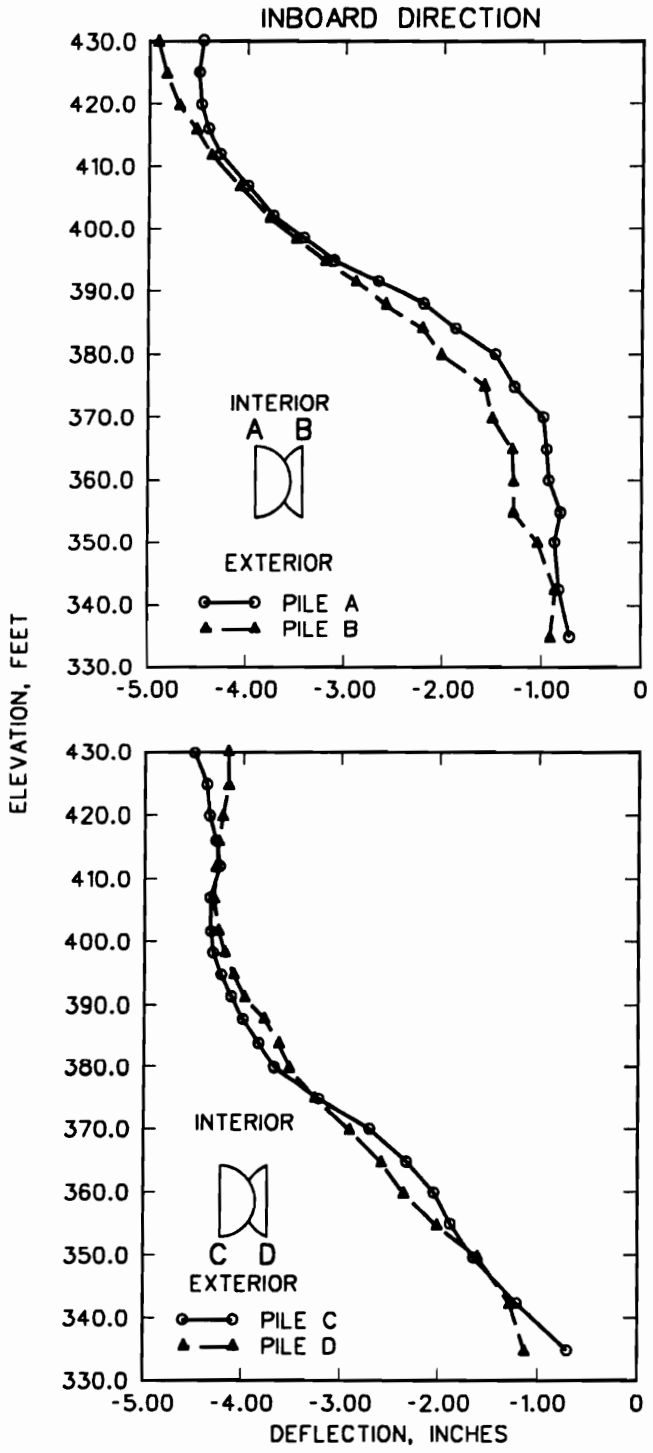

Figure 7.8: Movements of inboard and outboard walls for river at maximum flood stage.

7.4.3 Lateral Earth Pressure Coefficients

In Chapter 7, the behavior of the cofferdam during filling of the main and arc cells was studied in detail. Lateral earth pressures were investigated with respect to their influence on the interlock forces. During cell filling, changes in the lateral earth pressure coefficient adjacent to the sheet piling are directly related to changes in the maximum interlock forces. The lateral earth pressure coefficients, k, at the end of main and arc cell filling are shown in Figures 6.53, 6.55, and 6.56. The lateral earth pressure coefficients shown in these figures are oriented in the direction normal to the sheet piling.

Figure 7.9 shows the lateral earth pressure coefficients for the cell fill and surrounding soil at the end of the main and arc cell filling; values after the initial dewatering analysis in Figure 7.10. The lateral earth pressure coefficients in the x direction in the cell fill increased as a result of dewatering. The increase varies from approximately 30 to 40 percent in the upper portion of the cell to as high as 60 to 70 percent in the lower portion along the center line of the cell. Figure 7.11 shows the lateral earth pressure coefficient values during flood conditions. An additional increase in the lateral earth pressure coefficients over the values found after dewatering are seen under flood conditions.

In Chapter 2, Terzaghi's vertical shear method of analysis [60] for internal stability was presented. In this method, the lateral earth pressure is the key component in providing the shear resistance in the cell fill, and, as indicated, there has been controversy about the appropriate value of the lateral earth pressure coefficient to be used in the analysis.

Terzaghi suggested that a lateral earth pressure coefficient, k, with a value of

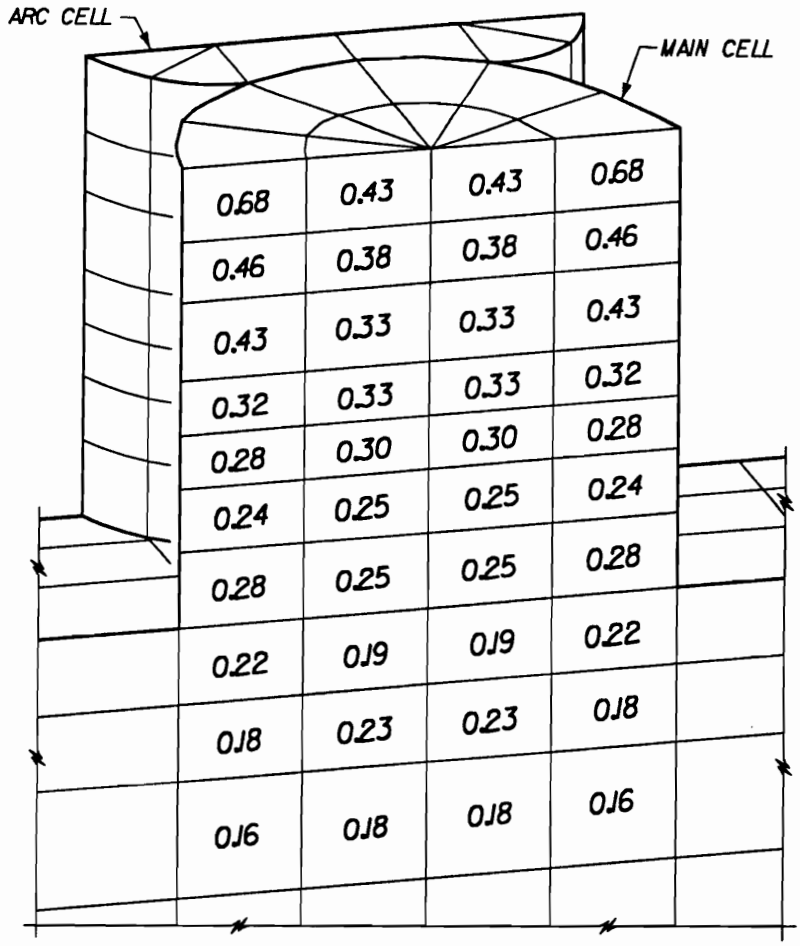

Figure 7.9: Lateral earth pressure coefficients in x direction at the end of main and arc cell filling.

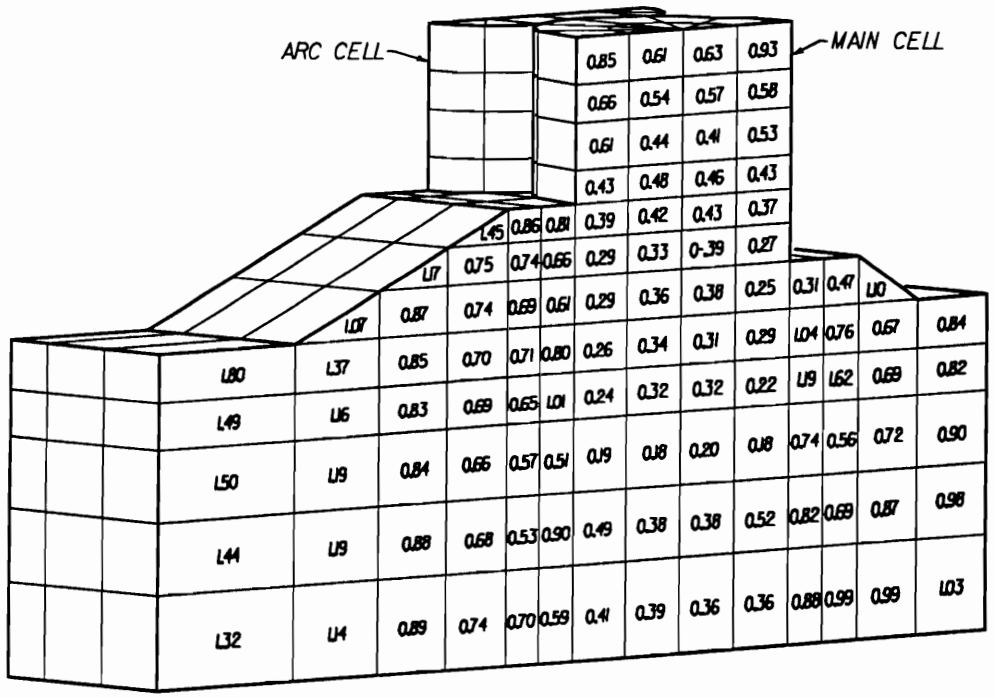

Figure 7.10: Lateral earth pressure coefficients in x direction after the initial dewatering.

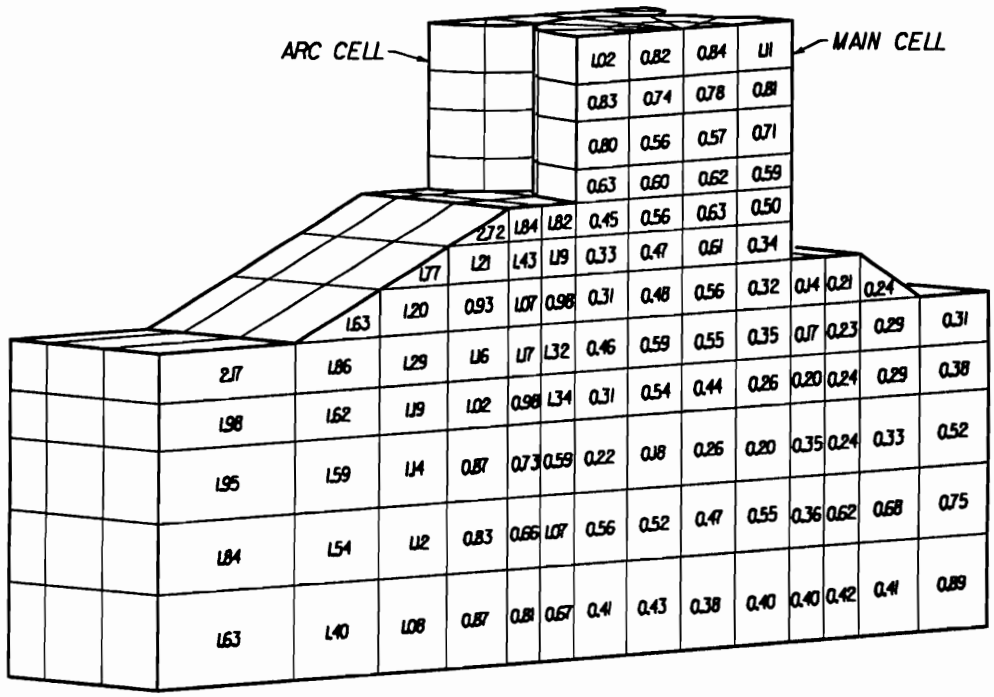

Figure 7.11: Lateral earth pressure coefficients in x direction during flood conditions.

0.4 be used to compute the normal force on the shear plane at the center of the cell. Krynine [32] pointed out that it was incorrect to use the Rankine active earth pressure coefficient to calculate vertical shear resistance in the cell fill because the failure plane (the vertical plane) cannot be a principal plane since shear stress acts on it. Terzaghi [60] concurred with Krynine's point and agreed that the lateral earth pressure coefficient would be greater than 0.4, possibly as high as 0.6.

Field observations by Schroeder et al. [50] have shown that k may be as high as 0.7 in cells used as bulkheads. In subsequent model tests, Schroeder and Maitland [51] argued that the overturning moment applied to the cell tends to compress the fill significantly on the inboard side, and, as a result, the lateral earth coefficient is appreciably increased. They suggested using $k = 1$, a value which yielded calculated values of ultimate overturning moment in good agreement with values obtained experimentally in model tests. Schroeder [49] was led to comment that the Schroeder and Maitland approach did not provide a fully rational explanation for the use of $k = 1$.

The results of the finite element analysis reported here show that the lateral loads applied to the cell from the differential water level causes an increase in the lateral stresses in the cell fill. This increase was also seen in the two–dimensional finite element analysis performed by Singh [56]. Unfortunately, the increase is not uniform throughout the cell fill making it difficult to draw a direct correlation to an increase in the lateral earth pressure coefficient that should be used in the vertical shear analysis.

7.4.4 Soil Stresses

The increase in the horizontal stress in the cell fill increases the confining stresses in the cell fill. Figures 7.12 and 7.13 show the mobilized shear strength in the soil after initial dewatering and during flood conditions, respectively. The effect of the increase in confining stresses is seen in these figures by the decrease in the level of mobilized shear strength in the cell fill as the differential water level changes from 48 ft at the initial dewatered stage, Figure 7.12, to 80 ft at the extreme flood stage, Figure 7.13.

The increase in confining stresses and the resulting decrease in mobilized shear strength with increasing differential water loading is the principal reason that cellular cofferdams can withstand extremely high lateral loads and lateral deformations without collapsing [35, 38, 60].

7.5 Response to Extreme Differential Loading

The second–stage cofferdam for Lock and Dam No. 26(R) was designed to provide a margin of safety against failure. The stresses and deflections of the second–stage cofferdam are well below those occurring as the cofferdam approaches failure. To study the response of a cellular cofferdam under extreme conditions, the lateral loads on the second–stage cofferdam model were increased by applying nine stages of load equal to one to nine times the lateral load used for the final flood condition presented in the preceding section.

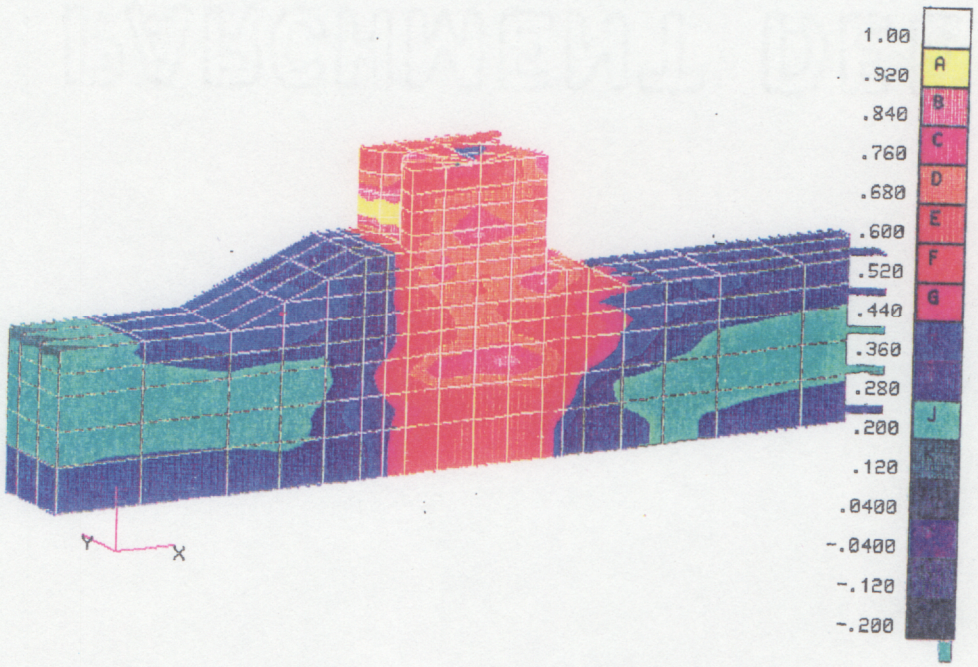

Figure 7.12: Mobilized shear strength after initial dewatering.

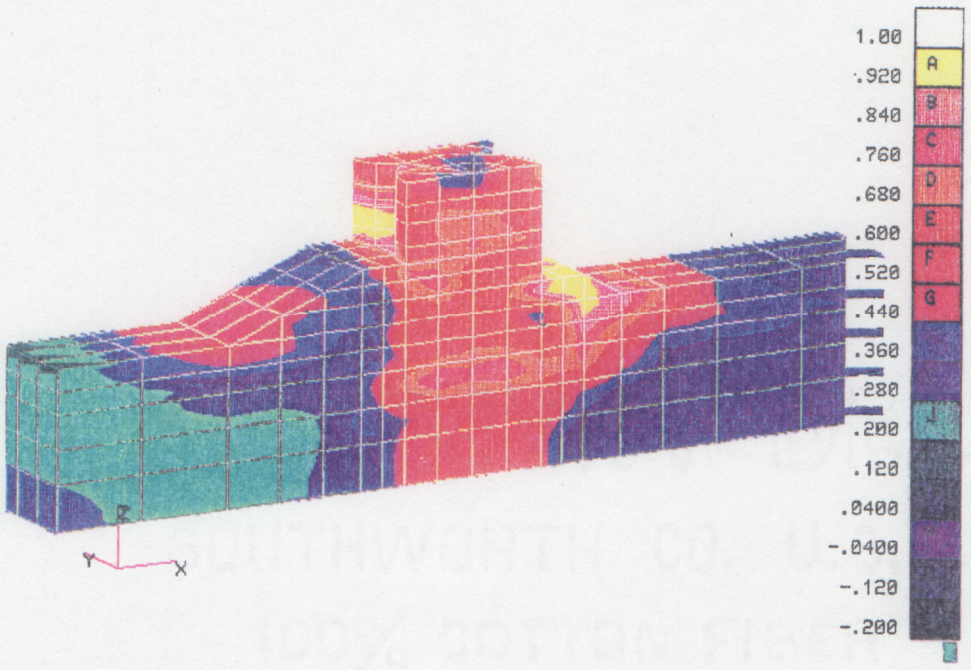

Figure 7.13: Mobilized shear strength during flood conditions.

7.5.1 Load–Deflection Response

The deflections of the sheet piling at the top of the cell for different multiples of the maximum flood lateral loading are plotted in Figure 7.14. The average deflection at the top of the cell for the maximum flood load, a fully dewatered interior and water to the top cells on the exterior, is approximately 4.5 in. The average deflection increases almost linearly from 4.5 in. for the maximum flood load to 18 in. for seven times the normal flood load. For loading greater than seven times the maximum flood load, the deflections increase more rapidly. Continued loading would result in greater deflections and eventually leading to the collapse of the cell.

Figure 7.15 shows the deformed shape of the model for a loading of nine times the maximum flood load. The main and arc cells move laterally and rotate towards the inboard. The greatest movements occur on the inboard wall above the top of the berm.

7.5.2 Lateral Earth Pressure Coefficient

Figure 7.16 shows the lateral earth pressure coefficients for the cell fill and surrounding soil after loading the cofferdam to nine times the maximum flood load. The lateral earth pressure coefficients in the x direction along the center line of the cell fill have significantly increased from those found under the maximum flood load, Figure 7.11. The increase varies from approximately 100 to 200 percent with an average at approximating 100 percent. The lateral earth pressure coefficients for the fill adjacent to the sheet piling, in general, decreased with increasing load. This decrease was accompanied with a decrease in the vertical stresses in this same region which results from the high level of shear stress between the sheet piling and

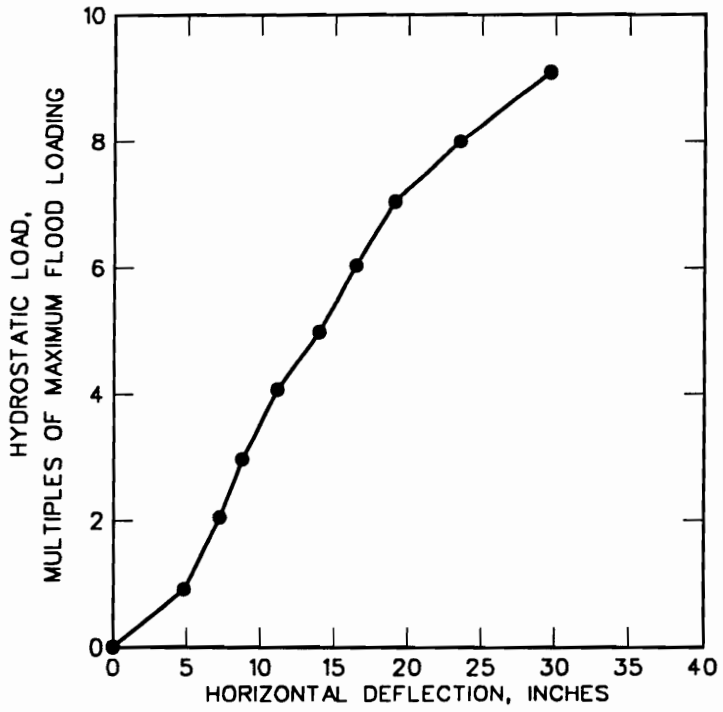

Figure 7.14: Lateral load versus deflection of top of sheet piling.

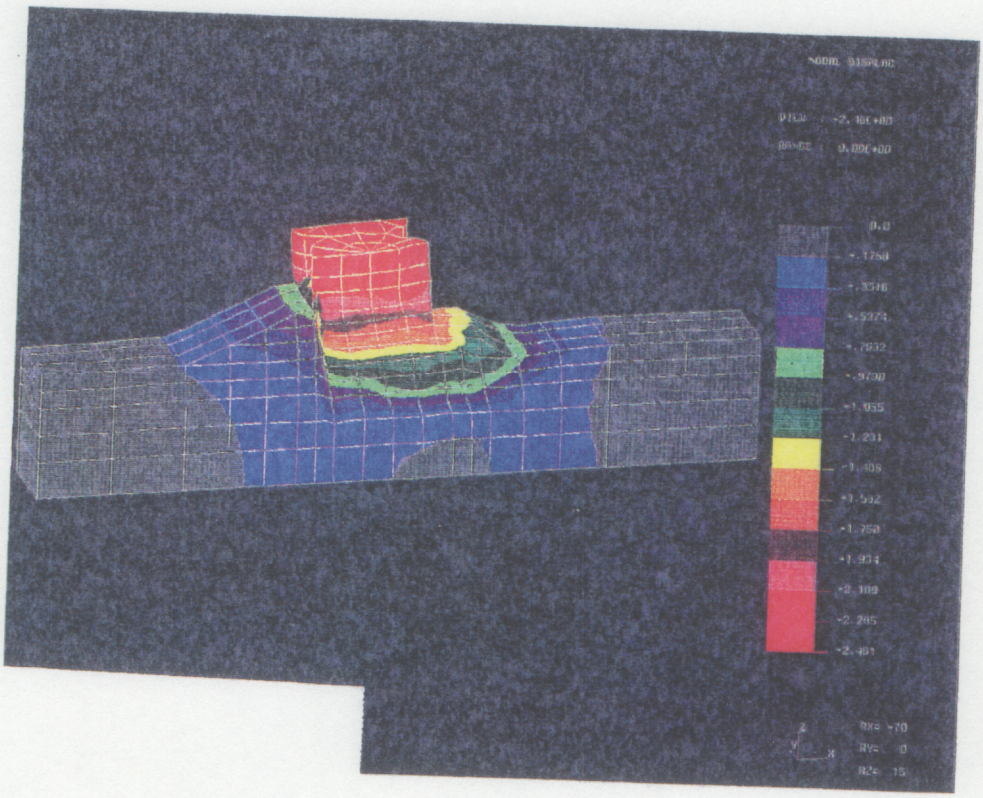

Figure 7.15: Deformed shape of model for nine times the normal flood load.

the cell fill.

These results further demonstrate the influence that the applied water load on the outboard of the cofferdam has on the confining stresses in the cell fill. In a reexamination of the results of his model studies, Schroeder [49] showed good agreement between the factor of safety computed with a new vertical shear analysis which includes an additional normal force on the vertical shear plane equal to the external applied load. The conventional vertical shear analysis proposed by Terzaghi [60] (Eq. 2.11) calculates the factor of safety as

$$FS = \frac{\gamma b H^2 (K_c \tan\phi + K_i f)}{3M} \tag{7.1}$$

The new procedure proposed by Schroeder calculates the factor of safety as

$$FS = \frac{\gamma b H^2 (K_c \tan\phi + K_i f) + \sum P \tan\phi}{3M} \tag{7.2}$$

where $\sum P \tan\phi$ is equal to the shear resistance on the vertical shear plane due to the external applied loads on the cofferdam. Using the Lock and Dam No. 26(R) cofferdam as a basis and keeping all similar terms the same, Figure 7.17 shows how the factor of safety from the vertical shear analysis with the external water force added as a normal force on the vertical shear plane as suggested by Schroeder [49] and the conventional analysis varies with increasing load by multiples of the maximum flood load. For the maximum flood load, the factor of safety is 2.94 as compared with 1.66 from the conventional analysis where the normal force acting on the centerline of the cell is computed using only the vertical overburden pressure in the cell fill and Krynine's lateral pressure coefficient. For Schroeder's approach, as the load increases, the factor of safety decreases, but at a lesser rate than the conventional analysis. Using the external water force added as a normal

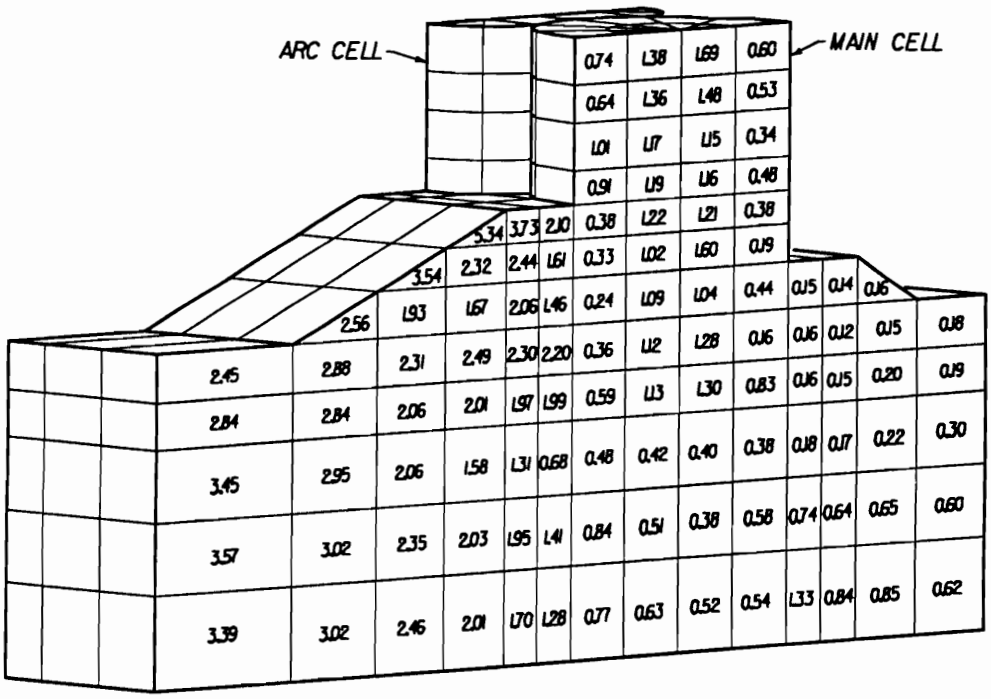

Figure 7.16: Lateral earth pressure coefficients in x direction at nine times the maximum flood load.

force on the vertical shear plane is the equivalent of having a lateral earth pressure coefficient of approximately 0.8 and 5.4 for the maximum flood load and nine times the maximum flood loading, respectively. The finite element analyses showed an increase in the lateral earth pressure coefficients for the cell, 100 to 200 percent, but not the 600–percent increase found in this vertical shear analysis.

Using the same basic cofferdam configuration, an alternative loading condition was examined. The height of cell and external water were raised and the factor of safety of vertical shear using Schroeder's and the conventional approach were determined. The results are shown in Figure 7.18. This shows that a cell with a diameter of 63 feet could reach a height of 140 feet before Schroeder's approach would say that failure would occur. The conventional approach would allow only a height of 108 feet. The equivalent lateral earth pressure coefficient from Schroeder's approach would be approximately 1.5.

7.5.3 Soil Stresses

Figures 7.19 and 7.20 show the mobilized strength shear in the soil at two and nine time the maximum flood load, respectively. Both figures show that the shear strength is fully mobilized in the soil outside the cell on the outboard side. This is consistent with the development of active lateral earth pressures in this area. In Figure 7.19, the mobilized shear strength ranges from a high of 0.9 in a small area adjacent to the berm to a low of 0.29 at the top of the cell. Along the centerline of the cell, the mobilized shear strength ranges from approximately 0.45 to 0.61. Figure 7.20 shows that the shear strength of soil is fully mobilized in the cell fill adjacent to the berm and outside the cell in the berm. The zone of high shear strength mobilization has greatly increased over that shown in Figure 7.19 for two

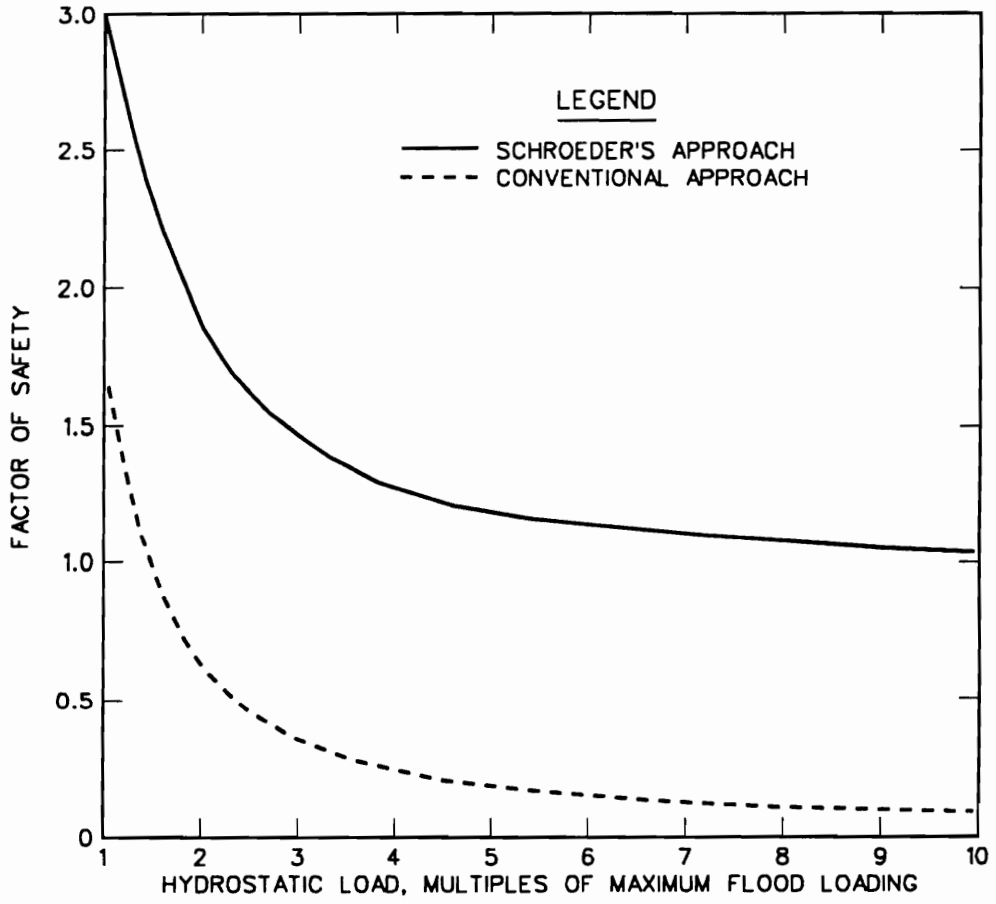

Figure 7.17: Vertical shear factor of safety versus multiples of normal flood load.

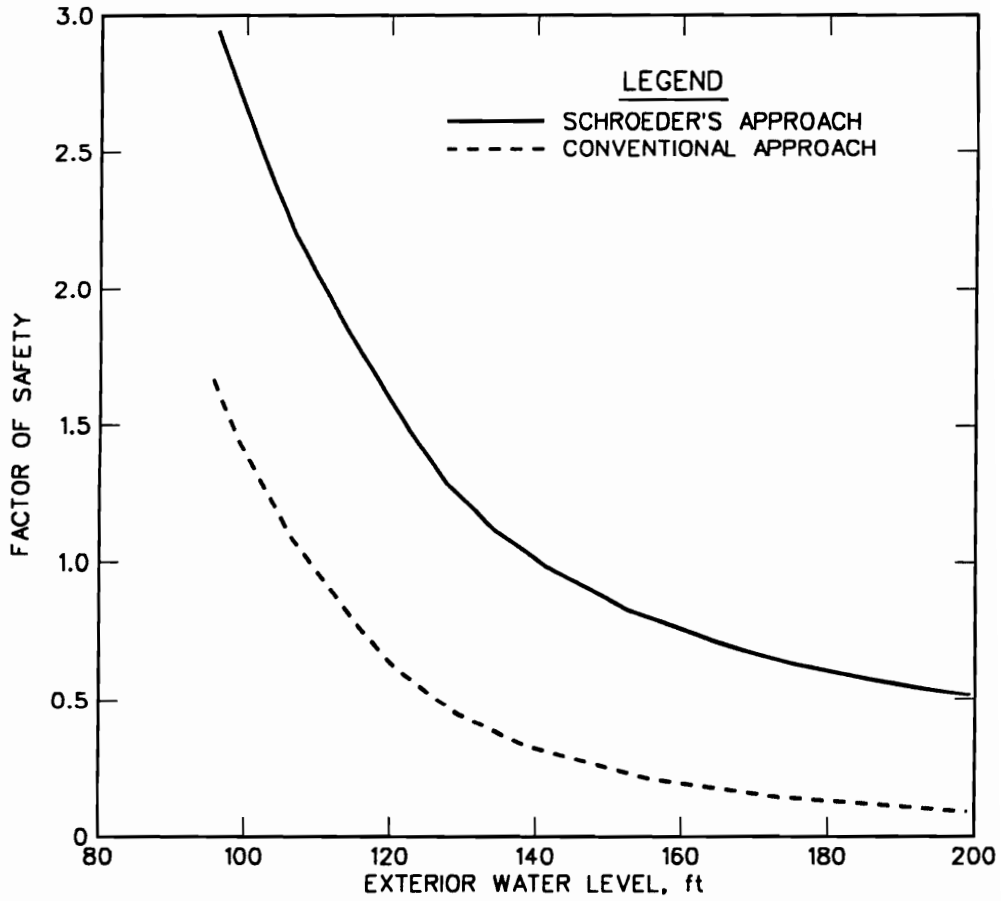

Figure 7.18: Vertical shear factor of safety versus water level.

times the maximum flood load. The mobilized shear strength along the centerline of the cell for nine times the normal flood load ranges from approximately 0.5 to 0.7.

There has been a shift in the mobilized shear strength for two times to nine times the maximum flood load. The mobilized shear strength has decreased slightly in the fill at the top of the cell and has increased significantly near the dredgeline as the loading has increased. This change is due to the shape of the pressure distribution used to define the loading. The pressure distribution on the cell is always zero at the top of the cell and the loading on the cofferdam is increased by increasing the slope of the pressure distribution. Thus, the pressures on the cell are greatly increased near the dredgeline. This also only increases the moment applied to the cofferdam by the equivalent lateral force from the pressure distribution with no change in the moment arm.

These results show that the cofferdam would have failed in sliding rather than by collapse due to shear failure of the cell fill.

7.6 Summary

The three–dimensional finite element analyses have provided new insight into the behavior of cell fill during differential water loading. First, the lowering of the phreatic surface in the cell fill during dewatering causes the inboard sheeting to move toward the interior of the cofferdam more than the outboard sheeting moves. The lowering of the phreatic surface increases the effective stresses in the cell fill which leads to vertical settlement and lateral spread of the unrestrained inboard wall. This lateral spread of the inboard wall coupled with the overall movement

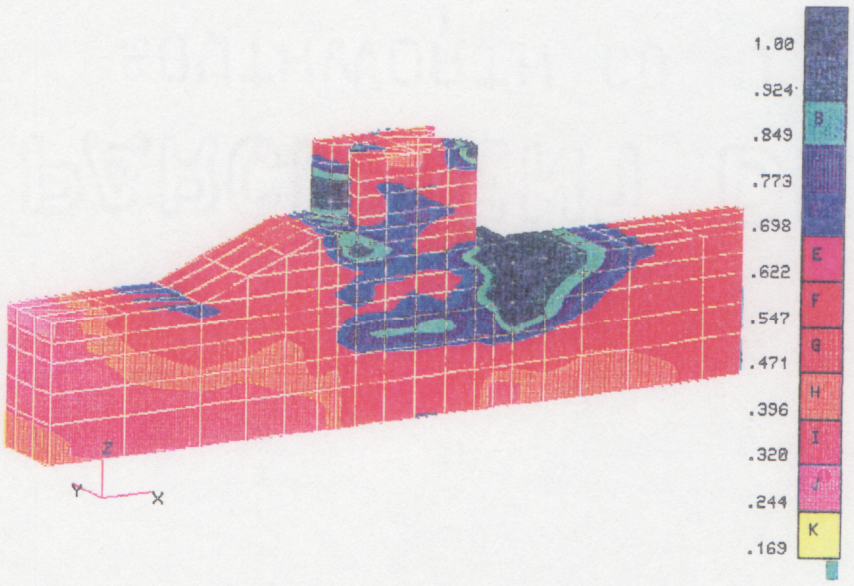

Figure 7.19: Mobilized shear strength at two times normal flood load.

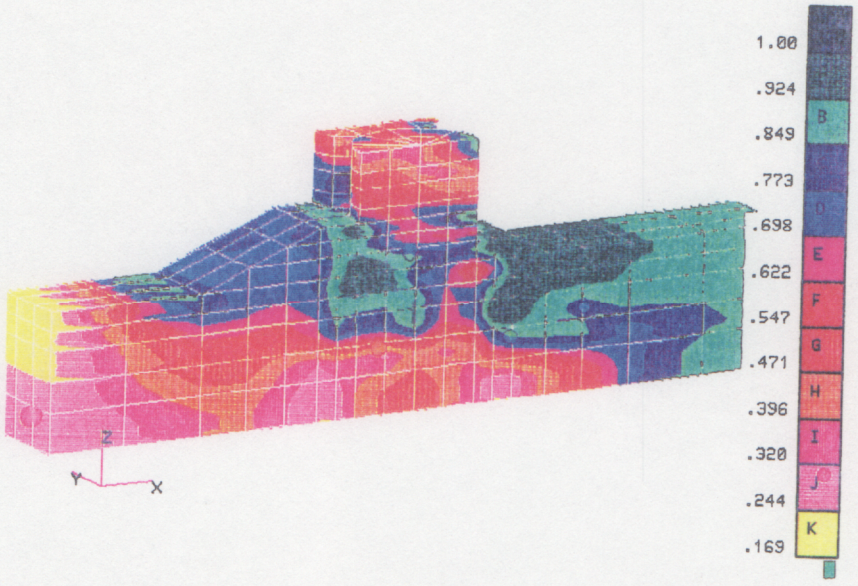

Figure 7.20: Mobilized shear strength at nine times normal flood load.

toward the interior cofferdam from the differential water loading results in a greater movement of the inboard wall than the outboard wall. Secondly, the finite element analysis results show that the lateral loads applied to the cell from the differential water level causes an increase in the lateral earth pressure coefficients, thus the horizontal stresses in the cell fill are increased. This increase in horizontal stresses increases the confining stresses in the cell fill. The effect of the increase in confining stresses results in a decrease in the level of mobilized shear strength in the cell fill as the differential water level increases.

The increase in confining stresses and the resulting decrease in mobilized shear strength with increasing differential water loading explains why the cellular cofferdam can withstand extremely high lateral loads and lateral deformations without collapsing.

Schroeder [49] proposed a new procedure to account for this increase in confining stresses in the conventional vertical shear analysis by adding the force due to the external differential water as a normal force on the vertical shear plane through the cell fill. While this proposed approach recognizes that the differential water loading increases the shearing resistance of the cell fill, it significantly underestimated the capacity of a cofferdam to endure differential loading.

Chapter 8

SUMMARY AND CONCLUSIONS

Conventional design methods for sheet–pile cellular cofferdams were developed in the 1940's and 1950's based primarily on field and experimental observations. The analytical techniques of the day were unable to account for the complexities involved. The procedures used only rudimentary concepts of soil–structure interaction which do not exhibit the true response of the cofferdam for most circumstances. Furthermore, no attempt were made to determine the possible cofferdam deformations that could be expected under the various loading conditions. This last deficiency is an important aspect in performance when deformations must be limited or when the deformations are used to monitor the field performance of the cofferdam.

Computational capabilities have greatly improved since the early investigations. Many of the complexities that were ignored or crudely approximated can now be considered through the use of the finite element method. Early efforts in the finite element analysis of cellular cofferdams were performed without due consideration

of the soil–structure interaction involved in the sheet pile–soil system. Clough and his associates [7, 8] first demonstrated that with proper consideration of the soil–structure interaction effects, the finite element method could be a powerful tool for the investigation of cellular cofferdam behavior. Importantly, it provided the means to predict cofferdam deformations which were lacking in previous methods. Considerable success was obtained in predicting the response of the instrumented cofferdam for the Lock and Dam No. 26(R) project. The results also showed that most conventional techniques were overly conservative and led to more costly designs than necessary. While attempts have been made to generalize the findings of these analyses, this could not be done since uncertainties remained about the assumptions made in the two–dimensional models. The only way to address the uncertainties was through a three–dimensional analysis.

The focus of this investigation was to develop a new three–dimensional soil–structure interaction finite element code for cellular cofferdam modeling and apply the new code to study the behavior of the first– and second–stage cofferdams at Lock and Dam No. 26 (R). The purpose of the work was to allow a more complete assessment of the validity of existing cofferdam analysis and design procedures than had been possible in the past.

8.1 Development of New Three–Dimensional Finite Element Code

An important decision faced in undertaking a three–dimensional finite element analysis was whether to use an existing general–purpose finite element code. After study,

it was found that as general as these codes may be, they were developed with a certain class of problems in mind. These codes lacked one or more of the following modeling capabilities necessary for the analysis of a cellular cofferdam: nonlinear soil behavior, incremental fill placement, initial gravity stress generation, interface elements, seepage effects, and construction simulation. In addition, they contained numerous other options not needed for the cofferdam analysis. Furthermore, the commercially available codes required a payment of fees for their use and are difficult, if not impossible, to modify. It was decided to develop a new code which could accommodate for the unique aspects of the cofferdam problem.

The philosophy for developing the new three–dimensional finite element code was to do only the things necessary to have a functioning code which could be verified and documented rapidly so that it could used to test critical phases of the Lock and Dam No. 26(R) cofferdam. Also, the modeling procedures were to be kept in line with the two–dimensional codes used in earlier cofferdam studies when possible, so that the two–dimensional codes could be validated. Further, the code would be kept flexible so that changes could be made in the future.

Once it was decided to develop a code, and a philosophy was established, the next step was to formulate the necessary requirements for the code. In keeping with the development philosophy, the capabilities of the two–dimensional code, **SOILSTRUCT**, were used to form the initial requirements for the three–dimensional code.

To accurately model a sheet–pile cellular cofferdam through its construction and operation, the key aspects that are fundamental to its behavior must be represented as closely as possible. It was felt the code should have the capability to:

- Model the geometry of the cellular cofferdam.

- Model the anisotropic response of the sheet–pile assemblage.
- Model the interaction between the sheet piles and the soil.
- Model the nonlinear response of the soil.
- Determine the initial state of stress in the soil prior to construction.
- Simulate the process of construction of the cellular cofferdam.
- Model the various events experienced during the operation of the cofferdam.

To simulate these aspects, a number of features were required in the code. These included:

- Higher–order isoparametric elements to allow the actual representation of curved cell geometry.
- Three–dimensional interface elements to allow relative movements to occur between the sheet piling and the soil.
- Three–dimensional shell and/or membrane elements to model the sheet piling with anisotropic capabilities to allow for different Young's modulus values in the horizontal and vertical directions.
- A three–dimensional nonlinear constitutive model to represent the stress–strain response of the soil.
- Procedures to simulate the construction process of the cofferdam. This includes the calculation of initial stresses in the foundation, placement of the sheet pile and cell fill, dewatering of the interior of the cofferdam, placement of the berms, and raising of the river level on the exterior of the cofferdam.

Knowing that the development of a three–dimensional finite element code would require a significant effort in both time and money, consideration was given to modifying an existing code that had some of the features needed for the cofferdam analysis. Instead of using one of the existing general–purpose finite element codes, the decision was made to develop a new code by enhancing a basic linear elastic code written by Kasali and Clough [29] . The code written by Kasali and Clough has many of the features needed for the analysis of a sheet–pile cellular cofferdam, including the use of a higher–order three–dimensional solid element and an efficient element assemblage and equation solution routine. While the Kasali and Clough code met the basic requirements for this study, it required considerable modification for three–dimensional analysis of sheet–pile cellular cofferdams.

8.2 Additions to The Element Library

One of the most important aspects in soil–structure interaction analysis is the simulation of the behavior of the interface where the soil and the structure meet. To model this phenomenon, a new three–dimensional interface element was developed and implemented. The new interface element used relative displacements as independent degrees of freedom. This formulation avoids the possible ill conditioning of the stiffness matrix due to very large off–diagonal terms or very small diagonal terms which can occur in other formulations. Advantages of the new interface element were demonstrated in terms of improved stability and modeling of soil–structure interaction.

The geometry of the cofferdam required the use of wedge–shaped elements in locations to generate a smooth consistent mesh. In the process of verifying the

code, it was discovered that the quadratic forms of the brick element in the original code would not yield the correct displacements when they degenerate to a wedge element. To solve this problem, a procedure was implemented that modified the serendipity–shape functions to accommodate the degeneration of the brick–type element.

The small cross-sectional thickness of the sheet piles, 0.5 in., and the large number of elements needed to model the problem made it necessary to have a shell element in the new code. The presence of such an element simplifies mesh generation around the connection of the arc cell to the main cell. A functional shell element was selected which allows for:

- Nodes only at the midsurface of the element.
- Higher–order shape functions to approximate the curved geometry of the cells.
- Anisotropic stress–strain properties to allow for a different Young's modulus value in the tangential and vertical direction.

8.3 Three–Dimensional Soil Model

For the analysis of the cofferdam, it was important to capture the key aspects of the soil behavior and the parameters that control that behavior within a constitutive relationship. In keeping with the general philosophy for developing the finite element code, the constitutive model for the soil was to be of the same order of complexity as the one employed in the finite element code, **SOILSTRUCT**, used in the two–dimensional analyses of the Lock and Dam 26(R) cofferdam. **SOILSTRUCT** uses a version of the Duncan–Chang model which is often referred to as the hyperbolic

model because a hyperbola is used to approximate the relationship between shear stress and strain during primary loading.

A new three–dimensional constitutive model for soil was developed based on the variable moduli concept. The primary criteria for the model were: to keep it simple, conceptually similar to the Duncan–Chang model, and to have parameters definable by commonly used laboratory tests. The three important characteristics of the stress–strain response of soils that the model had to emulate were nonlinearity, stress–dependency, and inelasticity.

The new model was formulated in terms of the tangent shear modulus, G_t, and bulk modulus, K_t. For the tangent shear modulus, it was assumed that the relationship between shear stress and strain could be represented by a hyperbolic curve, and the stiffness was dependent on the mean normal stress and the shear stress ratio. For the tangent bulk modulus, it was assumed that the relationship between mean normal stress and volumetric strain could be represented by power function, and the stiffness was a function of the mean normal stress.

To assess the new soil model and refine the parameters of the model, the three–dimensional finite element code with the new constitutive model was used to predict the stress–strain response from the compression and extension triaxial test and cubical shear tests. The differences in predictions of the cubical shear test results between the two–dimensional and three–dimensional soil models led to several interesting discoveries. First, even though the shear strength determined from compression and extension tests was the same, the stiffness of the stress–strain curves was different. The differences were not great, but they were significant. Secondly, the stiffness parameters that matched the extension tests also gave the best match to the cubical shear tests. Finally, the difference in the formulation of the three–dimensional model

in terms of shear and bulk moduli from that used in the two–dimensional model in terms of Young's modulus and Poisson's ratio provided a significant advantage for the three–dimensional model in predicting the cubical shear tests.

8.4 Analysis of an Isolated Main Cell

The behavior of the second–stage Lock and Dam No. 26(R) cellular cofferdam was analyzed for the filling conditions. This analysis allowed confirmation of the basic formulation of the elements and the incremental analysis procedure used in the new finite element code and provided verification of the new three–dimensional constitutive soil model.

The radial deflections computed by the new three–dimensional code compared well with two–dimensional finite element results. Predicted distributions of interlock forces were comparable to those from two–dimensional axisymmetric finite element results and compared well with the mean of the instrumentation measurements. The location of the maximum interlock force approximately coincided with the location of the maximum bulge in the sheet–pile cell wall. Arching in the cell fill had a substantial effect on the lateral earth pressures applied to the sheet–pile cell walls. In large part, the arching was attributable to friction developing between the sheet piles and the cell fill. Lateral earth pressures in the cell were above active values in the upper to midportion of cell fill but less than active in the lower portion of the cell. Arching served to reduce the effective vertical stresses from the gravity conditions throughout the cell fill.

A general conclusion from the study of the isolated main cell problem is that the three–dimensional and two–dimensional analyses predicted essentially the same

response of the isolated main cell, and the results are supported by the instrumentation measurements. These analyses provided confidence in the new code for its application to more complex aspects of the cofferdam.

8.5 Analysis of Main and Arc Cells During Filling

After confirmation of the new three–dimensional finite element code by the study of the isolated main cell problem, the code was used to study the filling of the main and arc cells. This problem is a three–dimensional problem that no two–dimensional analysis is fully capable of modeling. The point of primary interest is the effect of the arc cell filling on the interlock forces in the common wall. This has been studied with the two–dimensional generalized plane strain finite element analyses [8, 33, 53] which assume that both the main and arc cells are filled simultaneously. This is not the actual case in the field. The three–dimensional analyses used a scenario that has the main cell being filled first, followed by the filling of the arc cell.

At completion of the filling of the main cell, the analyses revealed that the deformations of the sheet piling were generally radial in direction (normal to the sheet piling), as in the isolated main cell analyses, but are slightly smaller in magnitude due to the closest of the side boundary of the model. The interlock forces were also less than those reported in the isolated main cell analyses. The reason for this is that a higher degree of arching is taking place in the cell fill for this model.

After the filling of the arc cell, the cell movements were no longer simply radial as would be expected. They varied depending on their location with respect to arc cell, but are in the range of observed values at Lock and Dam No. 26(R). The

interlock forces in the main cell were approximately the same as those reported in the isolated main cell analyses, although they were increased over those reported at the end of main cell filling. The interlock forces in the common wall were 29 to 35 percent higher than those in the main cell. These interlock forces in the common wall were less than those calculated by conventional methods and compare well with the measured values at Lock and Dam No. 26(R). The interlock forces in the arc cell were significantly less than those found in the main cell. This can be attributed to the lower lateral earth pressures in the arc cell due to the high level of arching taking place. This high level of arching results from the small size of the arc cell.

The arching in the cell fill in the three–dimensional analyses is believed to be one of the reasons that the generalized plane strain model is unable to accurately predict the interlock forces in the common wall. A second factor is the limitation of assuming simultaneous placement of the main and arc cell fill in the generalized plane strain model. The filling of the main cell in three–dimensional analyses has the effect of stiffening the main cell prior to the arc cell fill placement and altering the overall response of the model as compared with the general plane strain analysis. Finally, the generalized plane strain model is unable to consider the three–dimensional response of the soil.

8.6 Differential Loading of the Cofferdam

Following modeling of the filling, the three–dimensional analysis of the second–stage Lock and Dam No. 26(R) cofferdam was used to simulate the cofferdam under differential loading due to initial dewatering of the interior of the cofferdam and changes in river levels. The second–stage Lock and Dam No. 26(R) cofferdam was

modeled from the time of berm placement and initial dewatering through a major flood event. The deflections of the cofferdam were compared to the survey data collected from the second–stage cofferdam and the instrumentation results from the first–stage cofferdam. Changes in stresses were reported and related to the overall performance of the cofferdam. The three–dimensional finite element model was also loaded to near collapse to study the behavior of cofferdams under extreme loading conditions. The deflections and the related stresses were examined to explain the unusual resistance of cellular cofferdams to lateral loads.

The three–dimensional finite element analyses provided new insight into the behavior of cell fill during differential water loading. The most significant finding was that the lateral loads applied to the cell from the differential water level cause an increase the horizontal stresses in the cell fill. In turn, this increased the confining stresses in the cell fill. The increase in confining stresses had the positive effect of lowering the level of mobilized shear strength in the cell fill, under conditions covering a maximum flood load (water to the top of the cells) to nine times the maximum load. The decrease in mobilized shear strength in the cell fill with increasing differential water loading explains why the cellular cofferdam appears to gain strength as the water rises. In addition, because the cellular structure is flexible, it can withstand the associated large lateral deformation without failure.

Schroeder [49] proposed a new procedure to account for some increase in confining stresses in the conventional vertical shear analysis by adding the force due to the external differential water as a normal force on the vertical shear plane through the cell fill. While this proposed approach recognized that the differential water loading increases the shearing resistance of the cell fill, it significantly underestimated the degree of this effect.

8.7 Conclusion

The principal conclusions from this investigation include:

- **Cell Filling**

  1. Conventional design methods for determining interlock forces in the common wall yield higher maximum values than those from the three–dimensional finite element analysis. While Swatek's formula [19] gives the best agreement, with the three–dimensional finite element results, the agreement is essentially fortuitous. The Swatel's formula does not consider the arching in the cell fill which is the most significant phenomena controlling the interlock forces.
  2. Sequential filling of the main cell followed by filling of the arc cell is necessary for accurate representation of a cofferdam when investigating common wall or arc cell response. This is possible to simulate only by a three–dimensional analysis.
  3. Interlock forces in the main cell after arc cell filling compare well with those from the isolated main cell analyses. Thus, the two–dimensional axisymmetric model is sufficiently accurate for determining the interlock force in the main cell.

- **Differential Loading**

  1. Conventional methods are conservative in predicting the cofferdam capacity under differential loads. The finite element analyses explain this, showing the differential loading led to an increase in lateral confining stress in the fill and a reduced level of mobilized shear strength.

2. The three–dimensional response more closely represented the observed cell behavior under differential loading than those predicted by two–dimensional, vertical slice, plane strain model.

3. The greater movement of the inboard cell wall as compared to the outboard wall during dewatering can be explained by examining the effects of the lowering of the phreatic surface in the cell fill. As the phreatic surface is lowered, the effective stresses in the cell fill increases leading to vertical settlement and lateral spread of the unrestrained inboard wall. Coupling this with the overall movement toward the interior of the cofferdam from the differential water loading results in a greater movement of the inboard wall than of the outboard wall.

Bibliography

[1] Tennessee Valley Authority. *Steel Sheet Piling Cellular Cofferdam on Rocks.* TVA Technical Monograph No. 75, Vol 1, Tennessee Valley Authority, 1957. pp 61–62, 66–67, and 69.

[2] R. Barker, C. Lewis, W. Oliver, and Mould K. *Sheetpile Interlock Connection Testing Program, Final Report - Task 1.1 Through 1.3.* prepared for US Army Engineer Waterways Experiment Station VPI/CE-ST-85/01, Department of Civil Engineering, Virginia Polytechnic Institute and State Universty, Blacksburg, VA, may 1985.

[3] C. S. Boardman. Discussion of: Coffer–dam for 1000–Foot Pier. *Transactions, ASCE*, Vol 81, Paper No. 1391, pp 553–569, 1917.

[4] D. N. Buragohain and V. L. Shah. Curved isoparametric interface surface element. *Journal of the Structural Division, ASCE*, Technical Notes, Vol. 104, No. ST1,(), January, 1978.

[5] G. W. Clough and J. M. Duncan. *Finite Element Analyses of Port Allen and Old River Locks.* Contract Report S-69-6, US Army Engineer Waterways Experiment Station, Vicksburg, MS, September, 1969.

[6] G. W. Clough and P. M. Goeka. In–situ testing for lock and dam no. 26 cellular cofferdam. *Proceedings, Use of In-Situ tests in Geotechnical Engineering, ASCE Specialty Conference*, Geotechnical Special Publication No. 6:pp 131–145, 1986.

[7] G. W. Clough and L. A. Hansen. *A Finite Element Study of the Behavior of the Willow Island Cofferdam.* Technical Report No. CE–218, Department of Civil Engineering, Stanford University, Stanford, CA, may 1977. prepared for US Army Engineer District, Huntington.

[8] G. W. Clough and T. Kuppusamy. Finite Element Analyses of Lock and Dam 26 Cofferdam. *Journal of the Geotechnical Engineering Division, ASCE*, Vol 3, No. 4, pp 521–544, April 1985.

[9] Woodward–Clyde Consultants. *Cofferdam Cell Fill Evaluation – Lock and Dam No. 26 (Replacement).* Under Contract No. DACW43–82–D–0047, Prepared for the U.S. Army Engineer District, St. Louis, St. Louis, Missouri, June 1982.

[10] E. M. Cummings. Cellular Cofferdams and Docks. *Journal of the Waterways and Harbors Division, ASCE*, Vol 83, WW3, Proc. Paper 1366, pp 13–45, Sept. 1957.

[11] Corps of Engineers Department of the Army. *An Analysis of Cellular Sheet Pile Cofferdams Failures.* Technical Report, Ohio River Division, Cinicinnati, PA, 1974.

[12] Department of the Army, Corps of Engineer. *Design of Sheet Pile Cellular Structures Cofferdams and Retaining Structures,.* Engineering Manual 1110–2–2906, US Army, Washington, DC, To be Publised 1988.

[13] Department of the Army, Corps of Engineers. *Design of Pile Structures and Foundations.* Engineering Manual 111–2–2906 (Draft), US Army, Washington, DC, November 1970.

[14] C. S. Desai, M. M. Zaman, J. G. Ligther, and H. J. Siriwardane. Thin-layer element for interfaces and joints. *International Journal for Numerical and Analytical Methods in Geomechanics*, Vol. 8, pp 19-43,, 1984.

[15] L. Domaschuk and N. H. Wade. A study of bulk and shear moduli of a sand. *Journal of the Soil Mechanics and Foundations Division, ASCE*, Vol. 95, No. SM2(Proc. Paper 6461):pp 561–581, March 1969.

[16] J. M. Duncan, P. Byrne, K. S. Wong, and P. Mabry. *Strength, Stress–Strain and Bulk Modulus Parameters for Finite Element Analyses of Stresses and Movements in Soil M.* Geotechnical Engineering, Dept. of Civil Engineering, University of California, Berkeley, CA, report no. ucb/gt/80-01 edition, August 1980.

[17] J. M. Duncan and C-Y Chang. Nonlinear analysis of stress and strain in soils. *Journal of the Soil Mechanics and Foundations Division, ASCE*, Vol. 96, No. SM5():pp.1629–1653, September 1970.

[18] E. P. Swatek, Jr. Cellular cofferdams design and practice. *Journal of the Waterways and Harbors, ASCE*, Vol. 93, No.WW3(Proc. Paper 5398):pp. 109–132, Aug., 1967.

[19] E. P. Swatek, Jr. Summary cellular structure design and installation. In Fang and Dismuke, editors, *Design and Installation of Pile Foundations and Cellular*

Structures, pages 413–424, Envo Publishing Co., Inc., Lehigh Valley, Pennsylvania, 1970.

[20] C. Z. Erzen. Discusion of: Cellular Cofferdams and Docks by E. M. Cummings. *Journal of Waterways and Harbors Division, ASCE*, Vol 83, WW3, Proc. Paper 1366, pp 37–43, Sept 1957.

[21] J. Ghaboussi, E. L. Wilson, and J. Isenberg. Finite element for rock joints and interfaces. *Journal of the Soil Mechanics and Foundations Division, ASCE*, Vol. 99, No. SM10, pp 833-848, October, 1973.

[22] R. E. Goodman, R. L. Taylor, and T. L Brekke. A model for the mechanics of jointed rock. *Journal of the Soil Mechanics and Foundations Division, ASCE*, Vol. 94, No. SM3, pp 637-659, May, 1968.

[23] J. B. Hansen. *Earth Pressure Calculations.* Danish Technical Press, Institution of Danish Civil Engineers, Copenhagen, 1963.

[24] J. B. Hansen. *The Internal Forces in a Circle of Repture.* Bulletin No. 2, Danish Geotechnical Institute, Copenhagen, 1957.

[25] K. O. Hardin. *Finite Element Analysis of Cellular Steel Sheet Pile Cofferdams.* PhD thesis, Virginia Polytechnic Institute and State University, Blacksburg, VA, October, 1990.

[26] C. Y. Huang and R. M. Barker. *Comparison and Result of Sheet Pile Interlock Analysis, Final Report.* Technical Report No. VPI/CE-ST-88/101, Virgina Polytechnic Institute and State University, Blacksburg, VA, 1988.

[27] B. M. Irons. A technique for degenerating brick–type isoparametric elements using hierarchical midside nodes. *International Journal on Numerical Methods in Engineering*, Vol. 8, pp 203-209, 1974.

[28] N. Janbu. Soil compressibility as determined by oedometer and triaxial tests. *European Conference on Soil Mechanics and Foundation Engineering*, Wissbadan, Germany, Vol. 1, pp. 19–25:, 1963.

[29] G. Kasali and G. W. Clough. *Development of a Design Technology for Ground Support for Tunnels in Soil - Volume II: Three-Dimensional Finite Element Analysis of Advanced and Conventional Shiel Tunneling.* Prepared by Dept. of Civil Engineering, Stanford University DOT-TSC-UMTA-82-54,2, US Department of Transportation, Washingtion, DC, February 1983.

[30] T. Khuayjarernpanishk. *Behavior of a Circular Cell Bulkhead During Construction.* PhD thesis, Oregon State University, Corvallis, OR, 1975.

[31] L. Kittisatra. *Finite Element Analysis of Circular Cell Bulkheads.* PhD thesis, Oregon State University, Corvallis, OR, June 1976.

[32] D. P. Krynine. Discussion of: Stability and Stiffness of Cellular Cofferdams by K. Terzaghi. *Transactions, ASCE*, Vol 110, Paper No. 2253, pp 1083–1202, 1945.

[33] T. Kuppusamy, G. W. Clough, and R. J. Finno. Finite Element Analyses of Cellular Cofferdams Including Three Dimensional Cell Interaction. *Proceedings of the 11th International Conference on Soil Mechanics and Foundation Engineering*, Vol 4, pp 1993–1996, Aug. 1985.

[34] Naval Research Laboratory. *Trident Cofferdam Analysis.* NRL Memorandum Report 3869, Naval Research Laboratory, Washington, DC, 1979.

[35] Y. Lacroix, M. I. Esrig, and U. Lusher. Design, Construction, and Performance of Cellular Cofferdams. *Proceedinds, ASCE Specialty Conference on Lateral Stresses in the Ground and Earth Retaining Structures*, pp 271–328, June 1970.

[36] R. S. Ladd. Preparing test specimens using under–compaction. *ASTM Geotechnical Testing Journal*, No. 1:pp. 16–23, 1978.

[37] J. K. Maitland and W. L. Schroeder. Model Study of Circular Sheetpile Cells. *Journal of the Geotechnical Engineering Division, ASCE*, Vol 105, No. GT7, pp 805–821, July 1979.

[38] J. R. Martin and G. W. Clough. *A Study of the Effects of Differential Loading on Cofferdams.* Technical Report under Contract No. DACW39–86–0007, Virginia Polytechnic Institute and State University, Blacksburg, VA, January 1988.

[39] B. H. Moore and M. M. Alizadeh. Design of Circular Cofferdam Instrumentation. In *Proceeding, International Symposium of Field Measurements in Geomechanics*, pages 503–512, 1983.

[40] D. J. Naylor. *Non–linear Finite Element Models for Soils.* PhD thesis, Univeristy college of Swansea, 1975.

[41] I. Nelson and M. L. Baron. Application of variable moduli models to soil behavior. *International Journal of Solids and Structures*, Vol. 7,:pp. 399–417, 1971.

[42] R. E. Newton. Degeneration of brick-type isoparametric elements. *International Journal on Numerical Methods in Engineering*, Vol. 7, No. 4, pp 579-581, 1974.

[43] E. F. O'Neil and W. E. McDonald. *Lock and Dam No. 26 (Repalcement) Cofferdam Experimental and Analytical Study - Tensile Tests of Steel Sheet Piles.* Technical Report ITL–88–3, US Army Engineer Waterways Experiment Station, Vicksburg, MS, September 1988.

[44] N. K. Ovesen. *Cellular Cofferdams, Calculation Methods and Model Tests.* Bulletin No. 14, Danish Geotechnical Institute, Copenhagen, 1962.

[45] R. P. Pennoyer. Discussion of: Stability and Stiffness of Cellular Cofferdams by K. Terzaghi. *Transactions, ASCE*, Vol 110, Paper No. 2253, pp 1083–1202, 1945.

[46] R. P. Pennoyer. Gravity Bulkheads and Cellular Cofferdams. *Civil Engineering*, Vol 4, pp 301–305, 1934.

[47] J. N. Reddy. *Energy and Variation Methods in Applied Mechanics.* John Wiley and Sons, New York, NY, 1984.

[48] M. Rossow, E. Demsky, and R. Mosher. *Theoretical Manual for Design of Cellular Sheet Pile Structures (Cofferdams and Retaining Structures).* Technical Report ITL–87–5, US Army Engineer Waterways Experiment Station, Vicksburg, MS, May 1987.

[49] W. L. Schroeder. Cellular sheetpile bulkheads. In P. C. Lamber and L. A. Hansen, editors, *Proceeding, Conference on Design and Performance of Earth*

Retaining Structures, pages pp. 190–216, ASCE, Geotechnical Engineering Division, Geotechnical Special Publication No. 25, Cornell University, June 18-21, 1990.

[50] W. L. Schroeder, Marker D. K., and T. Khuayjarernpanishk. Performance of a Cellular Wharf. *Journal, Geotechnical Engineering Division, ASCE*, Vol 103, No. GT12, Paper No. 16758, pp 1643–1655, March 1977.

[51] W. L. Schroeder and J. K. Maitland. Cellular Bulkheads and Cofferdams. *Journal of the Geotechnical Engineering Division, ASCE*, Vol 105, No. GT7, pp 823–838, July 1979.

[52] A. Sehn, G. W. Clough, Y. P. Singh, and T. Kuppusamy. *Cell Fill Testing Program - Final Report -Task 3.* Technical Report under Contract No. DACW 39-84-C-0031 Geotechnical Engineering, Virginia Polytechnic Institute and State University, Blacksburg, VA, June 1985.

[53] Shannon and Wilson, Inc. *Final Report Tasks 3.2, 3.3, and 3.4; Finite Element Models for Lock and Dam No. 26 (Replacement) First Stage Cofferdam.* Technical Report, prepared for US Army Engineer District, St. Louis, November 1982.

[54] Shannon and Wilson, Inc. *Final Report Tasks 6.1 Through 6.7; Sheet Pile Interlock Testing for Lock and Dam No. 26 (Replacement) First Stage Cofferdam.* Technical Report, prepared for US Army Engineer District, St. Louis, March 1983.

[55] Shannon and Wilson, Inc. *Summary Report, Instrumentation Data Analysis and Finite Element Studies for First Stage Cofferdam, Lock and Dam 26(R).*

Technical Report, prepared for US Army Engineer District, St. Louis, November 1983.

[56] Y. P. Singh. *Finite Element Analyses of Cellular Cofferdams.* PhD thesis, Virginia Polytechnic Institute and State University, Blackburg, VA, 1988.

[57] M. D. Sorota and E. B. Kinner. Cellular Cofferdam for Trident Drydock: Design. *Journal of Geotechnical Division, ASCE*, Vol 107, No. GT12, Proc. Paper 16732, pp 1643–1655, Dec. 1981.

[58] M. D. Sorota, E. B. Kinner, and M. X. Haley. Cellular Cofferdam for Trident Drydock: Performance. *Journal of Geotechnical Division, ASCE*, Vol 107, No. GT12, Proc. Paper 16733, pp 1657–1676, Dec. 1981.

[59] R. F. Stevens. *Study of the Behavior of a Cellular Cofferdam.* PhD thesis, Duke University, Durham, NC, 1980.

[60] K. Terzaghi. Stability and Stiffness of Cellular Cofferdams. *Transactions, ASCE*, Vol 110, Paper No. 2253, pp 1083–1202, 1945.

[61] A. White, J. A. Cheney, and M. Duke. Field Study of a Circular Bulkhead. *Journal, Soil Mechanics and Foundations Division, ASCE*, Vol 87, No. SM4, Paper No. 2902, pp 89-124, August 1971.

[62] L. White and E. A. Prentis. *Cofferdams.* Columbia University Press, New York, N. Y., second edition, 1950.

[63] E. L. Wilson. *Finite Elements in Geomechanics*, chapter Chapter 10, pages pp 319–350. John Wiley and Sons, 1977.

[64] J. Y. Wu and R. M. Barker. *Analytical Study of Sheet Pile Interlocks, Final Report - Task 1.1 Through 1.2.* Technical Report No. VPI/CE-ST-87/01, Virginia Polytechnic Institute and State University, Blacksburg, VA, January 1987.

[65] O. C. Zienkiewicz, B. Best, C. Dullage, and K. G. Stagg. Analysis of nonlinear problems in rock mechanics with particular reference to jointed rock systems. In *Proceedings of 2nd Conference of the International Society of Rock Mechanics*, pages Belgrade, Vol. 3, pp 501–509,, 1970.

Appendix A

Derivation of the Goodman Interface Element

The element was derived based on the principle of minimum potential energy. Using the local coordinate system shown in Figure A.1, the stored energy element is

$$\phi = \frac{1}{2}\int_{-L/2}^{L/2} w_i P_j dx \tag{A.1}$$

or in matrix notation

$$\phi = \frac{1}{2}\int_{-L/2}^{L/2} \{w\}^T \{P\}\, dx \tag{A.2}$$

where $\{w\}$ is the relative displacement vector given by

$$\{w\} = \left\{ \begin{array}{c} w_s^{top} - w_s^{bottom} \\ w_n^{top} - w_n^{bottom} \end{array} \right\} \tag{A.3}$$

and $\{P\}$ is the force vector per unit length given by

$$\{P\} = \left\{ \begin{array}{c} P_s \\ P_n \end{array} \right\} \tag{A.4}$$

The vector, $\{P\}$, may be expressed in terms of the unit joint stiffness and relative displacements as

$$\{P\} = [k]\{w\} \tag{A.5}$$

where $[k]$ is the diagonal material matrix expressing the stiffness in the normal and tangential directions,

$$[k] = \begin{bmatrix} k_s & 0 \\ 0 & k_n \end{bmatrix} \tag{A.6}$$

Substituting Eq. A.5 into Eq. A.2 yields

$$\phi = \frac{1}{2}\int_{-L/2}^{L/2} \{w\}^T [k]\{w\}\, dx \tag{A.7}$$

The displacements, $\{w\}$, may be expressed in terms of the nodal point displacements, $\{u\}$, through linear shape functions. With components of $\{u\}$ being the displacements in tangential, u_i, and normal, v_i, directions, respectively, the displacements may be expressed along the bottom of the joint element as

$$\begin{Bmatrix} w_s^{bottom} \\ w_s^{bottom} \end{Bmatrix} = \frac{1}{2}\begin{bmatrix} A & 0 & B & 0 \\ 0 & A & 0 & B \end{bmatrix} \begin{Bmatrix} u_1 \\ v_1 \\ u_2 \\ v_2 \end{Bmatrix} \tag{A.8}$$

and along the top of the joint element as

$$\begin{Bmatrix} w_s^{top} \\ w_s^{top} \end{Bmatrix} = \frac{1}{2}\begin{bmatrix} B & 0 & A & 0 \\ 0 & B & 0 & A \end{bmatrix} \begin{Bmatrix} u_3 \\ v_3 \\ u_4 \\ v_4 \end{Bmatrix} \tag{A.9}$$

where $A = 1 - 2\frac{x}{L}$ and $B = 1 + 2\frac{x}{L}$. The relative displacements in the joint element are

$$\{w\} = \begin{Bmatrix} w_s^{top} - w_s^{bottom} \\ w_n^{top} - w_n^{bottom} \end{Bmatrix} \tag{A.10}$$

which equals

$$\{w\} = \frac{1}{2}\begin{bmatrix} -A & 0 & -B & 0 & B & 0 & A & 0 \\ 0 & -A & 0 & -B & 0 & B & 0 & A \end{bmatrix} \begin{Bmatrix} u_1 \\ v_1 \\ u_2 \\ v_2 \\ u_3 \\ v_3 \\ u_4 \\ v_4 \end{Bmatrix} \tag{A.11}$$

Writing this in matrix form

$$\{w\} = \frac{1}{2}[D]\{u\} \tag{A.12}$$

with $[D]$ and $\{u\}$ as defined above. Substituting this into Eq. A.2 yields

$$\phi = \frac{1}{2}\int_{-L/2}^{L/2} \frac{1}{4}\{u\}^T [D]^T [k] [D] \{u\}\, dx \tag{A.13}$$

Performing the matrix multiplication gives

$[D]^T [k] [D] =$

$$\begin{bmatrix} A^2k_s & 0 & ABk_s & 0 & -ABk_s & 0 & -A^2k_s & 0 \\ 0 & A^2k_n & 0 & ABk_n & 0 & -ABk_n & 0 & -A^2k_n \\ ABk_s & 0 & B^2k_s & 0 & -B^2k_s & 0 & -ABk_s & 0 \\ 0 & ABk_n & 0 & B^2k_n & 0 & -B^2k_n & 0 & -ABk_n \\ -ABk_s & 0 & -B^2k_s & 0 & B^2k_s & 0 & ABk_s & 0 \\ 0 & -ABk_n & 0 & -B^2k_n & 0 & B^2k_n & 0 & ABk_n \\ -A^2k_s & 0 & -ABk_s & 0 & ABk_s & 0 & A^2k_s & 0 \\ 0 & -A^2k_n & 0 & -ABk_n & 0 & ABk_n & 0 & A^2k_n \end{bmatrix} \tag{A.14}$$

Since the material matrix is independent of length, the integration of the terms A^2, AB, and B^2 can be performed independently. The results of the integration yields the stored energy as

$$\phi = \frac{1}{2} L \{u\}^T [K] \{u\} \tag{A.15}$$

in which

$$[K] = \begin{bmatrix} 2k_s & 0 & 1k_s & 0 & -1k_s & 0 & -2k_s & 0 \\ 0 & 2k_n & 0 & 1k_n & 0 & -1k_n & 0 & -2k_n \\ 1k_s & 0 & 2k_s & 0 & -2k_s & 0 & -1k_s & 0 \\ 0 & 1k_n & 0 & 2k_n & 0 & -2k_n & 0 & -1k_n \\ -1k_s & 0 & -2k_s & 0 & 2k_s & 0 & 1k_s & 0 \\ 0 & -1k_n & 0 & -2k_n & 0 & 2k_n & 0 & 1k_n \\ -2k_s & 0 & -1k_s & 0 & 1k_s & 0 & 2k_s & 0 \\ 0 & -2k_n & 0 & -1k_n & 0 & 1k_n & 0 & 2k_n \end{bmatrix} \tag{A.16}$$

is the joint stiffness matrix.

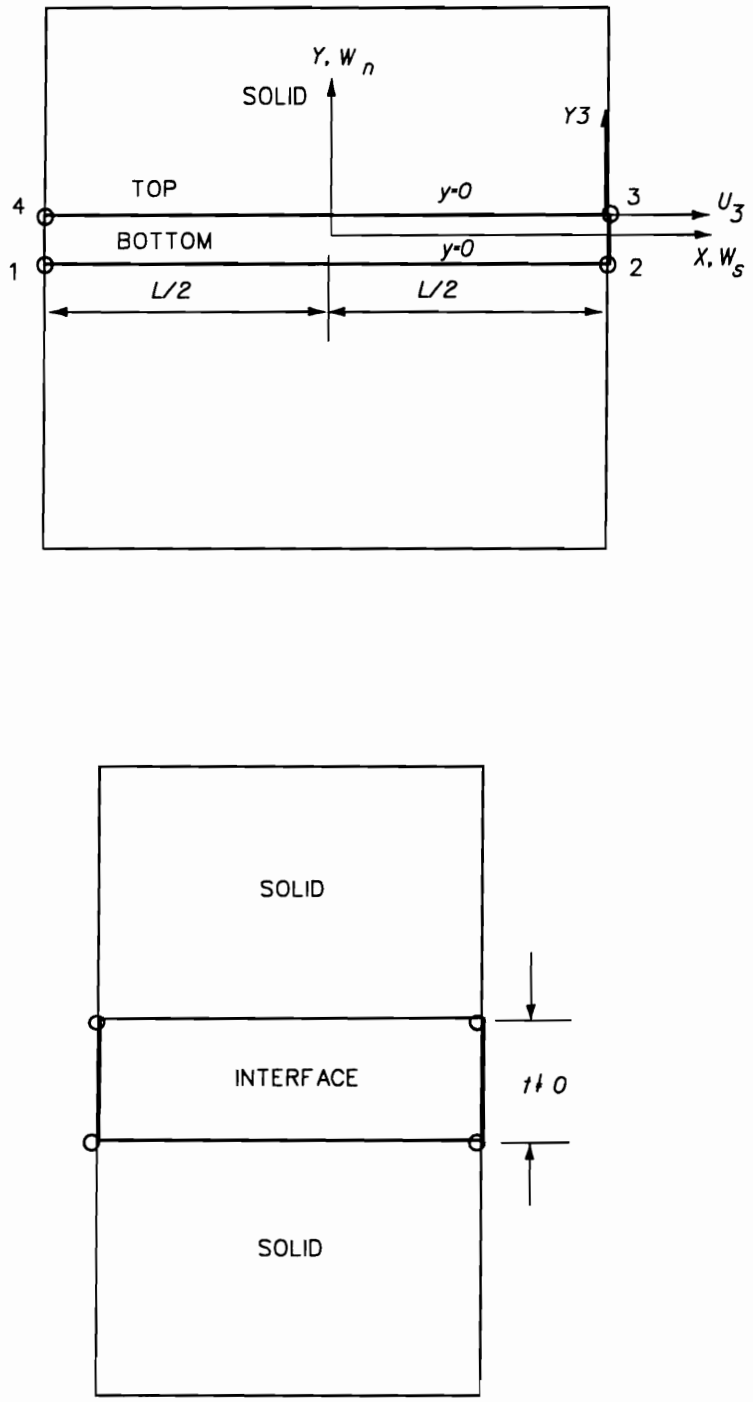

Figure A.1: Goodman, Taylor, and Berkke Interface Element [22].

Appendix B

1–D Example of the Goodman Interface Element

The stiffness is formulated in terms of the absolute displacments:

$$\begin{Bmatrix} P_1 \\ - \end{Bmatrix} = \begin{bmatrix} 1.5 & 0 \\ 0 & 0 \end{bmatrix} \begin{Bmatrix} u_1 \\ u_2 \end{Bmatrix} \quad \text{or} \quad \{P_1\} = [K_1]\{u\} \tag{B.1}$$

$$\begin{Bmatrix} - \\ P_2 \end{Bmatrix} = \begin{bmatrix} 0 & 0 \\ 0 & 1.5 \end{bmatrix} \begin{Bmatrix} u_1 \\ u_2 \end{Bmatrix} \quad \text{or} \quad \{P_2\} = [K_2]\{u\} \tag{B.2}$$

$$\begin{Bmatrix} P_1 \\ P_2 \end{Bmatrix} = \begin{bmatrix} 1000.0 & -1000.0 \\ -1000.0 & 1000.0 \end{bmatrix} \begin{Bmatrix} u_1 \\ u_2 \end{Bmatrix} \quad \text{or} \quad \{P_3\} = [K_3]\{u\} \tag{B.3}$$

The value of the stiffness coefficients for the interface element was chosen to illustrate what may happen when large values of the stiffness coefficients are used for normal stiffness in a zero thickness two–dimensional or three–dimensional interface element.

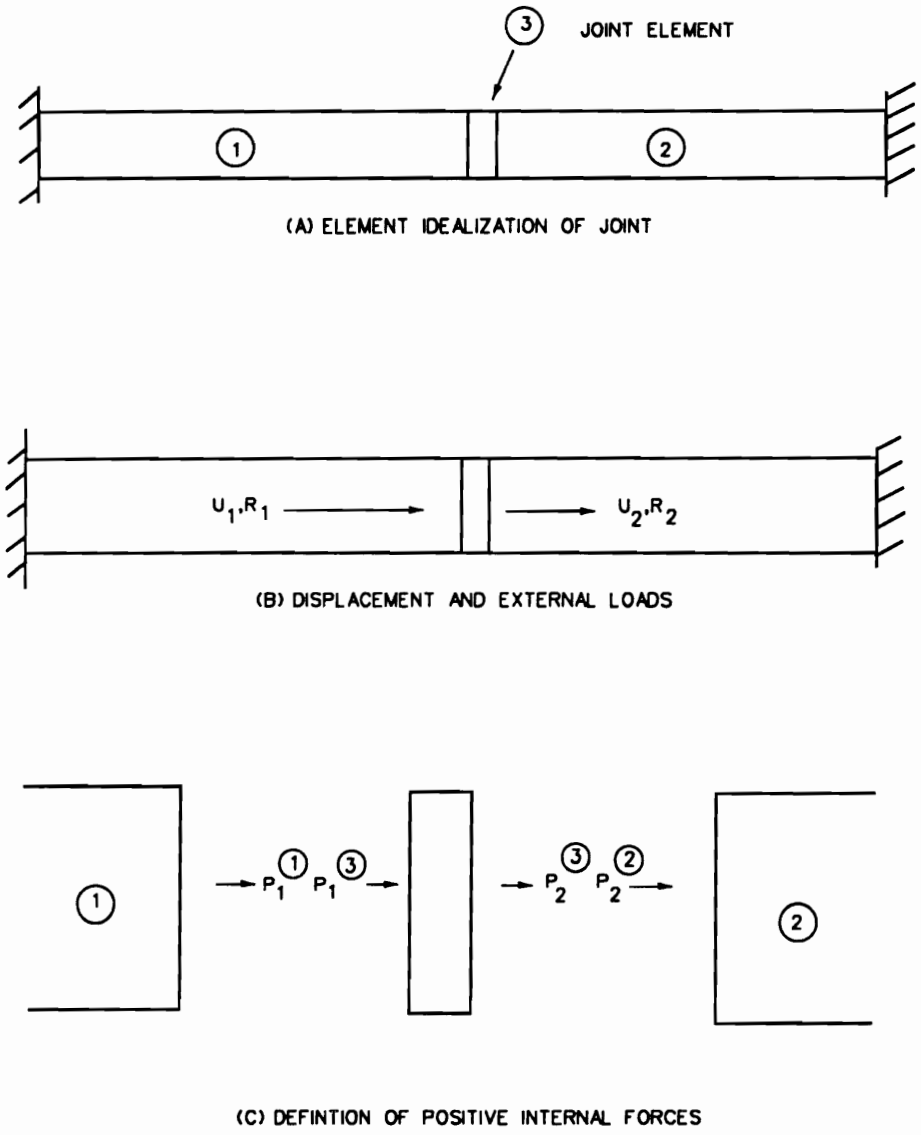

Figure B.1: Example problem to evaluate interface element [63].

The global equilibrium equations for the system are

$$\{F\} = \left\{ \begin{array}{c} F_1 \\ \\ F_2 \end{array} \right\} = \{P_1\} + \{P_2\} + \{P_3\} = \Big[[K_1] + [K_2] + [K_3]\Big] \{u\} \tag{B.4}$$

or in matrix

$$[K]\{u\} = \{F\} \tag{B.5}$$

If the external forces are $F_1 = 0$ and $F_2 = 1.0$, the global equilibrium equations are

$$\left[\begin{array}{cc} 1001.5 & -1000.0 \\ -1000.0 & 1001.5 \end{array} \right] \left\{ \begin{array}{c} u_1 \\ \\ u_2 \end{array} \right\} = \left\{ \begin{array}{c} 0 \\ \\ 1.0 \end{array} \right\} \tag{B.6}$$

Retaining the five significant figures shown in the stiffness matrix during the solution of equilibrium equations yields

$$u_1 = 0.33283 \quad \text{and} \quad u_2 = 0.33333 \tag{B.7}$$

If only four significant figures are possible for the stiffness matrix, the solution will be

$$\left[\begin{array}{cc} 1001 & -1000 \\ -1000 & 1001 \end{array} \right] \left\{ \begin{array}{c} u_1 \\ \\ u_2 \end{array} \right\} = \left\{ \begin{array}{c} 0 \\ \\ 1.0 \end{array} \right\} \quad \text{or} \quad \left\{ \begin{array}{c} u_1 \\ \\ u_2 \end{array} \right\} = \left\{ \begin{array}{c} 0.4995 \\ \\ 0.5000 \end{array} \right\} \tag{B.8}$$

If only three significant figures are possible, the set of equations are singular and $u_1 = u_2 = \infty$.

Appendix C

Basic Shell Element Formulation

The shell element proposed by Reddy [47] uses a doubly curved isoparametric rectangular anisotropic shell element used in the code. Orthogonal curvilinear coordinates (shell coordinates) are denoted by ξ_1, ξ_2, and ζ such that ξ_1 and ξ_2 correspond to the lines of curvature of the midsurface (reference surface) of the shell element, and $\zeta = 0$, and ζ coincide with straight lines perpendicular to the midsurface (Figure C.1). The lines of the principal curvature coincide with the ξ_1 and ξ_2 coordinate lines. The values of the principal radii of curvature of the midsurface of the element are specified by R_1 and R_2. A point on the midsurface is denoted by the position vector r, and a point at a distance from the reference surface is denoted by the position vector R, Figure C.1b.

The distance ds between points $(\xi_1, \xi_2, 0)$ and $(\xi_1 + d\xi_1, \xi_2 + d\xi_2, 0)$ is defined by

$$(ds)^2 = dr \cdot dr = \alpha_1^2 (d\xi_1)^2 + \alpha_2^2 (d\xi_2)^2 \tag{C.1}$$

where $dr = r_1 d\xi_1 + r_2 d\xi_2$, the vectors r_1 and r_2 ($r_i = \partial r / \partial \xi_i$) are tangent to the ξ_1 and ξ_2 coordinate lines and α_1 and α_2 are surface metrics defined as

$$\alpha_i^2 = r_i \cdot r_i \quad \text{where} \quad i = 1, 2 \tag{C.2}$$

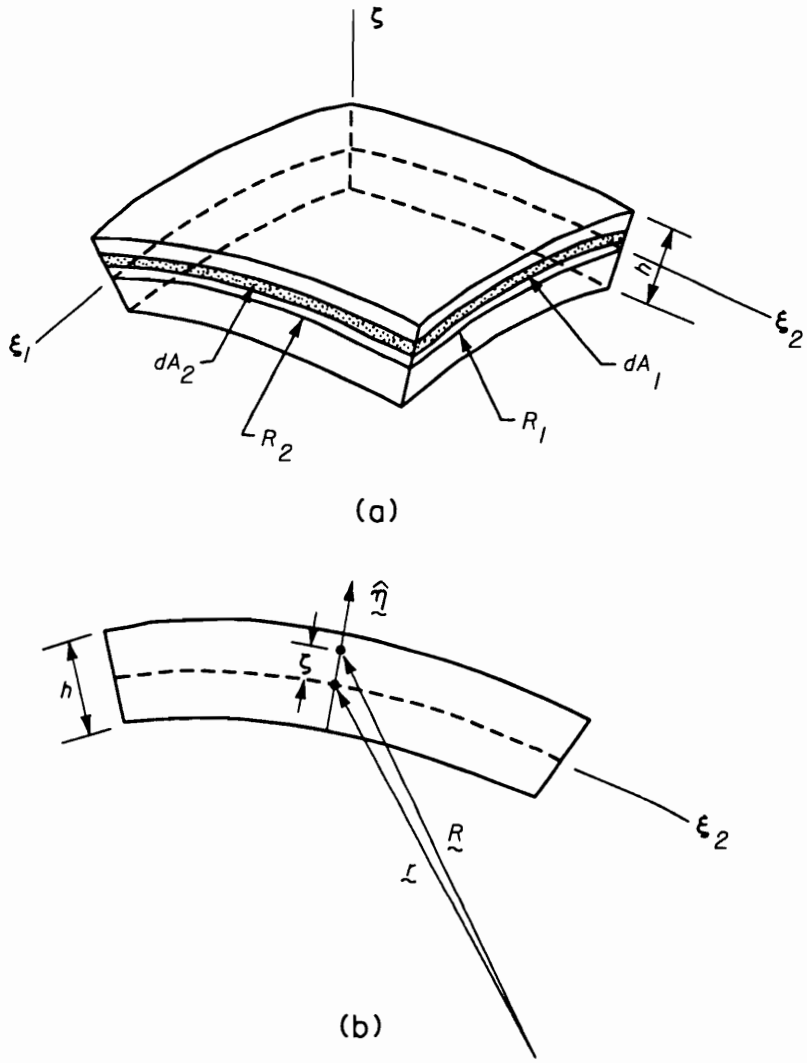

Figure C.1: Geometry of the shell element [47].

The position vector R of a point at distance ζ from the midsurface can be expressed as

$$R = r + \hat{n}\zeta \tag{C.3}$$

where $\hat{n}$ is the unit vector normal to the midsurface and is determined by

$$\hat{n} = \frac{r_1 \times r_2}{\alpha_1 \alpha_2} \tag{C.4}$$

By differentiation

$$\frac{\partial R}{\partial \xi_i} = \frac{\partial r}{\partial \xi_i} + \frac{\partial \hat{n}}{\partial \xi_i}\zeta \quad \text{where} \quad i = 1,2 \tag{C.5}$$

from a theorem of Rodrigues [47]

$$\frac{\partial \hat{n}}{\partial \xi_i} = \frac{1}{R_i}\frac{\partial r}{\partial \xi_i} \quad \text{where} \quad i = 1,2 \tag{C.6}$$

Substituting Eq. C.6 into Eq. C.5

$$\frac{\partial R}{\partial \xi_i} = \left(1 + \frac{\zeta}{R_i}\right)\frac{\partial r}{\partial \xi_i} \quad \text{where} \quad i = 1,2 \tag{C.7}$$

Using these geometrical relations, the distance dS between points (ξ_1, ξ_2, ζ) and $(\xi_1 + d\xi_1, \xi_2 + d\xi_2, \zeta + d\zeta)$ is given by

$$(dS)^2 = dR \cdot dR = L_1^2(d\xi_1)^2 + L_2^2(d\xi_2)^2 + L_3^2(d\zeta)^2 \tag{C.8}$$

where

$$dR = \left(\frac{\partial R}{\partial \xi_1}\right) d\xi_1 + \left(\frac{\partial R}{\partial \xi_2}\right) d\xi_2 + \left(\frac{\partial R}{\partial \zeta}\right) d\zeta \tag{C.9}$$

and L_1, L_2, and L_3 are the *Lamé coefficients* which are defined as

$$L_i = \alpha_i \left(1 + \frac{\zeta}{R_i}\right) \quad \text{where} \quad i = 1,2 \quad \text{and} \quad L_3 = 1 \tag{C.10}$$

It should be noted that vectors $\partial R/\partial \xi_1$ and $\partial R/\partial \xi_2$ are parallel to the vectors $r_1 = \partial r/\partial \xi_1$ and $r_2 = \partial r/\partial \xi_2$.

The stress resultants are obtained by integrating the corresponding stress components over the thickness. If N_1 is the tensile force measured per unit length along the coordinate line ξ_2 on the cross section perpendicular to the ξ_1 direction, the total tensile force in that direction is $N_i \alpha_2 d\xi_2$. This force is equal to the integral of $\sigma_1 dA_2$ over the thickness

$$N_i \alpha_2 d\xi_2 = \int_{-h/2}^{h/2} \sigma_1 dA_2 \tag{C.11}$$

where h is the shell thickness. Using *Lamé coefficients*, the elements of the area of the cross sections can be defined as

$$dA_i = L_i d\xi_i d\zeta = \alpha_i \left(1 + \frac{\zeta}{R_i}\right) d\xi_i d\zeta \quad \text{where} \quad i = 1, 2 \tag{C.12}$$

Substituting Eq. C.12 into Eq. C.11 and rearranging gives

$$N_1 = \int_{-h/2}^{h/2} \sigma_1 \left(1 + \frac{\zeta}{R_2}\right) d\zeta \tag{C.13}$$

The other stress resultants can be derived in a similar manner and given as

$$\begin{Bmatrix} N_1 \\ N_2 \\ N_{12} \\ N_{21} \\ Q_5 \\ Q_4 \\ M_1 \\ M_2 \\ M_{12} \\ M_{21} \end{Bmatrix} = \int_{-h/2}^{h/2} \begin{Bmatrix} \sigma_1 \left(1 + \frac{\zeta}{R_2}\right) \\ \sigma_2 \left(1 + \frac{\zeta}{R_1}\right) \\ \sigma_6 \left(1 + \frac{\zeta}{R_2}\right) \\ \sigma_6 \left(1 + \frac{\zeta}{R_1}\right) \\ \sigma_5 \left(1 + \frac{\zeta}{R_2}\right) \\ \sigma_4 \left(1 + \frac{\zeta}{R_1}\right) \\ \zeta\sigma_1 \left(1 + \frac{\zeta}{R_2}\right) \\ \zeta\sigma_2 \left(1 + \frac{\zeta}{R_1}\right) \\ \zeta\sigma_6 \left(1 + \frac{\zeta}{R_2}\right) \\ \zeta\sigma_6 \left(1 + \frac{\zeta}{R_1}\right) \end{Bmatrix} d\zeta \tag{C.14}$$

For thin shells, ζ/R_1 and ζ/R_2 can be assumed to be negligible in comparison to unity. For this assumption, $N_{12} = N_{21}$ and $M_{12} = M_{21}$ can be replaced by N_6 and M_6, respectively.

The strain–displacement equations for the shell are an approximation based on the following assumptions [47]

- The thickness of the shell is small compared to the principal radii of the curvature $(h/R_1, h/R_2 \ll 1)$.
- The transverse strain energy is negligible.
- Normals to the reference surface of the shell before deformation remain straight but not necessarily normal to the surface after deformation.

In view of the first assumption, the stress resultants in Eq. C.14 can be expressed as

$$N_i = \int_{h/2}^{h/2} \sigma_i d\zeta, \text{ where } i = 1,2,6 \tag{C.15}$$

$$M_i = \int_{h/2}^{h/2} \sigma_i \zeta d\zeta, \text{ where } i = 1,2,6 \tag{C.16}$$

$$Q_i = K_i^2 \int_{h/2}^{h/2} \sigma_i d\zeta, \text{ where } i = 4,5 \tag{C.17}$$

where K_i equals the shear correction factors. It is also assumed that transverse displacement u_3 does not vary with ζ so that $u_3 = u_3(\xi_1, \xi_2)$. The displacement field for the shell is

$$\bar{u_i} = \frac{1}{\alpha_i}(L_i u_i) + \zeta \phi_i \quad \text{where} \quad i = 1,2 \quad \text{and} \quad \bar{u_3} = u_3 \tag{C.18}$$

where $\bar{u_1}$, $\bar{u_2}$,$\bar{u_3}$ are displacements of a point (ξ_1, ξ_2, ζ) and u_1, u_2,u_3 are the displacements of a point $(\xi_1, \xi_2, 0)$ on the midsurface. ϕ_1 and ϕ_2 are the rotations about

the ξ_2 and ξ_1 coordinate lines of the midsurface, respectively. Substituting Eq. C.18 into Sander's strain–displacement relationship [47] for an orthogonal curvilinear coordinate system gives

$$\left\{ \begin{array}{c} \epsilon_1 \\ \epsilon_2 \\ \epsilon_4 \\ \epsilon_5 \\ \epsilon_6 \end{array} \right\} = \left\{ \begin{array}{c} \epsilon_1^0 + \zeta\kappa_1^0 \\ \epsilon_2^0 + \zeta\kappa_2^0 \\ \epsilon_4^0 \\ \epsilon_5^0 \\ \epsilon_6^0 + \zeta\kappa_6^0 \end{array} \right\} \tag{C.19}$$

where

$$\epsilon_1^0 = \frac{1}{\alpha_1}\frac{\partial u_1}{\partial \xi_1} + \frac{u_3}{R_1} \tag{C.20}$$

$$\epsilon_2^0 = \frac{1}{\alpha_2}\frac{\partial u_2}{\partial \xi_2} + \frac{u_3}{R_2} \tag{C.21}$$

$$\epsilon_4^0 = \frac{1}{\alpha_2}\frac{\partial u_3}{\partial \xi_2} + \phi_2 - \frac{u_2}{R_2} \tag{C.22}$$

$$\epsilon_5^0 = \frac{1}{\alpha_1}\frac{\partial u_3}{\partial \xi_1} + \phi_1 - \frac{u_1}{R_1} \tag{C.23}$$

$$\epsilon_6^0 = \frac{1}{\alpha_1}\frac{\partial u_2}{\partial \xi_1} + \frac{1}{\alpha_2}\frac{\partial u_1}{\partial \xi_2} \tag{C.24}$$

$$\kappa_1^0 = \frac{1}{\alpha_1}\frac{\partial \phi_1}{\partial \xi_1} \tag{C.25}$$

$$\kappa_2^0 = \frac{1}{\alpha_2}\frac{\partial \phi_2}{\partial \xi_2} \tag{C.26}$$

$$\kappa_6^0 = \frac{1}{\alpha_1}\frac{\partial \phi_2}{\partial \xi_1} + \frac{1}{\alpha_2}\frac{\partial \phi_1}{\partial \xi_2} + \frac{1}{2}\left(\frac{1}{R_2} - \frac{1}{R_1}\right)\left(\frac{1}{\alpha_1}\frac{\partial u_2}{\partial \xi_1} + \frac{1}{\alpha_2}\frac{\partial u_1}{\partial \xi_2}\right) \tag{C.27}$$

For the most general case of anisotropy, the number of independent elastic constants is 21. This number can be significantly reduced by limiting the anisotropy to the three mutually orthogonal planes of symmetry. The sheet piles of the cellular cofferdam possess this type of symmetry, with the midsurface being a symmetric plane at each point $(\xi_1, \xi_2, 0)$. If the material and geometric reference systems are

parallel, the general strain–stress relationship is given as

$$\sigma_i = c_{ij}\epsilon_j \quad \text{or} \quad \{\sigma\} = [C]\{\epsilon\} \tag{C.28}$$

Based on the assumption of zero normal stress, $\sigma_3 = 0$, the stress and strain vectors are

$$\{\sigma\} = \{\sigma_1, \sigma_2, \sigma_4, \sigma_5, \sigma_6\}^T \tag{C.29}$$

$$\{\epsilon\} = \{\epsilon_1, \epsilon_2, \epsilon_4, \epsilon_5, \epsilon_6\}^T \tag{C.30}$$

and the constitutive matrix, C, relating the stresses and strains is denoted as

$$[C] = \begin{bmatrix} C_{11} & C_{12} & 0 & 0 & 0 \\ C_{12} & C_{22} & 0 & 0 & 0 \\ 0 & 0 & C_{44} & 0 & 0 \\ 0 & 0 & 0 & C_{55} & 0 \\ 0 & 0 & 0 & 0 & C_{66} \end{bmatrix} \tag{C.31}$$

where the elastic constants C_{ij} can be expressed as functions of Young's moduli, Poisson's ratios, and shear moduli

$$C_{11} = \frac{E_1}{(1 - \nu_{12}\nu_{21})} \tag{C.32}$$

$$C_{22} = \frac{E_2}{(1 - \nu_{12}\nu_{21})} \tag{C.33}$$

$$C_{12} = \frac{E_2\nu_{12}}{(1 - \nu_{12}\nu_{21})} \tag{C.34}$$

$$C_{44} = G_{23} \tag{C.35}$$

$$C_{55} = G_{13} \tag{C.36}$$

$$C_{66} = G_{12} \tag{C.37}$$

If the principal axes of anisotropy does not coincide with the reference lines (ξ_1, ξ_2)

but are rotated to the reference lines by a certain angle θ, the new constitute matrix C' is determined from the following transformation

$$\{\sigma'\} = [T]\{\sigma\} \tag{C.38}$$

$$\{\epsilon'\} = [T']\{\epsilon\} \tag{C.39}$$

where

$$[T] = \begin{bmatrix} [T_1] & 0 \\ 0 & [T_2] \end{bmatrix} \tag{C.40}$$

in which

$$[T_1] = \begin{bmatrix} \cos^2\theta & \sin^2\theta \\ \sin^2\theta & \cos^2\theta \end{bmatrix} \tag{C.41}$$

and

$$[T_2] = \begin{bmatrix} \cos\theta & \sin\theta & 2\sin\theta\cos\theta \\ -\sin\theta & \cos\theta & -2\sin\theta\cos\theta \\ -\sin\theta\cos\theta & \cos\theta\sin\theta & \left(\cos^2\theta - \sin^2\theta\right) \end{bmatrix} \tag{C.42}$$

and

$$[T'] = \begin{bmatrix} [T_1] & 0 \\ 0 & [T_2'] \end{bmatrix} \tag{C.43}$$

in which

$$[T_2'] = \begin{bmatrix} \cos\theta & \sin\theta & \sin\theta\cos\theta \\ -\sin\theta & \cos\theta & -\sin\theta\cos\theta \\ -2\sin\theta\cos\theta & 2\sin\theta\cos\theta & \left(\cos^2\theta - \sin^2\theta\right) \end{bmatrix} \tag{C.44}$$

From Eq. C.38 and Eq. C.39, the relation between stresses and strains can be written as

$$\{\sigma\} = [C']\{\epsilon\} \tag{C.45}$$

where C' is the general constitutive matrix, which is given by

$$[C'] = [T]^{-1}[C][T'] = \begin{bmatrix} C'_{11} & C'_{12} & 0 & 0 & C'_{16} \\ C'_{12} & C'_{22} & 0 & 0 & C'_{26} \\ 0 & 0 & C'_{44} & C'_{45} & 0 \\ 0 & 0 & C'_{45} & C'_{55} & 0 \\ C'_{16} & C'_{26} & 0 & 0 & C'_{66} \end{bmatrix} \tag{C.46}$$

Using Eq. C.15, C.16, and C.17 in Eq. C.19, the stress resultants, (N_i, M_i, Q_i), can be related to ϵ_i^0 and κ_i^0 as

$$N_i = A_{ij}\epsilon_i^0 + B_{ij}\kappa_i^0, \text{ where } i,j = 1,2,6 \tag{C.47}$$

$$M_i = B_{ij}\epsilon_i^0 + D_{ij}\kappa_i^0, \text{ where } i,j = 1,2,6 \tag{C.48}$$

$$Q_i = A_{ij}\epsilon_j^0, \text{ where } i,j = 4,5 \tag{C.49}$$

where A_{ij}, B_{ij}, and D_{ij} are for the extension, flexural–extension coupling, and flexural stiffness, respectively, and determined by

$$A_{ij} = \int_{-h/2}^{h/2} C'_{ij}\,d\zeta, \text{ where } i,j = 1,2,6 \tag{C.50}$$

$$B_{ij} = \int_{-h/2}^{h/2} C'_{ij}\zeta\,d\zeta, \text{ where } i,j = 1,2,6 \tag{C.51}$$

$$D_{ij} = \int_{-h/2}^{h/2} C'_{ij}\zeta\,d\zeta^2, \text{ where } i,j = 1,2,6 \tag{C.52}$$

$$A_{ij} = \int_{-h/2}^{h/2} K_i K_j C'_{ij}\,d\zeta, \text{ where } i,j = 4,5 \tag{C.53}$$

Applying the principle of virtual work yields

$$\begin{aligned} 0 = \int_{h/2}^{h/2} \{ \int_\Omega & [\sigma_1\delta\epsilon_1 + \sigma_2\delta\epsilon_2 + \sigma_3\delta\epsilon_3 + \sigma_4\delta\epsilon_4 \\ & + \sigma_5\delta\epsilon_5 + \sigma_6\delta\epsilon_6]\,\alpha_1\alpha_2 d\xi_1 d\xi_2 \} d\zeta \end{aligned} \tag{C.54}$$

Substituting into the expression for $\delta\epsilon_i$ and σ_i in terms of ϵ_i^0 and κ_i^0 and the stress resultants, (N_i, M_i, Q_i), respectively, gives

$$\begin{aligned} 0 &= \int_\Omega \Big[N_1\delta\epsilon_1^0 + N_2\delta\epsilon_2^0 + N_6\delta\epsilon_6^0 + M_1\delta\kappa_1^0 + M_2\delta\kappa_2^0 + M_6\delta\kappa_6^0 \\ &\quad + Q_1\delta\epsilon_4^0 + Q_2\delta\epsilon_5^0 - q\delta u_3\Big]\,\alpha_1\alpha_2 d\xi_1 d\xi_2 \end{aligned} \tag{C.55}$$

For the finite element formulation, the displacements $(u_1, u_2, u_3, \phi_1, \phi_2)$ of the shell element are interpolated over the surface of the shell element by expressions of the form

$$u_i = \sum_{j=1}^{n} u_i^j \psi_j(\xi_1\xi_2), \quad \text{where } i = 1,2,3 \tag{C.56}$$

$$\phi_i = \sum_{j=1}^{n} \phi_i^j \psi_j(\xi_1\xi_2), \quad \text{where } i = 1,2 \tag{C.57}$$

where ψ_j are interpolation functions and u_i^j and ϕ_i^j are the nodal values of u_i and ϕ_i. By substituting Eq. C.56 and C.57 into the virtual work principle, Eq. C.55 , the element equations are obtained as

$$[K]\{\Delta\} = \{F\} \tag{C.58}$$

where $\{\Delta\}$ is the nodal point displacement vector, $[K]$ is the element stiffness matrix, and $\{F\}$ is the force vector. The stiffness matrix coefficients for the five degrees of freedom at a given nodal point are [47]

$$\begin{aligned} K_{11} &= \int_R \sum_{i=1}^{n}\sum_{j=1}^{n} \Bigg[A_{11}\frac{\partial\psi_i}{\partial x_1}\frac{\partial\psi_j}{\partial x_1} + (A_{16} + c_0 B_{16})\left(\frac{\partial\psi_i}{\partial x_1}\frac{\partial\psi_j}{\partial x_2} + \frac{\partial\psi_i}{\partial x_2}\frac{\partial\psi_j}{\partial x_1}\right) \\ &\quad + \left(A_{66} + 2c_0 B_{66} + c_0^2 D_{66}\right)\frac{\partial\psi_i}{\partial x_2}\frac{\partial\psi_j}{\partial x_2} + \frac{1}{R_1^2}A_{55}\psi_i\psi_j\Bigg]\,\alpha_1 d\xi_1 \alpha_2 d\xi_2 \\ K_{12} &= \int_R \sum_{i=1}^{n}\sum_{j=1}^{n} \Bigg[(A_{16} - c_0 B_{16})\frac{\partial\psi_i}{\partial x_1}\frac{\partial\psi_j}{\partial x_1} + \left(A_{66} - c_0^2 D_{66}\right)\frac{\partial\psi_i}{\partial x_2}\frac{\partial\psi_j}{\partial x_1} \end{aligned}$$

$$+A_{12}\frac{\partial\psi_i}{\partial x_1}\frac{\partial\psi_j}{\partial x_2}+(A_{26}+c_0B_{26})\frac{\partial\psi_i}{\partial x_2}\frac{\partial\psi_j}{\partial x_2}+\frac{1}{R_1R_2}A_{45}\psi_i\psi_j\Big]\alpha_1 d\xi_1\alpha_2 d\xi_2$$

$$K_{13} = \int_R\sum_{i=1}^{n}\sum_{j=1}^{n}\Big[\Big(\frac{A_{11}}{R_1}+\frac{A_{12}}{R_2}\Big)\frac{\partial\psi_i}{\partial x_1}\psi_j+\Big[\frac{A_{16}}{R_1}+\frac{A_{26}}{R_2}+c_0\Big(\frac{B_{16}}{R_1}+\frac{B_{26}}{R_2}\Big)\Big]\frac{\partial\psi_i}{\partial x_2}\psi_j$$
$$-\frac{1}{R_1}\Big(A_{45}\psi_i\frac{\partial\psi_j}{\partial x_2}+A_{55}\psi_i\frac{\partial\psi_j}{\partial x_1}+\Big)\Big]\alpha_1 d\xi_1\alpha_2 d\xi_2$$

$$K_{14} = \int_R\sum_{i=1}^{n}\sum_{j=1}^{n}\Big[B_{11}\frac{\partial\psi_i}{\partial x_1}\frac{\partial\psi_j}{\partial x_1}+B_{16}\frac{\partial\psi_i}{\partial x_1}\frac{\partial\psi_j}{\partial x_2}+(B_{16}+c_0D_{16})\frac{\partial\psi_i}{\partial x_2}\frac{\partial\psi_j}{\partial x_1}$$
$$+(B_{66}+c_0D_{66})\frac{\partial\psi_i}{\partial x_2}\frac{\partial\psi_j}{\partial x_2}+\frac{1}{R_1}A_{55}\psi_i\psi_j\Big]\alpha_1 d\xi_1\alpha_2 d\xi_2$$

$$K_{15} = \int_R\sum_{i=1}^{n}\sum_{j=1}^{n}\Big[B_{12}\frac{\partial\psi_i}{\partial x_1}\frac{\partial\psi_j}{\partial x_2}+B_{16}\frac{\partial\psi_i}{\partial x_1}\frac{\partial\psi_j}{\partial x_1}+(B_{26}+c_0D_{26})\frac{\partial\psi_i}{\partial x_2}\frac{\partial\psi_j}{\partial x_2}$$
$$+(B_{66}+c_0D_{66})\frac{\partial\psi_i}{\partial x_2}\frac{\partial\psi_j}{\partial x_1}+\frac{1}{R_1}A_{45}\psi_i\psi_j\Big]\alpha_1 d\xi_1\alpha_2 d\xi_2$$

$$K_{22} = \int_R\sum_{i=1}^{n}\sum_{j=1}^{n}\Big[A_{22}\frac{\partial\psi_i}{\partial x_2}\frac{\partial\psi_j}{\partial x_2}+(A_{26}-c_0B_{26})\Big(\frac{\partial\psi_i}{\partial x_1}\frac{\partial\psi_j}{\partial x_2}+\frac{\partial\psi_i}{\partial x_2}\frac{\partial\psi_j}{\partial x_1}\Big)$$
$$+\Big(A_{66}-2c_0B_{66}+c_0^2D_{66}\Big)\frac{\partial\psi_i}{\partial x_1}\frac{\partial\psi_j}{\partial x_1}+\frac{1}{R_2^2}A_{45}\psi_i\psi_j\Big]\alpha_1 d\xi_1\alpha_2 d\xi_2$$

$$K_{23} = \int_R\sum_{i=1}^{n}\sum_{j=1}^{n}\Big\{\Big[\frac{A_{16}}{R_1}+\frac{A_{26}}{R_2}-c_0\Big(\frac{B_{16}}{R_1}+\frac{B_{26}}{R_2}\Big)\Big]\frac{\partial\psi_i}{\partial x_1}\psi_j\Big(\frac{A_{11}}{R_1}+\frac{A_{12}}{R_2}\Big)\frac{\partial\psi_i}{\partial x_2}\psi_j$$
$$-\frac{1}{R_2}\Big(A_{44}\psi_i\frac{\partial\psi_j}{\partial x_2}+A_{45}\psi_i\frac{\partial\psi_j}{\partial x_1}+\Big)\Big\}\alpha_1 d\xi_1\alpha_2 d\xi_2$$

$$K_{24} = \int_R\sum_{i=1}^{n}\sum_{j=1}^{n}\Big[(B_{16}-c_0D_{16})\frac{\partial\psi_i}{\partial x_1}\frac{\partial\psi_j}{\partial x_1}+(B_{66}-c_0D_{66})\frac{\partial\psi_i}{\partial x_1}\frac{\partial\psi_j}{\partial x_2}$$
$$+B_{12}\frac{\partial\psi_i}{\partial x_2}\frac{\partial\psi_j}{\partial x_1}+B_{26}\frac{\partial\psi_i}{\partial x_2}\frac{\partial\psi_j}{\partial x_2}-\frac{1}{R_2}A_{45}\psi_i\psi_j\Big]\alpha_1 d\xi_1\alpha_2 d\xi_2$$

$$K_{25} = \int_R\sum_{i=1}^{n}\sum_{j=1}^{n}\Big[B_{22}\frac{\partial\psi_i}{\partial x_2}\frac{\partial\psi_j}{\partial x_2}+B_{26}\frac{\partial\psi_i}{\partial x_2}\frac{\partial\psi_j}{\partial x_1}+(B_{26}-c_0D_{26})\frac{\partial\psi_i}{\partial x_1}\frac{\partial\psi_j}{\partial x_2}$$
$$+(B_{66}-c_0D_{66})\frac{\partial\psi_i}{\partial x_1}\frac{\partial\psi_j}{\partial x_1}+\frac{1}{R_2}A_{44}\psi_i\psi_j\Big]\alpha_1 d\xi_1\alpha_2 d\xi_2$$

$$K_{33} = \int_R\sum_{i=1}^{n}\sum_{j=1}^{n}\Big[A_{45}\frac{\partial\psi_i}{\partial x_1}\frac{\partial\psi_j}{\partial x_2}+A_{55}\frac{\partial\psi_i}{\partial x_1}\frac{\partial\psi_j}{\partial x_1}+A_{44}\frac{\partial\psi_i}{\partial x_2}\frac{\partial\psi_j}{\partial x_2}+A_{45}\frac{\partial\psi_i}{\partial x_2}\frac{\partial\psi_j}{\partial x_1}$$
$$+\Big[\Big(\frac{A_{11}}{R_1}+\frac{A_{12}}{R_2}\Big)\frac{1}{R_1}+\Big(\frac{A_{12}}{R_1}+\frac{A_{22}}{R_2}\Big)\frac{1}{R_2}\Big]\psi_i\psi_j\Big]\alpha_1 d\xi_1\alpha_2 d\xi_2$$

$$
\begin{aligned}
K_{34} &= \int_R \sum_{i=1}^{n}\sum_{j=1}^{n}\left[A_{55}\frac{\partial\psi_i}{\partial x_1}\psi_j + A_{45}\frac{\partial\psi_i}{\partial x_2}\psi_j + \left(\frac{B_{11}}{R_1}+\frac{B_{12}}{R_2}\right)\psi_i\frac{\partial\psi_j}{\partial x_1}\right.\\
&\quad \left. + \left(\frac{B_{16}}{R_1}+\frac{B_{16}}{R_2}\right)\psi_i\frac{\partial\psi_j}{\partial x_2}+\right]\alpha_1 d\xi_1\alpha_2 d\xi_2\\
K_{35} &= \int_R \sum_{i=1}^{n}\sum_{j=1}^{n}\left[A_{45}\frac{\partial\psi_i}{\partial x_1}\psi_j + A_{45}\frac{\partial\psi_i}{\partial x_2}\psi_j + \left(\frac{B_{11}}{R_1}+\frac{B_{12}}{R_2}\right)\psi_i\frac{\partial\psi_j}{\partial x_2}\right.\\
&\quad \left. + \left(\frac{B_{16}}{R_1}+\frac{B_{16}}{R_2}\right)\psi_i\frac{\partial\psi_j}{\partial x_1}+\right]\alpha_1 d\xi_1\alpha_2 d\xi_2\\
K_{44} &= \int_R \sum_{i=1}^{n}\sum_{j=1}^{n}\left[D_{11}\frac{\partial\psi_i}{\partial x_1}\frac{\partial\psi_j}{\partial x_1} + D_{16}\frac{\partial\psi_i}{\partial x_1}\frac{\partial\psi_j}{\partial x_2} + D_{16}\frac{\partial\psi_i}{\partial x_2}\frac{\partial\psi_j}{\partial x_1}\right.\\
&\quad \left. + D_{66}\frac{\partial\psi_i}{\partial x_2}\frac{\partial\psi_j}{\partial x_2} + A_{55}\psi_i\psi_j\right]\alpha_1 d\xi_1\alpha_2 d\xi_2\\
K_{45} &= \int_R \sum_{i=1}^{n}\sum_{j=1}^{n}\left[D_{12}\frac{\partial\psi_i}{\partial x_1}\frac{\partial\psi_j}{\partial x_2} + D_{16}\frac{\partial\psi_i}{\partial x_1}\frac{\partial\psi_j}{\partial x_1} + D_{26}\frac{\partial\psi_i}{\partial x_2}\frac{\partial\psi_j}{\partial x_2}\right.\\
&\quad \left. + D_{66}\frac{\partial\psi_i}{\partial x_1}\frac{\partial\psi_j}{\partial x_2} + A_{45}\psi_i\psi_j\right]\alpha_1 d\xi_1\alpha_2 d\xi_2\\
K_{55} &= \int_R \sum_{i=1}^{n}\sum_{j=1}^{n}\left[D_{26}\frac{\partial\psi_i}{\partial x_1}\frac{\partial\psi_j}{\partial x_2} + D_{66}\frac{\partial\psi_i}{\partial x_1}\frac{\partial\psi_j}{\partial x_1} + D_{22}\frac{\partial\psi_i}{\partial x_2}\frac{\partial\psi_j}{\partial x_2}\right.\\
&\quad \left. + D_{26}\frac{\partial\psi_i}{\partial x_2}\frac{\partial\psi_j}{\partial x_1} + A_{44}\psi_i\psi_j\right]\alpha_1 d\xi_1\alpha_2 d\xi_2
\end{aligned}
$$

where n is the total number of nodes for a given element and

$$c_0 = \frac{1}{2}\left(\frac{1}{R_1} - \frac{1}{R_2}\right)$$

Appendix D

Determination of Soil Model Parameters

The first step in evaluating any parameters for a constitutive model is to select data appropriate to the problem being analyzed. In the case of cell fill, the laboratory tests were performed using specimens compacted to the same density as found in the cell fill. The tests were performed at pressures that were in the range of those present in the field.

The results were inspected closely to ensure correctness and consistency. The triaxial test data were replotted to form new stress–strain curves. The stress–strain curve from a conventional triaxial test is normally reported as the measure of shear stress versus axial strain (major principal strain). The two–dimensional hyperbolic model was developed to relate shear stress to the major principal strain as would be found in the conventional triaxial test. In the two–dimensional incremental analysis, the incremental shear stress is related to the incremental major principal strain through a Young's tangent modulus. The new three–dimensional hyperbolic model

relates the shear stress to the shear strain. In the new finite element code, the incremental shear stress is related to incremental shear strain through a tangent shear modulus. For the triaxial state of stress, the shear stress is

$$q = (\sigma_1 - \sigma_3) \tag{D.1}$$

and the shear strain is

$$\epsilon_s = \frac{2}{3}(\epsilon_1 - \epsilon_3) \tag{D.2}$$

The strength parameters c and ϕ were evaluated by plotting the Mohr's circles. The cell fill is a medium dense sand, therefore, the value of c is zero. The values of ϕ were determined by drawing the failure envelope and measuring the angle of inclination. The Mohr–Coulomb failure envelope for almost all soils is curved to some extent. The wider the range of pressures involved, the greater the curvature. For the cell fill, the range of pressures are such that one value for the angle of internal friction is sufficient to describe the failure envelope.

The evaluation of the stress–strain curve parameter K and n is a two–step procedure. The first step is to determine the values for the initial slope for each test by plotting the test data in the form of $\epsilon_s/(\sigma_1 - \sigma_3)$ normalized by the mean normal stress versus ϵ_s. The second step is to plot the initial slope values versus mean normal stress on a log–log scale to determine the values of K and n. The initial slope and mean normal stress are normalized by atmosphere pressure. By drawing a straight line through the data points, the value of K is equal to the value of the normalized initial slope at the point where the normalized mean normal stress is equal to unity . The value of n is equal to the slope of a straight line drawn through the data points.

The stress–dependency of the asymptote, q_{ult}, was shown earlier to relate to the

shear stress at failure based on Mohr–Coulomb failure criterion by R_f as

$$R_f = \frac{q_{ult}}{q_f} \tag{D.3}$$

The asymptotic value obtained from the plot of the data on the transformed axis is

$$b = \frac{1}{q_{ult}p} \tag{D.4}$$

Therefore, R_f is found from the data plotted on the transformed axis as

$$R_f = \frac{q_{ult}p}{q_f p_f} \tag{D.5}$$

Most actual stress–curves are approximated only by the hyperbolic expression. Duncan and Chang [17] found that for the two–dimensional hyperbolic model the best fit is usually attained by determining initial slopes (reciprocals of the intercepts) and asymptotic values (reciprocals of the slope) from the points on experimental curves corresponding to 70 and 95 percent of the strength. This was based on the fact that at low strain values the triaxial curves diverge from the hyperbolic expression. This same phenomena is true for the reduction of the data for the new three–dimensional model, Figure D.1. Based on these findings, it was necessary to analyze the test data to find the best procedure to follow to fit the hyperbolic expression to the triaxial data.

To examine the fitting of the hyperbolic expression to the compressive triaxial test data, the initial slope normalized by the mean normal stress and R_f were calculated by fitting a straight line through each data point and the data point corresponding to 99 percent of the failure stress.

Using the data for the relative densities of 55 and 70 percent, the approximate relative densities of the cell fill and foundation soil, the values of normalized initial

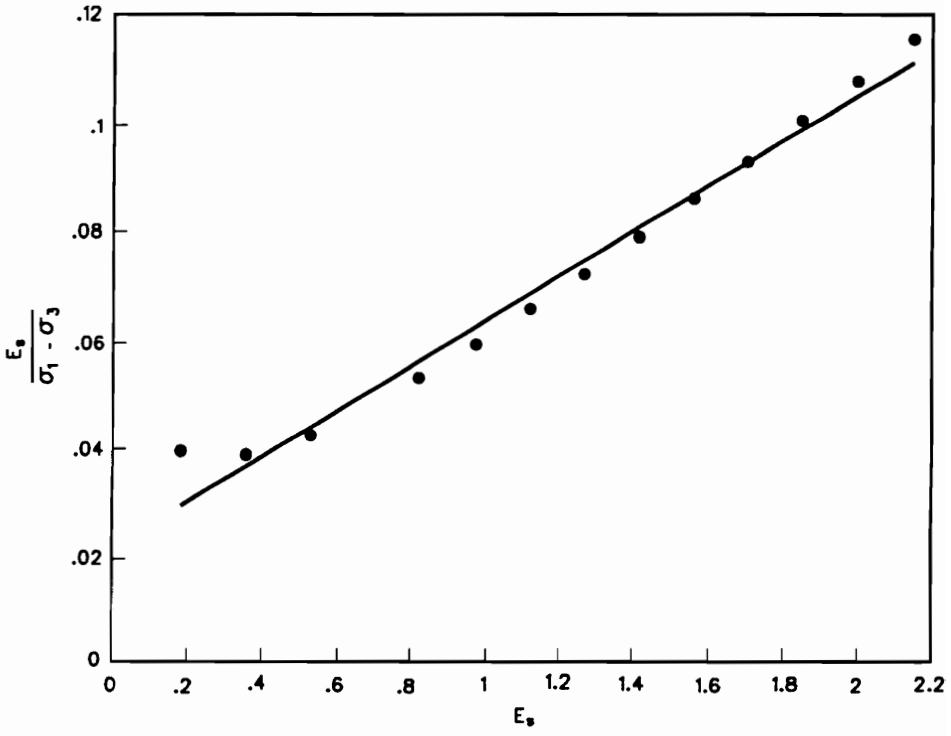

Figure D.1: Diverge from hyperbolic expression.

slope were plotted against the corresponding values of R_f, Figures D.2 and D.3, respectively. The plots show that the initial slope and R_f are interdependent. For each confining pressure, the value of the normalized initial slope increases as the R_f value increases where different points are used in the fitting process. Similarly, Figures D.4 and D.5 show the plot of the normalized initial slope versus the percent of shear strength developed of the data point used in fitting the curve parameters for relative densities of 55 and 70 percent, respectively. The relationship between normalized initial slope and percent of shear strength is not as consistent as the one between initial slope and R_f. Figures D.6 and D.7 show plots of percent of shear strength versus R_f for relative densities of 55 and 70 percent, respectively. If there were a one–to–one correspondence between the two, the tests would form one line. Figures D.8 and D.9 show plots of the normalized initial slope values versus the normalized mean normal stress on a log–log scale for common values of R_f as obtain from Figures D.2 and D.3 for relative densities of 55 and 70 percent, respectively. The values of normalized initial slope corresponding to a given R_f form a straight line from which the parameters K and n can be determined. Tables D.1 and D.2 show the values of K and n corresponding to the plots in Figures D.8 and D.9.

This analysis to determine the best curve fit of the compression triaxial test data show that R_f is a better means of selection of data points for the fitting of the hyperbolic curve to the test data than using the percent of shear strength. R_f serves as a measure of the rate of curvature of the hyperbolic curve; as R_f increases, the greater the rate of curvature.

The extension triaxial tests did not show the divergence from hyperbolic expression at low strain rate as found in the compression tests. Figures D.10 and D.11 show that the data conforms to the hyperbolic expression. One reason is that there

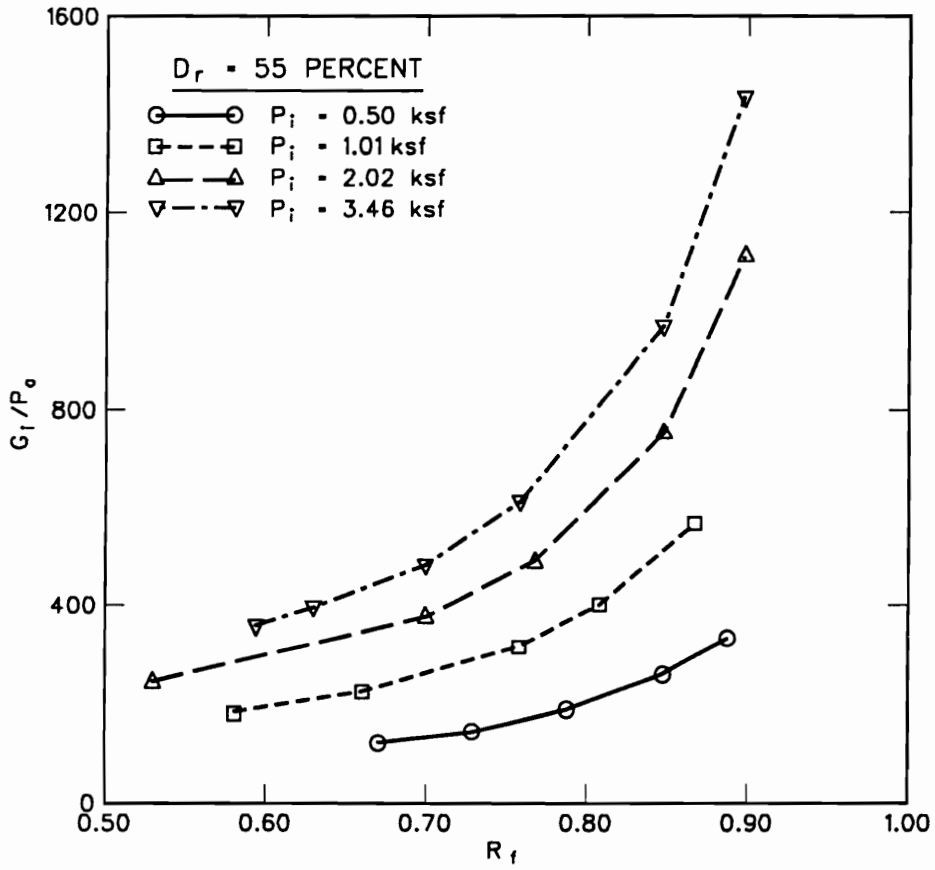

Figure D.2: Relationship between normalized initial slope and R_f for a relative density of 55 percent.

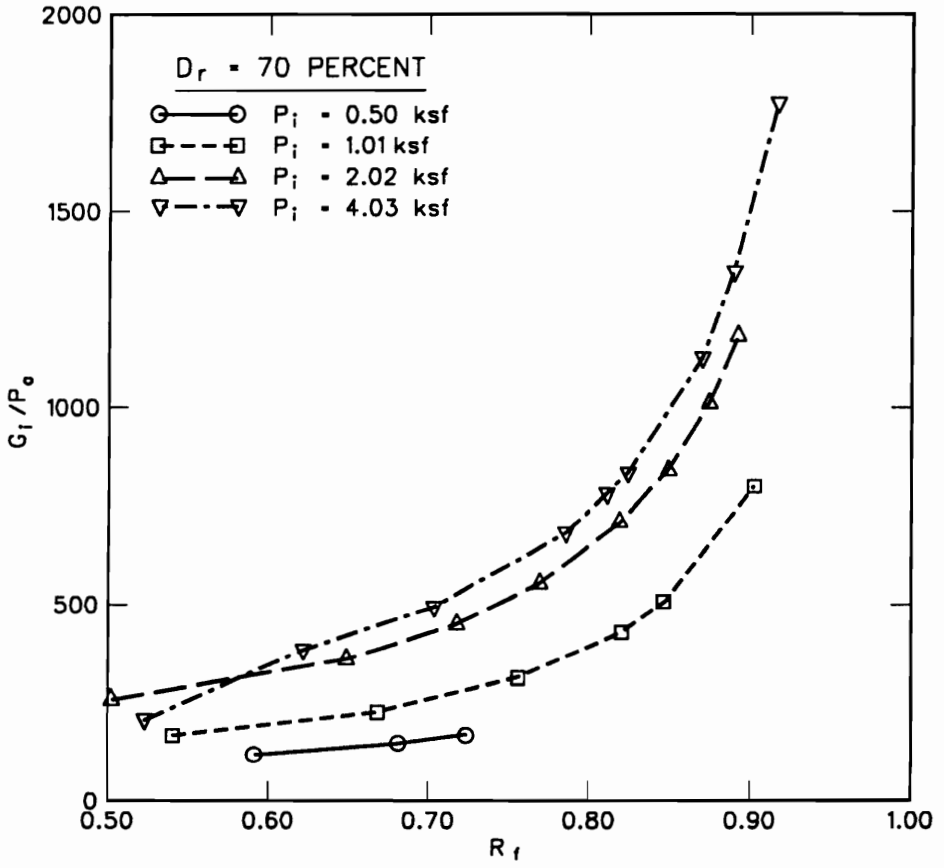

Figure D.3: Relationship between normalized initial slope and R_f for a relative density of 70 percent.

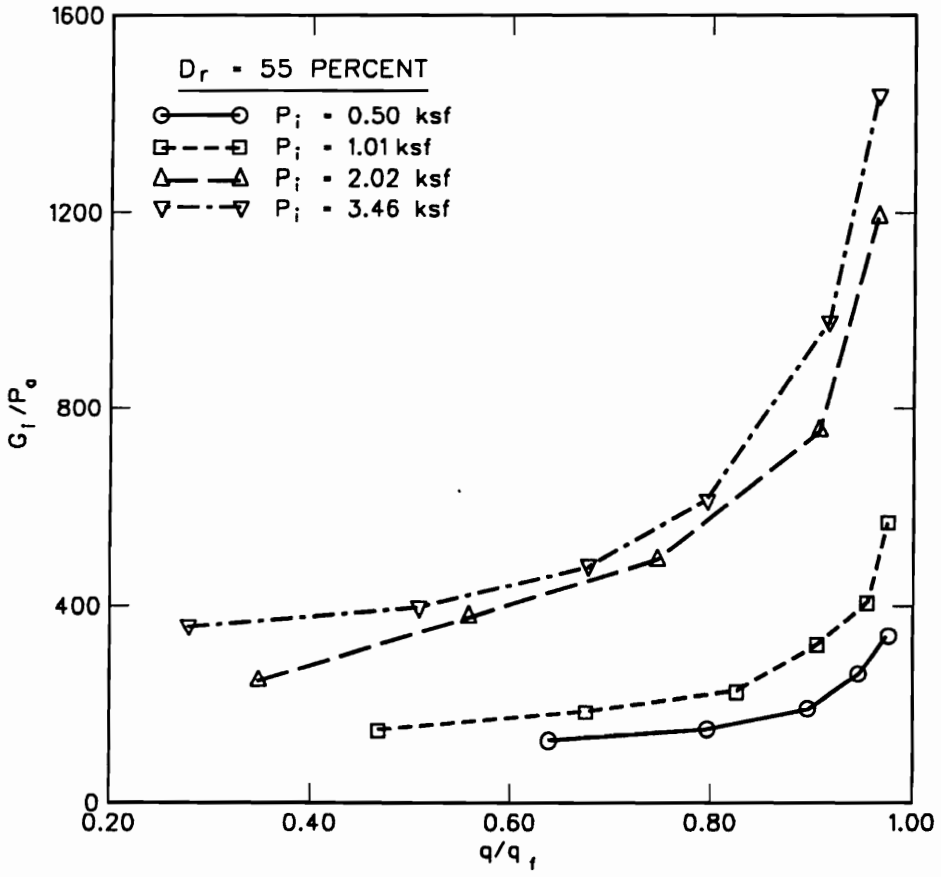

Figure D.4: Relationship between normalized initial slope and shear strength for a relative density of 55 percent.

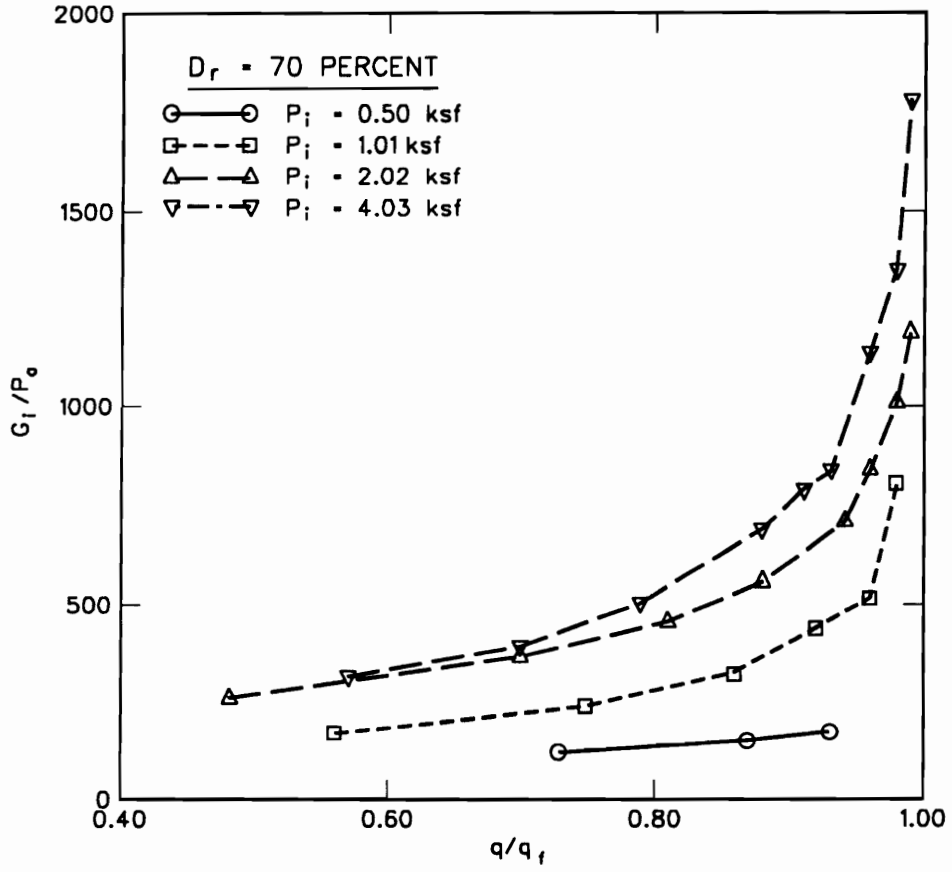

Figure D.5: Relationship between normalized initial slope and shear strength for a relative density of 70 percent.

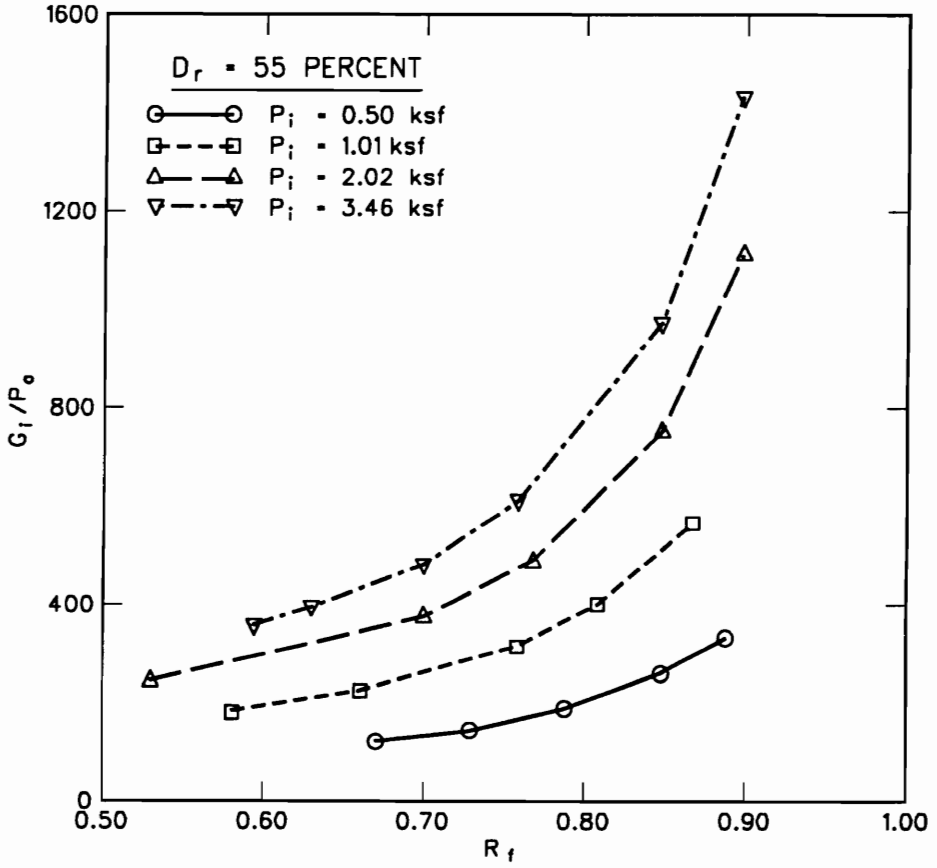

Figure D.6: Relationship between shear strength mobilized and R_f for a relative density of 55 percent.

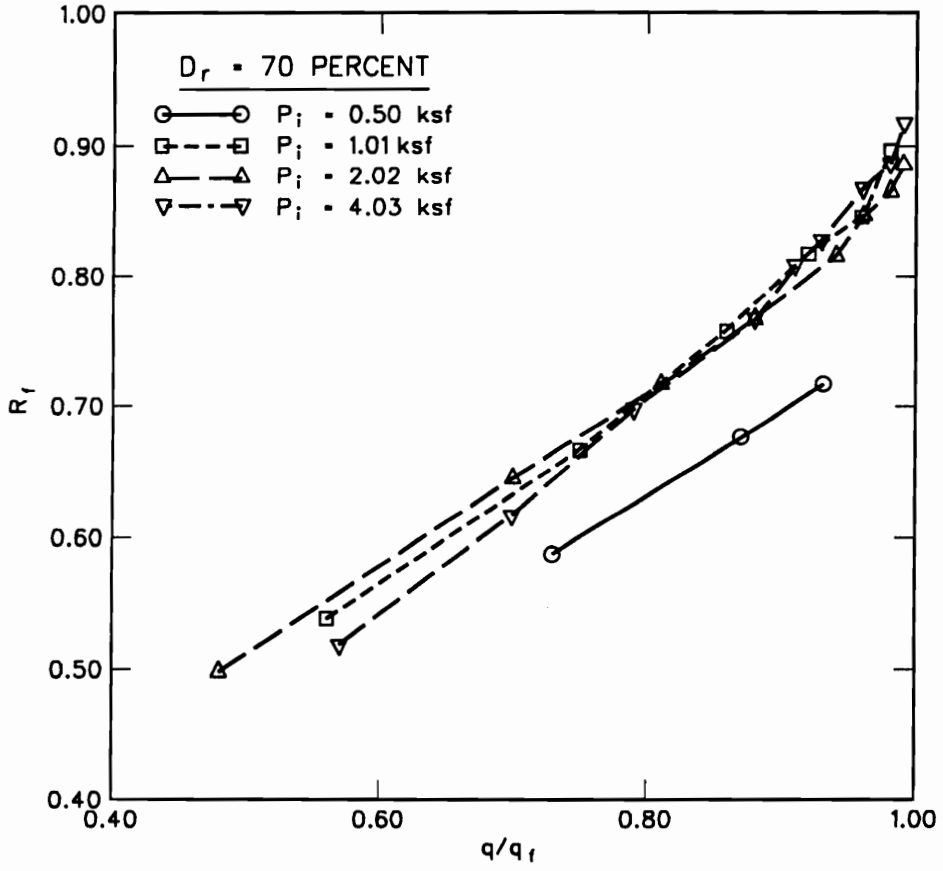

Figure D.7: Relationship between shear strength mobilized and R_f for a relative density of 70 percent.

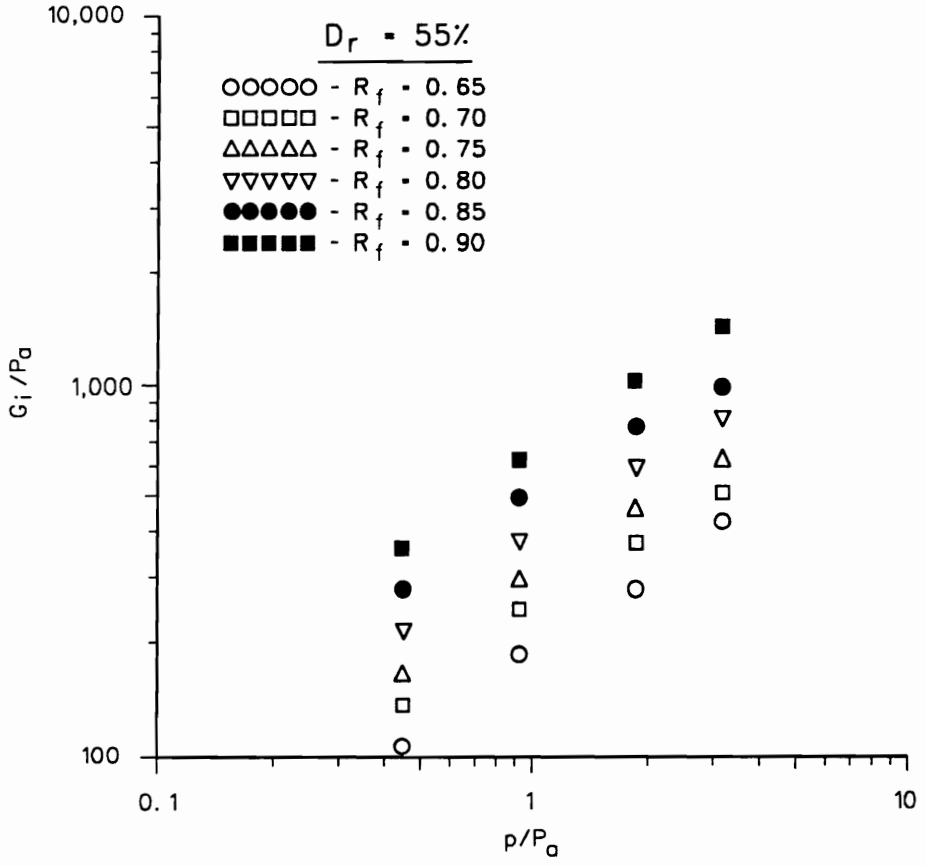

Figure D.8: Relationship between normalized initial slope and normalized mean normal stress for a relative density of 55 percent.

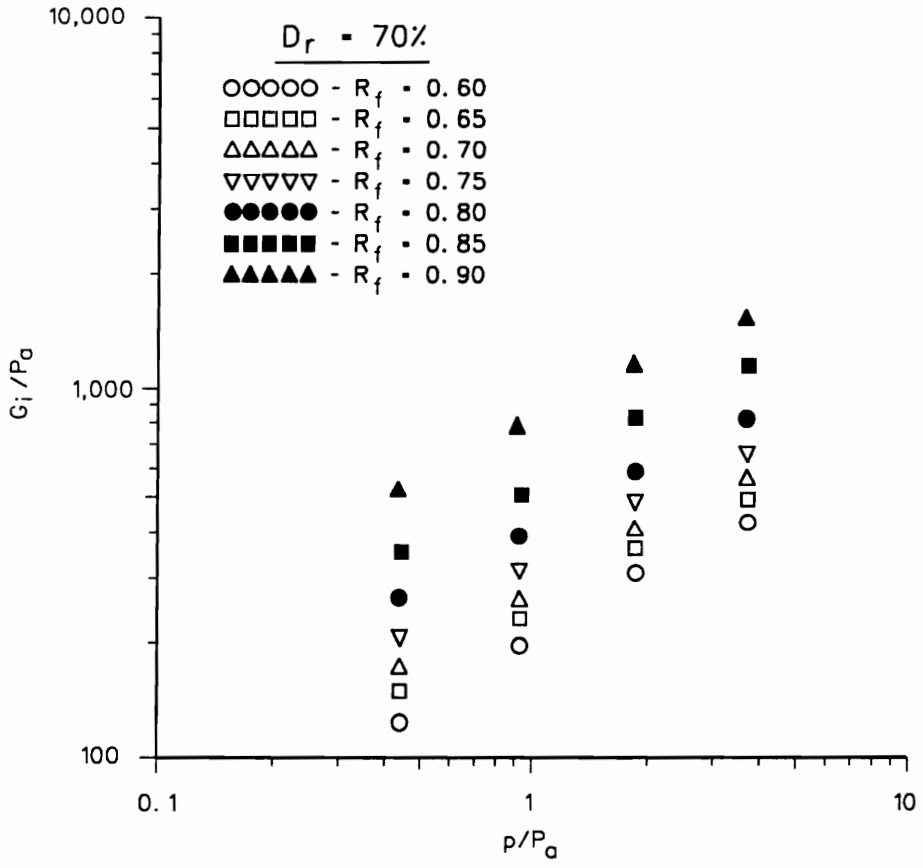

Figure D.9: Relationship between normalized initial slope and normalized mean normal stress for a relative density of 70 percent.

Table D.1: Three–dimensional hyperbolic model parameters determined from triaxial tests for a relative density of 55 percent.

R_f	K	n
0.65	190	.68
0.70	230	.68
0.75	290	.68
0.80	350	.68
0.85	450	.68
0.90	600	.68

Table D.2: Three–dimensional hyperbolic model parameters determined from triaxial tests for a relative density of 70 percent.

R_f	K	n
0.60	200	.53
0.65	230	.53
0.70	280	.53
0.75	350	.53
0.80	450	.53
0.85	580	.53
0.90	800	.53

are fewer data points in the low stress range, while the rate of curvature was high. R_f ranged between 0.95 to 0.99. The straight lines shown in Figures D.10 and D.11 were formed using a least squares fit and resulted in the normalized initial slope values that are compared with the compression test values in Figures D.12 and D.13. The extension tests are similar to compression tests, but the magnitude of the normalized initial slope for a given R_f would appear to be less than the compression tests.

The bulk modulus of the soil was assumed to be independent of changes in shear stress and to vary with the mean normal stress. This approximation is reasonable and provides the best possible representation of soil behavior within the framework of this incremental elasticity methodology. It assumes that changes in volume are due only to changes in mean normal stress.

Since real soils undergo some volume change as a result of changes in shear stress, in addition to those caused by changes in mean normal stress, the values of the bulk modulus computed from a triaxial test depend upon the stage in the test when it is calculated. Figure D.14 shows a plot of mean normal stress versus volumetric strain during a triaxial test. As the mean normal stress increases, the soil specimen contracts and volumetric strain is approximately linear. As the mean normal stress levels off, the volumetric strain changes direction and the soil specimen starts to dilate. The dilation is due to the shearing of the soil. At zero volumetric strain in triaxial tests, some volume change has already taken place due to consolidation. It appears impossible to separate the volume change due to the mean normal stress from that due to shearing in the triaxial tests.

To determine the model parameters K_b and m, the volumetric strain due to consolidation of the triaxial tests was plotted against mean normal stress (confining

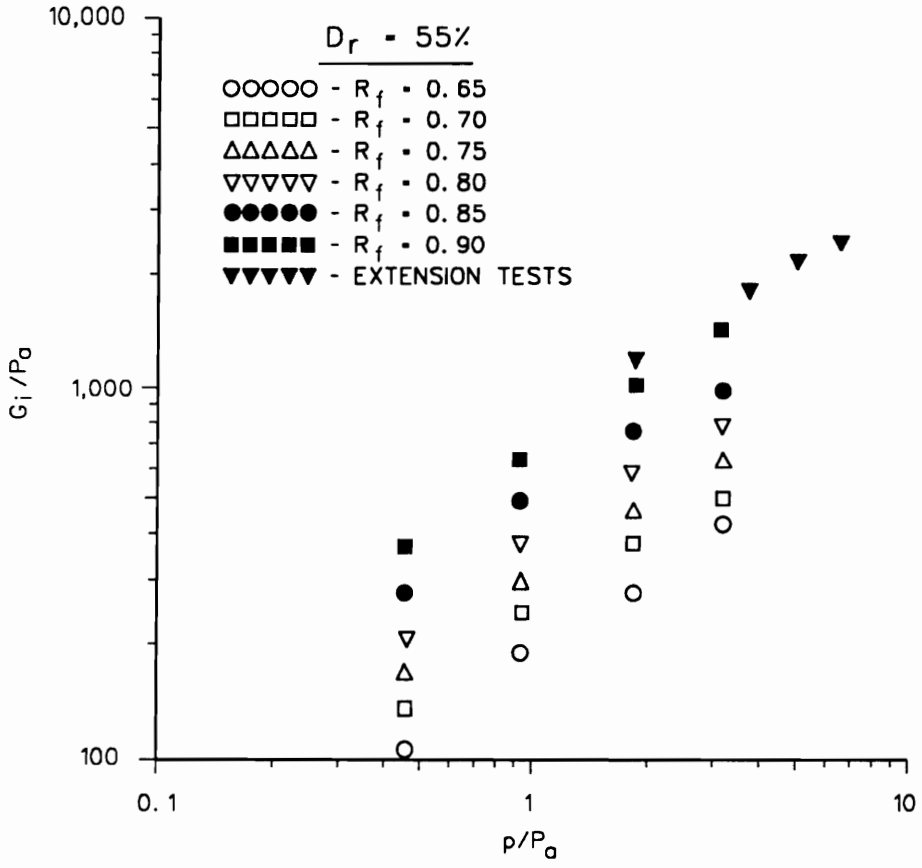

Figure D.10: Extension triaxial test data plotted transformed axis for relative density of 55 percent.

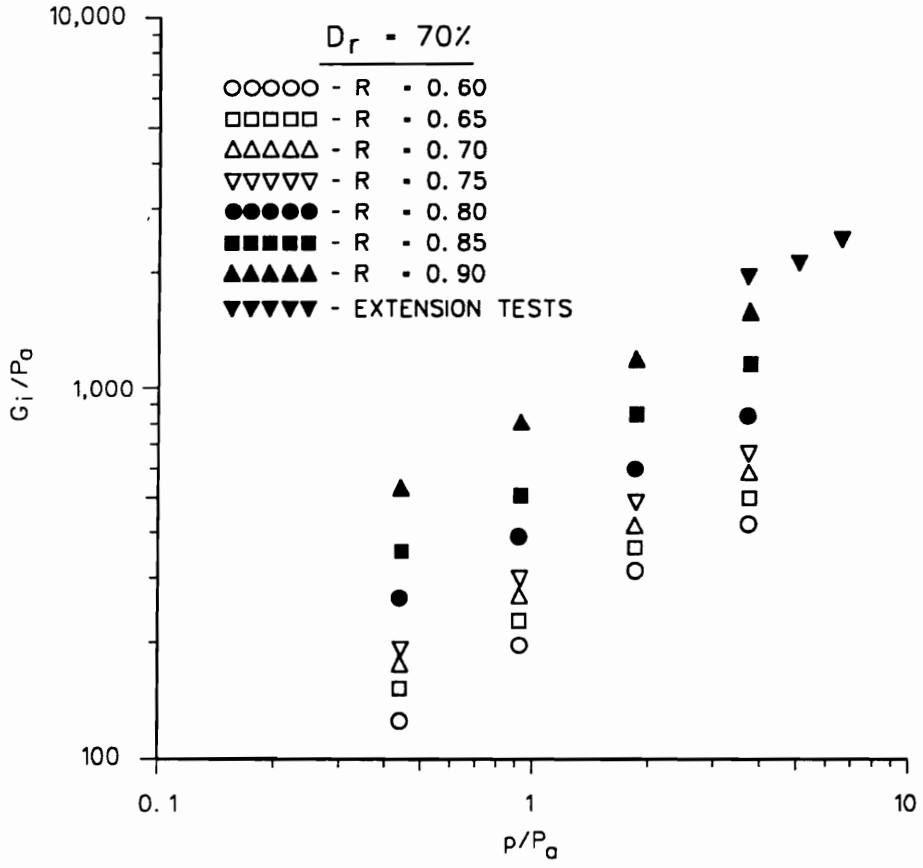

Figure D.11: Extension triaxial test data plotted transformed axis for a relative density of 70 percent.

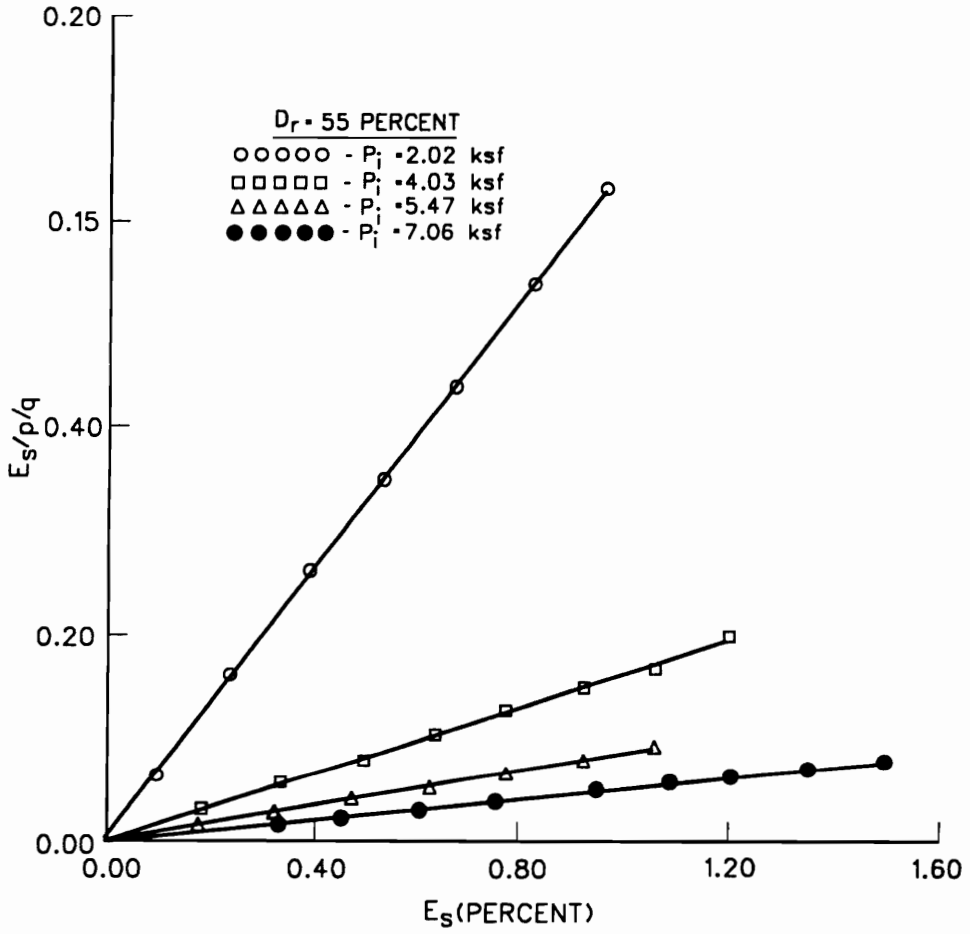

Figure D.12: Comparison of initial slope versus mean normal stress between extension and compression triaxial test data for relative density of 55 percent.

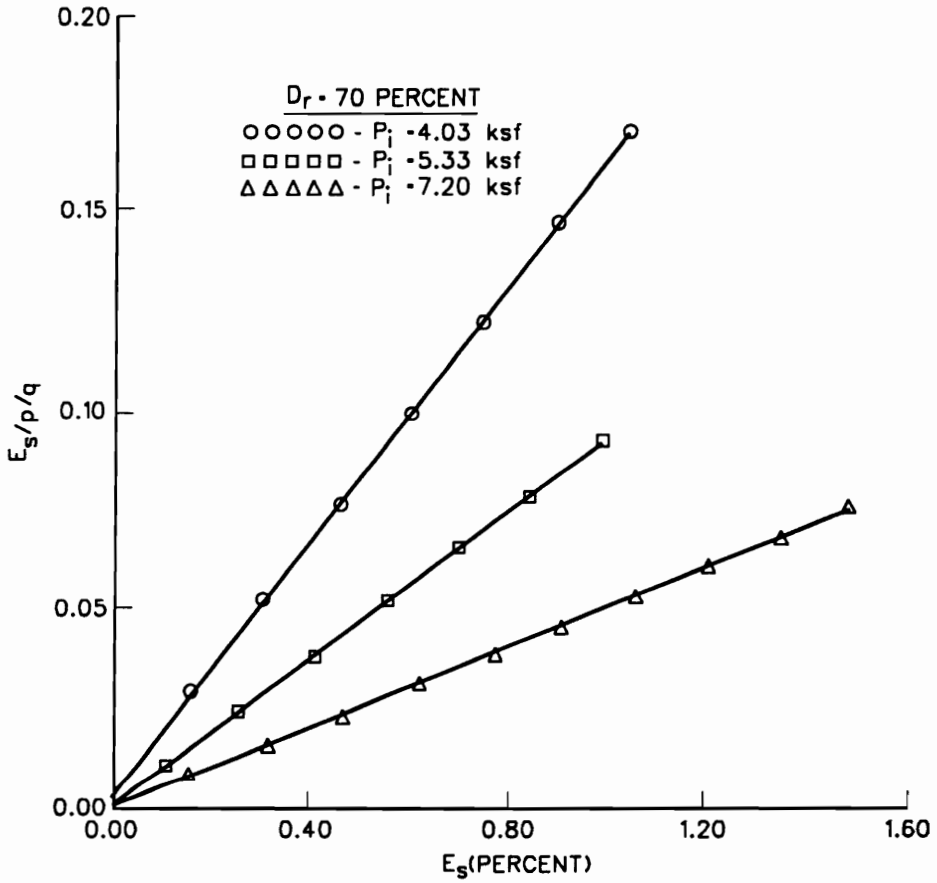

Figure D.13: Comparison of initial slope versus mean normal stress between extension and compression triaxial test data for a relative density of 70 percent.

stress) on a log–log scale. To supplement this data, volumetric strain at low shear stress levels from the triaxial tests was included in the data base. The parameters K_b and m can be found directly from this plot of the data. By drawing a straight line through the data points, the value of K_b is equal to the volumetric strain at a normalized mean normal stress value of unity and the value of m is equal to the slope of the line.

Figures D.15 and D.16 show plots of volumetric strain versus normalized mean normal stress for the compression triaxial tests for relative densities of 55 and 70 percent, respectively. Figures D.17 and D.18 show plots of volumetric strain versus normalized mean normal stress for the compression triaxial tests for relative densities of 55 and 70 percent, respectively. Table D.3 gives the values of the parameters K_b and m calculated from these plots.

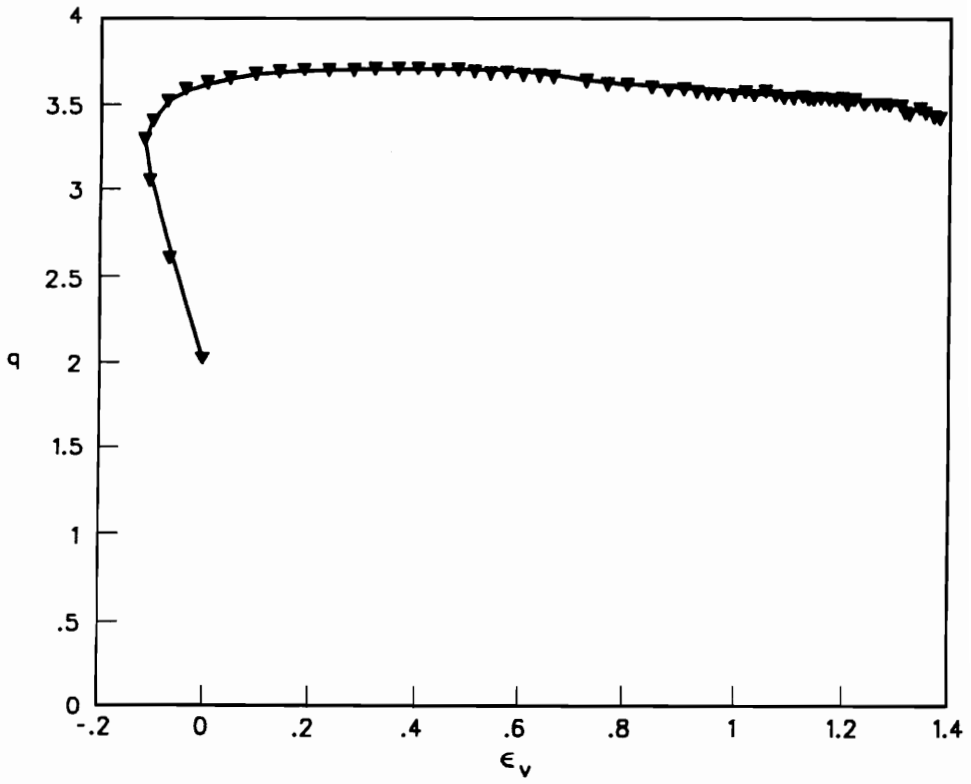

Figure D.14: Volumetric strains occurring during a triaxial test.

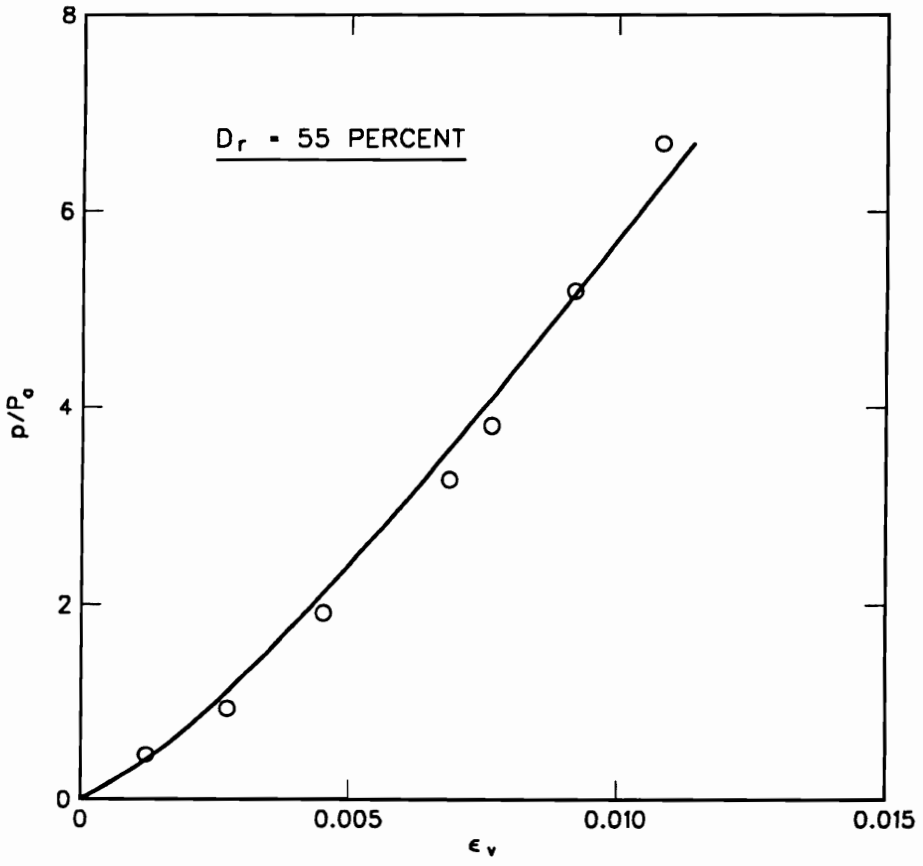

Figure D.15: Mean normal stress versus volumetric strain for relative density of 55 percent.

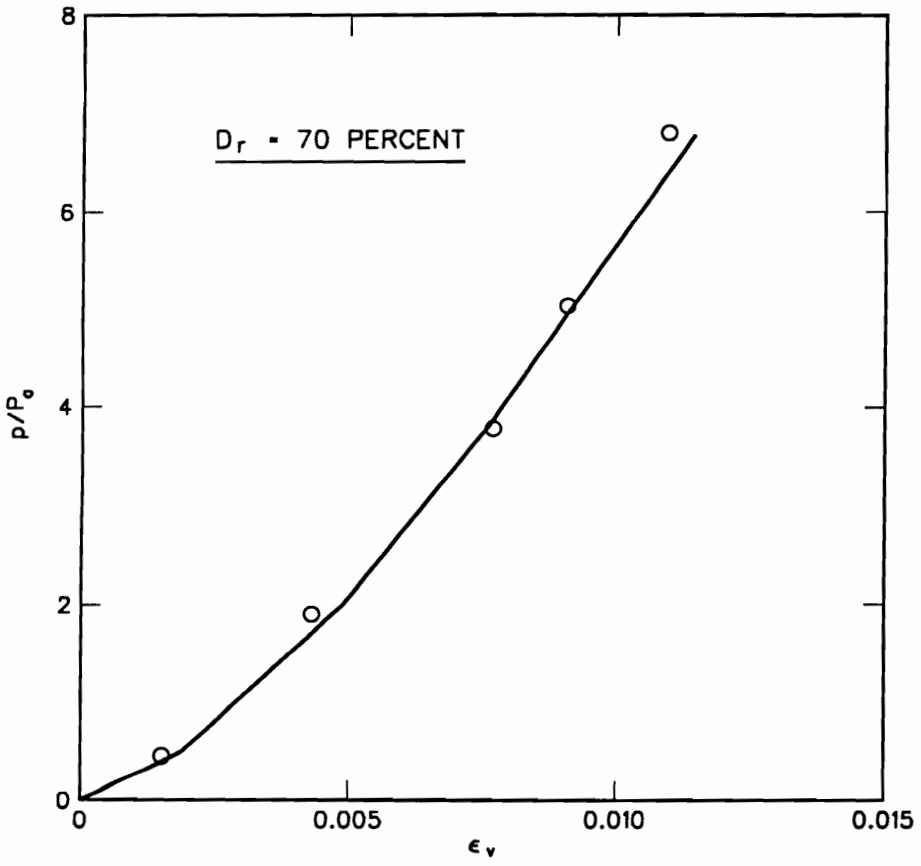

Figure D.16: Mean normal stress versus volumetric strain for relative density of 70 percent.

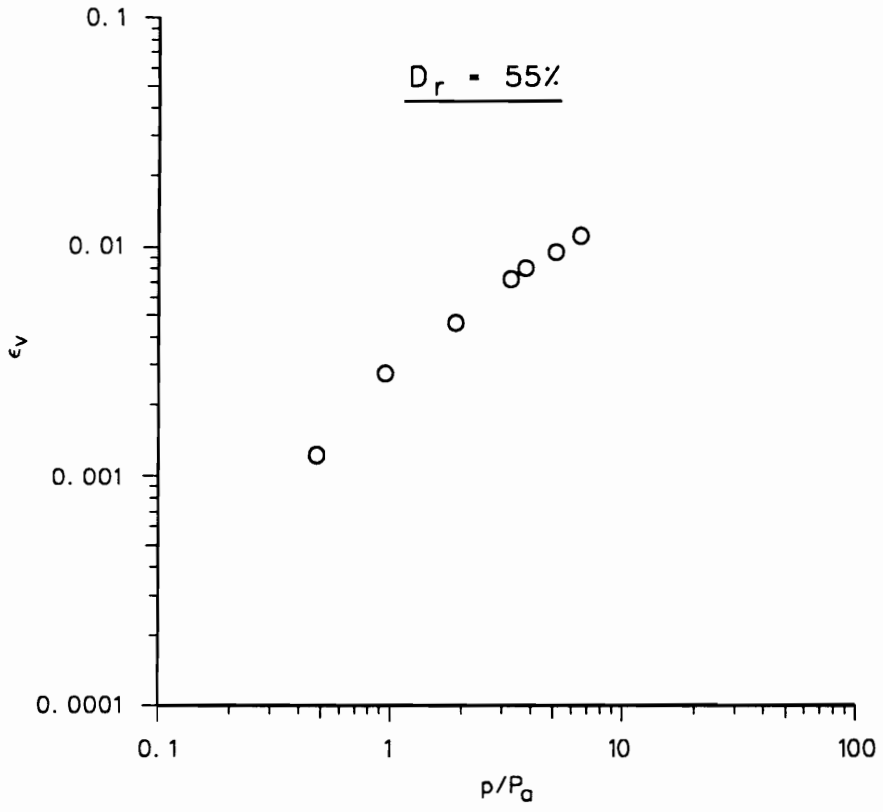

Figure D.17: Volumetric strain versus mean normal stress on a log–log scale for a relative density of 55 percent

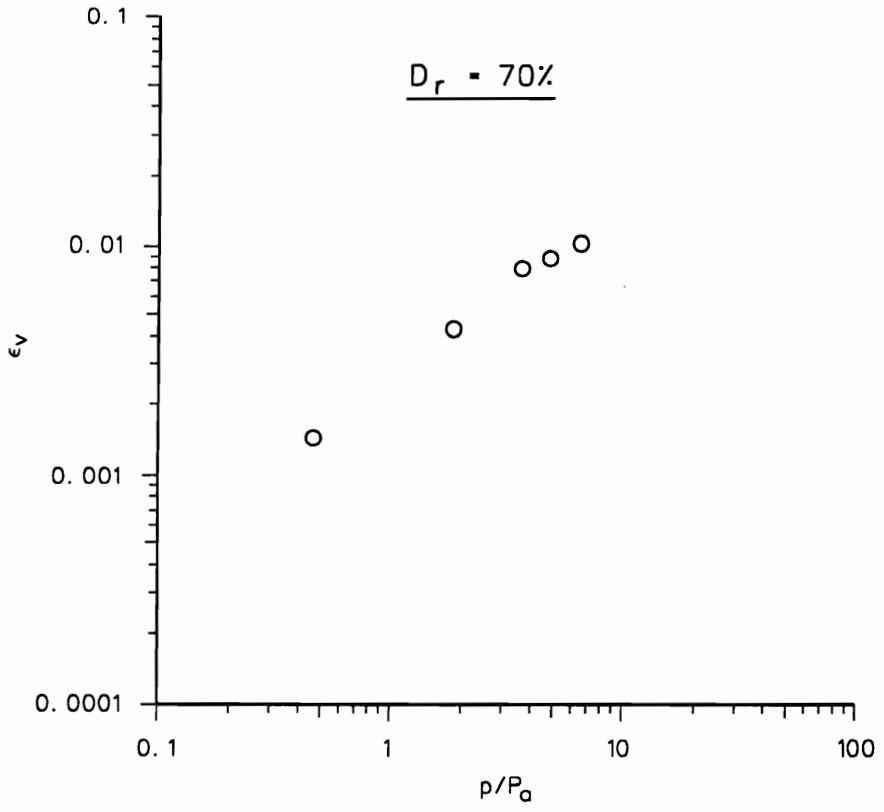

Figure D.18: Volumetric strain versus mean normal stress on a log–log scale for a relative density of 70 percent

Table D.3: Parameters of the bulk modulus model.

Relative Density (percent)	K_b	m
55	0.0025	0.8
70	0.0030	0.7

VITA

Dr. Mosher, born on November 8, 1954, grew up in Temple, Maine. He graduated from Mt. Blue High School, Farmingtion, Maine where he excelled in mathematic and science and was a standout in football and wrestling. He attended Worcester Polytechnic Institute and received a Bachelor of Science degree in Civil Engineering in 1977. His major qualifying project for his bachelors degree was entitled *Design of a Gravity Type Offshore Drilling Structure.* While at Worcester Polytechnic Institute he was a member of Chi Epsilon, a national civil engineering honorary society, and held the post of Vice President.

After working for a year for Raymond International, Inc., Dr. Mosher joined the U.S. Army Engineers Waterway Experiment Station in Vicksburg, Mississippi. In January 1979, he initiated graduate studies at the Waterways Experiment Station Graduate Center. He received a Master of Science degree in Civil Engineering in 1982 from Mississippi State University through the Graduate Center. His masters' thesis was entitled *Numerical Analysis of Axially Loaded Piles in Sand.*

In 1982, Dr. Mosher was selected for the U.S. Army Engineers long–term training program. During the 1982–1983 school year, he attended Virginia Tech. After completing his course work and Ph.D qualifying exams, he returning to the Waterways Experiment Station to begin his Ph.D dissertation research. The research was

conducted under the supervision of Professor G. Wayne Clough.

Dr. Mosher is still employed as a senior Research Civil Engineer at the Waterways Experiment Station where he has authored or co–authored over 35 technical reports, papers, and articles. He has received the Commander and Director's Research and Development Achievement Award and was the U.S. Army Engineers nominee for the Department of Army Researcher of the Year.